Fundamental Insights into the Dissolution and Precipitation of Cellulosic Biomass from Ionic Liquid Mixtures

By

David L. Minnick

Submitted to the graduate degree program in Chemical and Petroleum Engineering and the Graduate Faculty of the University of Kansas in partial fulfillment of the requirements for the degree of Doctor of Philosophy.

_____

Chairperson: Aaron M. Scurto

_____

Bala Subramaniam

_____

Raghunath V. Chaudhari

_____

Laurence Weatherley

_____

Belinda Sturm

Date Defended: July, 14th 2016

The Dissertation Committee for David L. Minnick certifies that this is the approved version of the following dissertation:

Fundamental Insights into the Dissolution and Precipitation of Cellulosic Biomass from Ionic Liquid Mixtures

_____

Chairperson: Aaron M. Scurto

Date approved: July, 22nd 2016

Abstract

Ionic liquids (ILs) are a unique class of molecular salts that melt at temperatures below 100^{o}C. The ionic functionality of ILs provide this class of molecules numerous advantages for applications in reactions, separations, and materials processing due to their molecular flexibility through cation/anion selection. Additionally, ionic liquids possess negligible vapor pressures and may lead to more sustainable or "green" processes by eliminating solvent-based air pollution. For these reasons ionic liquids are being targeted for implementation in a range of industrial processes as sustainable solvent technologies.

The primary objective of this dissertation targets the application of ionic liquids to cellulosic biomass processing. For instance, chemical processing of biomass remains a challenge as the rigid inter- and intra- molecular hydrogen bonding network of cellulose renders it insoluble in nearly all aqueous and organic solvents. Alternatively, select ionic liquids (ILs) are capable of dissolving significant quantities. Through an ionic liquid mediated dissolution and precipitation process cellulose crystallinity is significantly reduced consequently enhancing subsequent chemical and biochemical reaction processes. Therefore, understanding the thermodynamics of ionic liquid – cellulose mixtures is imperative to developing an IL based biomass processing system. This dissertation illustrates the solid-liquid phase behavior for the dissolution and precipitation of cellulose in various IL/cosolvent, IL/antisolvent, and IL/mixed solvent systems with the ionic liquid 1-ethyl-3-methylimidazolium diethyl phosphate ([EMIm][DEP]). The vast majority of molecular solvents dramatically decrease cellulose solubility in ILs and are therefore considered "antisolvents". However, select quantities of polar aprotic solvents, when mixed with ILs, (despite having negligible solubility on their own) are capable of enhancing the

thermodynamic solubility limit, even beyond the measured cellulose solubility limits of pure ILs. Furthermore, cosolvents enhance transport properties of IL/biomass mixtures and reduce ionic liquid moisture (H_2O) sensitivity which is known to severely impact the dissolution capacity of cellulose. Spectroscopic techniques including Kamlet Taft solvatochromic analysis, FTIR, and NMR elucidate molecular interactions between the ionic liquid and solvent species and provide an understanding of the solvation sphere around the IL in relation to cellulose dissolution within the various IL-solvent mixtures. The phase equilibrium results indicate that mixed IL/cosolvent systems are even better solvents for cellulose dissolution than pure ILs from thermodynamic, transport, and economic perspectives.

The majority of ionic liquid research targets biomass transformation and little consideration has been given to product extraction. Nonetheless, the high cost of the ionic liquid feedstock will require near quantitative recovery and recycle of the IL for the process to be economically viable. Therefore, efficient extraction of cellulose from ionic liquid mixtures is imperative for IL pretreatment processes. Conventional antisolvents for biomass precipitation include polar protic liquids which are highly effective at disrupting IL-cellulose interactions. For instance, liquid antisolvents are so effective that as little as 1 mass% residual water on an IL can reduce its cellulose capacity by as much as 55%. Therefore, ILs must be highly purified from liquid antisolvents prior to recycle. Preliminary analyses indicate that quantitative separation of an IL from a liquid antisolvent is highly energy intensive and could potentially impede large scale viability. Therefore, a novel gas antisolvent method which precipitates cellulosic biomass by compressed carbon dioxide at low to moderate pressures is presented. The gas antisolvent separation process is especially unique as it is non-reactive and completely reversible. By simple depressurization of CO_2 to just a few bar pressure below the separation point, ionic liquid

solvation power for cellulose is completely regenerated. The second research objective of this dissertation highlights the solid-liquid phase equilibrium effects of both conventional and novel separation processes. Spectroscopic techniques identify key trends within the separation data. Finally, an energy analysis is presented to demonstrate the advantages of this novel CO_2 based precipitation process relative to liquid antisolvent separations.

The third thrust of this dissertation investigates biomass conversion in mixed IL/cosolvent systems with emphasis on the transformation of fructose to 5-hydroxymethylfurfural. Preliminary results indicate that polar aprotic cosolvents both enhance the 5-HMF reaction rate as well as stabilize the product. Therefore, mixed IL/cosolvent systems are promising for both dissolution and conversion of biomass. A second component of this objective targets the chemical transformation of platform chemicals from biomass that are highly soluble in ILs into less polar value-added products that exhibit low miscibility and spontaneously phase separate. For instance, hydrogenation of cellulose derived 5-hydroxymethylfurfural and hemicellulose based furfural yield furan products that are applicable as "drop-in" fuel replacements and industrial solvents. Significant emphasis is placed on tuning hydrogen solubility with compressed CO_2 since previous studies demonstrate that liquid phase H_2 concentration can be rate limiting for hydrogenation reactions in ILs.

The majority ionic liquid synthesis methods utilize batch scale operations with limited knowledge of the chemical kinetics and purification techniques. Moreover, most IL synthesis methods use many of the hazardous solvents that ILs will purportedly replace. For ionic liquids to be part of a sustainable process they must also be synthesized in a likewise sustainable manner. Therefore, the fourth objective of this dissertation is to develop thermodynamic,

process, and life cycle assessment models for the continuous synthesis of an ionic liquid. Experimental vapor-liquid and liquid-liquid equilibrium involved in the production of the model ionic liquid 1-hexyl-3-methylimidazolium bromide ([HMIm][Br]) are presented and modeled using the Peng-Robinson equation of state and Gibbs excess activity coefficient models. In conjunction with previously measured kinetic reaction parameters, the thermodynamic modeling results are used to develop an Aspen Plus process model for the continuous production of [HMIm][Br]. Finally, a cradle-to-gate life cycle assessment is presented to compare the environmental impacts associated with the synthesis of [HMIm][Br] in a range of reaction solvents.

The final dissertation objective investigates the application of ionic liquids to CO_2 sequestration. Select ionic liquids have some of the largest CO_2 absorption capabilities of any known solvent indicating a competitive advantage for utilization in carbon dioxide capture processes. However, the characteristically high viscosities and slow mass transport properties of ionic liquids create potential barriers to industrial implementation. Therefore, the performance of ionic liquids in packed absorption towers for CO_2 capture are presented and discussed. The computational findings suggest that packed absorption towers designed to accommodate ionic liquids with even the highest known CO_2 capacities yield capital costs in excess of towers designed for conventional amine based solvents due to the comparatively slow gas-liquid mass transfer rates of ILs. These results indicate that process intensification techniques should be considered to take advantage of the thermodynamic benefits of ionic liquids.

Acknowledgements

Six years ago after completing a bachelor's degree in chemistry, making the transition into chemical engineering and pursuing a doctoral degree seemed but a pipe dream. Yet, here I stand today looking back on what a fun experience it has been thanks to the many great people who have accompanied and supported me along the journey.

First and foremost, thank you to my advisor Aaron Scurto. Early on in my academic career you identified potential within me. It is because of your mentorship and guidance that I have developed into the Ph.D. scientist that I am today. Thank you for being a role model, teammate, and friend. I am deeply grateful for the investment you made in my education and look forward to our future collaborations as colleagues.

I would also like to thank my committee members including Professors Bala Subramaniam, R.V. Chaudhari, Laurence Weatherley, and Belinda Sturm. Each of you made significant contributions to my academic development at the University of Kansas through coursework and research meetings. I am grateful for the knowledge you imparted on me and thank you for the time and talent you dedicated to reviewing this dissertation.

Special thanks are given to the many colleagues I worked alongside over the years. First to Sylvia Nwosu; thanks for being my role model as a young graduate student and for continuing to provide mentorship to this day. Additionally, thanks to Andrew Danby and Michael Lundin. You both provided a wealth of technical knowledge and were always there to help troubleshoot when things went wrong. I also am grateful for the friendships we developed over the years, it truly made working at the CEBC a fun and enjoyable experience.

I am eternally grateful to the many undergraduate researchers who spent countless hours in the lab alongside me. To Raul Flores and Kyle Harrigan, thank you for your time and talent. I am proud of your accomplishments and look forward to the day when each of you will defend your Ph.D. theses. Thank you to Ryan McDonough and Matt DeStefano who dedicated their summers as REU-NSF students and made valuable contributions to my research success. Also thank you to Maeley Brown, Phuc Nguyen, Mark Vu, and Elisabeth Maurer who dedicated time as undergraduate research assistants in the Scurto laboratory.

I want to extend special thanks to my family and friends who have supported my success over the past six years. To my mom and dad, Matt and Julie Minnick, thank you for always believing in me and giving me the ability to pursue my dreams. I am constantly amazed at the love and support you provide on a daily basis. You are my heroes and I can't thank you enough. Additionally, thank you to my brother and sister, Ben and Angie; because of family support this was possible. To the many friends I have made during my time in Lawrence, thanks for the amazing memories that made my experience at KU unforgettable. Also I want to extend a special thanks to Lindsey Ott for your love, support, and guidance over the past four years.

Thank you to Madison and Lila Self. It is because of your selflessness and generosity that I was able to pursue a doctoral degree. The Self Fellowship program was instrumental in my professional development while at the University of Kansas and I am eternally grateful for the opportunity that you gave me.

Finally, I want to thank God who is my guiding light and who makes all things possible.

Ad Majorem Dei Gloriam

Dedicated To:

Matt and Julie Minnick

for the unending love and support
you continuously provide

Table of Contents

List of Tables

List of Figures

1. Introduction

Between 2009 and 2012 the price per barrel of Brent crude oil tripled, increasing from approximately $40 to $120 per barrel as market speculation forecasted potential supply issues of this fossil resource.[1] Today with the discovery of U.S. shale gas reserves the price of oil has declined to approximately $30 per barrel. Yet, the reality remains that a finite amount of fossil resources exist and the demand for petroleum continues to increase. Liquid petroleum is incorporated into a majority of consumer items including textiles, paints, polymers, plastics, and fuels among others. The theory of peak oil indicates that at some future time world oil production will reach a maximum and then decline causing supply restrictions and increased prices. While the current market appears saturated with oil reserves, the reality remains that a fixed amount of fossil resources exist. The question is not "if" demand for petroleum will exceed supply but "when". Therefore, alternative energy technologies based on renewable resources must be developed in preparation for the future when energy security becomes a significant problem.

Lignocellulosic biomass is a renewable resource that consists of three primary components: cellulose (30-50 wt.%), hemicellulose (20-35 wt.%), and lignin (18-35 wt.%).[2] An estimated 1.3 billion dry tons of lignocellulosic biomass are annually available within the United States and are sourced from a range of waste agricultural residues including switchgrass, wheat straw, bagasse, corn stover, and forestry byproducts. [3, 4] [3, 4] Unlike first generation biofuels (*i.e.* corn ethanol); the lignocellulosic biomass feedstock is not food vs. fuel competitive. Additionally, cellulose and hemicellulose can be chemically converted into a range of value added products including fuels, solvents, and polymers. While lignocellulosic biomass appears

promising, feedstock recalcitrance inhibits facile chemical conversion and has prevented the development of industrial processing technology. For instance, a significant limitation of lignocellulosic biomass is the lack of aqueous and organic solvents available to dissolve cellulose and hemicellulose.[5]

Owing to their cation/anion charged character, select ionic liquids (ILs) are capable of preferentially interacting with hydrogen bonding functional groups of cellulose thus disrupting the inter- and intra- molecular bonding structure of the biopolymer. As a result, certain ILs are capable of dissolving significant quantities of cellulose. While preliminary studies have highlighted the general benefits of ILs for biomass processing, very little is currently understood about the thermodynamics of cellulose dissolution in ionic liquids. For instance, few solubility data points exist for cellulose in ionic liquids and most are provided as a range of concentrations (*i.e.* 8-10 mass.%).[6] For ILs to be a viable industrial biomass processing solution, thermodynamic datasets must be acquired to develop accurate models of the dissolution process.

For the first time, quantitative thermodynamic solid-liquid-equilibrium datasets on cellulose dissolution in an ionic liquid have been developed and are presented herein. The results demonstrate the significant biomass solubility of pure ILs and potential dissolution mechanisms. Despite their excellent biomass dissolution capacities, ILs are criticized for being expensive relative to conventional solvents. To overcome this limitation, novel ionic liquid - cosolvent mixtures have been developed. Whereas polar aprotic cosolvents demonstrate negligible solubility of cellulose, when combined with an ionic liquid the thermodynamic and rheological properties of the mixture are significantly enhanced. The results presented herein indicate that inexpensive and environmentally friendly cosolvents can reduce the amount of ionic liquid

required by as much as 50 mass% while concurrently enhancing the cellulose capacity of the mixture. By exchanging the comparatively expensive ionic liquid with a conventional organic solvent both process performance and economics are improved.

Following the dissolution process, cellulose can be chemically converted in the IL or separated for non-IL processing. Removal of cellulose from ILs by precipitation yields a reduced crystallinity product (cellulose II) that has applications ranging from coatings and films to insulation. Additionally, amorphous cellulose demonstrates significantly enhanced chemical and biochemical conversion properties compared to native crystalline cellulose.[7] Cellulose precipitation from ILs requires changing the solvent environment of the system. Preliminary studies have demonstrated that precipitation of cellulosic biomass could be accomplished by contacting the IL-cellulose mixture with a protic liquid antisolvent. Molecules including water and alcohols actively participate in hydrogen bonding interactions and disrupt cellulose-IL bonds thus precipitating the biopolymer from solution.

Herein, the first quantitative solid-liquid equilibrium studies are presented and demonstrate the substantial negative impact that protic solvents have on biomass solubility in ionic liquid mixtures. While protic antisolvents are highly effective at precipitating cellulose from ionic liquids, it has been determined that removal of liquid antisolvents are cost prohibitive due to the energy requirement needed to recover and recycle the IL. Therefore, a novel gas antisolvent method has been developed that relies on compressed carbon dioxide.[8] A full phase equilibrium and process economics study demonstrates the advantages associated with this novel processing technology.

Provided the limitations discussed above, the primary purpose of this research is to investigate cellulosic biomass as an alternative resource for the production of chemicals and fuels traditionally sourced from petroleum. Efficient processing of recalcitrant cellulosic biomass requires dissolution into a liquid reaction phase. Therefore, identifying effective solvent technologies is imperative to utilizing this renewable resource. The current chapter provides an introduction into ionic liquid synthesis and solvent selection as well as an overview of IL applications to the fields of biomass processing and carbon dioxide capture. Thermodynamic considerations are targeted within each section and attempts are made to optimize IL solvent performance with cost. A comprehensive literature review is included within each section to demonstrate the relevant work that has been established within our research group and the greater scientific community. The chapter is concluded by summarizing the dissertation objectives, outline, and outcomes of the research presented herein.

1.1. Room Temperature Ionic Liquids

Ionic liquids are traditionally defined as liquid salts that melt at temperatures below 100^{o}C. The characteristic ionic interactions between cation and anion constituents of ILs afford them interesting properties including negligible vapor pressures. For this reason, ionic liquids are commonly referred to as environmentally friendly "green" solvents. Ionic liquids also possess excellent thermal stability and have decomposition temperatures greater than 500 K allowing them to be applied in high temperature processes without degradation. Ionic liquids are deemed "designer solvents" as an estimated 10^{14} unique cation/anion combinations are theoretically possible.[9]

Figure 1.1 displays the common classes of IL cation and anion constituents. By altering the ion pairs, IL properties including but not limited to melting point, viscosity, density, heat capacity, hydrophobicity, gas solubility, hydrogen bond accepting ability (acidity), and hydrogen bond accepting ability (basicity) can be tuned. Therefore, the vast number of unique cation/anion combinations allows IL functionality and performance to be tailored to the desired application.

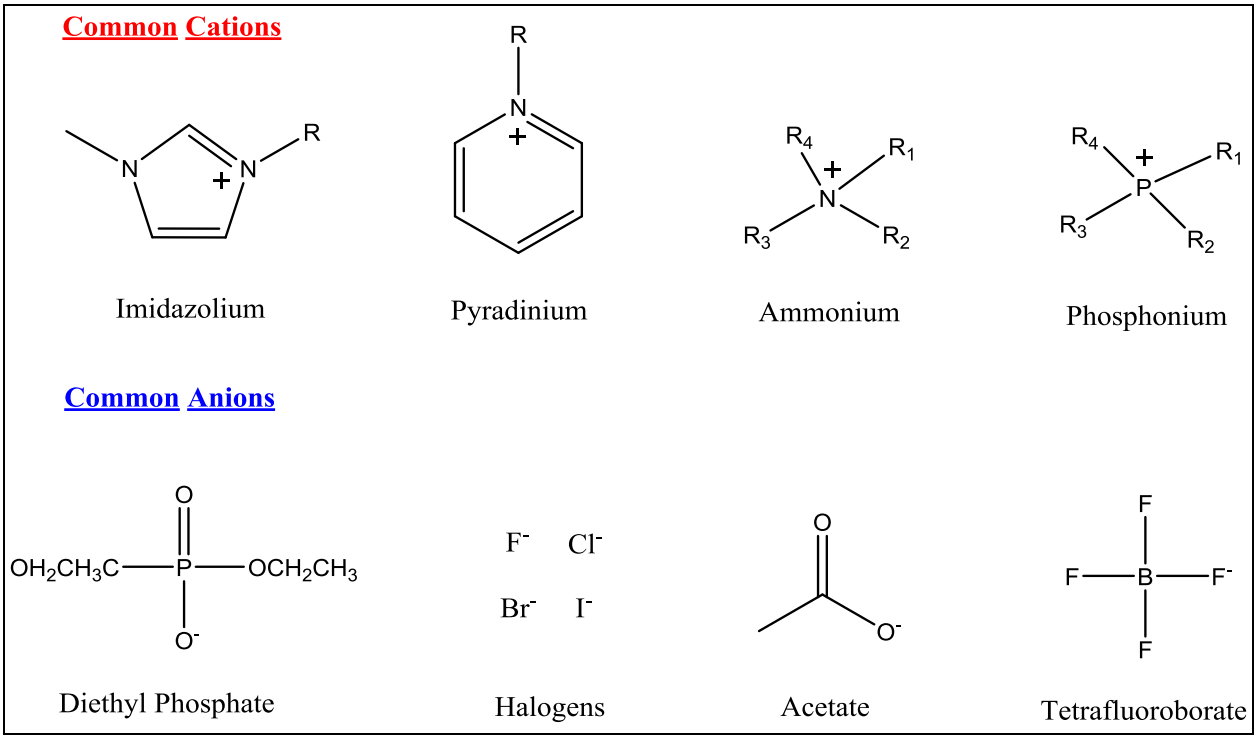

Figure 1.1: Classes of cation and anion constituent groups that form common ionic liquids.

Despite these advantages, the high cost of ionic liquid synthesis often precludes ILs from consideration in industrial processes.[10] Many ILs are also hygroscopic and display moderate viscosities which could be problematic in large scale applications. Nonetheless, research on ionic liquids continues to demonstrate excellent performance in extraction, chemical reaction,

and materials processing fields. Furthermore, select imidazolium based ionic liquids have shown great potential for lignocellulosic biomass dissolution and conversion.

1.2. Ionic Liquid Synthesis

While ionic liquids are conventionally referred to as environmentally friendly "green" solvents, the source of their precursor molecules has recently been called into question.[11] In reality, ILs are only as "green" as the chemicals they are synthesized from. For instance, ionic liquids possessing halogen based anions (*i.e.* 1-hexyl-3-methylimidazolium bromide [HMIm][Br]) must be synthesized from 1-bromohexane, a halogenated compound that presents a significant environmental hazard. Attempts should be made to use non-halogen based ILs and increasingly green precursor molecules. Additionally, solvents are utilized in the IL synthesis process to mitigate exothermic heat effects and improve reaction kinetics. The solvent must be removed from the ionic liquid and recycled after the reaction. Depending on the solvent selected, the ionic liquid purification process can be both energy intensive and cost prohibitive. Therefore, solvent selection also plays a role in the environmental impact of the IL synthesis process.

Ionic liquids, being an emerging technology, are currently produced in small batch scales and are expensive relative to conventional solvents. Understanding the costs of ionic liquid synthesis is imperative to successful implementation of this novel solvent technology as they can be 2-100 times more expensive than organic solvents.[12] Previous attempts to improve the economics of IL processes have targeted synthesizing less expensive protic ILs from acid-base precursor molecules.[13] However, thus far new inexpensive ILs do not match the performance of imidazolium ILs, especially in biomass applications. Therefore, new strategies must be

developed to reduce the cost of ionic liquid based processes while maintaining their competitive advantage relative to conventional solvents.

1.2.1. Thermal Quaternization Reactions

Imidazolium-based ionic liquids are often synthesized by a quaternization reaction between an alkyl halide and a 1-alkyl-imidazole. For the production of the model ionic liquid 1-hexyl-3-methylimidazolium bromide ([HMIm][Br]), this reaction occurs between 1-bromohexane and 1-methylimidazole, shown in Figure 1.2. The reaction of a haloalkane with the substituted imidazole proceeds by a S_N2 nucleophilic backside attack mechanism where a lone pair of electrons on the imidazole ring attacks the carbon adjacent to bromine on the haloalkane thus cleaving off the halogen atom, forming the cation/anion pair. The reaction is thermally driven with reaction temperatures ranging from 80-100^{o}C and reaction times between 24 and 72 hours to reach ~100% conversion.[14] Upon completion, volatile impurities and the reaction solvent are removed by vacuum distillation. After producing the platform ionic liquid, further functionalization can be added through ion exchange reactions. For instance, [HMIm][Br] can be reacted with a 30% excess of lithium bistrifluoromethylsulfoxideamide ($LiTf_2N$) to form the ionic liquid 1-hexyl-3-methylimidazolium bistrifluoromethylsulfoxideamide [HMIm][Tf_2N].[14]

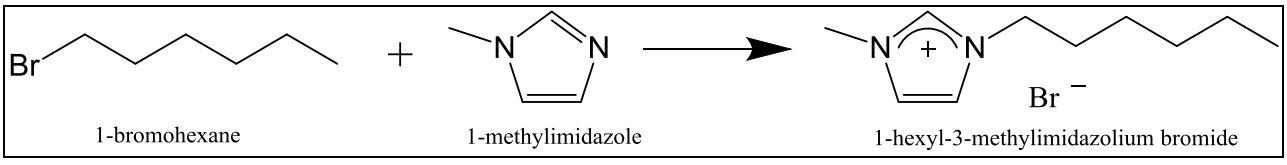

Figure 1.2: Reaction of 1-bromohexane and 1-methylimidazole to produce the ionic liquid 1-hexyl-3-methylimidazolium bromide [HMIm][Br].[15]

1.2.2. Microwave Reactions for IL Synthesis

Select ionic liquids including 1-ethyl-3-methylimidazolium diethyl phosphate [EMIm][DEP], shown in Figure 1.3, can be synthesized by thermal methods but proceed at prohibitively slow reaction rates. For instance, [EMIm][DEP] synthesis at 120^{o}C requires reaction times greater than 3 days.[16] Alternatively, microwave synthesis methods have been developed which significantly enhance the reaction rate. Microwave reactions utilize electromagnetic microwave radiation to provide uniform distribution of heat directly into the sample as opposed to thermal methods which operate by conductive heating methods. The advantages of microwave reactions include: reaction rate acceleration, lowering required reaction temperatures, enhanced selectivity, greater yields, and reduced energy consumption.[17] Despite these advantages, scale up of microwave synthesis methods is still in the early stages and therefore this methodology may be currently limited to small batch production systems.

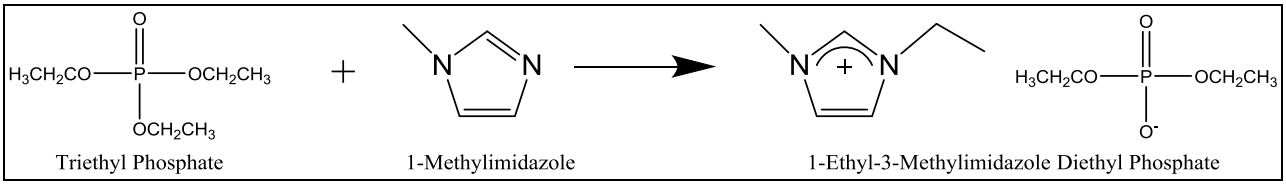

Figure 1.3: The reaction of triethyl phosphate and 1-methylimidazole to produce the ionic liquid 1-ethyl-3-methylimidazolium diethyl phosphate [EMIm][DEP].

1.3. Solvent Selection for IL Synthesis

Organic solvents are utilized in ionic liquid synthesis processes for multiple reasons. First and foremost, ionic liquid synthesis reactions are highly exothermic generating heat as a byproduct of the reaction. Solvents act as a heat sink and reduce thermal and pressure hazards associated with the process. For select ILs solvents also bring the reactants and product into a single

homogeneous phase and reduce mass transfer limitations. Furthermore, many ionic liquids, despite melting at temperatures below 100^{o}C, are not liquid at room temperature. By dilution with a solvent, ILs can be handled and processed in the liquid phase at milder temperatures. Finally, solvent effects on S_N2 reactions between amines and haloalkanes have been well documented in the literature. Menshutkin investigated kinetics of the S_N2 reaction mechanism for the production of quaternary ammonium salts from amines and haloalkanes in 23 solvents and found that the reaction rate is highly solvent dependent. [18-20] [18-20] ILs have been synthesized in a range of solvents including acetonitrile, acetone, dichloromethane, methanol, ethanol, and dimethyl sulfoxide among others.[21] While solvents serve an important role in the synthesis process, environmental aspects must be considered as the ionic liquid is only as "green" as the reagents used to in its synthesis. In an attempt to investigate environmentally benign solvents for IL synthesis, Nwosu investigated the production of [HMIm][Br] in supercritical CO_2 as well as in CO_2 expanded liquids (CXLs). [22, 23] [22, 23] Compressed carbon dioxide is advantageous as it has a large heat capacity, low viscosity, and low environmental impact. Despite the mass transport advantages of supercritical CO_2, the [HMIm][Br] reaction kinetics are not equivalent to synthesis in organic solvents. Table 1.1 displays reaction rate as a function of solvent selection.

Solvent	**K x 10^6 (M^{-1} s^{-1})**	
	313.15 K	333.15 K
Dimethyl Sulfoxide	77.9 +/- 1.7	322.3 +/- 3.5
Acetonitrile	21.6 +/- 0.2	110.6 +/- 1.4
Neat (Solvent Free)	17.63 +/- 0.06	106.3 +/- 1.3
CO2 @ 30 Bar	14.9 +/- 0.5	107.0 +/- 2.8
CO2 @ 60 Bar	8.2 +/- 0.8	69.0 +/- 1.0
CO2 @ 90 Bar	8.0 +/- 0.2	59.9 +/- 0.8
CO2 @ 140 Bar	5.9 +/- 0.1	49.2 +/- 1.0
Cyclopentanone	15.1 +/- 0.1	76.1 +/- 1.7
Acetone	12.67 +/- 0.06	63.7 +/- 0.6
2-Butanone	11.56 +/- 0.08	58.8 +/- 0.3
Dichloromethane	8.5 +/- 0.1	N/A
Ethyl Formate	8.0 +/- 0.1	N/A
Methanol	2.03 +/- 0.08	17.1 +/- 0.1

Table 1.1: Reaction rate of 1-bromohexane and 1-methylimidazole to produce the ionic liquid [HMIm][Br] in various solvents.[22]

The reaction in dimethyl sulfoxide is kinetically optimal having a reaction rate that is nearly four times as fast as the next best solvent. However, tradeoffs exist when selecting solvents for IL synthesis. DMSO is highly polar and demonstrates mutual miscibility with the ionic liquid. Separation methods to purify the IL from DMSO require thermal distillation methods. Provided the high boiling point of DMSO ~189^{o}C, the costs of IL purification may counteract the economic and environmental solvent effects of DMSO. Alternatively, from a separation standpoint, dichloromethane is ideal as it boils at ~40^{o}C and requires far less thermal energy input for IL purification. However, DCM has a large environmental impact and demonstrates low kinetic reaction rates for IL synthesis. These results demonstrate that solvent selection requires an optimization of kinetic performance, volatility, and environmental impact.

1.3.1. IL Purification and Solvent Recycle

Ionic liquids have been successfully utilized in a range of applications including CO_2 capture and lignocellulosic biomass processing. In each of these applications IL purity is critical to performance. For instance, Aki *et al.* determined that the CO_2 capacity of ionic liquid [BMIm][PF_6] changed from 38 mol% to 43 mol% simply by removing IL degradation products and impurities from the synthesis procedure.[24] These results demonstrate the impact of residual reactants in solution after the IL synthesis process. Furthermore, in biomass processing protic solvents significantly affect the dissolution and reaction process. Water and ethanol can completely inhibit biomass dissolution in ILs by competitively interacting with IL ions and residual reactants such as 1-methylimidazole can chemically complex with biomass in solution forming insoluble humins.[25] It is therefore evident that producing high purity ionic liquids will be necessary for implementation in industrial processes.

Purification of ionic liquids synthesized via metathesis reactions (*i.e.* [HMIm][Br]) require the removal of trace quantities of unreacted 1-bromohexane and 1-methylimidazole as well as the reaction solvent and residual water. Previous attempts have been made at assessing the energy of IL purification by utilizing the latent heat of vaporization of the solvent selected for synthesis.[21] However, to provide a detailed and accurate understanding of the actual separation process the full vapor-liquid equilibrium of the various solvents and ionic liquids must be known. To this point, no such study has investigated the phase equilibrium thermodynamics of the reactants, product, and solvent involved in an ionic liquid synthesis system. Thermodynamic data developed from vapor-liquid equilibrium experiments is utilized by process simulators (Aspen Plus) to accurately predict the energy required to produce ILs with 99+%

purity. Furthermore, the phase equilibrium data can be utilized within life cycle assessment models to predict the environmental footprint of the cradle to gate ionic liquid synthesis process.

1.4. Ionic Liquid Applications

Ionic liquids have been intentionally designed and applied to a broad range of problems facing the chemical industry due to their molecularly tunable nature. Select application areas include: reaction engineering, separations, nanomaterials, electrolytes, heat storage, solvents, and analytical instrumentation. While academic research on ILs has demonstrated exponential growth between 2010 and 2014, commercialization of ionic liquid technologies has been limited. Common criticisms of ILs include: expensive feedstock cost, comparatively high viscosities, impurity effects, and limited knowledge of physio-chemical properties. Despite these detractors, when used correctly ILs can demonstrate a competitive advantage over other technologies. For instance, BASF is currently operating the "BASIL" (Biphasic Acid Scavenging Utilizing Ionic Liquids) process to remove HCl from a reaction mixture producing the photoinitiator diethoxyphenylphosphine.[26]

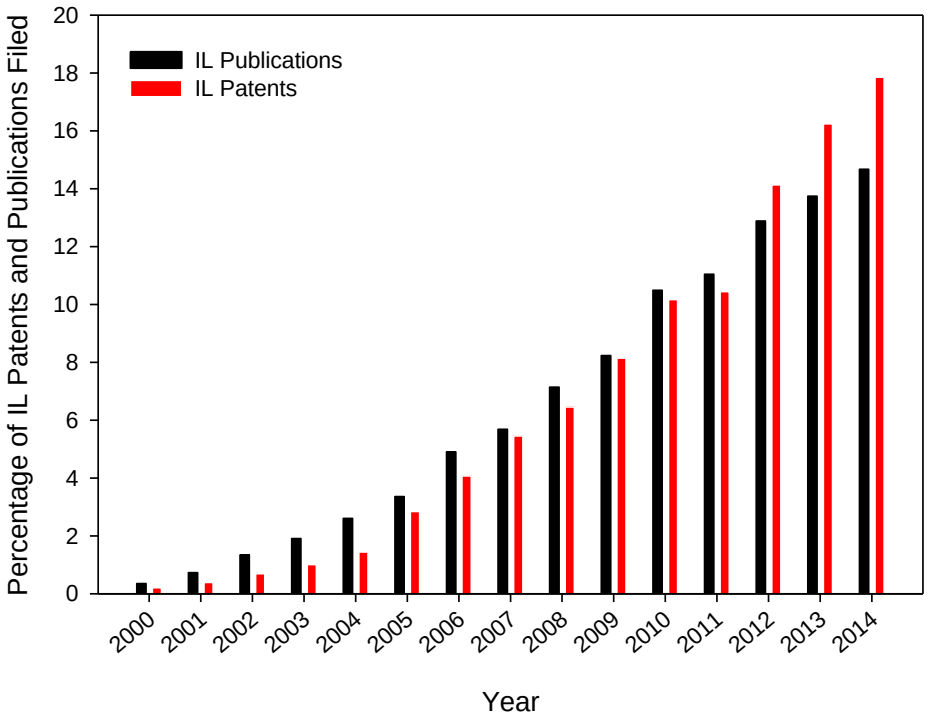

Figure 1.4: Percentage of total publications and patents on ionic liquids accepted by year as found on SciFinder.

Additionally, Air Products is using select imidazolium ILs, on a commercial scale, to transport hazardous gases at reduced pressures. As shown in Figure 1.4, growth in patents on ionic liquid technologies has recently surpassed that of publications. Therefore, industrialization of ionic liquid based processes may still be in the future. For ILs to overcome the "valley of death" facing all new technologies, ionic liquids must be developed as "drop in" replacements in conventional processes and must demonstrate a significant economic benefit relative to current operations. While comprehensive overviews of IL application areas can be found in the literature, carbon dioxide capture and biomass processing will be reviewed as they pertain to the research presented herein.

1.4.1. Carbon Dioxide Capture

As of November, 2015, the concentration of atmospheric carbon dioxide (CO_2) was 400.38 ppm, approximately 40% higher than 200 years ago.[27] Furthermore, atmospheric CO_2 levels have been increasing at a rate of ~2ppm per year since 2004.[28] The increase in CO_2 concentration primarily stems from the combustion of fossil fuels to produce energy. In an effort to reduce greenhouse gas emissions, carbon dioxide capture technologies are being developed to sequester CO_2 from post combustion flue gas using physical and chemical absorbents.

First generation absorbent technologies consist of amine based solvents (*i.e.* monoethanolamine) which physically and chemically absorb CO_2 through a flue gas scrubbing process. [29-33] [29-33] CO_2 is subsequently liberated from the solvent by a high temperature desorption process and stored in reservoirs including evacuated oil wells. While moderately effective, monoethanolamine is volatile, corrosive to metals, and moderately unstable.[34] Additionally, preliminary calculations estimate that separation of the amine solvent and CO_2 could require as much as 30% of the power generated by the plant due to the large heat of reaction between CO_2 and MEA.[35]

Ionic liquids have garnered significant interest as alternative solvents for CO_2 capture. Conventional room temperature ionic liquids demonstrate moderate CO_2 capacities and primarily absorb CO_2 through a physical mechanism thus eliminating the need for energy intensive desorption processes required by amine solvents. For instance, imidazolium ILs with the hexafluorophosphate, tetrafluoroborate, and bis(trifluoromethane)sulfonamide anions have shown promise as alternative solvents for CO_2 capture.[36] Additionally, task specific ionic liquids (TSILs) have been designed to capture carbon dioxide through both chemical and

physical absorption mechanisms.[37] TSILs demonstrate enhanced selectivity towards CO_2 and preferentially absorb carbon dioxide over other components such as N_2 and H_2S in the flue gas mixture. IL based CO_2 absorption is strongly influenced by the anion and select TSILs incorporating functionalized anions can absorb up to 1:1 mole ratio quantities of CO_2 relative to the IL.[38] Despite the thermodynamic advantages that ILs possess, moderate ionic liquid viscosity causes mass transport limitations of CO_2 in the liquid solvent. Diffusion coefficients of CO_2 in ILs are typically one to two orders of magnitude smaller than in amine based solvents thus limiting the absorption rate of the greenhouse gas. [39, 40] [39, 40] Current CO_2 capture processes are designed as packed tower absorption processes. Therefore, for ILs to be an effective technology they will have to demonstrate enhanced thermodynamic and transport properties and be successfully implemented as "drop-in" replacements for amine based solvent technologies.

1.4.2. Dissolution of Cellulosic Biomass

The complex inter- and intra- molecular hydrogen bonding network of cellulose renders it insoluble in nearly all aqueous and organic solvents. However, select ionic liquids are capable of dissolving large quantities.[41] Ionic liquid anions preferentially hydrogen bond to cellulose and solubilize the polymer through a non-derivitizing process. Anion basicity (hydrogen bond accepting ability) is primarily attributed to the successful dissolution of cellulose in ILs. Spectroscopic studies indicate that ILs possessing the chloride and diethyl phosphate anions display some of the highest measured solvatochromic basicity (β) values of any known ionic liquids. [41, 42] [41, 42] Correspondingly these ILs also dissolve large quantities of cellulose. However, the presence of water and other protic solvents can interfere with the hydrogen

bonding ability of ILs and reduce their cellulose dissolution capacities.[25] Elevated melting points and moderate viscosities are two other limitations of select biomass dissolving ILs. For example, while [EMIm][DEP] is a liquid at room temperature, [BMIm][Cl] melts at 70^{o}C and [EMIm][Cl] melts at 77^{o}C. Additionally, at 80^{o}C the viscosities of [BMIm][Cl] and [EMIm][Cl] are 142 and 65 cP respectively.[43] The addition of biomass further increases mixture viscosity and at high loadings IL/biomass mixtures can display thick gel-like rheological behavior. Mass transport limitations can inhibit cellulose dissolution and conversion indicating the importance of utilizing low viscosity ionic liquids like [EMIm][DEP] which has a viscosity of 20 cP at 80^{o}C.[44] Additionally, polar aprotic cosolvents have been shown to reduce mixture viscosities without precipitating biomass and could be a feasible solution.[45] Despite these drawbacks, a unique feature of ionic liquid based biomass dissolution is that cellulose degree of polymerization (chain length) is unaltered while the degree of crystallinity (intramolecular bonding) is largely reduced.[46] Kinetic studies on the acid catalyzed hydrolysis of cellulose to glucose indicate that crystallinity is a significant barrier to the chemical conversion of polymeric carbohydrates.[47] Therefore, in combination with their comparatively high biomass solubilities, the increased reaction performance of cellulose in ionic liquids indicates several advantages ILs possess over organic and aqueous solvents.

1.4.3. Precipitation of Cellulosic Biomass

Once dissolved in an ionic liquid, cellulosic biomass can be directly precipitated to form a de-crystallized product with value added materials applications including coatings and films. Alternatively, as addressed in section 1.4.4 cellulose can be directly converted to value added

chemicals within the ionic liquid solvent. A general process flow diagram of both processing routes is displayed in Figure 1.5.

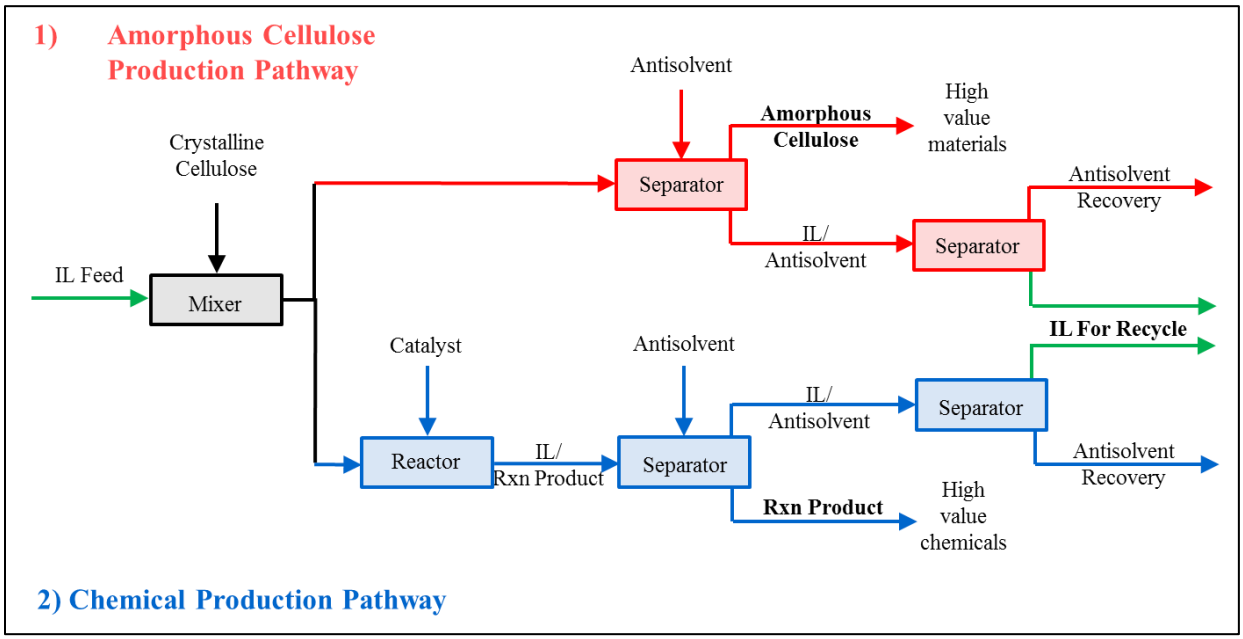

Figure 1.5: Ionic liquid processing of cellulosic biomass to produce 1) amorphous cellulose and 2) value added chemicals.

The dissolution of cellulose in ionic liquids is highly dependent on the ability of select ILs to preferentially bond into the inter- and intra- molecular hydrogen bonding structure of cellulose. Therefore, precipitation of cellulose can be achieved by adding an additional component to disrupt the IL-cellulose interactions. Protic solvents including water and alcohols contain acidic hydrogen atoms that competitively interact with the IL anion thus disrupting IL-cellulose bonds and precipitating the biopolymer. Protic liquid antisolvents are highly effective and as little as 1 mass% water can reduce the cellulose solubility of an ionic liquid by as much as 55%.[8] However, solubility data indicates saturation conditions of cellulose in solution. Saturation is distinctly different from separation which requires significantly larger antisolvent quantities to

overcome the large mixture viscosities and IL inclusion bodies that are formed as cellulose precipitates from the mixture.

Alternative cellulose separation methods have also been developed using a gas antisolvent method. For instance, Barber and Sun have recently demonstrated the use of carbon dioxide as a reactant to precipitate cellulose from imidazolium ionic liquids with acetate anions [Ac], *e.g.* 1-ethyl-3-methylimidazolium acetate [EMIm][Ac]. [48, 49] [48, 49] The IL-CO_2 reaction produces a mixture of 1-alkyl-3-methylimidazolium-2-carboxylate zwitterion complex and acetic acid which is unable to solubilize cellulose. [50, 51] [50, 51] Additionally, research herein demonstrates the precipitation of cellulose from [EMIm][DEP]-cosolvent mixtures by a physical non-reactive method. The production of cellulose, being a relatively inexpensive product, will require highly efficient separations and ionic liquid recycle operations.

1.4.4. Chemical Conversion of Cellulosic Biomass

Cellulosic biomass can be converted into a range of value added chemicals including sugar (glucose, fructose, *etc.*), sugar alcohols (sorbitol, ethylene glycol, *etc.*), organic acids (formic acid, levulinic acid, *etc.*) and furans (5-hydroxymethylfurfural, 2,5-dimethylfuran, *etc.*). Figure 1.6 displays the general chemical conversion pathways of cellulose.

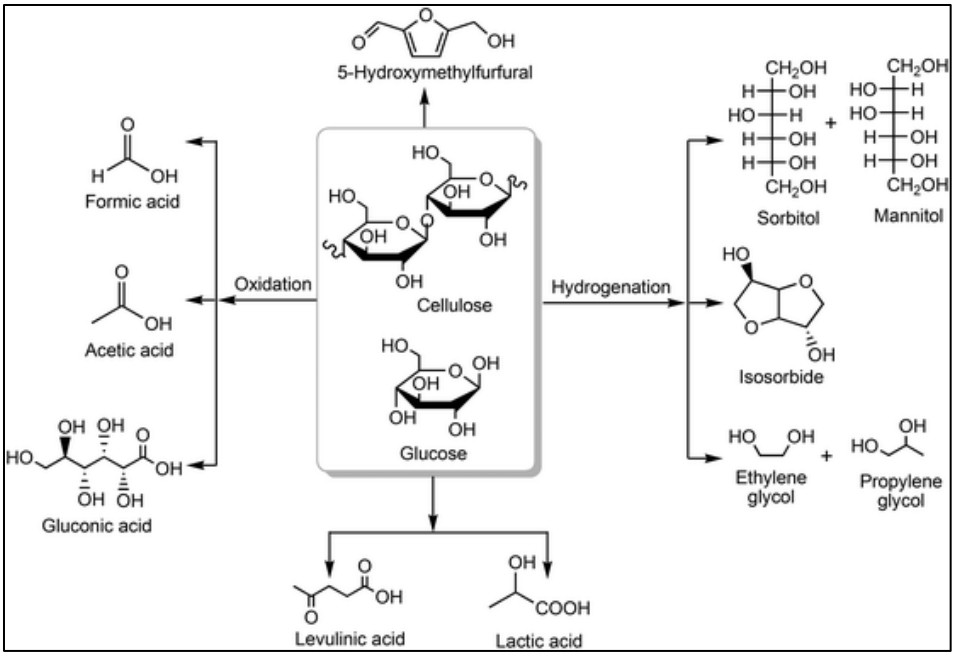

Figure 1.6: Value added chemical products from cellulosic biomass conversion.[52]

Direct production of 5-hyroxymethylfurfural (5-HMF) and furfural from cellulose and hemicellulose respectively is one of the most researched areas of lignocellulosic biomass conversion. [53-60] [53-60] Motivation for making these two products is primarily attributed to the ability of a catalytic mechanism to simultaneously perform several chemical conversion steps in a one-pot system. In the case of 5-HMF production a combination of mineral and Lewis acids are capable of hydrolyzing cellulose to glucose, isomerizing glucose to fructose, and dehydrating fructose to 5-HMF with moderate selectivity.[52] Studies have shown that Lewis acids including chromium chloride ($CrCl_3$),[61] tin chloride ($SnCl_4$)[62], and copper chloride ($CuCl_2$)[63] are highly effective at isomerizing aldose sugars to ketose sugars. Therefore, in conjunction with mineral acids (H_2SO_4 *etc.*) that are effective for hydrolysis and dehydration reactions, 5-HMF can be produced directly from cellulose. Select studies have also shown that the combination of ionic liquids and Lewis acids can directly convert cellulose to 5-HMF without the use of a strong

acid. [63-65] [63-65] Interestingly, the production of furfural from xylan, occurs by an analogous mechanism to that of 5-HMF from cellulose with similar reaction conditions.[66] Attempts at the concomitant production of 5-HMF and furfural from lignocellulose have been attempted but demonstrate lower selectivity and conversion compared to reacting pure cellulose and hemicellulose feedstocks separately.[58] Nonetheless, initial studies with ionic liquid solvents show an opportunity for improvement and continued research is expected to demonstrate advances in this area.[67]

1.5. Dissertation Objectives

The research presented in this dissertation targets environmental and economic aspects pertaining to the synthesis of ionic liquids and their applications to the fields of biomass processing and carbon dioxide capture. The core of this dissertation investigates utilizing ionic liquids for the dissolution, precipitation, and chemical conversion of cellulosic biomass. The first quantitative thermodynamic solid-liquid equilibrium datasets are presented for cellulose solubility in pure ionic liquid systems. Additionally, polar aprotic liquids are investigated as cosolvents for cellulose dissolution. Efficient product extraction and IL recycle will be imperative to creating a viable ionic liquid based process. Herein, precipitation of cellulosic biomass from ionic liquid solvent systems is investigated by conventional liquid antisolvents and a novel non-reactive gas antisolvent method. Solid-liquid phase equilibrium measurements and spectroscopic techniques are utilized to understand the separation process. Furthermore, vapor-liquid equilibrium datasets are acquired to assess the energy required to purify and recycle the ionic liquid and antisolvent. Process modeling is applied to the thermodynamic data to understand the economics of biomass separations from ionic liquids.

This work also considers optimizing solvent selection for ionic liquid synthesis by investigating the separation energies required to purify an IL product from the reaction mixture. Experimental vapor-liquid and liquid-liquid equilibria pertaining to the reactants, products, and solvent in the synthesis of the model ionic liquid [HMIm][Br] are investigated. The phase equilibrium data has been regressed by Equation of State and Gibbs Excess activity coefficient models and utilized by Aspen Plus to build accurate ionic liquid synthesis process models. Separation energies and process parameters gained from the simulations are utilized by life cycle assessment methods to investigate the environmental aspects of solvent selection for IL synthesis. The work generated herein is intended to provide an enhanced understanding of large scale ionic liquid synthesis processes and guide the scientific community towards increasingly economic and environmental IL synthesis methods.

Finally, a computational study is utilized to assess the ability of ionic liquids as solvents for carbon dioxide capture. Capital and operating cost estimations are generated through the design of a theoretical packed absorption and flash unit desorption process. Comparisons are made between conventional amine solvent technology and ionic liquids and recommendations are provided to guide future research activities in this area.

1.6. Outline of Chapters

Chapter two outlines the experimental methods and modeling used in this study. Ionic liquid synthesis and purification procedures are provided and described in detail. Experimental thermodynamic techniques including solid-liquid equilibrium cloud point measurements, liquid-liquid equilibrium measurements, isobaric vapor-liquid equilibrium measurements, and isothermal vapor-liquid equilibrium measurements are reviewed. Additionally, a new vapor-

liquid-liquid equilibrium measurement technique is presented as proof of concept. Analytical techniques used in this study including various modes of NMR, FTIR, UV-Vis spectroscopy, rheology, and high performance liquid chromatography (HPLC) are discussed. Phase equilibrium modeling including Equation of State and Gibbs excess models used in this study are presented and reviewed. Finally, a comprehensive list of materials used to perform the studies herein is included.

In chapter three, cellulose dissolution in ionic liquid systems is investigated. Solid-liquid equilibrium results are presented for cellulose dissolution in pure ionic liquids as well as mixed IL-cosolvent systems. Spectroscopic techniques are utilized to assess the cellulose dissolution mechanism and rheology studies are employed to assess the mass transfer aspects of biomass containing ionic liquid systems.

Chapter four details the precipitation of cellulosic biomass from ionic liquid systems. Solid-liquid equilibrium measurements explore cellulose precipitation by conventional polar protic liquid antisolvents. Additionally, a novel gas antisolvent method utilizing compressed carbon dioxide is investigated. Precipitation studies conducted in an autoclave are supported by high pressure vapor-liquid equilibrium experiments. Spectroscopic techniques are also utilized to understand the separation process. Characterization of the amorphous cellulose product is examined by solid state NMR.

Chapter five provides a preliminary investigation on the chemical conversion of cellulosic biomass in ionic liquids. Cellulose hydrolysis and isomerization to form fructose are initially discussed. Subsequently, results detailing the effects of polar aprotic cosolvents on 5-hydroxymethylfurfural production in mixed IL-cosolvent systems are presented. Further

conversion of 5-HMF to furan products is also discussed as an opportunity for further exploration.

Chapter six investigates the separation energies required for the purification of the ionic liquid [HMIm][Br] from its reaction mixture. Isobaric vapor-liquid equilibrium data is presented for binary systems composed of the reactants 1-bromohexane and 1-methylimiazole, product [HMIm][Br], and reaction solvent: acetone, acetonitrile, dichloromethane, and dimethyl sulfoxide. The experimental datasets are modeled by Equation of State and Gibbs Excess functions.

Chapter seven presents Aspen Plus simulations for the continuous production of model ionic liquid [HMIm][Br] based on the thermodynamic phase equilibrium measurements discussed in chapter six. The Aspen Plus simulations are utilized to estimate the quantity of energy required to produce an ionic liquid product with a desired purity level. Additionally, cradle to gate life cycle assessment methodologies are employed to measure the environmental impact of ionic liquid synthesis.

Chapter eight investigates the capital and operating costs associated with carbon dioxide capture using ionic liquid solvent technologies in packed absorption towers. Absorption tower specifications are computed including heights and numbers of transfer units as well as hydraulic parameters. Comparisons are made to conventional amine based CO_2 capture solvents and general recommendations are provided to guide future research in this area.

Finally, chapter nine completes the thesis by providing conclusions and recommendations for future research.

1.7. Research Outcomes

The goal of this research is to propel the field of ionic liquid research by developing environmental and economically efficient applications of ionic liquids to problems facing the chemical engineering industry.

References

1. Nasdaq. *Latest Price & Chart for Crude Oil Brent*. 2016; Available from: http://www.nasdaq.com/markets/crude-oil-brent.aspx.
2. Luterbacher, J.S., D. Martin Alonso, and J.A. Dumesic, *Targeted chemical upgrading of lignocellulosic biomass to platform molecules.* Green Chemistry, 2014. **16**(12): p. 4816-4838.
3. Perlack, R.D., Stokes, B.J., *U.S. Billion Ton Update: Biomass Supply for a Bioenergy and Bioproducts Industry.* Oak Ridge National Laboratory, Oak Ridge, TN. 227p., U.S. Department of Energy 2011. **ORNL/TM-2011/224**
4. Perlack, R.D.W., Lynn L. ; Turhollow, Anthony F. ; Graham, Robin L. ; Stokes, Bryce J. ; Erbach, Donald C., *Biomass as Feedstock for a Bioenergy and Bioproducts Industry: The Technical Feasibility of a Billion-Ton Annual Supply*, U.S.D.o. Energy, Editor 2005: Oak Ridge National Laboratory.
5. Horvath, A.L., *Solubility of structurally complicated materials: I. Wood.* Journal of Physical and Chemical Reference Data, 2006. **35**(1): p. 77-92.
6. Wang, H., G. Gurau, and R.D. Rogers, *Ionic liquid processing of cellulose.* Chemical Society Reviews, 2012. **41**(4): p. 1519-1537.
7. Hall, M., et al., *Cellulose crystallinity - a key predictor of the enzymatic hydrolysis rate.* Febs Journal, 2010. **277**(6): p. 1571-1582.
8. Minnick, D.L. and A.M. Scurto, *Reversible and non-reactive cellulose separations from ionic liquid mixtures with compressed carbon dioxide.* Chemical Communications, 2015. **51**(63): p. 12649-12652.
9. Holbrey, D.J. and R.K. Seddon, *Ionic Liquids.* Clean Products and Processes. **1**(4): p. 223-236.
10. Rogers, R.D., K.R. Seddon, and S. Volkov, *Green industrial applications of ionic liquids*. NATO science series Series II, Mathematics, physics, and chemistry. 2002, Dordrecht ; Boston: Kluwer Academic Publishers. xxiv, 553 p.
11. Clough, M.T., et al., *Ionic liquids: not always innocent solvents for cellulose.* Green Chemistry, 2015. **17**(1): p. 231-243.
12. Sowmiah, S., et al., *On the Chemical Stabilities of Ionic Liquids.* Molecules, 2009. **14**(9): p. 3780-3813.
13. Greaves, T.L. and C.J. Drummond, *Protic ionic liquids: Properties and applications.* Chemical Reviews, 2008. **108**(1): p. 206-237.
14. Ahosseini, A. and University of Kansas., *Homogeneous catalysis and mass transfer in biphasic ionic liquid systems with compressed carbon dioxide and organic compounds*. p. 233 p.
15. Minnick, D.L. and A.M. Scurto, *Vapor-liquid equilibrium in the production of the ionic liquid, 1-hexyl-3-methylimidazolium bromide ([HMIm][Br]), in acetone.* Fluid Phase Equilibria, 2014. **365**: p. 11-19.
16. Kuhlmann, E., et al., *Imidazolium dialkylphosphates - a class of versatile, halogen-free and hydrolytically stable ionic liquids.* Green Chemistry, 2007. **9**(3): p. 233-242.

17. Loupy, A., *Microwaves in organic synthesis*. 2nd, completely rev. and enlarged ed. 2006, Weinheim: Wiley-VCH.
18. Menshutkin, N.Z., Physical Chemistry, 1890. **5**(589).
19. Menshutkin, N.Z., Physical Chemistry, 1980. **6**(41).
20. Reichardt, C., *Solvatochromic Dyes as Solvent Polarity Indicators.* Chemical Reviews, 1994. **94**(8): p. 2319-2358.
21. Schleicher, J.C. and A.M. Scurto, *Kinetics and solvent effects in the synthesis of ionic liquids: imidazolium.* Green Chemistry, 2009. **11**(5): p. 694-703.
22. Nwosu, S.O., J.C. Scheicher, and A.M. Scurto, *Kinetics and polarity effects in the synthesis of the ionic liquid, 1-hexyl-3-methyl-imidazolium bromide, using compressed CO2.* Journal of Supercritical Fluids, 2015. **96**: p. 171-179.
23. Nwosu, S.O., J.C. Schleicher, and A.M. Scurto, *High-pressure phase equilibria for the synthesis of ionic liquids in compressed CO2 for 1-hexyl-3-methylimidazolium bromide with 1-bromohexane and 1-methylimidazole.* Journal of Supercritical Fluids, 2009. **51**(1): p. 1-9.
24. Aki, S.N.V.K., et al., *High-pressure phase behavior of carbon dioxide with imidazolium-based ionic liquids.* Journal of Physical Chemistry B, 2004. **108**(52): p. 20355-20365.
25. Khupse, N.D. and A. Kumar, *Delineating Solute-Solvent Interactions in Binary Mixtures of Ionic Liquids in Molecular Solvents and Preferential Solvation Approach.* Journal of Physical Chemistry B, 2011. **115**(4): p. 711-718.
26. Plechkova, N.V. and K.R. Seddon, *Applications of ionic liquids in the chemical industry.* Chemical Society Reviews, 2008. **37**(1): p. 123-150.
27. Dlugokencky, E., Tans, P., *Trends in Atmospheric Carbon Dioxide.* NOAA/ESRL, 2015.
28. Agency., I.E., *CO2 Emissions From Fuel Combustion.* 2015.
29. Maceiras, R., E. Alvarez, and A.A. Cancela, *Effect of temperature on carbon dioxide absorption in monoethanolamine solutions.* Chemical Engineering Journal, 2008. **138**(1-3): p. 295-300.
30. Puxty, G. and M. Maeder, *A simple chemical model to represent CO2-amine-H2O vapour-liquid-equilibria.* International Journal of Greenhouse Gas Control, 2013. **17**: p. 215-224.
31. Aronu, U.E., et al., *Solubility of CO2 in 15, 30, 45 and 60 mass% MEA from 40 to 120 degrees C and model representation using the extended UNIQUAC framework.* Chemical Engineering Science, 2011. **66**(24): p. 6393-6406.
32. Darde, V., et al., *Process simulation of CO2 capture with aqueous ammonia using the Extended UNIQUAC model.* International Journal of Greenhouse Gas Control, 2012. **10**: p. 74-87.
33. Zhang, Y., et al., *Rate-Based Process Modeling Study of CO2 Capture with Aqueous Monoethanolamine Solution.* Industrial & Engineering Chemistry Research, 2009. **48**(20): p. 9233-9246.
34. Luis, P., *Use of monoethanolamine (MEA) for CO2 capture in a global scenario: Consequences and alternatives.* Desalination, 2016. **380**: p. 93-99.
35. Hammond, G.P. and S.S.O. Akwe, *Thermodynamic and related analysis of natural gas combined cycle power plants with and without carbon sequestration.* International Journal of Energy Research, 2007. **31**(12): p. 1180-1201.

36. Bara, J.E., et al., *Guide to CO2 Separations in Imidazolium-Based Room-Temperature Ionic Liquids.* Industrial & Engineering Chemistry Research, 2009. **48**(6): p. 2739-2751.
37. Bates, E.D., et al., *CO2 capture by a task-specific ionic liquid.* Journal of the American Chemical Society, 2002. **124**(6): p. 926-927.
38. Torralba-Calleja, E., J. Skinner, and D. Gutierrez-Tauste, *CO2 Capture in Ionic Liquids: A Review of Solubilities and Experimental Methods.* Journal of Chemistry, 2013.
39. Camper, D., et al., *Diffusion and solubility measurements in room temperature ionic liquids.* Industrial & Engineering Chemistry Research, 2006. **45**(1): p. 445-450.
40. Kuntz, J. and A. Aroonwilas, *Mass-transfer efficiency of a spray column for CO2 capture by MEA.* Energy Procedia, 2009. **1**(1): p. 205-209.
41. Gericke, M., P. Fardim, and T. Heinze, *Ionic Liquids - Promising but Challenging Solvents for Homogeneous Derivatization of Cellulose.* Molecules, 2012. **17**(6): p. 7458-7502.
42. Stark, A., et al., *The effect of hydrogen bond acceptor properties of ionic liquids on their cellulose solubility.* Science China-Chemistry, 2012. **55**(8): p. 1663-1670.
43. Fendt, S., et al., *Viscosities of Acetate or Chloride-Based Ionic Liquids and Some of Their Mixtures with Water or Other Common Solvents.* Journal of Chemical and Engineering Data, 2011. **56**(1): p. 31-34.
44. Abd Ghani, N., et al., *Density, Surface Tension, and Viscosity of Ionic Liquids (1-Ethyl-3-methylimidazolium diethylphosphate and 1,3-Dimethylimidazolium dimethylphosphate) Aqueous Ternary Mixtures with MDEA.* Journal of Chemical and Engineering Data, 2014. **59**(6): p. 1737-1746.
45. Raines, R.T., *Fermentable sugars by chemical hydrolysis of biomass in an ionic liquid.* Abstracts of Papers of the American Chemical Society, 2010. **240**.
46. Ingildeev, D., et al., *Comparison of direct solvents for regenerated cellulosic fibers via the lyocell process and by means of ionic liquids.* Journal of Applied Polymer Science, 2013. **128**(6): p. 4141-4150.
47. Xiang, Q., et al., *Heterogeneous aspects of acid hydrolysis of alpha-cellulose.* Applied Biochemistry and Biotechnology, 2003. **105**: p. 505-514.
48. Barber, P.S., et al., *Coagulation of Chitin and Cellulose from 1-Ethyl-3-methylimidazolium Acetate Ionic-Liquid Solutions Using Carbon Dioxide.* Angewandte Chemie-International Edition, 2013. **52**(47): p. 12350-12353.
49. Sun, X.F., Y.L. Chi, and T.C. Mu, *Studies on staged precipitation of cellulose from an ionic liquid by compressed carbon dioxide.* Green Chemistry, 2014. **16**(5): p. 2736-2744.
50. Besnard, M., et al., *CO2 in 1-Butyl-3-methylimidazolium Acetate. 2. NMR Investigation of Chemical Reactions.* Journal of Physical Chemistry A, 2012. **116**(20): p. 4890-4901.
51. Denning, D.M. and D.E. Falvey, *Solvent-Dependent Decarboxylation of 1,3-Dimethylimdazolium-2-Carboxylate.* Journal of Organic Chemistry, 2014. **79**(10): p. 4293-4299.
52. Song, J.L., et al., *Conversion of glucose and cellulose into value-added products in water and ionic liquids.* Green Chemistry, 2013. **15**(10): p. 2619-2635.
53. Deng, W.P., Q.H. Zhang, and Y. Wang, *Catalytic transformations of cellulose and cellulose-derived carbohydrates into organic acids.* Catalysis Today, 2014. **234**: p. 31-41.
54. Mika, L.T., E. Cséfalvay, and I.T. Horváth, *The role of water in catalytic biomass-based technologies to produce chemicals and fuels.* Catalysis Today, (0).

55. Shi, J.C., et al., *Production of 5-Hydroxymethylfurfural from Mono- and Disaccharides in the Presence of Ionic Liquids.* Catalysis Letters, 2014. **144**(2): p. 252-260.
56. Xiao, S.H., et al., *Efficient conversion of cellulose into biofuel precursor 5-hydroxymethylfurfural in dimethyl sulfoxide-ionic liquid mixtures.* Bioresource Technology, 2014. **151**: p. 361-366.
57. Yabushita, M., H. Kobayashi, and A. Fukuoka, *Catalytic transformation of cellulose into platform chemicals.* Applied Catalysis B-Environmental, 2014. **145**: p. 1-9.
58. Zakrzewska, M.E., E. Bogel-Lukasik, and R. Bogel-Lukasik, *Ionic Liquid-Mediated Formation of 5-Hydroxymethylfurfural-A Promising Biomass-Derived Building Block.* Chemical Reviews, 2011. **111**(2): p. 397-417.
59. Zhou, L.L., et al., *One-step degradation of cellulose to 5-hydroxymethylfurfural in ionic liquid under mild conditions.* Carbohydrate Polymers, 2015. **117**: p. 694-700.
60. Zhu, Y.H., et al., *Conversion of Cellulose to Hexitols Catalyzed by Ionic Liquid-Stabilized Ruthenium Nanoparticles and a Reversible Binding Agent.* Chemsuschem, 2010. **3**(1): p. 67-70.
61. Li, C.Z., Z.H. Zhang, and Z.B.K. Zhao, *Direct conversion of glucose and cellulose to 5-hydroxymethylfurfural in ionic liquid under microwave irradiation.* Tetrahedron Letters, 2009. **50**(38): p. 5403-5405.
62. Hu, S.Q., et al., *Efficient conversion of glucose into 5-hydroxymethylfurfural catalyzed by a common Lewis acid SnCl4 in an ionic liquid.* Green Chemistry, 2009. **11**(11): p. 1746-1749.
63. Yu, S., et al., *Single-step conversion of cellulose to 5-hydroxymethylfurfural (HMF), a versatile platform chemical.* Applied Catalysis a-General, 2009. **361**(1-2): p. 117-122.
64. Qi, X.H., et al., *Fast Transformation of Glucose and Di-/Polysaccharides into 5-Hydroxymethylfurfural by Microwave Heating in an Ionic Liquid/Catalyst System.* Chemsuschem, 2010. **3**(9): p. 1071-1077.
65. Wang, P., et al., *Catalytic hydrolysis of lignocellulosic biomass into 5-hydroxymethylfurfural in ionic liquid.* Bioresource Technology, 2011. **102**(5): p. 4179-4183.
66. Binder, J.B., et al., *Synthesis of Furfural from Xylose and Xylan.* Chemsuschem, 2010. **3**(11): p. 1268-1272.
67. Cai, C.M., et al., *Coupling metal halides with a co-solvent to produce furfural and 5-HMF at high yields directly from lignocellulosic biomass as an integrated biofuels strategy.* Green Chemistry, 2014. **16**(8): p. 3819-3829.

2. Experimental Methods and Modeling

2.1. Ionic Liquid Synthesis

2.1.1. [HMIm][Br]

The ionic liquid 1-hexyl-3-methylimidazolium bromide [HMIm][Br] was synthesized from 1-bromohexane and 1-methylimidazole by a thermally driven quaternization reaction. The reaction mixture was prepared by charging a measured quantity of 1-methylimidazole into a round bottom flask containing a stir bar. Next, a 1:1 mol ratio of reaction solvent acetonitrile, relative to 1-bromohexane, was added to the flask to mitigate heat effects as the reaction is *highly exothermic*. Finally, a 6 mass% excess of 1-bromohexane relative to the mass of 1-methylimidazole was added. The flask headspace was purged with an inert gas (N_2, Ar, *etc.*) and stoppered. The reaction was placed on a hot plate (IKA RCT Basic) at 80^{o}C and allowed to react for ~7 days under vigorous mixing conditions. Prior to purification, [HMIm][Br] conversion was measured by proton (^{1}H) NMR by analytically quantifying reactant and product peaks. After conversion reached ~99% the ionic liquid was placed on a Buchi rotary evaporator at 60^{o}C and 100 mBar for one hour to remove acetonitrile. The [HMIm][Br] was then washed three times with ethyl acetate to remove residual unreacted 1-bromohexane and 1-methylimiazole. The ionic liquid was again put on the rotovap for one hour at 60^{o}C and 100 mBar to remove ethyl acetate. Finally, the [HMIm][Br] sample was placed on high vacuum ($P < 10^{-4}$ Torr) at 100^{o}C for 2 days to remove trace impurities including water, excess reactants, and residual acetonitrile. Water content on the IL was measured using a Mettler Toledo DL32 Karl Fisher Coulometric titrator. IL purity was measured by proton NMR on a Bruker Avance 400 MHz spectrometer. All [HMIm][Br] utilized in this study met the minimum specifications of: $H_2O < 500$ ppm and

purity > 99%. Proton NMR chemical shifts of [HMIm][Br] prepared in deuterated chloroform (relative to TMS internal standard) are as follows: δ (ppm) 10.23 (s, 1H), 7.64 (s, 1H), 7.47 (s, 1H), 4.24 (t, 2H), 4.05 (s, 3H), 1.85 (q, 2H), 1.24 (m, 6H), 0.78 (t, 3H).

2.1.2. [BMIm][Cl]

The ionic liquid 1-butyl-3-methylimdazolium chloride was synthesized from 1-methylimidazole and 1-chlorobutane by a similar procedure to that described for [HMIm][Br] in section 2.1.1. All [BMIm][Cl] utilized in this study met the minimum specifications of: H_2O < 500 ppm and purity > 99%. Proton ^{1}H NMR chemical shifts of [BMIm][Cl] prepared in deuterated chloroform (relative to TMS internal standard) are as follows: $\delta \times 10^{-6}$: 9.95 (1H, s, NC*H*N), 7.32 (1H, s, NC*H*CHN), 7.20 (1H, m, NCHC*H*N), 3.81 (2H, t, $NCH_2(CH_2)_2CH_3$), 3.58 (3H, s, NCH_3), 1.36 (2H, m, $NCH_2CH_2CH_2CH_3$), 0.81 (2H, m, $N(CH_2)_2CH_2CH_3$), 0.39 (3H, t, $N(CH_2)_3CH_3$).

2.1.3. [EMIm][DEP]

The ionic liquid 1-ethyl-3-methylimidazolium diethyl phosphate [EMIm][DEP], was synthesized by a solvent free, microwave reaction method. Thermal synthesis preparation methods were attempted but the reaction was prohibitively slow reaching less than 75% conversion after 30 days at 100^{o}C. Alternatively, [EMIm][DEP] synthesis in the microwave reactor (Biotage Initiator) was able to reach ~99% conversion in 100 minutes at a reaction temperature of 170^{o}C. Equal molar quantities of 1-methylimiazole and triethyl phosphate were added to a 1L glass bottle and stored under an inert gas atmosphere. A 15 mL aliquot of the reaction mixture was charged into a microwave reaction vial and sealed by a crimp top cap. The vial was then inserted into the microwave reactor and set to react at the previously specified time and temperature.

Most often a series of reactions were performed to make ~250 mL batches of [EMIm][DEP] at a time. Trace impurities from unconverted reactants were removed by liquid-liquid extraction with ethyl acetate. The purified ionic liquid was subsequently placed on a rotary evaporator at 60^{o}C and 100 mBar for one hour to remove residual ethyl acetate. Finally the IL was placed on high vacuum for two days at 100^{o}C to remove water. All [EMIm][DEP] utilized in this study met the minimum specifications of: H_2O < 300 ppm and purity > 99%. Proton ^{1}H NMR chemical shifts of [EMIm][DEP] prepared in deuterated chloroform (relative to TMS internal standard) are as follows: $\delta \times 10^{-6}$: 9.92 (1H, s, NC*H*N), 7.22 (1H, s, NC*H*CHN), 7.18 (1H, s, NCHC*H*N), 3.77 (2H, q, NC*H*$_2$CH$_3$), 3.46 (3H, s, NC*H*$_3$), 3.31 (4H, m, P(OC*H*$_2$CH$_3$)$_2$), 0.95 (3H, t, NCH$_2$C*H*$_3$), 0.57 (6H, t, P(OCH$_2$C*H*$_3$)$_2$).

2.2. Phase Equilibrium Measurements

2.2.1. Isobaric Vapor-Liquid Equilibrium

A modified Othmer style recirculation still (Ace Glass) was used to obtain vapor-liquid equilibrium measurements at atmospheric pressure. The still, shown in Figure 2.1, contains a liquid sampling port and a condenser that allows the condensate to be sampled before returning to the bottom of the still. Heating is provided by a Ni/Cr heating coil immersed in the liquid phase that is controlled by a Variac, Inc. controller. Fiberglass insulation tape was placed around the exterior of the cell to minimize temperature fluctuations. In all cases, a 300 mL sample was charged to the still and heated. Equilibrium of the liquid and vapor phases was established in approximately 30 minutes for each trial as indicated by the stabilization of the vapor/liquid interfacial temperature and consistent liquid phase compositions. An additional 15 minutes were provided per trial after temperature stabilization to ensure the system had reached equilibrium.

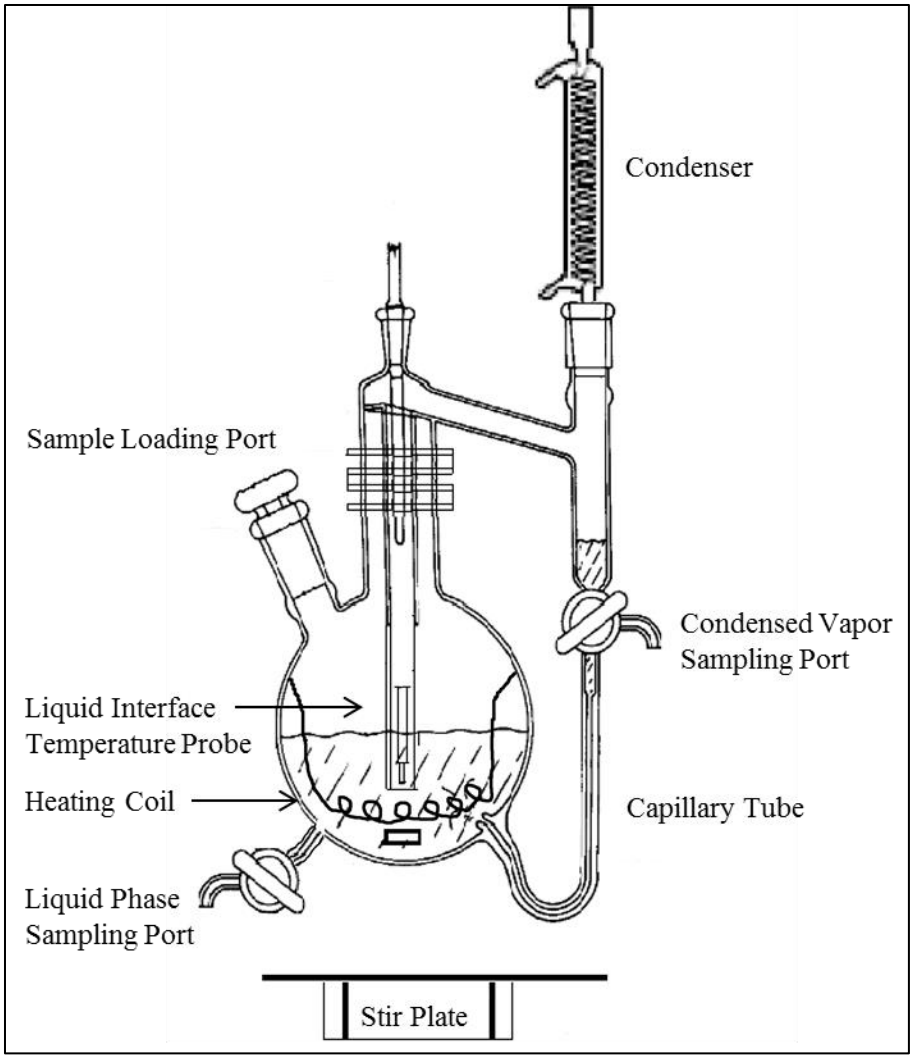

Figure 2.1: Modified Othmer Still diagram adapted from [1].

Temperature measurements were taken by a RTD temperature probe (Hart Scientific) calibrated against a NIST-traceable thermistor (Ertco, Inc.) with an accuracy of at least ±0.1 K at the highest temperatures and ±0.02 K at the lower temperatures, *i.e.* <100°C. The vapor phase was condensed by a water-cooled jacket condenser and returned to the still through the vapor phase sampling port for recirculation. Condensed vapor and liquid samples were obtained via their respective ports and cooled to room temperature prior to analysis. A refractometer (Reichert,

Inc., Abbe Mark II) with an uncertainty of +/- 0.0001 was used to analyze the vapor and liquid samples. Temperature of the spectrometer was maintained constant at 20.4°C by a water bath and fluctuated by less than 0.1°C. Sample composition was determined from a calibration curve of gravimetrically prepared standard solutions (Mettler Toledo) with an accuracy of 0.1 mg. Experimentally measured liquid and vapor samples had a mole fraction uncertainty range [u(x)=u(y)] of 0.0005 to 0.001. Atmospheric pressure was measured for each sample by a Fisher Scientific Traceable compact digital barometer accurate to +/- 5mBar. The National Institute of Standards and Testing (NIST) evaluated Sydney Young equation was applied to normalize experimental atmospheric pressures to 1.01325 bar:

$$T_{adj} = 0.0009\left(101.3 - P_{exp}\right)\left(273 + T_{exp}\right) \qquad \text{Eqn. 2.1}$$

where P_{exp} and T_{exp} are the experimentally observed pressure and temperature in kPa and degrees Celsius respectively.[2] T_{adj} is the temperature adjustment due to pressure normalization. When added to the experimentally measured boiling point, the temperature reflects the boiling point at 1.01325 bar.

2.2.2. Isothermal Vapor-Liquid Equilibrium

A static high pressure apparatus for the measurement of isothermal vapor-liquid equilibrium has previously been developed and discussed by Ren and Scurto.[3, 4] The apparatus, shown in Figure 2.2, consists of a high pressure viewcell, a 100 dM Isco syringe pump, and thermostatic water bath. Precision pressure and temperature transducers measure the P-T properties of the system and are accurate to +/- 0.01^{o}C and +/- 0.2 bar. A cathetometer is used to measure the height of the liquid meniscus which, through a calibration equation, computes the volume of the

liquid phase. Through a synthetic material balance method the apparatus calculates the solubility of compressed gases in liquid phases with a mol fraction accuracy of (x) +/- 0.001.

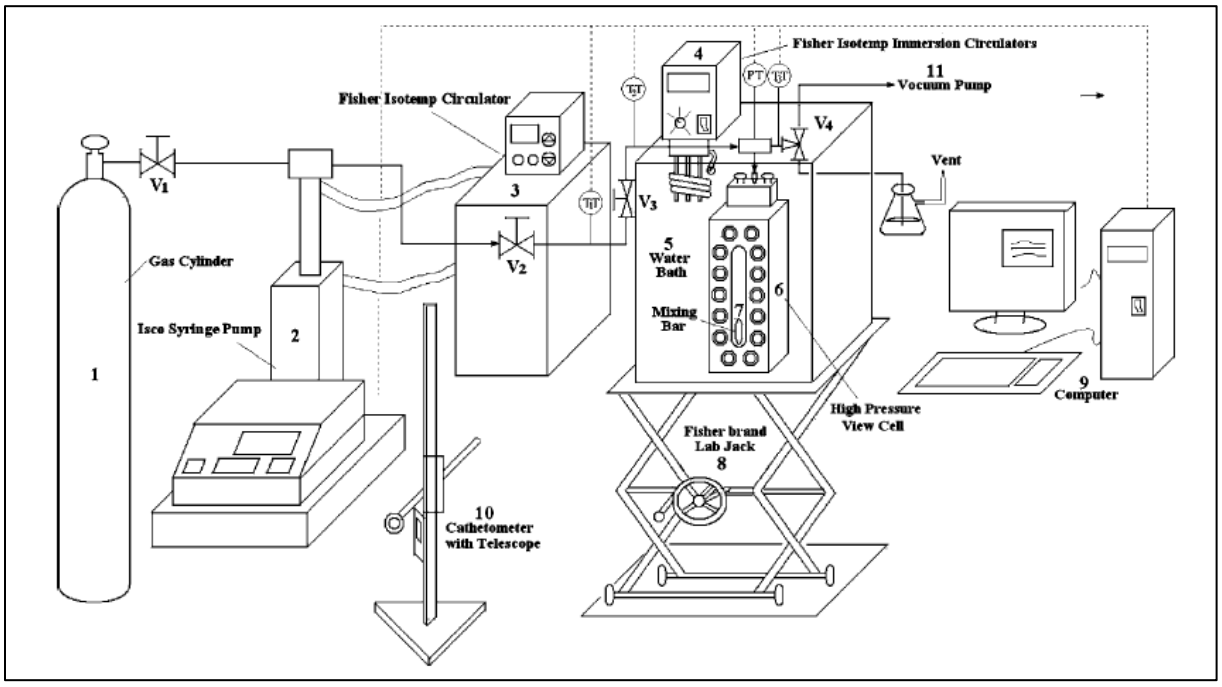

Figure 2.2: Schematic describing the detailed layout of a static high pressure apparatus for the determination of isothermal vapor-liquid equilibrium.[4]

The initial apparatus design utilized a high pressure viewcell with a total volume of 5.718 mL. Recently this component was compromised and is no longer available. Therefore, a new larger cell has been obtained for future use. The total cell volume was determined by measuring the volume displacement of nitrogen in the Isco pump needed to restore the initial pump pressure. The total cell volume was measured in triplicate to be 25.498 mL. Additionally, the incremental cell volume was determined by a height-volume calibration conducted in triplicate with n-tetradecane. The calibration equation is displayed in Eqn. 2.2:

$$V(20^oC) = 0.1548 * (H) - 0.2249$$ Eqn. 2.2

Thermal expansion of the high pressure viewcell must be considered when measuring systems at elevated temperatures. For instance, the measured cell volume at 60°C was 0.192% greater than an identical system at 20°C. Eqn. 2.3 accounts for thermal expansion of the steel cell in three dimensions. Alpha is the coefficient of linear thermal expansion for steel α=1x10^{-5} (1/K), *V(T)* is the cell volume at the temperature of interest, T is the measured cell temperature, and *V(20°C)* is the cell volume based on the calibration equation computed at 20°C : Eqn. 2.2.

$$V(T) = V(20^oC)[1 + 3\alpha(T - 20)]$$ Eqn. 2.3

For each trial an initial quantity of liquid sample was drawn into a volumetric syringe with an eight inch needle. The sample was weighed on an analytical balance (Ohaus Analytical) and carefully deposited into the bottom of the high pressure viewcell. The final mass of the syringe and needle were determined and the mass of liquid sample added to the cell was computed. The cell was then connected to the high pressure line, purged three times with the compressed gas of interest, and subsequently placed in the thermostatic water bath for 30 minutes to reach thermal equilibrium. For each phase equilibrium data point, compressed gas was slowly added to the viewcell until the desired pressure was reached. During this process vigorous mixing of the vapor-liquid interface was achieved by a magnetic stirbar contained within the viewcell. Vapor-liquid equilibrium was determined by the stabilization of the cell pressure and temperature for at least 30 minutes. Mass of the compressed gas added to the liquid phase (*i.e.* gas solubility) was determined by measuring the difference between initial and final pump volumes while accounting for the volume of the high pressure lines and cell headspace through the mass balance

method previously detailed.[4] Additional calculations including liquid phase molar volume, volume expansion, molarity, and molality are also possible using the mass balance method.

2.2.3. Isothermal Vapor-Liquid-Liquid Equilibrium

The same isothermal vapor-liquid equilibrium device described in section 2.2.2 has also been recently applied for the determination of three-component, three-phase, vapor-liquid-liquid equilibrium measurements. The Gibbs Phase Rule is shown in Eqn. 2.4 where (*DOF*) indicates the degrees of freedom that exist for a phase equilibrium system, (*C*) is the number of components, and (*P*) is the number of phases.

$$DOF = C - P + 2 \qquad \text{Eqn. 2.4}$$

For a three-component, three-phase system two degrees of freedom exist. The static high pressure isothermal phase equilibrium method requires specification of the system temperature and pressure thereby restricting all other intensive variables including phase composition and molar volume. For instance, if three different loadings are investigated in the VLLE region at identical temperatures and pressures the resulting systems will flash into three phases of identical composition irrespective of initial loading.

Determination of vapor-liquid-liquid equilibrium phase compositions requires measuring the phase equilibrium of three distinctly different initial component loadings at a specified temperature and pressure. As described in section 2.2.2, the initial loading of liquid components is known by measurement on an analytical balance and moles of CO_2 are determined by the volume change of the Isco pump, height of the liquid phases as measured by the cathetometer, and the mass balance method. From the phase equilibrium results of the three loadings, a system

of nine equations and nine unknowns is developed and can be solved for the mole fraction phase compositions and molar volumes. The equations are specified as follows:

Loading 1

Component 1: $N_1 = x_1^I \frac{V^I}{\underline{V}^I} + x_1^{II} \frac{V^{II}}{\underline{V}^{II}} + y_1 \frac{V^V}{\underline{V}^V}$ Eqn. 2.5

Component 2: $N_2 = \left(1 - x_1^I - x_3^I\right)\frac{V^I}{\underline{V}^I} + \left(1 - x_1^{II} - x_3^{II}\right)\frac{V^{II}}{\underline{V}^{II}} + \left(1 - y_1 - y_3\right)\frac{V^V}{\underline{V}^V}$ Eqn. 2.6

Component 3: $N_3 = x_3^I \frac{V^I}{\underline{V}^I} + x_3^{II} \frac{V^{II}}{\underline{V}^{II}} + y_3 \frac{V^V}{\underline{V}^V}$ Eqn. 2.7

Loading 2

Component 1: $N_1' = x_1^I \frac{V^{I'}}{\underline{V}^I} + x_1^{II} \frac{V^{II'}}{\underline{V}^{II}} + y_1 \frac{V^{V'}}{\underline{V}^V}$ Eqn. 2.8

Component 2: $N_2' = \left(1 - x_1^I - x_3^I\right)\frac{V^{I'}}{\underline{V}^I} + \left(1 - x_1^{II} - x_3^{II}\right)\frac{V^{II'}}{\underline{V}^{II}} + \left(1 - y_1 - y_3\right)\frac{V^{V'}}{\underline{V}^V}$ Eqn. 2.9

Component 3: $N_3' = x_3^I \frac{V^{I'}}{\underline{V}^I} + x_3^{II} \frac{V^{II'}}{\underline{V}^{II}} + y_3 \frac{V^{V'}}{\underline{V}^V}$ Eqn. 2.10

Loading 3

Component 1: $N_1'' = x_1^I \frac{V^{I''}}{\underline{V}^I} + x_1^{II} \frac{V^{II''}}{\underline{V}^{II}} + y_1 \frac{V^{V''}}{\underline{V}^V}$ Eqn. 2.11

Component 2: $N_2'' = \left(1 - x_1^I - x_3^I\right)\frac{V^{I''}}{\underline{V}^I} + \left(1 - x_1^{II} - x_3^{II}\right)\frac{V^{II''}}{\underline{V}^{II}} + \left(1 - y_1 - y_3\right)\frac{V^{V''}}{\underline{V}^V}$ Eqn. 2.12

Component 3: $N_3'' = x_3^I \frac{V^{I''}}{\underline{V}^I} + x_3^{II} \frac{V^{II''}}{\underline{V}^{II}} + y_3 \frac{V^{V''}}{\underline{V}^V}$ Eqn. 2.13

From these nine equations the variables $(N_1,\ N_2,\ N_3,\ N_1',\ N_2',\ N_3',\ N_1'',\ N_2'',\ N_3'')$ are the moles of the three components in the cell at equilibrium. The two liquid components are determined by the initial gravimetric loading while the moles of CO_2 are calculated by the mass balance method. Volumes of all three phases $\left(V^I, V^{II}, V^{III},\ V^{I'}, V^{II'}, V^{III'}, V^{I''}, V^{II''}, V^{III''}\right)$ are measured experimentally by the cathetometer. Therefore, nine unknowns remain including the mole fractions of each component in each phase and the molar volumes of each phase $\left(x_1^I, x_3^I, x_1^{II}, x_3^{II}, y_1, y_3, \underline{V}^I, \underline{V}^{II}, \underline{V}^V\right)$. By convention, component (1) is CO_2, component (2) is water, and component (3) is acetone. Phase (I) is the lowest liquid phase (H_2O rich), phase (II) is the middle liquid phase (acetone rich), and the vapor phase (V) is CO_2 rich. N_i indicates loading (1) which was 40 mass% acetone and 60 mass% water, $N_i^{'}$ indicates loading (2) and was 50 mass% acetone and 50 mass% water, and $N_i^{''}$ indicates loading (3) which was 60 mass% acetone and 40 mass% water. Careful measurements were made for each loading to ensure that the temperature was within +/- 0.01^{o}C and pressure was +/- 0.05 bar of the target value.

Determination of the unknown parameters requires the simultaneous solution of the nine non-linear equations presented above. If one can accurately assume that the vapor phase is pure compressed gas $(y_1 \approx 1\ and\ y_2 = y_3 = 0)$ then the equations can be reduced to a series of six equations and six unknowns. In this preliminary solution the 9 equation 9 unknown system was solved using the Microsoft Excel solver function with the constraint that all mole fraction values must be in the range: (0<x, y<1). Additionally, the vapor phase molar volume was restricted not to be larger than the molar volume of pure CO_2 at the system temperature and pressure. Initial guesses were made for the system variables as follows: $x_1^I = 0.05, x_1^{II} = 0.50, x_1^v = 1.00, x_3^I =$

$0.25, x_3^{II} = 0.50, x_3^{v} = 0.00, MV^{I} = 25\ \frac{cm^3}{mol}, MV^{II} = 50\ \frac{cm^3}{mol}, MV^{v} = MV_{CO2}(T, P)$. Unknown variables were optimized using the following objective function by minimizing F_T.

$$F_1 = Eqn.\,2.5 + Eqn.\,2.8 + Eqn.\,2.11 \qquad \text{Eqn. 2.14}$$

$$F_2 = Eqn.\,2.6 + Eqn.\,2.9 + Eqn.\,2.12 \qquad \text{Eqn. 2.15}$$

$$F_3 = Eqn.\,2.7 + Eqn.\,2.10 + Eqn.\,2.13 \qquad \text{Eqn. 2.16}$$

$$F_T = 0 = F_1 + F_2 + F_3 \qquad \text{Eqn. 2.17}$$

A proof of concept study was conducted on acetone, water, and carbon dioxide to validate the above method. Table 2.1 and Table 2.2 present a direct comparison of the experimental and literature results from Mauer *et al.* and the corresponding error analysis.[5] Absolute average mole fraction errors in the three phases were: L(1) = 0.011, L(2) = 0.030, and V = 0.000. The largest mole fraction error was observed in the acetone rich (middle) phase. This could be due to the added experimental error of relying on two independent meniscus height measurements and/or the optimization algorithm. An increased deviation of the experimental data from literature was also observed at elevated pressures. For instance, at 32.10 bar the percent absolute average relative deviation (%AARD) between experimental and literature values was 8.64%. At 39.98 bar the %AARD was 12.28% and at 51.00 bar the deviation was 12.56%. Increased error at elevated pressures is likely due to the inability of the synthetic method to measure the concentration of volatile organic compounds in the vapor phase. Nonetheless, the proof of concept study demonstrated herein displays that this synthetic method is applicable for the measurement of three component, three phase, vapor-liquid-liquid equilibrium with moderate accuracy.

Data Type	Temp (K)	Pressure (bar)	Liquid Phase I				Liquid Phase II				Vapor Phase			
			X CO_2	X Ace	X H_2O	MV	X CO_2	X Ace	X H_2O	MV	X CO_2	X Ace	X H_2O	MV
Lit.	313.15	32.10	0.033	0.816	0.151	26.41	0.318	0.196	0.486	54.21	1.000	0.000	0.000	688.27
Exp.	313.19	32.15	0.018	0.823	0.159	30.28	0.309	0.166	0.525	55.79	1.000	0.000	0.000	688.27
Lit.	313.15	39.88	0.031	0.865	0.104	23.88	0.454	0.115	0.431	55.46	1.000	0.000	0.000	525.81
Exp.	313.19	39.98	0.015	0.870	0.115	26.39	0.456	0.071	0.473	60.87	1.000	0.000	0.000	525.81
Lit.	313.15	51.02	0.025	0.912	0.063	21.63	0.617	0.064	0.319	54.91	1.000	0.000	0.000	376.95
Exp.	313.19	51.14	0.011	0.928	0.061	24.90	0.610	0.039	0.352	57.49	1.000	0.000	0.000	376.88

Table 2.2: Vapor-liquid-liquid equilibrium results obtained by the synthetic mass balance method for a three component carbon dioxide, acetone, water system compared to published literature data by Maurer et al.

Error Type	Temp (K)	Pressure (bar)	Liquid Phase I				Liquid Phase II				Vapor Phase			
			X CO_2	X Ace	X H_2O	MV	X CO_2	X Ace	X H_2O	MV	X CO_2	X Ace	X H_2O	MV
Absolute	313.15	32.10	0.015	0.007	0.008	3.87	0.009	0.030	0.039	1.58	0.000	0.000	0.000	0.00
%AARD	313.19	32.15	43.73	0.89	5.17	14.66	2.85	15.18	7.99	2.91	0.000	0.000	0.000	0.00
Absolute	313.15	39.88	0.016	0.005	0.011	2.51	0.002	0.044	0.042	5.41	0.000	0.000	0.000	0.00
%AARD	313.19	39.98	50.63	0.57	10.39	10.52	0.48	38.67	9.81	9.76	0.000	0.000	0.000	0.00
Absolute	313.15	51.02	0.014	0.016	0.002	3.27	0.007	0.025	0.033	2.58	0.000	0.000	0.000	0.07
%AARD	313.19	51.14	57.97	1.76	2.52	15.14	1.21	39.32	10.22	4.70	0.000	0.000	0.000	0.02

Table 2.1: Vapor-Liquid-Liquid equilibrium error analysis between measured and literature data.

2.2.4. Liquid-Liquid Equilibrium

Isobaric liquid-liquid equilibrium experiments were conducted in sealed 20mL vials at atmospheric pressure. Phase equilibrium was established at constant temperature and controlled by an IKA RCT Basic hot plate with an aluminum block that surrounded the vials. Temperature measurements of the samples were obtained by the same probe described in section 2.2.1 and trials and were accurate to at least $\pm 0.1^{o}$C or better. Effective mass transfer and phase equilibrium was accomplished by vigorous stirring over a period of 24 hours followed by settling. Samples were obtained and prepared for quantitative NMR (QNMR) analysis (section 2.3.3.2) in deuterated chloroform (Cambridge Isotopes) using a Bruker Avance 400 MHz NMR-spectrometer. ^{1}H NMR acquisition parameters consisted of 10 scans with a relaxation delay time (d_1) of 30 seconds as determined by (T_1) analysis to ensure all nuclei had fully relaxed prior to subsequent pulsing. Sample composition was accurate to [u(x)] 0.001.

2.2.5. Solid-Liquid Equilibrium

Solid liquid equilibrium measurements for cellulose in pure ionic liquid [EMIm][DEP] and IL/solvent mixtures were obtained by an optical cloud point method. For each trial ionic liquid and solvent (when applicable) were added into a 20 mL glass scintillation vial and sealed. The relative masses of the components were obtained by a gravimetric balance (Mettler Toledo) accurate to 0.1 mg. The samples were heated to the desired temperature in aluminum pie blocks to ensure uniform temperature distribution on a thermostatic hot plate (IKA RCT Basic) calibrated by a NIST Traceable RTD temperature probe, accurate to +/- 0.1^{o}C. After reaching the desired temperature, cellulose was massed out and quantitatively added to the liquid sample, the vials were then sealed and allowed to equilibrate under constant mixing by rare earth metal

stir bars (Bel-Art). This process was repeated until the liquid sample transitioned from a clear/transparent state to one that was opaque/cloudy indicating cellulose saturation within the liquid sample. Dissolution times ranged from minutes to hours for different samples and contrary to previous reports, extended dissolution times up to 48 hours should be provided to ensure that true thermodynamic equilibrium is established as highly viscous systems require extended time scales for dissolution. All solid-liquid equilibrium measurements were replicated to confirm the saturation point. Solvent concentration is reported on a solute (cellulose) free basis while cellulose concentration is reported on a total solution basis. The saturation point measurements were accurate to [u(x)] +/- 0.2 mass%.

$$mass\%\ solvent = \frac{mass\ solvent}{mass\ solvent + mass\ IL} \qquad \text{Eqn. 2.18}$$

$$mass\%\ Cellulose\ Solubility = \frac{mass\ cellulose}{mass\ cellulose + mass\ solvent + mass\ IL} \qquad \text{Eqn. 2.19}$$

2.2.6. Autoclave Viewcells

Autoclave viewcells were utilized to observe global phase transitions at elevated pressures (*i.e.* vapor-liquid to vapor-liquid-solid and vapor-liquid to vapor-liquid-liquid). The cells consist of a stainless steel body with two end caps and an internal volume of ~5mL. The end caps are assembled by first inserting the O-ring assembly, followed by the viewcell window, spacer, and threaded nut. The cells consisted of an HIP valve to control pressure, a pressure transducer, and a port for a temperature probe. All parts of the autoclave are depicted in Figure 2.3.

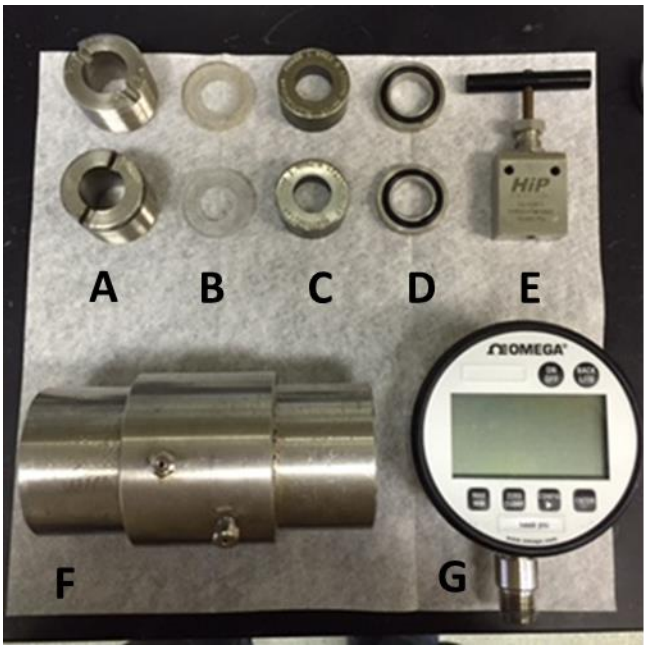

Figure 2.3: Autoclave parts: A) threaded nut, B) plastic spacer, C) viewcell, D) O-Ring assembly, E) HIP valve, F) autoclave body, G) Omega pressure transducer.

For the high pressure cellulose precipitation studies, mixtures of IL [EMIm][DEP] and cosolvent (DMF used here for illustration purposes) were prepared in sealed glass vials and mechanically mixed by a rare earth metal magnetic stir bar. Microcrystalline cellulose was fed into the vial at 80^{o}C with constant mixing. Cellulose was dissolved in approximately 10 minutes. The homogeneous IL/DMF/cellulose solution was then cooled to room temperature and loaded into a steel autoclave cell. The resulting cellulose compositions at room temperature were always sub-saturated. Compressed CO_2 was added into the autoclave cell by a high-pressure syringe pump (ISCO 260D) and temperature was maintained by a thermostatic hot plate (IKA RCT Basic). CO_2 was dosed to a loading just prior to cellulose precipitation and allowed to equilibrate for approximately 20 minutes. Mixing inside of the autoclave was accomplished by a stir bar. After reaching equilibrium an additional small quantity of CO_2 was added to the cell and cellulose precipitation was visually determined by cloud point analysis, rapid viscosity increase, and the

presence of solid amorphous cellulose within the cell. Precipitation trials were repeated in triplicate both from lower to higher pressure and higher pressure to lower pressure to confirm the separation point. Separation pressures were measured accurate to +/- 1 bar.

2.3. Chemical Analysis

2.3.1. Karl Fisher Coulometric Titration

Water content of the ionic liquids and organic solvents were measured by Karl Fisher (KF) coulometric titration. The titration operates by generation of I_2 from I^- in solution at the platinum anode of the KF. The I_2 subsequently oxidizes SO_2 in solution based on the stoichiometric amount of water present in the sample per Eqn. 2.20 and 2.21.[6]

$$ROH + SO_2 + R'N \rightarrow (R'NH)SO_3R \qquad \text{Eqn. 2.20}$$

$$(R'NH)SO_3R + H_2O + I_2 + 2R'N \rightarrow (R'NH)I + (R'NH)SO_4R \qquad \text{Eqn. 2.21}$$

The titration end point is reached when excess I_2 appears in solution and a sizable voltage drop occurs thus indicating the equivalence point has been reached. Based on the energy required to produce the stoichiometric quantity of I_2 consumed the amount of water in solution is computed.

For each measurement approximately 1 mL of sample was drawn into a 5mL syringe through a needle. The needle should be 16G or larger when working with ILs as they are highly viscous and can be difficult to inject. The sample was initially weighed on an analytical balance (Mettler Toledo) accurate to 0.0001 mg. After pre-titrating the working solution the sample was slowly added to ensure that splashing did not occur. The vessel was carefully inspected to ensure that

viscous ionic liquid dissolved into solution and did not accumulate on the glass walls. The emptied syringe and needle were again massed to obtain the amount of sample added to the Karl Fisher. Upon reaching equilibrium the water content in ppm was calculated. The Karl Fisher was calibrated with Hydranal water standards at 100 ppm and 1000 ppm and was accurate to +/- 20 ppm on any measurement in that range.

2.3.2. Refractive Index Spectroscopy

Refractive index (RI) spectroscopy is a universal detection method based on the bending of light after transmission through a sample. A refractometer (Reichert, Inc., Abbe Mark II) with an uncertainty of +/- 0.0001 was used to analyze the vapor and liquid samples in the ionic liquid synthesis solvent selection project. Temperature of the spectrometer was maintained constant at 20.4°C by a water bath and fluctuated by less than 0.1°C. Sample composition was determined from a calibration curve of gravimetrically prepared standard solutions (Mettler Toledo) with an accuracy of 0.1 mg. Experimentally measured liquid and vapor samples had a mole fraction uncertainty range [u(x)=u(y)] of 0.0005 to 0.001.

2.3.3. Nuclear Magnetic Resonance (NMR) Spectroscopy

Nuclear magnetic resonance (NMR) spectroscopy is an analytical technique used for the qualitative detection and quantitative analysis of components within a sample. The technique is particularly advantageous as it is non-destructive to the sample, fast, moderately inexpensive, and reliable. In this study, NMR was applied for the analysis of ionic liquid synthesis samples, the quantification of phase equilibrium mixtures, the analysis of IL properties at high pressure, and the determination of cellulose crystallinity.

2.3.3.1. Proton [^{1}H] NMR

Atomic nuclei within a molecule spin according to the number of protons and neutrons they contain thus generating a randomly oriented magnetic moment. When placed in a strong magnetic field (B_o) the nuclei align in the direction of the field. The theory of NMR is formed on the basis of manipulating the magnetic moments of atomic nuclei and measuring their response. As shown in Figure 2.4, a radio frequency pulse is applied to the sample perpendicular to (B_o) causing select nuclei absorb energy and shift to a new orientation relative to the magnetic field.

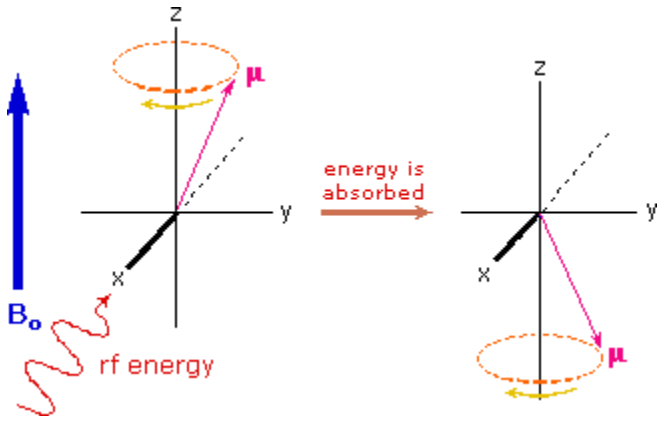

Figure 2.4: 90^o NMR radio frequency pulse inverting the spin of a nucleus.[7]

When the pulse is turned off the nuclei relax and re-align with the original magnetic field (B_o). Energy emitted by the relaxing nuclei is detected forming a free induction decay (FID) signal. Through a Fourier transform process the FID signal is converted from time domain to frequency domain thus generating the NMR spectrum. The proton NMR the spectrum ranges from 0-13 ppm. Field shifts of protons in the NMR spectrum are determined by the chemical environment (*i.e.* electrons) surrounding the atomic nucleus. A difference between the applied and the effective magnetic field felt by the nucleus occurs based on the degree of shielding provided by

the electrons around a nucleus. Field shifts in proton NMR are measured relative to tetramethylsilane (TMS) which has the highest degree of electron shielding. The corresponding NMR proton [^{1}H] peak for TMS is typically set at 0.00 ppm and all other shifts are measured relative to this benchmark. Figure 2.5 displays a diagram of peak shifts and spin-spin coupling for common functional groups in proton NMR. Spin-spin coupling is generated by interactions between protons on neighboring atoms and appears as multiplicity in NMR peaks. Multiplicity is determined by counting the number of neighboring protons and adding one (*i.e.* n+1 rule) due to the different interference patterns neighboring protons have. Further detailed explanations of NMR theory can be found in a comprehensive text by Gunther *et al*.[8]

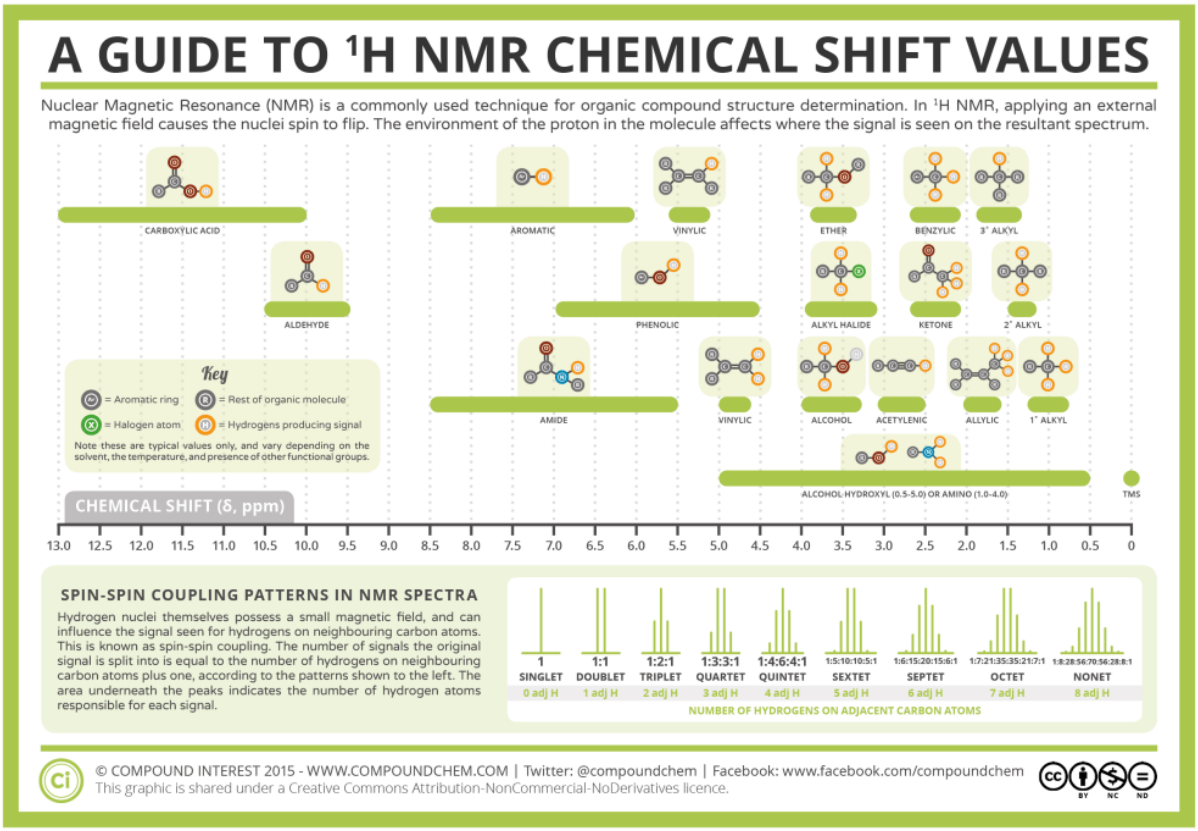

Figure 2.5: Proton NMR peak shifts and spin coupling patterns for common functional groups.[9]

Proton NMR has been utilized throughout this study for a variety of applications. Most specifically, NMR peak shift theory was applied to investigate the interactions between polar protic and polar aprotic cosolvents with ionic liquids in section 3.6.3. As electron shielding causes proton peak shifts, NMR can be used to analyze the chemical (*i.e.* solvent) environment surrounding an ionic liquid.[10, 11] Downfield shifts (higher ppm) indicate reduced electron shielding and thus fewer interactions between molecules in solution while upfield shifts (lower ppm) indicate increased interactions between ILs and the solvent environment. Figure 2.6

demonstrates the peak shift effect that varying concentrations of water have on the acidic proton 2 of the [EMIm] cation due to increased electron shielding.

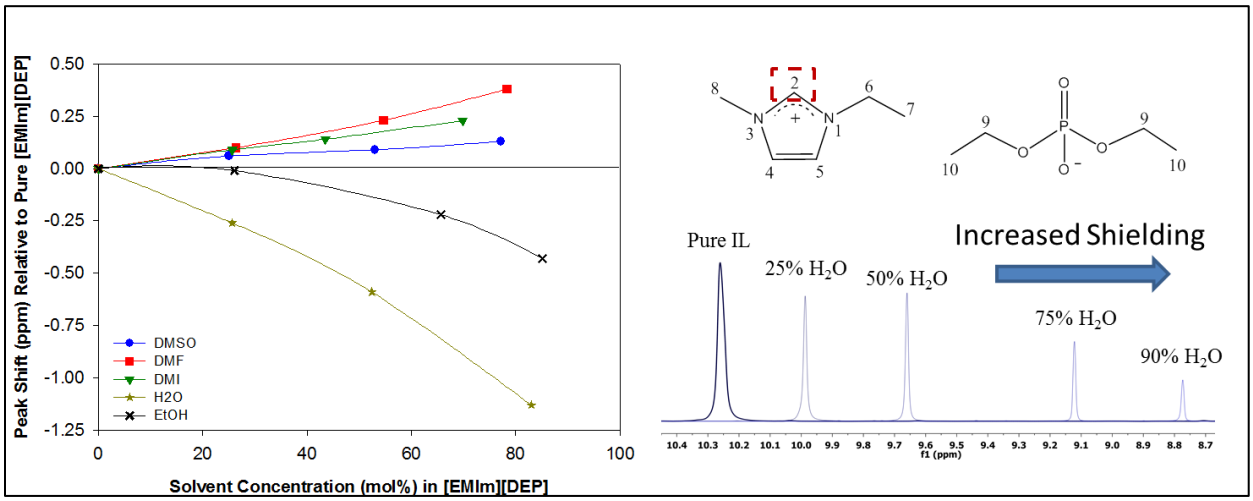

Figure 2.6: Chemical shifts on proton 2 of the [EMIm] cation due to solvation by water.

Proton NMR has additionally been used for the qualitative detection of species in a sample. The spectral database for organic compounds presents a substantial catalog of NMR peak shifts for common chemicals and has been an excellent resource for compound identification.[12]

2.3.3.2. Quantitative Proton [^{1}H] NMR

The signal from proton [^{1}H] NMR is directly proportional to molar concentration of protons in a sample when it is generated by full relaxation of pulsed nuclei. Therefore, proton NMR can be utilized for quantitative purposes when the acquisition parameters are set such that all nuclei in the sample fully relax between pulse cycles. Longitudinal relaxation time measurements, performed by T_1 analysis, determine the length of time required for nuclei to relax after a pulse sequence. For quantitative NMR, the instrument delay time (d_1) which sets the time between

pulses is conventionally set at 5 times the T_1 value ($d_1=5*T_1$) to ensure full relaxation of the sample.

Proton NMR is particularly advantageous for the quantitative determination of analytes in solution as the method does not require a calibration curve. Alternatively, an internal standard must be used as ^{1}H NMR measures proton concentration proportional to peak area. Ideal internal standards are chemically inert, have low volatility, have high stability, and known concentrations in the sample. Therefore, ionic liquids are advantageous for this purpose provided their negligible vapor pressures, thermal stability, and inert nature. The concentration of an analyte in solution is calculated according to Eqn. 2.22 by comparing a ratio of peak areas and concentration where N_{ref} is the number of moles of the internal standard, A_{unk} is the area of the analyte peak, A_{ref} is the area of the internal standard peak, I_{unk} is the number of protons corresponding to the analyte peak, and I_{ref} is the number of protons corresponding to the reference peak.

$$N_{unk} = N_{ref} * \frac{\left(\frac{A_{unk}}{I_{unk}}\right)}{\left(\frac{A_{ref}}{I_{ref}}\right)} \qquad \text{Eqn. 2.22}$$

The quantitative NMR method presented has been applied for the purity analysis of all in-house synthesized ionic liquid samples, the determination of phase equilibrium samples for the dichloromethane vapor-liquid equilibrium study, and for product quantification in the 5-HMF reaction study.

2.3.3.3. High Pressure Proton [^{1}H] NMR

High pressure NMR experiments were performed in sealed 10mm sapphire NMR tubes shown in Figure 2.7. Three sapphire 10mm tubes were custom grown by Saint Gobain Crystals and high pressure valve stems were custom fabricated at the University of Kansas by Geoff Aiken and Allen Walker.

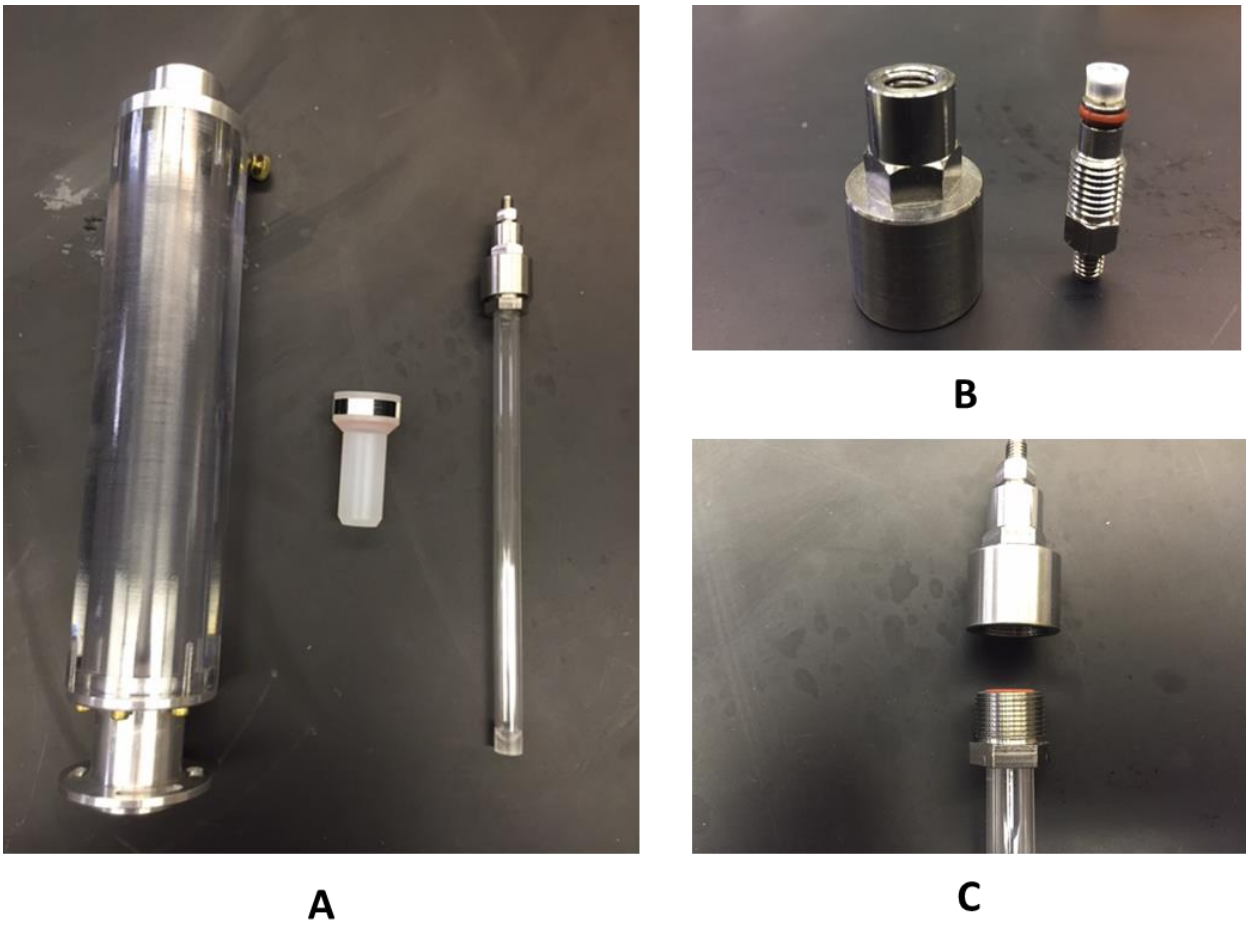

Figure 2.7: A) High pressure 10mm sapphire NMR tube, spinner, and protective shell B) Valco high pressure connection and custom fabricated valve stem C) Valve and NMR tube connection.

The high pressure NMR tubes were utilized to measure the chemical interactions between compressed carbon dioxide and select ionic liquids [EMIm][DEP] and [EMIm][Ac] at elevated pressures. Gravimetrically prepared samples were loaded into the NMR tube and pressurized to 100 bar by a syringe pump (ISCO 260D). Samples were provided 72 hours to equilibrate prior to testing. A Bruker Avance 500 MHz NMR-spectrometer was used to process the samples. Due to a broken proton channel, only coupled ^{13}C-^{1}H results were obtained. Acquisition parameters for the high pressure NMR consisted of 128 scans with a delay time (d_1) of 5 seconds.

2.3.3.4. Solid State Carbon [^{13}C] NMR

Solid state NMR was utilized to measure the degree of crystallinity of microcrystalline cellulose before and after ionic liquid pretreatment. Cross polarization/magic angle spinning (CP/MAS) solid state ^{13}C NMR experiments were performed on a Bruker Avance 500 MHz spectrometer. Spectral parameters were set at 10240 scans with a relaxation delay time of 1 second. As a result of ionic liquid processing inter- and intra- molecular bonds within cellulose are disrupted forming amorphous cellulose. Correspondingly, the ^{13}C NMR resonances of carbon atoms C_4 and C_6 which participate in the crystalline bonding network are altered through the pretreatment process. As shown in Figure 2.8, crystalline cellulose is represented by the C_4 peak at 92 ppm while the amorphous cellulose C_4 peak is located at 87ppm.

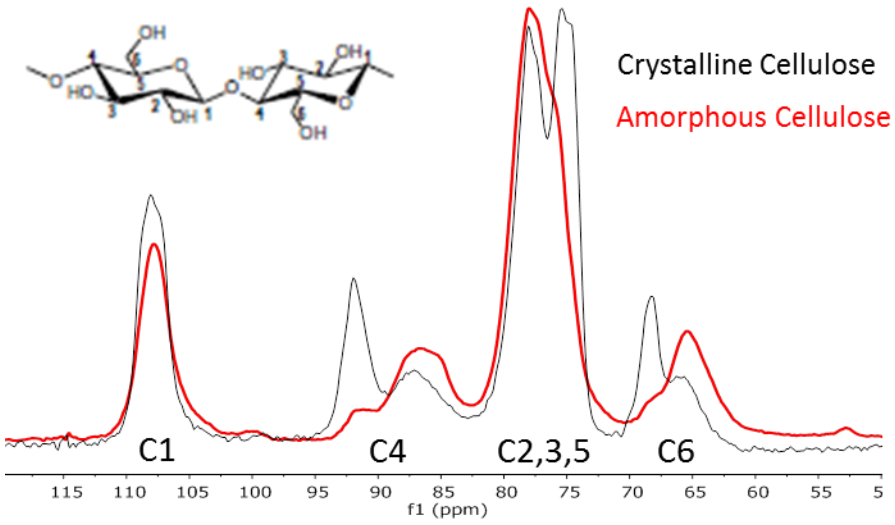

Figure 2.8: Solid State ^{13}C NMR spectra of crystalline cellulose (black) and amorphous cellulose (red). The C_4 and C_6 peaks broaden and shift as a result of the pretreatment process.

Degree of crystallinity was calculated by taking the ratio of integrated C_4 crystalline peak height to total C_4 peak height per Newman's C_4 peak separation method shown in Eqn. 2.23. Additional information describing the measurement of cellulose crystallinity by solid state NMR is provided in detail by Park *et al*.[13, 14]

$$Crystallinity\ Index = \frac{Area_{Crystalline\ C4\ Peak}}{Area_{Crystalline\ C4\ Peak} + Area_{Amorphous\ C4\ Peak}} * 100 \qquad \text{Eqn. 2.23}$$

2.3.4. Ultraviolet-Visible (UV-Vis) Spectroscopy

Ultraviolet-visible (UV-Vis) spectroscopy was applied for the analysis of solvent parameters using solvatochromic dyes as well as for the detection and quantification of products in the reaction of fructose to 5-hydroxymethylfurfural. All benchtop UV-Vis measurements were obtained using a Varian Carry 300 Bio UV-Visible dual beam spectrophotometer equipped with a dual cell Peltier accessory that facilitated temperature control and mixing of the samples. The

spectrophotometer was given one hour to warm up prior to any measurements. Sample analysis was conducted using the Carry WinUV 3.0 software. All UV-Vis measurements were obtained at atmospheric pressure and 25^{o}C using a 1cm path length quartz cuvette.

2.3.5. Kamlet Taft Solvatochromic Polarity Analysis

Kamlet Taft (KT) solvatochromic dyes including 4-nitroaniline (4-NA), N,N-diethyl-4-nitroaniline (NNDE-4-NA), and Reichardt's Betaine Dye 30 (Re.D.) were used to measure the acidity (α), basicity (β), and polarizability (π^*) of mixed ionic liquid – molecular solvent systems. Kamlet Taft parameters were calculated from the absorbance peaks of the three dye molecules in the ultraviolet and visible region of the electromagnetic spectrum. The wavelength of maximum absorbance corresponding to a particular dye depends on the identity and composition of species in its solvation sphere. Dye molecules are classified into two categories based on the direction which their absorbance band shifts in solvents of increasing polarity. Absorbance peak shifts towards shorter wavelengths indicate hypsochromic behavior and that a dye is negatively solvatochromic. Alternatively, absorbance peak shifts towards longer wavelengths (bathochromic shifts) indicate that the dye is positively solvatochromic.

Solvatochromism occurs due to the preferential stabilization of a solvatochromic probes ground and first Franck-Condon excited electronic state by its solvation shell.[15] The ground state of a negatively solvatochromic molecule is more dipolar than its excited state and experiences increasingly favorable interactions as the polarity of its solvation sphere increases. These interactions lower the energy of the solvatochromic probes ground electronic state and cause the probe to absorb light at shorter wavelengths, detected as a hypsochromic (blue) shift. For probes

that exhibit positive solvatochromism the excited state of the probe molecule is more dipolar than its ground state. Increasingly polar solvents stabilize and lower the energy of the Frank-Condon excited electronic state causing the probe wavelength of maximum absorbance to shift towards longer wavelengths of light. In this study, Reichardt's dye exhibits negative solvatochromism while NNDE-4-Na and 4-Na exhibit positive solvatochromism.

The solvatochromic shift of a dye molecule is affected by three properties of its solvation shell including: polarity, as well as the ability of the solvent to donate and accept hydrogen bonds. Through the appropriate linear combination of maximum absorbing wavelengths for each dye in the solvent system, polarizability, acidity, and basicity of a solvent can be assessed.[16-18] Polarizability (π^*) of a solvent, is calculated from the wavelength of maximum absorbance of NNDE-4-Na. Solvent basicity (β) is computed from the linear combination of spectral data for 4-Na and NNDE-4-Na. The 4-nitroaniline probe is a hydrogen bond donor that is also susceptible to polarity interactions. Alternatively, NNDE-4-Na is only affected by solvent polarity and does not participate in H-bond interactions. Therefore, solvent basicity is computed by subtracting the polarity effects, accounted for by NNDE-4-Na, from the combined contribution of solvent polarity and H-bond accepting ability which are detected by 4-Na. Solvent acidity (α) is calculated from the wavelength of maximum absorbance of Re. D, which is a hydrogen bond accepting probe molecule. Reichardt's dye is also affected by solvent polarity and therefore NNDE-4-Na is subtracted from Re.D. to obtain a parameter which is solely dependent on the hydrogen bond donating ability of the solvent.

Previous studies indicate that Kamlet-Taft properties are roughly temperature independent therefore measurements were conducted at 25^{o}C as maintained by a Peltier plate.[19] Three dyes

4-nitroaniline, N,N-diethyl-4-nitroaniline, and Reichardt's Dye 30 were used to obtain the wavelength of maximum absorbance. From the spectroscopic data, acidity (α), basicity (β), and dipolarizability (π^*) were calculated with the equations shown below.[18]

$$\pi^* = \frac{27.52 - \nu(NNDE-4-Na)_{Max}}{3.182} \quad \text{Eqn. 2.24}$$

$$\beta = \frac{1.035 * \nu(NNDE-4-NA)_{max} - \nu(4-NA)_{max} + 2.64}{2.80} \quad \text{Eqn. 2.25}$$

$$\alpha = 0.1856 * \nu(Re.D)_{max} - 2.03 - 0.72\pi^* \quad \text{Eqn. 2.26}$$

Previous studies in our group utilized an acidity (α) equation that included an adjustable polarizability correction term (δ), which takes on a value of 1.00 for aromatic solvents, 0.50 for poly-halogenated solvents and a value of 0.00 for non-halogenated aliphatic solvents.[20, 21] The acidity correlation utilizing the polarizability correction parameter could not be applied to mixed solvents in a straightforward manner as the varying composition of ionic liquid and organic solvent changed for different trials making it unclear how to account for different degrees of solvent loading. It should be mentioned that the KT parameters can vary based on the choice of probes and correlation used and that comparing KT parameters from one study to another should be done with caution.

Pure organic solvent samples were prepared for solvatochromic analysis by mixing 3 mg of dye with 3 mL of the organic solvent of interest in a 20 mL scintillation vial forming a stock solution. The vial was stirred until complete dissolution of the dye was observed. Between 20-500 µL of the stock dye solution was then added into a 2nd scintillation vial containing ~3 mL of the same pure organic solvent. This mixture was thoroughly mixed and subsequently put into a 1 cm path

length quartz cuvette, placed into the spectrophotometer, and tested. If the samples absorbance was too low then it was put back into its scintillation vial, where it was dosed with more dye solution. This was repeated until the dye concentration was such that the absorbance on the spectrophotometer was roughly 1.0.

The procedure for obtaining the spectrum of the pure ionic liquid samples was different than what was outlined above due to the comparatively high IL viscosity. Instead, a concentrated dye solution was initially made in dichloromethane. The pure IL was then doped with this dye solution and the absorbance was measured. Dye solution was added to the IL sample until an absorbance of approximately 1.0 was observed. Dichloromethane was then evaporated on a rotovap for 2-3 hours at 60°C and 300 mbar. After removing dichloromethane, the sample was analyzed to obtain the final, pure IL data.

The sample preparation procedure for IL-organic solvent mixtures varied depending on the dye. For NNDE-4-Na and 4-Na, concentrated dye solutions were prepared as previously outlined for the pure organic solvent systems. The IL-organic solvent mixtures (dye free) were prepared gravimetrically at 25, 50, 75 and 90 percent organic solvent loadings. Stock dye solutions within the selected solvent were then added until the absorbance was roughly 1.0. For NNDE-4-Na and 4-Na the amount of dye solution needed to achieve the required absorbance was about 20 μL and was small enough that it did not appreciably affect the IL-solvent mass fraction. Reichardt's dye samples were prepared by a different method as the amount of dye required to get the mixture to an absorbance value of 1.0 was large enough to affect the ratio of IL and solvent. To accommodate this, an initial dye solution was prepared in the organic solvent of interest by adding 6-10 mg of dye to 3 mL of solvent. In the process of adding the concentrated dye

solution to the IL a considerable amount of solvent was introduced into the mixture. Once the absorbance of the IL-concentrated dye solution reached ~1.0, additional pure (dye free) solvent was added to obtain the desired mass fraction.

Initial spectra for each sample were obtained at a scan rate of 600 nm/min across the entire UV-Vis region from 800 to 200 nm. Wavelengths of maximum absorbance were detected for each dye within the following regions: Re.D. (580-670 nm), NNDE-4-NA (415-390 nm), and 4-NA (405-360 nm). After locating the peak of maximum absorbance for a particular dye, the scan rate was reduced to 150 nm/min and measured through the wavelength region applicable to each dye. For each sample a series of four scans were performed from which the average was obtained for use by the KT equations.

2.3.6. High Performance Liquid Chromatography (HPLC)

High performance liquid chromatography (Varian Pro Star) equipped with an autosampler and dual channel UV-Vis detector was used to analyze components in the fructose to 5-hydroxymethylfurfural (5-HMF) reaction study. Wavelengths of maximum absorption were initially determined using the Varian Carry 300 Bio UV-Visible dual beam spectrophotometer. Subsequently the HPLC UV-Vis detector was set at the appropriate wavelengths to detect the reactants and products. The HPCL was equipped with a Bio-Rad Aminex HPX-87H column ideal for separating sugars and sugar alcohols. Water containing five millimolar sulfuric acid was utilized as the mobile phase at a flowrate of 0.4 mL/min. The column was operated at ambient temperature 25^{o}C +/- 2^{o}C. Table 2.3 displays the elution time, concentration range, and detection wavelength for select compounds in the study.

Component	Elution Time	Concentration Range	Detection Wavelength
Fructose	22 minutes	0.25 – 10.25 mass%	280 nm
Formic Acid	32 minutes	0.11 - 9.60 mass%	254 nm
Levulinic Acid	42 minutes	0.10 - 9.90 mass%	280 nm
5-HMF	112 minutes	0.25 - 10.50 mass%	330 nm

Table 2.3: HPLC parameters for fructose conversion studies utilizing a Bio-Rad Aminex HPX-87H column, 0.4 mL/min H_2O + 5 mM H_2SO_4 mobile phase at ambient temperature.

Calibration curves for fructose, formic acid, levulinic acid, and 5-HMF are displayed on a mass percent basis in Figure 2.9. All calibration curves were linear with an R^2 value of 0.999 or greater.

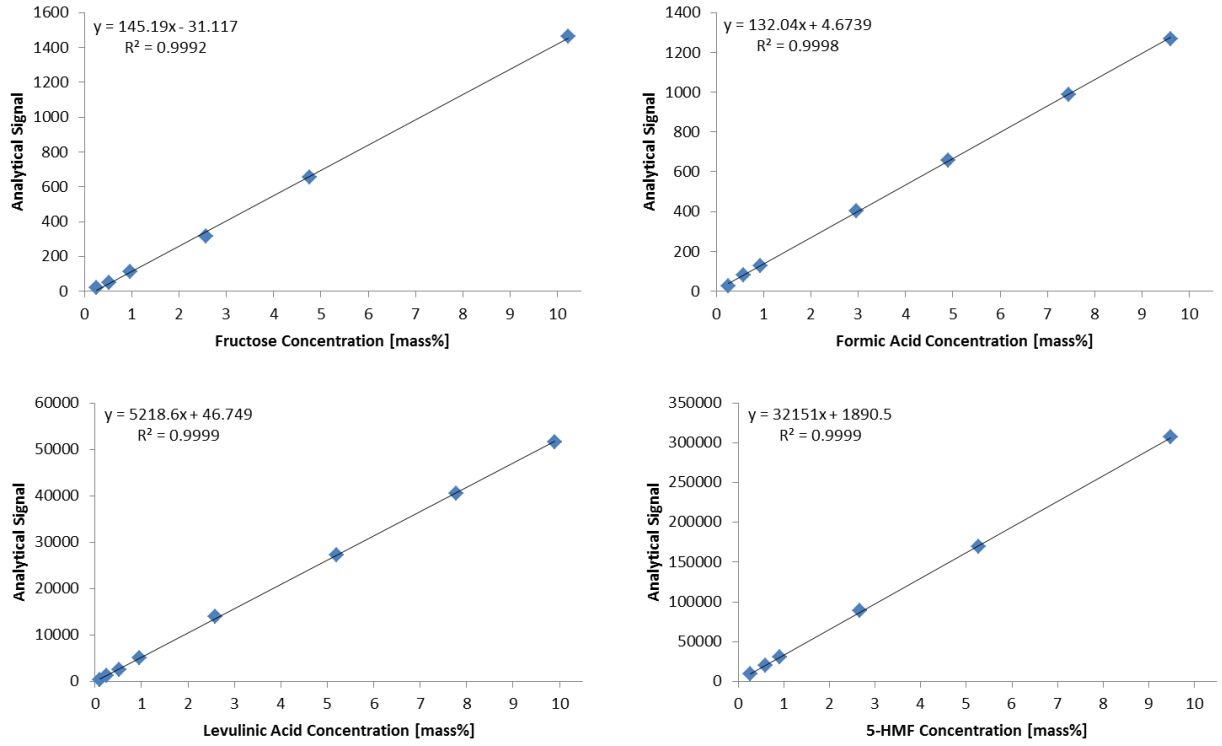

Figure 2.9: HPLC calibration curves for the major species in the fructose to 5-HMF reaction

2.3.7. ReactIR

In-situ Fourier transform infrared (FTIR) measurements were performed using a ReactIR iC10 instrument (Mettler Toledo) equipped with a silicon SiComp probe at ambient pressure and 25^{o}C previously described by our research group.[22] IR spectra were analyzed between 4000 cm^{-1} and 650 cm^{-1} by taking 1800 scans with a 1 cm^{-1} resolution. For each sample the probe was thoroughly cleaned with acetone and dried using compressed air. IR characterization of the diethyl phosphate anion was obtained from literature and the anion P=O stretching peak at 1240 cm^{-1} was analyzed for solvent dependent interactions with the IL anion.[23] The pure molecular solvents were also investigated to ensure that the P=O stretching resonance at 1240 cm^{-1} was non-convoluted and did not overlap with any of the solvent peaks. Increasing concentration of the polar aprotic cosolvent DMSO resulted in blue shifts (increased wavenumber) of the P=O stretching resonance while the protic antisolvent yielded red shifts (decreased wavenumber).[24] Figure 2.10 displays the red and blue shifts in the P=O resonance caused by polar aprotic and polar protic solvents respectively.

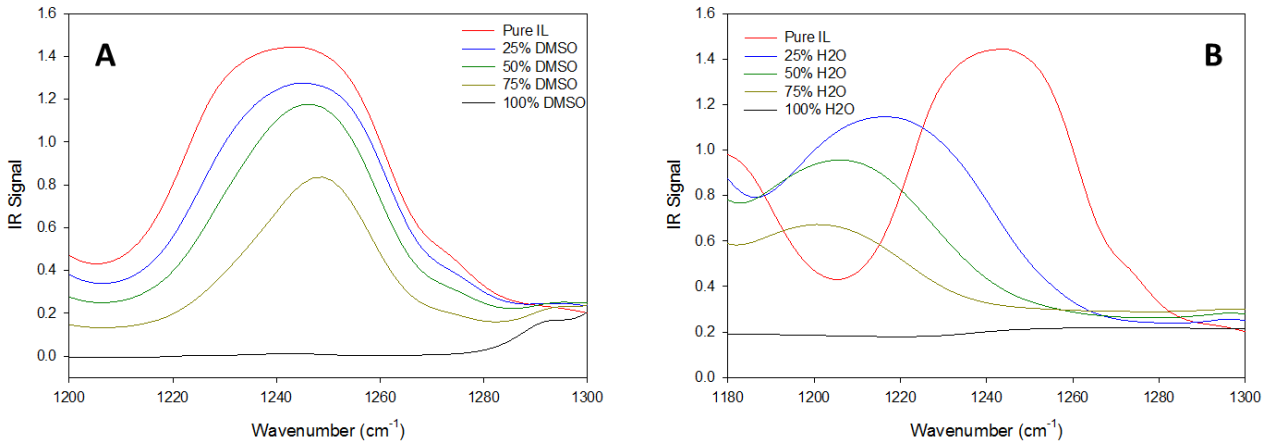

Figure 2.10: A) FTIR blue shift of the P=O stretching resonance on the [EMIm][DEP] anion due to solvation by the polar aprotic cosolvent DMSO B) FTIR red shift due to solvation by H_2O.

2.4. Rheology

2.4.1. Viscosity Measurements

Mixture viscosity of [EMIm][DEP]-DMSO-cellulose mixtures were measured using an AR-2000 rheometer (TA Instruments) with a 40mm roughed plate-plate geometry. Samples were loaded onto a Peltier plate which maintained a constant temperature of 40^{o}C and 60^{o}C (+/- 0.1^{o}C). Sheer rate was ramped from 10 – 1000 (1/sec) and mixture viscosity was obtained. All measurements were conducted in triplicate to obtain average and standard deviation data.

2.4.2. Viscosity Average MW Measurements

Average molecular weight of cellulose was determined by a viscometric method using a Cannon Fenske (150) viscometer with a calibration constant of 0.0351233. Standard solutions of cellulose ranging from 0.1 to 0.8 mass% were dissolved in a solvent mixture of

dimethylacetamide with 9 wt.% lithium chloride (cellulose free basis). Viscosity measurements were obtained by measuring the length of time it took the liquid samples to flow between indicated lines on the capillary tube. Each sample was collected at 30^{o}C in triplicate and averaged to obtain the viscosity of the cellulose containing sample relative to the viscosity of the blank solvent (n_{rel}). Equations 2.27 – 2.29 and previously published Mark Howink parameters are used to calculate the average molecular weight of cellulose from the viscosity data.[25]

$$\eta_{relative} = \frac{\eta_{cellulose\ sample}}{\eta_{pure\ solvent}} = \frac{t_{cellulose\ sample}}{t_{pure\ solvent}} \qquad \text{Eqn. 2.27}$$

$$\eta_{specific} = \eta_{relative} - 1 \qquad \text{Eqn. 2.28}$$

The plot of $\frac{\eta_{specific}}{cellulose\ concentration}$ vs. cellulose concentration for a range of cellulose loadings produces a linear line where the y-intercept is the actual viscosity η of the sample. Figure 2.11 displays a sample plot of specific viscosity vs. concentration for cellulose.

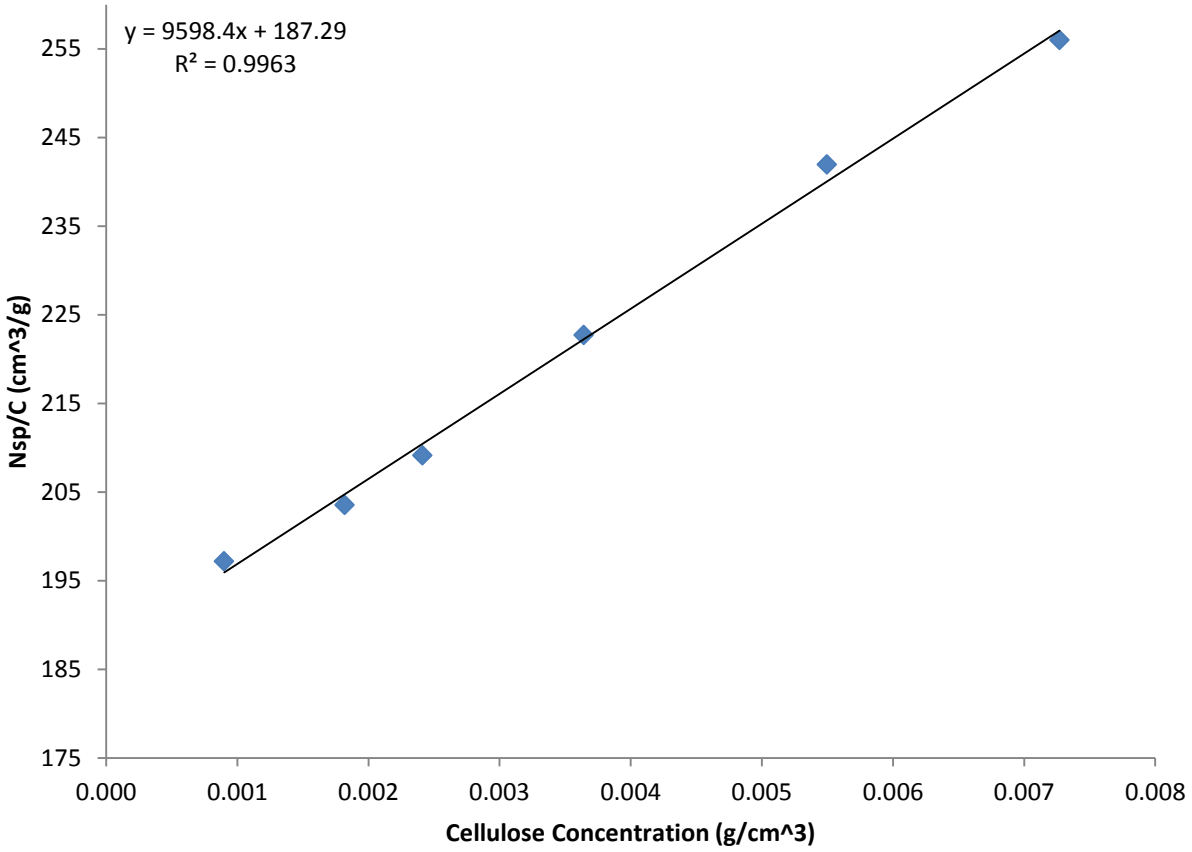

Figure 2.11: Plot of solution viscosity as a function of cellulose concentration used to compute the viscosity average molecular weight of the microcrystalline cellulose.

After obtaining the actual viscosity η of the sample Eqn. 2.29 can be applied with the Mark Howink parameters for microcrystalline cellulose to determine the viscosity average molecular weight of the polymer where a=1.19 and k=1.278*10^{-4} at 30^{o}C for cellulose.

$$\overline{MW_v} = \left(\frac{\eta}{k}\right)^{1/a} \qquad \text{Eqn. 2.29}$$

The viscosity average molecular weight of native microcrystalline cellulose used throughout this study was determined to be 152,000 g/mol (+/- 3,000 g/mol) and the degree of polymerization was ~937 anhydroglucose units (+/- 19 AGU).

2.5. Phase Equilibrium Modeling

Thermodynamic models transform complex experimental multi parameter phase equilibrium data into simplified mathematical formulas that can be utilized by process simulation software. The two most common models include those based on an Equations of State and Gibbs Excess Activity Coefficients. For multicomponent systems both models are formulated from the initial criteria that within each phase temperature, pressure, and fugacity of each species are equal.

$$T^I = T^{II} \ldots = T^n \qquad \text{Eqn. 2.30}$$

$$P^I = P^{II} \ldots = P^n \qquad \text{Eqn. 2.31}$$

$$\bar{f}^I{}_i = \bar{f}^{II}{}_i \ldots = \bar{f}^n{}_i \qquad \text{Eqn. 2.32}$$

Fugacity is an adjusted pressure measurement accounting for the non-ideal interactions of real gas systems and therefore has units of pressure (bar *etc.*). By normalizing the fugacity of the real gas to its ideal gas reference state, the fugacity coefficient is formed, a dimensionless quantity that indicates departure of the real gas system from ideality.

$$\overline{\varphi}_i{}^l = \frac{f_i{}^l}{y_i P} \quad and \quad \overline{\varphi}_i{}^v = \frac{f_i{}^v}{x_i P} \qquad \text{Eqn. 2.33}$$

Through the fugacity coefficient, components in a mixture can be related to their *P-V-T* properties using an appropriate thermodynamic model. By accounting for the "real" fluid behavior of pure components and mixtures, thermodynamic models are able to accurately simulate phase equilibrium and separation processes. The Equation of State and Gibbs Excess models that regress binary interaction parameters to correlate experimental data used in this study will be overviewed herein.

2.5.1. Vapor-Liquid Equilibrium

2.5.1.1. Peng Robinson Equation of State

Equation of State (EoS) models mathematically describe the state of matter under a given set of physical conditions and relate state variables including temperature, pressure, volume, internal energy, enthalpy, and entropy.[26] Boyle's Law and the Ideal Gas Law represent two of the earliest developed equation of state models and are applicable to light gases at low pressures and high temperatures. However, these preliminary models fail to accurately capture the thermodynamic behavior of low temperature high pressure systems with heavy molecules. No current equation of state model is applicable to any chemical component at any condition. Instead, each model has limitations that must be understood and accounted for.

In this study, the Peng Robinson Equation of State (PR-EoS) was applied to model the vapor and liquid phase fugacity components of the *T-x-y* data obtained in the ionic liquid synthesis experiments. The Peng Robinson cubic Equation of State is shown in Eqn. 2.34:

$$P = \frac{RT}{\underline{V}-b} - \frac{a(T,\omega)}{\underline{V}(\underline{V}-b)+b(\underline{V}-b)} \qquad \text{Eqn. 2.34}$$

where *a(T,ω)* is the temperature dependent mixture attractive parameter,

$$a(T,\omega) = \left(0.45724 \frac{R^2 T_c^2}{P_c}\right) \alpha(T) \qquad \text{Eqn. 2.35}$$

and *(b)* is the co-volume parameter that accounts for repulsive intermolecular interactions.

$$b = 0.7780 \frac{RT_c}{P_c} \qquad \text{Eqn. 2.36}$$

The temperature dependent alpha function within the *a(T,ω)* equation was formulated by regressing vapor pressure vs. temperature data for a range of fluids and is utilized to increase the accuracy of vapor pressure calculations. At the critical point the alpha function equals one.

$$\alpha(T,w) = \left[1 + k\left(1 - \sqrt{\frac{T}{T_c}}\right)\right]^2 \qquad \text{Eqn. 2.37}$$

k is expressed as:

$$k = 0.37464 + 1.54226\omega - 0.26992\omega^2 \qquad \text{Eqn. 2.38}$$

where omega (ω) is the acentric factor which accounts for the non-spherical nature of molecules and is calculated from the vapor pressure and critical properties of a given component.

$$\omega = -1.0 - \log_{10}\left[\frac{P^{vap}(T_r=0.7)}{P_c}\right] \qquad \text{Eqn. 2.39}$$

For multicomponent systems, a mixing function is required for the PR-EoS. The van der Waals 1-parameter mixing rule (vdW1) has been utilized in this study and is shown in Eqns. 2.40-2.42:

$$a_m = \sum_{i=1}^{C} \sum_{j=1}^{C} \left(x_i x_j a_{ij} \right) \quad \text{Eqn. 2.40}$$

$$a_{ij} = \left(1 - k_{ij}\right) \sqrt{a_i a_j} \quad \text{Eqn. 2.41}$$

$$b_m = \sum_{i=1}^{C} (y_i b_i) \quad \text{Eqn. 2.42}$$

where a_i a_j and b_i are parameters of the pure components and k_{ij} is the regressed binary interaction parameter. The Peng Robinson Equation of State model utilizes the critical properties of components in the system (T_c, P_c) as well as the acentric factor and one adjustable binary interaction parameter. Due to the non-volatile nature of ionic liquids and the lack of experimental data on precursor molecules 1-bromohexane and 1-methylimidazole, a modified Joback group contribution method was applied to estimate the necessary critical properties T_c and P_c.[27]

2.5.1.2. Non-Random Two Liquid Activity Coefficient Model

Activity coefficient models utilize Gibbs Excess relations to model the liquid phase while using an equation of state method for the vapor phase. In the ionic liquid synthesis solvent selection project, the Non-Random Two Liquid (NRTL) activity coefficient method was used to model the liquid phase assuming a saturated fugacity coefficient of the pure component equal to one, a Poyntig correction equal to one, and an ideal mixture vapor phase (vapor fugacity coefficients of one). The NRTL activity coefficient model represents an empirical correlation with two adjustable parameters τ_{ij} and τ_{ji} with the non-randomness factor α fixed at a value of 0.20.

$$\ln(\gamma_i) = x_j^2 \left[\tau_{ji} \left(\frac{G_{ji}}{x_i + x_j G_{ji}} \right)^2 + \frac{\tau_{ij} G_{ij}}{(x_j + x_i G_{ij})^2} \right]$$ Eqn. 2.43

$$\ln G_{ij} = -\alpha \tau_{ij}$$ Eqn. 2.44

$$\tau_{ij} = \frac{\Delta g_{ij}}{RT} \qquad \tau_{ji} = \frac{\Delta g_{ji}}{RT}$$ Eqn. 2.45

For the NRTL model, γ_i represents the activity coefficient, x_i and x_j are the liquid phase mole fractions of the components in the binary mixture, and τ_{ij} and τ_{ji} are the binary interaction parameters regressed to the experimental data.

2.5.1.3. UNIquac Functional-group Activity Coefficient Method

Select phase equilibrium systems cannot be experimentally measured. In the case of 1-methylimidazole and 1-bromohexane, the two components react to form the ionic liquid [HMIm][Br] within the timescale required to measure each phase equilibrium point. Therefore, the UNIquac Functional-group Activity Coefficient (UNIFAC) model was utilized to predict the vapor-liquid equilibrium data and activity coefficients for the mixture. The UNIFAC activity coefficient model utilizes an index of functional groups that have been correlated to experimental phase equilibrium data. In the UNIFAC model, molecules are built from a combination of their constituent functional groups and thus a mixture of molecules effectively becomes a mixture of functional groups. Activity coefficients are calculated based on the interactions between functional groups of the compounds in the mixture.

The UNIFAC model consists of a combinatorial term dependent on the surface area and volume of each functional group, as well as a residual term that accounts for the interaction energies between groups.

$$\ln \gamma_i = \ln \gamma_i(combinatorial) + \ln \gamma_i(residual) \quad \text{Eqn. 2.46}$$

$$\ln \gamma_i(combinatorial) = \ln \frac{\phi'_i}{x_i} + 1 - \frac{\phi'_i}{x_i} - \frac{z}{2} q_i \left(1 + \ln \frac{\phi_i}{\theta_i} - \frac{\phi_i}{\theta_i}\right) \quad \text{Eqn. 2.47}$$

$$\phi'_i = \frac{x_i r_i^{3/4}}{\sum_j x_j r_j^{3/4}} \quad \text{Eqn. 2.48}$$

$$\theta_i = \frac{x_i q_i}{\sum_j x_j q_j} \quad \text{Eqn. 2.49}$$

ϕ'_i is the volume parameter and θ_i is the area fraction for species (i) in the mixture. Additionally, (*r*) and (*q*) are the specific volume and surface area parameters for the functional groups defined within the UNIFAC database and (*z*) is the average coordination number.

$$\ln \gamma_i(residual) = \sum_k \upsilon_k^{(i)} \left[\ln \Gamma_k - \ln \Gamma_k^{(i)}\right] \quad \text{Eqn. 2.50}$$

$$\ln \Gamma_k = Q_k \left[1 - \ln\left(\sum_m \Theta_m \psi_{mk}\right) - \sum_m \frac{\Theta_m \psi_{km}}{\sum_n \Theta_n \psi_{nm}}\right] \quad \text{Eqn. 2.51}$$

$$\Theta_m = \frac{X_m Q_m}{\sum_n X_n Q_n} \quad \text{Eqn. 2.52}$$

$$\psi_{mn} = \exp\left[\frac{-(u_{mn} - u_{nn})}{kT}\right] = \exp \frac{-a_{mn}}{T} \quad \text{Eqn. 2.53}$$

Where, X_m is the mole fraction of group m in the mixture, $\upsilon_k^{(i)}$ is the number of k groups present in species *I*, R_i and Q_i are known surface and volume parameters, and α_{mn} is the interaction energy between groups in the mixture which is computed from the regression of thermodynamic data from many functional groups.

The UNIFAC parameters used to approximate 1-bromohexane and 1-methylimdiazole are shown in Table 2.4. Due to a current lack of data on imidazole rings within the database, the 1-methylimidazole molecule was approximated by carbon-nitrogen and carbon-carbon groups currently within the database.

Component	UNIFAC Functional Groups							
	$-CH_3$	$-CH_2$	-Br	$-CH_3N$	A-C_2H_2N	A-CH	-Cl	DMSO
1-Bromohexane	1	5	1	-------	-------	-------	-------	-------
1-Methylimidazole	-------	-------	-------	1	1	1	-------	-------
Dichloromethane	-------	1	-------	-------	-------	-------	2	-------
Dimethyl Sulfoxide	-------	-------	-------	-------	-------	-------	-------	1

Table 2.4: Functional group parameters used to formulate 1-bromohexane, 1-methylimidazole, dichloromethane, and dimethyl sulfoxide with the UNIFAC predictive activity coefficient model.

2.5.2. Liquid-Liquid Equilibrium Modeling

The 1-bromohexane/[HMIm][Br] system exhibits liquid-liquid equilibrium behavior. For this regression the NRTL model described in section 2.5.1.2 was applied and used with temperature-dependent interaction parameters:

$$\tau_{ij} = A_{ij} + \frac{B_{ij}}{T} \qquad \tau_{ji} = A_{ji} + \frac{B_{ji}}{T} \qquad \text{Eqn. 2.54}$$

where the regressed parameters are A_{ij} and B_{ij}. The temperature dependent parameter B_{ij} allowed for superior performance over the traditional NRTL model and was therefore implemented for this LLE system.

2.5.3. Objective Function

The Peng Robinson Equation of State, NRTL, and UNIFAC activity coefficient models were applied within the Aspen Plus and XSEOS software suites to model all of the VLE datasets in this study. Both software packages utilized an ordinary least squares objective function to regress binary interaction parameters to the experimental data.[28] Alternatively, the liquid-liquid equilibrium modeling was solely performed in Aspen Plus with the Britt-Luecke Maximum Likelihood method for regression of the NRTL binary interaction parameters.[29]

Binary interaction parameters (BIPs) were regressed to each vapor-liquid equilibrium dataset by a bubble-point temperature calculation. The experimental pressure *(P)* and liquid mole fractions (x_i) were used to predict the temperature *(T)* and vapor phase mole fraction (y_i). The objective function for all VLE systems was chosen as the combined average absolute relative deviation (%AARD) of the vapor-phase composition and the temperature.

$$\%AARD = \frac{100}{n}\left[\sum_{i=1}^{n}\left|\frac{y_i^{exp}-y_i^{pred}}{y_i^{exp}}\right| - \sum_{i=1}^{n}\frac{T^{exp}-T^{pred}}{T^{exp}}\right] \qquad \text{Eqn. 2.55}$$

2.6. Safety

Select experiments performed in this study were conducted at elevated temperatures and pressures. As such, extra precautions were taken to mitigate risk. For instance, all pressure

vessels were inspected prior to use to ensure they were in good working order. Additionally, all pressure vessels were used within their designed pressure range (*i.e.* < 250 bar). Personal protective equipment including close toed shoes, a flame resistant laboratory coat, and goggles were worn at all times. Despite the negligible vapor pressure of ionic liquids, many of the organic chemicals utilized in this dissertation exhibited moderate volatility. Experimental studies at elevated temperatures (especially those generating VLE data with the Othmer still) were conducted within a fume hood to prevent exposure to vapor phase emissions. Additionally, select chemicals within the presented studies including dichloromethane and dimethyl imidazolidinone are known carcinogens. When handling these chemicals extra precautions were taken to mitigate exposure risk. Most importantly, these chemicals were always used sparingly and within a well-functioning fume hood. Furthermore, proper personal protective equipment including gloves, goggles, and a lab coat were worn to prevent exposure. All chemical waste was properly categorized (*i.e.* halogenated, non-halogenated, acid, base, *etc.*) and disposed of according to environmental health and safety guidelines. Finally, safety protocols were observed at all times to ensure a safe laboratory working environment.

2.7. Materials

1-methylimidazole (CAS 616-47-7) 99% and 1-bromohexane (CAS 111-25-1) 98% were obtained from Acros Organics. Acetone (CAS 67-64-1) 99.9+%, acetonitrile (CAS 75-05-8) >99.9%, dichloromethane (CAS 75-09-2) 99%, dimethyl sulfoxide (CAS 67-68-5) >99.9%, ethanol 99.5% (CAS 64-17-5), methanol (CAS 67-56-1) (99%), and triethyl phosphate (CAS 78-40-0) 99% were obtained from Sigma Aldrich. Dimethylformamide (CAS 68-12-2) 99%, ethyl acetate (CAS 141-78-6) 99%, HPLC water (CAS 7732-18-5), hydrochloric acid (CAS 7647-01-

0) trace metal grade, and sulfuric acid (CAS 7664-93-9) trace metal grade were obtained from Fisher Scientific. Microcrystalline cellulose powder (CAS 9004-34-6) and D-fructose (CAS 57-48-7) were obtained from Sigma Aldrich and used as received. Carbon dioxide (CAS 124-38-9) 99.99% was obtained from Matheson and was used as received. Deuterated solvents including water, dimethyl sulfoxide, and chloroform were obtained from Cambridge Isotopes at 99% purities. Kamlet-Taft spectroscopic studies were conducted with dyes: 4-nitroaniline (CAS 100-01-6) 99%, N,N-diethyl-4-nitroaniline (CAS 100-23-2) 99%, and Reichardt's Dye 30 (10081-39-7) 90% were supplied by Sigma Aldrich. All organic chemicals were stored under an inert argon atmosphere Matheson gas (CAS 7440-37-1) 99.99% pure and dried by 4Å molecular sieves supplied by Fisher Scientific. Distilled water was obtained from an in-house reverse osmosis system.

References

1. Dhanalakshmi, J., P.S.T. Sai, and A.R. Balakrishnan, *Effect of Inorganic Salts on the Isobaric Vapor-Liquid Equilibrium of the Ethyl Acetate-Ethanol System.* Journal of Chemical and Engineering Data, 2013. **58**(3): p. 560-569.
2. Ott, L.S., B.L. Smith, and T.J. Bruno, *Experimental test of the Sydney Young equation for the presentation of distillation curves.* Journal of Chemical Thermodynamics, 2008. **40**(9): p. 1352-1357.
3. Ren, W. and University of Kansas., *High-pressure phase equilibria of ionic liquids and compressed gases for applications in reactions and absorption refrigeration*. p. 426 p.
4. Ren, W. and A.M. Scurto, *High-pressure phase equilibria with compressed gases.* Review of Scientific Instruments, 2007. **78**(12).
5. Jodecke, M., A.P.S. Kamps, and G. Maurer, *Experimental investigation of the solubility of CO2 in (acetone plus water).* Journal of Chemical and Engineering Data, 2007. **52**(3): p. 1003-1009.
6. Millipore, E. *Karl Fisher Titration Basics*. 2012; Available from: https://www.emdmillipore.com/US/en/lab-technical-resources/karl-fischer-faqs/w5yb.qB.0VgAAAFE3oMWq.DH,nav.
7. Reusch, W. *Supplemental NMR Topics*. 2013; Available from: https://www2.chemistry.msu.edu/faculty/reusch/virttxtjml/spectrpy/nmr/nmr2.htm.
8. Gunther, H., *NMR Spectroscopy: Basic Principles, Concepts and Applications in Chemistry*. 3rd ed. 2013: Wiley.
9. Brunning, A. *Analytical Chemistry – A Guide to Proton Nuclear Magnetic Resonance (NMR)*. 2015; Available from: http://www.compoundchem.com/2015/02/24/proton-nmr/.
10. Hall, C.A., et al., *Macroscopic and Microscopic Study of 1-Ethyl-3-methyl-imidazolium Acetate-Water Mixtures.* Journal of Physical Chemistry B, 2012. **116**(42): p. 12810-12818.
11. Hesse-Ertelt, S., et al., *Solvent Effects on the NMR Chemical Shifts of Imidazolium-Based Ionic Liquids and Cellulose Therein.* Macromolecular Symposia, 2010. **294**(2): p. 75-89.
12. (AIST), N.I.o.A.I.S.a.T. *Spectral Database for Organic Compounds*. 2016; Available from: http://sdbs.db.aist.go.jp/sdbs/cgi-bin/cre_index.cgi.
13. Park, S., et al., *Cellulose crystallinity index: measurement techniques and their impact on interpreting cellulase performance.* Biotechnology for Biofuels, 2010. **3**.
14. Park, S., et al., *Measuring the crystallinity index of cellulose by solid state C-13 nuclear magnetic resonance.* Cellulose, 2009. **16**(4): p. 641-647.
15. Reichardt, C., *Solvatochromic Dyes as Solvent Polarity Indicators.* Chemical Reviews, 1994. **94**(8): p. 2319-2358.
16. Khupse, N.D. and A. Kumar, *Delineating Solute-Solvent Interactions in Binary Mixtures of Ionic Liquids in Molecular Solvents and Preferential Solvation Approach.* Journal of Physical Chemistry B, 2011. **115**(4): p. 711-718.
17. Marcus, Y., *The Properties of Organic Liquids That Are Relevant to Their Use as Solvating Solvents.* Chemical Society Reviews, 1993. **22**(6): p. 409-416.

18. Mellein, B.R., et al., *Solvatochromic studies of ionic liquid/organic mixtures.* Journal of Physical Chemistry B, 2007. **111**(1): p. 131-138.
19. Hauru, L.K.J., et al., *Role of Solvent Parameters in the Regeneration of Cellulose from Ionic Liquid Solutions.* Biomacromolecules, 2012. **13**(9): p. 2896-2905.
20. Nwosu, S.O. and University of Kansas., *Environmentally Benign Production of Ionic Liquids in CO2-Expanded Systems*. p. 337 p.
21. Schleicher, J. and University of Kansas., *Kinetics and solvent effects in the synthesis of ionic liquids*. p. 142 p.
22. Nwosu, S.O., J.C. Scheicher, and A.M. Scurto, *Kinetics and polarity effects in the synthesis of the ionic liquid, 1-hexyl-3-methyl-imidazolium bromide, using compressed CO2.* Journal of Supercritical Fluids, 2015. **96**: p. 171-179.
23. Azema, L., et al., *Does phosphoryl protonation occurs in aqueous phosphoesters solutions.* Spectrochimica Acta Part a-Molecular and Biomolecular Spectroscopy, 2005. **62**(1-3): p. 287-292.
24. Ding, Z.-D., et al., *Theoretical and experimental investigation of the interactions between [emim]Ac and water molecules.* Journal of Molecular Structure, 2012. **1015**: p. 147-155.
25. Mccormick, C.L., P.A. Callais, and B.H. Hutchinson, *Solution Studies of Cellulose in Lithium-Chloride and N,N-Dimethylacetamide.* Macromolecules, 1985. **18**(12): p. 2394-2401.
26. Perrot, P., *A to Z of thermodynamics*. 1998, Oxford ; New York: Oxford University Press. vi, 329 p.
27. Nwosu, S.O., J.C. Schleicher, and A.M. Scurto, *High-pressure phase equilibria for the synthesis of ionic liquids in compressed CO2 for 1-hexyl-3-methylimidazolium bromide with 1-bromohexane and 1-methylimidazole.* Journal of Supercritical Fluids, 2009. **51**(1): p. 1-9.
28. Castier, M., *XSEOS: An Open Software for Chemical Engineering Thermodynamics.* Chemical Engineering Education (CEE), 2008. **42**(2): p. 74-81.
29. Britt, H.I. and R.H. Luecke, *The Estimation of Parameters in Nonlinear, Implicit Models.* Technometrics, 1973. **15**(2): p. 233-247.

3. Solvent Effects on the Dissolution of Cellulosic Biomass in Ionic Liquids

3.1. Introduction

Lignocellulose is the most abundant naturally occurring biomass source on earth making it a promising renewable feedstock for the production of chemicals and fuels.[1-3] Within the United States alone there is an estimated 340 million tons of lignocellulosic biomass annually available from a diverse range of sources including but not limited to crop residues (corn stover), timber residues, and switchgrass.[4] Furthermore, lignocellulosic biomass is geographically distributed throughout the U.S., as displayed in Figure 3.1, indicating the versatility of this feedstock.[5] Unfortunately biomass utilization remains a challenge as recalcitrance of cellulose and hemicellulose hinder chemical processing of these carbohydrates in conventional solvents.

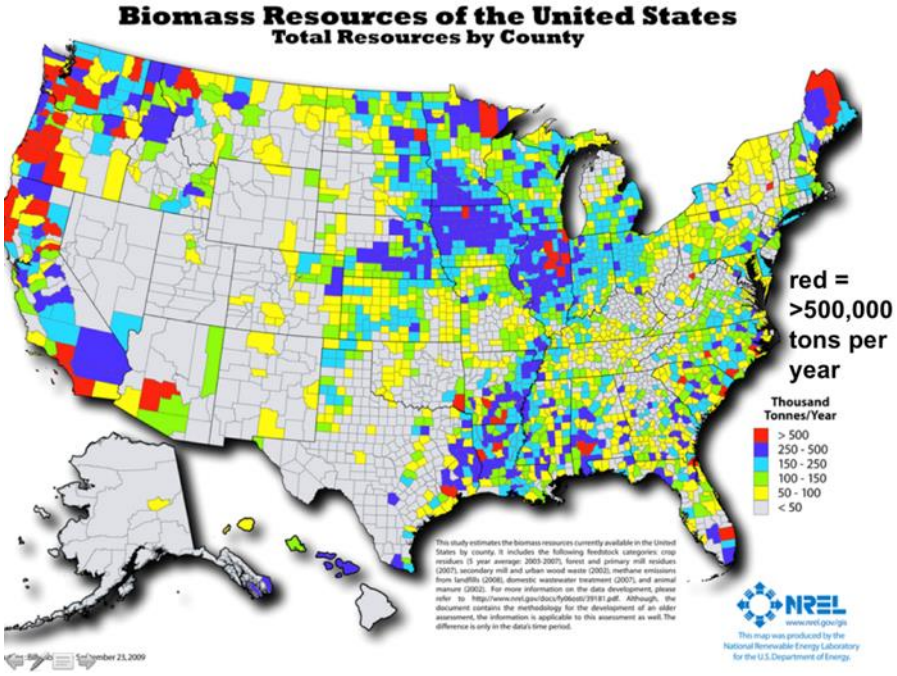

Figure 3.1: Distribution of lignocellulosic biomass resources within the United States.[5]

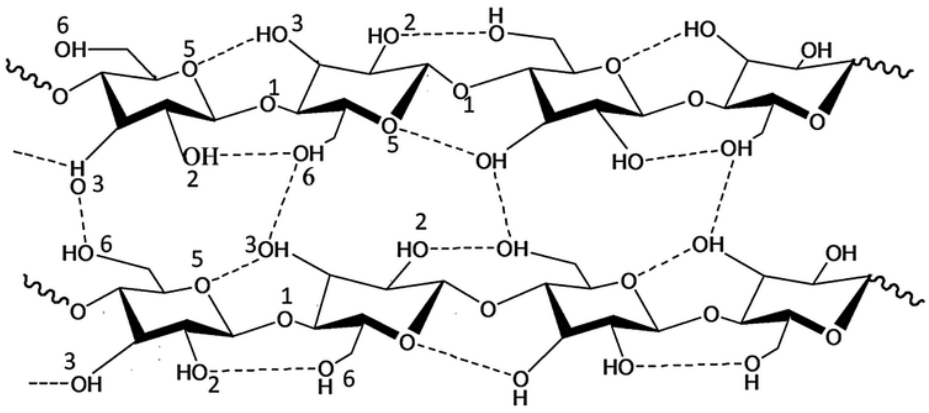

Figure 3.2: Inter- and intra- molecular hydrogen bonding between anhydroglucose units in the macroscopic cellulose structure. Adapted from [6, 7].

Lignocellulose is comprised of three primary components: cellulose (30-50 wt.%), hemicellulose (20-35 wt.%), and lignin (18-35 wt.%).[8] Cellulose is a carbohydrate comprised of six carbon sugar monomers linked by β-1,4 glycosidic bonds. For this reason cellulose is typically targeted for biomass conversion to value-added products. Despite the apparent advantages of cellulose, recalcitrance of lignocellulosic biomass prevents the facile conversion of these carbohydrates by conventional chemical processing routes. For example, the complex inter- and intra- molecular hydrogen bonding network of cellulose, shown in Figure 3.2, renders it insoluble in nearly all aqueous and organic solvents. However, select ionic liquids (ILs) can dissolve significant quantities.[9] Cellulose dissolution is primarily driven by the ability of IL anions to preferentially hydrogen bond to cellulose and solubilize the biopolymer through a non-derivatizing process; although a few ILs are known to react with cellulose.[10, 11] Correspondingly, hydrogen bond accepting ability (Kamlet-Taft Basicity) of the ionic liquid anion is largely attributed to successful dissolution of cellulose in an IL.[12-14] Table 3.1 presents a summary of solvents for biomass dissolution and their respective hydrogen bond accepting abilities as measured by Kamlet-Taft solvatochromic analysis.

Solvent	Temperature [^{o}C]	Cellulose Solubility [mass%]	Hydrogen Bond Accepting Ability
[EMIm][DEP]	100	19.8 [a]	1.07 [a]
[EMIm][Ac]	100	10.0 [c]	1.09 [d]
[BMIm][Ac]	100	12.0 [b]	1.05 [d]
[BMIm][Cl]	100	10.0 [b]	0.87 [d]
DMSO	100	0.0 [a]	0.69 [a]
DMF	100	0.0 [a]	0.64 [a]
DMI	100	0.0 [a]	0.79 [a]
EtOH	100	0.0 [a]	0.74 [a]
H_2O	100	0.0 [a]	0.47 [a]

[a] Experimental data obtained from **[15]**, [b] Solubility data obtained from **[9]**, [c] Solubility data obtained from **[2]**
[d] Kamlet-Taft data from **[14]**

Table 3.1: Cellulose solubility and hydrogen bond accepting ability (KT-Basicity) of select ionic liquids, organic, and aqueous solvents.

While a majority of findings on ionic liquid dissolution of cellulose show that the process is anion driven, select studies also indicate that the IL cation plays an ancillary role through interactions with oxygen atoms on the hydroxyl groups of cellulose.[7] Figure 3.3 displays the theoretical IL cation and anion interactions with cellulose that drive the dissolution process.

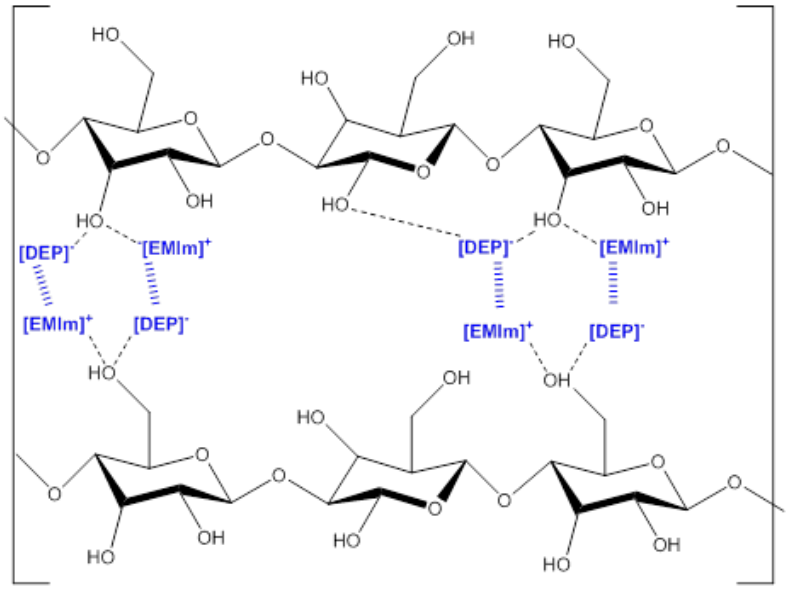

Figure 3.3: Interactions between the ionic liquid [EMIm][DEP] and cellulose that drive dissolution of the biopolymer.

Numerous ionic liquids for biomass dissolution have been investigated [2, 9] including the most widely studied ILs 1-butyl-3-methyl-imidazolium chloride ([BMIm][Cl]) [16-18] and 1-ethyl-3-methyl-imidazolium acetate ([EMIm][Ac]) [19-21]. Despite the large number of publications in this area, prior investigations on cellulose solubility in ionic liquids are mostly qualitative. Systematic approaches to determine the solid-liquid phase equilibrium thermodynamics of cellulose in ionic liquids have not been reported. Most ILs, especially [BMIm][Cl], have elevated melting points and moderate to high pure component viscosities. Moreover, upon the addition of biomass, IL-cellulose mixtures have been known to form gels and other solid-transitions with larger quantities of dissolved cellulose prohibiting quantitative measurement of cellulose solubility in an IL.[22] However, the ionic liquid 1-ethyl-3-methylimidazolium diethyl phosphate [EMIm][DEP] shown in Figure 3.4 may be a model IL for study as it has a comparatively low pure component viscosity 284 cP at 40°C, and does not appear to form gels even upon the addition of large cellulose quantities.[23] These attributes of [EMIm][DEP] allow more facile and standard experimental methods to determine the solid-liquid equilibrium conditions. In addition, [EMIm][DEP] does not react with cellulose as observed with acetate ILs [24, 25] and does not contain halides which could lead to possible corrosion issues with metals [26, 27].

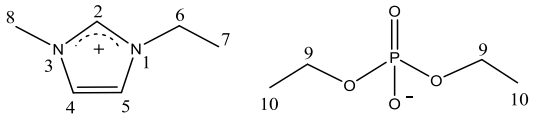

Figure 3.4: 1-Ethyl-3-Methylimidazolium Diethyl Phosphate [EMIm][DEP] structure.

Herein we present some of the most extensive thermodynamic solubility data for cellulose in mixtures of the model ionic liquid 1-ethyl-3-methylimidazolium diethyl phosphate

[EMIm][DEP] with aprotic cosolvents (DMSO, DMF, and DMI). Temperatures ranging from 40 to 120°C are investigated for cellulose solubility in the pure IL and 40 to 80°C for the mixed IL-molecular cosolvent systems.

3.2. Cellulose Solubility in Pure Model Ionic Liquid [EMIm][DEP]

The solid-liquid equilibrium of microcrystalline cellulose (*MW*~ 152,000 g/mol, 61% crystallinity) was measured in pure [EMIm][DEP] at temperatures ranging from 40°C to 120°C and reported in Table 3.2. As previously discussed, the system of cellulose and [EMIm][DEP] does not seem to incur gelation or other solid phase transitions at higher compositions which would obscure the solid-liquid saturation point thus allowing experimental acquisition of accurate thermodynamic measurements. At 40°C the saturation point of cellulose in [EMIm][DEP] is 9.1 mass% which is greater than the cellulose capacity of a majority of ILs investigated in literature at 100°C despite being at a much lower temperature. Furthermore, at 100°C the saturation point of cellulose in pure [EMIm][DEP] is 19.8 mass% indicating that [EMIm][DEP] has one of the highest measured cellulose capacities of any IL at 100°C.

Temperature [°C]	Cellulose Solubility [a] [mass%]	Anion: Cellulose -OH [Molar Ratio]	% of Maximum Theoretical Solubility
40	9.1	2.0	37.4
60	13.5	1.3	55.6
80	18.3	0.9	73.5
100	19.8	0.8	81.5
120	19.9	0.8	81.9

[a] Standard deviations are within ±0.2 mass% yielding a total potential uncertainty of ±0.4 mass%

Table 3.2: Solubility of microcrystalline cellulose in pure IL [EMIm][DEP].

The results displayed in Figure 3.5 demonstrate that the solubility of cellulose in the pure IL is directly proportional to temperature up to 100°C. However, the measured solubility of cellulose

in [EMIm][DEP] at 120°C was 19.9 mass%, only 0.1 mass% greater than the 100°C sample and within experimental error. This asymptotic maximum in solubility of cellulose in an ionic liquid with temperature has not previously been observed or reported in the literature.

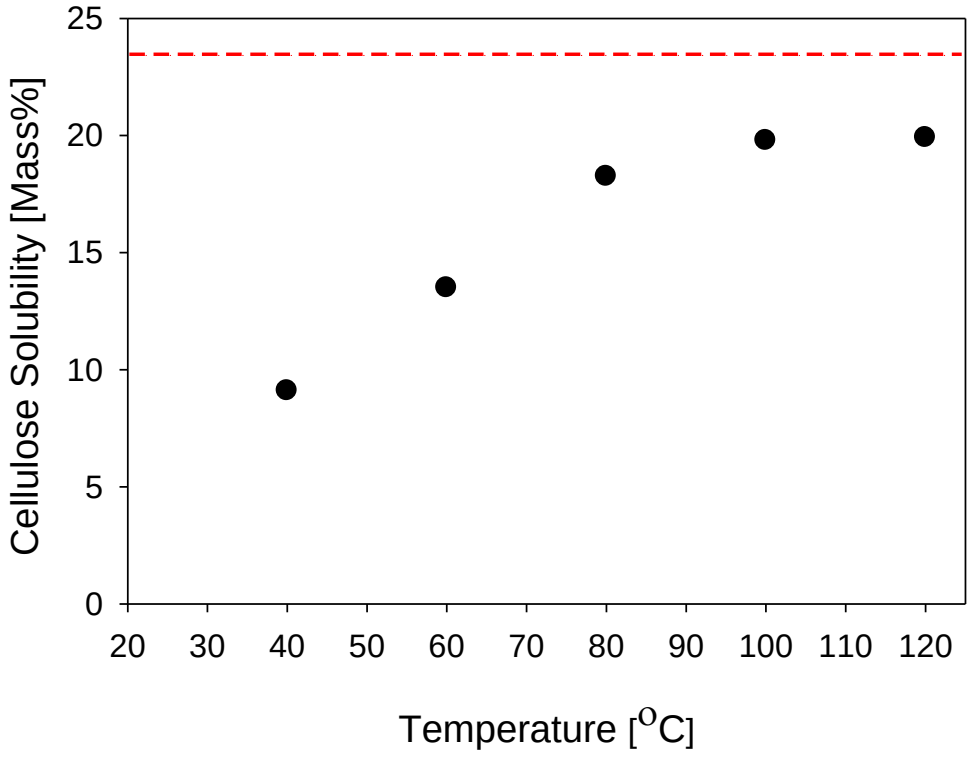

Figure 3.5: Cellulose solubility as a function of temperature. Error bars are approximately the size of the symbols. Dashed line is maximum theoretical solubility (see text).

Conventional solid-liquid equilibrium thermodynamic analysis is a function of the chemical potential (fugacity) of both the pure solid phase and mixture liquid phase. The ideal solubility of a solid in a liquid, assuming that the liquid phase is at the "ideal solution/mixture" reference state, is simply a function of the enthalpy of fusion, melting temperature (actually triple point), the experimental temperature of interest, and potentially heat capacities as small secondary corrections as shown in Eqn. 3.1.

$$\ln(x_1\gamma_1) = \frac{-\Delta H_{fus}}{RT}\left(1 - \frac{T}{T_m}\right) - \frac{1}{RT}\int_{T_m}^{T} \Delta C_p dT + \frac{1}{R}\int_{T_m}^{T} \frac{\Delta C_p}{T} dT \qquad \text{Eqn. 3.1}$$

Therefore, *ideal* solubility always increases with temperature and, thus the observed maximum in *real* solubility implies that the thermodynamic activity coefficient of cellulose in the IL has a significant effect on its solubility. It should be noted that changes in the solid phase due to temperature or due to IL absorption into the crystal structure have not been studied here. Wada and coworkers have investigated the effects of temperature on cellulose (I_β) structure and indicate that polymorphic transitions to the "high-temperature" phase and crystallinity do not occur until approximately 225°C.[28, 29] This would indicate that within our temperature range here, a solid-solid transition does not occur and thus typical solid-liquid equilibrium behavior and thermodynamic analysis may be appropriate. However, it is known that some organic solvents may swell solid cellulose fibers.[30, 31] If the resulting system has solvent molecules in the solid phase at the molecular level, the resulting solid-phase solution would possibly have different thermodynamic activity and temperature/composition trends. The effects of ILs and IL mixtures on the solid phase of cellulose are currently unknown.

The asymptotic maximum solubility of cellulose in [EMIm][DEP] with temperature was analyzed with respect to mechanisms of cellulose dissolution in ILs discussed in the literature. Several researchers have suggested that cellulose solubility in ILs is mainly governed by the ability of the anion to disrupt the cellulose inter- and intra- molecular hydrogen bonds.[9, 11, 12, 32-36] The dissolution phenomenon is believed to be driven by a quasi-chemical equilibrium where cellulose -OH functional groups are solvated by IL anions. Maximum liquid stability occurs when at least enough anions are present in solution to solvate all (or most, see below) hydroxyl groups on each molecule of cellulose. As a first approximation, one could envision

that a molecular ratio of anions to cellulose hydroxyl groups should be approximately equal to 1.0 as a limiting value. Here, the theoretical molar ratio of cellulose hydroxyl (-OH) groups to the IL (DEP) anion was calculated using the experimental data for cellulose solubility in pure [EMIm][DEP]. Utilizing the measured degree of polymerization of microcrystalline cellulose (DP~937), the ratio of [DEP] anions to cellulose -OH groups was calculated and the results are displayed in Table 3.2. At 40°C, the anion:OH ratio is ~2.0 indicating that at this temperature, a surplus of unbound IL anions exist in solution relative to cellulose –OH groups. Thus, it would seem that the solubility at this temperature is limited by the solid phase (cellulose) thermodynamic activity and not by a lack of anions for solvation. As temperature and cellulose solubility increase, we observe that the anion:OH ratio decreases and drops below a value of one at temperatures greater than 60°C. At both 100°C and 120°C, the anion:OH ratio is ~0.8. This indicates that some IL anions potentially interact with more than one hydrogen bond donating group on cellulose or some cellulose hydroxyl groups remain unbound in solution despite total dissolution of the polymer.

A recent molecular dynamics (MD) study investigating cellulose dissolution in 1-ethyl-3-methylimidazolium dimethyl phosphate [EMIm][DMP] indicates several interesting phenomena pertaining cellulose solvation by ILs. Rabideau and Ismail found that that a combination of 1:1 and 1:2 anion:-OH interactions occur between [DMP] anions and cellulose signifying that select anions are capable of interacting with more than one cellulose -OH group.[37] The MD findings indicate that [DMP] anions form stable interactions with two -OH groups on cellulose approximately 33% of the time while single anion:-OH interactions occur approximately 67% of the time. Additionally, they found that, on average, only 2.54 (out of 3) hydroxyl (-OH) groups per anhydroglucose unit (AGU) interact with [DMP] anions as opposed to simulation results on

chloride and acetate ILs in which all three -OH groups per anhydroglucose unit interacted with the IL anion. Thus, for cellulose solvation by [EMIm][DMP], select -OH groups remain unbound in solution despite complete dissolution of the biopolymer. Given the similarity between [DMP] targeted in the computational study and the [DEP] anion studied here, it is believed that similar 1:1 and 2:1 interactions occur and a similar number of H-bonds per AGU may exist for cellulose dissolution in [EMIm][DEP]. Based on this distribution of interactions, a theoretical limiting ratio of [DEP] anions to total cellulose hydroxyl groups [DEP]:-OH would be equal to 0.64 (not 1) for a system that has saturated all of the -OH bonds that participate in hydrogen bonding with [DEP] anions. This ratio corresponds to a maximum theoretical cellulose solubility of approximately 24 mass% in [EMIm][DEP]. As shown in Table 3.2, the measured asymptotic maximum solubility of cellulose in [EMIm][DEP] above 100°C corresponds to approximately 82% of the computed maximum theoretical solubility. Again, these calculations are using simulation data for a slightly different ionic liquid and the actual ratio of 1:1 and 2:1 anion:-OH interactions for this IL might be different and change to some extent with temperature, composition, *etc*. Based on the analysis presented herein, the quasi-chemical idea of cellulose solvation with the anions does seem to agree semi-quantitatively with both experiment and simulation.

Recent calorimetry studies for the dissolution of micro-crystalline cellulose in ILs may also help corroborate the solubility phenomena discovered here.[38, 39] Costa Gomes and coworkers found that the heat of dissolution of cellulose in [EMIm][Ac] (at near infinite dilution, <0.4 mass%) was exothermic.[38] Additionally, Nunes de Oliveira and Rinaldi illustrate that the heat of dissolution and mixing of cellobiose (the simplest β-1-4-disaccharide with a degree of polymerization, DP, of 2 anhydroglucose units) at infinite dilution in [BMIm][Ac] (and

extrapolated values for pure [BMIm][Cl]) is also exothermic.[40] While cellobiose is obviously much smaller than cellulose, it is believed that these molecules exhibit similar energetic interactions with ILs. These studies imply that the IL:cellulose interactions are enthalpically favorable, but also suggest that higher temperatures will lead to lower marginal solubility compared to solutes that have little exothermic or even endothermic heats of solution. Thus for this cellulose/IL system, we would expect the *slope* of solubility to decrease with increasing temperature. However, it is currently unknown how the enthalpy of dissolution changes at higher compositions (beyond infinite dilution) where solute-solute interactions in the liquid phase become more influential as is likely the case with solutions of approximately 20 mass% observed for [EMIm][DEP] at 100^{o}C.

3.3. Antisolvent Effects on Cellulose Dissolution

Nearly all aqueous and organic solvents precipitate cellulosic biomass from ionic liquid mixtures and thus are considered antisolvents. Furthermore, the majority of proposed processes for the separation of cellulose from ionic liquids utilize antisolvent precipitation.[41-46] Hydrogen bond donating solvents (*i.e.* water, alcohols, *etc.*) closely associate with negatively charged ionic liquid anions. When mixed with ILs, protic solvents compete for interactions with IL anions and interfere with their ability to dissolve cellulose. Thus, the preferential binding between IL anions and protic solvents results in precipitation of cellulose from IL-protic solvent mixtures.[20]

Protic solvents including ethanol, methanol, and water contain acidic hydrogen atoms and participate in hydrogen bond interactions. When protic solvents are added to IL-cellulose mixtures, they disrupt the favorable IL-cellulose interactions thus reducing the cellulose capacity of IL-antisolvent mixtures.[37, 47] To assess the thermodynamic effect of antisolvents on

cellulose dissolution, solid-liquid equilibrium measurements were conducted on mixtures of [EMIm][DEP] with 1, 3, and 5 mass% antisolvent loadings of ethanol, methanol, and water at 40°C. As these antisolvents have much lower molecular masses than the IL (264.26 g/mol), these mass fractions represent much higher mole fractions, *e.g.* for water 1 mass% = 12.9 mole%; 3 mass% = 31.2 mole% and 5 mass% = 43.6 mole%; less of a difference exists for methanol and ethanol. As displayed in Figure 3.6, ethanol, methanol, and water all significantly reduce the cellulose capacity of [EMIm][DEP]. Compared to the cellulose capacity of the pure IL which dissolves 9.1 mass% cellulose at 40°C, cellulose solubility in mixtures of [EMIm][DEP] with just 1 mass% antisolvent (cellulose-free basis) are 8.3 mass%, 7.6 mass%, and 6.6 mass% for ethanol, methanol, and water respectively. At a 3 mass% antisolvent loading, cellulose solubility in the same antisolvent systems are 6.9 mass%, 5.5 mass% and 0.5 mass% respectively. Therefore, inclusion of only 3 mass% antisolvent reduces the cellulose capacity of the IL-mixed solvent systems by 24% and 40% for ethanol and methanol and by 95% for water. At a 5 mass% antisolvent loading at 40°C, the solubility of cellulose in the IL mixture with water is undetectable by our current experimental method and is estimated to be less than 0.1 mass%.

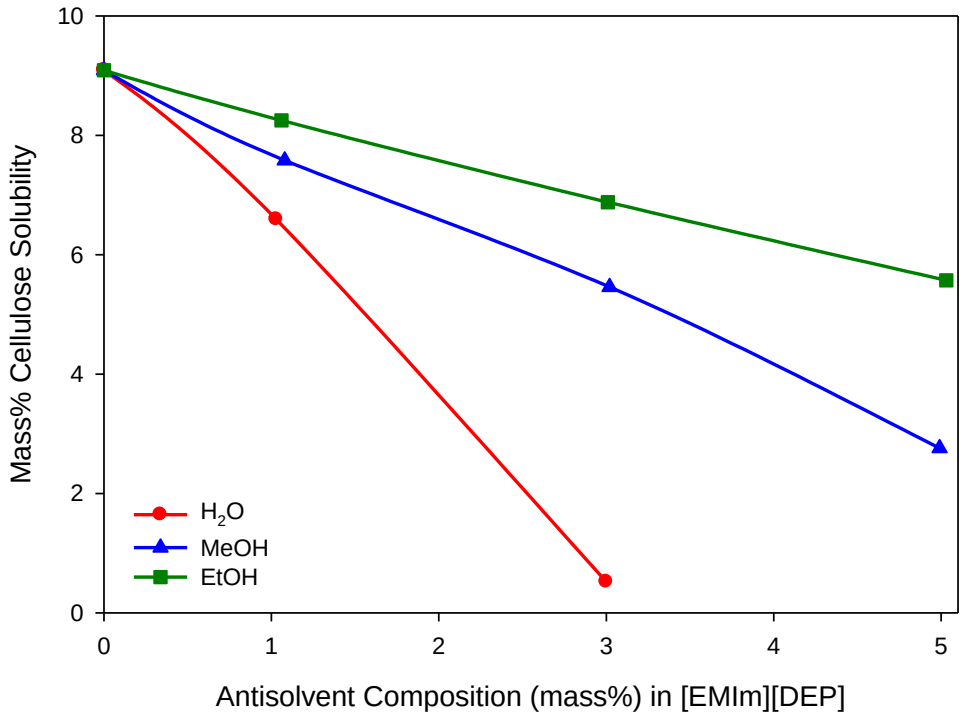

Figure 3.6: Thermodynamic solubility limit of cellulose in [EMIm][DEP]-antisolvent mixtures at 40°C. Lines are smoothed data.

As opposed to the pure IL case above, a simple quasi-chemical model could not be quantitatively applied here as cellulose and antisolvent molecules both contain hydroxyl groups. To evaluate the antisolvent effects, the anion: cellulose -OH ratio was computed for the mixed [EMIm][DEP]-antisolvent systems studied. At 80°C the anion:-OH ratio for cellulose dissolved in pure [EMIm][DEP] is 0.9. For cellulose dissolution in [EMIm][DEP] with 1 mass%, 3 mass%, and 5 mass% loadings of water at 80°C the anion:-OH mole ratios calculated from the experimental solubilities are: 1.0, 1.4, and 1.9 respectively. Therefore, the number of IL ions in solution relative to cellulose -OH groups appears to increase with higher antisolvent loadings and exceeds the required anion:-OH ratio for cellulose dissolution in the pure IL at the same

temperature. However in the presence of protic antisolvents, there is now competition for the IL anion between cellulose and antisolvent -OH groups. These competitive interactions were investigated by comparing the calculated IL: cellulose -OH and IL: antisolvent -OH ratios for all three systems (see Appendix 3). By determining the molar ratio of anions to antisolvent -OH groups it becomes evident that antisolvent molecules have a high probability of being in the cybotactic region of both the ionic liquid and cellulose thus disrupting IL solvation of the biopolymer. A computational study by Rabideau and Ismail similarly found that as water content in an IL increases, IL-water hydrogen bonds readily form and the frequency of IL-cellulose hydrogen bonds significantly decrease.[37] Therefore, decreased cellulose solubility with increased antisolvent (water) loading is likely caused by competitive interactions between the protic antisolvent and IL inhibiting hydrogen bond formation between the IL and cellulose and concomitantly promoting strong cellulose-cellulose interactions.

Increased temperature slightly mitigates antisolvent effects on cellulose dissolution capacity, as shown in Figure 3.7 for the [EMIm][DEP]-H_2O system. At a 3 mass% H_2O loading on [EMIm][DEP] (cellulose free basis), 0.5 mass% cellulose is soluble at 40°C. Increasing the temperature to 60°C and 80°C results in cellulose dissolution capacities of 9.6 and 12.7 mass% respectively. At a 5 mass% water loading, whereas cellulose is completely insoluble at 40°C, the same system at 60°C dissolves 5.3 mass% cellulose and at 80°C the system dissolves 6.3 mass% cellulose. Compared to the pure IL system at these temperatures, 5 mass% water on the IL reduces the cellulose capacity of the mixture by 100%, 61%, and 66% for the 40°C, 60°C, and 80°C temperatures.

Nunes de Oliveira and Rinaldi measured infinite-dilution heat of mixing (dissolution) values of cellobiose in [BMIm][Cl] with varying quantities of water. Whereas the heat of mixing for cellobiose dissolution in pure [BMIm][Cl] was exothermic, when approximately 4.5-5 mass% water was in the IL, the heat of mixing values were approximately zero. Furthermore, at water loadings greater than 5 mass% H_2O in [BMIm][Cl], the heat of mixing for cellobiose dissolution became endothermic. While the molecular weights of cellobiose and cellulose vary considerably, it is believed that the molecules will have similar energetic interactions with water and the IL. This implies that the cellulose interactions in the IL-water mixture are less energetically favorable at higher water compositions and that solubility should increase at a greater rate with increased temperatures as demonstrated experimentally here. Furthermore, MD simulations by Partharsarathi *et al.* illustrate that at high temperatures (~160°C) water in small proportions (<~2 mass%; <~20 mole%) has little effect on the number of H-bonds between cellulose and the anion of [EMim][Ac] compared to the pure IL.[48] However at lower temperatures, there is significant competition whereby the anions are solvated by water and unable to interact with cellulose.[37]

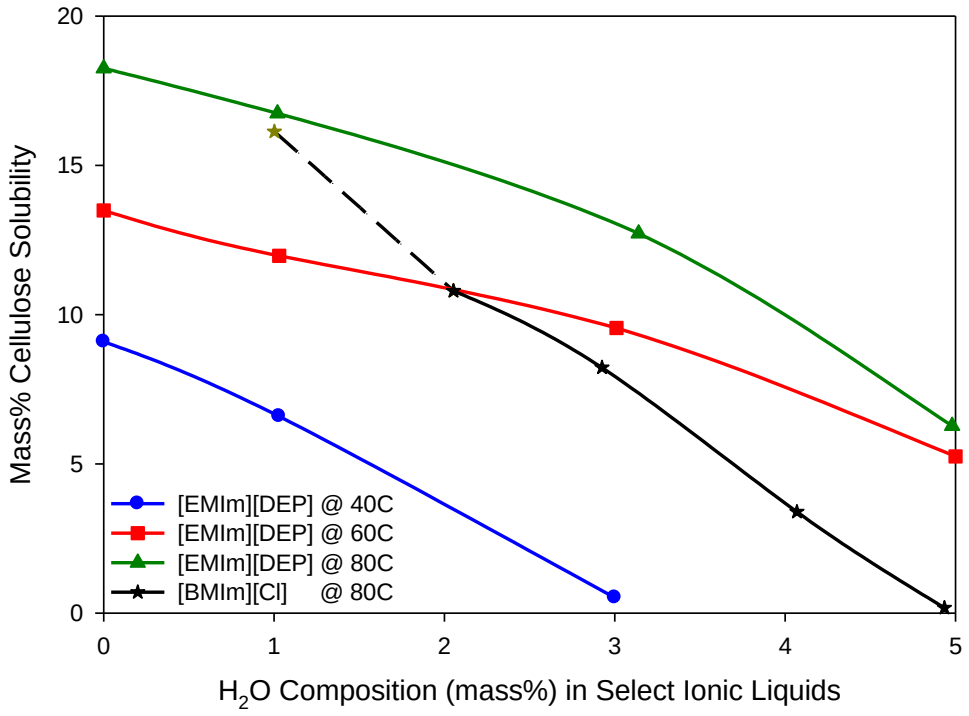

Figure 3.7: Thermodynamic solubility limit of cellulose in mixtures of ionic liquids [EMIm][DEP] and [BMIm][Cl] with H_2O at 40°C, 60°C, and 80°C, lines are smoothed data. Gold star indicates potential mass transfer limitations or gel effects.

The antisolvent effect of water was investigated in another ionic liquid, 1-butyl-3-methyl-imidazolium chloride ([BMIm][Cl]) at 80°C for comparison. Mixtures of [BMIm][Cl] and cellulose are highly viscous, even at elevated temperatures, thus inhibiting accurate thermodynamic solubility measurements of cellulose in the pure IL at 80°C. Many publications cite that the solubility of cellulose in pure [BMIm][Cl] at 100°C is between 10-25 mass% and much discrepancy exists in the exact value likely due to variation in IL purity, IL water content, cellulose source, and limitations caused by the high mixture viscosities of [BMIm][Cl] systems, *etc.*[2] However with the addition of water, we were able to quantitatively measure the solubility of cellulose down to 2 mass% H_2O (solute free basis; 16.5 mole %). For pure [BMIm][Cl] and

this IL with 1 mass% H_2O, the measurements became extremely difficult, even with equilibration times greater than one week, and the accuracy of the measurement was significantly diminished. When antisolvent (H_2O) quantities greater than 2 mass% were added to [BMIm][Cl], the biomass solubility of the mixture was reduced to a point where thermodynamic equilibrium could be obtained with high certainty and reproducibility. At a 2 mass% (solute free basis) water loading the solubility of cellulose in [BMIm][Cl] was 10.8 mass% (total solution basis). As water content in the IL increased the cellulose solubility of the mixture decreased significantly. At a 3 mass% loading of H_2O, cellulose solubility in [BMIm][Cl] was 8.2 mass%. For comparison, at the same temperature and water loading, [EMIm][DEP] dissolved 12.7 mass% cellulose, 35% more than [BMIm][Cl]. Additionally, the cellulose solubility in a solution of 5 mass% water with [BMIm][Cl] was 0.2 mass%. At these conditions [EMIm][DEP] dissolved 6.3 mass% cellulose. Therefore, based on the comparison of these two ILs at 80°C it is evident that [EMIm][DEP] has a better tolerance to water content on a more practical mass basis. The overall trend of cellulose solubility as a function of antisolvent quantity is roughly linear for both [EMIm][DEP] and [BMIm][Cl] with water, methanol, and ethanol. For instance, the change in solubility with water content is fairly linear between 1% and 5% for [BMIm][Cl] indicating that the data could potentially be extrapolated to estimate cellulose solubility in the pure IL. Based on this extrapolation method we estimate the solubility of cellulose in pure [BMIm][Cl] would be approximately 19.5 mass% which is well within the previously published literature range of cellulose solubility in this IL (and similar to the maximum cellulose solubility of [EMIm][DEP] at the same temperature). Thus, this antisolvent dilution method may help determine approximate solubilities of cellulose in pure ILs when direct measurement is difficult or impossible.

The solid-liquid equilibrium data presented demonstrate that small quantities of liquid antisolvents significantly impact cellulose solubility in ILs. The use of ILs and antisolvents for the pretreatment of cellulose has been highly investigated in the literature for the purpose of decreasing cellulose crystallinity and to improve conventional chemical or biochemical conversion methods to produce chemicals and fuels. The cellulose solubility data indicates that ionic liquids must be highly purified from the protic antisolvent before recycling the IL for subsequent biomass pretreatment cycles. Even small quantities of residual antisolvent in the IL such as 1 mass% could hinder the process by significantly reducing the biomass capacity of the ionic liquid. Moreover, most biomass contains at least 20% water, indicating that the separation of water will always be necessary for recycling the ionic liquid unless the biomass is highly dried at additional cost. Using the phase equilibrium data here as a guide, cellulose containing 20 mass% water would require approximately 50% more ionic liquid to dissolve a comparative amount of completely dry cellulose. While this solubility data also indicates that only small amounts of antisolvent are necessary to induce a separation of cellulose from the IL, we and others have observed that antisolvent quantities in significant excess of that required to reach the thermodynamic saturation point are needed to effectively precipitate cellulose from IL mixtures.[14] Antisolvent mass loadings of 1:1 (antisolvent:IL) 2:1 or greater are generally required to reduce the viscosity of the heterogeneous cellulose-IL/antisolvent mixtures, reduce mass transport limitations, remove adsorbed or trapped IL from the cellulose matrix, *etc*. Thus, separation of the antisolvent from the IL is a major consideration for potential applications and understanding the interactions between the IL and antisolvent become critical.

3.4. Mixed IL-Cosolvent Systems for Cellulosic Biomass Processing

Cellulose is negligibly soluble in a majority of aqueous and organic solvents. When added to IL/cellulose mixtures, most molecular solvents induce cellulose precipitation and thus, most are considered antisolvents.[41-46] However, we and others have found that some polar aprotic solvents may actually be considered cosolvents when mixed with an IL.[16, 21, 47, 49-51] For instance, in select mass ratios and at certain temperatures mixed IL-cosolvent systems can enhance the thermodynamic solubility of cellulose and dissolve more biomass than the pure ionic liquid at the same temperature. Furthermore, some recent experimental and computational studies may indicate additional advantages of mixed IL-cosolvent systems for cellulose dissolution.[16, 47] These studies demonstrate that dissolution time, temperature, and mixture viscosity of cellulose in IL solutions can be reduced by inclusion of a cosolvent.[50, 52]

The solubility of cellulose was investigated in mixtures of [EMIm][DEP] with DMSO, DMF, and DMI at temperatures between 40°C and 80°C. The selected cosolvents possess some of the highest Kamlet-Taft basicities (β) and lowest *KT* acidities (α) of any common polar aprotic solvent making them ideal candidates for the cellulose dissolving mixed solvent systems. Figure 3.8 illustrates the effect of increasing cosolvent (DMSO) composition on the solubility of cellulose at three temperatures. Surprisingly at 40°C and 60°C, cellulose solubility increases with cosolvent addition to a global maximum followed by a steep decrease in the solubility at higher cosolvent loadings. Thus despite the dilution of the IL on a mass basis, the solubility of cellulose actually increases with moderate amounts of cosolvent.

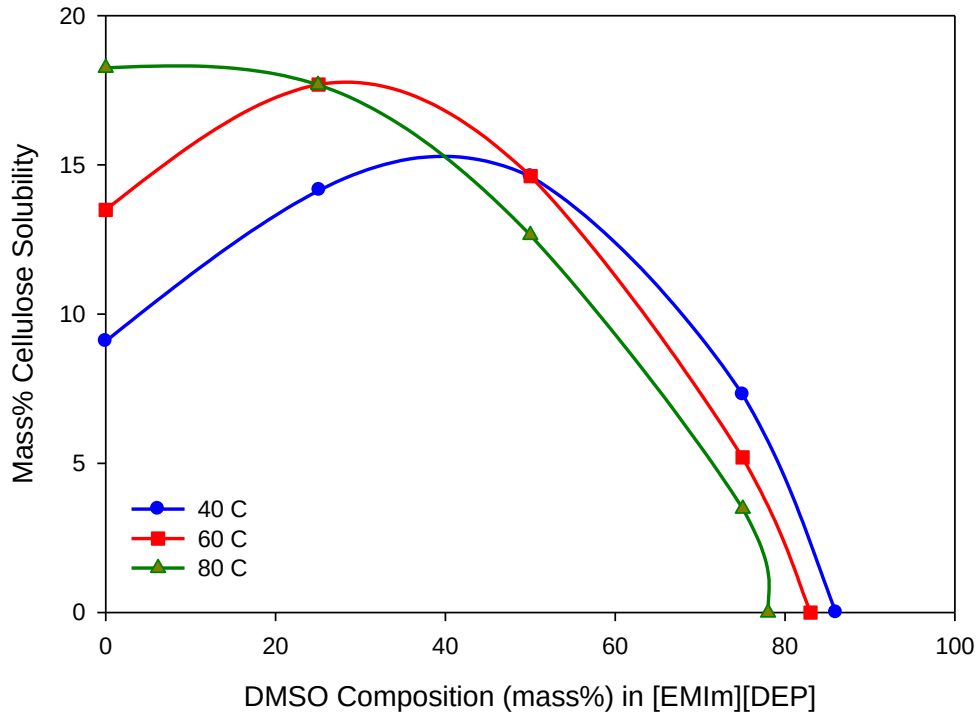

Figure 3.8: Cellulose solubility in [EMIm][DEP]/DMSO mixtures at 40°C, 60°C, and 80°C. Lines are smoothed data.

For instance, a 25 mass% DMSO-IL mixture (cellulose free basis) at 40°C dissolves 14.2 mass% cellulose (total solution basis), a 56% increase in cellulose capacity relative to the pure IL system at the same temperature. Furthermore, the maximum cellulose capacity at 40°C occurs at a 50 mass% cosolvent loading where the mixture solubility is 14.6 mass%; a 60% increase compared to the pure IL at 40°C. These results demonstrate that in select ratios, DMSO is capable of enhancing cellulose dissolution in IL mixtures allowing the mixed solvent system to dissolve more cellulose than the pure IL itself. It should be highlighted that these are true thermodynamic results and not due to mass transfer effects. At 60°C, the maximum cellulose solubility approximately occurs at a 25 mass% cosolvent loading. Interestingly at 80°C, increasing

cosolvent loadings up to 25 mass% appear to have little effect on the solubility. However beyond 25 mass%, there is a steeper decrease in solubility with increasing cosolvent composition than at the other temperatures.

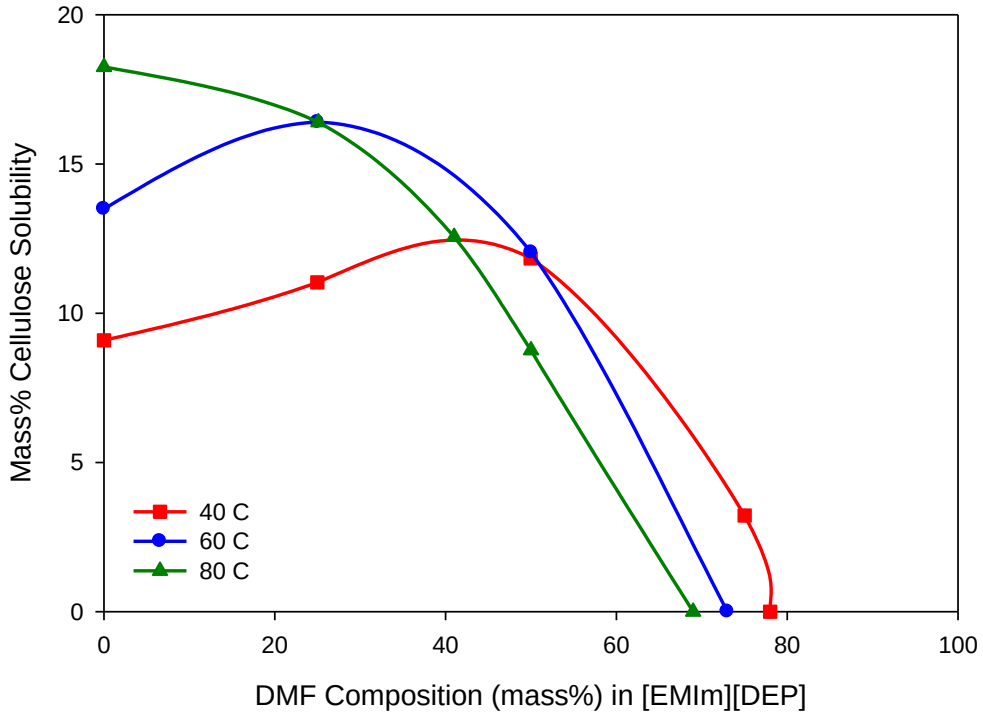

Figure 3.9: Cellulose solubility in [EMIm][DEP]/DMF mixtures at 40°C, 60°C, and 80°C. Lines are smoothed data.

Similar to the DMSO cosolvent system, at 40°C, [EMIm][DEP]-DMF mixtures, shown in Figure 3.9, display a maximum cellulose solubility of 11.0 mass% (total solution basis) at a 50 mass% cosolvent loading (cellulose free basis). This represents a 30% increase in cellulose capacity relative to pure [EMIm][DEP] at the same temperature. At 60°C, the maximum measured cellulose solubility (16.4 mass%, total solution basis) occurred at a 25 mass% DMF loading. This represents a 21% increase compared to cellulose solubility in the pure IL at the same

temperature. At 80^{o}C the maximum cellulose solubility was observed to occur in the pure [EMIm][DEP] system and similar to what was observed for the DMSO system and cosolvent additions of 25 mass% or greater negatively impacted cellulose solubility of the mixture.

Maximum cellulose solubilities for the DMI system again occurred at cosolvent loadings of 50 mass%, 25 mass%, and 0 mass% for the 40^{o}C, 60^{o}C, and 80^{o}C temperatures respectively as shown in Figure 3.10. At 40^{o}C the maximum measured cellulose solubility in the mixture was 12.4 mass% on a total solution basis at a 50 mass% DMI cosolvent loading marking a 36% enhancement in cellulose capacity of the mixture relative to pure [EMIm][DEP]. Furthermore, a 23% increase in cellulose capacity was observed in the 25 mass% DMI mixture at 60^{o}C which dissolved 16.6 mass% cellulose.

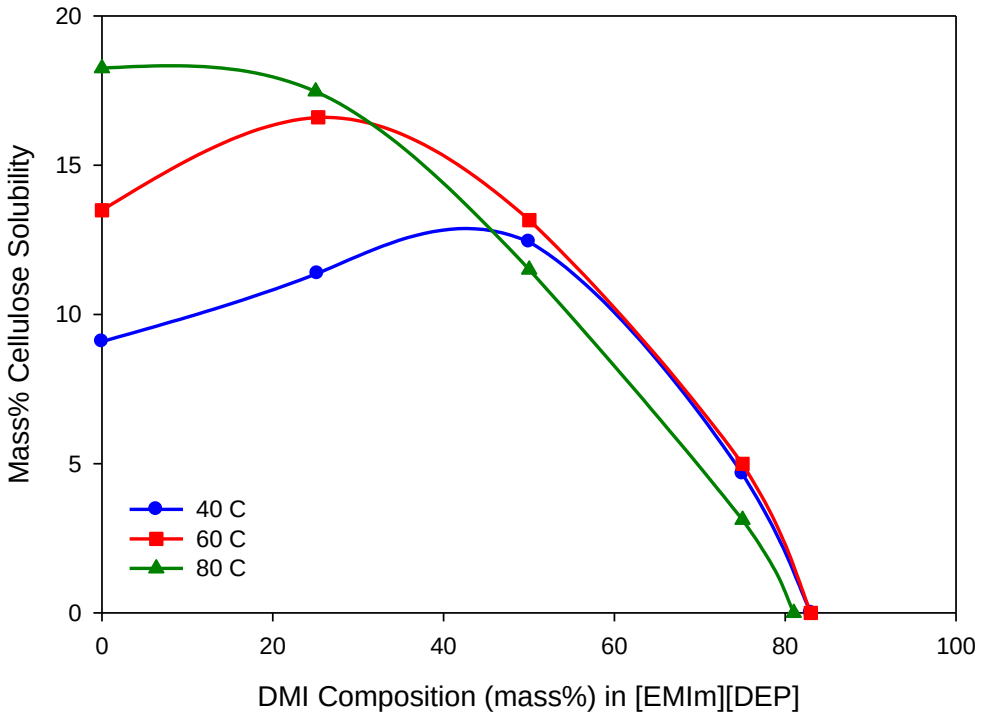

Figure 3.10: Cellulose solubility in [EMIm][DEP]/DMI mixtures at 40°C, 60°C, and 80°C. Lines are smoothed data.

Interestingly, for the DMSO, and DMF, and DMI systems several solubility data points are closely correlated despite being at different temperatures. For instance, the experimentally measured cellulose solubilities of the 25 mass% DMF cosolvent system at 40°C and 60°C are 11.8 mass% and 12.0 mass% respectively. Similarly, mixtures of 50 mass% DMF with [EMIm][DEP] at 60°C and 80°C display identical cellulose solubilities of 16.4 mass%. Therefore, from a process engineering perspective, inclusion of a cosolvent could lower the required operating temperature of the process while maintaining a fixed cellulose capacity of the mixture.

Table 3.3 displays the maximum cellulose solubilities at 40°C, 60°C, and 80°C for the various cosolvent systems. At both 40°C and 60°C the highest cellulose solubilities are observed in [EMIm][DEP]-DMSO mixtures followed by IL mixtures with DMI and DMF. Alternatively at 80°C no cosolvent was able to enhance cellulose dissolution and the pure IL system displayed the highest solubility. Therefore, by comparing the maximum cellulose solubility data it is evident that the order of effective cosolvents for cellulose dissolution is: DMSO > DMI > DMF. Complete solid-liquid equilibrium data sets and ternary diagrams for cellulose solubility in the [EMIm][DEP] cosolvent systems can be found in Appendix 3.

System	Temperature	Cellulose Solubility [Mass%]	%Increase in Cellulose Capacity Relative to Pure [EMIm][DEP]
25 mass% DMSO	40	14.6	32
25 mass% DMI	40	12.4	23
25 mass% DMF	40	11.8	21
50 mass% DMSO	60	17.7	61
50 mass% DMI	60	16.6	36
50 mass% DMF	60	16.4	30
Pure [EMIm][DEP]	80	18.3	N/A

Table 3.3: Maximum cellulose solubilities of the mixed IL-cosolvent systems and percent increase in cellulose capacity relative to pure [EMIm][DEP] at 40°C, 60°C, and 80°C.

The effect of temperature at constant cosolvent loadings is illustrated in Figure 3.11 for DMSO. As discussed above, a strong positive correlation between temperature and cellulose solubility is observed for pure [EMIm][DEP]. However, as the cosolvent loading is increased beyond 25 mass% the slope of cellulose solubility vs. temperature decreases and eventually inverts at compositions greater than 75 mass% DMSO. For instance, both the 25 and 50 mass% loadings initially exhibit an increase in solubility of cellulose with temperature. However for 50 mass%, the solubility changes little with temperature between 40 and 60°C followed by a steep decrease

in solubility with temperature beyond 60°C. At a 75 mass% cosolvent loading, cellulose solubility decreases with temperature throughout the range investigated.

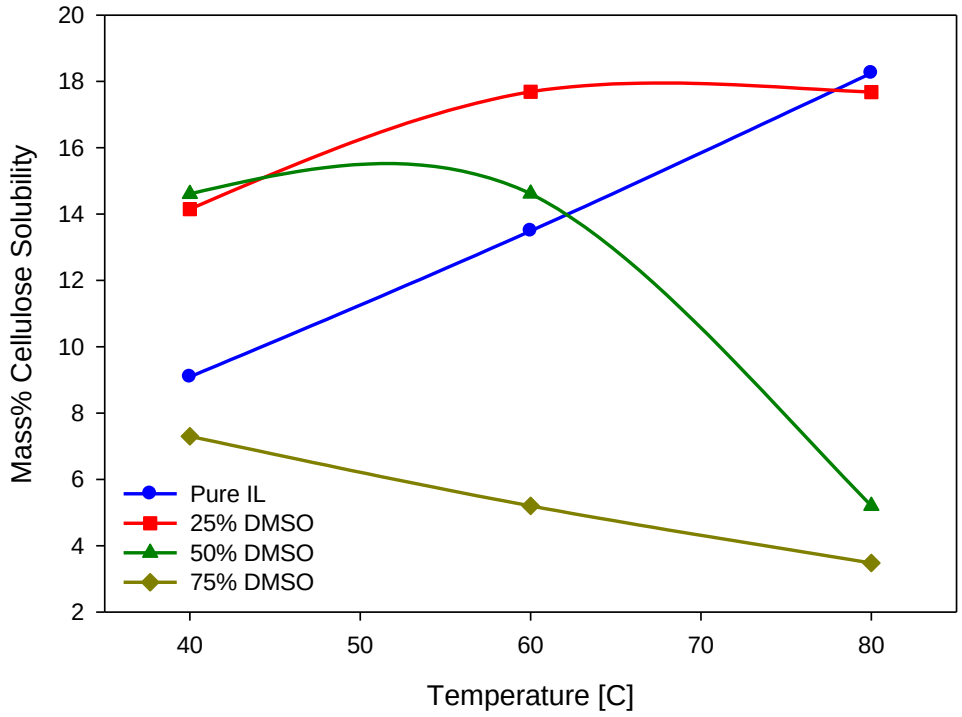

Figure 3.11: Effect of temperature on cellulose capacity in IL/DMSO mixtures of varying capacity. Lines are smoothed data.

At 40°C all three cosolvents, when loaded at concentrations greater than 50 mass%, cause a significant decrease in cellulose solubility. For the DMSO system, cellulose solubility transitions from 14.6 mass% to 7.3 mass% and finally to 0.0 mass% at cosolvent (DMSO) loadings of 50 mass%, 75 mass%, and 85 mass% respectively. On a molar basis, these DMSO loadings correspond to 77 mol%, 91 mol%, and 95 mol%. Similar solubility results are also observed for the DMF and DMI cosolvent systems when cosolvent loading is presented on a molar basis, as shown in Figure 3.12. Maximum cellulose solubility measurements in

[EMIm][DEP] mixtures with DMSO, DMF, and DMI were observed at molar cosolvent loadings of 77 mol%, 78 mol%, and 70 mol% respectively. Therefore, the ionic liquid is able to support cellulose dissolution even when significant molar cosolvent quantities are present. However, at high cosolvent loadings >80 mol% the ionic liquid concentration in the mixture is significantly diluted indicating that less anions are present in solution to solvate cellulose. As the dissolution process is driven by interactions between IL ions and cellulose, the dilution phenomena potentially explains the observed negative trend in cellulose solubility when cosolvent loadings exceed 50 mass% or 70-80% on a molar basis.

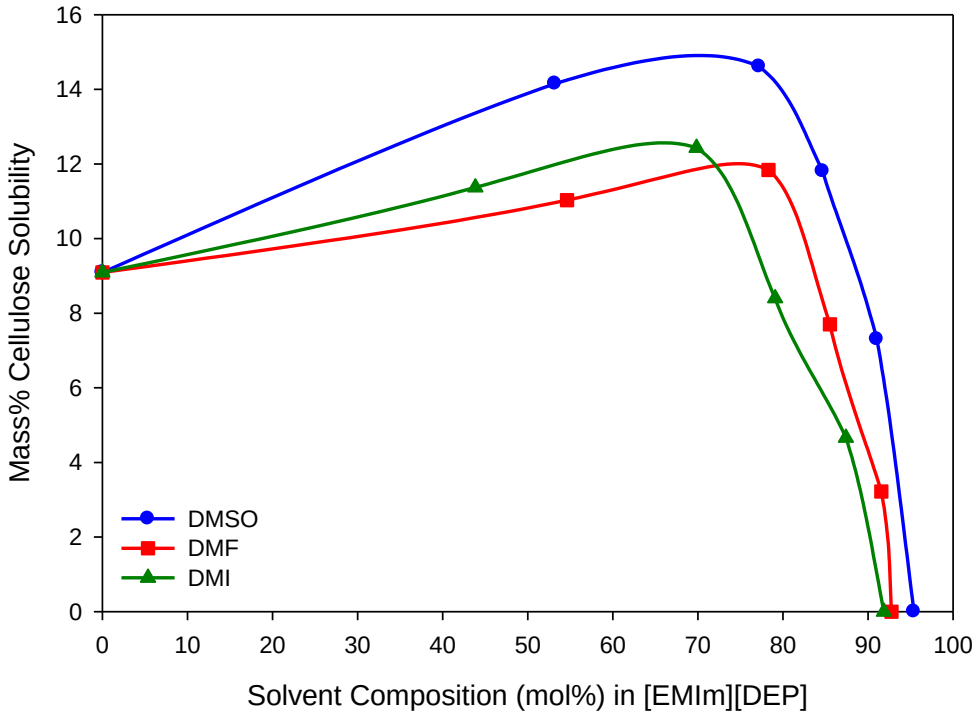

Figure 3.12: Cellulose solubility in [EMIm][DEP]-cosolvent mixtures at 40^{o}C where cosolvent loading is represented on a molar basis. Lines are smoothed data.

As previously discussed, computational findings on [EMIm][DMP] indicate that approximately 33% of IL anions are capable of forming interactions with multiple (two) cellulose hydroxyl groups while ~67% form single anion:-OH interactions. Additionally, simulation results show that only 2.54 (out of 3) hydroxyl groups per anhydroglucose unit interact with [DMP] anions; thus, a 0:1 anion:-OH bonding scenario exists for select cellulose hydroxyl groups in solution.[37] Similar trends to those observed computationally for [EMIm][DMP] are also presumed to occur for [EMIm][DEP]. Utilizing these computationally determined interaction scenarios, the anion to total cellulose -OH ratio was determined (0.64) and was used to calculate the theoretical maximum solubility of cellulose in pure [EMIm][DEP] (24.3 mass%). For cellulose solubility in the pure IL, this analysis scales well with the experimental behavior. Therefore, a similar treatment has been performed on the IL-cosolvent systems to assess the theoretical maximum solubility of cellulose in these mixed solvent systems as a function of cosolvent loading, see Appendix 3. To this point, no simulation study has investigated the anion:-OH interaction scenarios for cellulose and ionic liquids in mixed IL-cosolvent systems. Therefore, the number of 0:1, 1:1, and 1:2 interactions in the mixed solvent systems were assumed to occur in identical proportions to what was observed computationally for the pure IL. As shown in Figure 3.13 for the [EMIm][DEP]-DMSO system at 60°C the experimental and theoretical maximum solubilities are in close agreement except at high cosolvent loadings (>80+ mass% or >90+ mole%). For instance, both decrease as a function of increased cosolvent loading beyond 25 mass% DMSO. Therefore, the theoretical maximum solubility calculations may help elucidate what is physically occurring in the mixed IL-cosolvent-cellulose solutions. The theoretical maximum solubility calculations assume a specified number of anion: cellulose -OH interactions based on the previously discussed computational findings. Yet, despite

maintaining constant IL-cellulose interactions, similar decreases are observed for the theoretical and experimental solubilities. Therefore, the reduction of cellulose capacity at elevated cosolvent loadings in mixed solvent systems is likely due to ionic liquid dilution and reduction of the number of ions in solution as opposed to competition for IL anions with the solvent as was observed for the antisolvent systems. Similar findings to those presented in Figure 3.13 are also observed for the DMF and DMI cosolvent systems where the experimental and theoretical maximum solubility data correlate well, especially at 60°C and 80°C. Alternatively, for all three systems at 40°C, the maximum theoretical solubility appears to over-predict the experimental data as was similarly observed for the pure IL system at lower temperatures. These results may indicate that the solid phase thermodynamic activity could be the limiting factor for cellulose solubility at lower temperatures as opposed to the liquid phase environment. Furthermore, it is unlikely that the number and type of molecular interactions in the pure IL system would be identical to what occur in the mixed IL-cosolvent systems. Nonetheless, the presented findings may be used to quickly estimate the maximum solubility of cellulose in these mixed IL/cosolvent systems simply based upon the IL, some knowledge of the number and types of anion to cellulose -OH interactions (even from simulations), and the amount of cosolvent in the mixture.

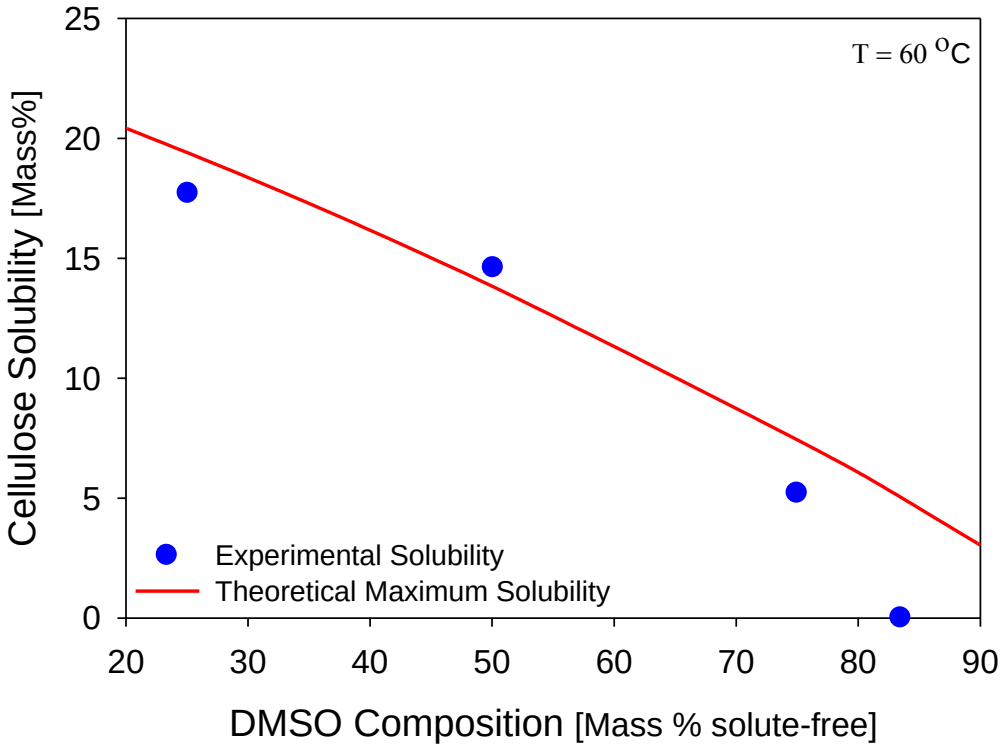

Figure 3.13: Comparison of the experimentally measured cellulose solubility and theoretical maximum solubility (based on anion:-OH interactions) at 60°C in [EMIm][DEP]-DMSO mixtures.

Costa Gomes and coworkers measured the heat of dissolution of cellulose at near infinite dilution in mixtures of [EMIm][Ac] and DMSO and found an exothermic process, although less exothermic as compared to the pure IL conditions.[50] Nunes de Oliveira and Rinaldi found that dissolution of small amounts of cellobiose in mixtures of ILs and polar aprotic cosolvents is mainly an exothermic event except at high compositions of cosolvents.[40] For instance, dissolution of cellobiose in mixtures containing cosolvent loadings greater than 50 mass% became endothermic. Assuming cellulose solubility in [EMIm][DEP] behaves similarly to cellobiose in [BMIm][Cl], it is evident that the dissolution process becomes enthalpically unfavorable as cosolvent:IL mass ratios exceed values of 1:1. Entropically, cellulose dissolution

requires a high level of coordination by IL anions to hydrogen bond to specific cellulose hydroxyl groups. As temperature increases these entropic contributions to Gibbs free energy become more influential and in conjunction with the shift in exothermic to endothermic heat of solution with increasing quantities of cosolvent it is reasoned that cellulose solubility would be negatively impacted by both temperature (at high cosolvent loadings) and at constant temperature (with cosolvent loadings beyond 1:1 mass ratios).

These results, demonstrating enhanced cellulose solubility in IL/cosolvent mixtures may have considerable practical implications for biomass processing and reactions. Cosolvents can increase cellulose capacity of IL-mixed solvent systems, lower necessary processing temperatures, improve rheological and transport properties of cellulose mixtures, and reduce the quantity of ionic liquid required by the process. Recent cellulose hydrolysis and isomerization studies indicate that polar aprotic cosolvents, when mixed with ILs, enhance reaction performance and selectivity of the conversion process to make 5-hydroxymethylfurfural.[53] Therefore, cosolvents may also have added benefits to downstream chemical conversion processes of cellulose.

3.5. Combined Anti- and Co-solvent effects on Cellulose Dissolution in an IL

Relatively small quantities of antisolvents in ILs are capable of reducing cellulose solubility to zero. However in IL/cosolvent mixtures, antisolvents seem to have slightly less of a negative effect on solubility. For instance, as shown in Figure 3.14, whereas the 97 mass% [EMIm][DEP] – 3 mass% water system (cellulose free basis) dissolves only 0.5 mass% cellulose (total solution basis), a comparative system containing 72 mass% [EMIm][DEP] – 25 mass% DMSO – 3 mass% H_2O (cellulose free basis) dissolves 10.3 mass% cellulose on a total solution basis.

Therefore, despite reducing the quantity of IL present in solution, the cosolvent significantly increases the biomass capacity of the mixture even with the same quantity of water present in solution. At a water content of 5 mass%, cellulose is completely insoluble in the binary IL-H_2O mixture at 40°C. However, when 25 mass% cosolvent (DMSO) is added to this mixture cellulose solubility increases to 4.6 mass%. Just as was observed for the IL-cosolvent systems, too much cosolvent can also significantly reduce the biomass capacity of these mixed IL-cosolvent-antisolvent systems. For instance, when 50 mass% DMSO is added to the 3 mass% water system the cellulose solubility is reduced to 7.0 mass%. This value is still significantly higher than the binary IL-water mixture solubility but is less than the mixture containing the IL, water, and 25 mass% DMSO. It is therefore evident that an optimal quantity of cosolvent exists that diminishes the antisolvent effects and concomitantly maximizes cellulose solubility in the mixed IL-cosolvent-antisolvent systems. Many ionic liquids including [EMIm][DEP], [BMIm][Cl], *etc.* are hygroscopic and readily absorb moisture from the atmosphere. Furthermore, even considerably "dry" biomass contains moderate quantities of water (*e.g.* 20+ %). As demonstrated above, water is a strong antisolvent for cellulose. Combining ILs with cosolvents may therefore improve the water tolerance for biomass processing.

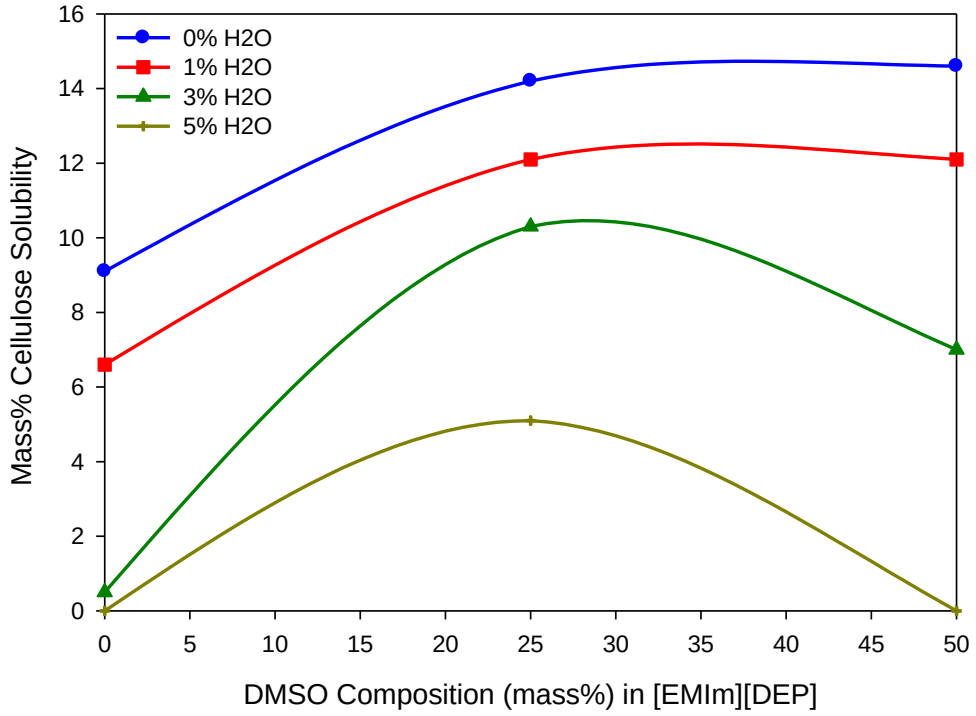

Figure 3.14: Cellulose solubility in [EMIm][DEP]+Cosolvent mixtures with varying quantities of antisolvent H_2O included at 40^{o}C. Lines are smoothed data.

3.6. Spectroscopic Analysis of Mixed IL-Solvent Systems for Cellulose

Interactions between the IL and molecular solvents were investigated by Kamlet-Taft solvatochromic analysis, FTIR, and NMR spectroscopy. The results indicate that preferential solvation of the IL cation and anion by co- and anti- solvents impact the ability of IL ions to interact with cellulose thus affecting the cellulose dissolution capacity of IL-solvent mixtures.

3.6.1. Kamlet Taft Solvatochromic Polarity Analysis

Kamlet-Taft properties of pure [EMIm][DEP] and mixed IL-solvent systems were measured to characterize the mixtures in terms of hydrogen bond donating ability or acidity (α), hydrogen

bond accepting ability or basicity (β), and dipolarity/polarizability (π^*). The large biomass capacity of pure [EMIm][DEP] (19.8 mass% at 100°C) is primarily attributed to the hydrogen bond accepting ability (basicity) of the IL anion.[13, 14, 16, 54-56] The basicity of [EMIm][DEP] (β=1.07) is comparatively higher than both [BMIm][Cl] (β=0.87)[57] and [EMIm][Ac] (β=0.95)[58] two of the most highly touted ILs for cellulosic biomass dissolution. The acidity of [EMIm][DEP] is primarily a function of the [EMIm] cation's bridging C-H group and was measured to be α=0.47 for the IL with a high polarizability at π^*=1.09.

Solvent	α	β	π^*
Water	1.17 (1.17)[a]	0.17 (0.14)[a]	1.09 (1.09)[a]
Ethanol	0.86 (0.86)[a]	0.75 (0.80)[a]	0.54 (0.54)[a]
DMF	0.17 (0.14)[b]	0.64 (0.69)[b]	0.87 (0.88)[b]
DMSO	0.15 (0.10)[b]	0.69 (0.76)[b]	1.04 (0.99)[b]
DMI	0.16 (N/A)	0.79 (N/A)	0.91 (N/A)
[EMIm][DEP]	0.46 (N/A)	1.07 (N/A)	0.98 (N/A)

Ref. **[59]** b) Ref. **[60]**.

Table 3.4: Pure component Kamlet-Taft parameters for select solvents of interest compared to published literature values in parentheses.

The Kamlet-Taft properties of the polar aprotic solvents DMSO, DMF, and DMI used in this study are presented in Table 3.4. All three cosolvents have moderate hydrogen bond accepting abilities (β>0.64) and correspondingly low hydrogen bond donating abilities (α<0.17). Therefore, these cosolvents do not compete with the IL anion for interactions with the hydroxyl groups on cellulose. To assess cosolvent effects on mixed IL-solvent systems, Kamlet-Taft parameters were measured across a range of cosolvent loadings for the DMSO, DMF, and DMI systems. It is well known that *KT* parameters of mixed solvents may be problematic if different local composition effects exist in the cybotactic region the dye molecule compared to the solute molecule of interest.[61] However, we assert that high polarity of both cellulose and the dyes will lead to similar solvent environments; at the very least qualitatively. At a cosolvent loading

of 25 mass% the basicity of all three IL-cosolvent mixtures are higher than any of the pure solvents as demonstrated in Figure 3.15. For instance, the 25 mass% DMF – 75 mass% IL system has a basicity value of β=1.12 which is approximately 5% greater than the basicity value of the pure IL and which is above and beyond the experimental uncertainty. Therefore, in the presence of mixed IL-cosolvent systems, Kamlet-Taft probes experience enhanced hydrogen bond accepting strength of the mixed solvent system relative to the pure IL. Rinaldi found that the *KT* parameters (especially β and π^*) of [EMIm][Ac] mixtures with a variety of solvents do not change significantly from the pure IL values except for compositions of solvents beyond approximately 80 mole%.[16] A maximum was not shown in this data, however, no *KT* parameters were measured in the dilute range between 0 to 50 mole% cosolvents, which is the region we observe most of these maxima.

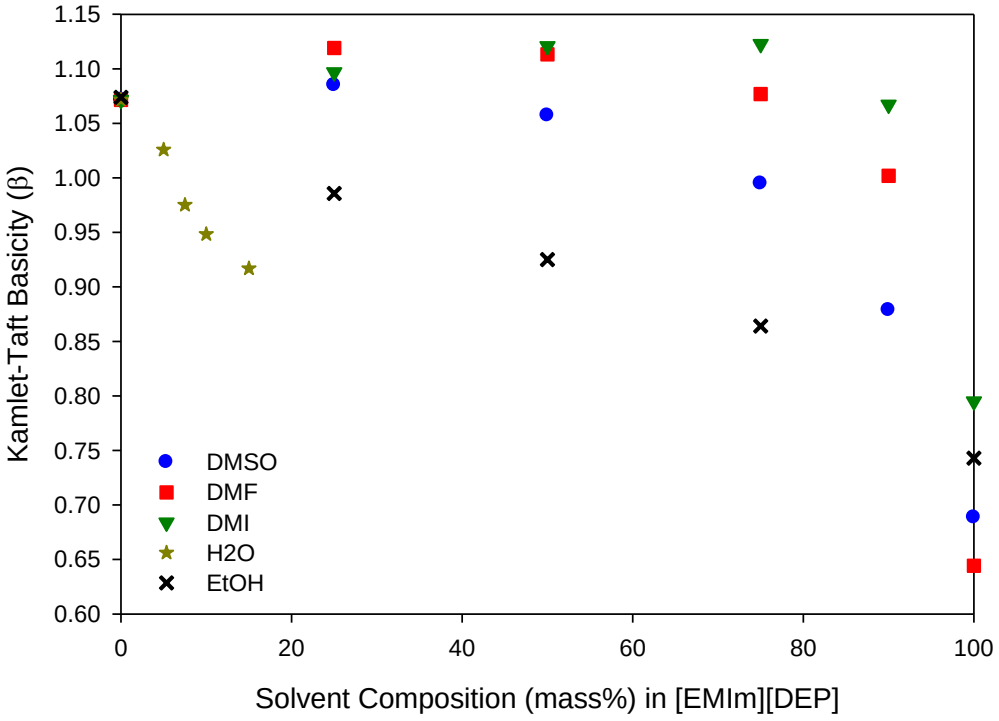

Figure 3.15: Kamlet-Taft basicity (β) of select mixed IL-cosolvent and IL-antisolvent systems.

Combining solvents that possess similar Kamlet-Taft properties can sometimes result in synergistic behavior on the mixture polarity as seen in other systems.[62] Here, only the basicity (β) was observed to have a higher value than the corresponding pure component value or any type of mole/mass fraction average of their values. Alternatively, acidity (α) decreased upon the addition of cosolvents likely due to the low α values of the pure organic cosolvents as shown in Figure 3.16.

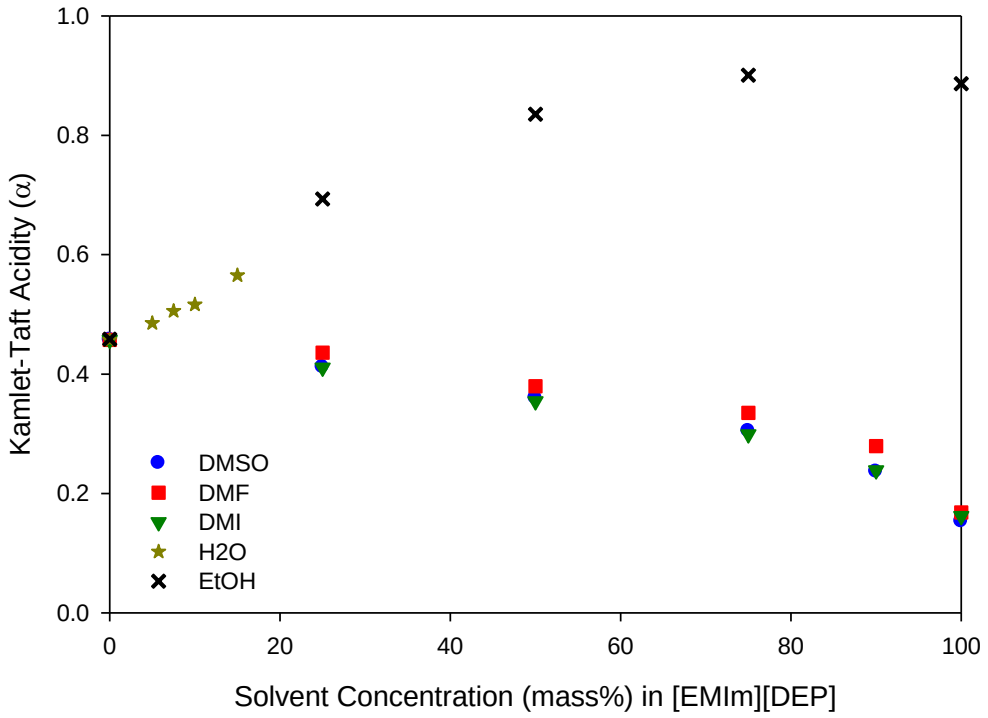

Figure 3.16: Kamlet-Taft acidity (α) of select IL-cosolvent and IL-antisolvent systems.

In addition, the cosolvents may also better solvate the imidazolium cation with its slightly acidic hydrogen reducing interactions with the probe and potentially anion. The Kamlet-Taft results for the IL-cosolvent mixtures demonstrate increased basicity (in select loadings) and decreased acidity, two essential characteristics required for cellulose dissolution. Correspondingly the solid-liquid equilibrium results demonstrate that cosolvent loadings between 25-50 mass% enhance the cellulose capacity of mixed IL-cosolvent systems relative to pure [EMIm][DEP] at 40°C and 60°C. Conversely, at high cosolvent loadings (*i.e.* >75 mass%) the cosolvent properties become increasingly dominant due to the reduced quantity of ionic liquid in solution causing a sharp decrease in the basicity value of the mixed solvent system. A comparison of the trends in cellulose solubility and Kamlet-Taft basicity is shown for the [EMIm][DEP]-DMF

cosolvent system at 40°C in Figure 3.17. The basicity data appears to correlate well to cellulose solubility in the IL-cosolvent systems with maxima in both basicity and solubility occurring within approximately 25 mass% of each other. Therefore, Kamlet-Taft polarity measurements could be utilized as future performance predictors of optimal mixed solvent systems for biomass processing.

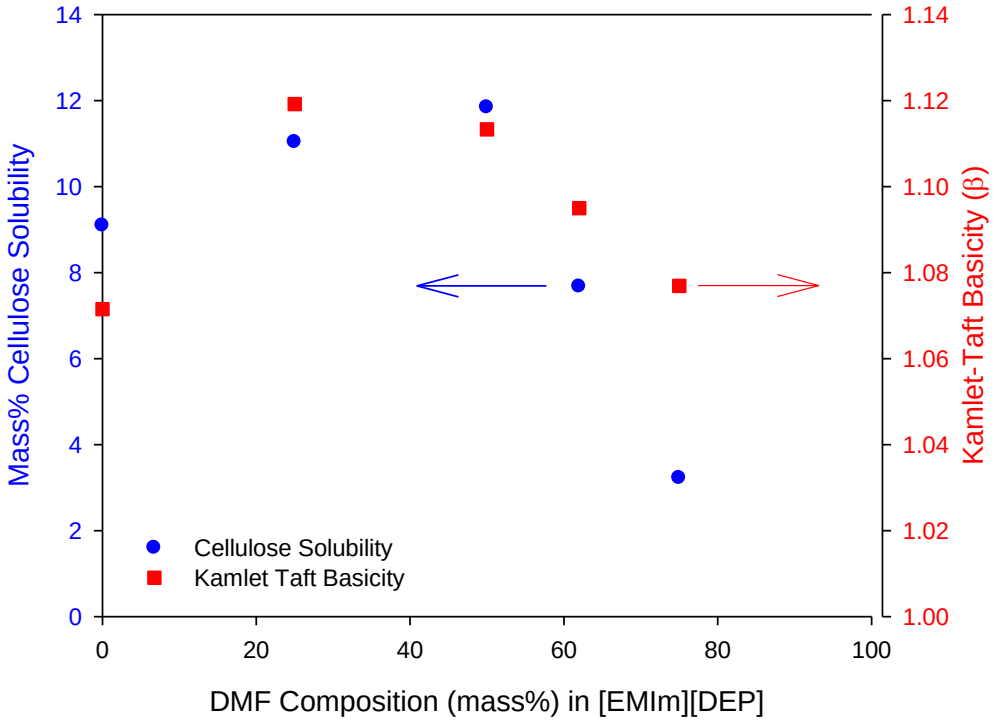

Figure 3.17: Comparison of the trends in cellulose solubility and Kamlet-Taft Basicity (β) for the [EMIm][DEP]-DMF mixed cosolvent system.

In contrast to aprotic cosolvents, protic antisolvents including water and ethanol possess hydrogen-bond donating atoms and demonstrate high Kamlet-Taft acidity values (α>0.86). When mixed with ionic liquids, protic antisolvents cause significant decreases in basicity (β) and sharp increases in acidity (α) of the IL-antisolvent mixture as shown in Figure 3.15 and Figure

3.16 respectively. Due to the limited solubility of Reichardt's Betaine (30) dye in water, Kamlet-Taft properties of [EMIm][DEP]-water mixtures were only measured up to 15 mass% H_2O loadings. Alternatively, measurements on the ethanol system were obtained across the entire composition range and demonstrate antisolvent effects at high mass loadings. The decrease in basicity of IL-water mixtures is notably steeper than that of IL-ethanol systems. The reduction in hydrogen bond accepting ability of the IL-antisolvent mixture is likely due to hydrogen bond formations between water and the [DEP] anion which reduce the quantity of hydrogen bond accepting sites available to interact with the solvatochromic probe. Therefore, it is possible that water forms stronger interactions with the IL anion and causes a greater decrease in the hydrogen bond accepting ability of the IL-water mixture. Correspondingly, solid-liquid equilibrium measurements demonstrate that water is a stronger antisolvent than ethanol for cellulose.

Assuming that the IL-antisolvent systems interact similarly with cellulose as compared to the solvatochromic probes this helps to explain the significant decrease in cellulose capacity upon the addition of protic antisolvents. However, the dramatic drop in cellulose solubility at only a few percent of antisolvent composition does not seem to quantitatively scale with the more gradual decrease in β and more gradual increase in α. From the current understanding on the more chemical/stoichiometric nature of cellulose dissolution with the IL anion, the differences in the nature of the solvatochromic probes and cellulose become more apparent.

3.6.2. Anion Solvation by Co- and Anti- Solvents assessed by ReactIR

Compared to ILs, protic and aprotic solvents demonstrate weak interactions with cellulose, reflective of their inability to dissolve the biopolymer.[47] Alternatively, molecular dynamics

studies indicate that cosolvents and antisolvents demonstrate moderate interactions with IL cations and anions.[63] Therefore, the change in cellulose capacity of mixed solvent systems relative to pure ILs is primarily due to direct interactions between ionic liquid and solvent molecules which alter the ILs ability to interact with cellulose. Solvent effects on the [DEP] anion were investigated by studying spectral shifts in the IR spectra of the mixed IL-solvent systems. The P=O stretching resonance of the diethyl phosphate anion was selected to assess solvent interactions with the pure IL and occurs at 1240 cm^{-1}.[64, 65] When cosolvents, investigated herein by DMSO, are present in solution, the P=O resonance experiences a solvent dependent blue shift and moves to higher wavenumbers as shown in Figure 3.18.

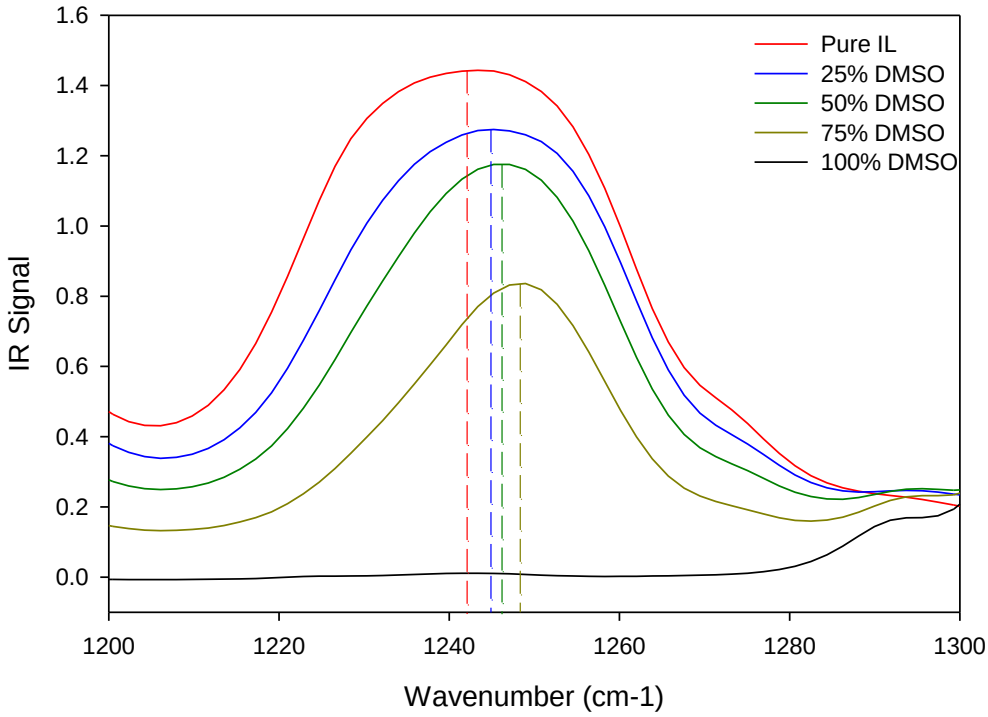

Figure 3.18: FTIR blue shift of the P=O stretching resonance on the [EMIm][DEP] anion due to solvation by the polar aprotic cosolvent DMSO. Vertical dashed lines are provided as a reference to identify the peak maximum and display the solvent induced blue shift.

Therefore, the dipole of the anion is altered by the cosolvent environment causing the P=O bond to be strengthened. In conjunction with the Kamlet-Taft results we hypothesize that electron density from the P=O bond may be shifted towards the electronegative oxygen atom [O^-] of [DEP] causing the anion to exhibit increased hydrogen bond accepting behavior (basicity) when solvated by polar aprotic molecules. Alternatively, when protic antisolvents, demonstrated by water, are mixed with the IL we observe a strong red shift of the P=O bond and the resonance shifts to lower wavenumbers as shown in Figure 3.19.

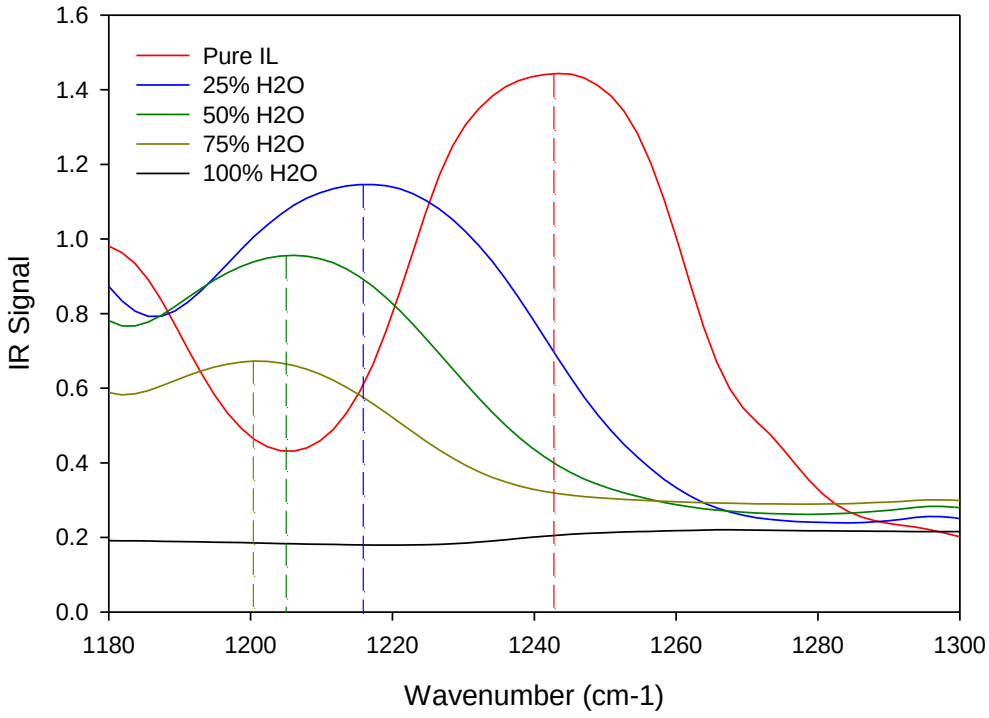

Figure 3.19: FTIR red shift of the P=O stretching resonance on the [EMIm][DEP] anion due to solvation by the polar protic antisolvent H_2O. Vertical dashed lines are provided as a reference to identify the peak maximum and display the solvent induced blue shift.

While water should preferentially interact with the electronegative oxygen atom [O^-] on the anion it is also likely that secondary interactions form between water and the oxygen atom in the P=O functional group. Electron transfer from the oxygen in P=O to the proton donor in water results in a weakening and elongation of the P=O bond thus potentially generating the red shift observed in the IR spectrum.[66, 67] The shift caused by protic antisolvents is opposite and in greater magnitude compared to the cosolvent shift. Therefore, these results seem to confirm that that protic antisolvents interact more strongly with the IL anion.[68]

A recent publication on the intermolecular interactions between 1-butyl-3-methylimidazolium acetate [BMIm][Ac] and water found that the presence of water caused a blue shift in the C=O acetate anion functional group.[69] We have experimentally confirmed similar results with [EMIm][Ac] in our laboratory. Alternatively, a study on mixtures of 1-ethyl-3-methylimidazolium ethyl sulfate [EMIm][$EtSO_4$] found that water causes red shifts in the S=O stretching resonance of the [$EtSO_4$] anion similar to what we have observed for the [DEP] anion in this study.[70] The discrepancy in direction of IR shift upon the addition of water observed for the acetate anion could be due to the central atom hybridization (SP_2 for carbon in acetate vs. SP_3 for phosphorous in [DEP] and sulfur in [$EtSO_4$]), the electronic structure of the various anions, or other factors. A detailed understanding of this phenomenon is beyond the scope of this work and has been limited to the current analysis.

3.6.3. Cation Solvation by Co- and Anti- Solvents assessed by NMR

While the interactions with the anion are of primary concern for biomass processing, cation interactions are also known to produce secondary effects. The ^{1}H NMR field shift ($\Delta\delta$ ppm) of

[EMIm][DEP] resonances in mixed solvent systems were measured relative to the pure IL to assess the solvation shell of the cation when in the presence of aqueous and organic solvents. The proton on carbon 2 of [EMIm][DEP], shown in Figure 3.20, was selected to represent solvent interactions with the IL cation.

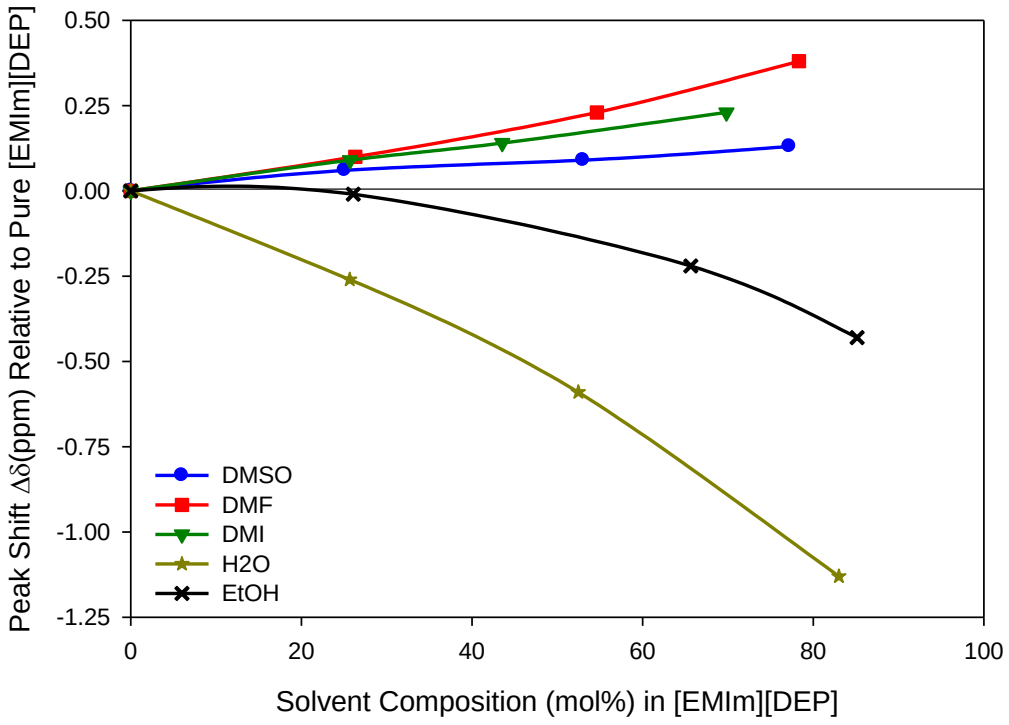

Figure 3.20: Proton 2 peak shift $\Delta\delta$ (ppm) of select mixed solvent systems relative to pure [EMIm][DEP]. Lines are smoothed data.

In the presence of aprotic cosolvents (*i.e.* DMSO *etc.*) protons on the [EMIm] cation experience a concentration dependent downfield shift of 0.1-0.4 ppm relative to the pure IL. Downfield shifts indicate that protons on the cation experience reduced shielding (less electron density) when in the presence of an aprotic solvent compared to the pure IL.[71, 72] This effect is potentially due to the solvent allowing greater separation (reduced interaction) between the

cation and anion due to solvation.[73] As a result of this solvation and reduced cation-anion interactions, the anion is potentially able make more and stronger interactions with cellulose hydroxyl- groups.

Protic antisolvents, demonstrated by water, cause up-field shifts in protons attached to the [EMIm] cation. As shown in Figure 3.20, the magnitude of the shift is significantly larger (-0.26 to -1.13) and in the opposite direction as the shift caused by aprotic solvents indicating that water and the IL cation experience stronger interactions than those between the cation and aprotic solvents. Similar up-field shifts are observed for the protic solvents methanol and ethanol. Up-field shifts indicate that electron density of this proton is increased in the presence of protic solvents relative to the pure IL.[69, 74] Interestingly, cellulose and cellobiose cause minor up-field shifts in protons on the [EMIm] cation indicating that protic solvents may form similar, but stronger, interactions with the IL cation compared to interactions formed between the cation and electronegative oxygen species within the cellulose structure.[75, 76] Therefore, these results indicate that water and other protic solvents closely associate with the [EMIm] cation potentially changing the system interactions with cellulose.[74] While IL anions are credited with driving cellulose dissolution, the role of the cation cannot be completely dismissed. Protons on the [DEP] anion were also probed by NMR spectroscopy but the observed shifts were small and inconclusive, likely due to their location on the aliphatic alkyl chain of the anion which does not actively participate in the hydrogen bonding process.

3.7. Rheological and Process Engineering Aspects of Mixed Solvent Systems

The large cation and anion substituents that provide ILs their characteristically low melting points also cause these molecules to have moderately high pure component viscosities compared

to most aqueous and organic solvents. Table 3.5 displays the pure component viscosities for several ionic liquids capable of dissolving cellulosic biomass at 40°C and 60°C.

Ionic Liquid	Viscosity at 40°C (cP)	Viscosity at 60°C (cP)
[BMIm][Cl]	3800 [A]	700 [A]
[BMIm][Ac]	112 [B]	43 [B]
[EMIm][Ac]	61 [C]	26 [C]
[EMIm][DEP]	146 [D]	60 [D]

[A)] Adapted from [77] [B)] Adapted from [78] [C)] Adapted from [79] [D)] Experimental Data

Table 3.5: Rheological properties of select ionic liquids that dissolve cellulosic biomass.

Whereas [BMIm][Cl] has a significant biomass dissolution capacity (estimated 19.5+ mass%) its pure component viscosity at 40°C is 3800 cP which, from a processing standpoint, presents severe mass transfer limitations to biomass dissolution and chemical conversion. Furthermore, mixtures of [BMIm][Cl] containing high cellulose loadings are known to form gels thus reducing their processability. Comparatively, acetate and diethyl phosphate ionic liquids demonstrate pure component viscosities that are an order of magnitude lower than [BMIm][Cl] at both 40°C and 60°C. Acetate ILs are known to become instable and degrade in the presence carbon dioxide[80-83], cellulosic biomass[24], and when exposed to elevated temperatures[84]. Alternatively, [EMIm][DEP] has demonstrated excellent thermal and chemical stability making it an ideal selection for applications in biomass conversion technology.

Despite the comparatively low pure [EMIm][DEP] viscosity of 140 cP at 40°C and 60 cP at 60°C, even small quantities of cellulose, when dissolved in the pure IL, cause exponential increases in the mixture viscosity. For instance, Figure 3.21 demonstrates that the dissolution of 3 mass% cellulose in [EMIm][DEP] at 40°C and 60°C results in an increase in the mixture viscosity by more than an order of magnitude. When 5 mass% cellulose is dissolved in the pure IL the mixture viscosities at 40°C and 60°C are 6870 cP and 2350 cP respectively. Considering

most IL-biomass processes will operate at high biomass loadings (*i.e.* 10-20 mass%) and that increased cellulose capacity has an exponential effect on the mixture viscosity, transport limitations of these solutions must be carefully understood and accounted for.

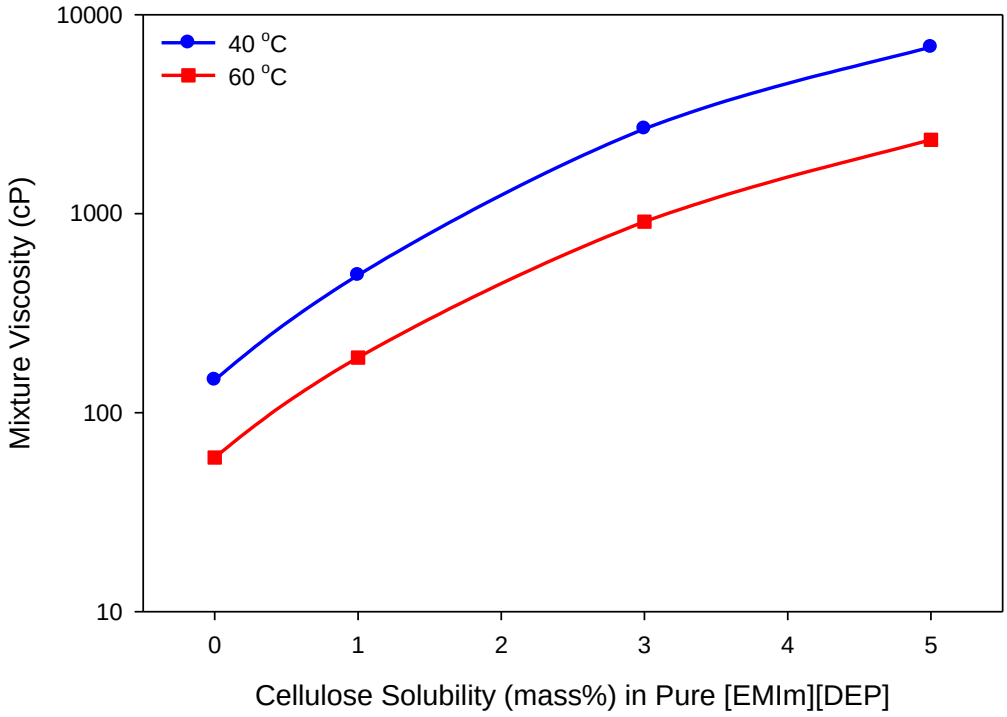

Figure 3.21: Experimental viscosities of [EMIm][DEP]-cellulose mixtures at 40 and 60°C.

As previously demonstrated in Section 3.4, at select temperatures and mass loadings, aprotic cosolvents increase the solubility of cellulose in ionic liquid mixtures. The cosolvent also enhances the mass transport properties of IL-cellulose mixtures. For instance, aprotic cosolvents significantly reduce the mixture viscosity of IL-biomass mixtures, thus improving the rheological behavior of cellulose containing solutions. The comparatively small cosolvent molecules (demonstrated by DMSO and applicable to all aprotic cosolvent systems studied herein) act as a

buffer between cellulose chains and IL molecules in solution thus reducing frictional interactions.[52, 85] The result is a significant reduction in mixture viscosity as shown in Figure 3.22 and Figure 3.23 for [EMIm][DEP]-cellulose solutions with varying DMSO cosolvent compositions at 40°C and 60°C respectively.

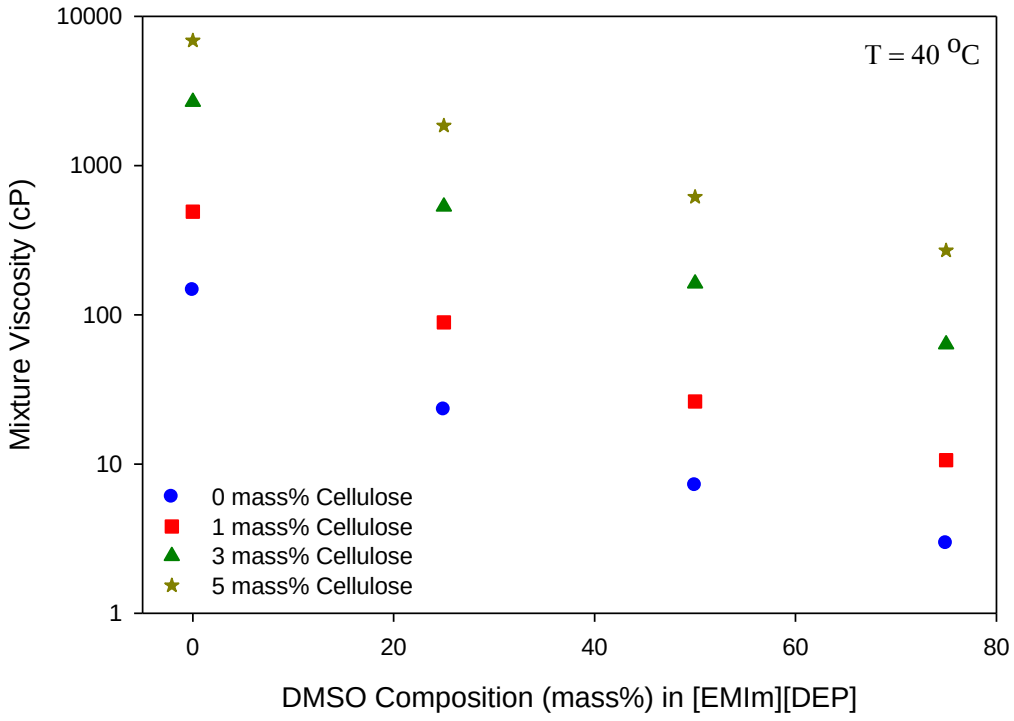

Figure 3.22: Viscosity of cellulose-IL mixtures as a function of cosolvent loading at 40°C

At 40°C a sample of pure [EMIm][DEP] containing 5 mass% cellulose (total solution basis) has a mixture viscosity of 6870 cP. At the same 5 mass% cellulose loading an IL-DMSO mixture containing 75 mass% DMSO (solute free basis) has a mixture viscosity of 270 cP. Again, these samples have identical cellulose compositions indicating that the significant reduction in mixture viscosity (one order of magnitude, 96%) is directly due to the presence of cosolvent in solution.

Similar results are observed for the pure IL system as well as [EMIm][DEP]-DMSO mixtures with 1 and 3 mass% cellulose loadings. Interestingly, plots displaying the natural log of mixture viscosity against DMSO composition result in fairly linear trends irrespective of cellulose loading. Therefore, the measured viscosity data presented here could potentially be extrapolated to predict the mixture viscosity of IL-cosolvent systems containing higher biomass loadings.

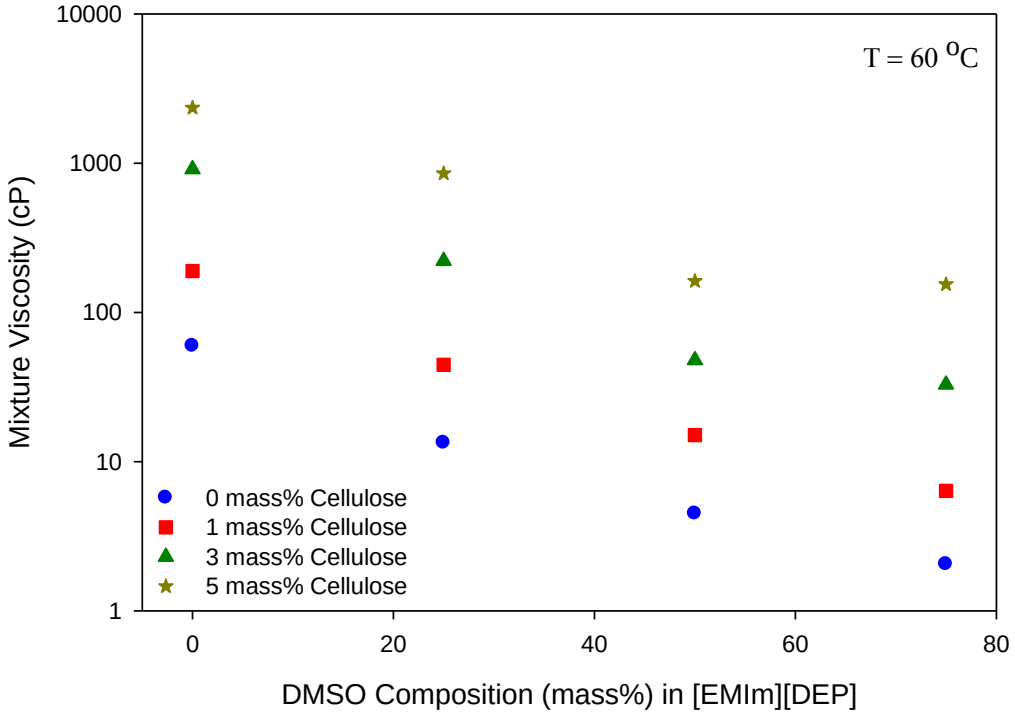

Figure 3.23: Viscosity of cellulose-IL mixtures as a function of cosolvent loading at 60°C

Temperature also has a moderate impact on mixture viscosity as displayed in Figure 3.24. For instance, the mixture viscosity of 1 mass% cellulose dissolved in pure [EMIm][DEP] is reduced from 491 cP to 189 cP by increasing the temperature from 40°C to 60°C. This corresponds to a 61% reduction in mixture viscosity by a 20°C temperature elevation. Alternatively, at a fixed

temperature of 40°C and a constant 1 mass% cellulose loading, increasing the DMSO cosolvent composition from 0 to 25 mass% (cellulose free basis) results in an 82% decrease in the mixture viscosity. Therefore, while both increased temperature (at a fixed cosolvent loading) and increased cosolvent composition (at a fixed temperature) have positive effects on mixture viscosity reduction, ultimately the cosolvent effects are more significant and have a larger impact on the mixture properties than the effects of temperature.

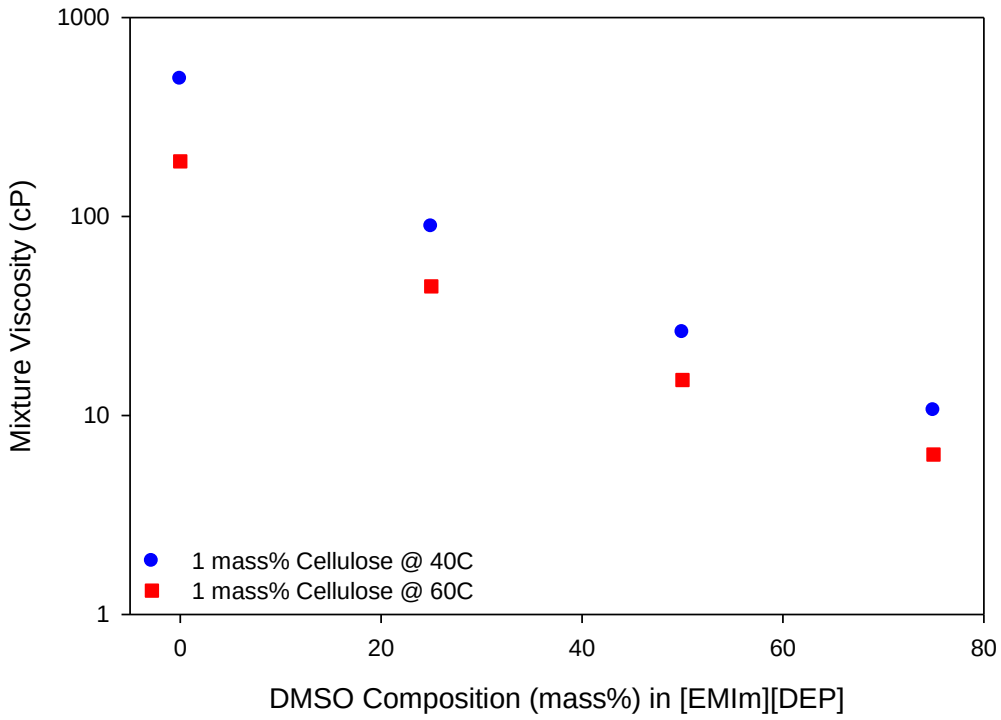

Figure 3.24: Temperature effect of mixture viscosity at various cosolvent (DMSO) compositions

3.8. Economics of Mixed IL-Cosolvent Systems for Cellulose Dissolution

From an economic perspective, inclusion of cosolvents in mixtures with ILs for biomass processing can significantly reduce the capital costs involved with purchasing the IL feedstock.

For instance, an economic study on biomass processing with ionic liquids indicated that ~93% of the operating costs were associated with purchasing the IL feedstock.[86] The findings further indicated that the IL purchase price (studied on [EMIm][Cl]) made the process economically prohibitive. Previous attempts at improving IL based processes have primarily focused on developing less expensive ionic liquids. While these efforts are indeed necessary the majority of inexpensive protic ILs developed do not have the characteristic high hydrogen bond accepting abilities found in imidazolium ILs are therefore not suitable for biomass applications.

Through the utilization of mixed IL-cosolvent systems an alternative approach for reducing the economic burden of the IL feedstock is presented. For instance, cosolvents can displace up to 75 mass% of the ionic liquid while still solubilizing cellulose. The cost of bulk production of [EMIm][Cl] (and presumed to be similar to the production costs of [EMIm][DEP]) was estimated in a techno-economic study to be ~$5.75 per kg [86] which is significantly more expensive than the bulk prices of dimethyl sulfoxide $1.30 per kg, dimethylformamide $0.89 per kg, and dimethyl imidazolidinone $4.88 per kg (based on the purchase of 1 metric ton).[87] A hypothetical process which requires 1000 kg of solvent to process lignocellulosic biomass would require an estimated $5750 to purchase a pure IL feedstock. Alternatively, if 50% of the IL were displaced with DMSO, ceteris paribus, the mixed solvent feedstock cost would be $3525, a ~39% reduction compared to the pure IL scenario. Additionally, blended IL-cosolvent mixtures of 25 mass% and 75 mass% DMSO would provide cost reductions of 58% and 19% respectively.

The cost of making a mixed solvent system required to process 1.0 kg of dry cellulosic biomass was also investigated based on the ternary cellulose solubility results presented herein and in conjunction with the pure solvent prices previously discussed. Figure 3.25 displays the

optimized solvent cost results for the [EMIm][DEP]-DMSO system at 40, 60, and 80°C as a function of cosolvent loading in the mixture. A similar analysis has been performed for the DMF and DMI mixed solvent systems and the results for all three cosolvent systems are displayed in Table 3.6.

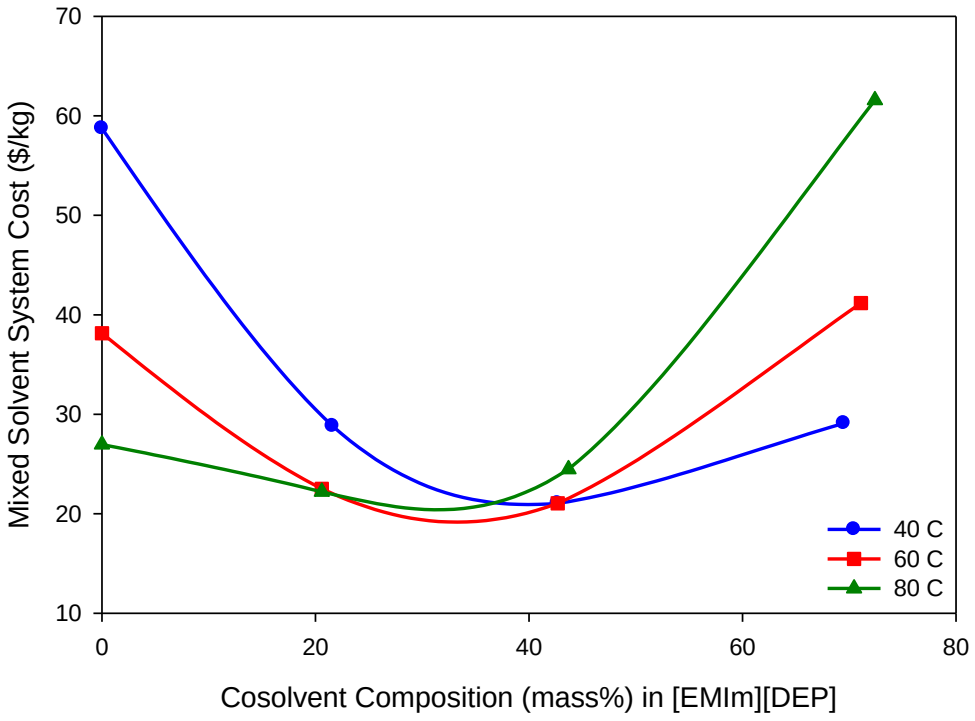

Figure 3.25: Cost of mixed [EMIm][DEP]-DMSO solvent systems for the dissolution of 1 kg of cellulosic biomass. Results presented based on optimizing the cellulose dissolution capacity of the mixed solvent systems with solvent cost.

At 40°C the mixed IL-cosolvent system cost for DMSO, DMF, and DMI were all approximately $19.50 per kg. However, the quantity of cosolvent which optimized the cellulose capacity and solvent cost varied significantly. For instance, the optimized DMSO system at 40°C consisted of a mixture of 46 mass% cosolvent and 39 mass% IL on a ternary basis which has an approximate

cellulose capacity of 14.1 mass%. Alternatively, the DMF solvent system at 40^{o}C was composed of a ternary mixture of 34.8 mass% cosolvent, 53.4 mass% [EMIm][DEP], and 11.8 mass% cellulose. The mixed solvent system of DMSO is slightly less expensive on a per kg basis compared to DMF likely due to the higher cellulose dissolution capacity of the [EMIm][DEP]-DMSO system at 40^{o}C compared to mixtures of the IL with DMF. However, the purchase price of pure DMF ($0.89 per kg) is marginally less expensive than DMSO ($1.30 per kg). Therefore, at 60 and 80^{o}C when the solubilities of the various cosolvent systems become increasingly similar, the lower DMF cost makes this mixed solvent less expensive. Furthermore, while DMI demonstrates the second best cellulose dissolution capacity of the three IL-cosolvent mixtures the high pure component DMI cost ($4.88 per kg) makes it comparatively expensive at 60 and 80^{o}C relative to DMSO and DMF. Interestingly, the least expensive mixed solvent costs required to solubilize 1 kg of cellulose are observed at 40^{o}C and are comparatively less than any solvent system at 60 and 80^{o}C. The data presented in Table 3.6 represents the raw material cost only and does not account for the cost of thermal energy required to heat the mixtures to their desired temperatures. Therefore, operating at lower temperatures (*i.e.* 40^{o}C) will have additional operating cost savings compared to the higher temperature systems. While a techno-economic evaluation is required to assess the quantitative savings of mixed IL-cosolvent systems, preliminary indicators demonstrate the potential for significant cost reduction relative to utilizing pure ILs.

Temperature [^{o}C]	Cosolvent mixed with [EMIm][DEP]	Optimized Cosolvent Loading (mass%)	Optimized Solvent Cost ($/kg)
40	DMSO	46.0	19.48
40	DMF	34.8	19.76
40	DMI	41.1	19.38
60	DMSO	34.2	28.44
60	DMF	30.5	22.62
60	DMI	33.4	23.63
80	DMSO	22.7	30.98
80	DMF	15.0	20.56
80	DMI	23.0	24.30

Table 3.6: Cost of mixed IL-cosolvent systems required to dissolve 1 kg of dry cellulosic biomass.

3.9. Summary

Several potential applications of ILs in biomass processing to fuels and chemicals have been proposed which often include the addition of other liquid solvents. We have demonstrated here that polar aprotic cosolvents can be used to significantly improve the thermodynamic solubility of cellulose depending on the composition and temperature. Cosolvents also demonstrate significant enhancements to mass transport limitations of IL-cellulose mixtures by reducing the mixture viscosity. Additionally, cosolvents improve the process economics of IL based biomass conversion technologies by reducing the quantity of IL required by the process and replacing it with a less expensive organic solvent. Alternatively, polar protic solvents, especially water, exhibit a dramatic decrease in cellulose solubility at relative low compositions. Therefore, any process that includes water intentionally or unintentionally will require high levels of IL purification prior to reuse. However, in IL/cosolvent mixtures the effect of the antisolvent at relatively low compositions is diminished, but still allows precipitation at higher loadings. Solvatochromic probes for determining mixture Kamlet-Taft polarity parameters of IL/cosolvent mixtures seem to correlate nearly quantitatively with these enhanced dissolution properties.

However, for antisolvents the *KT* parameters do not exhibit the same dramatic drop as is observed in the solubility measurements with increased antisolvent composition. NMR and FTIR spectroscopic shifts also trend with the behavior of both co- and anti-solvents. Thus, Kamlet-Taft and other spectroscopic techniques may be potential rapid screening tools for designing IL, cosolvent, and antisolvent systems for biomass processing.

References

1. Murugesan, S. and R.J. Linhardt, *Ionic liquids in carbohydrate chemistry - Current trends and future directions.* Current Organic Synthesis, 2005. **2**(4): p. 437-451.
2. Pinkert, A., et al., *Ionic Liquids and Their Interaction with Cellulose.* Chemical Reviews, 2009. **109**(12): p. 6712-6728.
3. Zhu, S.D., et al., *Dissolution of cellulose with ionic liquids and its application: a mini-review.* Green Chemistry, 2006. **8**(4): p. 325-327.
4. Energy, U.S.D.o., *U.S. Billion Ton Update: Biomass Supply for Bioenergy and Bioproducts Industry*, 2011, Oak Ridge National Laboratory.
5. Milbrandt, A., *A Geographic Perspective on the Current Biomass Resource Availability in the United States*, N.R.E. Laboratory, Editor 2005.
6. Yuan, X.M. and G. Cheng, *From cellulose fibrils to single chains: understanding cellulose dissolution in ionic liquids.* Physical Chemistry Chemical Physics, 2015. **17**(47): p. 31592-31607.
7. Lu, B.L., A.R. Xu, and J.J. Wang, *Cation does matter: how cationic structure affects the dissolution of cellulose in ionic liquids.* Green Chemistry, 2014. **16**(3): p. 1326-1335.
8. Luterbacher, J.S., D. Martin Alonso, and J.A. Dumesic, *Targeted chemical upgrading of lignocellulosic biomass to platform molecules.* Green Chemistry, 2014. **16**(12): p. 4816-4838.
9. Wang, H., G. Gurau, and R.D. Rogers, *Ionic liquid processing of cellulose.* Chemical Society Reviews, 2012. **41**(4): p. 1519-1537.
10. Vitz, J., et al., *Extended dissolution studies of cellulose in imidazolium based ionic liquids.* Green Chemistry, 2009. **11**(3): p. 417-424.
11. Zhao, Y.L., et al., *Effects of anionic structure on the dissolution of cellulose in ionic liquids revealed by molecular simulation.* Carbohydrate Polymers, 2013. **94**(2): p. 723-730.
12. Brandt, A., et al., *Deconstruction of lignocellulosic biomass with ionic liquids.* Green Chemistry, 2013. **15**(3): p. 550-583.
13. Doherty, T.V., et al., *Ionic liquid solvent properties as predictors of lignocellulose pretreatment efficacy.* Green Chemistry, 2010. **12**(11): p. 1967-1975.
14. Hauru, L.K.J., et al., *Role of Solvent Parameters in the Regeneration of Cellulose from Ionic Liquid Solutions.* Biomacromolecules, 2012. **13**(9): p. 2896-2905.
15. Minnick, D.L., Scurto, A.M., *Solvent Effects on the Dissolution and Precipitation of Cellulose from Ionic Liquids.* Journal of Physical Chemistry B, 2016.
16. Rinaldi, R., *Instantaneous dissolution of cellulose in organic electrolyte solutions.* Chemical Communications, 2011. **47**(1): p. 511-513.
17. Gross, A.S., A.T. Bell, and J.W. Chu, *Thermodynamics of Cellulose Solvation in Water and the Ionic Liquid 1-Butyl-3-Methylimidazolim Chloride.* Journal of Physical Chemistry B, 2011. **115**(46): p. 13433-13440.
18. Li, Y., et al., *Dissolving process of a cellulose bunch in ionic liquids: a molecular dynamics study.* Physical Chemistry Chemical Physics, 2015. **17**(27): p. 17894-17905.

19. Le, K.A., C. Rudaz, and T. Budtova, *Phase diagram, solubility limit and hydrodynamic properties of cellulose in binary solvents with ionic liquid.* Carbohydrate Polymers, 2014. **105**: p. 237-243.
20. Olsson, C., et al., *Influence of water on swelling and dissolution of cellulose in 1-ethyl-3-methylimidazolium acetate.* Carbohydrate Polymers, 2014. **99**: p. 438-446.
21. Xu, A.R., et al., *Cellulose dissolution at ambient temperature: Role of preferential solvation of cations of ionic liquids by a cosolvent.* Carbohydrate Polymers, 2013. **92**(1): p. 540-544.
22. Gericke, M., P. Fardim, and T. Heinze, *Ionic Liquids - Promising but Challenging Solvents for Homogeneous Derivatization of Cellulose.* Molecules, 2012. **17**(6): p. 7458-7502.
23. Normazlan, W.M.D.W., et al., *Composition and Temperature Dependence of Density, Surface Tension, and Viscosity of EMIM DEP/MMIM DMP + Water+1-Propano1/2-Propanol Ternary Mixtures and Their Mathematical Representation Using the Jouyban Acree Model.* Journal of Chemical and Engineering Data, 2014. **59**(8): p. 2337-2348.
24. Clough, M.T., et al., *Ionic liquids: not always innocent solvents for cellulose.* Green Chemistry, 2015. **17**(1): p. 231-243.
25. Du, H.B. and X.H. Qian, *The effects of acetate anion on cellulose dissolution and reaction in imidazolium ionic liquids.* Carbohydrate Research, 2011. **346**(13): p. 1985-1990.
26. Deetlefs, M. and K.R. Seddon, *Assessing the greenness of some typical laboratory ionic liquid preparations.* Green Chemistry, 2010. **12**(1): p. 17-30.
27. Francis, R., *The Effect of Chlorine Additions to Cooling Water on Corrosion of Copper Alloy Condenser Tubes.* Materials Performance, 1982. **21**(8): p. 44-49.
28. Wada, M., et al., *X-ray diffraction study on the thermal expansion behavior of cellulose Iβ and its high-temperature phase.* Polymer Degradation and Stability, 2010. **95**(8): p. 1330-1334.
29. Wada, M., *Lateral thermal expansion of cellulose Iβ and IIII polymorphs.* Journal of Polymer Science Part B: Polymer Physics, 2002. **40**(11): p. 1095-1102.
30. Fidale, L.C., et al., *Cellulose Swelling by Aprotic and Protic Solvents: What are the Similarities and Differences?* Macromolecular Chemistry and Physics, 2008. **209**(12): p. 1240-1254.
31. Chen, L., et al., *Comprehensive Study on Cellulose Swelling for Completely Recyclable Nonaqueous Reactive Dyeing.* Industrial & Engineering Chemistry Research, 2015. **54**(9): p. 2439-2446.
32. Payal, R.S., et al., *Dissolution of Cellulose in Room Temperature Ionic Liquids: Anion Dependence.* Journal of Physical Chemistry B, 2015. **119**(4): p. 1654-1659.
33. Remsing, R.C., et al., *Solvation of carbohydrates in N,N '-dialkylimidazolium ionic liquids: A multinuclear NMR spectroscopy study.* Journal of Physical Chemistry B, 2008. **112**(35): p. 11071-11078.
34. Remsing, R.C., et al., *Mechanism of cellulose dissolution in the ionic liquid 1-n-butyl-3-methylimidazolium chloride: a C-13 and Cl-35/37 NMR relaxation study on model systems.* Chemical Communications, 2006(12): p. 1271-1273.
35. Swatloski, R.P., et al., *Dissolution of cellose with ionic liquids.* Journal of the American Chemical Society, 2002. **124**(18): p. 4974-4975.

36. Xu, A.R., J.J. Wang, and H.Y. Wang, *Effects of anionic structure and lithium salts addition on the dissolution of cellulose in 1-butyl-3-methylimidazolium-based ionic liquid solvent systems.* Green Chemistry, 2010. **12**(2): p. 268-275.
37. Rabideau, B.D. and A.E. Ismail, *Mechanisms of hydrogen bond formation between ionic liquids and cellulose and the influence of water content.* Physical Chemistry Chemical Physics, 2015. **17**(8): p. 5767-5775.
38. Andanson, J.M., A.A.H. Padua, and M.F.C. Gomes, *Thermodynamics of cellulose dissolution in an imidazolium acetate ionic liquid.* Chemical Communications, 2015. **51**(21): p. 4485-4487.
39. de Oliveira, H.F.N. and R. Rinaldi, *Understanding Cellulose Dissolution: Energetics of Interactions of Ionic Liquids and Cellobiose Revealed by Solution Microcalorimetry.* Chemsuschem, 2015. **8**(9): p. 1577-1584.
40. Nunes de Oliveira, H.F.N. and R. Rinaldi, *Understanding Cellulose Dissolution: Energetics of Interactions of Ionic Liquids and Cellobiose Revealed by Solution Microcalorimetry.* Chemsuschem, 2015. **8**(9): p. 1577-1584.
41. Cheng, F., et al., *Facile pulping of lignocellulosic biomass using choline acetate.* Bioresource Technology, 2014. **164**: p. 394-401.
42. Dibble, D.C., et al., *A facile method for the recovery of ionic liquid and lignin from biomass pretreatment.* Green Chemistry, 2011. **13**(11): p. 3255-3264.
43. Laine, C., et al., *Simultaneous bench scale production of dissolving grade pulp and valuable hemicelluloses from softwood kraft pulp by ionic liquid extraction.* Carbohydrate Polymers, 2016. **136**: p. 402-408.
44. Suzuki, T., et al., *Preparation of cellulose particles using an ionic liquid.* Journal of Colloid and Interface Science, 2014. **418**: p. 126-131.
45. Voon, L.K., S.C. Pang, and S.F. Chin, *Highly porous cellulose beads of controllable sizes derived from regenerated cellulose of printed paper wastes.* Materials Letters, 2016. **164**: p. 264-266.
46. Wang, X.J., et al., *Cellulose extraction from wood chip in an ionic liquid 1-allyl-3-methylimidazolium chloride (AmimCl).* Bioresource Technology, 2011. **102**(17): p. 7959-7965.
47. Huo, F., Z.P. Liu, and W.C. Wang, *Cosolvent or Antisolvent? A Molecular View of the Interface between Ionic Liquids and Cellulose upon Addition of Another Molecular Solvent.* Journal of Physical Chemistry B, 2013. **117**(39): p. 11780-11792.
48. Parthasarathi, R., et al., *Theoretical Insights into the Role of Water in the Dissolution of Cellulose Using IL/Water Mixed Solvent Systems.* The Journal of Physical Chemistry B, 2015. **119**(45): p. 14339-14349.
49. Froschauer, C., et al., *Separation of Hemicellulose and Cellulose from Wood Pulp by Means of Ionic Liquid/Cosolvent Systems.* Biomacromolecules, 2013. **14**(6): p. 1741-1750.
50. Andanson, J.M., et al., *Understanding the role of co-solvents in the dissolution of cellulose in ionic liquids.* Green Chemistry, 2014. **16**(5): p. 2528-2538.
51. Zhao, Y.L., et al., *Insight into the Cosolvent Effect of Cellulose Dissolution in Imidazolium-Based Ionic Liquid Systems.* Journal of Physical Chemistry B, 2013. **117**(30): p. 9042-9049.

52. Wang, L.J., et al., *Rheological behaviors of cellulose in 1-ethyl-3-methylimidazolium chloride/dimethylsulfoxide.* Carbohydrate Polymers, 2014. **110**: p. 292-297.
53. Xiao, S.H., et al., *Efficient conversion of cellulose into biofuel precursor 5-hydroxymethylfurfural in dimethyl sulfoxide-ionic liquid mixtures.* Bioresource Technology, 2014. **151**: p. 361-366.
54. Stark, A., et al., *The effect of hydrogen bond acceptor properties of ionic liquids on their cellulose solubility.* Science China-Chemistry, 2012. **55**(8): p. 1663-1670.
55. Brandt, A., et al., *The effect of the ionic liquid anion in the pretreatment of pine wood chips.* Green Chemistry, 2010. **12**(4): p. 672-679.
56. Kyllonen, L., et al., *On the solubility of wood in non-derivatising ionic liquids.* Green Chemistry, 2013. **15**(9): p. 2374-2378.
57. Ohno, H. and Y. Fukaya, *Task Specific Ionic Liquids for Cellulose Technology.* Chemistry Letters, 2009. **38**(1): p. 2-7.
58. Zhang, S.G., et al., *Hydroxyl Ionic Liquids: The Differentiating Effect of Hydroxyl on Polarity due to Ionic Hydrogen Bonds between Hydroxyl and Anions.* Journal of Physical Chemistry B, 2010. **114**(11): p. 3912-3920.
59. Jessop, P.G., et al., *Solvatochromic parameters for solvents of interest in green chemistry.* Green Chemistry, 2012. **14**(5): p. 1245-1259.
60. Ali, A., et al., *Solvatochromic Absorbance Probe Behavior within Mixtures of the Ionic Liquid 1-Butyl-3-methylimidazolium Bis(trifluoromethylsulfonyl)imide plus Molecular Organic Solvents.* Journal of Chemical and Engineering Data, 2014. **59**(6): p. 1755-1765.
61. Acree, W.E., S.A. Tucker, and D.C. Wilkins, *Spectrochemical Investigations of Preferential Solvation - Fluorescence Emission Behavior of Select Polycyclic Aromatic Hydrocarbon Solute Probes Dissolved in Mixed-Solvents.* Journal of Physical Chemistry, 1993. **97**(43): p. 11199-11203.
62. Khupse, N.D. and A. Kumar, *Delineating Solute-Solvent Interactions in Binary Mixtures of Ionic Liquids in Molecular Solvents and Preferential Solvation Approach.* Journal of Physical Chemistry B, 2011. **115**(4): p. 711-718.
63. Gupta, K.M. and J.W. Jiang, *Cellulose dissolution and regeneration in ionic liquids: A computational perspective.* Chemical Engineering Science, 2015. **121**: p. 180-189.
64. Azema, L., et al., *Does phosphoryl protonation occurs in aqueous phosphoesters solutions.* Spectrochimica Acta Part a-Molecular and Biomolecular Spectroscopy, 2005. **62**(1-3): p. 287-292.
65. Zakzeski, J., P.C.A. Bruijnincx, and B.M. Weckhuysen, *In situ spectroscopic investigation of the cobalt-catalyzed oxidation of lignin model compounds in ionic liquids.* Green Chemistry, 2011. **13**(3): p. 671-680.
66. Li, X.S., L. Liu, and H.B. Schlegel, *On the physical origin of blue-shifted hydrogen bonds.* Journal of the American Chemical Society, 2002. **124**(32): p. 9639-9647.
67. Ratajczak, H., *Charge-transfer properties of the hydrogen bond. I. Theory of the enhancement of dipole moment of hydrogen-bonded systems.* The Journal of Physical Chemistry, 1972. **76**(21): p. 3000-3004.
68. Badger, R.M. and S.H. Bauer, *Spectroscopic studies of the hydrogen bond. II. The shift of the O-H vibrational frequency in the formation of the hydrogen bond.* Journal of Chemical Physics, 1937. **5**(11): p. 839-851.

69. Marekha, B.A., et al., *Intermolecular interactions in mixtures of 1-n-butyl-3-methylimidazolium acetate and water: Insights from IR, Raman, NMR spectroscopy and quantum chemistry calculations.* Journal of Molecular Liquids, 2015. **210**: p. 227-237.
70. Zhang, Q.G., N.N. Wang, and Z.W. Yu, *The Hydrogen Bonding Interactions between the Ionic Liquid 1-Ethyl-3-Methylimidazolium Ethyl Sulfate and Water.* Journal of Physical Chemistry B, 2010. **114**(14): p. 4747-4754.
71. Hesse-Ertelt, S., et al., *Solvent Effects on the NMR Chemical Shifts of Imidazolium-Based Ionic Liquids and Cellulose Therein.* Macromolecular Symposia, 2010. **294**(2): p. 75-89.
72. Wade, L.G., *Organic chemistry*. 3rd ed. 1995, Englewood Cliffs, N.J.: Prenctice Hall.
73. Radhi, A., et al., *Macroscopic and Microscopic Study of 1-Ethyl-3-methyl-imidazolium Acetate-DMSO Mixtures.* Journal of Physical Chemistry B, 2015. **119**(4): p. 1633-1640.
74. Hall, C.A., et al., *Macroscopic and Microscopic Study of 1-Ethyl-3-methyl-imidazolium Acetate-Water Mixtures.* Journal of Physical Chemistry B, 2012. **116**(42): p. 12810-12818.
75. Lovell, C.S., et al., *Influence of Cellulose on Ion Diffusivity in 1-Ethyl-3-Methyl-Imidazolium Acetate Cellulose Solutions.* Biomacromolecules, 2010. **11**(11): p. 2927-2935.
76. Zhang, J.M., et al., *NMR spectroscopic studies of cellobiose solvation in EmimAc aimed to understand the dissolution mechanism of cellulose in ionic liquids.* Physical Chemistry Chemical Physics, 2010. **12**(8): p. 1941-1947.
77. Seddon, K.R., A. Stark, and M.J. Torres, *Viscosity and density of 1-alkyl-3-methylimidazolium ionic liquids.* Clean Solvents, 2002. **819**: p. 34-49.
78. Almeida, H.F.D., et al., *Thermophysical Properties of Five Acetate-Based Ionic Liquids.* Journal of Chemical and Engineering Data, 2012. **57**(11): p. 3005-3013.
79. Freire, M.G., et al., *Thermophysical Characterization of Ionic Liquids Able To Dissolve Biomass.* Journal of Chemical and Engineering Data, 2011. **56**(12): p. 4813-4822.
80. Barber, P.S., et al., *Coagulation of Chitin and Cellulose from 1-Ethyl-3-methylimidazolium Acetate Ionic-Liquid Solutions Using Carbon Dioxide.* Angewandte Chemie-International Edition, 2013. **52**(47): p. 12350-12353.
81. Besnard, M., et al., *CO2 in 1-Butyl-3-methylimidazolium Acetate. 2. NMR Investigation of Chemical Reactions.* Journal of Physical Chemistry A, 2012. **116**(20): p. 4890-4901.
82. Denning, D.M. and D.E. Falvey, *Solvent-Dependent Decarboxylation of 1,3-Dimethylimdazolium-2-Carboxylate.* Journal of Organic Chemistry, 2014. **79**(10): p. 4293-4299.
83. Sun, X.F., Y.L. Chi, and T.C. Mu, *Studies on staged precipitation of cellulose from an ionic liquid by compressed carbon dioxide.* Green Chemistry, 2014. **16**(5): p. 2736-2744.
84. Clough, M.T., et al., *Thermal decomposition of carboxylate ionic liquids: trends and mechanisms.* Physical Chemistry Chemical Physics, 2013. **15**(47): p. 20480-20495.
85. Sammons, R.J., et al., *Rheology of 1-butyl-3-methylimidazolium chloride cellulose solutions. I. Shear rheology.* Journal of Applied Polymer Science, 2008. **110**(2): p. 1175-1181.
86. Sen, S.M., et al., *Conversion of biomass to sugars via ionic liquid hydrolysis: process synthesis and economic evaluation.* Biofuels Bioproducts & Biorefining-Biofpr, 2012. **6**(4): p. 444-452.

87. alibaba.com. *Bulk DMSO Purchase Price*.

4. Precipitation of Cellulosic Biomass from Ionic Liquid Mixtures via Traditional Liquid and Novel Gas Antisolvent Methods

4.1. Introduction

Select ionic liquids including 1-ethyl-3-methylimidazolium diethyl phosphate ([EMIm][DEP]) have demonstrated success for cellulose dissolution and pretreatment, as illustrated in Chapter 3.[1-4] Once dissolved in an ionic liquid, cellulose can undergo several processing routes including precipitation to produce amorphous cellulose or direct chemical conversion into value-added products including: glucose, 5-hydroxymethylfurfural, and 2,5-dimethylfuran among others as shown in Figure 4.1.[5-12]

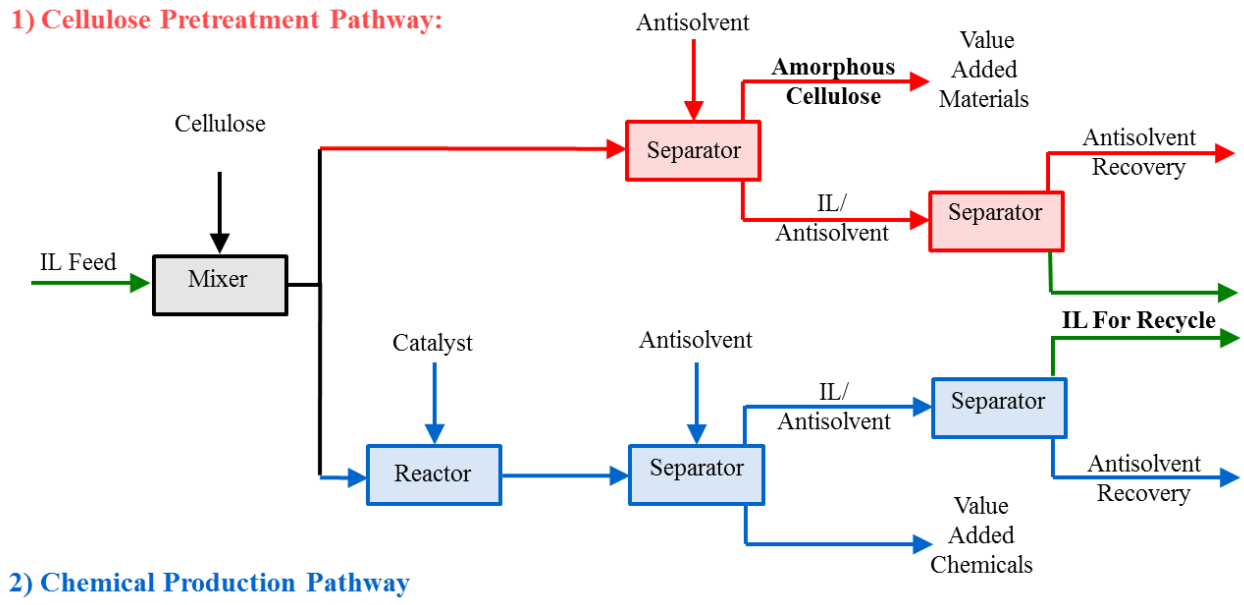

Figure 4.1: Potential pathways for cellulose processing in ionic liquid solvent systems.

While the majority of research on cellulose and ionic liquids targets chemical transformation pathways, the production of amorphous cellulose is also of significant interest for applications in

insulation, drug encapsulation, and fibers for clothing.[13] Additionally, amorphous cellulose has been correlated to superior chemical and biochemical conversion rates to glucose or other chemicals in non-ionic liquid based solvents even despite the heterogeneous (solid-liquid) reaction scenario.[14, 15]

Irrespective of the processing scheme, the high cost of the ionic liquid feedstock will require near quantitative recovery and recycle of the IL for the process to be economically viable.[16] As ionic liquids are non-volatile, the majority of scientific reports recommend using distillation to separate volatile products from ILs by thermal methods. Most studies assume that separation processes based on distillation will be low cost and neglect to perform engineering calculations which as a first approximation should at least account for the heat capacities, latent, and sensible heats of vaporization of the pure components to compute approximate separation energies. Despite these naive assumptions, distillation accounts for 60-80% of the total energy consumed by conventional chemical processes.[17] Therefore, attempts should be made to identify less energy intensive separation routes for the purification of chemical products, especially when designing new production methods based on ionic liquids.

Many products from biomass including cellulose, hemicellulose, and their respective monomers (glucose, xylose, *etc*.) are solids at temperatures below 300^{o}C and decompose at or slightly above their melting points.[18] Therefore, distillation is not directly applicable to separate these carbohydrate and sugar compounds from ILs. Instead, antisolvent technologies are traditionally employed to recover the biomass product and recycle the ionic liquid.[19-24] In this chapter conventional liquid antisolvents and novel gas antisolvents are investigated for precipitating cellulose from ionic liquid-cosolvent mixtures. The gas antisolvent process, when applied to

[EMIm][DEP] mixed solvent systems, is particularly interesting as the precipitation is completely reversible and rapid within small changes of pressure *i.e.* liquid phase CO_2 composition.[25]

4.2. Liquid Antisolvents for Cellulosic Biomass Precipitation

Extensive research has targeted dissolution of cellulose in ILs while only limited work has investigated the ensuing biomass precipitation step. Conventional antisolvents comprise the class of polar protic liquids which are effective at disrupting cellulose-IL interactions.[26-29] Characterization of the precipitated cellulose product displays a highly amorphous structure which has been correlated to superior chemical and biochemical conversion rates compared with alternative pretreatment methods.[14, 15]

The majority of aqueous and organic solvents have negligible cellulose solubility and most act as "antisolvents" when mixed with IL/cellulose mixtures leading to cellulose precipitation. Typical antisolvents in the literature are chosen among polar protic liquids (H_2O, MeOH, EtOH, *etc.*). These antisolvents induce cellulose precipitation by disrupting cellulose-IL hydrogen bonding interactions producing mostly amorphous cellulose.[26-29] Protic liquid antisolvents are so highly effective at precipitating biomass from ionic liquids that recent solubility studies in our group indicate that even trace amounts of these residual compounds in the ionic liquid can significantly inhibit further biomass dissolution. For example, we have found that cellulose solubility in [EMIm][DEP] at 40°C is reduced by more than 95% with only 3 mass% of residual water in the IL as shown in Figure 4.2.[30]

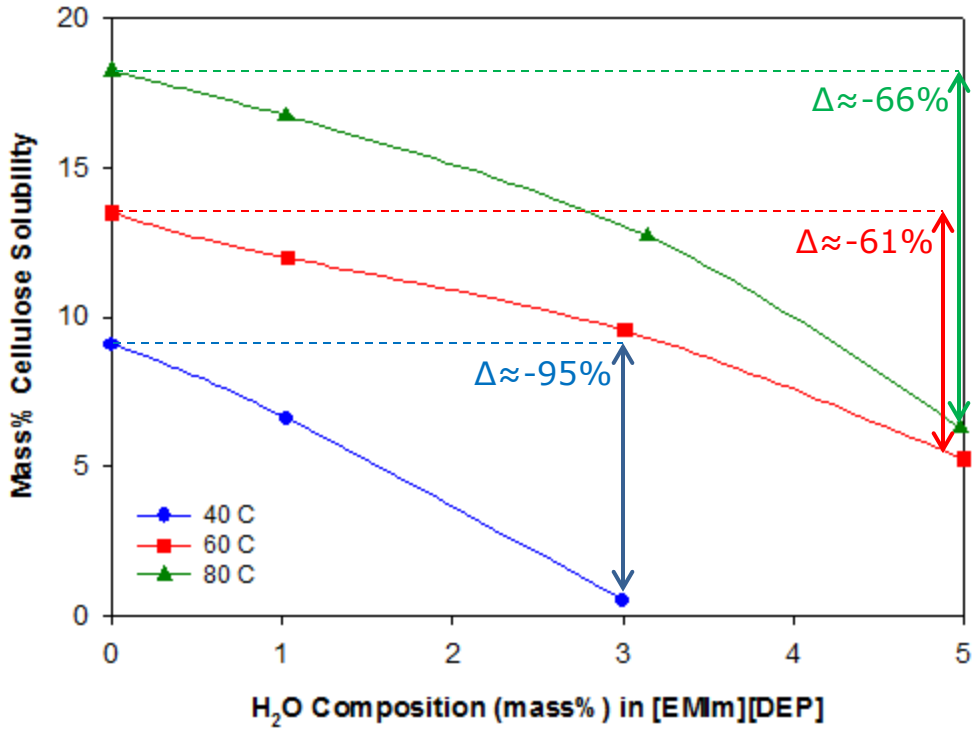

Figure 4.2: Effect of water as an antisolvents on the solubility of cellulose in [EMIm][DEP] at various temperatures.

While the results displayed in Figure 4.2 indicate that only small antisolvent quantities are required to reach the "saturation point" of cellulose in ionic liquid mixtures, significantly larger antisolvent loadings are required to "separate" biomass from IL mixtures. For instance, typical antisolvent precipitation methods utilize polar protic liquids in mass ratios of 1:1 (Antisolvent:IL), 2:1 and greater. Figure 4.3 displays the difference between "saturation" and "separation" for a mixture of [EMIm][DEP] and cellulose with various loadings of water as the antisolvent. Saturation, indicated by the mixture cloud point, is the thermodynamic limit of cellulose solubility in the ionic liquid. Alternatively, separation of the ionic liquid and cellulose

requires significantly larger antisolvent loadings to extract the IL and remove inclusion bodies of trapped or adsorbed IL from the cellulose matrix.

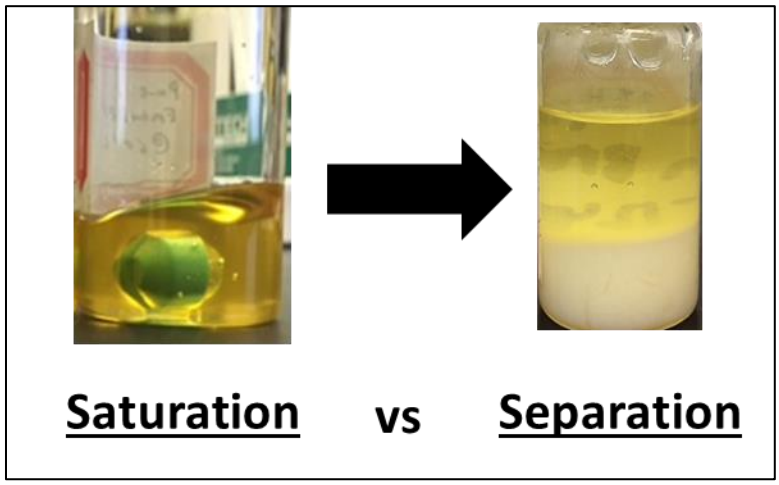

Figure 4.3: Demonstrating the difference between a saturated condition (point at which the thermodynamic cellulose solubility limit is reached) and separation (which is a quantitative precipitation of cellulose and extraction of the IL into the liquid, H_2O rich, phase).

While liquid antisolvents are highly effective at precipitating cellulose, several washing cycles are required to efficiently extract all of the ionic liquid from the amorphous cellulose product.[3, 31] After precipitation, the IL-antisolvent mixture is separated from cellulose via a bi-phasic (solid-liquid) extraction. The resulting pure amorphous cellulose product will likely require additional purification from the pretreatment solvent via thermal drying depending on the desired application. The ionic liquid must also be quantitatively separated from the liquid antisolvent prior to recycle. For instance, Figure 4.2 can alternatively be used to indicate the required separation of IL from the protic antisolvent such that subsequent biomass processing steps do not lose efficiency (*i.e.* cellulose dissolution capacity) because of residual antisolvent in the IL. For example, as shown in Figure 4.2, cellulose solubility in [EMIm][DEP] at 40°C is reduced by

more than 55% with only 1 mass% of residual water in the IL.[32] Furthermore, when 5 mass% H_2O is present in the IL, cellulose solubility is reduced by 100%, 61% and 66% respectively at 40, 60, and 80^{o}C. These results demonstrate that the IL must be highly purified from liquid antisolvents, herein demonstrated by water, prior to recycle for further processing.

4.2.1. Process Economics of IL-Liquid Antisolvent Separations

The energy required to purify [EMIm][DEP] from liquid antisolvents was computed by conducting a series of simulations based on thermodynamic models fit to experimental vapor-liquid equilibrium (*VLE*) data of IL/antisolvent systems.[33] The binary isobaric vapor-liquid equilibrium data for [EMIm][DEP] and H_2O at 1.01325 bar is presented in Figure 4.4.[34]

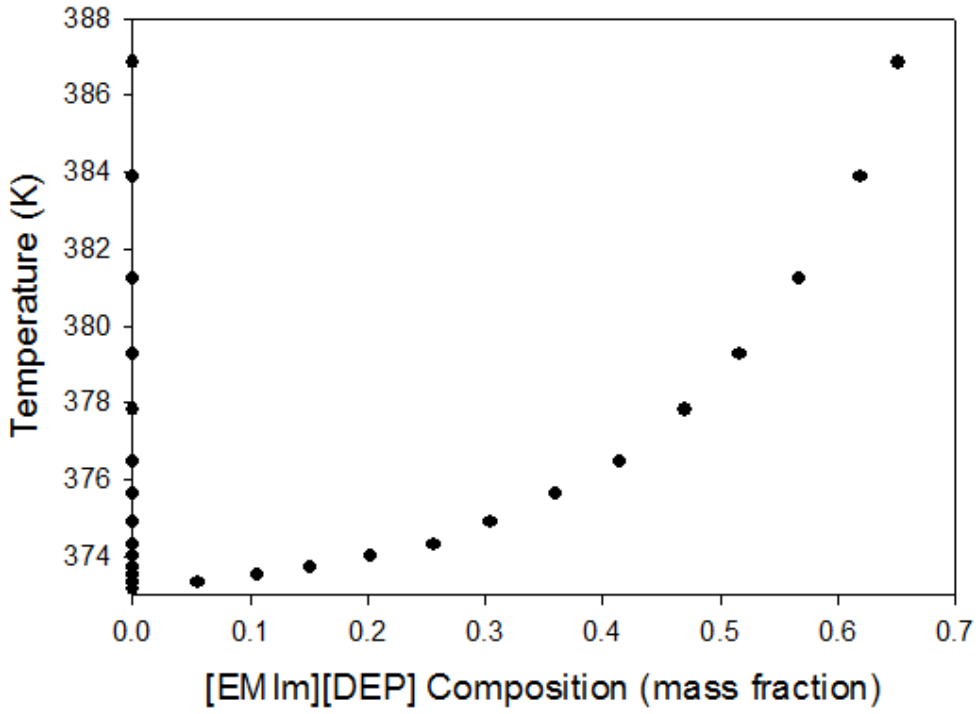

Figure 4.4: Isobaric vapor-liquid equilibrium data for mixtures of [EMIm][DEP] and H_2O at 1.01325 bar.[34]

The experimental phase equilibrium data displays a vertical dew point curve composed of pure H_2O and an exponential increase in the bubble point temperature with increasing liquid phase composition of the ionic liquid. Similar results to those obtained by Lu *et al.* are demonstrated in Chapter 6 for the investigation of environmentally friendly solvents for ionic liquid synthesis. The experimental data for the [EMIm][DEP]-H_2O system was regressed by the Non-Random-Two-Liquid (NRTL) activity coefficient model as well as the Peng-Robinson Equation of State with the Van der Waals 1-parameter mixing rule (PR-EoS VDW1). The critical properties and vapor pressure coefficients of [EMIm][DEP] and water are displayed in Table 4.1.

		Critical Properties			Antoine Constants (bar, K)		
Component	T_{Boil} (K)	T_c (K)	P_c (Bar)	ω	A	B	C
Water[a]	373.2	647.1	220.6	0.345	8.19626	-1482.28	-198.04
[EMIm][DEP][b]	658.6	750.0	21.46	0.722	5.08395	-3130.09	-43.00

[a] Obtained from NIST database [b] Estimated by Joback group contribution methods.

Table 4.1: Properties of water and [EMIm][DEP] used for PR-EOS and NRTL modeling of isobaric binary vapor-liquid equilibrium data in Aspen Plus.

Furthermore, the binary interaction parameters (BIPs) for the NRTL activity coefficient model and PR-EoS are displayed in Table 4.2 and Table 4.3 respectively.

System	A_{12}	A_{21}	B_{12}	B_{21}	$C_{12=21}$	$D_{12=21}$	E_{12}	E_{21}
H_2O (1) – [EMIm][DEP] (2)	7.15e-12	-3.9e-12	3480.64	-3090.09	0.1024	0	-1.1e-12	6.14e-13

Table 4.2: NRTL parameters regressed to the isobaric vapor liquid equilibrium data in Figure 4.4

Where the NRTL temperature dependent binary interaction parameter is defined as:

$$\tau_{ij} = A_{ij} + \frac{B_{ij}}{T} + E_{ij}\ln(T)$$

and the Peng Robinson temperature dependent parameters are:

$K_{ij} = K_{ij}^{I} + K_{ij}^{II}T$ and $L_{ij} = L_{ij}^{I} + L_{ij}^{II}T$

System	$K^{I}_{12=21}$	$K^{II}_{12=21}$	$L^{I}_{12=21}$	$L^{II}_{12=21}$
H_2O (1) – [EMIm][DEP] (2)	2.42	-0.008	-168.49	0.42

Table 4.3: PR-EOS parameters regressed to the isobaric vapor-liquid equilibrium data in Figure 4.4

Utilizing the isobaric VLE data and thermodynamic modeling (PR-EoS) presented above, a simulated separation process was created using Aspen Plus to obtain the estimated separation energies and operating conditions for purifying [EMIm][DEP] from the cellulose antisolvent (*i.e.* water). The Aspen model was designed to purify [EMIm][DEP] from a 2 kg feed mixture composed of a 1:1 mass ratio of IL to water at 1.01325 bar and 25^{o}C using a vacuum flash distillation process unit. The distillate from the process was pure water and the bottoms was composed of varying IL:H_2O compositions. The results of the simulation demonstrate that varying intensities of thermal and vacuum distillation are required to separate the compounds depending on the desired level of IL purity as shown in Figure 4.5.

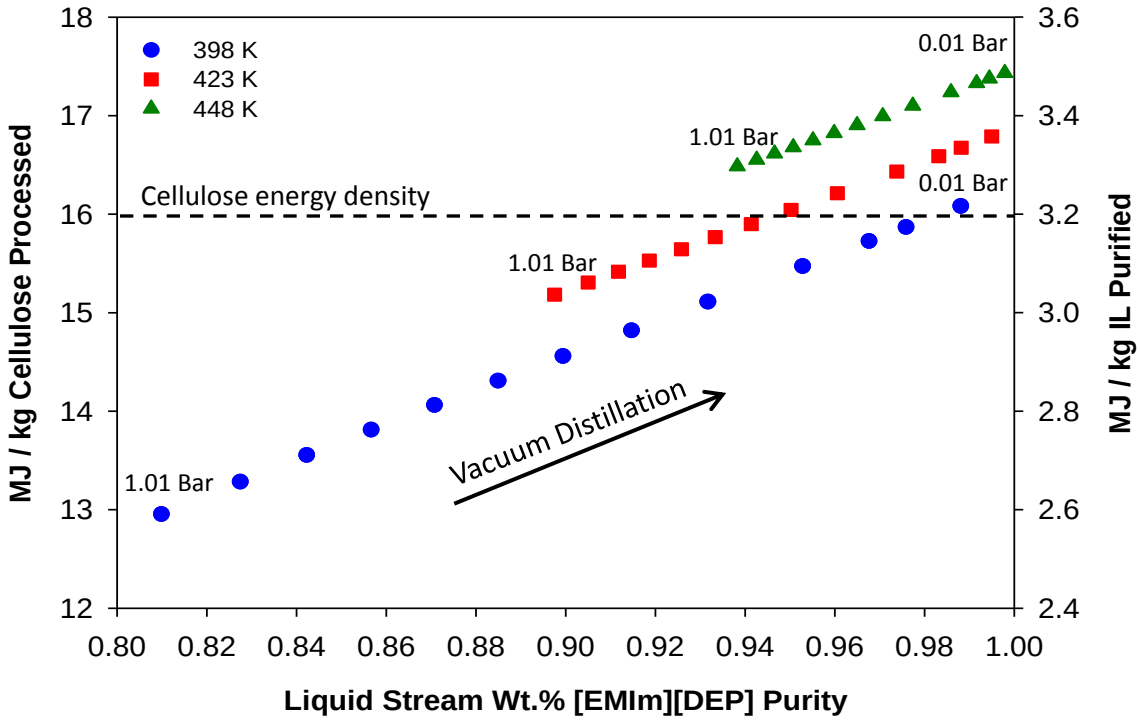

Figure 4.5: Separation energy for the purification of [EMIm][DEP] from water at 125, 150, and 175°C. The dashed line represents the energy density of cellulose based on its combustion value.

As displayed in Figure 4.5, thermal distillation at temperatures of 125, 150, and 175°C and 1.01325 bar is only capable of purifying the ionic liquid to approximate compositions of 81, 90, and 94 mass% [EMIm][DEP] respectively. Therefore, even at the highest temperature investigated (*i.e.* 175°C), without vacuum distillation, 6 mass% water remains in [EMIm][DEP]. At this composition of water in the IL, the cellulose solubility would be reduced by more than 61% at 60 and 80°C relative to pure [EMIm][DEP], and at 40°C cellulose would be rendered completely insoluble due to the antisolvent loading in the IL. Furthermore, at distillation temperatures below 175°C, and at 1.01325 bar, residual antisolvent (water) loadings greater than

10 mass% would remain on the IL making cellulose insoluble in the IL at our experimentally measured temperatures up to 80^{o}C and presumably much higher.

Therefore, a second simulation was performed to obtain increasingly pure [EMIm][DEP] by applying vacuum flash distillation at pressures between 1.01 and 0.01 bar. Industrial vacuum distillation units, utilized in the petroleum refining industry, are capable of achieving vacuum pressures as low as 0.01 bar, setting the basis for the process presented herein.[35] However, the capital and operating costs of vacuum distillation processes are significantly more expensive compared to conventional distillation units at atmospheric pressure and should be avoided when possible.[36]

Again, using the Peng-Robinson Equation of State (PR-EoS) thermodynamic package to model the separation process, it was determined that vacuum flash distillation at 0.01 bar could achieve [EMIm][DEP] purities of 85, 93, and 97 mass% at the flash unit operating temperatures of 125, 150, and 175^{o}C respectively. Therefore, even at the lowest vacuum pressure and highest temperature investigated herein, 3 mass% water still remains in the ionic liquid and will have adverse effects on recycle and second pass biomass dissolution processes; albeit less so compared to the larger antisolvent quantities residing on the IL following conventional distillation at atmospheric pressure.

The energy demand required to purify [EMIm][DEP] from water by conventional and vacuum flash distillation processes was examined and displayed in Figure 4.5. The results demonstrate that, as expected, increases in temperature and vacuum pressure result in significant increases in energy demand by the unit operation. The horizontal dashed line in Figure 4.5 represents the energy content of unprocessed cellulose based on its inherent heat of combustion which has been

experimentally measured to be approximately 16 MJ/kg.[37] Utilizing an assumed practical cellulose solubility limit of 15 mass% in pure [EMIm][DEP], based on experimental solubility data presented in Figure 4.5, the separation energy required to purify the IL and antisolvent can be compared to the inherent energy density of the biomass product. For instance, the calculations displayed in Figure 4.5 indicate that the separation of a 1:1 mass ratio of [EMIm][DEP] to water using vacuum flash distillation at 0.01 bar and 175°C would consume over 17 MJ of heat per kg cellulose processed, not including mechanical (vacuum) power. Thus, more energy would be consumed by the IL/water separation process than the energy content of the pretreated cellulose. Other antisolvents and lower quantities could potentially reduce the required separation energy, but the energy demand is still predicted to be of the same order of magnitude. Therefore, quantitative separation of the IL and liquid antisolvent for recycle is predicted to be highly energy intensive and could impede large-scale viability. Based on the analysis presented, a non-reactive, low-energy process for the precipitation of cellulose from ionic liquids would be highly useful for biomass pretreatment.

4.3. Compressed Carbon Dioxide as a Gas Antisolvent for Precipitating Cellulose from Ionic Liquid – Mixed Solvent Systems

Compressed carbon dioxide is moderately inexpensive, naturally abundant, non-toxic, non-flammable, and environmentally benign, especially when not released to the atmosphere making it an ideal antisolvent for precipitating cellulosic biomass from ionic liquid mixtures.[38-40] Additionally, most ILs demonstrate high carbon dioxide solubilities [41-45] and dissolution of CO_2 significantly reduces the viscosity of IL systems.[46-48] Therefore, a separation process designed to precipitate cellulosic biomass from ionic liquids using compressed CO_2 at low to

moderate pressures (*i.e.* below the CO_2 critical point: $T_c = 31.1^oC$ $P_c = 73.9$ bar) was developed as a competing technology to cellulose precipitation by liquid antisolvent methods detailed in Section 4.3. The process flow diagram demonstrating a hypothetical system for pretreating cellulosic biomass utilizing ionic liquids and CO_2 is presented in Figure 4.6.

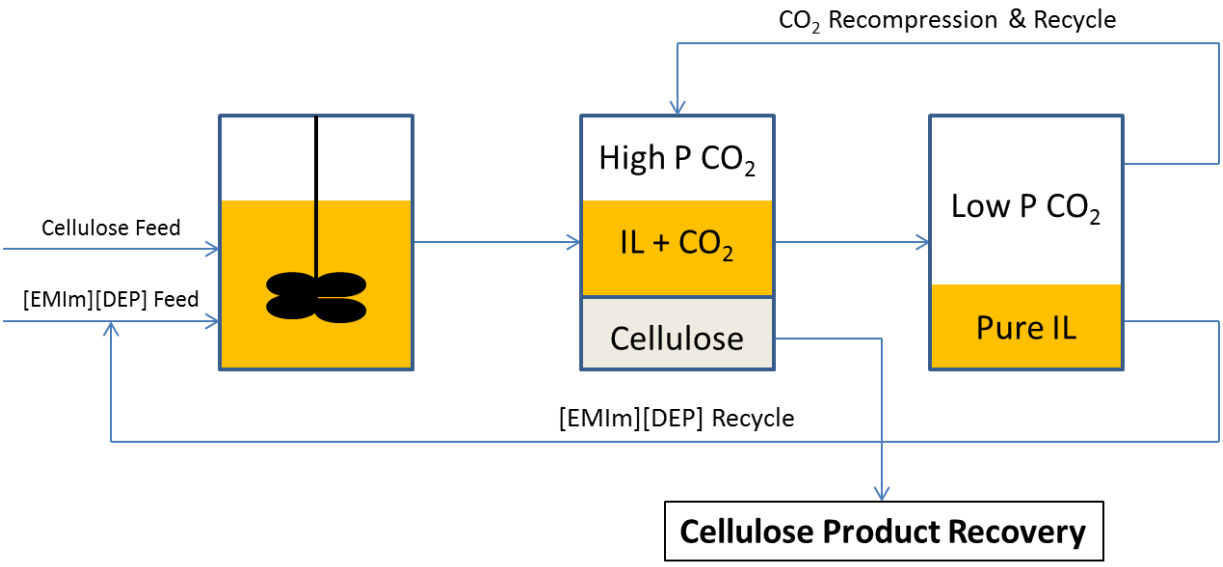

Figure 4.6: Hypothetical process flow diagram for continuous cellulose pretreatment using ionic liquids with biomass precipitation accomplished by a compressed carbon dioxide antisolvent.

4.3.1. Cellulose Precipitation by Reacting ILs with Carbon Dioxide

Barber *et al.* recently demonstrated the use of carbon dioxide as a reactant to precipitate cellulose and chitin from 1-ethyl-3-methylimidazolium acetate [EMIm][Ac].[49] Additionally, Sun *et al.* utilized compressed carbon dioxide at various pressures to precipitate cellulose from 1-butyl-3-methylimidazolium acetate [BMIm][Ac] in controlled stages based on the molecular weight of the biopolymer.[50] While these ILs are effective at precipitating cellulose in the presence of CO_2, spectroscopic studies demonstrate that acetate [Ac] ionic liquids readily react with carbon

dioxide to produce a mixture of 1-alkyl-3-methylimidazolium-2-carboxylate zwitterion and acetic acid.[51, 52] The reaction scheme, as confirmed by NMR, is displayed in Figure 4.7. Acetate ionic liquids are well known for their considerably basic character as indicated by the pKa of acetic acid (4.75) in water and presumably also in the ionic liquid. As such, spectroscopy studies indicate that the reaction of acetate ionic liquids in the presence of CO_2 is initially promoted by abstraction of the acidic proton on the IL cation (NC*H*N) by the basic acetate anion forming acetic acid. The cation is initially stabilized by carbon dioxide prior to reacting with CO_2 forming the stable carboxylate species shown in Figure 4.7.[51, 52] ^{13}C NMR characterization of [EMIm][Ac] before and after exposure to CO_2 is displayed in Figure 4.8.

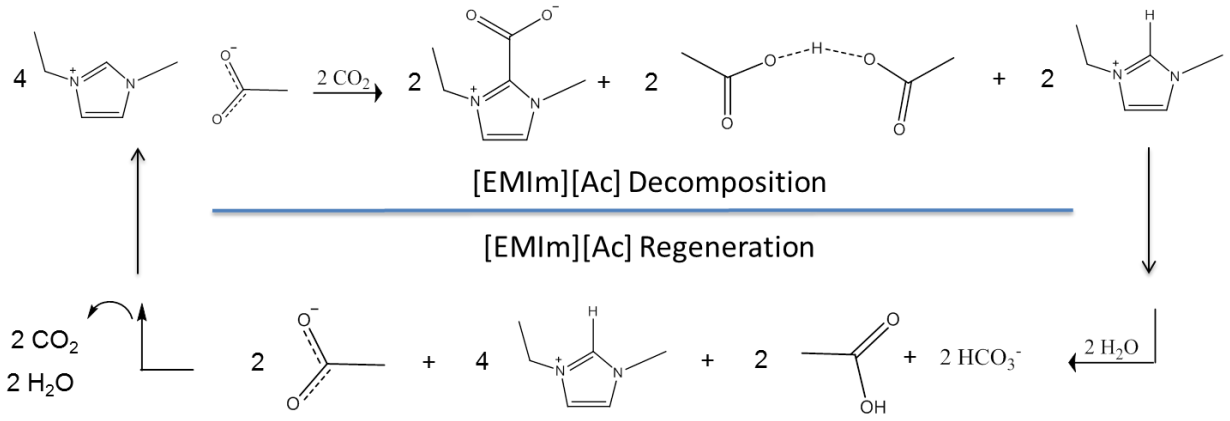

Figure 4.7: Decomposition and regeneration pathways for the complexation of CO_2 and an acetate ionic liquid modeled here by [EMIm][Ac]. [51, 52]

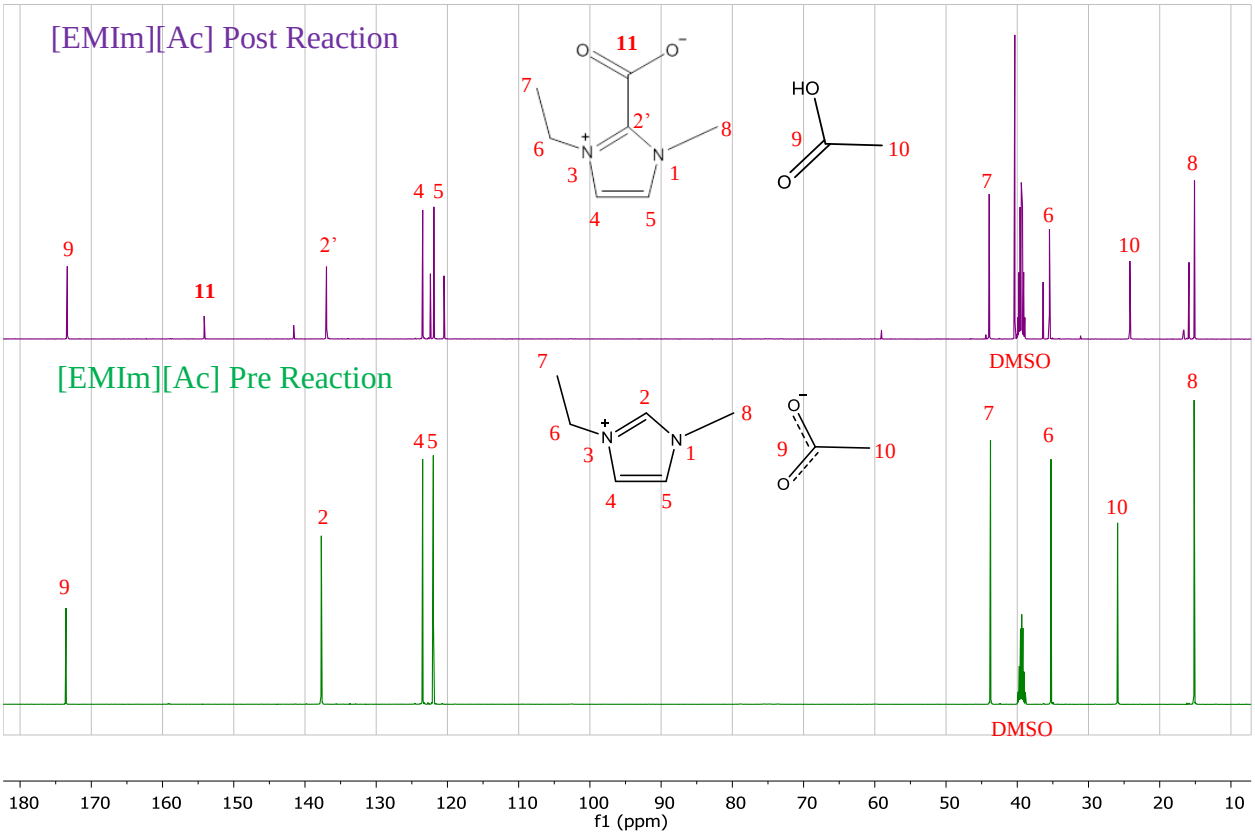

Figure 4.8: ^{13}C NMR pre- and post- reaction spectra for [EMIm][Ac] with compressed carbon dioxide. IL was exposed to CO_2 at 100 bar for 48 hours prior to obtaining the post reaction sample. Peak 11 at 155 ppm indicates the formation of carboxylate after reaction with CO_2.

Formation of the carboxylate species on the [EMIm] cation after reaction with CO_2 is demonstrated in Figure 4.8 by the ^{13}C NMR peak at ~155 ppm. Secondary resonances are also observed on carbon peaks 4, 5, 6, and 8 of the [EMIm] cation in the post processing spectra due to the equilibrium formation of the carboxylate zwitterion product. Previous studies by Besnard *et al.* estimate that approximately 16 mol% of [EMIm][Ac] is converted to the carboxylate degradation product when the IL was exposed to an atmosphere of 1 bar CO_2 at ~80°C for 30 hours.[51] Under these conditions the experimentally measured composition of carbon dioxide in the IL was X_{CO2} = 0.27. Therefore, the equilibrium behavior of the reaction explains the

observed “double” peak nature on select carbon resonances of the cation as well as the small yet non-negligible formation of the carboxylate peak at 155 ppm. Importantly, it should be noted that previous cellulose precipitation studies in the literature with acetate ILs and CO_2 were conducted at pressures far greater than 1 bar (*i.e.* 20-200 bar) and thus the equilibrium conversion of [EMIm][Ac] is likely to be significantly greater than 16 mol% at these conditions.

As the decomposition products from the acetate IL – CO_2 reaction are unable to solubilize cellulose, this forms the basis for the observed biomass precipitation. For instance, at process pressures (*i.e.* P_{CO2} > 60 bar) the acetate ionic liquid – cellulose mixture exhibits vapor-liquid equilibrium where the vapor phase is composed primarily of compressed carbon dioxide and the liquid phase consists of the acetate IL, cellulose, and absorbed CO_2. However, upon depressurization, the IL decomposes into the 1-alkyl-3-methylimidazolium-2-carboxylate zwitterion which is a white crystalline solid at atmospheric pressure and acetic acid neither of which are capable of dissolving cellulose. Separating cellulose from the IL degradation products is problematic as both amorphous cellulose and the imidazolium carboxylate zwitterion are white solids. Furthermore, while 1-alkyl-3-methylimidazolium-2-carboxylate zwitterion and acetic acid can be chemically reconverted into the ionic liquid by a reaction with water, IL stability and potential losses are of significant concern. Therefore, a non-reactive, low-energy process for the precipitation of cellulose from ionic liquids would be highly useful for biomass pretreatment.

4.4. Reversible and Non-Reactive Cellulose Separations from Ionic Liquid [EMIm][DEP] Mixtures with Compressed Carbon Dioxide

1-ethyl-3-methylimidazolium diethyl phosphate [EMIm][DEP] is a promising ionic liquid for biomass pretreatment as it dissolves significant quantities of cellulose (~20 mass% at 120^{o}C), has a low pure component viscosity (284 cP at 40°C), and is chemically & thermally stable.[53] Additionally, the infinite dilution Henry's constant of CO_2 in [EMIm][DEP] is $H_{CO2\ (x\rightarrow 0)}$ = 6.53 (at 30^{o}C) indicating that this IL also has a significant dissolution capacity of carbon dioxide.[44, 54] It was therefore hypothesized that compressed carbon dioxide could be used as an antisolvent to precipitate cellulose from [EMIm][DEP] and mixtures of this IL with polar aprotic cosolvents dimethyl sulfoxide (DMSO), dimethylformamide (DMF), and 1,3-dimethyl-2-imidazolidinone (DMI) which have been shown to enhance the thermodynamic solubility of cellulose in IL mixtures (see Chapter 3). In initial studies without cosolvents, only small quantities of cellulose precipitated from [EMIm][DEP] using compressed CO_2, even to high pressures (*i.e.* 200 bar). However, when precipitation studies were investigated on mixed IL-cosolvent-cellulose systems, dramatic separations were observed where solid cellulose rapidly precipitated from the liquid mixture. Thus, the cosolvent plays an ancillary but necessary role in intensifying the separation phenomena. Interestingly, upon decreasing the system pressure (*i.e.* liquid phase CO_2 composition) to values just below the precipitation point, cellulose spontaneously re-dissolved in the liquid mixture. Based on these results we demonstrate for the first time the use of compressed carbon dioxide as a physical (non-reactive) antisolvent for the precipitation of cellulose from IL/cosolvent mixtures.

4.4.1. Reversible and Non-Reactive Separation Process Overview

In this study, microcrystalline cellulose (Figure 4.9 A) was dissolved in a model system of ionic liquid [EMIm][DEP] with select cosolvent ratios. The liquid mixture was loaded into an autoclave viewcell and compressed carbon dioxide was added to the IL/cosolvent/cellulose liquid mixture resulting in vapor-liquid equilibrium with an IL/cosolvent/cellulose liquid phase and a CO_2-rich vapor phase absent of cellulose and the IL (Figure 4.9 B). At certain pressures (CO_2 compositions), cellulose dramatically precipitated from the liquid mixture forming a solid-liquid-vapor equilibrium (*SLV*) condition (Figure 4.9 C): solid cellulose, IL/cosolvent-rich liquid, CO_2-rich vapor. During the precipitation either a single mass of amorphous cellulose or a range of cellulose particles could be produced depending on the rate of CO_2 addition, mixing speed, *etc.* With a small pressure reduction to just a few bar below the precipitation point, cellulose re-dissolved in the liquid phase, and a clear homogeneous mixture (Figure 4.9 D) was recovered within minutes. Therefore, a narrow pressure - composition regime exists in which cellulose undergoes a transition from full to virtually no solubility in the IL/cosolvent liquid phase. From a practical engineering perspective, these results demonstrate that by simply reducing the CO_2 pressure, the antisolvent effect of CO_2 is eliminated and, importantly, the solvation ability of the IL for cellulose is completely regenerated. Therefore, this interesting phase behavior demonstrates the feasibility of using CO_2 composition as a separation switch for the precipitation of cellulose from ionic liquid mixtures.

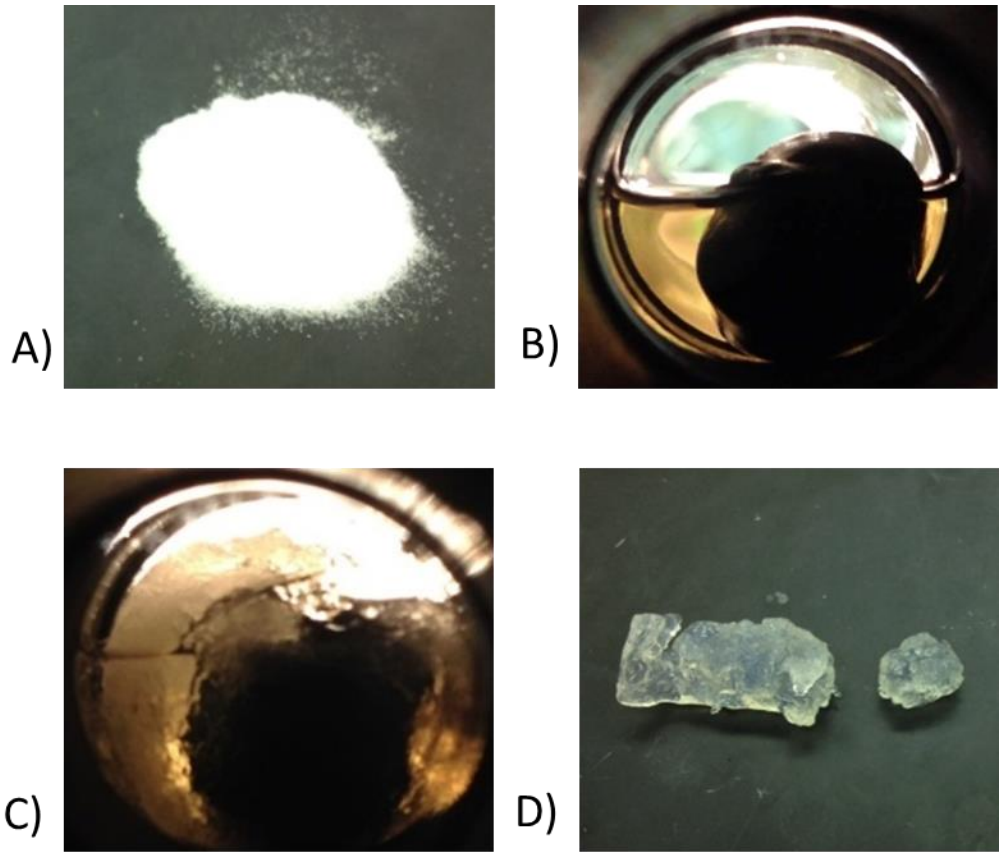

Figure 4.9: Images of A) microcrystalline cellulose; B) cellulose /IL/DMF (stirbar in windowed-pressure vessel); C) cellulose precipitating with CO_2; D) precipitated cellulose (washed).[25]

4.4.2. Cellulose Precipitation Parameters

4.4.2.1. Ionic Liquid Selection

The compressed carbon dioxide non-reactive antisolvent process was explored with three cellulose dissolving ionic liquids including 1-butyl-3-methylimidazolium chloride [BMIm][Cl], 1-methyl-3-methylimidazolium dimethyl phosphate [MMIm][DMP], and [EMIm][DEP] as well as mixtures of these ILs with the aprotic cosolvent DMSO. Whereas a clear cellulose separation was observed for [EMIm][DEP] and mixtures of this IL with aprotic cosolvents, cellulose did not precipitate from any of the other ILs including [BMIm][Cl] and [MMIm][DMP] or mixtures of

these ILs with DMSO at pressures up to 250 bar CO_2 (5 mass% initial cellulose loading). The solubility of CO_2 in [BMIm][Cl] and [EMIm][DEP] were compared and displayed in Figure 4.10. Despite being at slightly different temperatures, it is evident that CO_2 is significantly more soluble in [EMIm][DEP] at 60°C compared to [BMIm][Cl] at 80°C. Similar results are expected for these ILs at lower temperatures as well as for [MMIm][DMP] which has not been measured to this point. As carbon dioxide composition is believed to be the driving force for the physical (non-reactive) cellulose precipitation observed with [EMIm][DEP], it is hypothesized that the non-[EMIm][DEP] ILs investigated are incapable of precipitating cellulose in the presence of CO_2 as a critical composition of gas antisolvent is incapable of dissolving in the liquid mixture.

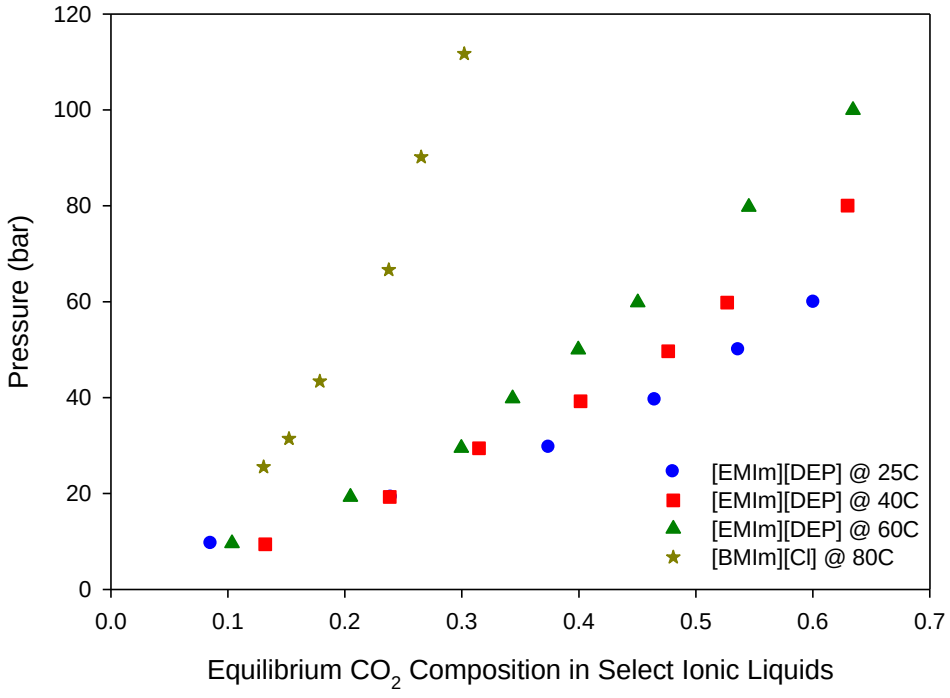

Figure 4.10: Solubility of carbon dioxide in select ionic liquids. [BMIm][Cl] data adapted from [43]. [EMIm][DEP] data experimentally measured.

4.4.2.2. Cosolvent Selection and Loading

Select cosolvents are advantageous for the CO_2-based separation process with [EMIm][DEP] since many polar aprotic molecules exhibit relatively high CO_2 solubilities.[44, 55] In addition, the presence of CO_2 itself decreases the mixture viscosity of ionic liquid systems, thus enhancing transport properties.[56] Furthermore, as shown in Chapter 3, select cosolvents do not significantly decrease the cellulose capacity of IL mixtures and can even enhance the thermodynamic solubility of cellulose in [EMIm][DEP] at select temperatures and loadings. Therefore, cosolvents including DMSO, DMF, and DMI were investigated for compatibility with the precipitation process. Additionally, acetone and acetonitrile were explored as they are two of the most common, inexpensive, polar aprotic solvents available.

Ionic Liquid	Cellulose Loading (mass%)	Cosolvent	Cosolvent Loading mass% [mol%][a]	Precipitation Pressure CO_2 (bar)	
				25°C	40°C
[EMIm][DEP]	5%	Acetone	25% [60.2%]	34	----
	5%	Acetonitrile	25% [68.2%]	43	62
	5%	DMSO	25% [54.8%]	54	----
	5%	DMF	25% [54.8%]	32	49
	5%	DMI	25% [43.5%]	53	68
	5%	DMSO	50% [78.3%]	53	----
	5%	DMF	50% [78.3%]	26	49
	5%	DMI	50% [69.8%]	40	57
[BMIm][Cl]	5%	DMSO	25% [42.9%]	----	----
	5%	DMF	25% [44.5%]	----	----

[a] solute-free composition; "—" indicates that precipitation did not occur at CO_2 pressures up to 250 bar

Table 4.4: Incipient conditions of cellulose precipitation (SLV Equilibrium) from IL/cosolvent mixtures with compressed CO_2.[25]

Table 4.4 illustrates the cellulose separation conditions (*SLV*) at 25°C and 40°C for two ionic liquids, five cosolvents, and two cosolvent compositions. For the system of 5 mass% cellulose dissolved in a mixture of 75 mass% [EMIm][DEP] and 25 mass% DMF at 25°C, (IL/cosolvent

compositions given on a solute-free basis) cellulose precipitates at just 32 bar pressure. Thus, the separation occurs by simply introducing CO_2 in its vapor phase at conditions much lower than its vapor pressure or critical point (31.1°C, 73.8 bar). Furthermore, by increasing the proportion of DMF in the mixture to an initial 50 mass% (solute-free basis) loading at 25°C the separation pressure is reduced to 26 bar. These results indicate that increased cosolvent loading can lower the required separation pressure in select conditions.

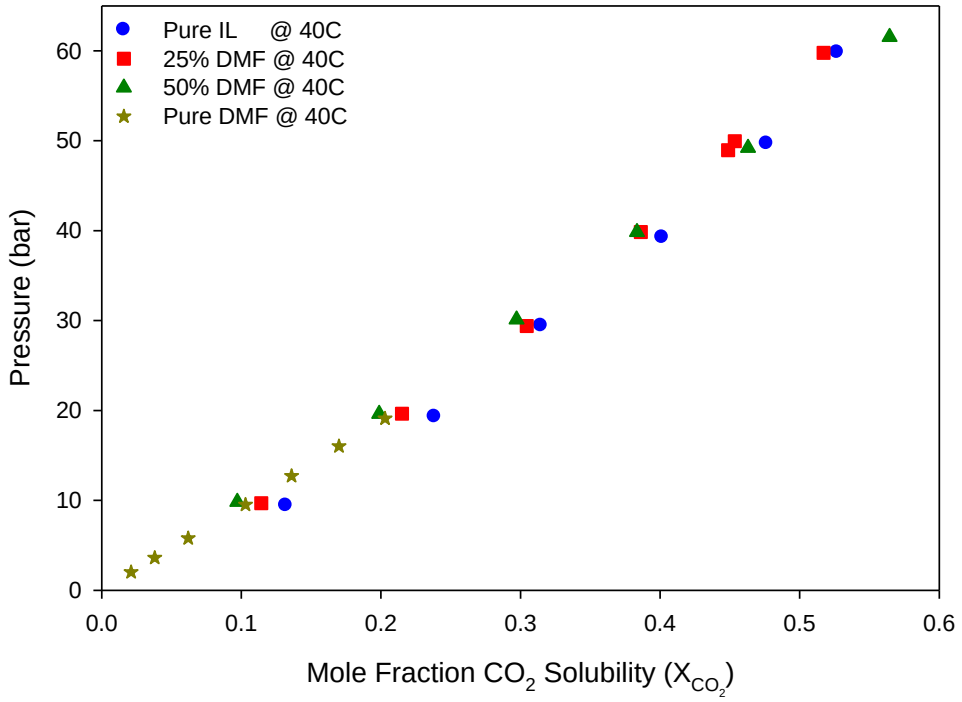

Figure 4.11: Solubility of carbon dioxide in [EMIm][DEP] mixtures with varying compositions of dimethylformamide at 40°C. Pure DMF data was adapted from [55].

Alternatively, as displayed in Table 4.4, [EMIm][DEP] mixtures at 25°C with 25 mass% and 50 mass% DMF cosolvent compositions (solute free basis) precipitate cellulose at identical 49 bar pressures. The indistinguishable separation pressures can be understood by investigating the

high pressure solubility data presented in Figure 4.11. Dimethylformamide and [EMIm][DEP] have nearly identical solubilities of CO_2 at 40°C. Therefore, the IL-DMF-cellulose mixtures at varying cosolvent loadings will have nearly equivalent CO_2 compositions in solution. As CO_2 composition is believed to be the primary driving force for cellulose precipitation from IL-cosolvent mixtures, the matching CO_2 solubilities for DMF and [EMIm][DEP] demonstrate that regardless of cosolvent loading the CO_2 capacity of the mixture and resulting precipitation point at 40°C should be unaffected.

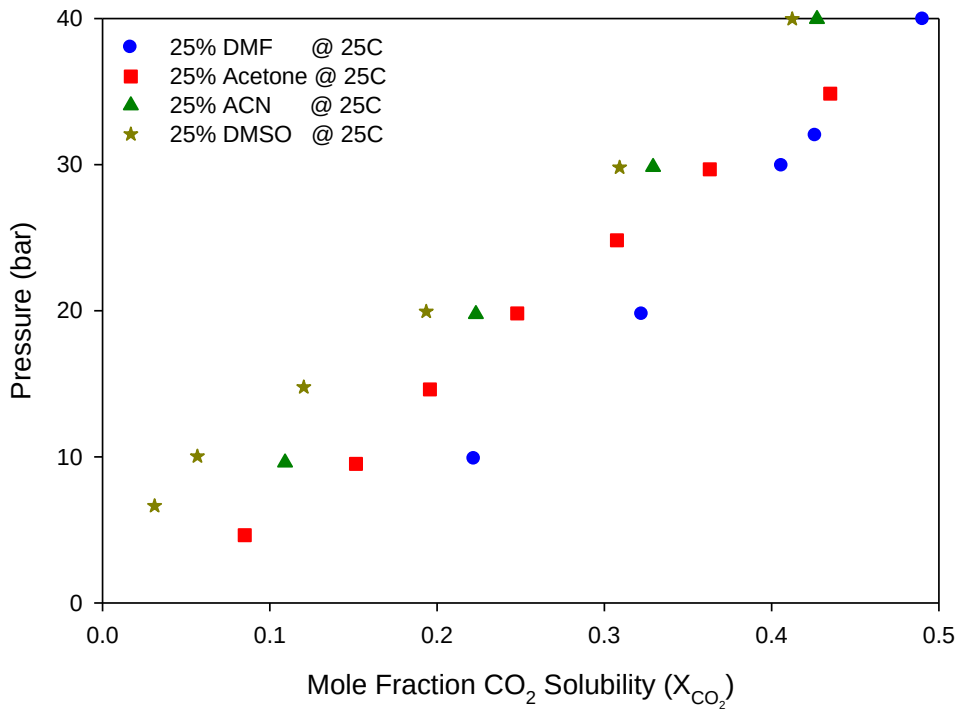

Figure 4.12: CO_2 solubility in select [EMIm][DEP] mixtures with 25 mass% cosolvent loadings (solute free basis) at 25°C

Utilizing the data displayed in Table 4.4, the pressure at which the cellulose separation occurs for various mixed IL systems can be explored at constant temperature and cosolvent loading. For

instance, at 25°C and 25 mass% cosolvent loadings (solute free basis) the order of separation pressures (*i.e.* P_{CO2}) is DMF < Acetone < ACN < DMSO ≈ DMI. This order can be understood by comparing the CO_2 solubilities in the resulting systems as shown in Figure 4.12. The high pressure solubility data indicate that the separation pressure is highly dependent on the mixed solvent system's CO_2 capacity and that mixed solvent systems with higher carbon dioxide solubilities precipitate cellulose at lower pressures. However, other factors must also be considered when comparing the various cosolvent systems. For instance, the 25 mass% DMI cosolvent system at 25°C, precipitates cellulose at 53 bar, which is 21 bar higher than DMF at the same cosolvent to IL mass ratio and temperature. The molar ratios of these cosolvent/IL systems are 55 mole% DMI vs. 44 mole% DMF, potentially explaining the difference in the observed precipitation points. Regardless of mechanism the results in Table 4.4 demonstrate that cosolvent selection and loading have a significant impact on the separation conditions.

4.4.2.3. Temperature Effects

The system temperature has a significant impact on the separation pressure as shown in Table 4.4. For instance, at a constant cosolvent loading of 25 mass% DMF, cellulose precipitation occurred at a CO_2 pressure of 32 bar. Alternatively, for the same system at 40°C, the precipitation pressure increased to 49 bar. Similar increases in precipitation pressure as a function of temperature are observed for the 25 mass% acetonitrile system, the 50 mass% DMF system, and the DMI systems at both 25 and 50 mass% loadings. The separation pressure-temperature dependence can be understood by investigating the high pressure phase equilibrium results for the 25 mass% DMF system at 25°C and 40°C, displayed in Figure 4.13. The results show that, as expected, increased temperature at a fixed cosolvent loading decreases the

solubility of CO_2 in the liquid phase. As the non-reactive separation appears to be a function of liquid phase CO_2 composition, it is therefore reasonable to expect higher required CO_2 partial pressures at elevated temperatures (*i.e.* 40°C).

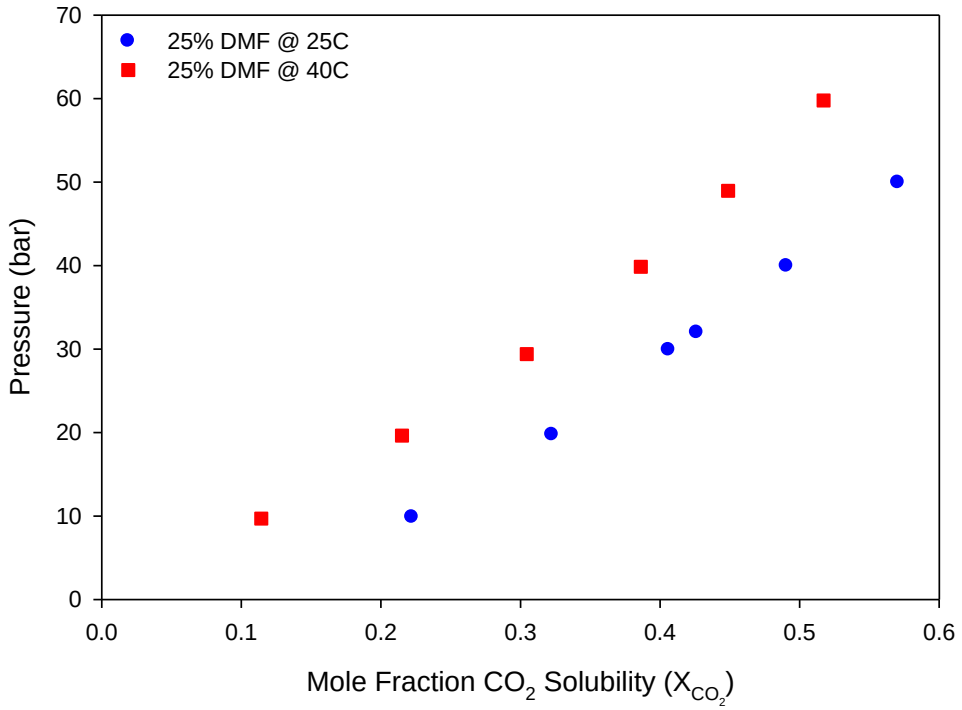

Figure 4.13: CO_2 solubility in a 25 mass% DMF – [EMIm][DEP] mixture as a function of temperature at 25°C and 40°C.

Not all systems precipitated cellulose at both 25°C and 40°C. For instance, the DMSO systems at both 25 and 50 mass% cosolvent loadings precipitated cellulose when the system temperature was at 25°C. However, at 40°C, neither cosolvent loading of DMSO was capable of generating a separation. Similar results were also observed for the 25 mass% acetone system at 25°C and 40°C. For these systems the phase equilibrium transitioned from an initial vapor-liquid state where the vapor phase was composed primarily of CO_2 and the liquid phase consisted of a

mixture of [EMIm][DEP], cosolvent, cellulose, and dissolved CO_2 to a vapor-liquid-liquid equilibrium (VLLE) scenario prior to precipitation of amorphous cellulose. In the VLLE cases, the phases consisted of an ionic liquid rich phase containing all of the cellulose, some cosolvent, and dissolved CO_2; a second liquid phase consisting of CO_2 expanded cosolvent; and a vapor phase of primarily compressed carbon dioxide with potential traces of some organic cosolvent. Therefore, at 40^{o}C, in cases where the precipitation did not occur, the cosolvent partitioned out of the initial liquid phase thus likely reducing the CO_2 capacity of the IL-cellulose rich phase and increasing the concentration of IL ions relative to cellulose hydroxyl groups both of which support greater cellulose stability in the ionic liquid mixture.

4.4.2.4. Cellulose Loading

For the 50 mass% DMF-IL system the effect of cellulose composition on the separation point was measured and displayed in Table 4.5.

Ionic Liquid	Cellulose Loading (mass%)	Cosolvent	Cosolvent Loading mass% [mol%][a]	Precipitation Pressure CO_2 (bar)	
				25^{o}C	40^{o}C
[EMIm][DEP]	2%	DMF	50% [78.3%]	33	NA
	5%			26	49
	8%			24	NA

"NA" indicates trial was not attempted

Table 4.5: Effect of cellulose loading on the separation pressure from a 50 mass% DMF cosolvent loading (solute free basis) in [EMIm][DEP].[25]

A system containing 5 mass% cellulose (total solution basis) in an IL-DMF mixture precipitated cellulose at a separation pressure of 26 bar. Comparatively, when only 2 mass% cellulose was loaded in the same IL-DMF mixture, the precipitation pressure increased to 33 bar. Therefore, the results appear to show that increased CO_2 pressure is required to remove trace quantities of

cellulose dissolved in the ionic liquid. Alternatively, a mixture containing 8 mass% cellulose demonstrated a precipitation pressure of 24 bar indicating that cellulose loading has a moderate impact on the separation pressure. Although pressure has been discussed as an operating parameter for the separation, it is the concomitant increase in CO_2 composition with pressure not hydrostatics that is the main driving force for cellulose precipitation.

The dependence of CO_2 precipitation pressure (liquid phase composition) on cellulose loading in the IL-cosolvent mixture may be potentially explained by the work of Sun *et al.* who investigated the staged precipitation of cellulose from acetate [Ac] ionic liquids using compressed carbon dioxide.[50] Despite investigating a reactive IL, this study concluded that the rate of cellulose precipitation from the IL was directly proportional to the degree of polymerization of the cellulose polymer chain.[57] For instance, they found that increased CO_2 exposure times were required to precipitate lower MW fractions of cellulose. While the precipitation mechanism for acetate ILs is based on a reaction between the IL and CO_2, similar separation phenomena associated with the size of the polymer chain may be occurring in our non-reactive systems. For instance, at lower partial pressures (*i.e.* liquid phase CO_2 compositions) the longer chain cellulose molecules may be precipitating from solution while higher pressures are required to separate the lower MW cellulose fractions. Alternatively, the bulk composition of cellulose may have a significant effect on the precipitation pressure. While hypothesized herein, to this point, the dependence of the precipitation pressure on liquid phase cellulose composition remains largely unknown in our systems.

Regardless of the precipitation mechanism, cellulose loading does not significantly impact the solubility of CO_2 in IL mixtures compared to what was observed for the impact of cosolvent

loading and temperature. For instance, Figure 4.14 demonstrates that the CO_2 solubility in a 50 mass% DMSO-[EMIm][DEP] mixture is negligibly affected by the presence of 5 mass% cellulose (total solution basis) in the mixture. Therefore, the pressure dependent separation phenomena correlated to cellulose loading is not due to any appreciable increase in CO_2 solubility associated with cellulose content.

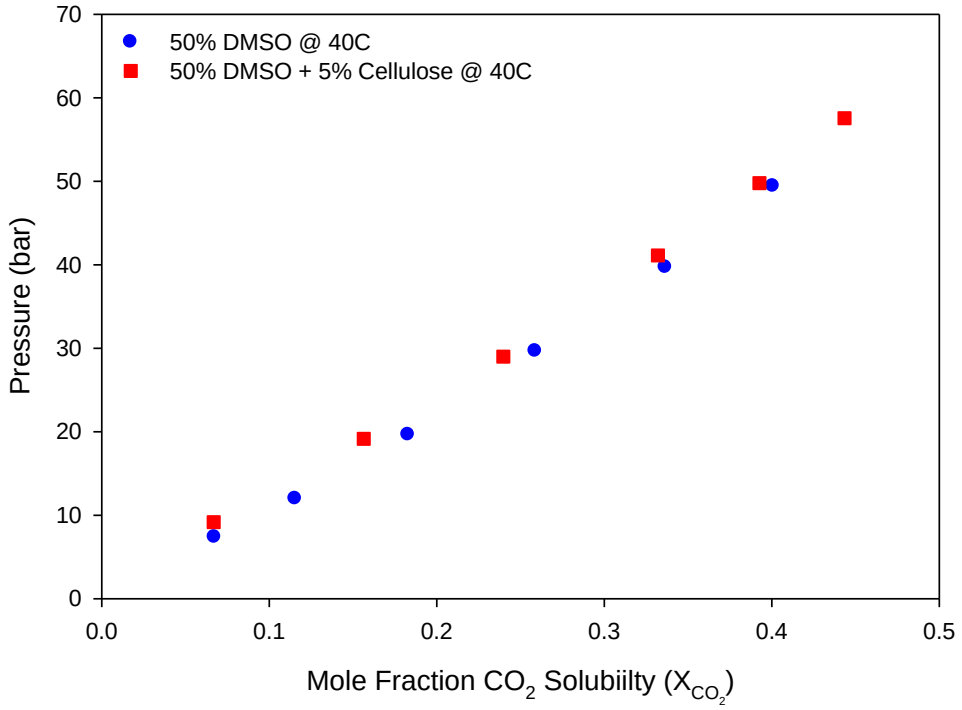

Figure 4.14: Effect of cellulose loading on CO_2 solubility of an [EMIm][DEP]-DMSO mixture.

4.4.2.5. Compressed Gases

Three compressed gases including carbon dioxide, nitrogen, and 1,1,1,2-tetrafluroroethane (R134a) were applied to investigate the role of the selected gas on the cellulose precipitation phenomena. Whereas CO_2 is highly soluble in most ionic liquids including [EMIm][DEP], both

nitrogen and R134a demonstrated limited solubilities. For instance, the addition of R134a formed a liquid-liquid equilibrium (LLE) condition at pressures up to 200 bar indicating that very little if any gas dissolved in the IL liquid phase. Furthermore, the separation was attempted with nitrogen and exhibited vapor-liquid equilibrium behavior up to 250 bar but did not produce any interesting results indicating that hydrostatics (*i.e.* pressure) is not the driving force for cellulose precipitation from [EMIm][DEP]-cosolvent mixtures.

Simulation studies show that ionic liquid solvation of cellulose is largely attributed to the disruption of inter and intra molecular hydrogen bonds within the crystalline cellulose structure by the IL anion.[58] Additionally, spectroscopic and simulation studies show that dissolved CO_2 preferentially interacts with ionic liquid anions.[59, 60] The presence of aprotic cosolvents, in limited amounts, does not seem to disrupt anion stabilization of dissolved cellulose to any great extent. Thus, the presence of CO_2 must interfere with the ability of the IL anion to solvate cellulose.

4.4.3. [EMIm][DEP] Stability: Confirming the Non-Reactive Separation Process

To confirm the physical (non-reactive) interactions between [EMIm][DEP] and CO_2, high pressure coupled ^{1}H-^{13}C NMR was measured on the pure IL and mixed IL cosolvent systems. [EMIm][DEP] was exposed to CO_2 at 100 bar pressure for 72 hours to ensure that chemical and thermodynamic equilibrium had been established. For reactive ILs with CO_2 such as [EMIm][Ac] shown in Section 4.3.1, the carboxylation of the imidazole ring produces a NMR resonance at ≈ 155 ppm.[51, 52] As shown in Figure 4.15, the NMR spectra of [EMIm][DEP] at 100 bar, a pressure significantly greater than what is required for cellulose precipitation, does not indicate a strong peak for the carboxylate at 155ppm even after

72 hours of exposure. Based on the signal-to-noise ratio, any carboxylate would be less than 1 mole%. Thus, the separation presented herein occurs by a physical, non-reactive, process.

The reaction mechanism between CO_2 and 1, 3-dialkyl-imidazolium acetate ILs is believed to occur in two steps: 1) deprotonation of the bridging carbon (C_2) in the imidazolium ring by the basic acetate anion to an imidazole carbene; 2) CO_2 reaction to form a stable carboxylate product.[51, 52] The diethyl phosphate anion is less basic (pKa ~1.4; at least in aqueous solution and presumed in ILs), compared to the acetate anion (pKa 4.75), and is unable to actively participate in the deprotonation of the imidazolium cation potentially explaining the enhanced stability of [EMIm][DEP] in the presence of CO_2. Additional ^{13}C NMR experiments have been conducted on pre- and post- pressurized [EMIm][DEP] to investigate IL stability before and after the separation process. The results shown in Figure 4.16 demonstrate that upon depressurization, [EMIm][DEP] is fully recovered and no degradation products are present in the spectra thus confirming that [EMIm][DEP]-CO_2 interactions are of the physical (non-reactive) regime.

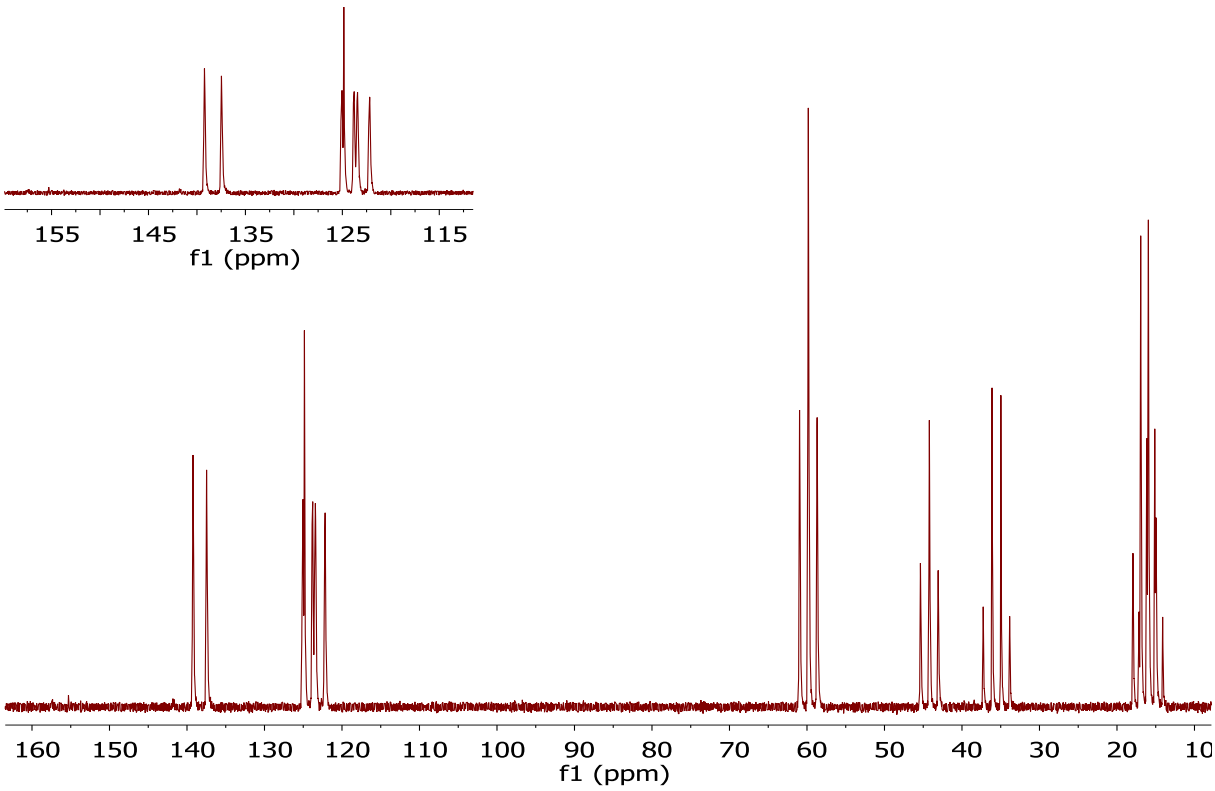

Figure 4.15: [EMIm][DEP]-CO_2 high-pressure coupled ^{1}H-^{13}C NMR at 100 bar after 72 hours. Inset: absence of resonance in imidazolium carboxylate region at ~155 ppm.

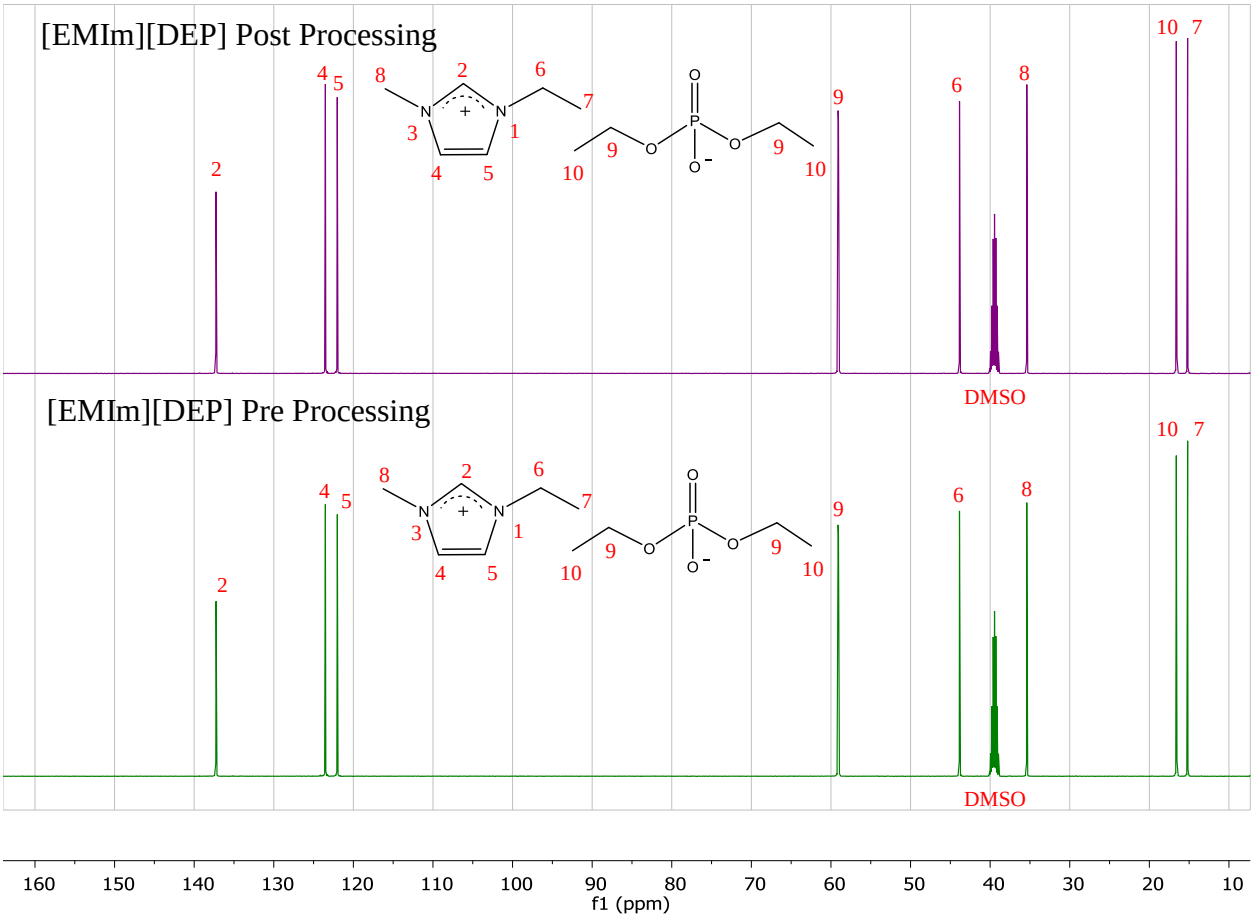

Figure 4.16: Stacked solution state proton NMR spectra displaying ionic liquid [EMIm][DEP] before (green) and after (purple) 72 hours of CO_2 exposure. Spectra perfectly align and display no formation of new proton resonances indicating IL stability. (DMSO d6 lock solvent)

4.4.4. Theoretical Physical (Non-Reactive) CO_2 Precipitation Mechanisms

While in-situ NMR studies confirm that [EMIm][DEP]-CO_2 interactions are physical (non-reactive) in nature, they are incapable of providing insight into the underlying separation mechanism. Spectroscopic techniques including Kamlet-Taft solvatochromic analysis and FTIR were applied to the high pressure separation studies but neither analytical technique yielded useful results. For instance, Kamlet-Taft studies on [EMIm][DEP]-CO_2 mixtures demonstrated

no change in acidity, basicity, or polarizability parameters of the system even with CO_2 loadings in excess of 200 bar ($X_{CO2} > 0.5$). Similar results were observed by Brennecke *et al.* who found that acidity and basicity parameters are "virtually independent" of CO_2 composition.[61] Furthermore, select *KT* probe molecules including Reichardt's Dye (30) precipitated from the liquid phase upon the addition of CO_2. Infrared spectroscopy studies investigated by ReactIR were similarly unable to detect changes in the spectra caused by CO_2.

4.4.4.1. CO_2 Solubility in mixed [EMIm][DEP]-Cosolvent Systems

As previously discussed, CO_2 is highly soluble in pure [EMIm][DEP] and IL-cosolvent mixtures investigated herein. The solubility and precipitation results for mixed [EMIm][DEP]-DMI systems at two cosolvent loadings and two temperatures is displayed in Figure 4.17.

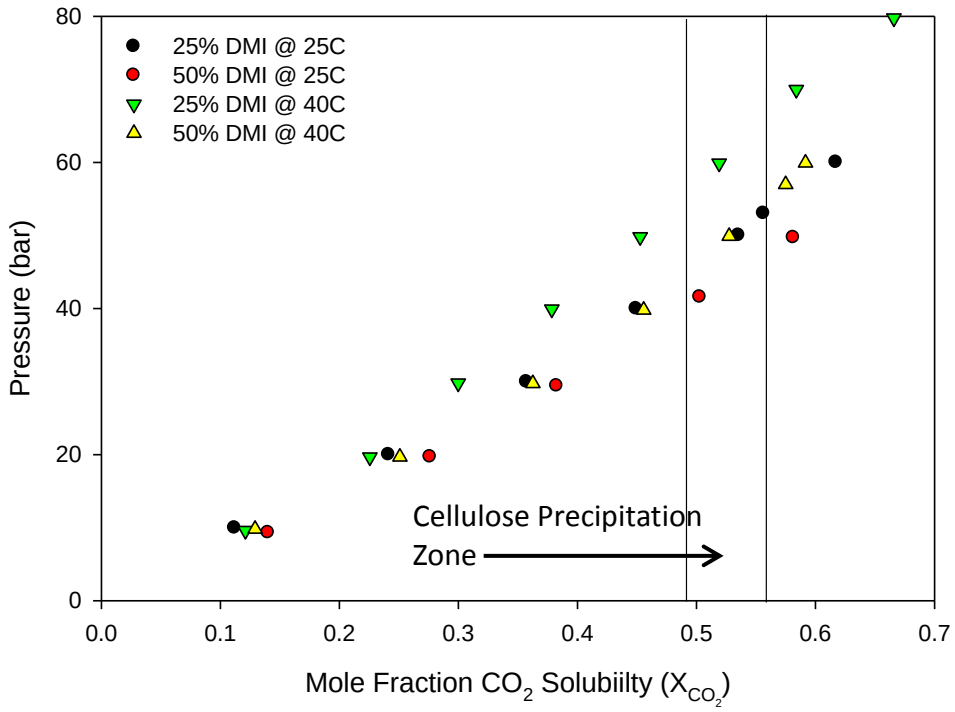

Figure 4.17: Solubility of CO_2 in [EMIm][DEP]-DMI mixtures and the effect of CO_2 capacity on the precipitation of cellulose.

From these solubility and separation results it is evident that cellulose precipitation occurs in a relatively narrow range of CO_2 compositions. For instance, at 40°C cellulose precipitates from the 25 mass% and 50 mass% DMI mixtures at 68 and 57 bar respectively. At these pressures, the corresponding CO_2 solubilities in these DMI mixtures are similarly ~58 mole%. Additionally, at 25°C the precipitation occurs at 53 bar and 40 bar for the 25 mass% and 50 mass% DMI cosolvent systems. These pressures correspond to liquid phase CO_2 compositions of 56 mole% and 49 mole% respectively. Therefore, the phase equilibrium results demonstrate that the separation is highly dependent on a critical liquid phase composition of compressed carbon dioxide.

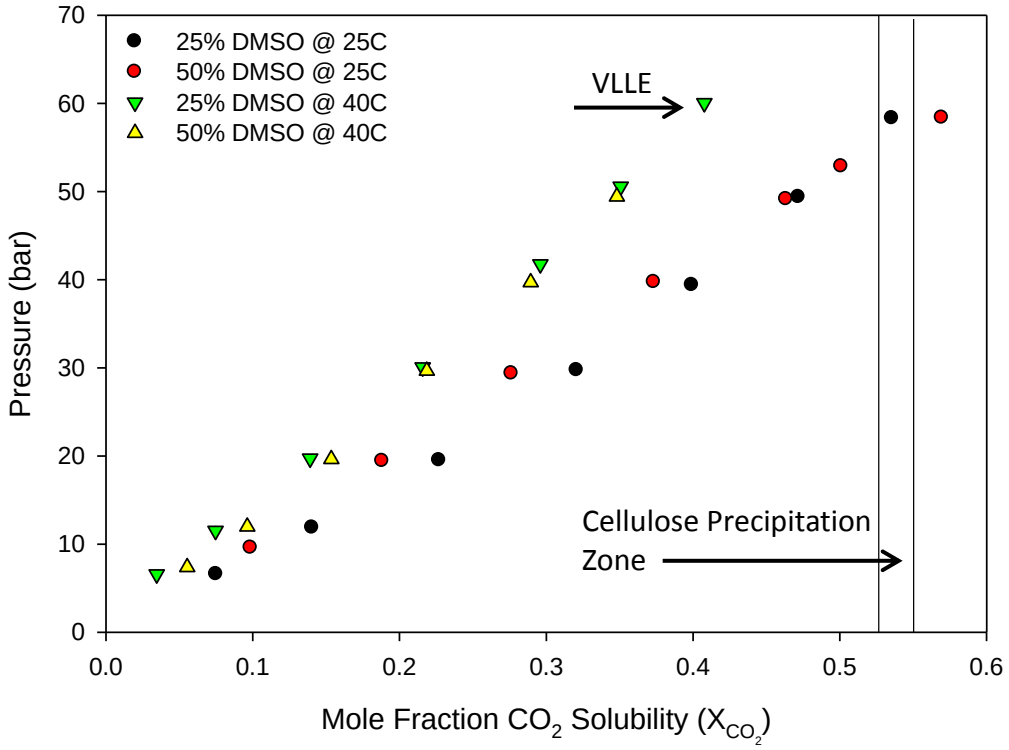

Figure 4.18: Solubility of CO_2 in [EMIm][DEP]-DMSO mixtures and the effect of CO_2 capacity on the precipitation of cellulose.

Despite the results demonstrated above for the DMI cosolvent systems, not all of the mixed [EMIm][DEP]-cosolvent systems demonstrated a separation at both 25°C and 40°C. For instance, the DMSO systems only precipitated cellulose when at 25°C. Alternatively both systems at 40°C transitioned to vapor-liquid-liquid equilibrium prior to reaching the separation point, as discussed above. To understand this phenomena in greater detail high pressure phase equilibrium CO_2 solubility data was obtained for the [EMIm][DEP]-DMSO systems at 25 mass% and 50 mass% cosolvent loadings and at 25 and 40°C. The 25 mass% and 50 mass% DMSO systems at 25°C precipitated cellulose at 54 and 53 bar respectively. The corresponding solubilities of CO_2 at these pressures were 57 mole% and 55 mole% for these same two

separation pressures. Therefore, as was observed for the DMI systems, the separation is highly dependent on the liquid phase CO_2 capacity.

However, separations were not observed for either the 25 mass% or 50 mass% DMSO system at 40^{o}C. The high pressure-solubility data for these systems shows that at 40^{o}C and approximately 60 bar pressure the system transitions to a VLLE scenario at which point the CO_2 solubility in the liquid phase becomes asymptotic with pressure. Therefore, the approximate maximum CO_2 capacity of both the 25 and 50 mass% DMSO systems at 40^{o}C is ~42 mole% which is significantly less than the quantity required to precipitate cellulose in either of the DMSO cosolvent systems at 25^{o}C (*i.e.* ~56 mole%). Based on this assessment it is hypothesized that cellulose precipitations from the mixed [EMIm][DEP]-DMSO systems at 40^{o}C were not observed due to the lack of CO_2 solubility in the liquid mixture. While not shown herein, similar results were also observed for the acetone system at 40^{o}C.

4.4.4.2. Volume Expansion of mixed [EMIm][DEP]-Cosolvent Systems

CO_2 dissolution in mixed [EMIm][DEP] cosolvent systems results in significant volume expansion of the liquid mixture. For instance, as shown in Figure 4.19 for the DMF system, at 25^{o}C and a cosolvent loading of 50 mass%, the liquid phase is expanded by as much as 60% relative to the liquid mixture prior to CO_2 addition. Mixed solvent systems containing only 25 mass% DMF demonstrated considerably lower volume expansions of ~20% at the highest CO_2 loadings (*i.e.* pressures) measured. Compared to ionic liquids, organic solvents (especially DMSO, DMF, and DMI) demonstrate significantly larger volume expansions by dissolved CO_2 explaining the observed trend in cosolvent loading and volume expansion.[62-64]

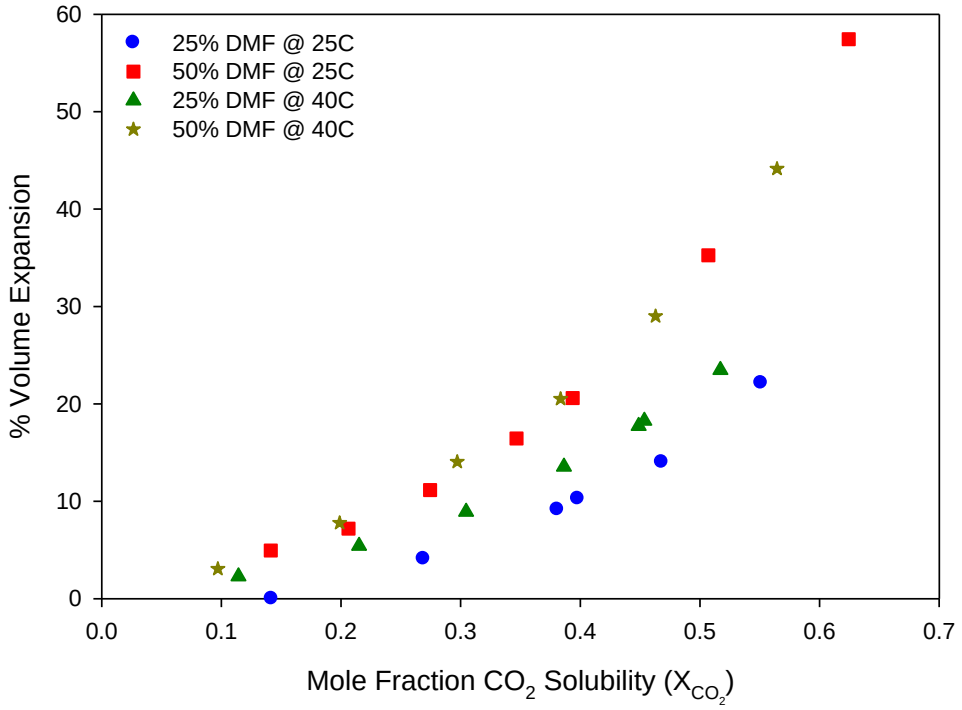

Figure 4.19: Volume expansion of mixed [EMIm][DEP]-DMF cosolvent systems as a function of CO_2 solubility.

Alternatively, temperature appears to have less of an effect on the volume expansion. For instance, the volume expansion curves of the 50 mass% DMF systems at 25°C and 40°C are perfectly overlaid indicating that the volume expansions of these systems are nearly identical. Similar results are also observed for the 25 mass% cosolvent loading systems although the volume expansion of the 40°C system is slightly greater than that of the 25°C system.

From a practical separation standpoint, volume expansion of the liquid mixture upon absorption of CO_2 potentially plays a significant role in the observed cellulose precipitation phenomena. At the separation point, mixtures of [EMIm][DEP] with 25 mass% DMF cosolvent loadings experience volume expansions of 10% and 15% at 25°C and 40°C respectively. Additionally, the

50 mass% DMF systems are expanded by 16% and 28% at these same two temperatures. Therefore, the liquid mixtures are significantly expanded prior to the separation point. Volume expansion may physically separate ionic liquid and cellulose in solution thus reducing the interaction probability between these molecules. Additionally, CO_2 may preferentially interact with the IL anion thus disrupting IL-cellulose bonding interactions. The volume expansion results clearly demonstrate that CO_2 changes the physiochemical properties of the liquid mixture at the separation point.

4.4.4.3. Molarity of mixed [EMIm][DEP]-Cosolvent Systems

Dissolution of CO_2 and volume expansion of the IL-cosolvent liquid mixture leads to a concomitant increase in liquid phase CO_2 composition and a nominal decrease in ionic liquid concentration (moles per volume) or, more importantly for cellulose solubility, a lower concentration of the IL anion. Ionic liquid [EMIm][DEP] molarity as a function of liquid phase CO_2 composition is displayed in Figure 4.20.

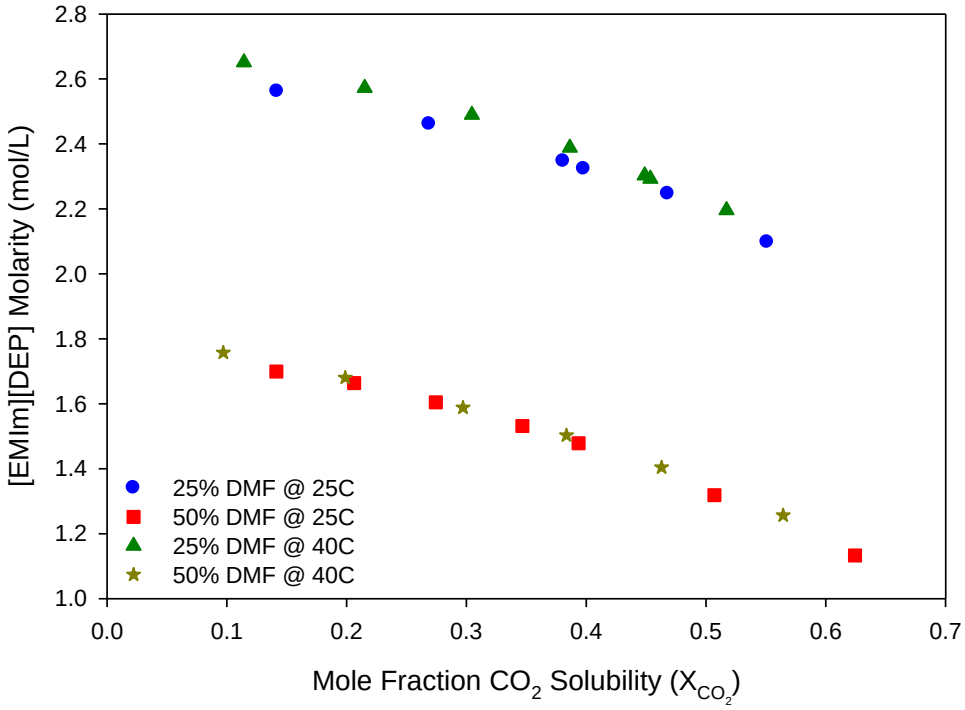

Figure 4.20: Concentration of [EMIm][DEP] (moles/L) as a function of liquid phase CO_2 capacity.

Cosolvent loading has a significant impact on the initial IL molarity in the mixed solvent systems as seen in Figure 4.20. For instance, the molarity of a pure [EMIm][DEP] system prior to CO_2 addition is 3.84 mol/L. Comparatively, when a cosolvent (DMF) is added in 25 mass% and 50 mass% loadings the resulting IL molarities are 2.75 and 1.76 respectively. Therefore, the addition of cosolvent alone has a significant impact on the concentration of IL ions in solution. Upon addition of CO_2 the concentration of the ionic liquid is further reduced. For instance, IL molarity is reduced by ~18% and ~34% at the highest CO_2 loadings in the 25 mass% DMF system (X_{CO2} ~ 0.55) and 50 mass% DMF system respectively (X_{CO2} ~ 0.63). Interactions between the ionic liquid and cellulose are hypothesized to be the driving force for biomass

dissolution in IL systems. Therefore, dilution of the ionic liquid by both cosolvents and compressed carbon dioxide potentially reduces the concentration of the IL below a critical amount which is required to solubilize cellulose.

4.5. Characteristics of the Amorphous Cellulose Product

Solid phase analysis of the cellulose product was performed by CP/MAS solid state NMR. Figure 4.21 displays the spectra of microcrystalline (pre-processed) cellulose and post-processed amorphous cellulose treated with an [EMIm][DEP]-DMSO mixed solvent system and CO_2 precipitation. Crystalline cellulose is characterized by sharp C_4 and C_6 peaks at 92 and 68 ppm respectively which are most actively involved in inter- and intra- molecular hydrogen bonding.[65-67] As shown, the C_4 and C_6 peaks of precipitated cellulose shift and broaden indicating reduced crystallinity. Degree of cellulose crystallinity was quantified using the C_4 peak separation and integration method.[66, 68] Native microcrystalline cellulose exhibited 61% crystallinity while the processed amorphous cellulose displayed <11% crystallinity. Therefore, total cellulose crystallinity was reduced by 80+% through IL/cosolvent and CO_2 antisolvent processing. From a reaction perspective, the highly amorphous precipitated cellulose product has been correlated to superior chemical and biochemical conversion rates to glucose or other chemicals.[14, 15] Importantly, the IL based dissolution and precipitation process is incapable of hydrolyzing the β-1,4 glycosidic bonds that connect the anhydroglucose monomers. Therefore, despite reducing the crystallinity of cellulose by IL pretreatment, the polymer MW is largely unaffected. Uniform polymer molecular weight distributions are preferred to produce an amorphous cellulose product that has consistent physical and chemical properties for materials or chemical conversion applications.

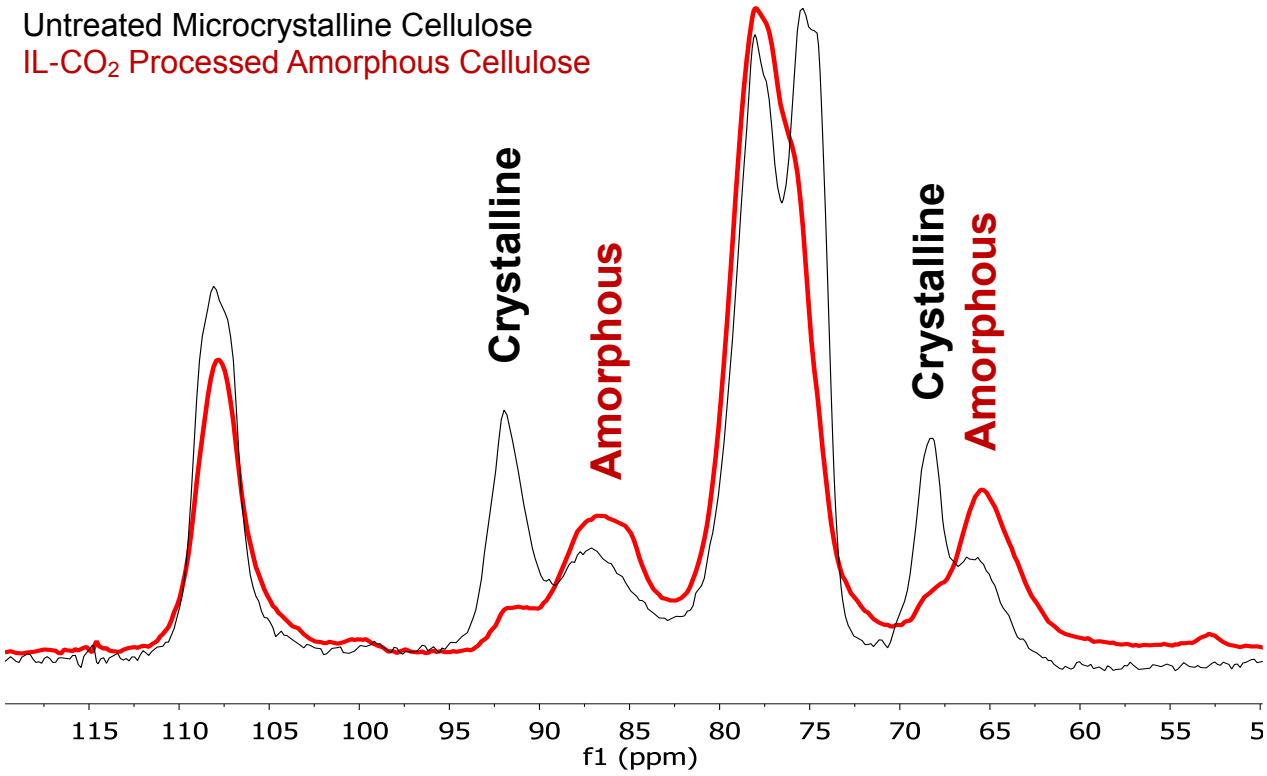

Figure 4.21: CP/MAS ^{13}C NMR on native microcrystalline cellulose (black) and processed amorphous cellulose via IL solvation and CO_2 precipitation (red).

4.6. Process Economics of CO_2 Based IL-Cellulose Separations

As detailed in section 4.2.1, cellulose antisolvent precipitation mechanisms utilizing liquid antisolvents (*e.g.* water) require energy intensive thermal separation processes (*i.e.* distillation) to purify the IL and antisolvent after recovering the solid amorphous cellulose product. Despite applying vacuum distillation at 175^{o}C and 0.01 bar, 3 mass% antisolvent still remains in the IL at an energy cost of 17 MJ/kg of cellulose processed. Thus, despite being currently economically prohibitive at these separation conditions, increasingly energy intensive separation methods are required to quantitatively separate the antisolvent from [EMIm][DEP]. Alternatively, compressed carbon dioxide based processing methods with [EMIm][DEP]-cosolvent mixtures

are completely reversible and controlled by the composition of CO_2 in the liquid phase. Therefore, the solvation power of the IL system can be regenerated by simply reducing the CO_2 pressure without requiring any thermal energy input. However, the novel CO_2 based process will require energy input in the form of CO_2 compression to regenerate the antisolvent power; for example from 1 bar to 26-54 bar at 25°C depending on the mixed IL-cosolvent system and cellulose loading.

An Aspen Plus simulation, based on the Peng Robinson Equation of State, was designed to compute the energy cost of CO_2 compression from 1 bar to 65 bar for a hypothetical gas antisolvent precipitation process. The EoS prediction indicates that this compression process would only require an estimated 1.1-1.4 MJ of mechanical energy per kg of cellulose processed (based on the same 15 mass% cellulose loading in [EMIm][DEP] as was used for the thermal separation energy analysis); thus requiring an order of magnitude less energy than the thermal distillation process with liquid antisolvents, *i.e.* ~20MJ/kg cellulose. While mechanical energy is more costly than heat, there is still significant potential energy savings for this new process.

4.7. Cellulose Recovery

The reversible nature of this compressed gas separation process indeed makes recovery of the amorphous cellulose product more complex than the liquid antisolvent systems. For instance, in order to recover a solid cellulose sample in our current experimental setup, a portion of cellulose was isolated above the IL/cosolvent liquid level and collected immediately upon depressurization before re-dissolution could occur by contact with the IL-phase. Subsequently, the sample was washed with ethanol to remove any residual IL, dried, and analyzed. Based on these initial experiments we believe the washing step could be eliminated or reduced through further

experimental design of a separation vessel capable of physically preventing contact between precipitated cellulose and the IL mixture at process pressure.

4.8. Summary

In summary, Chapter 4 demonstrates the first physical (non-reactive) and reversible precipitation of cellulosic biomass from an ionic liquid mixture using compressed carbon dioxide. High pressure NMR confirms that precipitation does not occur via chemical reaction with CO_2. Solid state NMR indicates an 80+% reduction in cellulose crystallinity. Cellulose precipitation is driven by liquid phase composition of carbon dioxide which dramatically reduces the cellulose solubility after a critical composition is obtained.

References

1. Holm, J., Lassi, U., *Ionic Liquids in the Pretreatment of Lignocellulosic Biomass*, in *Ionic Liquids: Applications and Perspectives*, P.A. Kokorin, Editor 2011, InTech.
2. Vitz, J., et al., *Extended dissolution studies of cellulose in imidazolium based ionic liquids.* Green Chemistry, 2009. **11**(3): p. 417-424.
3. Wang, H., G. Gurau, and R.D. Rogers, *Ionic liquid processing of cellulose.* Chemical Society Reviews, 2012. **41**(4): p. 1519-1537.
4. Zhao, D.S., et al., *Dissolution of cellulose in phosphate-based ionic liquids.* Carbohydrate Polymers, 2012. **87**(2): p. 1490-1494.
5. Deng, W.P., Q.H. Zhang, and Y. Wang, *Catalytic transformations of cellulose and cellulose-derived carbohydrates into organic acids.* Catalysis Today, 2014. **234**: p. 31-41.
6. Mika, L.T., E. Cséfalvay, and I.T. Horváth, *The role of water in catalytic biomass-based technologies to produce chemicals and fuels.* Catalysis Today, (0).
7. Shi, J.C., et al., *Production of 5-Hydroxymethylfurfural from Mono- and Disaccharides in the Presence of Ionic Liquids.* Catalysis Letters, 2014. **144**(2): p. 252-260.
8. Xiao, S.H., et al., *Efficient conversion of cellulose into biofuel precursor 5-hydroxymethylfurfural in dimethyl sulfoxide-ionic liquid mixtures.* Bioresource Technology, 2014. **151**: p. 361-366.
9. Yabushita, M., H. Kobayashi, and A. Fukuoka, *Catalytic transformation of cellulose into platform chemicals.* Applied Catalysis B-Environmental, 2014. **145**: p. 1-9.
10. Zakrzewska, M.E., E. Bogel-Lukasik, and R. Bogel-Lukasik, *Ionic Liquid-Mediated Formation of 5-Hydroxymethylfurfural-A Promising Biomass-Derived Building Block.* Chemical Reviews, 2011. **111**(2): p. 397-417.
11. Zhou, L.L., et al., *One-step degradation of cellulose to 5-hydroxymethylfurfural in ionic liquid under mild conditions.* Carbohydrate Polymers, 2015. **117**: p. 694-700.
12. Zhu, Y.H., et al., *Conversion of Cellulose to Hexitols Catalyzed by Ionic Liquid-Stabilized Ruthenium Nanoparticles and a Reversible Binding Agent.* Chemsuschem, 2010. **3**(1): p. 67-70.
13. Mondal, I.H., *Cellulose and Cellulose Derivatives: Synthesis, Modification and Applications*. 2015: Nova Science Publishers, Incorporated.
14. Li, C.L., et al., *Comparison of dilute acid and ionic liquid pretreatment of switchgrass: Biomass recalcitrance, delignification and enzymatic saccharification.* Bioresource Technology, 2010. **101**(13): p. 4900-4906.
15. Uppugundla, N., et al., *A comparative study of ethanol production using dilute acid, ionic liquid and AFEX (TM) pretreated corn stover.* Biotechnology for Biofuels, 2014. **7**.
16. Sen, S.M., et al., *Conversion of biomass to sugars via ionic liquid hydrolysis: process synthesis and economic evaluation.* Biofuels Bioproducts & Biorefining-Biofpr, 2012. **6**(4): p. 444-452.
17. King, C.J., *Separation processes*. 2d ed. McGraw-Hill chemical engineering series. 1980, New York: McGraw-Hill. xxvi, 850 p.
18. Maga, J.A., *An Overview of the Thermal-Decomposition of Carbohydrates.* Abstracts of Papers of the American Chemical Society, 1988. **196**: p. 37-Agfd.

19. Cheng, F., et al., *Facile pulping of lignocellulosic biomass using choline acetate.* Bioresource Technology, 2014. **164**: p. 394-401.
20. Dibble, D.C., et al., *A facile method for the recovery of ionic liquid and lignin from biomass pretreatment.* Green Chemistry, 2011. **13**(11): p. 3255-3264.
21. Laine, C., et al., *Simultaneous bench scale production of dissolving grade pulp and valuable hemicelluloses from softwood kraft pulp by ionic liquid extraction.* Carbohydrate Polymers, 2016. **136**: p. 402-408.
22. Suzuki, T., et al., *Preparation of cellulose particles using an ionic liquid.* Journal of Colloid and Interface Science, 2014. **418**: p. 126-131.
23. Voon, L.K., S.C. Pang, and S.F. Chin, *Highly porous cellulose beads of controllable sizes derived from regenerated cellulose of printed paper wastes.* Materials Letters, 2016. **164**: p. 264-266.
24. Wang, X.J., et al., *Cellulose extraction from wood chip in an ionic liquid 1-allyl-3-methylimidazolium chloride (AmimCl).* Bioresource Technology, 2011. **102**(17): p. 7959-7965.
25. Minnick, D.L. and A.M. Scurto, *Reversible and non-reactive cellulose separations from ionic liquid mixtures with compressed carbon dioxide.* Chemical Communications, 2015. **51**(63): p. 12649-12652.
26. Castro, M.C., et al., *Mixtures of Ethanol and the Ionic Liquid 1-Ethyl-3-methylimidazolium Acetate for the Fractionated Solubility of Biopolymers of Lignocellulosic Biomass.* Industrial & Engineering Chemistry Research, 2014. **53**(29): p. 11850-11861.
27. Gupta, K.M., Z.Q. Hu, and J.W. Jiang, *Molecular insight into cellulose regeneration from a cellulose/ionic liquid mixture: effects of water concentration and temperature.* Rsc Advances, 2013. **3**(13): p. 4425-4433.
28. Nakamura, A., et al., *Recovery of cellulose and xylan liquefied in ionic liquids by precipitation in anti-solvents.* Holzforschung, 2010. **64**(1): p. 77-79.
29. Shi, J., et al., *Understanding the role of water during ionic liquid pretreatment of lignocellulose: co-solvent or anti-solvent?* Green Chemistry, 2014. **16**(8): p. 3830-3840.
30. Minnick, D.L., Scurto, A.M., *Cellulose Solubility in Ionic Liquids: Cosolvent and Antisolvent Effects.* Manuscript In Preparation, 2015.
31. Hauru, L.K.J., et al., *Role of Solvent Parameters in the Regeneration of Cellulose from Ionic Liquid Solutions.* Biomacromolecules, 2012. **13**(9): p. 2896-2905.
32. Minnick, D.L., Scurto, A.M., *Solvent Effects on the Dissolution and Precipitation of Cellulose from Ionic Liquids.* Journal of Physical Chemistry B, 2016.
33. Minnick, D.L., McDonough, R., Scurto, A.M., *Solubility of Carbon Dioxide in Mixed Ionic Liquid + Co-Solvent Systems.* Manuscript in Preparation, 2015.
34. Peng, Y. and X.Y. Lu, *Isobaric Vapor-Liquid Equilibria for Water plus Acetic Acid + 1-Ethyl-3-methylimidazolium Diethylphosphate at 101.32 kPa.* Journal of Chemical and Engineering Data, 2014. **59**(2): p. 250-256.
35. Gary, J.H. and G.E. Handwerk, *Petroleum Refining*. 2001: Taylor & Francis.
36. Jobson, M., *Chapter 6 - Energy Considerations in Distillation A2 - Górak, Andrzej*, in *Distillation*, E. Sorensen, Editor. 2014, Academic Press: Boston. p. 225-270.

37. Goldberg, R.N., et al., *A thermodynamic investigation of the cellulose allomorphs: Cellulose(am), cellulose I beta(cr), cellulose II(cr), and cellulose III(cr).* Journal of Chemical Thermodynamics, 2015. **81**: p. 184-226.
38. Nwosu, S.O. and University of Kansas., *Environmentally Benign Production of Ionic Liquids in CO2-Expanded Systems*. p. 337 p.
39. Poliakoff, M., et al., *Green chemistry: Science and politics of change.* Science, 2002. **297**(5582): p. 807-810.
40. Wu, W.Z., et al., *A green and effective method to synthesize ionic liquids: supercritical CO2 route.* Green Chemistry, 2005. **7**(10): p. 701-704.
41. Ahosseini, A., et al., *Phase Equilibrium, Volumetric, and Interfacial Properties of the Ionic Liquid, 1-Hexyl-3-methylimidazolium Bis(trifluoromethylsulfonyl)amide and 1-Octene.* Journal of Chemical and Engineering Data, 2010. **55**(4): p. 1611-1617.
42. Lei, Z.G., C.N. Dai, and B.H. Chen, *Gas Solubility in Ionic Liquids.* Chemical Reviews, 2014. **114**(2): p. 1289-1326.
43. Fang, S., et al., *High-pressure phase behavior of CO2+1-butyl-3-methylimidazolium chloride system.* Fluid Phase Equilibria, 2010. **299**(2): p. 216-221.
44. Mejia, I., et al., *On the High-Pressure Solubilities of Carbon Dioxide in Several Ionic Liquids.* Journal of Chemical and Engineering Data, 2013. **58**(9): p. 2642-2653.
45. Ramdin, M., et al., *Solubility of CO2/CH4 gas mixtures in ionic liquids.* Fluid Phase Equilibria, 2014. **375**: p. 134-142.
46. Ahosseini, A., L.R. Weatherley, and A.M. Scurto, *Viscosity and Diffusivity for the Ionic Liquid 1-Hexyl-3-methylimidazolium Bis(trifluoromethylsulfonyl)amide with 1-Octene.* Journal of Chemical and Engineering Data, 2011. **56**(10): p. 3715-3721.
47. Ahosseini, A., et al., *Viscosity of n-alkyl-3-methyl-imidazolium bis(trifluoromethylsulfonyl)amide ionic liquids saturated with compressed CO2.* Fluid Phase Equilibria, 2009. **286**(1): p. 62-68.
48. Ahosseini, A. and A.M. Scurto, *Viscosity of imidazolium-based ionic liquids at elevated pressures: Cation and anion effects.* International Journal of Thermophysics, 2008. **29**(4): p. 1222-1243.
49. Barber, P.S., et al., *Coagulation of Chitin and Cellulose from 1-Ethyl-3-methylimidazolium Acetate Ionic-Liquid Solutions Using Carbon Dioxide.* Angewandte Chemie-International Edition, 2013. **52**(47): p. 12350-12353.
50. Sun, X.F., Y.L. Chi, and T.C. Mu, *Studies on staged precipitation of cellulose from an ionic liquid by compressed carbon dioxide.* Green Chemistry, 2014. **16**(5): p. 2736-2744.
51. Besnard, M., et al., *CO2 in 1-Butyl-3-methylimidazolium Acetate. 2. NMR Investigation of Chemical Reactions.* Journal of Physical Chemistry A, 2012. **116**(20): p. 4890-4901.
52. Denning, D.M. and D.E. Falvey, *Solvent-Dependent Decarboxylation of 1,3-Dimethylimdazolium-2-Carboxylate.* Journal of Organic Chemistry, 2014. **79**(10): p. 4293-4299.
53. Normazlan, W.M.D.W., et al., *Composition and Temperature Dependence of Density, Surface Tension, and Viscosity of EMIM DEP/MMIM DMP + Water+1-Propano1/2-Propanol Ternary Mixtures and Their Mathematical Representation Using the Jouyban Acree Model.* Journal of Chemical and Engineering Data, 2014. **59**(8): p. 2337-2348.

54. Ramdin, M., et al., *Solubility of CO2 and CH4 in Ionic Liquids: Ideal CO2/CH4 Selectivity.* Industrial & Engineering Chemistry Research, 2014. **53**(40): p. 15427-15435.
55. Shokouhi, M., H. Farahani, and M. Hosseini-Jenab, *Experimental solubility of hydrogen sulfide and carbon dioxide in dimethylformamide and dimethylsulfoxide.* Fluid Phase Equilibria, 2014. **367**: p. 29-37.
56. Ahosseini, A., et al., *Viscosity of n-alkyl-3-methyl-imidazolium bis(trifluoromethylsulfonyl)amide ionic liquids saturated with compressed CO2.* Fluid Phase Equilibria, 2009. **286**(1): p. 72-78.
57. Lu, Y., et al., *Dissolution and Regeneration of Cellulose and Development in Processing Cellulose-Based Materials with Ionic Liquids.* Chinese Journal of Organic Chemistry, 2010. **30**(10): p. 1593-1602.
58. Gupta, K.M. and J. Jiang, *Cellulose dissolution and regeneration in ionic liquids: A computational perspective.* Chemical Engineering Science, 2015. **121**(0): p. 180-189.
59. Bhargava, B.L. and S. Balasubramanian, *Probing anion-carbon dioxide interactions in room temperature ionic liquids: Gas phase cluster calculations.* Chemical Physics Letters, 2007. **444**(4-6): p. 242-246.
60. Indarto, A. and J. Palgunadi, *Prediction of binding bond energy between phosphorous-based ionic liquids and CO2. Assessment of the CO2-anion interactions.* Ionics, 2012. **18**(1-2): p. 143-150.
61. Fredlake, C.P., et al., *Solvent strength of ionic liquid/CO2 mixtures.* Physical Chemistry Chemical Physics, 2004. **6**(13): p. 3280-3285.
62. Blanchard, L.A., Z.Y. Gu, and J.F. Brennecke, *High-pressure phase behavior of ionic liquid/CO2 systems.* Journal of Physical Chemistry B, 2001. **105**(12): p. 2437-2444.
63. Denardin, F.G., Vieira de Melo, S.A.B., Mammucari, R., and Foster, N.R., *Phase Transition and Volume Expansion in CO2-Expanded Liquid Systems.* Chemical Engineering Transactions, 2013. **32**: p. 529-534.
64. Marr, R. and T. Gamse, *Use of supercritical fluids for different processes including new developments - a review.* Chemical Engineering and Processing, 2000. **39**(1): p. 19-28.
65. Kim, S.H., C.M. Lee, and K. Kafle, *Characterization of crystalline cellulose in biomass: Basic principles, applications, and limitations of XRD, NMR, IR, Raman, and SFG.* Korean Journal of Chemical Engineering, 2013. **30**(12): p. 2127-2141.
66. Park, S., et al., *Cellulose crystallinity index: measurement techniques and their impact on interpreting cellulase performance.* Biotechnology for Biofuels, 2010. **3**.
67. Zhao, H.B., et al., *Studying cellulose fiber structure by SEM, XRD, NMR and acid hydrolysis.* Carbohydrate Polymers, 2007. **68**(2): p. 235-241.
68. Park, S., et al., *Measuring the crystallinity index of cellulose by solid state C-13 nuclear magnetic resonance.* Cellulose, 2009. **16**(4): p. 641-647.

5. Chemical Conversion of Cellulosic Biomass in Ionic Liquids

5.1. Introduction

Conversion of biomass to chemicals and fuels will be vital to meet the long term global energy demand as fossil resources are depleted. Significant research and development was directed towards biofuels in the early 2000's with the emphasis on first generation feedstocks such as corn and sugarcane. Through fermentation, sugars are converted into bioethanol for applications in blended transportation fuels. While the chemical conversion process to produce first generation biofuels is straightforward; use of these agricultural resources has been criticized for several reasons. First, corn and sugarcane are used for food applications. Therefore, diversion of these resources to produce fuel has been shown to decrease the food supply and concomitantly increase the price of agricultural resources.[1] Furthermore, fermentation processes produce dilute aqueous feeds of alcohol in water making purification of the end product highly energy intensive.[2] Finally, the energy balance of the chemical conversion process is less than ideal, producing only 1.3 units of energy for every unit input.[3] For these reasons, research on second generation lignocellulosic biofuels, sourced from agricultural waste products (*i.e.* corn stover, switch grass, sugarcane bagasse, *etc.*), are currently being considered for the production of renewable fuels and chemicals.

Lignocellulosic biomass is renewable, diverse, inexpensive, and non-food vs. fuel competitive. For these reasons it is highly touted as a sustainable carbon source for the production of bio-fuels and bio-chemicals. Lignocellulose is comprised of three primary components: cellulose (30-50 wt.%), hemicellulose (20-35 wt.%) and lignin (18-35 wt.%).[4] Unfortunately recalcitrance of lignocellulosic biomass is problematic as cellulose and hemicellulose are insoluble in most

aqueous and organic solvents creating complex heterogeneous reaction scenarios. Alternatively, ionic liquids (ILs) demonstrate relatively large dissolution capacities of these carbohydrates indicating their competitive advantage as solvents for the chemical conversion of biomass.

Complete utilization of all three biomass components is ideal but not currently feasible due to the complex structure of lignin. However, mature conversion technologies exist for cellulose and hemicellulose which comprise up to 85% of biomass by weight. Select ionic liquids demonstrate significant solubilities of cellulose and hemicellulose while maintaining comparatively low solubilities of lignin making them ideal solvents for biomass conversion.[5-7] Once dissolved in ILs, cellulose and hemicellulose can be transformed into a range of products. For instance, significant research has been dedicated to the production of 5-hydroxymethylfurfural (5-HMF) from cellulose [8-15] and furfural from hemicellulose.[16-21] Despite the success of producing these platform chemicals with high conversion and selectivity, product separation from ionic liquids is problematic as polar molecules are highly miscible with ILs. Recommended separation procedures consist of energy intensive distillation and steam stripping processes for product recovery and IL recycle. Therefore, creating products which are separable via a bi-phasic process at reaction temperatures without extraction solvents or distillation would be superior to products that are widely miscible with the ionic liquid reaction phase.

Figure 5.1 demonstrates select value-added products that can be produced from cellulosic biomass. Efficient chemical conversion processes must hydrolyze the bio-polymers to produce their constituent sugars after which functionalization can occur using a range of chemistries including: dehydration, oxidation, hydrogenation, *etc*. to produce products.

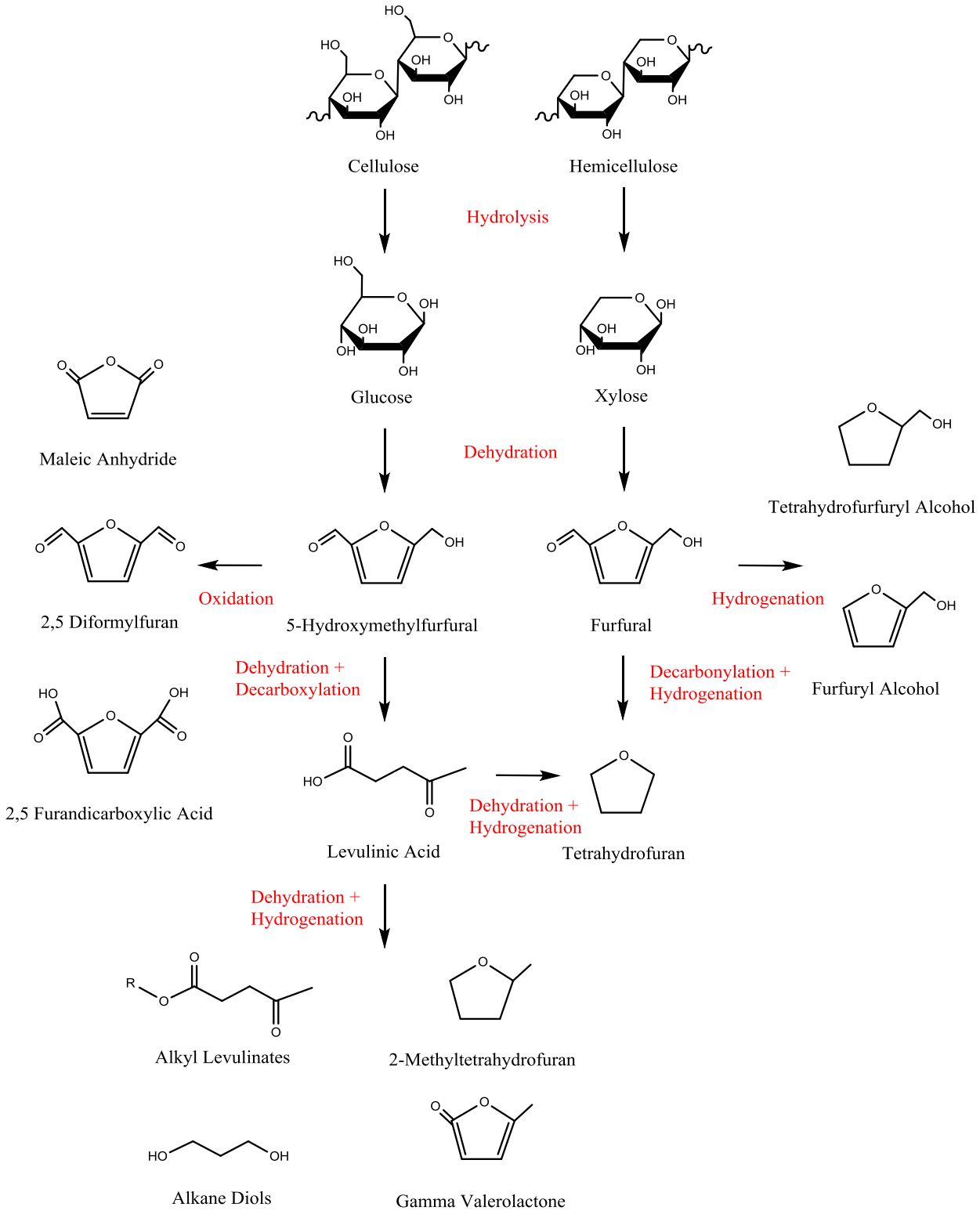

Figure 5.1: Chemical conversion of cellulose and hemicellulose to value added chemicals. Adapted from [22].

5.2. Overview

The current status of research on cellulosic biomass conversion in ionic liquids is reviewed in this chapter with a specific focus on the production of 5-hydroxymethylfurfural. While ionic liquids are ideal for cellulosic biomass dissolution, chemical conversion of biomass in ILs is comparatively slow relative to organic solvents due to the elevated viscosities of pure ILs. Additionally, 5-HMF degrades to form humins in ILs and aqueous solvents at reaction temperatures. Alternatively, polar aprotic solvents have been shown to stabilize 5-HMF and reduce the formation of degradation products. To understand how aprotic solvents affect the production and stability of 5-HMF, mixed [EMIm][DEP]-DMSO systems were experimentally investigated using a model compound (*i.e.* fructose). Results on the chemical conversion of fructose to 5-HMF at 100^{o}C using hydrochloric acid are presented to analyze the cosolvent effects on the reaction process. Finally, the chapter is concluded by presenting a new pathway to produce and separate low-polarity furan platform chemicals (*i.e.* 2,5-dimethylfuran) from 5-HMF. Preliminary results demonstrate the potential success of this reaction pathway.

5.3. Conversion of Fructose to 5-HMF in Mixed Ionic Liquid Cosolvent Systems

Direct production of 5-hyroxymethylfurfural (5-HMF) and furfural from cellulose and hemicellulose respectively is one of the most researched areas of lignocellulosic biomass conversion.[8, 11-14, 23-25] Motivation for making these two products is primarily attributed to the ability of a catalytic mechanism to simultaneously perform several chemical conversion steps in a one-pot system. In the case of 5-HMF production, as shown in Figure 5.2, a combination of mineral and Lewis acids are capable of hydrolyzing cellulose to glucose, isomerizing glucose to fructose, and dehydrating fructose to 5-HMF with moderate selectivity.[10]

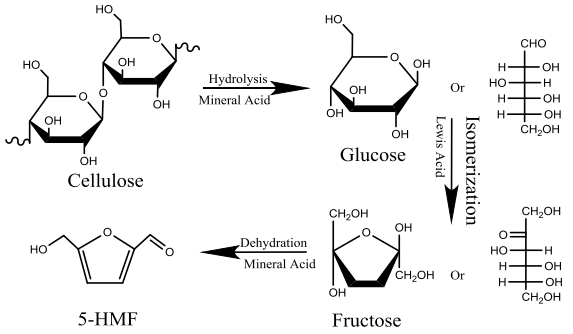

Figure 5.2: Reaction mechanism for the conversion of cellulose to 5-HMF.

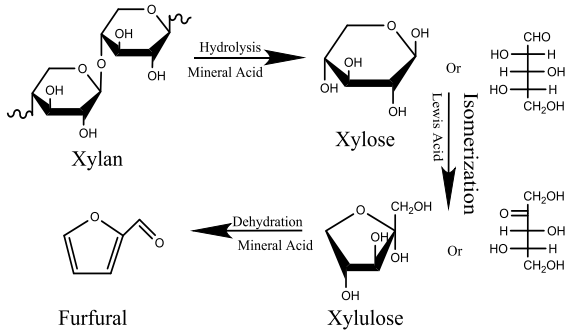

Figure 5.3: Reaction mechanism for the conversion of xylan to furfural.

Attempts at the concomitant production of 5-HMF and furfural from lignocellulose have been conducted but demonstrate lower selectivity and conversion compared to reacting pure cellulose and hemicellulose feedstocks separately.[13] Nonetheless, initial studies with ionic liquid solvents show an opportunity for improvement and continued research is expected to demonstrate advances in this area.[26]

Select literature results for the conversion of biomass derived compounds to 5-HMF are displayed in Table 5.1. The results indicate that 5-HMF can be produced in ILs with moderate yields dependent on the biomass source, catalyst used, reaction temperature, and reaction time.

Starting Material	Solvent	Catalyst	5-HMF Yield (mass%)	Conditions (^{o}C / hours)	Source
Cellulose	[BMIm][Cl]	$HCl/CrCl_3$	30	140 / 0.6 [A]	[27]
	[EMIm][Cl]	$CrCl_2/CuCl_2$	57	120 / 8	[28]
	[BMIm][Cl]/DMSO	$HCl/AlCl_3$	55	150 / 9	[11]
Glucose	[BMIm][Cl]	$CrCl_3$	65	120 / 1	[29]
	[BMIm][Cl]	$CrCl_3$	91	100 / 4	[30]
	[BMIm][Cl]	$CrCl_3$	50	90 / 5	[31]
Fructose	[BMIm][Cl]	$CrCl_3$	16	120 / 0.5	[30]
	[BMIm][Cl]	$CuCl_2$	80	80 / 0.16	[32]
	[BMIm][Cl]	H_2SO_4	70	80 / 0.16	[32]
	[BMIm][Cl]	HCl	3	80 / 0.16	[32]

Table 5.1: Chemical conversion of biomass derived compounds into 5-HMF in ionic liquids.

To this point, the majority of biomass conversion research with ionic liquids has focused on [BMIm][Cl]. While effective at dissolving cellulosic biomass [BMIm][Cl] is prohibitively viscous, even at elevated temperatures, which negatively impacts chemical reactions in this solvent especially in regards to mass transfer. Therefore, this study investigated the conversion of fructose to 5-HMF in [EMIm][DEP], a comparatively lower viscosity IL with superior biomass dissolution capacity. Furthermore, the reaction is investigated in mixtures of this ionic liquid with polar aprotic cosolvent DMSO. Preliminary results demonstrate that DMSO is beneficial for reactions producing 5-HMF as it reduces the activation energy barrier and stabilizes the end product thus preventing the formation of degradation products and humins.[33]

5.3.1. Reaction Parameter Selection

As shown in Table 5.1 a range of mineral acid, Lewis acid, and ion exchange resin catalysts are applicable for fructose dehydration. Lewis acid catalysts including chromium (III) chloride exhibit some of the best 5-HMF yields in [BMIm][Cl]. However, hexavalent chromium is known to cause severe health and environmental hazards and should therefore be avoided.[34] In this study, hydrochloric acid (HCl) was selected as the dehydration catalyst despite previous reports showing low fructose conversion and 5-HMF yield. A constant HCl loading of 5 mass% (total solution basis) was applied to all trials to eliminate the effect of catalyst loading on the results. Previous studies have shown that the reaction temperature can also accelerate the rate of 5-HMF formation but concomitantly accelerates the rate of 5-HMF degradation to form humins.[14] Reaction temperatures between 70^{o}C and 120^{o}C are conventionally employed in biomass conversion reactions and therefore, the temperature in this study was fixed at 100^{o}C to avoid any deviations due to thermal effects.[14] Finally, while reactant concentration has been

shown to be relatively independent of reaction performance, a constant initial fructose concentration of 10 mass% (total solution basis) was applied to all systems to eliminate any potential changes due to reactant loading.[32]

5.3.2. Fructose to 5-HMF Reaction Results

Chemical conversion of fructose to 5-HMF was performed in [EMIm][DEP]-DMSO mixtures at 100^{o}C with HCl as the catalyst. As shown in Figure 5.4, the DMSO composition within the sample had a significant impact on the reaction rate. For instance, 100% conversion of fructose was reached in approximately two minutes for the pure DMSO solvent system. Alternatively, the pure [EMIm][DEP] solvent system reached only 80% conversion after 1200 minutes (*i.e.* 20 hours). Extended time scales could be applied to allow the pure IL sample to reach 100% conversion but were beyond a practical limit for this study. Mixed [EMIm][DEP]-DMSO solvent systems were also explored at intermediate compositions. The results indicated that increased DMSO content in the mixture accelerated the rate of fructose conversion. Reaction samples were vigorously mixed by magnetic stir bars within sealed 1.5 mL glass vials and therefore bulk mass transfer effects are not believed to be a limiting factor in the reaction. Alternatively, the accelerated reaction rates at high DMSO loadings could theoretically be due to reduction of the solution viscosity or lowering of the activation energy barrier for fructose dehydration. For instance, a NMR study conducted by Amarasekara *et al.* found that the lone pair electrons on the oxygen atoms of DMSO molecules actively participate in the dehydration mechanism by abstracting hydrogen atoms from fructose thus promoting the reaction.[35]

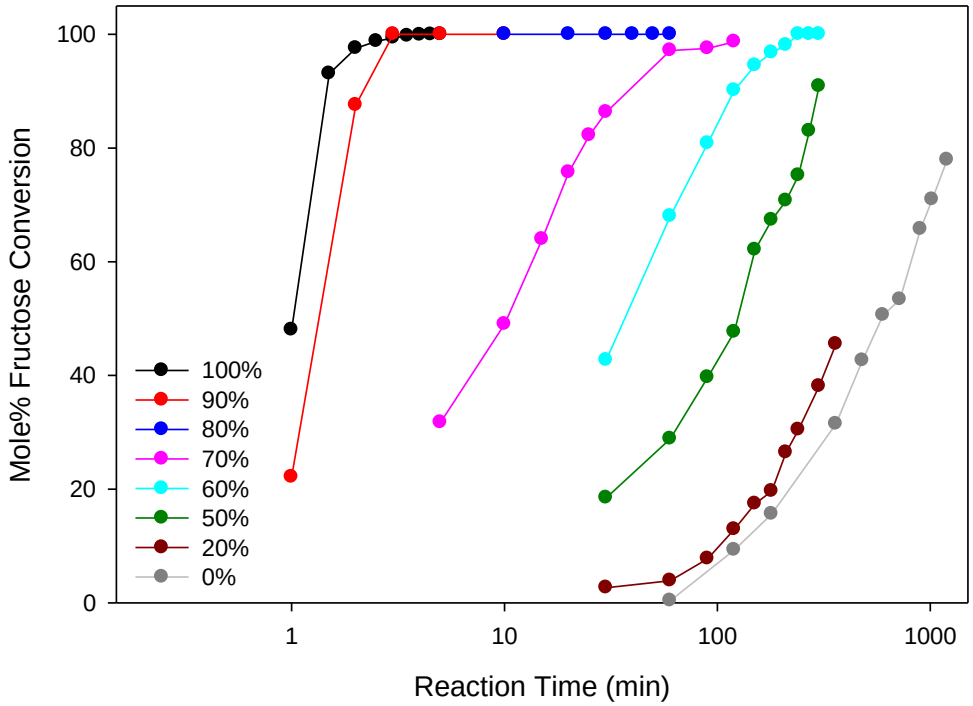

Figure 5.4: Fructose conversion vs. time as a function of DMSO composition (see legend) in the mixed [EMIm][DEP]-cosolvent systems.

Previously cited literature reports indicate that chemical conversion of fructose to 5-HMF proceeds by a first order reaction mechanism which is expressed in terms of conversion in Eqn. 5.1.[32, 36-38]

$$\ln(1 - X) = -kt \qquad \text{Eqn. 5.1}$$

Therefore, the reaction rate was analyzed as a function of DMSO composition (*ceteris paribus*) by generating a plot of *ln(1-X)* vs. *time*, where *X* represents molar fructose conversion. The linear regression is shown in Figure 5.5 where the slope represents the reaction rate in (min^{-1}).

Based on the results presented it is evident that DMSO composition has a pronounced effect on the rate of fructose dehydration.

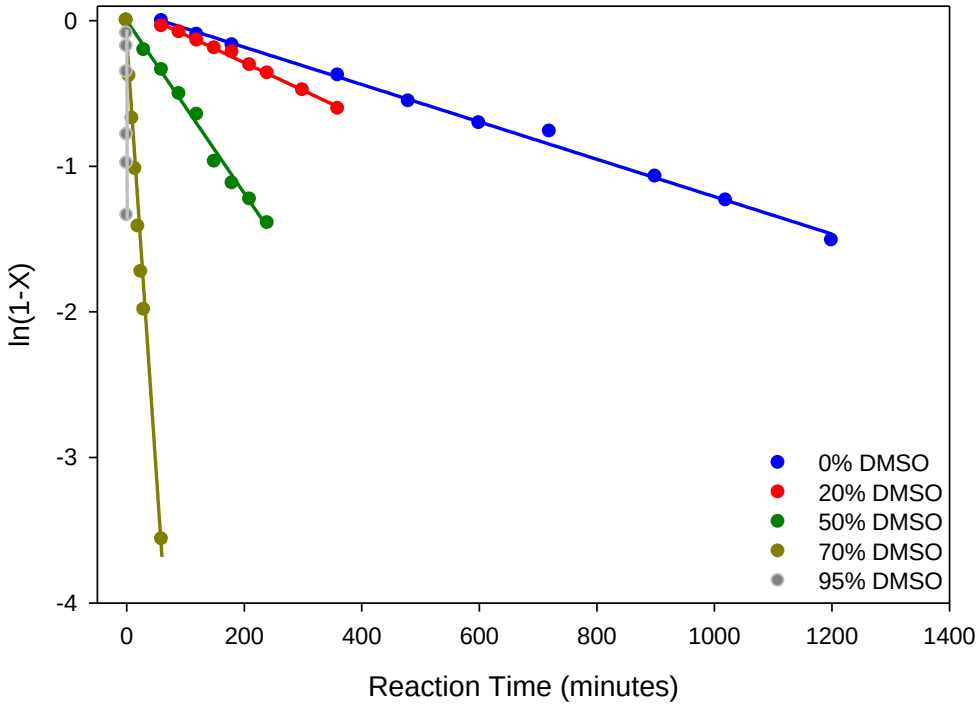

Figure 5.5: Determination of the first order reaction rate constants for the dehydration of fructose in [EMIm][DEP]-DMSO mixtures.

For a first order reaction, kinetic rate constants are determined by the slope of the conversion vs. time plot as shown in Figure 5.5. Table 5.2 displays the reaction rate constants for the various IL-DMSO solvent systems. Importantly, solvent composition was the only parameter probed in this study, thus all other variables were held constant. The results indicate that the reaction rate changes by three orders of magnitude dependent on DMSO composition in the sample.

DMSO Loading (mass% binary relative to IL)	Reaction Rate (min^{-1})
0% DMSO	$1.28 * 10^{-3}$
20% DMSO	$1.90 * 10^{-3}$
50% DMSO	$5.93 * 10^{-3}$
70% DMSO	$5.94 * 10^{-2}$
95% DMSO	$2.24 * 10^{0}$

Table 5.2: Fructose dehydration reaction rate as a function of cosolvent (DMSO) composition.

Figure 5.6 displays a bar graph of the maximum measured cellulose conversion for each binary IL-DMSO mixture with the yield of 5-HMF for each system overlaid (see blue data points). Complete conversion of fructose was observed in IL-cosolvent mixtures with DMSO loadings between 100 mass% and 60 mass%. For instance, solvent systems with DMSO loadings greater than 60 mass% demonstrated 5-HMF yields between 66 and 75 percent which meet or exceed the standards established in current literature reports. Alternatively, ionic liquid compositions greater than 40 mass% resulted in significant decreases in both the conversion of fructose and yield of 5-HMF despite extended reaction times in excess of 20 hours.

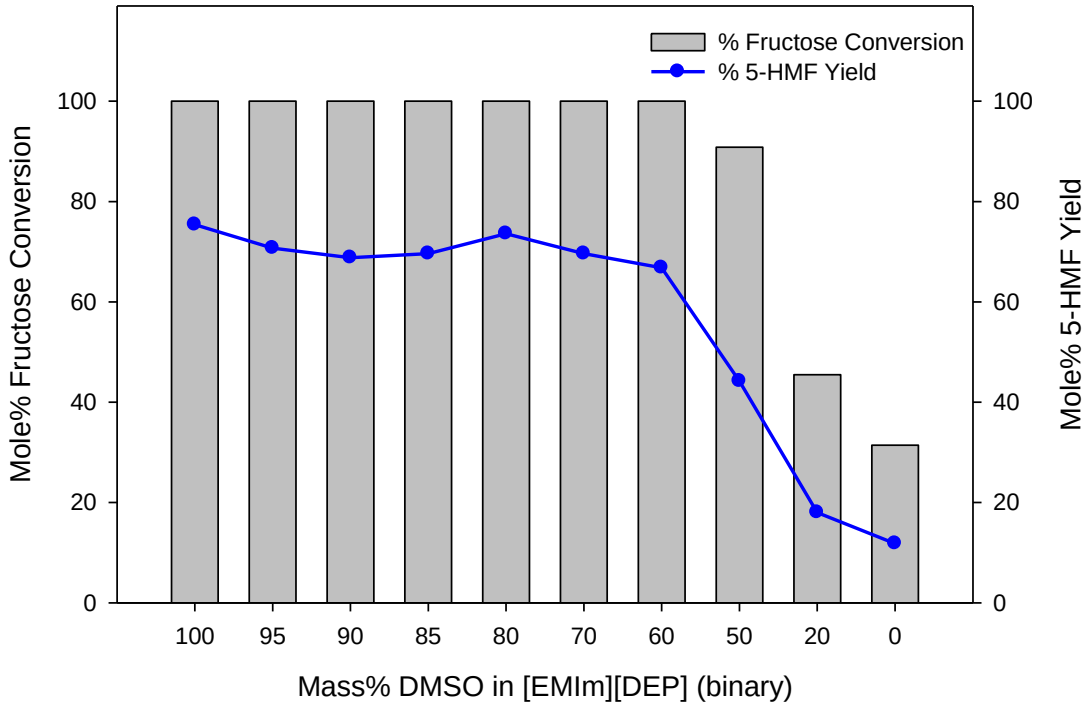

Figure 5.6: Effect of DMSO composition in mixed [EMIm][DEP] cosolvent systems on the conversion of fructose and yield of 5-HMF at 100^{o}C.

For instance, the pure [EMIm][DEP] and 20 mass% DMSO systems demonstrated fructose conversions of 45.5 and 31.5 percent respectively after 20 hours at 100^{o}C. Furthermore, the 5-HMF yield for these two systems were 18 and 11 percent indicating that the reaction is significantly inhibited by elevated concentrations of [EMIm][DEP]. Importantly, at a cosolvent loading of 60 mass% DMSO the system demonstrated 100% conversion and 67% 5-HMF yield after only 4 hours. As shown in Chapter 3, mixed IL: cosolvent systems also demonstrated enhanced cellulose dissolution when approximately 50 mass% DMSO was mixed with [EMIm][DEP]. Therefore, similar intermediate IL-cosolvent composition mixtures that enhanced cellulose solubility are applicable to the chemical conversion of biomass to 5-HMF.

While this study demonstrates preliminary results for one IL-cosolvent system with a single catalyst and temperature, it shows promise for future experiments investigating the chemical conversion of biomass in mixed solvent systems. Future work to extend the preliminary results demonstrated herein should include expanding the study to explore additional catalysts and temperatures as well as moving to a raw biomass feedstock (*i.e.* cellulose) as opposed to working with model compounds. These objectives are further outlined in section 9.2.2.

5.4. Limitations of Producing 5-HMF in Ionic Liquids

Furfural and 5-HMF are highly polar molecules that are completely miscible with ILs. Therefore, production of these molecules in an ionic liquid is limited by the energy intensive extraction process required for product recovery. Current commercial production of furfural requires steam stripping to separate the product and aqueous reaction mixture. The extraction produces a dilute 1-6 mass% furfural stream in water which then must be subsequently separated by distillation.[39] Similarly, lab-scale 5-HMF production requires an immiscible organic extraction phase to selectively remove products from the reaction mixture. Distillation is then applied to recover 5-HMF and recycle the solvent. Since both 5-HMF and furfural are moderately polar molecules, separating these components from an ionic liquid is particularly problematic. Experiments targeting the conversion of fructose to 5-HMF in ionic liquids demonstrate that mass based solvent: IL ratios of 64:1 and 53:1 are required to extract the product from [BMIm][Cl] with tetrahydrofuran and ethyl acetate respectively.[40] Initial research indicated that immediate separation of 5-HMF and furfural was required to prevent product degradation and humins formation. However, recent studies have shown that polar aprotic cosolvents, in combination with ILs, are capable of stabilizing furfural and 5-HMF thus

enhancing reaction selectivity.[11, 41] As shown in Figure 5.7, we have experimentally studied the stability of 5-HMF in the ionic liquid [EMIm][DEP] with a range of cosolvent (DMSO) loadings at a constant temperature of 100^{o}C. The results indicate that the polar aprotic solvent, when mixed with the IL, stabilizes 5-HMF. For instance, after 150 minutes at 100^{o}C, approximately 87% of the initially loaded 5-HMF in pure [EMIm][DEP] had degraded. Alternatively, the pure DMSO sample exhibited only 16% 5-HMF degradation over the same time span. Intermediate cosolvent loadings demonstrated varying degrees of enhanced product (*i.e.* 5-HMF) stability. Therefore, based on this improvement, furfural and 5-HMF can remain in the ionic liquid reaction phase for subsequent controlled chemical conversion to furan products by hydrogenation. Since non-polar molecules have limited miscibility with biomass dissolving ILs, chemistries which reduce the polarity of 5-HMF and furfural should be targeted to make products which are separable by less energy intensive processes.

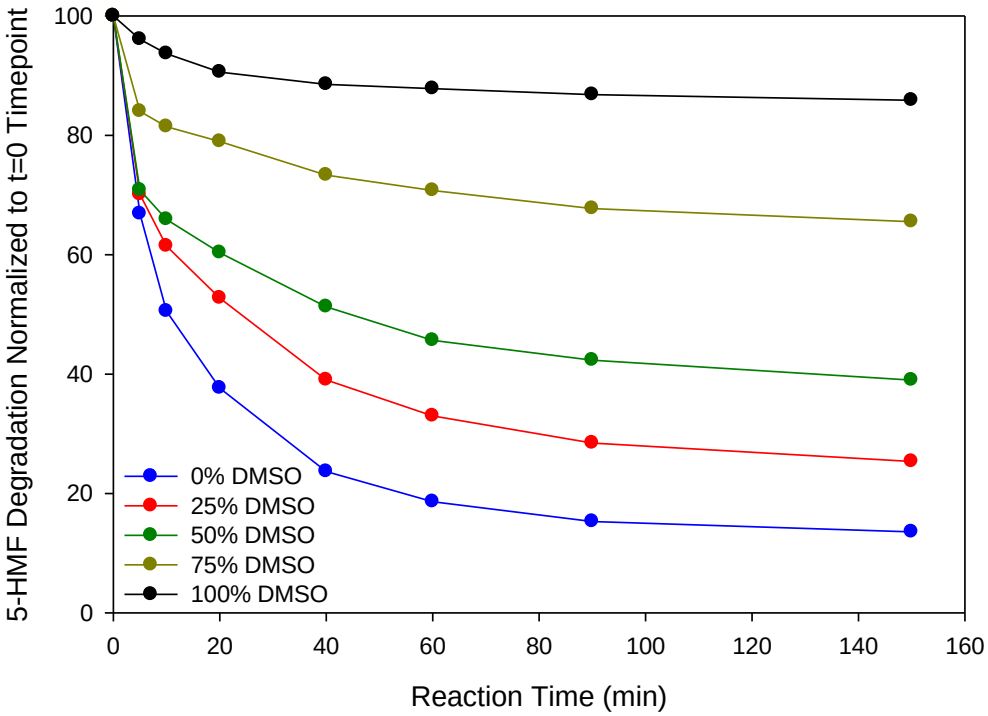

Figure 5.7: 5-HMF degradation as a function of time. All samples were normalized to the initial 5-HMF concentration in the sample at the initial t=0 time point.

5.5. Hydrogenation of 5-HMF and Furfural

The overarching goal of this section is to present preliminary results demonstrating the feasibility of transforming platform chemicals from biomass that are highly soluble in ILs into less polar value-added products that exhibit low miscibility with the IL reaction phase and spontaneously separate. The work presented herein investigates hydrogenation reactions 5-HMF and furfural which have been produced in ILs with high selectivity. Transformation of these molecules yields furan products that are applicable as "drop-in" fuel replacements, precursors for polymer production, and industrial solvents. For instance, 2,5-dimethylfuran has 40% greater energy density than ethanol, has a higher octane number than gasoline, and can be used as a feedstock

for the production of p-xylene.[42] Therefore, creating value-added furan products which are separable via a bi-phasic process at reaction temperatures without extraction solvents or distillation is superior to products that are widely miscible with the IL reaction phase.

5.5.1. Production of Furan Products by Hydrogenation of 5-HMF and Furfural

5-Hydroxymethylfurfural and furfural are highly oxygenated molecules that contain two carbon-carbon (C=C) double bonds and one carbon-oxygen (C=O) double bond. Transformation of these molecules occurs by catalytic hydrogenation to furans. Heterogeneous hydrogenation reactions proceed on the surface of supported metal catalysts where activated hydrogen attacks a double bonded functional group of the adsorbed substrate. While most hydrogenation reactions demonstrate high levels of conversion, product selectivity is problematic. This is especially true for molecules with multiple degrees of unsaturation since atoms bound to the catalyst surface are more likely to react and substrate adsorption heavily determines product selectivity. Proper catalyst selection is one way to overcome selectivity issues. For example, ruthenium, platinum, and palladium catalysts have high affinities for adsorbing C=C bonds while copper catalysts preferentially adsorb C=O functional groups as shown in Figure 5.8.[43, 44] Interestingly, furfural and 5-HMF have planar geometry which orients all three double bonded functional groups in the same plane. This allows Pt and Pd catalysts to simultaneously adsorb both C=C and C=O functional groups of furfural and 5-HMF as shown in Figure 5.9. Correspondingly, these catalysts favor the production of 2,5-dimethyltetrahydrofuran (2,5-DMTHF) and 2-methyltetrahydrofuran (2-MTHF) whereas copper

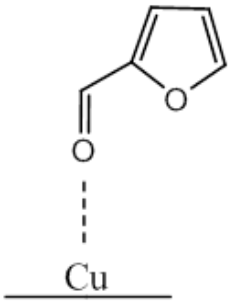

Figure 5.8: Furfural adsorption on copper.

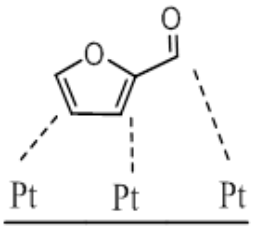

Figure 5.9: Furfural adsorption on platinum.

catalysts selectively produce 2,5-dimethylfuran (2,5-DMF) and 2-methylfuran from 5-HMF and furfural respectively.[45] Table 5.3 and Table 5.4 display a range of products formed by the hydrogenation of 5-HMF and furfural respectively with select catalysts including platinum, ruthenium, and palladium in aqueous, organic, and ionic liquid solvents.

Solvent	**Catalyst**	**Temp**	**P_{H2}/P_{CO2}**	**Conversion**	**Selectivity (%)**			
		(^oC)	(bar)	(%)	MF	DHMF	MFA	DMF
H_2O	Pt/MCM-41	120	8/0	100	1.1	--	98.9	--
THF	Ru/C	200	20/0	100	--	--	--	94.7
Sc-CO_2/H_2O	Pd/C	80	10/100	100	--	--	--	100
[EMIm][Cl]	Pd/C	120	62/0	19	51	9	7	13

Table 5.3: Chemical conversion of 5-HMF via hydrogenation reactions in select solvents and with select catalyst systems.[46, 47]

Solvent	**Catalyst**	**Temp**	**P_{H2}/P_{CO2}**	**Conversion**	**Selectivity (%)**		
		(^oC)	(bar)	(%)	FA	2-MF	2-MTHF
H_2O	Cu/Fe	180	90/0	99.4	82	10	--
Octane	Pd/C	80	10/0	100	--	--	100

Table 5.4: Chemical conversion of furfural via hydrogenation reactions in select solvents and with select catalyst systems.[46, 48]

Hydrogenation reactions of 5-HMF and furfural have been successfully demonstrated in organic and aqueous solvents. The primary reduction products are displayed in Figure 5.10 and Figure 5.11 for 5-HMF and furfural respectively. The first reported hydrogenation of 5-HMF produced 2,5-dimethylfuran with a 71% yield using a carbon supported Cu/Ru bi-metallic catalyst in 1-butanol.[47] An additional study demonstrated that 2,5-DMF could be produced in tetrahydrofuran with a yield of 80.6% using a carbon supported ruthenium catalyst.[49]

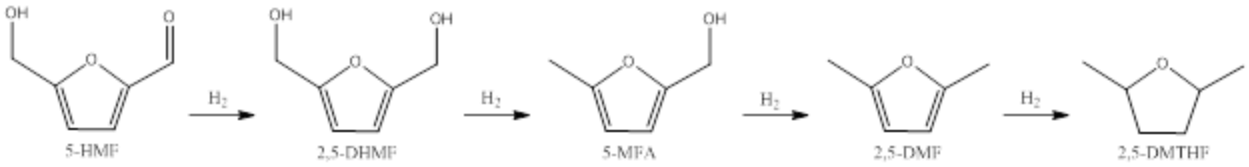

Figure 5.10: Primary hydrogenation products from 5-HMF: 2,5-dihydroxymethylfuran (DHMF), 5-methylfurfuryl alcohol (MFA), 2,5-dimethylfuran (2,5-DMF), and 2,5-dimethyltetrahydrofuran (2,5-DMTHF)

While effective, these reactions proceed at relatively high temperatures (T > 200 ^{o}C) and moderate hydrogen pressures (P_{H2} > 60 bar). Additionally, production of 2,5-DMF in nonpolar solvents necessitates energy intensive distillation processes for product recovery. For these reasons alternative hydrogenation solvents would be beneficial.

Compressed carbon dioxide is a particularly interesting medium for hydrogenation reactions since polar molecules including 5-HMF and furfural are relatively immiscible with CO_2 while less polar furan products are increasingly soluble. One select study has investigated the hydrogenation of 5-HMF and furfural in supercritical carbon dioxide-water mixtures using a Pd/C catalyst.[46] The results demonstrate that product selectivity can be controlled by CO_2 pressure tuning. Hydrogen partial pressure was set at 8 bar and the reaction temperature was held constant at 80 ^{o}C. Under these conditions and with 60 bar of CO_2 pressure the observed products favored 5-methylfurfuryl alcohol (5-MFA) with 57.8% selectivity. At 100 bar CO_2, 5-HMF was converted with 100% selectivity to 2,5-dimethylfuran (2,5-DMF). Finally, at CO_2 pressures above 160 bar product selectivity (67%) favored 2,5-dimethytetrahydrofuran (2,5-DMTHF). The unique CO_2 controlled product selectivity can be partially explained by examining the phase behavior of the system. At 60 bar the system exists in a vapor-liquid equilibrium state with a mixed CO_2/H_2 gas phase and a 5-HMF/H_2O liquid phase.

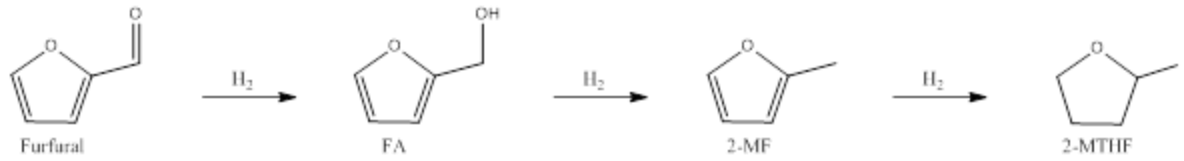

Figure 5.11: Primary hydrogenation products from furfural including: furfuryl alcohol (FA), 2-methylfuran (2-MF), and 2-methyltetrahydrofuran (2-MTHF).

Between 60 and 100 bar the system transitions from VLE to VLLE and a new immiscible CO_2/H_2 liquid phase forms on top of the reactant phase. Although not measured, it is hypothesized that increased solubility of hydrogen in the reaction phase likely aided selective formation of 2,5-DMF at 100 bar. Finally, at 160 bar pressure the CO_2/H_2 liquid phase was significantly expanded. Subsequent studies indicated that formed product 2,5-DMF partitioned into the upper CO_2/H_2 liquid phase where it further reacted to form 2,5-DMTHF.

Hydrogenation reactions have also been explored in ionic liquids on a range of reactants but no studies have explored the hydrogenation of furfural. Furthermore, only one study has investigated catalytic reduction of 5-HMF in ILs where a two-stage approach for the conversion of glucose to 2,5-dimethylfuran was attempted.[50] The results are displayed in Table 5.5. The hydrogenation of 5-HMF to 2,5-DMF using a Pd/C catalyst in [EMIm][Cl] was moderately unsuccessful, demonstrating only 47% conversion and 16% yield of the desired product. Poor catalytic reduction results were attributed to the lack of hydrogen in the IL reaction phase and further attempts at improving reaction performance were limited. As shown in Table 5.5, ILs exhibit lower hydrogen solubility compared to organic solvents which can lead to slow hydrogenation reaction rates in ILs.[51]

Solvent	Henry's Constant [H_{CO2} (MPa)]	Hydrogen Solubility at 100 bar [Mol/L]	Source
Methanol	6.6 x 10^2	3.75×10^{-3}	[52]
Ethanol	5.9 x 10^2	2.98×10^{-3}	[52]
Toluene	2.7 x 10^2	3.50×10^{-3}	[52]
[BMIm][Tf_2N]	4.5 x 10^2	7.7×10^{-4}	[53]
[BMIm][PF_6]	6.6 x 10^2	8.8×10^{-4}	[53]
[HMIm][BF_4]	5.7 x 10^2	7.9×10^{-4}	[53]

Table 5.5: Hydrogen solubility and Henry's constants in a range of organic solvents and ionic liquids. Measurements were conducted at 298K.

However, select studies have shown that CO_2 can significantly enhance the solubility of hydrogen in ILs and the mixed gas system can effectively be used for hydrogenation reactions.

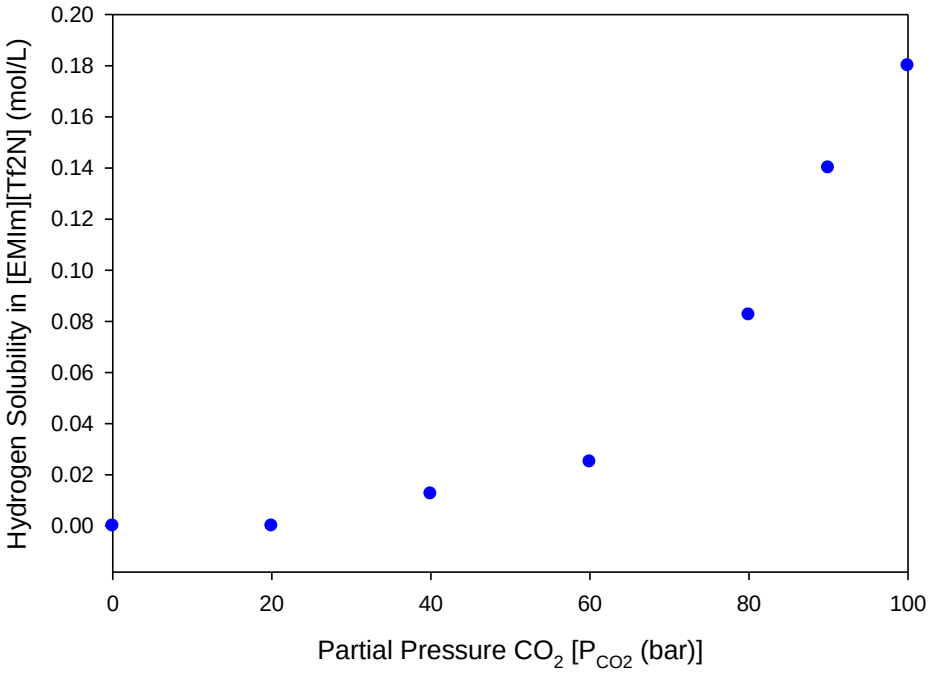

Figure 5.12: Solubility of hydrogen in the ionic liquid [EMIm][Tf_2N] as a function of CO_2 partial pressure at 298 K and a fixed hydrogen partial pressure of 30 bar.[54]

For example, the presence of one mole of compressed carbon dioxide at 38.7 bar increases the solubility of hydrogen in [EMIm][Tf_2N] by 28% as shown in Figure 5.12.[55] Experimental data on the mixed solubility of CO_2 and H_2 in biomass dissolving ionic liquids (*i.e.* [BMIm][Cl] or [EMIm][DEP]) does not currently exist and an urgent need of this information has been expressed.[56] In an effort to generate interest in this area a recent publication by Hiraga *et al*. utilized semi-empirical methodology to predict the CO_2 enhanced solubility of hydrogen in select biomass dissolving ionic liquids. Two of the most promising ILs identified in the study were [BMIm][Cl] and [EMIm][DEP]. Table 5.6 demonstrates the theoretical CO_2 enhanced solubility of hydrogen in these ILs at 100^{o}C based on PR-EoS thermodynamic modeling. Ratios greater than one indicate that hydrogen solubility in the ionic liquid is expected to be positively affected by carbon dioxide. The results demonstrate that [BMIm][Cl] and especially [EMIm][DEP] show promise for CO_2 enhanced hydrogen solubility.

Ionic Liquid	Estimated H_2 Enhancement Ratio	
	$m_{(CO2)}$ = 0.1 mol/kg $X_{CO2} \approx 0.03$	$m_{(CO2)}$ = 1.0 mol/kg $X_{CO2} \approx 0.21$
[EMIm][Tf_2N]	1.020	1.270
[BMIm][Cl]	1.016	1.162
[EMIm][DEP]	1.022	1.224

Table 5.6: Predicted enhancement of hydrogen solubility in select ionic liquids as a function of carbon dioxide concentration at 100^{o}C and 60 bar total pressure.[56]

The enhancement ratio displayed in Table 5.6 is defined as the molal concentration of hydrogen in the ternary (IL, CO_2, H_2) mixture relative to the molal concentration of hydrogen in the binary (IL, H_2) mixture as shown in Eqn. 5.2.

$$H_2\ Enhancement\ Ratio = \left(\frac{m_{H2}(T,P,m_{CO2})ternary}{m_{H2}(T,P')binary}\right)_{T,\,\hat{f}_{H2}} \qquad \text{Eqn. 5.2}$$

Based on the review of hydrogenation studies herein, compressed CO_2 is proposed to serve a dual function for the conversion of 5-HMF and furfural in ILs. First, CO_2 can increase hydrogen solubility in the IL reaction phase thereby enhancing the reaction rate and conversion. Second, phase tuning of the reactant/IL and reactant/product mixtures can be maintained for selective product formation. For these reasons, carbon dioxide enhanced hydrogenation of 5-HMF and furfural to furan products in ionic liquids appears promising.

5.5.2. Mass Transfer Resistance in Three Phase Catalysis

Catalytic hydrogenation reactions conventionally employ three phase gas-liquid-solid systems. In the case of furan production dissolved hydrogen reacts with liquid phase 5-HMF or furfural on the surface of a solid metal catalyst.

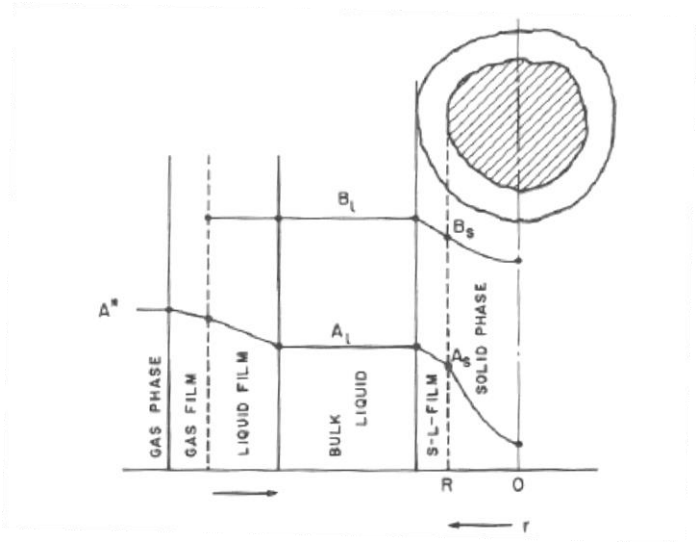

Figure 5.13: Mass transfer resistance within a three phase gas-liquid-solid catalyst system.[57]

Figure 5.13 demonstrates the sources of mass transfer resistance that can occur in three phase catalytic processes with one vapor phase reactant, one liquid phase reactant, and a solid catalyst.[57] In this system gaseous reactant (A^*) diffuses into the bulk liquid phase containing reactant (B_L). Subsequently both liquid species move to the catalyst where intra-particle diffusion transports the reactants to the surface. On the catalyst surface the reactants are converted to products. Finally, the products desorb from the catalyst surface and proceed back into the bulk liquid phase. Based on this model it is evident that many transport processes can influence the reaction rate. Previous studies demonstrate that gas-liquid mass transfer of sparingly soluble hydrogen is often the rate limiting step of three phase hydrogenation reactions. Therefore, a thorough analysis of transport and reaction mechanisms must be understood.

5.5.3. Bi-Phasic Product Separation

Energy efficient product separations are extremely important for industrial processes. Currently proposed lignocellulosic biomass conversion methods are insufficient as these produce dilute product streams in aqueous and organic media that must be separated by liquid-liquid extraction and distillation. To this point the majority of products from biomass conversion including 5-HMF and furfural display moderate to high polarity. Hydrogenation and hydrodeoxygenation are common reaction pathways to decrease the polarity of a molecule by reduction of oxygenated and unsaturated functional groups. As non-polar molecules are immiscible with biomass dissolving ionic liquids, hydrogenation of 5-HMF and furfural to furans generate a bi-phasic product separation without the need of an extraction solvent as shown in Figure 5.14. Whereas 5-HMF and furfural are completely miscible in [EMIm][DEP], Table 5.7 demonstrates the reduced miscibility of select furan products in this same IL at 25^{o}C and 1.01325 bar pressure.

Furan Product	Mol% [EMIm][DEP] in IL Rich Phase	Mass% [EMIm][DEP] in IL Rich Phase	Mass% [EMIm][DEP] in Furan Rich Phase
2-MF	32.7	61.0	0.0
2-MTHF	52.1	76.9	0.0
2,5-DMF	56.6	78.2	0.0
2,5-DMTHF	72.0	87.2	0.0

Table 5.7: Solubility of select furan products in [EMIm][DEP] at 25^{o}C and 1.01325 bar.

The results show that increased reduction of the furan product reduces its miscibility with the [EMIm][DEP] rich phase. For instance, at 25^{o}C and 1.01325 bar, thermodynamic equilibrium of 2,5-dimethylfuran (2,5-DMF) in the [EMIm][DEP] rich phase is 21.8 mass% and any additional 2,5-DMF partitions into a furan rich phase which contains no measurable quantity of IL, estimated to be less than 0.001 mole fraction. Furthermore, 2,5-dimethyltetrahydrofuran demonstrates even less miscibility with the IL rich phase as only 12.8 mass% 2,5-DMTHF is miscible with [EMIm][DEP].

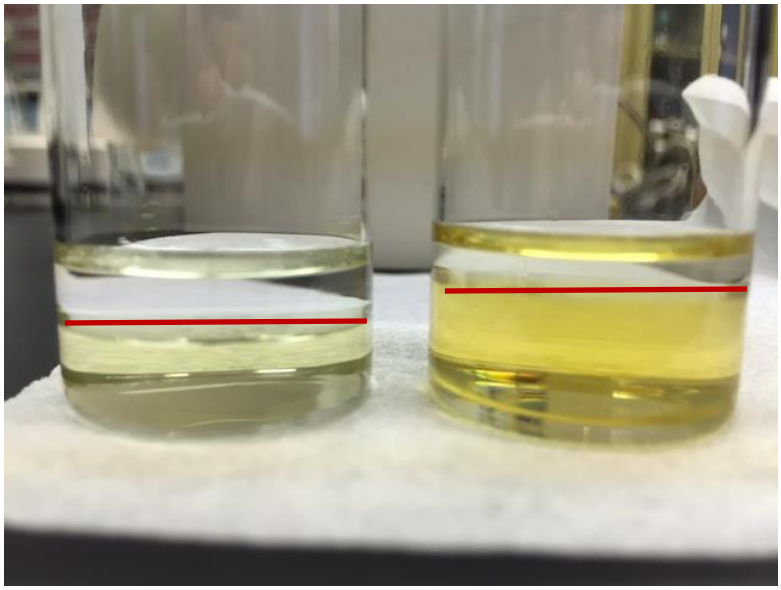

Figure 5.14: Thermodynamic liquid-liquid equilibrium of 2,5-dimethylfuran in [EMIm][DEP] (left) and [BMIm][Cl] (right) at 25^{o}C. IL rich phase on the bottom, furan rich phase on top. Red line utilized to indicate the phase partition.

Compressed carbon dioxide has previously been shown to partition organic and aqueous chemicals out of ionic liquids at low to moderate pressures.[58] Therefore, while ambient conditions are effective at generating a bi-phasic separation of furan products and ionic liquids, CO_2 was explored as a potential extraction enhancement technique. Preliminary phase equilibrium results for the CO_2 enhanced extraction are displayed in Figure 5.15. The experiment was conducted by loading a one phase mixture of 2-methylfuran (25 mass% binary, solute free) and [EMIm][DEP] (75 mass% binary, solute free) into an autoclave viewcell at 25^{o}C. Prior to CO_2 addition the mixture exists as a dark homogeneous phase with a stir bar in the middle of the cell to aid mixing. After reaching equilibrium at 10 bar CO_2 pressure, a second liquid phase forms on top of the IL rich phase, indicating partitioning of 2-methylfuran.

P = 0 Bar CO_2 P = 10 Bar CO_2 P = 25 Bar CO_2 P = 100 Bar CO_2

Figure 5.15: Extraction of 2-methylfuran from [EMIm][DEP] using select pressures (*i.e.* compositions of compressed carbon dioxide at 25^{o}C.

At 25 bar CO_2 increasing quantities of 2-methylfuran partition out of the IL rich phase and are expanded by carbon dioxide. Finally, at 100 bar, when CO_2 is beyond its liquefaction point, CO_2 and 2-MF form a homogeneous liquid phase on top of the IL rich liquid phase. Although not quantified here, the preliminary results of Figure 5.15 appear to indicate that compressed CO_2 is capable of extracting 2-methylfuran, and presumably other furan products, from ionic liquid mixtures and therefore should be considered as an effective separation enhancement technology.

5.6. Summary

Ionic liquids are ideal solvents for the chemical conversion of biomass as they are capable of dissolving significant quantities of raw cellulose and hemicellulose. However, chemical conversion of biomass in ILs, as demonstrated by the model reaction of fructose to 5-HMF in [EMIm][DEP], is comparatively slow relative to processes in organic solvents or mixed IL-cosolvent systems. Additionally, 5-HMF thermally degrades in ionic liquids and aqueous solvents. Polar aprotic cosolvents, when mixed with [EMIm][DEP] at loadings between 60-90 mass% enhanced fructose conversion and 5-HMF yield and were significantly greater than the

results obtained from the pure IL system even at extended time scales. Mixed IL polar aprotic cosolvent systems have been shown to enhance 5-HMF stability as well as biomass solubility and should therefore be targeted for future biomass conversion work.

Despite efficient chemical conversion of biomass in ILs, products from cellulose hydrolysis (*i.e.* glucose), isomerization (*i.e.* fructose), and dehydration reactions (*i.e.* 5-HMF) are polar and require energy intensive separation processes to isolate them from the reaction mixture. Products including 2,5-dimethylfuran, 2,5-dimethyltetrahydrofuran, 2-methylfuran, and 2-methyltetrahydrofuran are produced by hydrogenation of 5-hydroxymethylfurfural and furfural. These compounds demonstrate reduced polarities and lower miscibility with ILs allowing them to naturally partition out of ionic liquids thus generating a bi-phasic separation without the input of thermal energy. Finally, utilization of compressed CO_2 appears to be a promising method for enhancing hydrogen solubility in the IL reaction phase, controlling the reaction selectivity, and separating furan products from the reaction mixture. Goals to further the preliminary results demonstrated here are presented in the recommendations and future work section of Chapter 9.

References:

1. Tenenbaum, D.J., *Food vs. fuel: Diversion of crops could cause more hunger.* Environmental Health Perspectives, 2008. **116**(6): p. A254-A257.
2. Cardona, C.A., O.J. Sanchez, and L.F. Gutierrez, *Process synthesis for fuel ethanol production*. Biotechnology and bioprocessing series. 2010, Boca Raton, FL: CRC Press. xxi, 393 p.
3. Bourne, J.K., *Green Dreams*, in *National Geographic*2007.
4. Luterbacher, J.S., D. Martin Alonso, and J.A. Dumesic, *Targeted chemical upgrading of lignocellulosic biomass to platform molecules.* Green Chemistry, 2014. **16**(12): p. 4816-4838.
5. Gericke, M., P. Fardim, and T. Heinze, *Ionic Liquids - Promising but Challenging Solvents for Homogeneous Derivatization of Cellulose.* Molecules, 2012. **17**(6): p. 7458-7502.
6. Vitz, J., et al., *Extended dissolution studies of cellulose in imidazolium based ionic liquids.* Green Chemistry, 2009. **11**(3): p. 417-424.
7. Wang, H., G. Gurau, and R.D. Rogers, *Ionic liquid processing of cellulose.* Chemical Society Reviews, 2012. **41**(4): p. 1519-1537.
8. Deng, W.P., Q.H. Zhang, and Y. Wang, *Catalytic transformations of cellulose and cellulose-derived carbohydrates into organic acids.* Catalysis Today, 2014. **234**: p. 31-41.
9. Lima, S., et al., *Ionic Liquids as Tools for the Acid-Catalyzed Hydrolysis/Dehydration of Saccharides to Furanic Aldehydes.* Chemcatchem, 2011. **3**(11): p. 1686-1706.
10. Song, J.L., et al., *Conversion of glucose and cellulose into value-added products in water and ionic liquids.* Green Chemistry, 2013. **15**(10): p. 2619-2635.
11. Xiao, S.H., et al., *Efficient conversion of cellulose into biofuel precursor 5-hydroxymethylfurfural in dimethyl sulfoxide-ionic liquid mixtures.* Bioresource Technology, 2014. **151**: p. 361-366.
12. Yabushita, M., H. Kobayashi, and A. Fukuoka, *Catalytic transformation of cellulose into platform chemicals.* Applied Catalysis B-Environmental, 2014. **145**: p. 1-9.
13. Zakrzewska, M.E., E. Bogel-Lukasik, and R. Bogel-Lukasik, *Ionic Liquid-Mediated Formation of 5-Hydroxymethylfurfural-A Promising Biomass-Derived Building Block.* Chemical Reviews, 2011. **111**(2): p. 397-417.
14. Zhou, L.L., et al., *One-step degradation of cellulose to 5-hydroxymethylfurfural in ionic liquid under mild conditions.* Carbohydrate Polymers, 2015. **117**: p. 694-700.
15. Zhu Yinghuai, A.O.B., Xiao Siwei, Narayan S Hosmane and John A. Maguire *Ionic Liquids in Catalytic Biomass Transformation, Applications of Ionic Liquids in Science and Technology*, ed. P.S. Handy. 2011.
16. Binder, J.B., et al., *Synthesis of Furfural from Xylose and Xylan.* Chemsuschem, 2010. **3**(11): p. 1268-1272.
17. Choudhary, V., S.I. Sandler, and D.G. Vlachos, *Conversion of Xylose to Furfural Using Lewis and Bronsted Acid Catalysts in Aqueous Media.* Acs Catalysis, 2012. **2**(9): p. 2022-2028.

18. Hu, X., et al., *Acid-Catalyzed Conversion of Xylose in 20 Solvents: Insight into Interactions of the Solvents with Xylose, Furfural, and the Acid Catalyst.* Acs Sustainable Chemistry & Engineering, 2014. **2**(11): p. 2562-2575.
19. Kumar, S., et al., *Carbon Dioxide Promoted Hydrolysis of Xylose to Furfural Using 1,1,3,3-Tetramethyl Guanidinium Hydrogen Sulfate: A Remarkable Enhancement in Reaction Rate.* Industrial & Engineering Chemistry Research, 2014. **53**(40): p. 15571-15575.
20. Zhang, L.X., H.B. Yu, and P. Wang, *Solid acids as catalysts for the conversion of D-xylose, xylan and lignocellulosics into furfural in ionic liquid.* Bioresource Technology, 2013. **136**: p. 515-521.
21. Zhang, L.X., et al., *Conversion of xylan, D-xylose and lignocellulosic biomass into furfural using AlCl3 as catalyst in ionic liquid.* Bioresource Technology, 2013. **130**: p. 110-116.
22. Chatterjee, C., F. Pong, and A. Sen, *Chemical conversion pathways for carbohydrates.* Green Chemistry, 2015. **17**(1): p. 40-71.
23. Mika, L.T., E. Cséfalvay, and I.T. Horváth, *The role of water in catalytic biomass-based technologies to produce chemicals and fuels.* Catalysis Today, (0).
24. Shi, J.C., et al., *Production of 5-Hydroxymethylfurfural from Mono- and Disaccharides in the Presence of Ionic Liquids.* Catalysis Letters, 2014. **144**(2): p. 252-260.
25. Zhu, Y.H., et al., *Conversion of Cellulose to Hexitols Catalyzed by Ionic Liquid-Stabilized Ruthenium Nanoparticles and a Reversible Binding Agent.* Chemsuschem, 2010. **3**(1): p. 67-70.
26. Cai, C.M., et al., *Coupling metal halides with a co-solvent to produce furfural and 5-HMF at high yields directly from lignocellulosic biomass as an integrated biofuels strategy.* Green Chemistry, 2014. **16**(8): p. 3819-3829.
27. Wang, P., et al., *Catalytic hydrolysis of lignocellulosic biomass into 5-hydroxymethylfurfural in ionic liquid.* Bioresource Technology, 2011. **102**(5): p. 4179-4183.
28. Yu, S., et al., *Single-step conversion of cellulose to 5-hydroxymethylfurfural (HMF), a versatile platform chemical.* Applied Catalysis a-General, 2009. **361**(1-2): p. 117-122.
29. Cao, Q., et al., *Conversion of hexose into 5-hydroxymethylfurfural in imidazolium ionic liquids with and without a catalyst.* Carbohydrate Research, 2011. **346**(7): p. 956-959.
30. Lima, S., et al., *Conversion of mono/di/polysaccharides into furan compounds using 1-alkyl-3-methylimidazolium ionic liquids.* Applied Catalysis a-General, 2009. **363**(1-2): p. 93-99.
31. Zhang, J., et al., *Kinetic studies on chromium-catalyzed conversion of glucose into 5-hydroxymethylfurfural in alkylimidazolium chloride ionic liquid.* Chemical Engineering Journal, 2014. **237**: p. 55-61.
32. Qi, X.H., et al., *Efficient process for conversion of fructose to 5-hydroxymethylfurfural with ionic liquids.* Green Chemistry, 2009. **11**(9): p. 1327-1331.
33. Tsilomelekis, G., et al., *Origin of 5-Hydroxymethylfurfural Stability in Water/Dimethyl Sulfoxide Mixtures.* Chemsuschem, 2014. **7**(1): p. 117-126.
34. Younan, S., et al., *Chromium(VI) bioremediation by probiotics.* Journal of the Science of Food and Agriculture, 2016: p. n/a-n/a.

35. Amarasekara, A.S., L.D. Williams, and C.C. Ebede, *Mechanism of the dehydration of D-fructose to 5-hydroxymethylfurfural in dimethyl sulfoxide at 150 degrees C: an NMR study.* Carbohydrate Research, 2008. **343**(18): p. 3021-3024.
36. Qi, X.H., et al., *Catalytic dehydration of fructose into 5-hydroxymethylfurfural by ion-exchange resin in mixed-aqueous system by microwave heating.* Green Chemistry, 2008. **10**(7): p. 799-805.
37. Qi, X.H., et al., *Selective Conversion of D-Fructose to 5-Hydroxymethylfurfural by Ion-Exchange Resin in Acetone/Dimethyl sulfoxide Solvent Mixtures.* Industrial & Engineering Chemistry Research, 2008. **47**(23): p. 9234-9239.
38. Bicker, M., J. Hirth, and H. Vogel, *Dehydration of fructose to 5-hydroxymethylfurfural in sub- and supercritical acetone.* Green Chemistry, 2003. **5**(2): p. 280-284.
39. Zeitsch, K.J., *The chemistry and technology of furfural and its many by-products*. Sugar series. 2000, Amsterdam ; New York: Elsevier. xv, 358 p.
40. Chan, J.Y.G. and Y.G. Zhang, *Selective Conversion of Fructose to 5-Hydroxymethylfurfural Catalyzed by Tungsten Salts at Low Temperatures.* Chemsuschem, 2009. **2**(8): p. 731-734.
41. Caratzoulas, S., et al., *Challenges of and Insights into Acid-Catalyzed Transformations of Sugars.* Journal of Physical Chemistry C, 2014. **118**(40): p. 22815-22833.
42. Nagpure, A.S., N. Lucas, and S.V. Chilukuri, *Efficient Preparation of Liquid Fuel 2,5-Dimethylfuran from Biomass-Derived 5-Hydroxymethylfurfural over Ru-NaY Catalyst.* ACS Sustainable Chemistry & Engineering, 2015. **3**(11): p. 2909-2916.
43. Pang, S.H. and J.W. Medlin, *Adsorption and Reaction of Furfural and Furfuryl Alcohol on Pd(111): Unique Reaction Pathways for Multifunctional Reagents.* Acs Catalysis, 2011. **1**(10): p. 1272-1283.
44. Sitthisa, S., et al., *Kinetics and mechanism of hydrogenation of furfural on Cu/SiO2 catalysts.* Journal of Catalysis, 2011. **277**(1): p. 1-13.
45. Nakagawa, Y., M. Tamura, and K. Tomishige, *Catalytic Reduction of Biomass-Derived Furanic Compounds with Hydrogen.* Acs Catalysis, 2013. **3**(12): p. 2655-2668.
46. Chatterjee, M., T. Ishizaka, and H. Kawanami, *Hydrogenation of 5-hydroxymethylfurfural in supercritical carbon dioxide-water: a tunable approach to dimethylfuran selectivity.* Green Chemistry, 2014. **16**(3): p. 1543-1551.
47. Roman-Leshkov, Y., et al., *Production of dimethylfuran for liquid fuels from biomass-derived carbohydrates.* Nature, 2007. **447**(7147): p. 982-U5.
48. Yan, K. and A.C. Chen, *Selective hydrogenation of furfural and levulinic acid to biofuels on the ecofriendly Cu-Fe catalyst.* Fuel, 2014. **115**: p. 101-108.
49. Hu, L., et al., *Selective Transformation of 5-Hydroxymethylfurfural into the Liquid Fuel 2,5-Dimethylfuran over Carbon-Supported Ruthenium.* Industrial & Engineering Chemistry Research, 2014. **53**(8): p. 3056-3064.
50. Chidambaram, M. and A.T. Bell, *A two-step approach for the catalytic conversion of glucose to 2,5-dimethylfuran in ionic liquids.* Green Chemistry, 2010. **12**(7): p. 1253-1262.
51. Mukund Ghavre, S.M.a.N.G., *Hydrogenation in Ionic Liquids*, in *Ionic Liquids: Applications and Perspectives*, P.A. Kokorin, Editor. 2011, InTech.

52. Seidell, A. and W.F. Linke, *Solubilities of inorganic and metal organic compounds; a compilation of quantitative solubility data from the periodical literature*. 3d ed. 1940, New York,: D. Van Nostrand company, inc.
53. Dyson, P.J., et al., *Determination of hydrogen concentration in ionic liquids and the effect (or lack of) on rates of hydrogenation.* Chemical Communications, 2003(19): p. 2418-2419.
54. Solinas, M., et al., *Enantioselective hydrogenation of imines in ionic liquid/carbon dioxide media.* Journal of the American Chemical Society, 2004. **126**(49): p. 16142-16147.
55. Kumelan, J., D. Tuma, and G. Maurer, *Simultaneous solubility of carbon dioxide and hydrogen in the ionic liquid [hmim][Tf2N]: Experimental results and correlation (vol 311, pg 6, 2011).* Fluid Phase Equilibria, 2012. **329**: p. 92-92.
56. Hiraga, Y., Y. Sato, and R.L. Smith Jr, *Development of a simple method for predicting CO2 enhancement of H2 gas solubility in ionic liquids.* The Journal of Supercritical Fluids, 2015. **96**(0): p. 162-170.
57. Ramachandran, P.A. and R.V. Chaudhari, *Three-phase catalytic reactors*. Topics in chemical engineering,. 1983, New York: Gordon and Breach Science Publishers. xii, 427 p.
58. Scurto, A.M., S.N.V.K. Aki, and J.F. Brennecke, *CO2 as a separation switch for ionic liquid/organic mixtures.* Journal of the American Chemical Society, 2002. **124**(35): p. 10276-10277.

6. Vapor-Liquid Equilibrium in the Production of the model Ionic Liquid 1-hexyl-3-methylimidazolium bromide [HMIm][Br]

6.1. Introduction

Ionic liquids have numerous advantages for applications in reactions, separations, and materials processing due to their molecular flexibility for optimizing their physical and chemical properties by cation/anion design. In addition ionic liquids possess immeasurable vapor pressures (*i.e*. non-volatility) and may lead to more sustainable or "green" processes by eliminating solvent based air pollution. As the number of successful ionic liquid applications grows, the demand for larger quantities of ILs concomitantly increases. Yet, to this point few studies have focused on developing sustainable and continuous ionic liquid production methods.[1-3] Current ionic liquid synthesis methods, as found in the literature, are performed by batch scale operations with only limited knowledge of chemical kinetics and optimized purification techniques.[4, 5] Batch scale production methods yield small quantities of product at high costs potentially impeding industrial implementation. Additionally, batch methods are extremely inefficient and violate the principles of sustainable chemistry thereby challenging the "green" character of ionic liquids from a cradle to gate life cycle assessment.[6, 7] For ionic liquids to be an industrially viable technology continuous, benign, and cost effective production methods must be developed.

Isolated studies have characterized the reaction kinetics [1-3] and thermodynamics [8, 9] of select ionic liquid synthesis systems. However, no such study has investigated the phase equilibrium thermodynamics of the reactants, product, and solvent required to simulate the purification of an ionic liquid from its reaction mixture. Previous work within the Scurto research group by Schleicher *et al.* investigated the impact of solvent selection on reaction

kinetics in the synthesis of the model ionic liquid [HMIm][Br].[10] It is the aim of this chapter to build on the preceding work by incorporating experimentally measured phase equilibrium and separation energy data for the purification of [HMIm][Br].

6.2. Background: Kinetics of [HMIm][Br] Synthesis

Select imidazolium-based ionic liquids are synthesized by a quaternization reaction between an alkyl halide and a 1-alkyl-imidazole. For the production of the model ionic liquid 1-hexyl-3-methylimidazolium bromide ([HMIm][Br]), this reaction occurs between 1-bromohexane and 1-methylimidazole, shown in Figure 6.1.

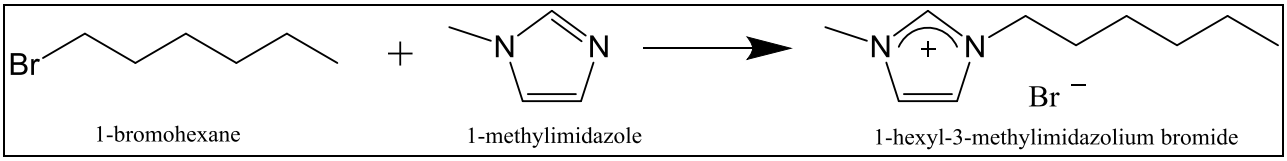

Figure 6.1: Reaction of 1-bromohexane and 1-methylimidazole to produce the ionic liquid 1-hexyl-3-methylimidazolium bromide [HMIm][Br].

Quaternization reactions are highly exothermic and require the use of solvents for safe heat dissipation. Additionally, solvents bring the reaction into a single homogeneous phase and enhance the reaction kinetics. Despite these advantages, ionic liquids are commonly criticized for being synthesized in many of the hazardous solvents they aim to replace. For ionic liquids to be part of a sustainable process and truly "green", they must also be synthesized in a likewise sustainable manner. Previous work in the Scurto group identified a solvent selection guide for IL synthesis by cross referencing reaction kinetics with environmental databases and approximate separation energies. The results of this work are shown in Table 6.1.[11]

Solvent	$K*10^6$ (M^{-1} sec^{-1})	Rowan Green Index (0 = Best)	Approx. Separation Energy (KJ/mol)[A]
Dimethyl Sulfoxide	77.89	0.42	65.89
Acetonitrile	21.56	3.21	33.59
Neat	17.63	>5 Est.	----
Cyclopentanone	15.11	3.6	52.78
Carbon Dioxide	7-17	0	----
Acetone	12.67	2.15	31.16
2-Butanone	11.56	3.6	37.65
Dichloromethane	8.47	5.36	28.04
Ethyl Formate	7.97	3.11	32.00
Chlorobenzene	3.64	>5 Est.	53.04
Ethyl Lactate	2.86	1.57	28.70
Methanol	2.03	2.52	37.21

[A] Approximate separation energy data based on the temperature difference between the solvent boiling point and a reaction conducted at 40°C assuming C_p constant over the entire temperature range.**[11]**

Table 6.1: Solvent selection guide for the synthesis of [HMIm][Br].

Whereas the best reaction kinetics were observed in dimethyl sulfoxide, a sustainable solvent system must also have a low energy of separation in addition to a low environmental impact. To estimate the approximate separation energies shown in Table 6.1, the latent and sensible heats of vaporization of the pure solvent were used. Environmental impacts of the various solvents were assigned based on the Rowan Green Index which is commonly used in the pharmaceutical industry.[12] From these combined results Schleicher *et al.* selected acetone as the optimal solvent for [HMIm][Br] synthesis. However, the full vapor-liquid equilibrium of the various solvents and ionic liquids must be known to provide a detailed and accurate understanding of the actual separation energies. Additionally, while the Rowan Green index provides a proxy for the environmental impacts of various chemicals, true sustainability should only be evaluated thorough life-cycle assessment (LCA) methodology.[6, 7]

6.3. Phase Equilibrium for [HMIm][Br] Synthesis

The [HMIm][Br] synthesis reaction mixture prior to complete conversion represents a quaternary mixture composed of the two reactants (1-bromohexane and 1-methylimidazole), one ionic liquid product ([HMIm][Br]), and the reaction solvent. While complete conversion is ideal, real processes will require removal of the solvent and unconverted reactants to obtain a high purity ionic liquid product. Phase equilibrium models and process simulators require specification of binary interaction parameters (BIPs) for each pair of components in the complex multi-component system. The [HMIm][Br] synthesis reaction is composed of six binary systems including mixtures of: solvent/1-bromohexane, solvent/1-methylimidazole, solvent/[HMIm][Br], 1-bromohexane/1-methylimizole, 1-bromohexane/[HMIm][Br], 1-methylimidazole/[HMIm][Br].

Experimental isobaric vapor liquid equilibrium measurements were obtained for most binary mixtures using a modified Othmer type recirculation still described in section 2.2.1. However, several systems were incapable of being measured by this method. For instance, 1-bromohexane and [HMIm][Br] are only partially miscible. Therefore, liquid-liquid equilibrium was measured for this binary system. Additionally, 1-bromohexane and 1-methylimidazole readily react to form [HMIm][Br] thus inhibiting experimental acquisition of accurate phase equilibrium measurements. Phase equilibrium data for reactive systems were obtained by the UNIFAC predictive Gibbs Excess activity coefficient model using the parameters displayed in Table 2.4.

Four solvents including dichloromethane (DCM), acetone, acetonitrile (ACN), and dimethyl sulfoxide (DMSO) were selected for phase equilibrium studies from the list of kinetically investigated solvents in Table 6.1. Of the four solvents selected, dichloromethane demonstrated the slowest reaction kinetics and highest environmental impact. However, DCM has the highest

vapor pressure of any solvent in this study with a pure component boiling point of 39^{o}C indicating that it may require the least energy for separation and IL purification. Acetone demonstrates significantly better environmental and kinetic properties compared to dichloromethane but will theoretically require higher separation energies due to its comparatively higher boiling point, 56^{o}C. Acetonitrile, one of the most common reaction solvents for IL synthesis, provided a combination of intermediate reaction kinetics, environmental impacts, and pure component boiling point (81^{o}C). Finally, dimethyl sulfoxide demonstrates the fastest reaction kinetics and lowest environmental impact of any solvent in Table 6.1 with the exception of carbon dioxide. However, DMSO boils at 189^{o}C and thus theoretically will require the most energy for solvent removal and IL purification. The four solvents selected in this study represent a cross section of performance with regards to reaction kinetics, environmental impact, and separation energy. By combining the previously acquired kinetic rate constants with the experimental phase equilibrium data and analysis presented herein, full process simulation models can be developed to analyze the costs of large-scale ionic liquid production. Additionally, life cycle assessment models can estimate the environmental impacts associated with continuous IL synthesis. The combination of process and LCA models allows for the recommendation of an optimal reaction solvent for IL synthesis.

6.4. Method Validation

A newly modified Othmer-type recirculation still was used to obtain the experimental isobaric vapor-liquid equilibrium (*Txy*). The ability of this apparatus to measure mixed organic solvent systems was confirmed by measuring vapor-liquid equilibrium data of the acetone/methanol binary system as shown in Figure 6.2 which has been well-studied in the literature.[13, 14]

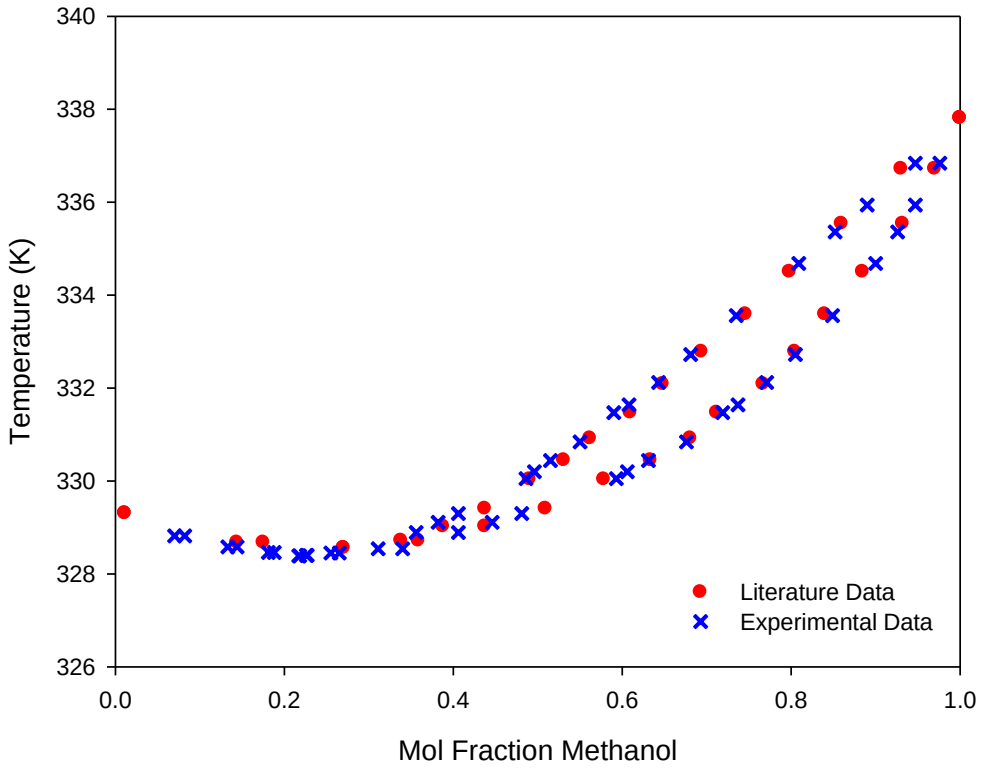

Figure 6.2: Comparison of experimental and literature data for the binary Acetone (1) / Methanol (2) system.[13]

The data measured in this study for the acetone/methanol system displays excellent agreement with literature sources exhibiting an average deviation from the interpolated literature data of 3.3% from the combined average deviations of both temperature and vapor phase compositions.

Very few studies have utilized a modified Othmer still apparatus for vapor-liquid equilibrium measurements involving ionic liquid systems.[15, 16] To validate our experimental method for these systems we investigated the ethanol/1-butyl-3-methylimidazolium chloride [BMIm][Cl] system which has been presented in the literature.[17] As shown in Figure 6.3 our data is again well correlated to data previously published in the literature with a combined average deviation of 5.25%.

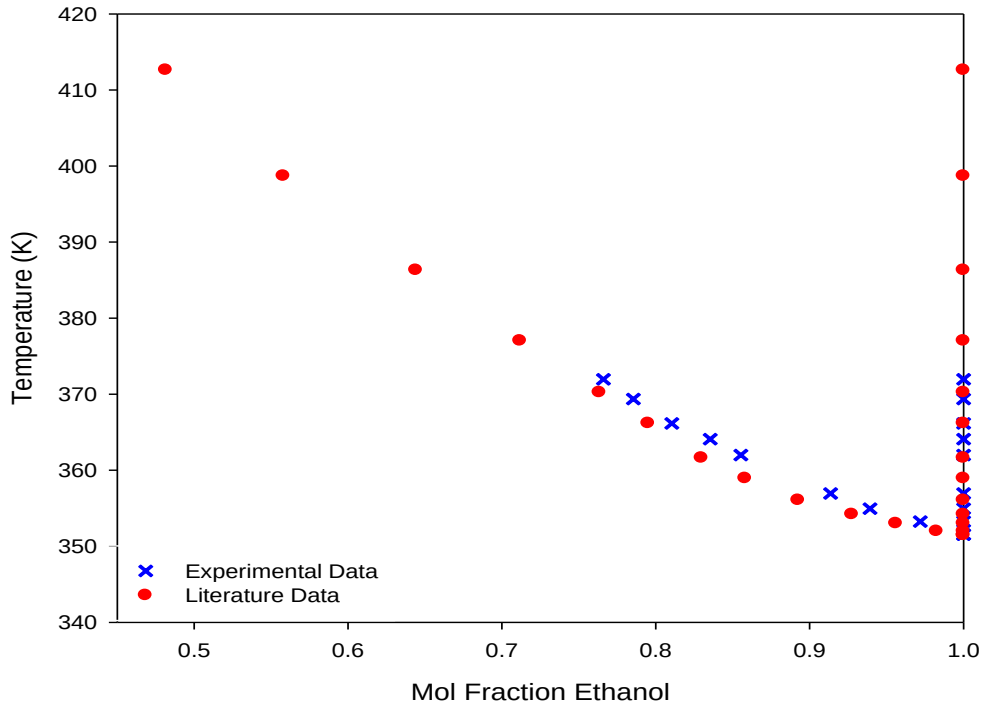

Figure 6.3: Comparison of experimental and literature data for the binary Ethanol (1) / [BMIm][Cl] (2) system.[17]

Unlike the acetone/methanol VLE system which demonstrates a conventional phase envelope, the ethanol/[BMIm][Cl] system displays a vertical dew point curve which is composed of pure ethanol across the entire temperature range. As ionic liquids are non-volatile they are unable to enter the vapor phase thus leading to the experimentally observed pure ethanol dew point curve. The bubble point curve for the ethanol/[BMIm][Cl] system is only measured to a composition of 0.75 mol fraction ethanol or, alternatively, a 0.25 mole fraction ionic liquid loading. However, due to the difference in molecular weights (MW) of these components (MW [BMIm][Cl] = 174.67 and MW ethanol = 46.07) 0.25 mole fraction ionic liquid corresponds to a 0.56 mass fraction IL loading. Ionic liquids are highly viscous and create transport limitations even at elevated temperatures. Therefore, accurate measurement of this IL-solvent system could not be attained at IL loadings greater than X_{IL}=0.25. However, in the measured regions both the

acetone/methanol and ethanol/[BMIm][Cl] trials proved that the modified Othmer still was capable of accurately measuring phase equilibrium for organic and ionic liquid containing systems. Table 6.2 and Table 6.3 represent the experimentally acquired phase equilibrium data for the acetone/methanol system and the ethanol/[BMIm][Cl] system respectively.

Temperature [K]	Liquid Mole Fraction, (x_1)	Vapor Mole Fraction, (y_1)
329.3	1.0000	1.0000
328.7	0.8560	0.8247
328.6	0.7298	0.7298
328.7	0.6412	0.6618
329.0	0.5623	0.6118
329.4	0.4906	0.5623
329.9	0.4379	0.5057
330.4	0.3663	0.4689
330.9	0.3271	0.4346
331.5	0.2880	0.3901
332.1	0.2329	0.3520
332.8	0.1953	0.3059
333.6	0.1599	0.2538
334.5	0.1150	0.2017
335.5	0.0676	0.1400
336.7	0.0298	0.0694
337.8	0.0000	0.0000

Table 6.2: Isobaric (1.01325bar) Vapor-Liquid Equilibrium of Acetone (1)/ Methanol (2) u(T)=0.1K u(x)=u(y)=0.001

Temperature [K]	Liquid Mole Fraction, (x_1)	Vapor Mole Fraction, (y_1)
351.5	1.0000	1.0000
353.3	0.9719	1.0000
354.9	0.9392	1.0000
356.9	0.9136	1.0000
362.0	0.8553	1.0000
364.1	0.8354	1.0000
366.2	0.8104	1.0000
369.4	0.7854	1.0000
372.0	0.7660	1.0000

Table 6.3: Isobaric (1.01325bar) Vapor-Liquid Equilibrium of Ethanol (1)/ 1-Butyl-3-Methylimidazolium Chloride ([BMIm][Cl]) (2). u(T)=0.1 K u(x)=u(y)=0.001

6.5. Binary Phase Equilibrium of Reactants and Solvents

Experimental vapor-liquid-equilibrium measurements were obtained for the reactant molecules 1-bromohexane and 1-methylimidazole with each solvent system including dichloromethane, acetone, acetonitrile, and dimethyl sulfoxide. These systems investigated the behavior and interactions of each individual reactant with the solvent involved in ionic liquid synthesis. As the reactant and solvent molecules are miscible with each other and volatile, full vapor-liquid phase equilibrium diagrams were developed for each pair of components. Experimental phase equilibrium data sets were modeled by the Peng-Robinson Equation of State (PR-EoS) and the Non-Random Two Liquid (NRTL) Gibbs Excess activity coefficient model. Critical properties for all components, utilized by PR-EoS regressions, are displayed in Table 6.4.

		Critical Properties		
Component	T_{Boil}[K]	T_c [K]	P_c [Bar]	ω
Dichloromethane [A]	312.9	510.0	60.80	0.199
Acetone [A]	329.3	508.2	47.01	0.306
Acetonitrile [A]	355.0	545.5	48.30	0.338
Dimethyl Sulfoxide [A]	462.2	729.0	56.50	0.281
1-Bromohexane [B]	428.5	626.8	31.30	0.384
1-Methylimidazole [B]	471.6	742.4	55.61	0.279
[HMIm][Br] [B]	-------	841.1	26.68	0.607

[A)] Critical properties obtained from NIST database. [B)] Critical properties obtained from Ref. **[18]**

Table 6.4: Critical properties used for Peng Robinson Equation of State modeling.

Additionally, Table 6.5 displays the Antoine type vapor pressure coefficients utilized by the NRTL activity coefficient model. The NIST validated extended Antoine type vapor pressure equation shown in Eqn. 6.1 was utilized to compute the vapor pressure of all components except 1-bromohexane which was specified by a Wagner25 type vapor pressure equation shown in Eqn. 6.2 where T_{ri} is the reduced temperature of the component of interest.

$$\ln(P^{vap}, bar) = A - \frac{B}{(T,K)+C} + D(T,K) + Eln(T,K) + F(T,K)^G \qquad \text{Eqn. 6.1}$$

$$\ln(P^{vap}, bar) = \ln(P_{ci}) + \frac{[A(1-T_{ri})+B(1-T_{ri})^{1.5}+C(1-T_{ri})^{2.5}+D(1-T_{ri})^5]}{T_{ri}} \qquad \text{Eqn. 6.2}$$

	Antoine Constants for the Calculation of Vapor Pressure (bar, K)						
Component	A	B	C	D	E	F	G
Dichloromethane [A]	90.0871	-6541.6	0	0	-12.247	1.2311E-5	2
Acetone [A]	57.4931	-5599.6	0	0	-7.0985	6.2237E-6	2
Acetonitrile [A]	46.7891	-5385.6	0	0	-5.4954	5.3634E-6	2
Dimethyl Sulfoxide [A]	44.7601	-7620.6	0	0	-4.6279	4.3819E-7	2
1-Bromohexane [A, B]	-8.86284	4.47543	-6.13716	-1.6837	3.44369	353.65	----
1-Methylimidazole [A, C]	13.0834	-6172.53	0.68805	0	0	0	0

[A)] Antoine constants from NIST database applied using the extended Antoine equation PLXANT [B)] Antoine constants applied using the WAGNER25 vapor pressure equation [C)] Antoine constants fitted to data from vapor pressure data from Ref. **[19]** Application of all vapor pressure data performed in Aspen Plus V.8.0.

Table 6.5: Antoine constants used for the calculation of vapor pressure in the Gibbs Excess NRTL activity coefficient model.

6.5.1. Dichloromethane – Reactant Systems

Dichloromethane represents the most volatile solvent investigated in this study and has a pure component boiling point of 312.8 K. Therefore, DCM readily evaporates even at room temperature. To obtain accurate experimental measurements and prevent the evaporation of dichloromethane during sample collection a special adapter was constructed from a rubber septum. The phase envelopes of binary mixtures of dichloromethane with 1-bromohexane and 1-methylimidazole are shown respectively in Figure 6.4 and Figure 6.5. Both systems have been modeled by the NRTL activity coefficient method and the Peng Robinson Equation of State with a Van der Waals 1 parameter mixing rule.

As shown in Figure 3.4, the Peng Robinson and NRTL models perform comparatively well for the DCM/1-bromohexane system. At compositions near the pure component boiling points both models accurately regress the bubble and dew point curves. However, at intermediate

compositions especially between 0.5 and 0.9 mole fraction dichloromethane loadings the models slightly under predict the dew point composition and temperature.

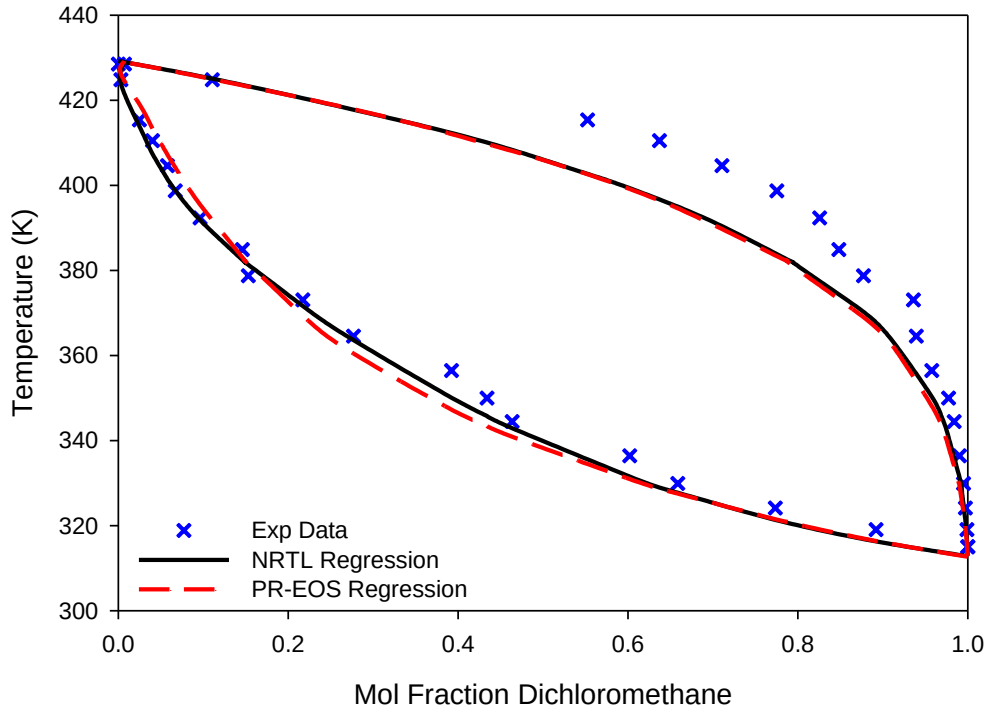

Figure 6.4: Experimental and modeled VLE data for the binary Dichloromethane (1) / 1-bromohexane (2) system.

Deviations in the vapor phase composition and temperature between the experimental and regressed data in this composition range were between 20-30 %AARD for y_1 and 0.5-2.0 %AARD for T. The overall %AARD in y_1 and T for the DCM-1-bromohexane system were 10.60 and 2.76 respectively. This represents the largest difference between measured and modeled data of any experimentally investigated vapor-liquid equilibrium system.

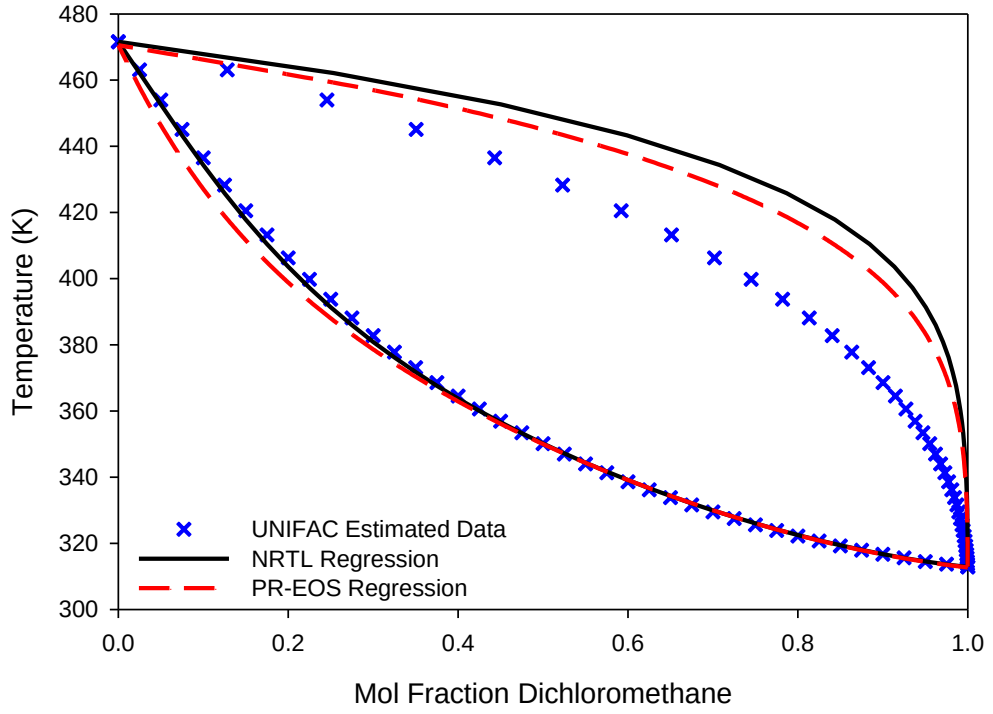

Figure 6.5: Experimental and modeled VLE data for the binary Dichloromethane (1) / 1-Methylimidazole (2) system.

Figure 6.5 displays the UNIFAC predicted vapor liquid equilibrium results for the binary mixture of dichloromethane and 1-methylimidazole. Multiple attempts were made to experimentally measure VLE data for this system. However, at temperatures above 353 K dichloromethane and 1-methylimidazole reacted to form a white crystalline precipitate. At elevated temperatures the reaction and precipitate formation became rapid and prevented accurate measurement of thermodynamic data points. Additional crystal growth occurred upon cooling of the liquid mixture. Images of the crystalline product are displayed in Figure 6.6.

Figure 6.6: White crystalline product formed from the reaction of dichloromethane and 1-methylimidazole at temperatures above 80^{o}C. Product in reaction mixture (left), isolated and purified product (right).

Previous kinetic studies by Schleicher *et al.* investigated the production of [HMIm][Br] in dichloromethane and did not report any side reactions between DCM and 1-methylimidazole.[10] However, these studies were performed low temperatures (40^{o}C) and without a metal heating coil which potentially acts as a catalyst. Alternatively, a well-studied reaction between dichloromethane and pyridine demonstrates that consecutive S_N2 reactions occur at elevated temperatures to form a di-cationic pyridine dimer and a pair of chloride anions.[20] Pyridine is an aromatic nitrogen containing molecule with similar structure to 1-methylimidazole. Therefore, a similar reaction mechanism could also theoretically occur between DCM and 1-methylimidazole. To investigate this hypothesis the crystalline product was dissolved in deuterated $DMSO_{d6}$ and analyzed by NMR spectroscopy. Similar to what was found for the pyridine system, NMR confirmed that DCM and 1-methylimidazole do react to produce an imidazole dimer. The formation of chloride ions could not be confirmed by this method but is presumed to occur based on similar findings from the pyridine study. The proposed reaction between 1-methylimidazole and dichloromethane is shown in Figure 6.7.

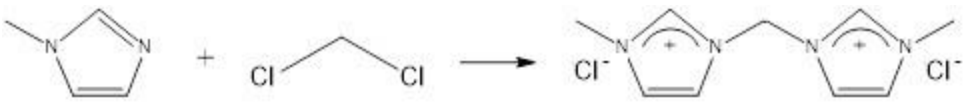

Figure 6.7: Proposed reaction between dichloromethane and 1-methylimidazole to produce an imidazole dimer and a pair of chloride ions.

Di-cationic imidazole based liquids with halogenated anions have been synthesized for use in carbon dioxide capture applications.[21] Conventional synthesis methods for producing these molecules involve a reaction between a di-halogenated alkane and an alkyl imidazole ring. Under elevated temperature conditions the imidazole rings undergo consecutive substitution reactions. Therefore, based on these findings and in conjunction with reaction studies on pyridine and DCM, it is believed that similar reactions, though currently undocumented in the literature, occur between dichloromethane and 1-methylimidazole.[22, 23]

Due to the reactive interactions of dichloromethane and 1-methylimidazole at elevated temperatures, accurate experimental vapor-liquid equilibrium data could not be acquired. Therefore, the UNIFAC group contribution based predictive activity coefficient method was utilized to generate the *Txy* data shown in Figure 6.5. Dichloromethane and 1-methylimidazole have very different pure component boiling points with an approximate difference of 158 K. The UNIFAC model predicts a narrow phase envelope with a gradual increase in the dew point temperature as the vapor phase composition becomes increasingly rich in 1-methylimidazole. Alternatively, both the Peng Robinson Equation of State and the NRTL activity coefficient models predict an initial sharp increase in the dew point temperature upon addition of small amounts of 1-methylmidazole leading to a wider phase envelope. For instance, both the NRTL and PR-EOS models estimate an 81^{o}C increase in dew point temperature in response to a

concomitant 5 mol% 1-methylimidazole vapor phase composition increase. The dichloromethane and 1-methylimidazole system demonstrates minor deviations between UNIFAC and modeled bubble and dew point temperatures with %AARD values for the PR-EOS and NRTL models of 2.04 and 1.69 respectively. However, the models were unable to predict the dew point composition with as much certainty. Vapor phase deviations for the PR-EOS and NRTL models were 16.14 and 17.75 %AARD respectively with the largest differences occurring at vapor phase compositions of 80 mol% 1-methylimidazole and greater. As the UNIFAC model can not specify the exact 1-methylimiazole structure due to the lack of adequate functional groups it is possible that the predictive model under-estimates the dew point composition of dichloromethane in the vapor phase.

6.5.2. Acetone – Reactant Systems

Figure 6.8 and Figure 6.9 present the experimental and modeled vapor-liquid equilibrium data for the acetone solvent system with 1-bromohexane and 1-methylimidazole respectively. Both systems exhibit a relatively wide boiling envelope with a steep increase in boiling point temperature in the approximate range of 0-20 mol% acetone. The acetone/1-bromohexane system had a slightly narrower composition difference between the liquid and vapor phases and exhibited a more gradual increase in boiling point temperature with increased 1-bromohexane composition.

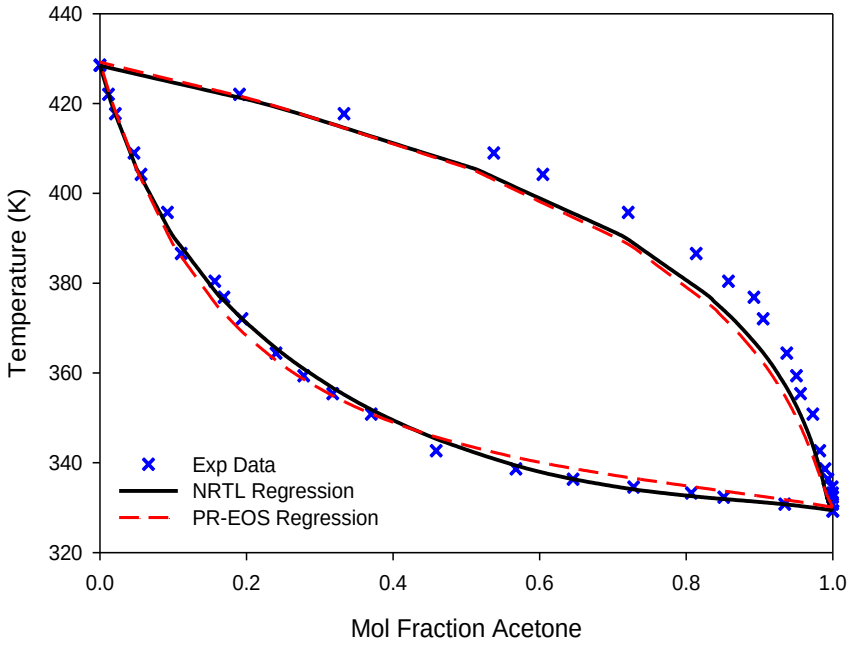

Figure 6.8: Experimental and modeled VLE data for the binary Acetone (1) / 1-Bromohexane (2) system.

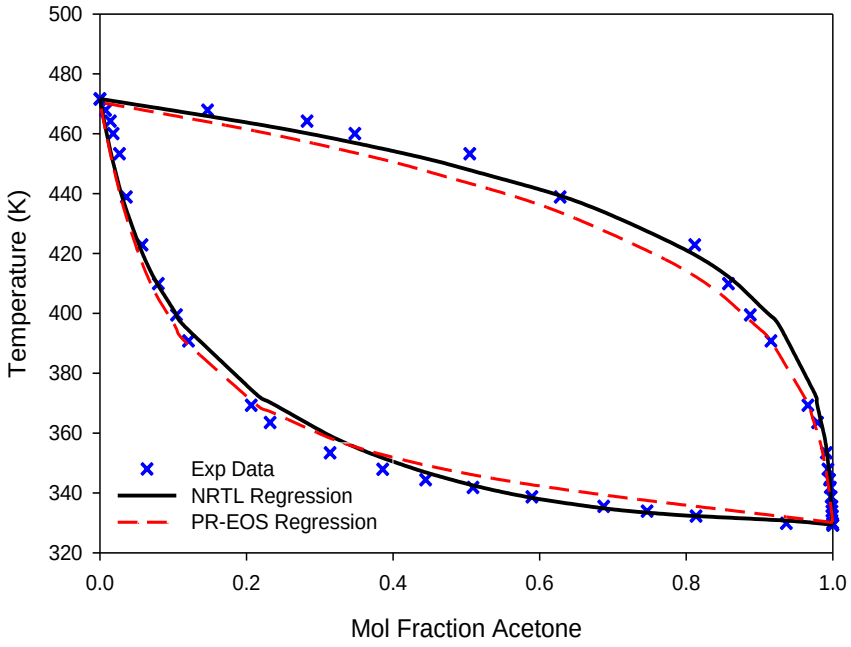

Figure 6.9: Experimental and modeled VLE data for the binary Acetone (1) / 1-Methylimidazole (2) system.

Activity coefficient and equation of state models accurately regressed the experimental data for both acetone solvent/reactant systems. It was observed that the NRTL regression of the acetone/1-bromohexane system performed marginally better than that of the acetone/1-methylimidazole system. Currently, limited vapor-liquid equilibrium data have been reported for 1-methylimidazole (with water [24]) and no full vapor-liquid equilibrium studies known to the authors have been attempted with 1-bromohexane. Therefore, some of this discrepancy may be due to the relatively large interpolation and extrapolation of the Antoine-type vapor pressure correlation for 1-methylimidazole and not to the model itself.[19, 25] In contrast, the Peng Robinson model performed comparatively well for both systems. Both models had minor difficulties modeling the dew points in the acetone/1-bromohexane system especially in the 50-90% mole acetone range. However, this inaccuracy only resulted in a dew point deviation (%AARD) of approximately 5.0 to 7.9% for the NRTL and PR-EoS models respectively.

6.5.3. Acetonitrile – Reactant Systems

Acetonitrile is the most commonly used reaction solvent for the production of [HMIm][Br] in the Scurto laboratory as it has an optimal combination of moderate reaction kinetics, relatively low pure component boiling point, and does not participate in any side reactions. Experimental vapor-liquid equilibrium measurements were obtained for the acetonitrile/1-bromohexane system and are displayed along with the NRTL and PR-EOS modeling results in Figure 6.10. A traditional phase envelope is observed and is narrower than that of the acetone/1-bromohexane system potentially due to the comparatively higher pure component boiling point of acetonitrile. Interestingly, at high concentrations of acetonitrile ($X_{ACN} > 0.95$) the phase envelope narrows significantly. The experimental data was replicated and while the dew point envelope appears to

meet the bubble point curve near the pure acetonitrile data point, an azeotrope does not form for this binary system.

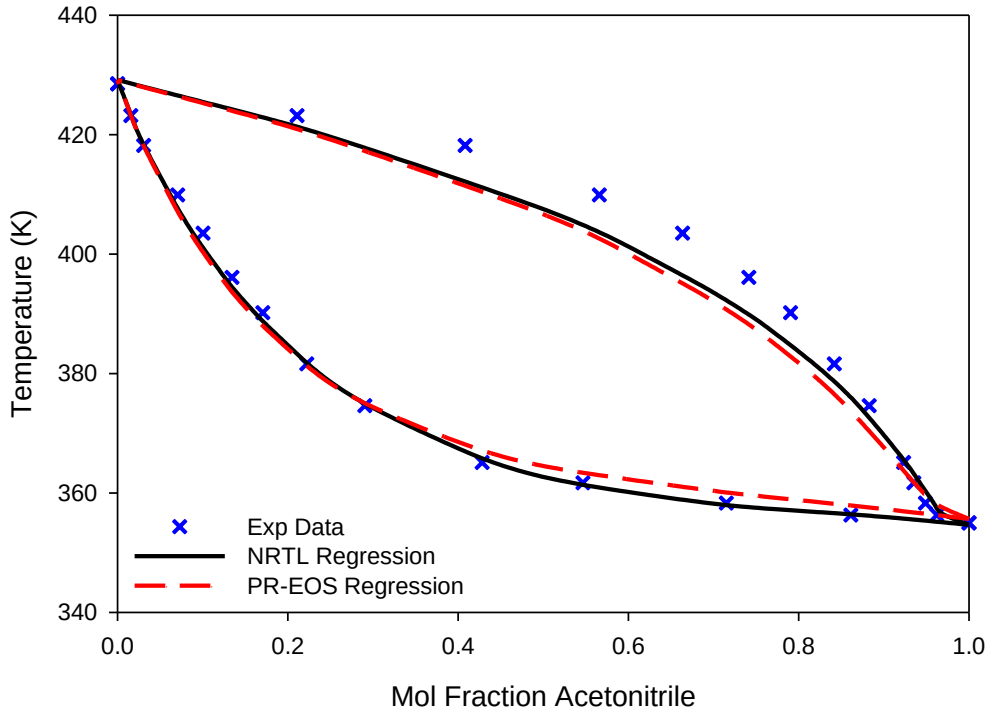

Figure 6.10: Experimental and modeled VLE data for the binary Acetonitrile (1) / 1-Bromohexane (2) system.

The activity coefficient and equation of state models both accurately regressed the experimental data for the acetonitrile/1-bromohexane system with a similar under prediction of the dew point composition and temperature at intermediate solvent loadings. Deviations in the experimental and regressed vapor-liquid data were 0.85 and 6.62 %AARD for the temperature and vapor phase composition respectively for the NRTL activity coefficient model. Alternatively, for the Peng Robinson Equation of State these values were 1.31 and 7.82 for the same two parameters. Therefore, both models accurately represent the experimental phase equilibrium data.

A conventional phase envelope is observed for the acetonitrile/1-methylimidazole system in Figure 6.11. Unlike the mixtures of acetonitrile and 1-bromohexane which display a narrower phase envelope, especially at high acetonitrile concentrations, for the 1-methylimidazole/ACN system we observe a steep increase in dew point temperature as the concentration of 1-methylimidazole increases. Similar increases in the experimental dew point temperature upon the addition of 1-methylimidazole were observed for the acetone solvent system. Alternatively, the UNIFAC dichloromethane/1-methylimidazole system demonstrated a narrower phase envelope. The conflicting results from the DCM and 1-methylimidazole system may indicate that the UNIFAC model is incapable of accurately predicting the dew point temperature and composition for this pair of components and that the results should be used with caution.

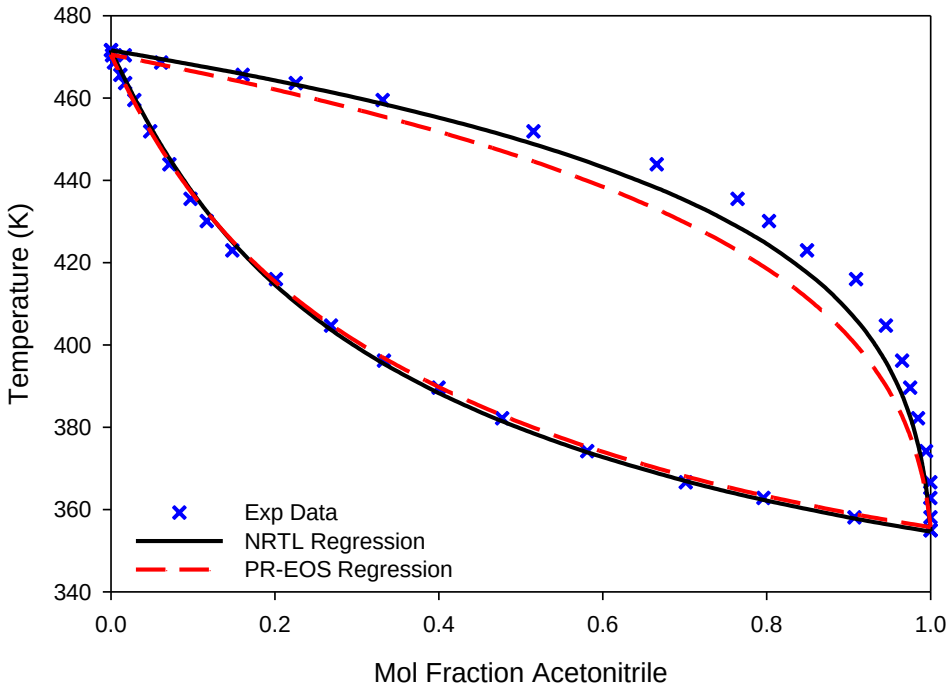

Figure 6.11: Experimental and modeled VLE data for the binary Acetonitrile (1) / 1-Methylimidazole (2) system.

The NRTL model accurately regressed the experimental vapor-liquid equilibrium data for the acetonitrile/1-methylimidazole system with calculated %AARD values of y_1 and T of 0.92 and 4.60 respectively. Alternatively, the Peng Robinson Equation of State accurately modeled both end points of the phase envelope but deviated slightly at intermediate mixture concentrations between 0.25 and 0.95 mole fraction acetonitrile. Despite these deviations, the %AARD in vapor phase composition and temperature from the regression for the PR-EOS were 0.62 and 11.47 respectively. Therefore, both models capture the phase behavior of this binary system.

6.5.4. Dimethyl Sulfoxide – Reactant Systems

The dimethyl sulfoxide solvent system demonstrated the fastest reaction kinetics for the synthesis of [HMIm][Br] of any solvent investigated but also has the highest pure component boiling point potentially leading to the largest separation energies for IL purification. To investigate the separation energy for IL synthesis in DMSO, phase equilibrium experiments were conducted with this solvent and reactant molecules 1-bromohexane and 1-methylimidazole.

Phase equilibrium experiments of 1-bromohexane and dimethyl sulfoxide were experimentally attempted but were not able to be completed due to a vigorous reaction between the components at the pure component boiling point of DMSO. In the failed experiments, 300 mL of DMSO was heated to reflux in the still. After initial equilibrium was achieved, 20 mL of 1-bromohexane was added to the still. Approximately one minute after 1-BH addition rapid boiling was observed in the still and the volume of distillate was far greater than the 1-bromohexane addition. The rate of vapor phase formation was too great for the condenser and escaped the system. Furthermore, condensed vapor solidified in the reflux arm forming a white crystalline precipitate.

A mixture of 1-bromohexane and DMSO was also heated in a scintillation vial at 100^{o}C and was found to react and form two immiscible liquid phases after approximately one hour. Previous reactions between 1-bromohexane and DMSO were not previously reported by our laboratory which could be due to the significantly lower reaction temperatures previously investigated. However, due to the high reactivity of these two chemicals at the elevated temperatures investigated herein (T > 155^{o}C) the UNIFAC model was again used to predict the phase equilibrium of this solvent-reactant system. The binary phase equilibrium of DMSO and 1-bromohexane is displayed in Figure 6.12. While the phase envelope narrows at compositions near pure 1-bromohexane, no azeotrope was detected. Importantly, both the Equation of State and Gibbs Excess models accurately regress the experimentally predicted UNIFAC data.

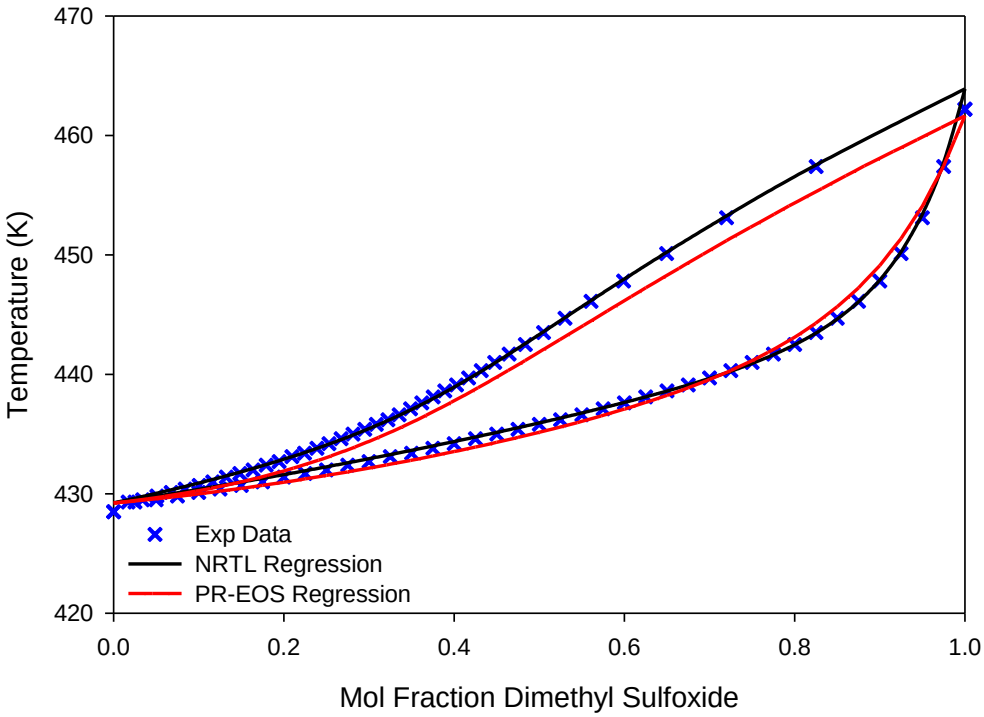

Figure 6.12: Experimental and modeled VLE data for the binary Dimethyl Sulfoxide (1) / 1-Bromohexane (2) system.

Mixtures of dimethyl sulfoxide and 1-methylimidazole did not react at the elevated temperatures thus allowing acquisition of experimental vapor-liquid equilibrium measurements, shown in Figure 6.13. The pure component boiling points of DMSO and 1-methylimidazole are only ~ 10 K different and represent the highest boiling pair of components investigated in this study. Due to the similarity in boiling points and vapor pressures of DMSO and 1-MI, the phase envelope of these components is very narrow. The NRTL model appears to inaccurately fit the phase envelope but only deviates from the pure DMSO boiling point by approximately 3 K. Alternatively, the Peng Robinson Equation of State under predicts both pure component boiling points as well as temperatures across the entire composition range by approximately 1 K.

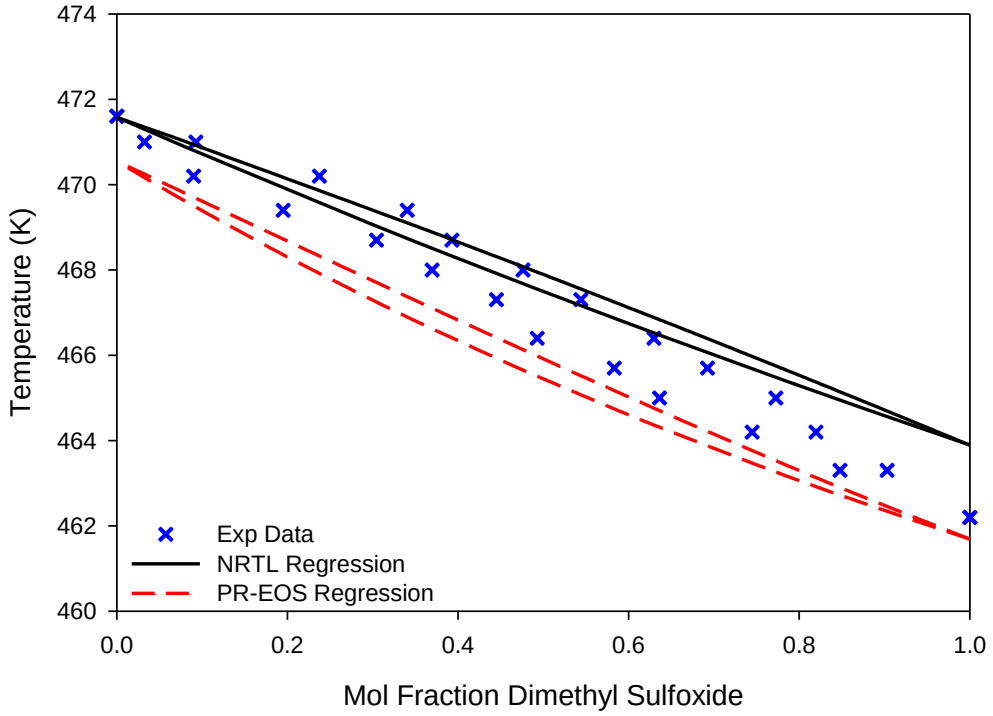

Figure 6.13: Experimental and modeled VLE data for the binary Dimethyl Sulfoxide (1) / 1-Methylimidazole (2) system.

6.5.5. Phase Equilibrium Modeling Results: Reactants and Solvents

From the results of the NRTL activity coefficient model for each binary solvent-reactant system, it was observed that the acetone, acetonitrile, and dimethyl sulfoxide systems exhibit positive deviations from Raoult's law. In all three cases, the activity coefficient of the solvent γ_1 was greater than one while γ_2 was approximately equal to one across the composition range. From a separations standpoint, a γ_1 for the solvent greater than one indicates a reduced bubble point temperature and thus a lower energy separation. Alternatively, the dichloromethane solvent system displayed negative deviations from Raoult's law with both 1-bromohexane and 1-methylimidazole. Negative Raoult's law deviations are a result of strong intermolecular

interactions between dichloromethane and the reactant molecules, likely due to hydrogen bond interactions between the compounds. Therefore, the energy required to separate these components is greater than what is estimated in ideality as determined by a combination of the pure component vapor pressures of each component according to Raoult's law.

Deviations between the modeled and experimental results, especially in intermediate solvent compositions, were common for every solvent system with 1-bromohexane and 1-methylimidazole. Although this appears problematic, ideal reactors will operate at high conversion (X > 90%). Therefore, the most important phase equilibrium results for the solvent – reactant systems are at mixture compositions of 90 mol% solvent and greater which is well modeled by both Peng Robinson and NRTL models. A table of binary interaction parameters and %AARD for each model solvent-reactant system is presented in Table 6.6. Additionally, tables of phase equilibrium data for all of the solvent – reactant binary systems are provided in Appendix 1.

System	NRTL[a]				PR-vdW1		
	Δg_{12}	Δg_{21}	%AARD		k_{12}	%AARD	
	J/mol.K	J/mol.K	T	y_1		T	y_1
Dichloromethane (1)/1-Bromohexane (2)	-7147.52	11319.76	2.76	10.60	-0.0313	4.29	12.64
Dichloromethane (1)/1-Methylimidazole (2)	1009.72	-4564.24	1.69	17.75	-0.0374	2.04	16.14
Acetone (1)/1-Bromohexane (2)	15331.93	-6139.86	0.67	6.70	0.0380	0.50	6.50
Acetone (1) /1-Methylimidazole (2)	11866.74	-5189.64	0.78	7.71	-0.2819	0.74	2.80
Acetonitrile(1)/1-Bromohexane (2)	10267.12	-3706.76	0.85	6.62	0.0719	1.31	7.82
Acetonitrile(1)/1-Methylimidazole (2)	-6804.72	9835.21	0.92	4.60	-0.0374	0.62	11.47
Dimethyl Sulfoxide(1)/1-Bromohexane (2)	8688.38	-3067.38	0.05	2.06	0.0189	0.12	8.99
Dimethyl Sulfoxide(1)/1-Methylimidazole(2)	-7376.70	13328.26	0.17	14.49	0.0032	0.20	16.28

[a] The NRTL α value was set to 0.20; [b] as this system cannot be experimentally measured, these results were the deviation between the NRTL model and UNIFAC VLE prediction.

Table 6.6: VLE regression parameters and %AARD deviation for the solvent-reactant systems.

6.6. Binary Phase Equilibrium of Ionic Liquid and Solvent

Isobaric VLE measurements of binary systems containing the solvent and ionic liquid product were measured to determine thermodynamic solvent/product interactions. Unlike the previous solvent/reactant non-IL systems, the non-volatile ionic liquid results in an ionic-liquid-free vapor phase across the temperature range measured within experimental accuracy, *i.e.* <<0.001 mole fraction, represented by a vertical dew point curve. While most ILs are considered non-volatile, there are a few ionic liquids whose vapor pressures have been high enough to quantify. [26-28] Extrapolating this data by a Clausius-Clapeyron methodology indicates that the normal boiling point of even the most volatile ILs is over 625°C (898 K). However, most ILs decompose before reaching this temperature. The pure component boiling point of [HMIm][Br] at atmospheric pressure has not been experimentally measured but we estimate it to be in excess of 700 °C (973 K) with decomposition well before this point.

Both Equation of State and Gibbs excess models have been applied to ionic liquid VLE systems. According to Maia *et al.* the NRTL model is the most commonly used local composition model for regressing VLE data. [29] It has been applied to both binary and ternary ionic liquid containing systems, most commonly focused on breaking azeotropes. [14, 17, 30] Alternatively, the Peng-Robinson EoS model has been primarily applied to ionic liquid VLE systems containing CO_2 or other high-pressure gases as the secondary component. [31-33] To our knowledge, this is the first time the Peng Robinson EoS has been applied to a VLE study of ionic liquid systems at atmospheric pressure.

Equation of State models require critical property data for the calculation of attractive and co-volume parameters needed to accurately regress experimental vapor-liquid equilibrium data. As

ionic liquids are non-volatile, experimental determination of their critical points is not possible. Therefore, T_c, P_c, and ω have been estimated from Joback group contribution methods for [HMIm][Br] in this study. Despite many successful applications of group contribution methods, the lack of critical property data necessary to define the pure component parameters of ionic liquids is commonly cited as the primary drawback of Equation of State models for IL containing systems. [29]

6.6.1. Dichloromethane – [HMIm][Br] System

Experimental phase equilibrium data for the dichloromethane-[HMIm][Br] system regressed by the Peng Robinson Equation of Sate and NRTL Gibbs Excess models are displayed in Figure 6.14. The experimental data demonstrates an exponential increase in boiling point temperature with a concomitant increase in liquid phase ionic liquid concentration. For instance, the mixture boiling point increases by ~36 K when the composition of IL in the liquid phase is x_{IL} = 0.47 mole fraction compared to the pure DCM boiling point. Boiling point elevation is likely due to physical and chemical interactions between DMC and the IL. Dichloromethane is highly polar and therefore interacts with the ions of [HMIm][Br] thus suppressing its vapor pressure. Additionally, the dichloromethane – [HMIm][Br] mixture exhibited negative deviations to Raoult's law. Negative Raoult's law deviations indicate that the vapor pressure of the mixture is lower (*i.e.* higher mixture boiling point temperature) than what would be predicted by a linear combination of mole fraction averaged pure component vapor pressures. Therefore, from a separations perspective, removing dichloromethane from [HMIm][Br] will require additional energy for IL purification compared to the ideal Raoult's law prediction.

The NRTL and PR-EoS models both regressed the experimental data for the DCM-[HMIm][Br] system with moderate accuracy. Both Equation of State and Gibbs Excess models correctly represent the pure component dichloromethane vapor phase indicative of the non-volatility of [HMIm][Br]. However, the models differ slightly in their regression of the bubble point temperature curve. The Peng Robinson EoS model indicates a nearly linear increase in temperature with liquid phase composition of [HMIm][Br]. Alternatively, the NRTL model more accurately models the experimental behavior of an exponential increase in bubble point temperature with liquid phase IL composition. Deviations between the experimental and modeled data were computed for the NRTL and PR-EoS models. Negligible differences were observed between the experimental and regressed vapor phase compositions (y_1). However, the dew point temperature calculation yielded deviations of 1.69 and 3.89 %AARD for the NRTL and Peng Robinson models respectively.

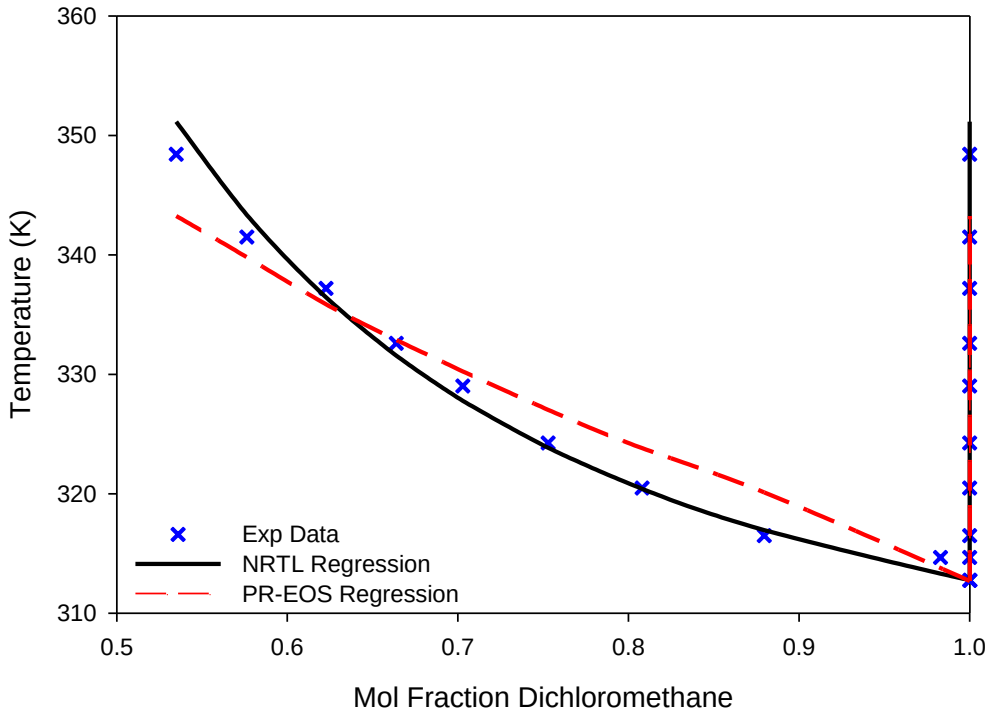

Figure 6.14: Experimental and modeled VLE data for the binary Dichloromethane (1) / [HMIm][Br] (2) system.

6.6.2. Acetone – [HMIm][Br] System

Similar phase behavior to the DCM-[HMIm][Br] system is observed in Figure 6.15 for the acetone solvent system with the IL. Compared to the dichloromethane system, the boiling point elevation due to IL in the liquid phase is less than what was observed for the DCM system. For instance, at an acetone composition of 0.47 mole fraction [HMIm][Br] the bubble point temperature is only ~ 25 K higher than the pure acetone boiling point which is 11 degrees less than what was observed for DCM. Dichloromethane is more polar than acetone potentially resulting in stronger interactions of DCM with the IL compared to the IL and acetone, thus greater boiling point temperature elevation for the dichloromethane solvent system.

Additionally, the acetone-[HMIm][Br] system displayed positive deviations to Raoult's law whereas the inverse was observed for dichloromethane. Comparing the acetone and DCM solvent systems it is apparent that the intermolecular interactions between solvent and product molecules in the post reaction mixture have a significant impact on bubble point temperature elevation, and more importantly, the energy required to purify the ionic liquid.

Again in the acetone-[HMIm][Br] system, the NRTL model preforms comparatively better than the Peng Robinson Equation of State, likely due to having two adjustable parameters compared to a single parameter EoS model. Both models accurately account for the [HMIm][Br] free vapor phase and show the exponential increase in bubble point temperature with IL composition.

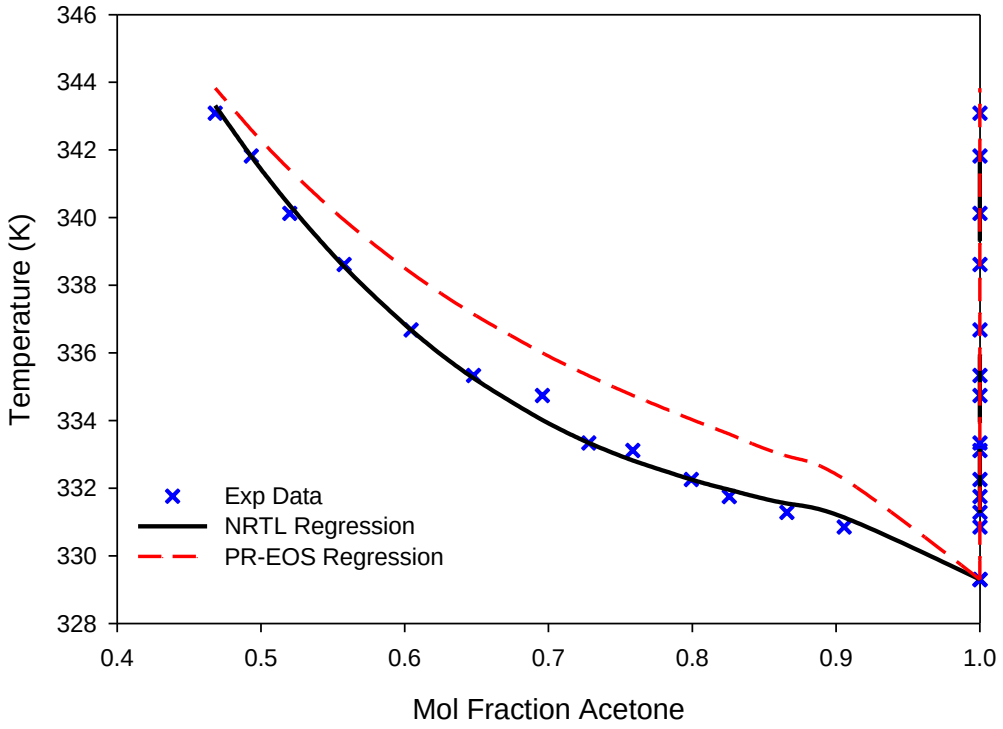

Figure 6.15: Experimental and modeled VLE data for the binary Acetone (1) / [HMIm][Br] (2) system.

6.6.3. Acetonitrile – [HMIm][Br] System

Phase equilibrium modeling by the NRTL and PR-EoS models exhibited the best results of any solvent-IL mixture for the acetonitrile solvent system as evidenced by Figure 6.16. For the Peng Robinson EoS the accurate regression is a function of the critical properties of the IL and acetonitrile as well as the ability of the model to fit one adjustable interaction parameter. Alternatively, the NRTL model utilized vapor pressure coefficients for each component as well as two adjustable binary interaction parameters to regress the experimental *Txy* data. The acetonitrile-[HMIm][Br] mixture again displays the expected exponential increase in temperature with increased composition of IL in the liquid phase as well as the pure solvent (IL-free) vapor phase. The bubble point temperature increase for the acetonitrile system was ~30 K upon the addition of 0.47 mol fraction ionic liquid, and was comparable to that observed for the acetone and dichloromethane solvent systems. Therefore, based on the three low-boiling reaction solvents investigated herein, it is evident that to purify the IL to approximately 50 mol% composition, a 20-30 K increase in liquid phase temperature will be required over the pure reaction solvent boiling point. Unfortunately the current experimental modified Othmer still apparatus was unable to obtain vapor-liquid equilibrium results at concentrated IL compositions. By extrapolating the modeling results of the ACN-[HMIm][Br] system it is estimated that temperatures between 438 K and 505 K could be required to purify the IL to 99+% from the reaction solvent. This forecasting indicates that IL purification has the potential to be highly energy intensive and that utilizing a solvent with a moderate to high vapor pressure could be essential to minimizing the economic impact of the post reaction separation train.

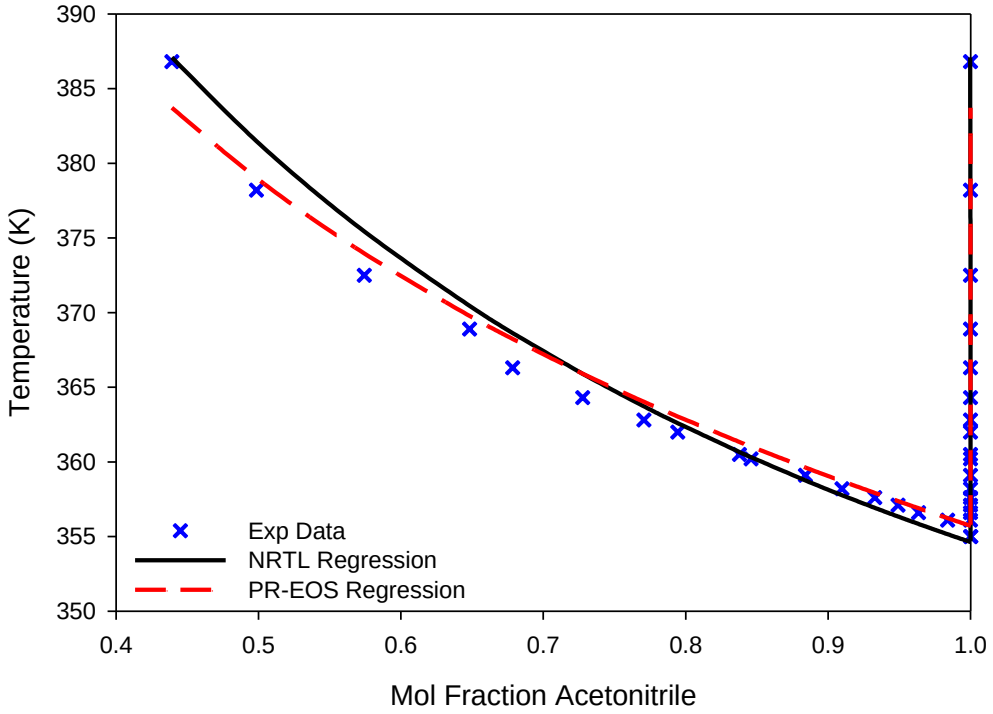

Figure 6.16: Experimental and modeled VLE data for the binary Acetonitrile (1) / [HMIm][Br] (2) system.

6.6.4. Dimethyl Sulfoxide – [HMIm][Br] System

Phase equilibrium results for the DMSO-[HMIm][Br] system are displayed in Figure 6.17. The DMSO system presented the greatest difficulty for both NRTL and PR-EOS models. The NRTL model accurately regressed the pure component DMSO boiling point but significantly over-predicted the bubble and dew point temperatures of IL-DMSO mixtures, especially at IL loadings greater than 30 mol%. For instance, at the highest [HMIm][Br] liquid phase composition, the NRTL model over-estimates the mixture boiling point by ~10 K. Alternatively, the PR-EoS model performs comparatively better relative to the NRTL model but still deviates from the measured bubble point temperature by ~ 5 K throughout most of the composition range.

For the PR-EoS model to accurately regress the experimental data the critical temperature of the IL was modified to T_c=1200 K due to the elevated pure component boiling point of DMSO. Upon alteration of IL properties for both the NRTL and PR-EoS models, the regressions performed significantly better than prior attempts with the conventional parameters applied for the other solvent systems. Despite the adjustment, current errors in both the NRTL model and PR-EOS are believed to be due to the high pure component boiling point of DMSO as these issues were not observed for the other solvent systems.

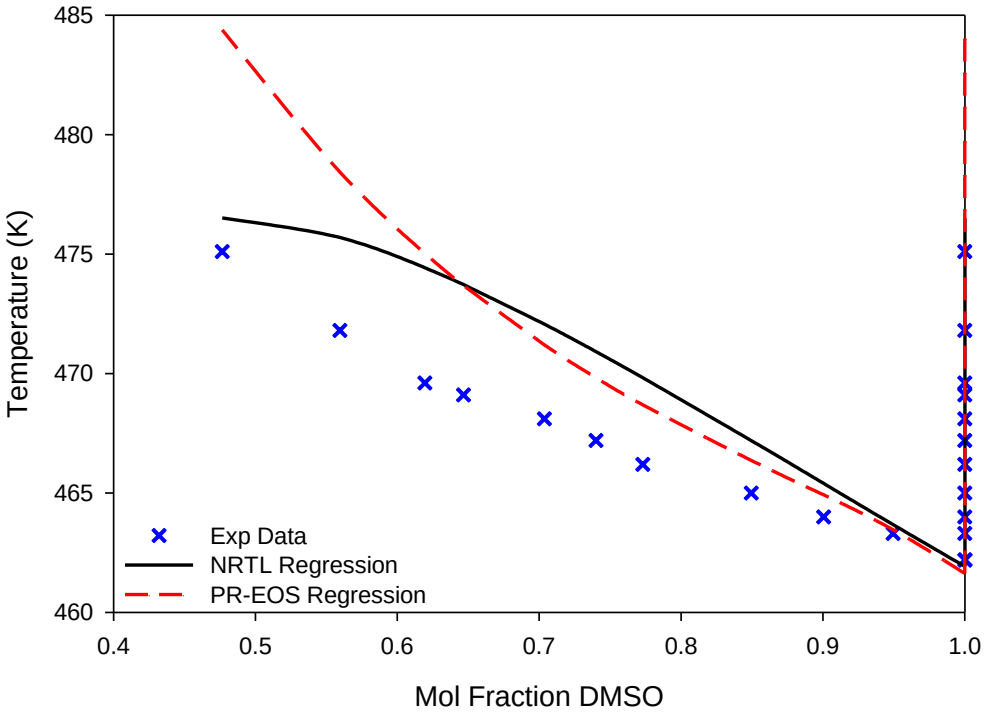

Figure 6.17: Experimental and modeled VLE data for the binary Dimethyl Sulfoxide (1) / [HMIm][Br] (2) system.

6.6.5. Phase Equilibrium Modeling Results: Solvents and [HMIm][Br]

Ideal reaction scenarios operate at high levels of conversion ~90+% thereby leaving trace quantities of reactants in the post-reaction mixture. Alternatively, solvents which are used to mitigate exothermic heat effects in the reaction as well as accelerate the reaction rate will be present in significant quantities upon reaction completion. Therefore, the separation of the reaction solvent from the ionic liquid is expected to have the largest impact on the post reaction separation train for purification of the ionic liquid product. Each solvent investigated herein demonstrated an exponential increase in mixture boiling point temperature as the concentration of ionic liquid increased. For most solvent systems the boiling point elevation was between 20-30 K to achieve 50 mol% IL liquid phase purities. This liquid phase IL concentration corresponds to 74, 81, 86, and 76 mass% IL for the dichloromethane, acetone, acetonitrile, and dimethyl sulfoxide systems respectively. Based on the exponential increase in bubble point temperature with increasing IL concentration through the experimentally measured composition range, the largest temperature increases are expected as IL purity increases. For instance, extrapolation of the experimental data for the acetonitrile-[HMIm][Br] system indicates a potential bubble point temperature between 438 K and 505 K to obtain a 99% pure IL liquid phase. This is a 19 to 42% increase relative to the pure component boiling point temperature of pure ACN. Similar temperature increases are expected for the other solvent systems and the separations could be more or less costly depending on the pure solvent volatility. A detailed analysis of separation energies are provided via process modeling simulations in Section 7.4.

The NRTL activity coefficient and Peng Robinson Equation of State regressed interaction parameters are displayed in Table 6.7. For binary systems containing the ionic liquid we found

that the regression ability of the activity coefficient model outperformed the equation of state model. We believe that the increased accuracy of the NRTL model was partially due to its two adjustable parameters as opposed to the one parameter of the EoS model. Furthermore, the EoS model may not have the most accurate attractive and co-volume parameters for the ionic liquid systems due to the experimentally-inaccessible critical points of the ionic liquid, and the use of estimated values for T_c, P_c, and ω from group contribution methods. This lack of critical property data necessary to define the pure component parameters of ionic liquids is commonly cited as the primary drawback of EoS models [29]. While the estimated critical properties are capable of generating a fairly accurate regression, as evidenced by our data, they are not capable of matching the ability of the more empirical activity coefficient model.

System	NRTL[a]				PR-vdW1		
	Δg_{12}	Δg_{21}	%AARD		k_{12}	%AARD	
	J/mol	J/mol	T	y_1		T	y_1
Dichloromethane (1)/[HMIm][Br] (2)	-18290.1	8800.45	1.69	----	-0.0401	3.89	----
Acetone (1)/[HMIm][Br]	3154.81	83140.0	2.66	----	0.0215	2.27	----
Acetonitrile(1)/[HMIm][Br] (2)	-3692.2	3312.88	1.14	----	0.0017	1.00	----
Dimethyl Sulfoxide(1)/[HMIm][Br] (2)[b]	58231.3	-15607.4	0.58	----	-0.0940	0.72	----

[a] The NRTL α value was set to 0.20; [b] Due to the high boiling point of DMSO the (A) parameter in the Antoine constant for [HMIm][Br] was modified to a value of 69.0 and T_c = 1200 K

Table 6.7: VLE regression parameters and %AARD deviation for the solvent-[HMIm][Br] systems

6.7. Binary Phase Equilibrium of Ionic Liquid and Reactants

Most IL synthesis reactions are conducted at high levels of conversion. For instance, we determined that for the ionic liquid [HMIm][Br] applied in this study, that reaction times of 48 hours or greater are sufficient to reach 99+% conversion levels of [HMIm][Br] when conducted at 70^{o}C in acetonitrile. Therefore, upon completion of the reaction only trace quantities of un-reacted 1-bromohexane and 1-methylimidazole will remain in the post-reaction mixture.

However, in the event that the reaction is not run to completion, an accurate understanding of the phase equilibrium thermodynamics for binary mixtures of the ionic liquid with each reactant, 1-bromohexane and 1-methylimidazole, must be understood.

6.7.1. 1-Bromohexane / [HMIm][Br] System

The components 1-bromohexane and [HMIm][Br] are only partially miscible, therefore liquid-liquid equilibrium (LLE) was used to generate the binary interaction parameters between these components. As displayed in Figure 6.16, 1-bromohexane is moderately miscible in the ionic liquid-rich phase but [HMIm][Br] is immiscible in the 1-bromohexane-rich phase within the experimental accuracy over all measured temperatures <0.0005 mole fraction. This system was modeled by a temperature dependent NRTL model to accurately account for the effect of temperature on solubility. The results of the regression are shown in Table 6.8.

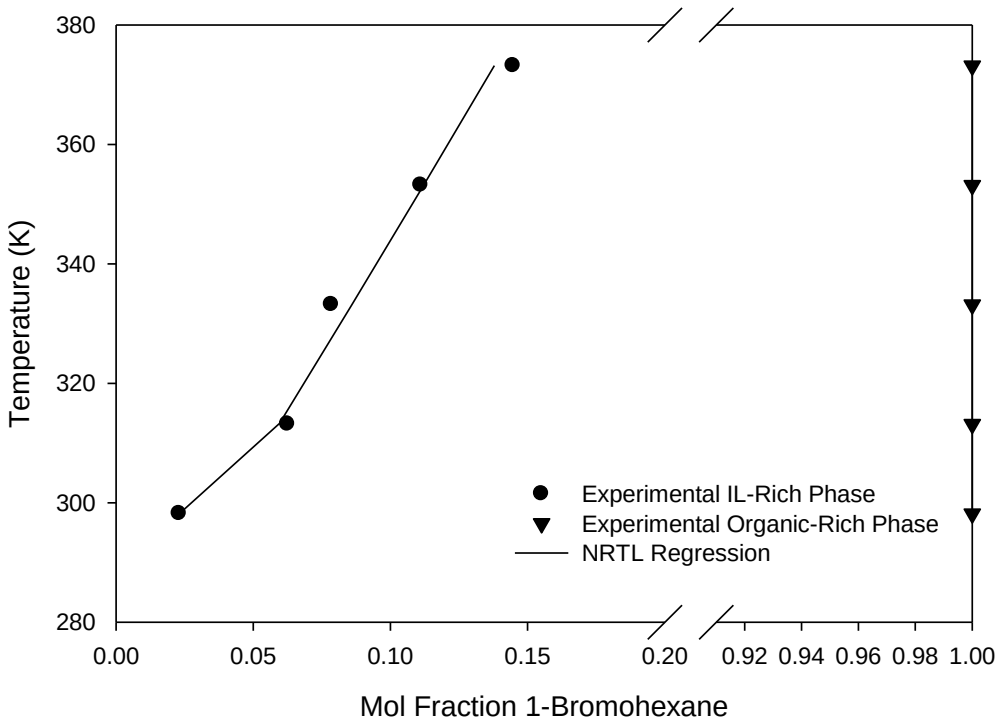

Figure 6.18: Experimental and modeled LLE data for the 1-Bromohexane (1) / [HMIm][Br] (2) system.

	NRTL					
System	A_{12}	A_{21}	B_{12}	B_{21}	*%AARD T*	*%AARD* x_1^{II}
1-Bromohexane (1) + [HMIm][Br] (2)	3.17244	1389.674	1.9620	2589.705	0.02	3.94

Table 6.8: Liquid-liquid equilibrium NRTL regression parameters for the binary 1-bromohexane (1) / [HMIm][Br] (2) system.

6.7.2. 1-Methylimidazole / [HMIm][Br] System

Phase equilibrium for the binary reactant-product mixture of 1-methylimidazole and [HMIm][Br] were measured using the modified Othmer still as the components were completely miscible over the experimental temperature range studied. Much like the solvent-IL systems we observe that the vapor phase consists of pure 1-methylimidazole even at the highest measured mixture

boiling point of 484 K. This is a true indication of the non-volatility which ILs possess. In Figure 6.19 we observe that both models accurately regress the pure 1-methylimidazole vapor phase. However, the NRTL activity coefficient method regressed the bubble point temperature with greater accuracy than the Peng Robinson Equation of State. Therefore, based on these results and those for the solvent-IL systems, the NRTL model is preferred over the PR-EOS. Model results for the activity coefficient and equation of state methods for the 1-methylimidazole/[HMIm][Br] system are displayed in Table 6.9.

System	**NRTL**[a]				**PR-vdW1**		
	Δg_{12}	Δg_{21}	*%AARD*		k_{12}	*%AARD*	
	J/mol	*J/mol*	*T*	y_1		*T*	y_1
1-Methylimidazole (1)/[HMIm][Br] (2)	15130.14	17507.60	0.14	-	0.1340	0.65	0.10

[a] The NRTL α value was set to 0.20

Table 6.9: Regression parameters for the binary 1-methylimidazole (1) / [HMIm][Br] (2) system.

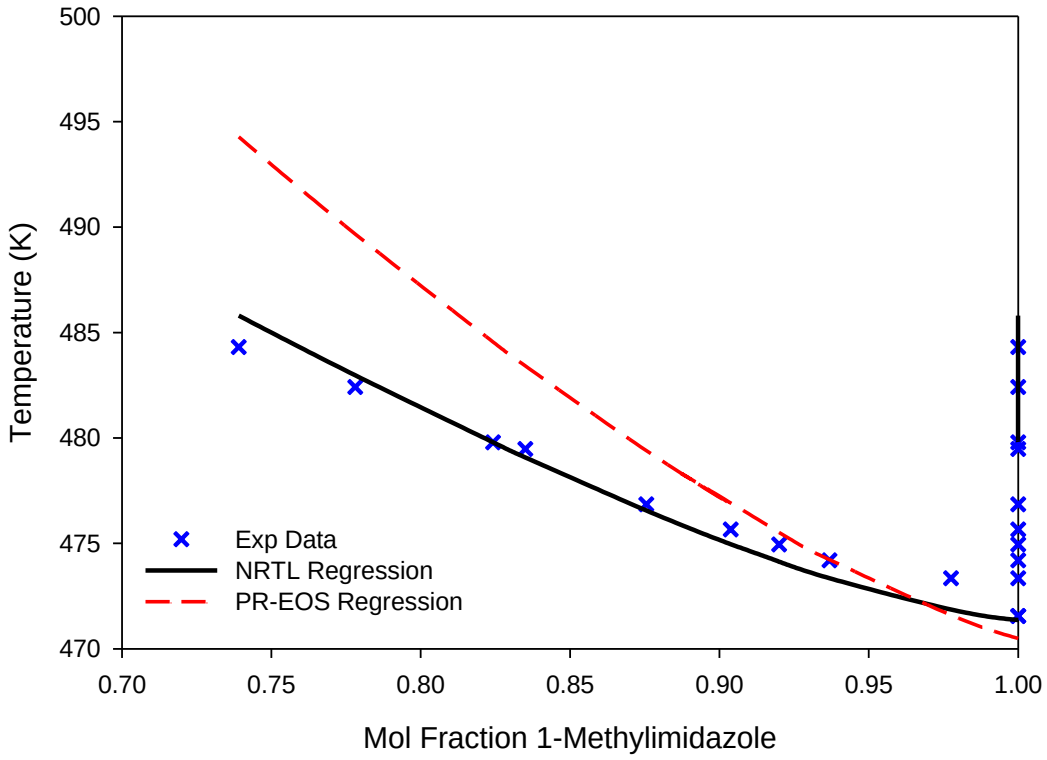

Figure 6.19: Experimental and modeled VLE data for the binary 1-Methylimidazole (1) / [HMIm][Br] (2) system.

6.8. Binary Phase Equilibrium of Ionic Liquid Reactant Molecules

The reactive nature of 1-bromohexane and 1-methylimidazole to make the ionic liquid [HMIm][Br], prevents VLE measurements from being obtained at temperatures that would be encountered at 1.01325 bar. Therefore, we have utilized the UNIFAC predictive activity coefficient model to generate the hypothetical binary vapor-liquid equilibrium data for this system. Figure 6.20 displays the predicted (*Txy*) plot for the 1-bromohexane/1-methylimidazole system.

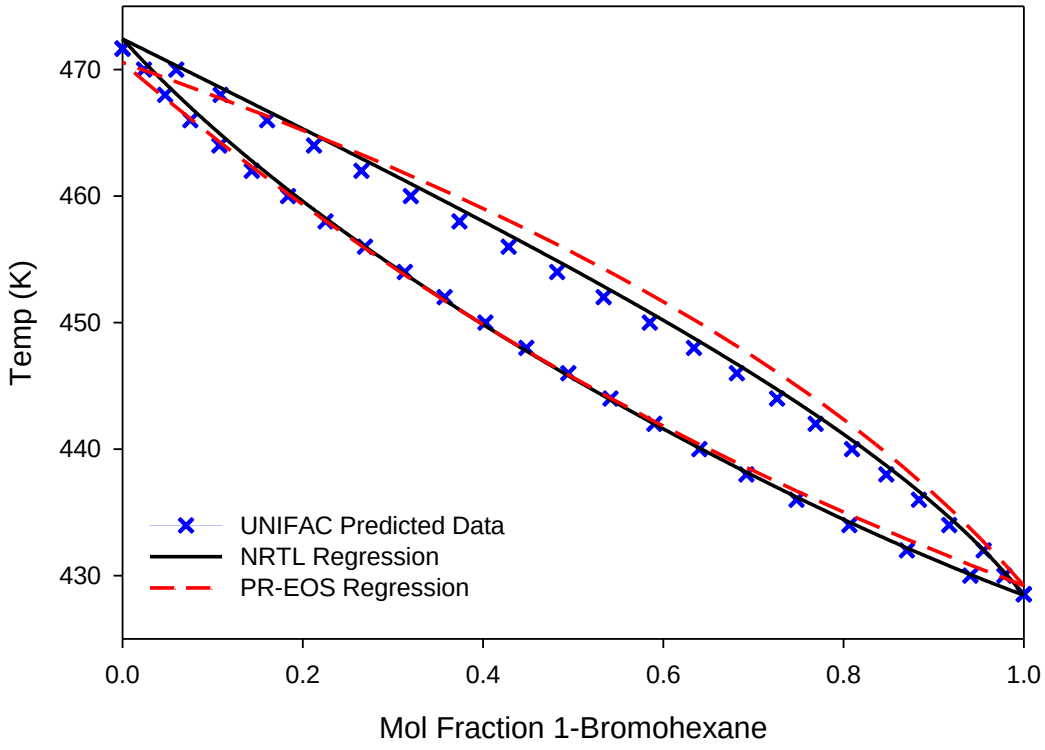

Figure 6.20: UNIFAC computational prediction and modeling of the binary 1-Bromohexane (1) / 1-Methylimidazole (2) system.

To analyze the accuracy of using the UNIFAC model for 1-bromohexane and 1-methylimidazole, we compared our experimentally measured data for the acetone/1-methylimidazole and acetone/1-bromohexane systems to data generated by the UNIFAC predictive model. Generally, UNIFAC was able to yield good correlation of the binary mixtures of the reactants with acetone. For the acetone/1-methylimidazole system, the bubble point temperature curve was elevated in the UNIFAC estimation relative to the experimental data. We believe the error was due to the lack of explicit functional group data for the 1-methylimidazole molecular structure. Current UNIFAC group contribution methods do not allow for exact design of the imidazole ring structure needed to accurately model this molecule. Despite this

discrepancy for 1-methylimidazole we note that the error in dew point temperature was higher than the experimental value. The over-prediction of the bubble point by the UNIFAC model would therefore provide conservative estimates of the amount of energy needed for thermal separation. The NRTL model was fit to this UNIFAC prediction to complete the necessary binary interaction parameters required for a multi-component prediction (see Table 6.10).

System	NRTL[a]				PR-vdW1		
	Δg_{12}	Δg_{21}	%AARD		k_{12}	%AARD	
			T	y_1		T	y_1
1-Bromohexane (1)/1-Methylimidazole (2)	3743.20	-4128.31	0.08[b]	2.79[b]	0.0499	0.09[b]	6.30[b]

[a] The NRTL α value was set to 0.20; [b] as this system cannot be experimentally measured, these results were the deviation between the NRTL model and UNIFAC VLE prediction.

Table 6.10: VLE Regression parameters for the 1-bromohexane/1-methylimidazole system.

Raoult's law analysis of the binary mixture indicated negative deviations indicative of mixture boiling point elevation due to intermolecular interactions between the components. Furthermore, 1-bromohexane and 1-methylimidazole are the highest boiling point components (except for the IL itself) in the synthesis system and will correspondingly require the most energy for removal. This analysis demonstrates the importance of proper reactor design for continuous ionic liquid synthesis. Operating a continuous reactor at high conversion levels will minimize excess reactants for post reaction separation, thus reducing the overall energy consumption of the separation process.

6.9. Summary

Ionic liquids are currently synthesized by batch methodologies with incomplete understanding of the reaction kinetics and phase equilibrium thermodynamics adding to their high costs and small production volumes. To meet the growing demand continuous ionic liquid synthesis methods

will eventually be necessary, requiring complete knowledge of the reaction kinetics, reaction engineering, and post reaction separations characterized by vapor-liquid equilibrium. In an attempt to address the aforementioned limitations, this chapter presents the first comprehensive experimental phase equilibrium study for all components involved in the production of an ionic liquid. Vapor-liquid and liquid-liquid equilibrium measurements were conducted on binary systems involved in the production of the ionic liquid [HMIm][Br] including solvent: reactant, reactant: reactant, solvent: product, and reactant: product mixtures to characterize the separation phenomena of the post-reaction system. Furthermore, four IL synthesis solvents including acetone, acetonitrile, dichloromethane, and dimethyl sulfoxide were investigated to compare the relative impacts of their volatilities on the separation phenomena. For each solvent system VLE experiments were performed on three binary systems including solvent/1-methylimidazole, solvent/1-bromohexane, and solvent/[HMIm][Br]. Additionally, vapor liquid equilibrium measurements were conducted on the 1-methylimidazole/[HMIm][Br] system. A liquid-liquid equilibrium experiment was conducted on the 1-bromohexane/[HMIm][Br] system to study its phase behavior. Finally, the 1-bromohexane/1-methylimidazole system was predicted using the UNIFAC predictive activity coefficient model. When compiled, the phase equilibrium data presented in this study fully characterize a pre- and post-reaction mixture for the production of the ionic liquid [HMIm][Br]. Tables containing the experimental *Txy* data for all experimentally measured systems are presented in Appendix 1.

Raoult's law modeling was conducted on each binary system to obtain a first pass understanding of separation energies required to purify the IL from its reaction mixture. The results indicated that all binary systems except those containing dichloromethane exhibited positive deviations to Raoult's law. Alternatively, mixtures containing dichloromethane exhibited negative deviations

to Raoult's law indicating that the components are increasingly stable in the liquid mixture due to favorable molecular interactions. The experimental phase equilibrium results were also modeled by the Peng Robinson Equation of State and NRTL activity coefficient methods to obtain binary interaction parameters. In general, the NRTL model outperformed the Peng-Robinson EoS model likely due to the increased number of adjustable and temperature dependent parameters it contains. Importantly, the phase equilibrium modeling results, presented herein, have been applied in Chapter 7 to design a continuous IL production process model in Aspen Plus.

References

1. Große Böwing, A. and A. Jess, *Kinetics of single- and two-phase synthesis of the ionic liquid 1-butyl-3-methylimidazolium chloride.* Green Chemistry, 2005. **7**(4): p. 230-235.
2. Große Böwing, A. and A. Jess, *Kinetics and reactor design aspects of the synthesis of ionic liquids—Experimental and theoretical studies for ethylmethylimidazole ethylsulfate.* Chemical Engineering Science, 2007. **62**(6): p. 1760-1769.
3. Hu, S.Z., et al., *Kinetic study of ionic liquid synthesis in a microchannel reactor.* Chemical Engineering Journal, 2010. **162**(1): p. 350-354.
4. Iken, H., et al., *Scalable synthesis of ionic liquids: comparison of performances of microstructured and stirred batch reactors.* Tetrahedron Letters, 2012. **53**(27): p. 3474-3477.
5. Willmes, S. and A. Jess, *Efficient continuous production of ionic liquids in a loop reactor – Experimental and theoretical studies for the example of 1-ethyl-3-methylimidazolium ethyl sulphate.* Chemical Engineering Journal, 2013. **222**(0): p. 198-208.
6. Anastas, P.T. and J.B. Zimmerman, *Design through the 12 principles of green engineering.* Environmental Science & Technology, 2003. **37**(5): p. 94a-101a.
7. Zhang, Y., B.R. Bakshi, and E.S. Demessie, *Life cycle assessment of an ionic liquid versus molecular solvents and their applications.* Environmental Science & Technology, 2008. **42**(5): p. 1724-1730.
8. Paulechka, Y.U., et al., *Thermodynamics of Ionic Liquid Precursors. 1-Bromobutane and Its Isomers.* Journal of Chemical and Engineering Data, 2011. **56**(12): p. 4891-4899.
9. Paulechka, Y.U., et al., *Thermodynamic properties of 1-alkyl-3-methylimidazolium bromide ionic liquids.* Journal of Chemical Thermodynamics, 2007. **39**(1): p. 158-166.
10. Schleicher, J.C. and A.M. Scurto, *Kinetics and solvent effects in the synthesis of ionic liquids: imidazolium.* Green Chemistry, 2009. **11**(5): p. 694-703.
11. Nwosu, S., *Environmentally Benign Production of Ionic Liquids in CO2-Expanded Systems*, in *C&PE*2012, University of Kansas.
12. Slater, C.S. and M. Savelski, *A method to characterize the greenness of solvents used in pharmaceutical manufacture.* Journal of Environmental Science and Health Part a-Toxic/Hazardous Substances & Environmental Engineering, 2007. **42**(11): p. 1595-1605.
13. Hiaki, T., K. Kurihara, and K. Kojima, *Vapor-Liquid-Equilibria for Acetone Plus Chloroform Plus Methanol and Constituent Binary-Systems at 101.3 kPa.* Journal of Chemical and Engineering Data, 1994. **39**(4): p. 714-719.
14. Orchilles, A.V., et al., *Ionic liquids as entrainers in extractive distillation: Isobaric vapor-liquid equilibria for acetone plus methanol plus 1-ethyl-3-methylimidazolium trifluoromethanesulfonate.* Journal of Chemical and Engineering Data, 2007. **52**(1): p. 141-147.
15. Li, Q.S., et al., *Isobaric vapor-liquid equilibrium for methanol+benzene+1-octyl-3-methylimidazolium tetrafluoroborate.* Korean Journal of Chemical Engineering, 2012. **29**(7): p. 941-945.

16. Liu, X.L., Z.; Wang, T.; Li, Q.; Zhu, J., *Isobaric Vapor-Liquid Equilibrium for the Ethanol + Water + 2-Aminoethanol Tetrafluoroborate System at 101.3 kPa.* Journal of Chemical & Engineering Data, 2012.
17. Calvar, N., et al., *Vapor-liquid equilibria for the ternary system ethanol plus water plus 1-butyl-3-methylimidazolium chloride and the corresponding binary systems at 101.3 kPa.* Journal of Chemical and Engineering Data, 2006. **51**(6): p. 2178-2181.
18. Nwosu, S.O., J.C. Schleicher, and A.M. Scurto, *High-pressure phase equilibria for the synthesis of ionic liquids in compressed CO2 for 1-hexyl-3-methylimidazolium bromide with 1-bromohexane and 1-methylimidazole.* Journal of Supercritical Fluids, 2009. **51**(1): p. 1-9.
19. Verevkin, S.P., et al., *Thermodynamics of Ionic Liquids Precursors: 1-Methylimidazole.* Journal of Physical Chemistry B, 2011. **115**(15): p. 4404-4411.
20. Rudine, A.B., M.G. Walter, and C.C. Wamser, *Reaction of Dichloromethane with Pyridine Derivatives under Ambient Conditions.* Journal of Organic Chemistry, 2010. **75**(12): p. 4292-4295.
21. Zhang, Y., et al., *CO2 Capture by imidazolate-Based Ionic Liquids: Effect of Functionalized Cation and Dication.* Industrial & Engineering Chemistry Research, 2013. **52**(18): p. 6069-6075.
22. Zhao, D.S., et al., *Synthesis, characterization, and properties of imidazole dicationic ionic liquids and their application in esterification.* Chemical Engineering Journal, 2013. **221**: p. 99-104.
23. Zhang, Y., et al., *Synthesis and thermophysical properties of imidazolate-based ionic liquids: Influences of different cations and anions.* Journal of Chemical Thermodynamics, 2014. **74**: p. 209-215.
24. Petek, A.S., et al., *Distillation of water-N-methylimidazole system.* Acta Chimica Slovenica, 2001. **48**(4): p. 515-520.
25. Almeida, A.R.R.P. and M.J.S. Monte, *Thermodynamic study of phase transitions of imidazoles and 1-methylimidazoles.* The Journal of Chemical Thermodynamics, 2012. **44**(1): p. 163-168.
26. Rebelo, L.P.N., et al., *On the Critical Temperature, Normal Boiling Point, and Vapor Pressure of Ionic Liquids.* The Journal of Physical Chemistry B, 2005. **109**(13): p. 6040-6043.
27. Rocha, M.A.A., et al., *High-Accuracy Vapor Pressure Data of the Extended [CnC1im][Ntf_2] Ionic Liquid Series: Trend Changes and Structural Shifts.* The Journal of Physical Chemistry B, 2011. **115**(37): p. 10919-10926.
28. Zaitsau, D.H., et al., *Experimental Vapor Pressures of 1-Alkyl-3-methylimidazolium Bis(trifluoromethylsulfonyl)imides and a Correlation Scheme for Estimation of Vaporization Enthalpies of Ionic Liquids.* The Journal of Physical Chemistry A, 2006. **110**(22): p. 7303-7306.
29. Maia, F.M.C., N.; Gonzalez, E.J.; Carneiro, A.P.; Rodriguez, O.; Macedo, E.A., *Modeling of Ionic Liquid Systems: Phase Equilibria and Physical Properties*, in *Ionic Liquids - New Aspects for the Future*, J.-i. Kadokawa, Editor. 2013, InTech.

30. Li, Q., et al., *Effect of Ionic Liquids on the Isobaric Vapor–Liquid Equilibrium Behavior of Methanol–Methyl Ethyl Ketone.* Journal of Chemical & Engineering Data, 2013. **58**(5): p. 1133-1140.
31. Arce, P.F., et al., *Modeling of high-pressure vapor–liquid equilibrium in ionic liquids + gas systems using the PRSV equation of state.* Fluid Phase Equilibria, 2010. **295**(1): p. 9-16.
32. Macías-Salinas, R., et al., *Accurate Modeling of CO_2 Solubility in Ionic Liquids Using a Cubic EoS.* Industrial & Engineering Chemistry Research, 2013. **52**(22): p. 7593-7601.
33. Ren, W. and A.M. Scurto, *Phase equilibria of imidazolium ionic liquids and the refrigerant gas, 1,1,1,2-tetrafluoroethane (R-134a).* Fluid Phase Equilibria, 2009. **286**(1): p. 1-7.

7. Process and Life Cycle Assessment Modeling for the Continuous Production of Model Ionic Liquid [HMIm][Br]

Utilization of ionic liquids on industrial scales will require efficient, continuous production methods. Yet, ILs are currently produced in small quantities by batch methods and relatively few studies have investigated the scale-up of IL synthesis.[1-3] Furthermore, laboratory based ionic liquid synthesis procedures utilize many of the hazardous solvents that ILs are intended to replace, most notably including dichloromethane. Solvents serve a vital role in the IL synthesis process by bringing the reaction into a single phase, accelerating the reaction rate, and quenching exothermic heat effects. However, ionic liquid purification requires removal of the volatile solvent and unconverted reactants. Therefore, solvent selection for IL synthesis requires an optimization of kinetic, thermodynamic, economic, and environmental aspects. To investigate the continuous synthesis of an ionic liquid, Aspen Plus process models were developed for the production of [HMIm][Br] from 1-methylimidazole and 1-bromohexane in a solvent mediated reaction. The solvents investigated include: acetone, acetonitrile, dichloromethane, and dimethyl sulfoxide. The goal of this study was to investigate the impact of solvent selection on the reactor size and energy consumption of a theoretical isothermal reaction process coupled with flash distillation producing approximately 30 metric tons of 99% pure [HMIm][Br] per day.

7.1. Process Model Overview

The process model, shown in Figure 7.1, was applied to all four solvent systems and consists of three feed streams including the reactants 1-bromohexane and 1-methylimidazole as well as the solvent. In this first pass approach, the solvent was fed into the reactor in a 1:1 mole ratio with

reactant 1-bromohexane. Therefore, the total feed into the reactor consisted of an equal molar mixture of 1-bromohexane, 1-methylimidazole, and the reaction solvent. The reactants and solvent entered the process at 25^{o}C and 1.01325 bar and were pressurized to maintain a liquid phase reaction. For temperatures below the pure solvent boiling point, a pressure of 1.5 bar was utilized for safety purposes. However, when the reaction temperature exceeded the pure solvent boiling point, overpressure was applied to maintain the liquid phase. After pressurization, the reactants and solvents were heated to the desired reaction temperature using process steam. Subsequently, the raw materials were combined at a mixing point and fed to the plug flow reactor. The PFR reactor was designed to achieve 99% conversion at the specified temperatures of 50^{o}C and 100^{o}C. The post-reaction mixture was fed into a flash unit which utilized a thermally driven separation mechanism for all solvent systems except DMSO which required vacuum operation. The distillate, composed primarily of the reaction solvent with trace quantities of 1-bromohexane and 1-methylimidazole, was cooled and pressurized prior to entering a purge unit to remove degradation products from the system. The solvent recycle stream was then reheated to the process temperature and fed into the mixing point. The purified ionic liquid (99 mass% minimum) was recovered from the bottom of the flash unit and cooled to 25^{o}C in preparation for distribution. The process unit specifications within the simulation varied depending on the solvent and operating conditions selected and are described in greater detail within the following sections.

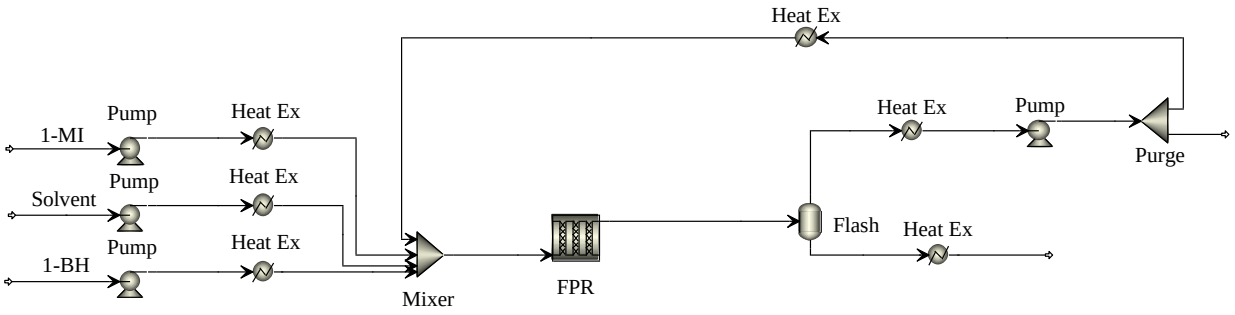

Figure 7.1: Aspen Plus process model for the continuous synthesis of [HMIm][Br].

7.2. Isothermal Plug Flow Reactor Sizing

Plug flow reactions occur in tubular geometries under laminar flow conditions where perfect radial mixing is assumed with negligible axial mixing. Therefore, conversion of reactants to products is a function of residence time (*i.e.* reactor length for a constant area pipe). A schematic of a typical PFR reactor is displayed in Figure 7.2 for theoretical component (*A*) where inlet mass flow rate of component (*A*) is F_{Ao} and outlet mass flowrate of component (*A*) is defined by F_A. Heat and work flows into/out of the reactor are defined by $\dot{Q}$ and $\dot{W}$ respectively.

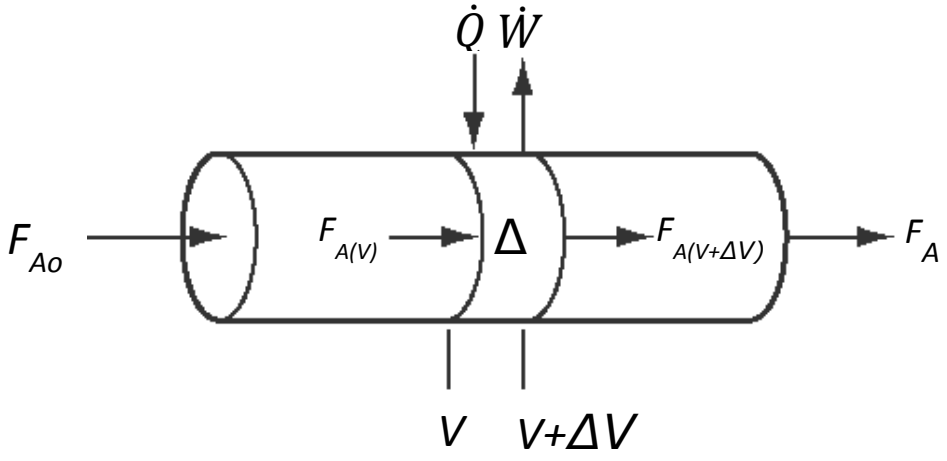

Figure 7.2: Plug flow reactor schematic.

The general PFR mass balance equation is displayed in Eqn. 7.1. At steady state accumulation equals zero and the rate of generation is determined by the reaction kinetics.

$$In - Out + Generation = Accumulation \quad \text{Eqn. 7.1}$$

For a plug flow reaction at steady state the mass balance equation is expressed in terms of theoretical component (*A*) in Eqn. 7.2 where (r_A) is the reaction rate and (*dV*) is the incremental volume in which the reaction takes place.

$$F_{Ao} - F_A + \int r_A dV = 0 \quad \text{Eqn. 7.2}$$

From Eqn. 7.2 the general PFR reactor sizing equation can be developed in terms of conversion and is shown in Eqn. 7.3.

$$dV = F_{Ao} \int_0^X \frac{dX}{-r_A} \quad \text{Eqn. 7.3}$$

The synthesis of ionic liquid [HMIm][Br] occurs by a reaction which is first order in terms of each reactant and second order overall per the general expression shown in Eqn. 7.4.

$$-r_A = kC_A C_B \quad \text{Eqn. 7.4}$$

In terms of conversion, the second order rate expression is shown in Eqn. 7.5.

$$-r_A = kC_{Ao} C_{Bo} (1 - X)^2 \quad \text{Eqn. 7.5}$$

Therefore, for an isothermal liquid phase reaction with negligible change in volumetric flowrate the PRF reactor sizing equation can be solved analytically for a desired level of conversion. The isothermal PFR sizing equation used to design the reactors in this study is expressed in Eqn. 7.6.

$$V = \frac{F_{Ao}}{kC_{Ao}C_{Bo}}\left[\frac{X}{(1-X)}\right] \qquad \text{Eqn. 7.6}$$

The second order reaction was modeled by a power law methodology by Schleicher *et al.* as shown in Eqn. 7.7 with the parameters displayed in Table 7.1.[4]

$$k = k_o e^{\left(\frac{-E_A}{RT(K)}\right)} \qquad \text{Eqn. 7.7}$$

Solvent	$\mathbf{k_o\ x\ 10^{-6}\ \left(\frac{1}{M.sec}\right)}$	$\mathbf{E_A\ \left(\frac{kJ}{mol}\right)}$
Acetone	2.20	67.26
Acetonitrile	6.51	68.73
Dichloromethane	1.85	67.98
Dimethyl Sulfoxide	2.51	63.05

Table 7.1: Kinetic parameters for the synthesis of [HMIm][Br] in select solvent systems.[4]

Based on the methodology presented above, PFR reactors were sized to achieve 99% conversion of 1-bromohexane and 1-methylimidazole assuming an equal molar feed of reactants $\left(C_{Ao} = C_{Bo} = 2.95\ \frac{mol}{L}\right)$ and a total flowrate into the reactor (F_{Ao}) of 1.405 $\frac{mol}{sec}$. These quantities were computed with the intention of producing 30 metric tons of [HMIm][Br] per day.

As previously discussed, reaction rate, and therefore reactor size, are highly dependent on the selected reaction solvent. The effect of solvent selection on reactor volume to achieve a desired level of conversion at a constant temperature of 50^{o}C is displayed in Figure 7.3.

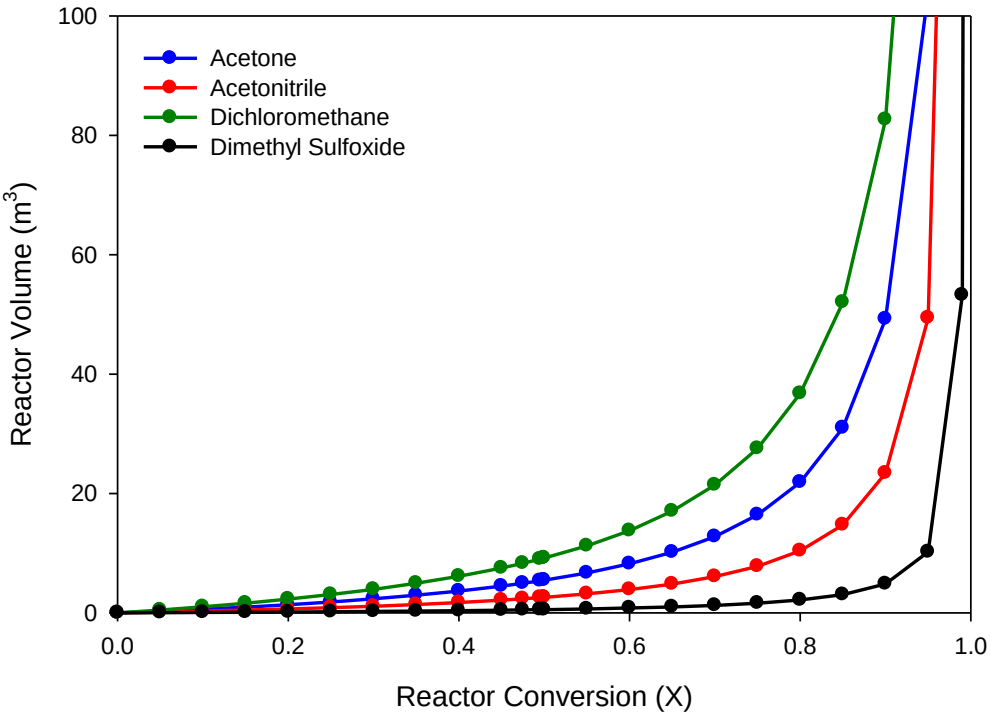

Figure 7.3: Isothermal PFR reactor volume for the production of [HMIm][Br] at 50°C as a function of solvent selection.

The results demonstrate that the plug flow reactor volume increases exponentially (at a fixed temperature) as higher levels of conversion are demanded due to the decrease in reactant concentration and concomitant reduction in reaction rate at extended reactor lengths. Therefore, desiring near quantitative conversion of reactants in plug flow reactor geometry can cause the reactor to become exponentially large. However, the reactor size can also be reduced by raising the reaction temperature as shown for the acetonitrile solvent system in Figure 7.4.

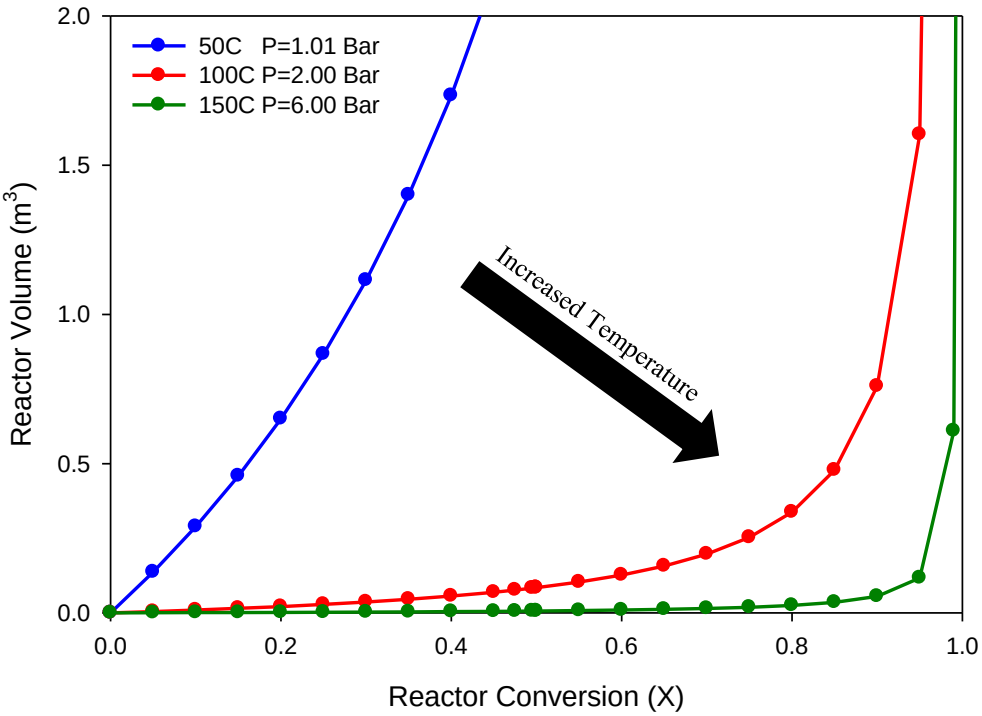

Figure 7.4: Isothermal PFR reactor volume for the production of [HMIm][Br] in acetonitrile as a function of temperature.

Whereas at 50°C a reactor volume of 2 m^3 is only able to achieve approximately 42% conversion for the acetonitrile system, at 100°C the reaction conversion reaches 96% at this same reactor volume. Furthermore, at 150°C a reaction conversion of 99.9% is achieved with a reactor volume of only 0.78 m^3. These results indicate that elevating the reaction temperature has a significant effect on reactor size. However, increased temperature also has several negative impacts on the reaction process. For instance, quaternization reactions are highly exothermic. Therefore, accelerating the rate by increased reaction temperature could lead to a runaway reaction scenario; especially if the rate of cooling is unable to exceed the rate of heat generation. Additionally, ILs including [HMIm][Br] thermally decompose at temperatures above

approximately 200°C indicating that operating conditions should avoid elevated temperatures when possible. Based on these criteria, isothermal reaction conditions of 50°C and 100°C were selected to examine the continuous production of [HMIm][Br]. Table 7.2 displays the reactor sizes (volumes) and process unit costs at these two temperatures necessary to achieve 99% conversion of 1-bromohexane and 1-methylimidazole.

Solvent	V_R (m^3) (99% Conversion)		Reactor Price (USD)	
	50°C	100°C	50°C	100°C
Acetone	103.9	3.6	160,800	33,700
Acetonitrile	49.4	1.6	97,600	31,200
Dichloromethane	174.4	5.9	235,100	43,300
Dimethyl Sulfoxide	10.2	0.4	48,200	20,200

Table 7.2: Effect of temperature and solvent selection on reactor volume. Reactor price calculated by the Aspen Plus economics package.

As expected, the fastest reaction kinetics required the smallest and least expensive reactor geometries. Reactor size increased in the following order based on the selected reaction solvent: dimethyl sulfoxide < acetonitrile < acetone < dichloromethane. Therefore, as previously discussed, while dichloromethane is an optimal solvent from a separation perspective, the kinetics and reactor size are the least favorable of the solvents investigated. The results also demonstrate that elevated reaction temperatures significantly reduce the size and cost of the PFR equipment.

7.3. Isothermal Plug Flow Reactor Heat Duty

The synthesis of [HMIm][Br] from 1-bromohexane and 1-methylimidazole is highly exothermic and therefore must be cooled in order to prevent thermally accelerated reaction rates and potential runaway reactions. The heat of reaction can be calculated from the heats of formation

of the various reactants and products at 298K. The heat of formation of [HMIm][Br] has not been experimentally measured but has been estimated by the Joback group contribution method. The estimated heat of formation value of [HMIm][Br] at 298K and 1.01325 bar was -134.32 $\frac{\text{kJ}}{\text{mol}}$ which is similar to the experimental value measured for a [BMIm][Br] $\Delta H_f = -96 \frac{\text{kJ}}{\text{mol}}$ an analogous ionic liquid with butyl alkyl chain functionality as opposed to hexyl in [HMIm][Br].[5] Furthermore, Verevkin *et al*. found that a linear correlation exists between cation alkyl chain length and liquid phase IL heat of formation at 298K indicating that [HMIm][Br] is expected to have a larger heat of formation than [BMIm][Br] and that the estimated value, presented herein, is reasonably accurate.[6] Based on these calculations the required cooling duty for the isothermal reactor can be determined by Eqn. 7.10.

$$\frac{dT}{dV} = \frac{Ua(T_a - T) + r_A(\Delta H_{rxn})}{F_{Ao} \sum C_{pi} + \Delta C_p X} \qquad \text{Eqn. 7.10}$$

For an isothermal reaction the temperature is constant along the volume (*i.e.* length) of the reactor making $\left(\frac{dT}{dV}\right)$ equal to zero. Thus, the minimum quantity of heat removal for the reaction is equal to the quantity of heat generated by the reaction. For the two temperature conditions investigated herein, the reaction conversion was maintained constant by varying the reactor size; thus, the heat generated by the reaction was also constant for all systems involved. The required cooling duty predicted by Aspen Plus for the synthesis of [HMIm][Br] was approximately -167.8 $\frac{kJ}{mol\ IL}$ for all solvent systems at both 50^{o}C and 100^{o}C which is slightly greater than what was predicted by the heat of formation of the IL. This difference could be due to a combination of effects including heat of mixing (*i.e.* partial molar enthalpies) of the reactants, solvent, and

product as well as the required heat of reaction adjustment with respect to temperature which is a function of individual pure component heat capacities.

7.4. Isothermal Flash Calculations

Following production of [HMIm][Br] in the plug flow reactor the post-reaction mixture was sent to a flash vessel where the IL was purified by thermal and (if necessary) vacuum methods. In all simulations the flash calculations were conducted in Aspen Plus based on the experimental NRTL thermodynamic modeling presented in sections 6.5 thru 6.8. The flash calculations utilized an "inside-out" iterative algorithm which first computed K-values followed by computation of mass and energy balances. Pre-defined product specifications required the production of 99 mass% pure [HMIm][Br] and therefore the flash temperature and pressure were set to achieve this condition. The flash temperatures, pressures, and heat duties required to purify [HMIm][Br] are displayed in Table 7.3.

Solvent	Flash Temp [^{o}C]	Flash Pressure [bar]	Separation Energy (kJ/mol IL)	
			50^{o}C Rxn	100^{o}C Rxn
Acetone	125	1.01325	79.7	46.6
Acetonitrile	145	1.01325	89.9	60.8
Dichloromethane	120	1.01325	74.2	43.6
Dimethyl Sulfoxide	190	0.15	292.0	240.9

Table 7.3: Flash conditions to produce 99 mass% pure [HMIm][Br] from the post-reaction synthesis stream.

For the acetone, acetonitrile, and dichloromethane solvent systems, thermally driven separations at temperatures well below 200^{o}C were sufficient to purify [HMIm][Br] to 99 mass% from the reaction mixture. Alternatively, dimethyl sulfoxide required vacuum flash operation to remove the high boiling solvent from the IL while maintaining temperatures below 200^{o}C. The flash

temperature and required heat duties trend in the general order of increasing pure component boiling point for each solvent (*i.e.* dichloromethane < acetone < acetonitrile << dimethyl sulfoxide). Schleicher *et al.* previously calculated the separation energy for purifying [HMIm][Br] from the reaction solvent using latent and sensible heats of vaporization. His results, based on a 40^{o}C reaction temperature, found that the separation energies required for IL purification were $Q_{(DCM)}$ = 56.12 kJ/mol IL, $Q_{(Acetone)}$ = 62.32 kJ/mol IL, $Q_{(ACN)}$ = 67.18 kJ/mol IL, and $Q_{(DMSO)}$ = 131.78 kJ/mol IL (values have been adjusted to reflect separation of a 2:1 solvent: IL molar ratio). Therefore, while the trend of separation energies determined by the heats of vaporization are in agreement with the NRTL calculations, the ideal method significantly under predicted the required quantity of energy necessary to separate the IL and reaction solvent. The strong intermolecular interactions between solvent and ionic liquid molecules in solution were previously found to generate significant boiling point elevation of the solvent when mixed with the ionic liquid. This potentially explains why the rigorous methods estimate that more separation energy is required for IL purification than what is predicted by ideal calculation methods based on latent and sensible heats of vaporization of the pure solvent.

7.5. Mass and Energy Balances for the Continuous IL Synthesis Process

Mass balance results from the Aspen Plus simulations for reactants, products, and solvent entering and exiting the process are displayed for the various solvent systems at 50^{o}C in Tables 7.4 to 7.7. The feed and product specifications at the 100^{o}C operating temperature were nearly identical to the 50^{o}C results due to the modified reactor and flash unit design to meet the desired [HMIm][Br] product specifications and therefore have not been shown. Importantly, the process has been designed to maintain a 1:1 mole solvent: 1-bromohexane ratio. Therefore, while only

small quantities of solvent are fed to the process, 5,057.4 $\frac{mol}{hr}$ continuously circulate through the reactor based on an initial solvent loading. The purge stream was specified to remove 5% of the distillate leaving the flash unit to extract any inert or volatile decomposition products formed in the process. This stream was primarily composed of the reaction solvent with some trace quantities of 1-bromohexane. With the exception of the DMSO solvent system, the flash unit temperature was not sufficient to volatilize 1-methylimidaozle and therefore all unreacted 1-MI exited in the product stream. Despite specifying the vapor pressure and BIP's to approximate the IL as being non-volatile, trace quantities were observed in the vapor phase exiting the flash unit as a consequence of the non-conventional nature of ionic liquids and moderate incompatibility with Aspen simulations. Therefore, small quantities of IL exiting the purge unit in the vapor phase (*i.e.* less than 1% of the flash unit feed) were observed for all systems and temperatures. While this theoretically should not occur, it is likely that in an actual process some IL will enter the vapor phase through entrainment thus rationalizing the observed results.

Component	Feed (In) (kg/hr)	Product (Out) (kg/hr)	Purge (Out) (kg/hr)
1-bromohexane	834.77	4.50	3.61
1-methylimidazole	415.18	4.05	0.00
[HMIm][Br]	0.00	1237.79	0.03
Acetone	19.17	3.81	15.36

Table 7.4: Mass balance results for the acetone solvent mediated [HMIm][Br] synthesis reaction at 50^{o}C.

Component	Feed (In) (kg/hr)	Product (Out) (kg/hr)	Purge (Out) (kg/hr)
1-bromohexane	834.77	2.22	3.68
1-methylimidazole	415.18	2.94	0.00
[HMIm][Br]	0.00	1241.10	0.12
Acetonitrile	16.91	6.80	10.11

Table 7.5: Mass balance results for the acetonitrile solvent mediated [HMIm][Br] synthesis reaction at 50^{o}C.

Component	Feed (In) (kg/hr)	Product (Out) (kg/hr)	Purge (Out) (kg/hr)
1-bromohexane	834.77	3.56	3.37
1-methylimidazole	415.18	3.45	0.00
[HMIm][Br]	0.00	1239.58	0.03
Dichloromethane	26.07	4.90	21.17

Table 7.6: Mass balance results for the dichloromethane solvent mediated [HMIm][Br] synthesis reaction at 50^{o}C.

Component	Feed (In) (kg/hr)	Product (Out) (kg/hr)	Purge (Out) (kg/hr)
1-bromohexane	834.77	0.75	12.10
1-methylimidazole	415.18	6.15	0.25
[HMIm][Br]	0.00	1218.27	12.41
Dimethyl Sulfoxide	36.33	17.32	19.01

Table 7.7: Mass balance results for the dimethyl sulfoxide solvent mediated [HMIm][Br] synthesis reaction at 50^{o}C.

Energy balance results for the process units including: pumps, heat exchangers, reactors, and flash units are displayed in tables 7.8 and 7.9 for the 50^{o}C and 100^{o}C reaction conditions respectively. Power supplied to pumps within the system for pressurization of the feed and recycle streams required relatively negligible energy quantities compared to the reactor and flash unit heat duties. Small heat duties were required by the heat exchangers which brought the reactants and solvent to the desired reaction temperature. Comparing Table 7.8 and Table 7.9 demonstrates that a non-negligible difference in energy is consumed by heating the components to 50^{o}C vs. 100^{o}C due to the change in sensible heat. However, the difference in heat duty experienced by the pre-heating process units are recovered within a few percent by the flash unit heat duty which is lower at the 100^{o}C operating condition relative to 50^{o}C due to the higher temperatures and enthalpies of the reactor effluent entering the flash drum.

The isothermal reactor unit consumed the most energy to cool the exothermic ionic liquid synthesis reaction. Cooling energy of approximately -167 kJ/mol of IL produced was required to maintain the isothermal reaction conditions independent of solvent selected or operating

temperature. The reactor cooling duty accounted for approximately half of the total energy consumed by the process. The second largest energy consuming process was the flash unit which varied depending on the solvent. The flash unit consumed between 25 and 30 percent of the total energy input to the process with the exception of the DMSO systems which required significantly greater duties. The mass and energy flows presented have been used as the inputs for the life cycle assessment comparing the various IL synthesis methods and solvent selection.

Process Unit	Acetone (kJ/mol IL)	Acetonitrile (kJ/mol IL)	Dichloromethane (kJ/mol IL)	Dimethyl Sulfoxide (kJ/mol IL)
Pumps	0.03	0.03	0.05	0.03
Heaters	10.85	10.78	12.96	8.65
Coolers	-43.28	-43.50	-39.96	-155.85
Reactor	-170.44	-167.66	-168.36	-168.07
Flash Unit	79.74	89.94	74.20	291.96

Table 7.8: Energy balance for process units at the 50^{o}C reaction condition.

Process Unit	Acetone (kJ/mol IL)	Acetonitrile (kJ/mol IL)	Dichloromethane (kJ/mol IL)	Dimethyl Sulfoxide (Q) (kJ/mol IL)
Pumps	0.16	0.04	0.26	0.03
Heaters	42.08	39.49	42.25	26.89
Coolers	-88.67	-101.58	-87.78	-241.65
Reactor	-168.40	-166.79	-166.57	-168.46
Flash Unit	46.62	60.82	43.61	240.85

Table 7.9: Energy balance for process units at the 100^{o}C reaction condition.

7.6. Optimization of Reaction and Separation Process

In this first pass approach to continuous ionic liquid synthesis process modeling several design assumptions were made. For instance, the plug flow reactor was sized to achieve 99% conversion of 1-bromohexane and 1-methylimidazole with the intention of reducing the quantity of unconverted reactants fed into the flash unit. While this design specification reduced the separation temperature and energy demand, the capital costs required to design the reactor were

significantly larger than what would have been observed at lower conversion levels. Additionally, an isothermal reactor design was selected to quickly compute the reactor size and heat duties. However, "real" reactors do not operate under completely isothermal conditions. Instead, cooling fluid is applied co- or counter- current to the process stream to remove heat from the reactor. Furthermore, select reactions can be run adiabatically (*i.e.* without heat removal). In theory an adiabatic reactor could be utilized for IL synthesis but careful calculation of mass and energy balance would be required to ensure safe operating conditions and prevent the possibility of a runaway reaction scenario. A second significant assumption specified in this initial case study required the [HMIm][Br] product to be at minimum 99 mass% pure. Based on this criterion the operating temperature and pressure of the flash unit were specified. While ionic liquid performance is directly correlated to its purity, an economic evaluation of market demand, IL purity, and IL price must be conducted. Future iterations of the project should consider optimization of the product purity as well as optimization of the flash unit operating temperature and pressure. Finally, rigorous design of a continuous IL synthesis process requires optimization of the process units and operating conditions with constraints such as the minimization of operating and capital cost. A full economic optimization is beyond the scope of this study but has been proposed for future work.

7.7. Life Cycle Assessment for the Continuous Production of [HMIm][Br]

Ionic liquids have been proclaimed as environmentally friendly "green" solvents in large part due to their negligible vapor pressures. However, while non-volatility does eliminate the environmental impact of vapor phase emissions, many other factors contribute to the sustainability of a molecule. Life cycle assessment (LCA) is the methodology by which the

comprehensive environmental impact of a molecule is determined. Three common types of LCA's exist including: cradle-to-gate, gate to gate, and cradle to grave. Cradle-to-gate investigates the synthesis and production of a particular chemical but omits the use and disposal impacts. A gate-to-gate LCA investigates only the hazards associated with the use of a particular chemical and omits both the production and disposal processes. Finally, a cradle-to-grave LCA accounts for all parts of a chemical's life including synthesis, application, and disposal. To this point, few studies have applied life cycle assessment methodology to ionic liquids.[7-10] Furthermore, even fewer studies have investigated the environmental impacts of ionic liquid synthesis primarily due to the lack of mass and energy balance data as well as limited life cycle impact data on precursor molecules which ILs are produced from.[11]

In the production of [HMIm][Br] 1-bromohexane and 1-methylimidazole are reacted in the presence of a solvent to mitigate heat effects. While a range of polar solvents concomitantly accelerate and quench the exothermic reaction, dichloromethane has been commonly selected for laboratory scale production due to its high vapor pressure; allowing relative ease of removal from the IL product. Despite its advantageously high volatility, DCM is a known carcinogen and demonstrates high levels of ecological and human toxicity. Therefore, when synthesized by a route utilizing DCM the IL is potentially less sustainable compared to its production in other synthesis solvents. Alternatively, dimethyl sulfoxide is a non-toxic, environmentally benign solvent which promotes the fastest [HMIm][Br] synthesis kinetics. However, DMSO boils at 180^{o}C making separations increasingly energy intensive; thus, potentially penalizing IL synthesis with this solvent. A comprehensive cradle to gate LCA is presented herein according to ISO 14040 guidelines for the production of [HMIm][Br] in four solvents including acetone,

acetonitrile, dichloromethane, and dimethyl sulfoxide to assess the impacts of continuous IL synthesis in various solvents.[12]

7.7.1. Goal

This study was intended to comparatively analyze the environmental impacts associated with synthesizing the ionic liquid [HMIm][Br] in a range of solvents including acetone, acetonitrile, dichloromethane, and dimethyl sulfoxide. The product of this report provides a definitive solvent recommendation for ionic liquid synthesis. Additionally, the results are intended to allow future life cycle assessments to compare the impacts of producing an ionic liquid to the impacts associated with the synthesis of common organic chemicals. A detailed report is provided to guide the scientific community in future research efforts investigating ionic liquid synthesis and applications. Finally, the report is intended to guide the future efforts of private industry in developing a continuous IL synthesis process.

7.7.2. Scope and System Boundary

The scope of this LCA study includes the cradle to gate life cycle assessment impacts pertaining to the synthesis of the ionic liquid [HMIm][Br]. The system boundaries are defined to contain all mass and energy flows necessary to produce the ionic liquid, precursor molecules 1-bromohexane and 1-methylimidazole, and the reaction solvent involved in the IL synthesis process. The system boundaries are displayed in Figure 7.5.

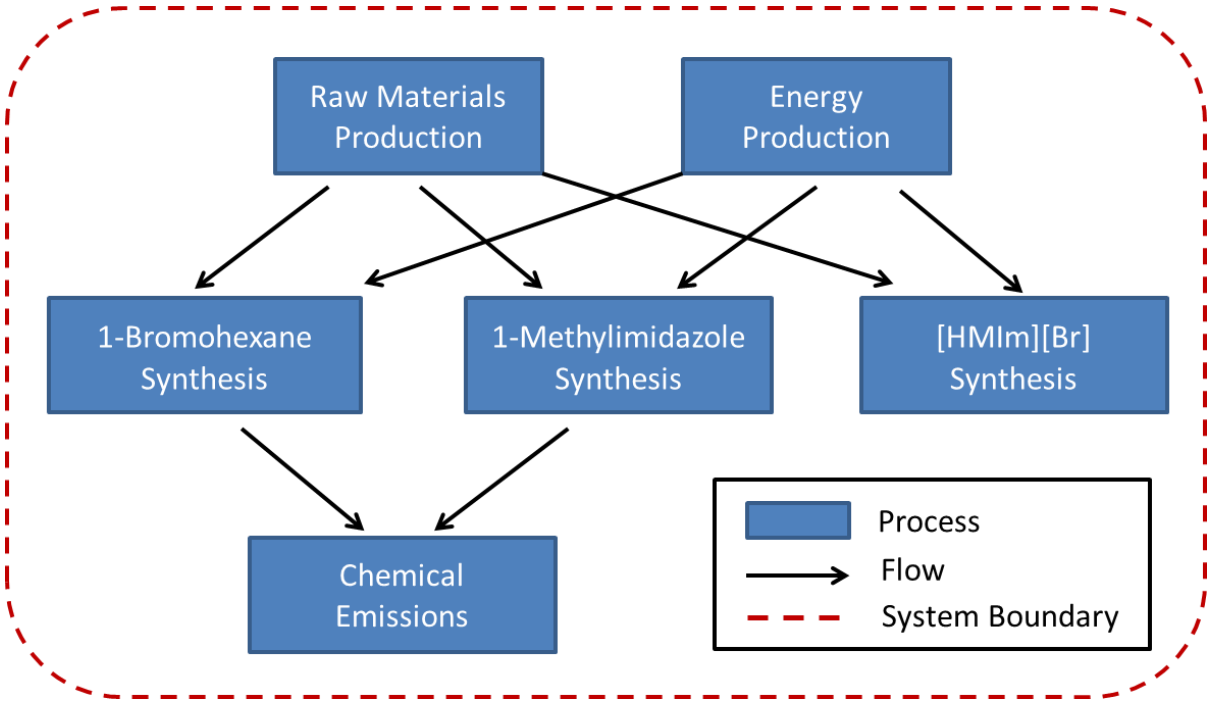

Figure 7.5: LCA System boundary for the continuous [HMIm][Br] production.

7.7.3. Functional Unit

The functional unit selected for this study was 1 kg of 99 mass% pure [HMIm][Br]. The functional unit is appropriate as the quantity 99% pure ionic liquid produced is the driving force for all raw material and energy inputs.[13] Finally, the selected functional unit will allow for a fair comparison between the four synthesis solvents and reaction conditions probed in this study by encompassing key areas where each system differs, especially including heat duties for the IL purification process and the environmental impacts of the reaction solvents.

7.7.4. Impact Categories

Life cycle inventories utilized in this study were obtained from the EcoInvent database using the SimaPro life cycle assessment software suite. The impact categories represent a midpoint level

approach to LCA modeling and utilize the U.S. EPA developed TRACI 2.1 methodology. The impact categories to be examined in this study include carcinogenicity [comparative toxic units-human (CTUh)], eco-toxicity [comparative toxic units-ecological (CTUe)], eutrophication [kg N equivalents], global warming potential [kg CO_2 equivalents], ozone depletion [kg CFC equivalents], and smog formation [kg O_3 equivalents]. These categories are highly relevant to the study since select components within the ionic liquid synthesis production process will produce both vapor and liquid phase emissions affecting human and environmental endpoints. Impacts can vary significantly depending on methodology, scope, and assumptions. Therefore, the preceding impact categories were chosen to align as closely as possible with prior studies while addressing the perceived impacts of ionic liquid synthesis.

7.7.5. Limitations

Mass and energy balance information as well as life cycle assessment inventories for ionic liquids and their precursor molecules remain widely unavailable. For instance, life cycle inventory data for 1-bromohexane and 1-methylimidazole are currently not specified within the EcoInvent database. Therefore, alternative methods have been utilized to approximate the impacts of these compounds. The life cycle inventory of 1-methylimidazole is approximated by the material and energy inputs for its synthesis including: glyoxal (proxy by ethylene glycol), methylamine, formaldehyde, ammonia, thermal energy (natural gas combustion), and electric energy (U.S. grid mix) shown in Figure 7.6.[10]

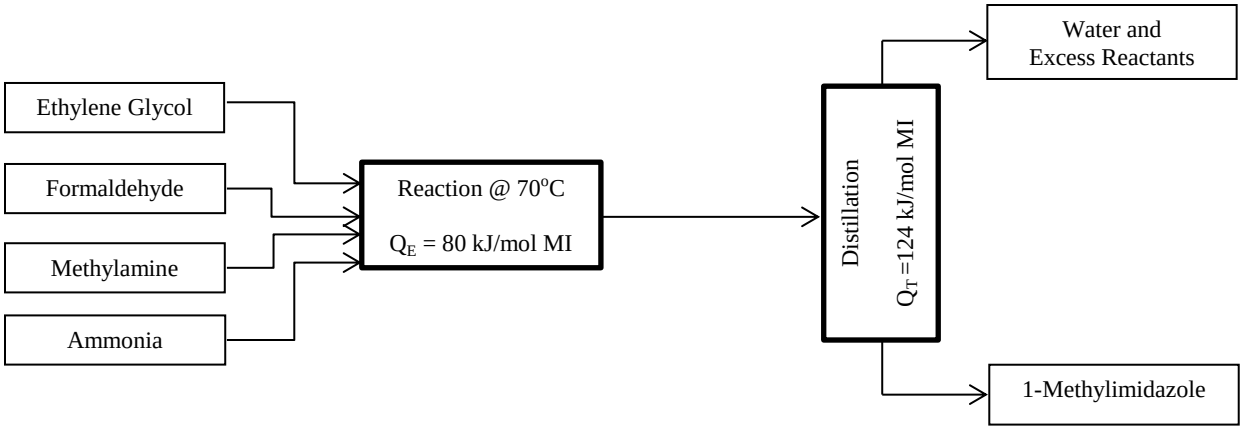

Figure 7.6: Synthesis of 1-methylimidazole from compounds and energy sources specified within the EcoInvent life cycle inventory database.

The inputs required to simulate the synthesis of 1-bromohexane are not available in the EcoInvent database creating a further limited situation for this precursor compound. Therefore, to approximate the life cycle inventory of 1-bromohexane, a similar halogenated compound, 1-chlorobutane, was utilized as a proxy. While the EcoInvent database does not contain 1-chlorobutane it does have LCI impact data for the components it is synthesized from including butanol and hydrochloric acid shown in Figure 7.7.[10]

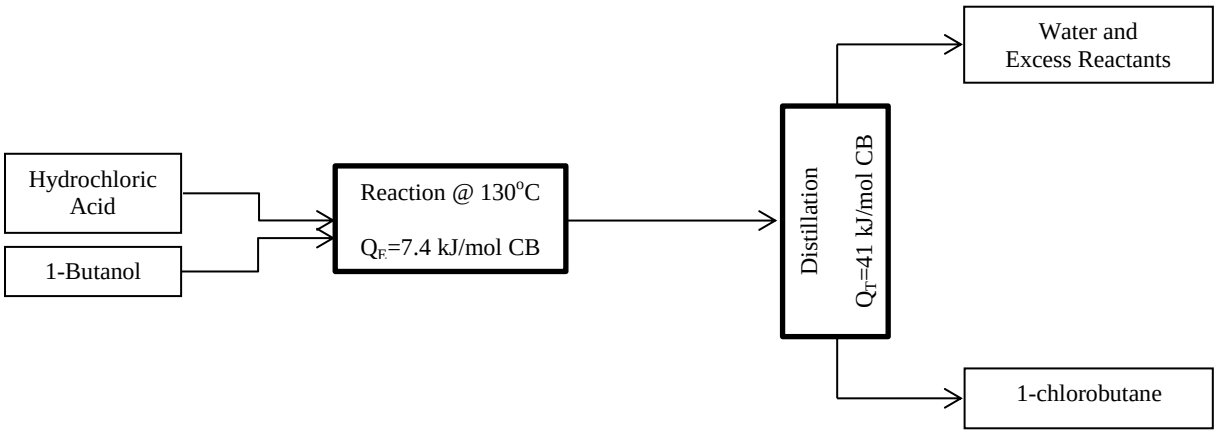

Figure 7.7: Synthesis of 1-chlorobutane (as a proxy for 1-bromohexane) from compounds and energy sources specified within the EcoInvent life cycle inventory database.

Mass and energy inputs associated with the continuous ionic liquid synthesis process were approximated using the previously discussed Aspen Plus process modeling results. While the process models were constructed on the basis of laboratory developed kinetic and thermodynamic data, there is a strong likelihood that some error is present in the resulting mass and energy balance values. Therefore, sensitivity and Monte Carlo analyses have been performed on each process utilizing the list of continuous variables displayed in Table 7.10. The continuous variables represent the simulated energy inputs required to synthesize and purify each of the reactant molecules as well as the ionic liquid. Additionally, the solvent recycle ratio was probed to assess the impact of solvent consumption on the overall LCA impacts.

IL Synthesis Solvent	Continuous Variable	Units	Minimum Value	Median Value	Maximum Value	Source
Acetone	Q_E (pumps) IL	(kJ/kg IL)	0.115	0.121	0.127	Aspen
	Q_E (heater) IL	(kJ/kg IL)	41.700	43.895	46.090	Aspen
	Q_E (cooler) IL	(kJ/kg IL)	-166.340	-175.095	-183.850	Aspen
	Q_T (reactor) IL	(kJ/kg IL)	-620.584	-689.538	-758.492	Aspen
	Q_T (flash) IL	(kJ/kg IL)	290.339	322.599	354.859	Aspen
	Solvent Recycle	N/A	0.75	0.99	1.00	Minnick
Acetonitrile	Q_E (pumps) IL	(kJ/kg IL)	0.115	0.121	0.127	Aspen
	Q_E (heater) IL	(kJ/kg IL)	41.431	43.612	45.793	Aspen
	Q_E (cooler) IL	(kJ/kg IL)	-167.186	-175.985	-184.784	Aspen
	Q_T (reactor) IL	(kJ/kg IL)	-610.462	-678.291	-746.120	Aspen
	Q_T (flash) IL	(kJ/kg IL)	327.478	363.864	400.251	Aspen
	Solvent Recycle	N/A	0.75	0.99	1.00	Minnick
Dichloromethane	Q_E (pumps) IL	(kJ/kg IL)	0.192	0.202	0.212	Aspen
	Q_E (heater) IL	(kJ/kg IL)	49.810	52.431	55.053	Aspen
	Q_E (cooler) IL	(kJ/kg IL)	-153.580	-161.664	-169.747	Aspen
	Q_T (reactor) IL	(kJ/kg IL)	-613.011	-681.123	-749.235	Aspen
	Q_T (flash) IL	(kJ/kg IL)	270.167	300.186	330.205	Aspen
	Solvent Recycle	N/A	0.75	0.99	1.00	Minnick
Dimethyl Sulfoxide	Q_E (pumps) IL	(kJ/kg IL)	0.115	0.121	0.127	Aspen
	Q_E (heater) IL	(kJ/kg IL)	33.245	34.995	36.744	Aspen
	Q_E (cooler) IL	(kJ/kg IL)	-598.987	-630.512	-662.038	Aspen
	Q_T (reactor) IL	(kJ/kg IL)	-611.955	-679.950	-747.945	Aspen
	Q_T (flash) IL	(kJ/kg IL)	1063.047	1181.164	1299.280	Aspen
	Solvent Recycle	N/A	0.75	0.99	1.00	Minnick
Reactants	Q_E (MI Synthesis)	(kJ/kg MI)	432	480	528	[10]
	Q_T (MI Synthesis)	(kJ/kg MI)	1359	1510	1661	[10]
	Q_E (BH Synthesis)	(kJ/kg BH)	117.90	131	144.10	[10]
	Q_T (BH Synthesis)	(kJ/kg BH)	2034	2260	2486	[10]

Table 7.10: Continuous variable list and ranges used in the sensitivity and Monte Carlo analyses. (Q_E represents electrical energy inputs) (Q_T represents thermal energy inputs)

7.7.6. Assumptions

The following assumptions were made to effectively conduct the life cycle assessment provided the limited process engineering and life cycle assessment inventory data available.

- For a basic LCA comparison of continuous ionic liquid synthesis production methods, it is assumed that the extrapolation from bench to commercial scale will be effective.

- Transportation of the raw materials has been assumed negligible and is not included since it will be equivalent for the various solvent systems.

- The waste and by-product streams from the production of all raw materials and energy production in this study were factored into the overall life cycle assessment. However, due to the small quantities and unknown nature of by-products potentially formed during the IL synthesis process it is assumed that the purged waste solvent and chemicals contribute negligibly to the overall impacts of the process and therefore have not been accounted for.

- Life cycle inventory data for 1-bromohexane was approximated by 1-chlorobutane synthesis as neither 1-bromohexane nor its precursors were available in the inventory database.

- The synthesis of 1-methylimidazole requires glyoxal which is not contained within the life cycle inventory databases. Glyoxal is formed by the oxidation of ethylene glycol. Therefore ethylene glycol was utilized as a proxy to represent the impacts of this raw material.

7.7.7. Cut off Criteria

Due to the scope of this study being focused on the continuous synthesis of ionic liquids, several facets of a complete chemical plant have been presumed negligible in this LCA study. They include plant maintenance, infrastructure modifications, human capital, and land impact.[14, 15] Additionally, the impact of the solid catalyst, zinc chloride, used in the synthesis of 1-chlorobutane has been neglected due to its reusable nature.

7.7.8. Geographic and Temporal Boundaries

The geographic scope of this study is limited to the United States. The temporal scope of the study is less restrictive and is extended ten years into the future with the understanding that this, and other LCAs, may help shape the development of continuous IL synthesis processes in the future. Future practices and improvements are not considered here, nor are any methods to model or predict such advances taken into account.

7.7.9. Life Cycle Inventories

Life cycle inventory data was collected from SimaPro LCA software and the EcoInvent database. Specific inventories used in this study include: acetone, acetonitrile, dichloromethane, dimethyl sulfoxide, ammonia gas, carbon dioxide, ethyl acetate, ethylene glycol, formaldehyde, methylamine, butanol, hydrochloric acid, U.S. grid mix electricity, and natural gas.

7.8. Nominal Results

The comparative cradle-to-gate life cycle assessment, presented herein, investigated the production of 1 kg of 99% pure ionic liquid [HMIm][Br] in four different reaction solvents. Figure 7.8 demonstrates the environmental impacts of the various IL synthesis processes across six impact categories normalized to the results from the acetone solvent system. The results demonstrate that ionic liquid synthesis in acetone produces the lowest environmental impacts, of the four solvents investigated, in every impact category except smog formation where [HMIm][Br] synthesis in acetonitrile produced marginally lower emissions of CFC equivalents (*i.e.* ~5% lower). Acetone is a moderately benign solvent and has the second lowest separation energy of the solvents probed potentially explaining the observed results. Interestingly, using acetonitrile as the reaction solvent generated similar environmental impacts as acetone with the exception of the eutrophication impact category. Eutrophication measures the potential introduction of inorganic nutrients to an ecosystem thereby penalizing acetonitrile for its nitrogenous functionality and the nitrogen based chemicals (*i.e.* ammonia) which are used in its synthesis.

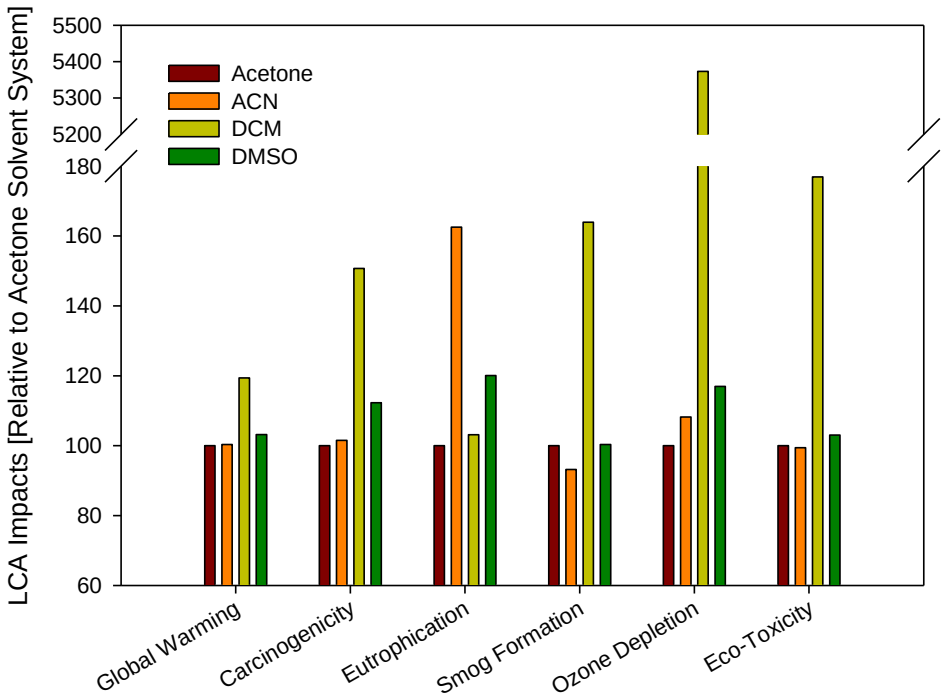

Figure 7.8: Life cycle impacts of [HMIm][Br] synthesis in the selected reaction solvents normalized to the impacts from the acetone solvent system.

Ionic liquid synthesis in dimethyl sulfoxide demonstrated the third highest life cycle assessment impacts in all assessed categories. As DMSO has the highest boiling point of all solvent systems investigated, the impact of separation energy on the LCA results was examined. Global warming impacts, measured by the quantity of equivalent CO_2 units produced per the functional unit (*i.e.* 1 kg of [HMIm][Br]) were investigated for the four solvent systems. The results demonstrated that the DMSO solvent system produced approximately 5% greater global warming impacts compared to IL synthesis in acetone. These impacts are a direct result of the increased energy demand for IL purification in DMSO relative to the other, lower boiling solvents. However, [HMIm][Br] synthesis in DMSO produced the lowest eco-toxicity and smog formation impacts

due to its environmentally benign nature and low vapor pressure indicating a tradeoff of beneficial and detrimental LCA results.

Finally, IL synthesis in dichloromethane generated the largest environmental impacts in every category except eutrophication. Dichloromethane is a known cancer-causing agent and thus IL synthesis in this solvent demonstrated significantly greater values of carcinogenicity and eco-toxicity compared to the other solvent systems. The DCM solvent system also produced the highest impacts in the global warming, smog formation, and ozone depletion categories likely due to its own synthesis process, high volatility, and probability of vapor phase release. Therefore, despite requiring the least separation energy for IL purification, the environmental and human hazards associated with the production and utilization of dichloromethane outweigh the reduced energy requirements.

The raw life cycle assessment data for each of the IL synthesis systems and the six impact categories are presented in Table 7.11. Importantly, this data represents all components of the IL synthesis process including all mass and energy flows required to synthesize the precursor molecules and [HMIm][Br] itself. Also presented are life cycle impacts for the production of CO_2 capture solvent monoethanolamine (MEA) and cellulose processing solvent N-methylmorpholine-N-oxide (NMMO).

IL Synthesis Solvent	Global Warming (kg CO_2 Eq.)	Ozone Depletion (kg CFC Eq.)	Eutrophication (kg N Eq.)	Smog Formation (kg O_3 Eq.)	Eco-Toxicity (CTUe Eq.)	Carcinogenicity (CTUh Eq.)
ACE	3.302	4.632E-07	4.532E-03	1.403E-01	2.589	9.545E-08
ACN	3.313	5.013E-07	7.380E-03	1.299E-01	2.573	9.692E-08
DCM	3.977	2.489E-05	4.674E-03	2.381E-01	4.623	1.440E-07
DMSO	3.412	5.416E-07	5.445E-03	1.410E-01	2.669	1.072E-07
MEA [(A)]	3.728	4.047E-07	1.169E-02	1.393E-01	3.854	1.258E-07
NMMO [(B)]	3.300	1.000E-07	N/A	N/A	N/A	N/A

Table 7.11: Life cycle assessment results for [HMIm][Br] synthesis in the selected reaction solvent systems compared to monoethanolamine (MEA) and N-methylmorpholine-N-oxide (NMMO). [(A)] LCA data adapted from EcoInvent database. [(B)] LCA data adapted from [10]

Compared to the production of 1kg of monoethanolamine, synthesis of an equivalent amount of [HMIm][Br] produces less environmental impacts in all but one category. For instance, synthesis of 1 kg of [HMIm][Br] in acetone, acetonitrile, and dimethyl sulfoxide produce lower environmental impacts than the production of MEA in terms of global warming, eutrophication, smog formation, eco-toxicity, and carcinogenicity. However, production of MEA is less hazardous by approximately an order of magnitude in terms of ozone depletion relative to the production of [HMIm][Br]. Limited life cycle impact data is available for the production of cellulose solvent N-methylmorpholine-N-oxide. Nonetheless, the global warming emissions associated with the production of [HMIm][Br] in acetone are approximately equivalent to the production of an identical amount of NMMO.[10] In terms of ozone depletion, however, production of 1 kg of NMMO emits less CFC equivalents than production of the IL regardless of the synthesis solvent used. While [HMIm][Br] is not traditionally applied to either CO_2 capture or cellulose dissolution the results indicate promise for ILs as comparable solvents for industrial applications from an environmental perspective. Furthermore, similar ILs including [BMIm][Cl] and [EMIm][Ac] have significant potential for applications in industrial processes and likely have similar environmental impacts to those presented herein for the synthesis of [HMIm][Br]. Application of ILs in a gate-to-gate process are likely to produce less environmental impacts compared with volatile organic compounds due to the non-volatility of the IL. Therefore,

utilization of ILs should enhance their environmentally beneficial attributes compared to volatile organic solvents when probed by a life cycle assessment that incorporates both the synthesis and application stages of an industrial process.

The disposal and end fate of ionic liquids remain largely unknown due to the lack of degradation studies. Vapor phase emissions from IL disposal will most likely be considered negligible due to the characteristic low volatility of ionic liquids. Therefore, disposal of ILs will most likely target solid and liquid point sources. Few studies have investigated the disposal of ILs and one specific study examined the biodegradability of [BMIm][Cl] over a 28 day period. The results indicated that this IL, similar to [HMIm][Br], was not biodegradable.[16] However, chemical methods have been successfully applied using UV light and oxidation to decompose imidazole based ILs.[17, 18] Regardless, a full understanding of the impacts of IL disposal on aqueous and land impacts cannot be fully understood at this time due to a lack of scientific data. The impacts associated with the disposal of ILs are likely to significantly affect their overall performance compared to conventional organic chemicals and future studies should address these unknown parameters to extend the boundaries of future LCA studies to encompass cradle-to-grave impacts.

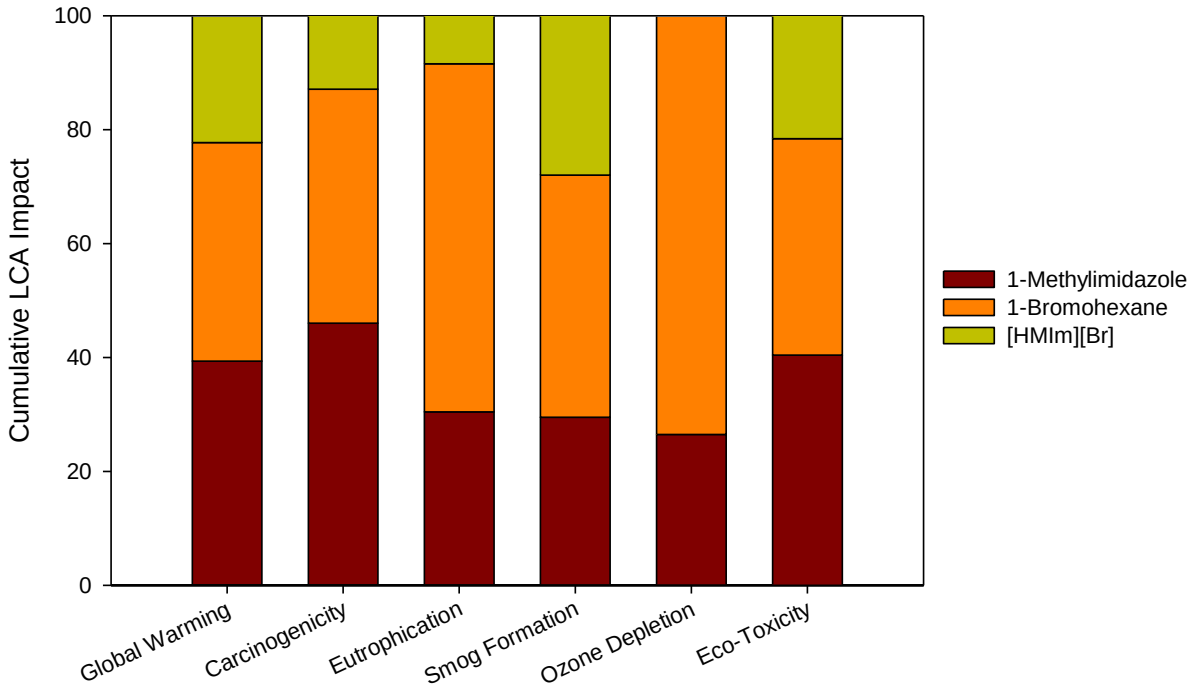

Figure 7.9: Contributions of 1-methylimidazole synthesis, 1-bromohexane synthesis and IL synthesis to the total life cycle impacts of [HMIm][Br] production.

The continuous IL synthesis process was divided into three constituent processes including: (1) production of 1-methylimidazole, (2) production of 1-bromohexane, and (3) production of [HMIm][Br] from its raw materials (*i.e.* 1-BH and 1-MI). The impacts of each production stage were assessed and normalized to the total LCA impacts of the entire 3-stage process. The results, displayed in Figure 7.9 demonstrate that in all impact categories investigated the contributions of IL production from its raw materials which account for the solvent used, IL synthesis reaction, and IL purification process contribute the least to the overall impact of the cradle to gate LCA study which encompasses all three process steps. For instance, the [HMIm][Br] synthesis step accounts for 22% of the total global warming and eco-toxicity impacts, 13% of the

carcinogenicity, 8% of eutrophication, 28% of the smog formation, and less than 1% of the ozone depletion. Alternatively, the majority of the impacts in these categories are sourced to the production of 1-bromohexane and 1-methylimidazole. This is likely due to the assignment of the raw materials within these processing steps whereas the IL synthesis step only accounts for the reaction solvent and energy consumed by the IL production process. Importantly, while the IL synthesis step is comparatively benign relative to the production of precursor molecules this study clearly demonstrates that a molecule is only as "green" as the components it is made from. Therefore, to reduce the environmental impacts associated with synthesizing ILs, increased attention should be placed on utilizing increasingly benign precursors.

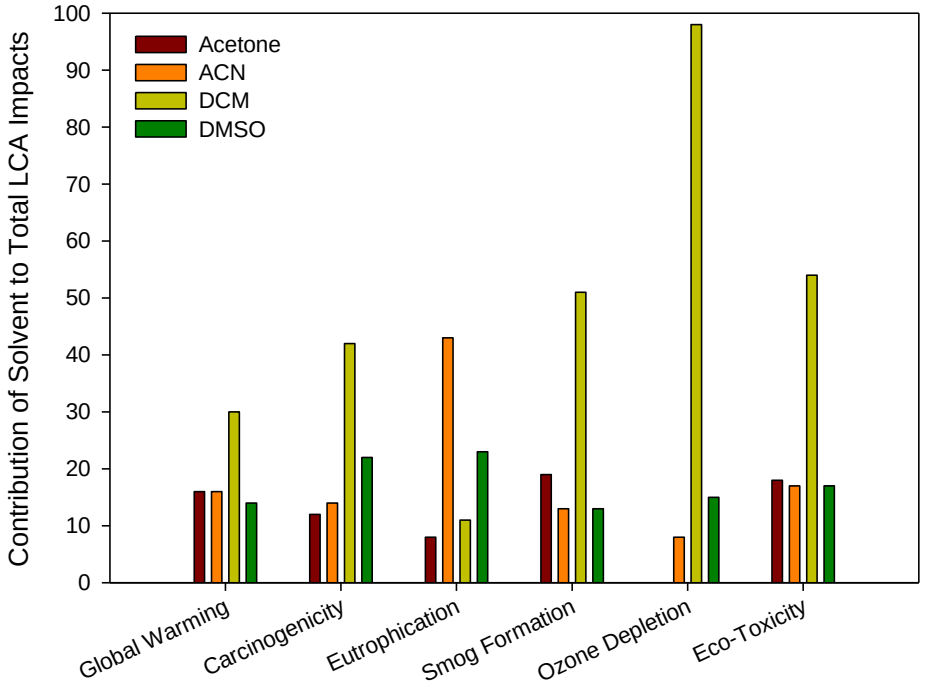

Figure 7.10: Isolated life cycle impacts due to utilization of the IL synthesis solvent. Results are normalized to the overall LCA impacts of the [HMIm][Br] synthesis process for each solvent.

The life cycle assessment impacts associated solely with utilization of the IL synthesis solvent were isolated and presented in Figure 7.10. The results represent the contributions of each solvent utilized within the IL synthesis process to the total life cycle impacts of continuous [HMIm][Br] production. For instance, utilization of dichloromethane as the reaction solvent accounts for approximately 54% of the total eco-toxicity impacts and 42% of the carcinogenetic impacts of the entire IL synthesis process using this solvent. Furthermore, DCM contributes the most of any solvent to the total process impacts in all categories assessed. The solvent impacts associated with acetone, acetonitrile, and dimethyl sulfoxide are all significantly lower than those observed for the DCM system and are moderately comparable. For instance, the global warming and eco-toxicity impacts for acetone, acetonitrile, and DMSO are nearly equivalent. Alternatively, for the carcinogenic, eutrophication, and ozone depletion categories the order of solvent impacts increases from acetone < acetonitrile < DMSO. To further analyze the effects of solvent selection on the IL synthesis process sustainability, the energy requirements for IL synthesis were evaluated relative to the total impacts of the process. The results from the energy analysis, which include the thermal and electrical energy required to operate the pumps, heaters, reactor, flash, and flash unit are displayed in Figure 7.11.

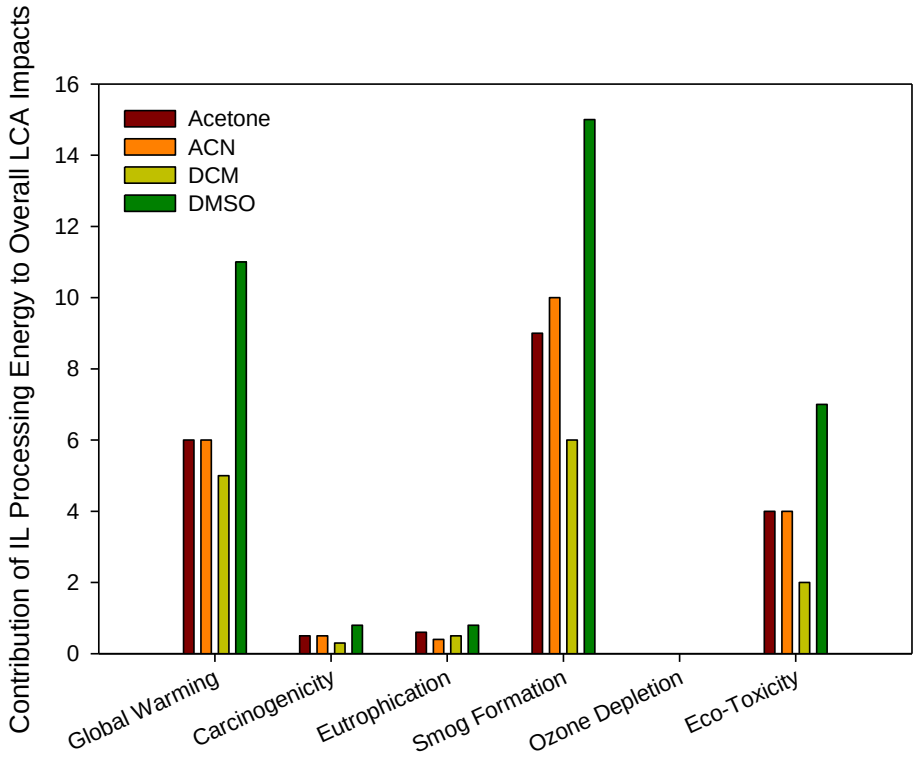

Figure 7.11: Life cycle impacts due to the thermal and electrical energy inputs required by the IL synthesis process. Results are normalized to the overall LCA impacts of the [HMIm][Br] synthesis process for each solvent.

The energy analysis results indicate that three primary LCA categories are affected by the production of thermal and electrical energy including: global warming, smog formation, and eco-toxicity. Analyzing these impact categories demonstrates that utilization of DMSO as the reaction solvent significantly increases the contributions of IL synthesis energy to the total life cycle assessment of the process. Alternatively, due to the high volatility of dichloromethane, this solvent system requires the least amount of energy for IL synthesis and concomitantly contributes the lowest amounts of LCA impacts of the solvents investigated.

Based on the previous discussions and the life cycle assessment impacts presented in Table 7.11 an overall rank of IL synthesis solvents was generated and displayed in Table 7.12 where (1) represents the lowest impact and (4) represents the highest impact.

Solvent	Global Warming	Carcinogenicity	Eutrophication	Smog Formation	Ozone Depletion	Eco-Toxicity
Acetone	1	1	1	2	1	2
Acetonitrile	2	2	4	1	2	1
Dichloromethane	4	4	2	4	4	4
Dimethyl Sulfoxide	3	3	3	3	3	3

Table 7.12: Rank of IL synthesis solvents based on LCA results for the production of 1 kg of [HMIm][Br]. (1) indicates the lowest LCA impacts and (4) indicates the highest LCA impacts.

The cumulative results from the six LCA impact categories allow for the recommendation of an optimal reaction solvent for the production of [HMIm][Br]. Clearly, acetone is the ideal reaction solvent from a comparative cradle-to-gate LCA perspective, having the lowest impacts in four of the six categories and the second lowest impacts in the remaining two. IL synthesis in acetonitrile produces the second best LCA results having a mix of intermediate impact results. Dimethyl sulfoxide ranks third across the board in every impact category and dichloromethane, despite its high volatility, is the most hazardous solvent in all but one impact category. Therefore, based on this assessment acetone and acetonitrile are recommended as ideal reaction solvents for continuous IL production.

7.9. Sensitivity Analysis

Uncertainty in LCA methodologies occur due to the limited availability of accurate scientific data for many emerging technologies. For this reasons, sensitivity analyses are vital to understanding the limitations within life cycle assessment calculation methods. For a given LCA study, many input parameters are unknown or known with limited confidence. Therefore, ranges

are established around input parameters to assess the significance of their contributions to the total environmental impacts of the given process. In this study the parameter ranges for continuous [HMIm][Br] synthesis are displayed in Table 7.10. For continuous IL synthesis, the material balance is fixed by the stoichiometry of the reaction (*i.e.* requiring a 1:1 molar feed of 1-BH and 1-MI). However, the thermal and electrical energy required to operate the IL synthesis process contains moderate uncertainty as it has been estimated based on Aspen Plus simulations which utilize mathematically modeled laboratory thermodynamic and kinetic data. The continuous variables probed in this LCA study consisted of all energy inputs to the IL synthesis process. These variables were bound by a range of +/- 10% to account for the influence of potential uncertainties. Furthermore, the solvent recycle ratio which dictates the quantity of solvent that can be reused remains unknown. Therefore, a range for this parameter was set between 0.75 and 1.00 as recycling less than 75% of the solvent would likely be prohibitive by both environmental and economic standards. By varying the range of values for a set of input parameters, the sensitivity of an LCA impact category can be quantified. Sensitivity analyses are integral to the life cycle assessment methodology, as they demonstrate which continuous variables have the most influence on each impact category. Due to the large number of input variables, impact categories, and processes examined only the most sensitive parameters for each process are presented. Importantly, the solvent recycle ratio significantly affected all impact categories. Alternatively, the LCA impacts from energy inputs into the IL synthesis process only significantly affected three categories including: global warming, eco-toxicity, and smog formation as shown in Figure 7.11. For this reason, the sensitivities of these three impact categories have been shown. Furthermore, while each IL synthesis solvent system has its own independent sensitivity results, only the results pertaining to the acetone system are displayed as

this was determined to be the most optimal reaction solvent. Sensitivity analyses for the acetonitrile, dichloromethane, and dimethyl sulfoxide solvent systems demonstrate similar trends to those observed for acetone.

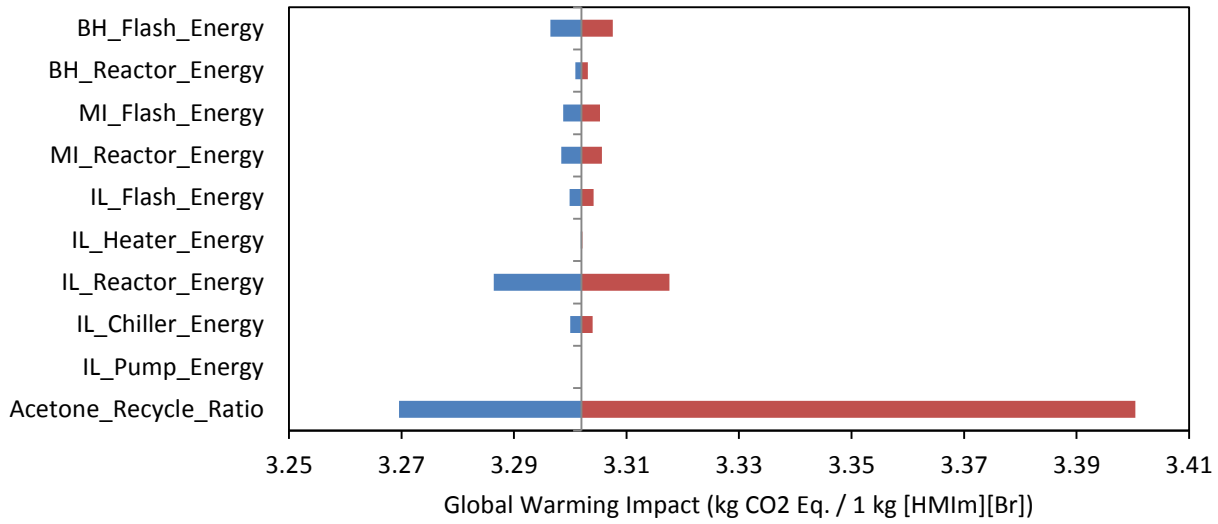

Figure 7.12: Sensitivity analysis probing the influence of the select continuous variables on the overall global warming impacts of [HMIm][Br] synthesis in acetone.

The global warming impact sensitivity results for [HMIm][Br] synthesis in acetone are displayed in Figure 7.12. Variations in the acetone recycle ratio demonstrate the greatest variation in total global warming impacts of the process. The Aspen Plus simulations for this system indicated that 93% of acetone could be effectively recycled within the process with small quantities leaving in the product stream and trace quantities being purged. An ideal reaction setup would continuously recycle 100% of the acetone initially fed to the process. Under this process condition, the global warming impacts could be reduced from 3.3 kg CO_2 equivalents to 3.27 kg CO_2 equivalents, approximately 1% less emissions relative to the nominal case. Alternatively, if the acetone recycle ratio were only 75%, the global warming impacts increase by approximately

3% to 3.40 kg CO_2 equivalents. Energy inputs including the thermal and electrical duties to the IL synthesis reactor and flash units have minor effects on the global warming impacts of the process and are less than 1% based on the applied ranges in this initial study. Therefore, optimizing the reaction and separation processes to efficiently recycle the reaction solvent will be important to minimizing the global warming impacts of the process.

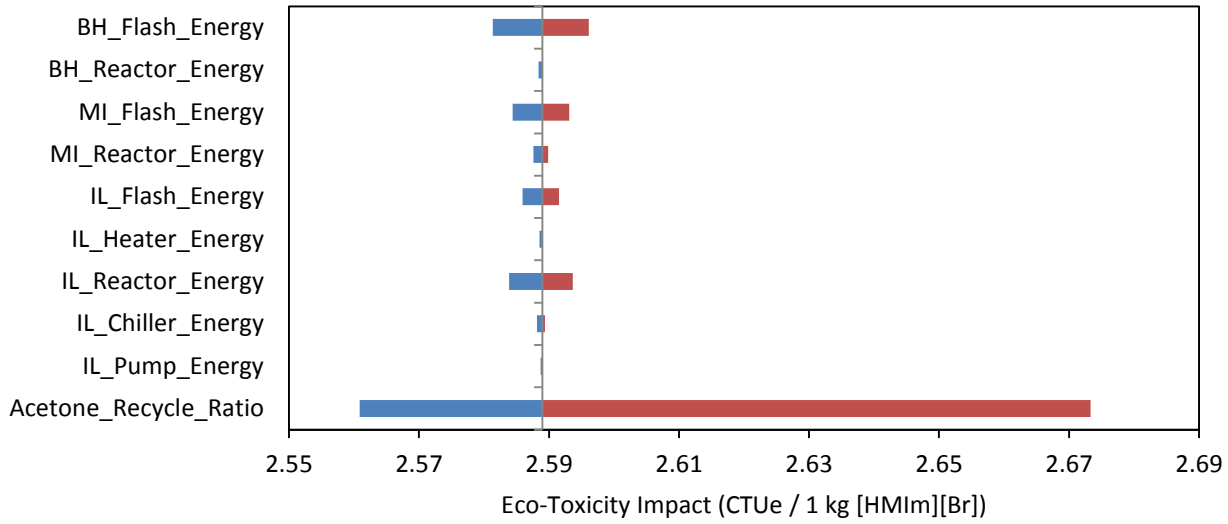

Figure 7.13 Sensitivity analysis probing the influence of the select continuous variables on the overall eco-toxicity impacts of [HMIm][Br] synthesis in acetone.

Figure 7.13 presents the eco-toxicity sensitivity results for the continuous variables probed in this study. As was observed for the global warming impacts, the recycle ratio of acetone most significantly affects the overall eco-toxicity impacts of the [HMIm][Br] synthesis process. Alternatively, varying the energy inputs to the system by +/- 10% does not have an appreciable impact on the overall eco-toxicity impacts of the process. Eco-toxicity measures the comparative toxic units emitted to aquatic point sources. As the majority of emissions due to energy production are air based, it is therefore reasonable that emissions targeting aqueous point sources

would be minimal for the thermal and electrical energy inputs. Alternatively, the solvent is traditionally sourced from the reaction of benzene with propylene followed by oxidation to produce acetone and phenol. Therefore, the eco-toxicity impacts of acetone consumption by the IL synthesis process are most likely tied to the carcinogenicity of benzene and chemical intermediates in the acetone synthesis process.

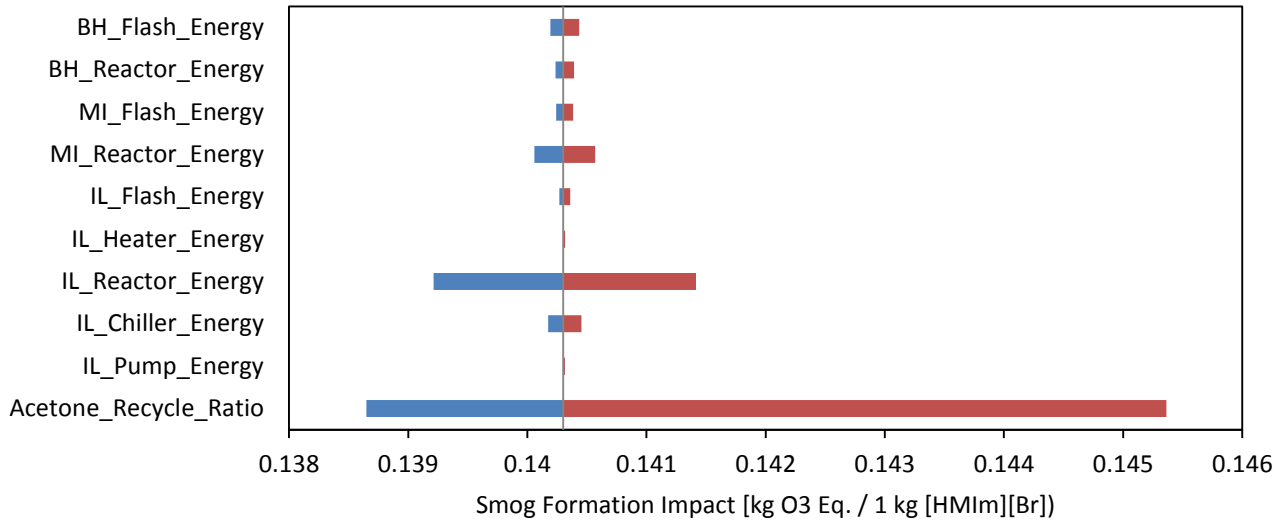

Figure 7.14: Sensitivity analysis probing the influence of the select continuous variables on the overall smog formation impacts of [HMIm][Br] synthesis in acetone.

The smog formation sensitivity analysis was conducted to assess the impact of energy inputs on the air based emissions of the process. The results indicate that while the acetone recycle ratio again has the largest impact on smog formation, power generation supplied to the reactor and other process units are also important. Select unit operations within the IL synthesis process do not consume significant quantities of energy. For instance, power supplied to the pumps and heaters are negligibly small compared to the power required to cool the isothermal reactor. Therefore, in the sensitivity analysis pump energy does not significantly affect the total

emissions from the IL synthesis process. However, the isothermal reactor does consume a significant quantity of energy to maintain the reaction temperature. The sensitivity results indicate that reducing power consumption by 10% relative to the baseline operation would reduce smog formation impacts by approximately 3%. Smog is produced from the combustion of fossil fuels and therefore these results demonstrate that the sustainability of the IL synthesis process is partially tied to the consumption of fossil fuels for power generation.

7.10. Monte Carlo Uncertainty Analysis

As previously discussed, LCA results are significantly impacted by the specified mass and energy inputs provided to the life cycle assessment solution algorithm. Therefore, Monte Carlo methodologies are traditionally utilized within LCA studies to evaluate the range and probability of life cycle impacts due to uncertainty in the input mass and energy parameters. While the nominal results reported in Section 7.8 reflect the life cycle impacts for the simulated [HMIm][Br] synthesis operating conditions, LCA impact ranges determined by Monte Carlo analyses are typically more informative for emerging technologies.[19] By generating random combinations of the continuous variables within their specified ranges, Monte Carlo calculations are capable of determining how closely the distribution of life cycle impact values for each process correlate to the nominal outcomes shown in Table 7.11. In this study 10,000 Monte Carlo simulations were performed for each impact category to assess the uncertainty in life cycle assessment results for [HMIm][Br] synthesis in the various solvent systems.

Table 7.13 presents the average and standard deviation results from 10,000 Monte Carlo simulations for [HMIm][Br] synthesis in the acetone, acetonitrile, dichloromethane, and dimethyl sulfoxide reaction solvent systems. The Monte Carlo results deviated from those

obtained by the nominal base case trial indicating the sensitivity of the LCA output results to the input parameters. Importantly, while the average results varied for each solvent and impact category, the results held the same overall trends as what was observed from the nominal base case. For instance, based on the Monte Carlo analysis, acetone remains the optimal IL synthesis solvent. One standard deviation of the mean was calculated to quantify the sensitivity of the LCA impact results to the specified parameter ranges. The standard deviation results indicated that the global warming, eco-toxicity, and smog formation impact categories were most significantly impacted by the range of continuous variables specified in Table 7.10. Alternatively, the ozone depletion, eutrophication, and carcinogenicity impact categories were comparatively less sensitive to variations of the continuous variables. The latter three impact categories were highly affected by the raw material inputs to the system including 1-bromohexane and 1-methylimidazole and therefore it is reasoned that the contributions of the solvent and energy inputs to the system were not large enough to make a significant impact in the overall distribution of results from the Monte Carlo analysis.

	Global Warming (kg CO_2 Eq.)	Ozone Depletion (kg CFC Eq.)	Eutrophication (kg N Eq.)	Smog Formation (kg O_3 Eq.)	Eco-Toxicity (CTUe Eq.)	Carcinogenicity (CTUh Eq.)
			Acetone			
Nominal	3.302	4.632E-7	4.532E-3	0.140	2.589	9.545E-8
Average	3.335	4.672E-7	4.533E-3	0.142	2.617	9.651E-8
Std. Dev.	0.039	1.300E-11	2.444E-5	0.002	0.033	8.064E-10
			Acetonitrile			
Nominal	3.313	5.013E-7	7.380E-3	0.130	2.573	9.692E-8
Average	3.336	5.028E-7	7.509E-3	0.131	2.593	9.747E-8
Std. Dev.	0.039	2.554E-9	2.150E-5	0.001	0.031	8.984E-10
			Dichloromethane			
Nominal	3.977	2.489E-5	4.674E-3	0.238	4.623	1.440E-7
Average	4.052	2.632E-5	4.704E-3	0.246	4.773	1.477E-7
Std. Dev.	0.085	1.662E-7	3.407E-5	0.009	0.170	4.142E-9
			Dimethyl Sulfoxide			
Nominal	3.412	5.416E-7	5.445E-3	0.141	2.669	1.072E-7
Average	3.608	5.441E-7	5.507E-3	0.154	2.740	1.082E-7
Std. Dev.	0.038	5.203E-9	8.307E-5	0.002	0.032	1.537E-9

Table 7.13: Uncertainty analysis based on Monte Carlo simulations comprised of 10,000 iterations. Nominal, average, and standard deviation results are presented for [HMIm][Br] synthesis in each solvent system.

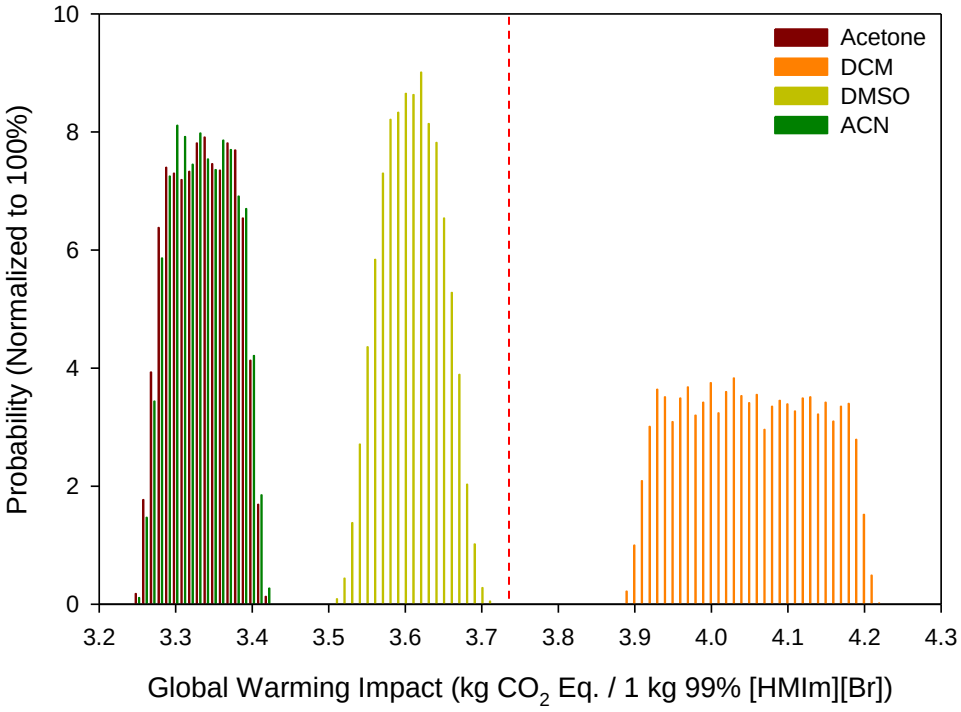

Figure 7.15: Monte Carlo results comparing the life cycle global warming impact ranges for [HMIm][Br] synthesis in the various reaction solvent systems.

The Monte Carlo simulation results for the global warming impact category are graphically depicted in Figure 7.15. Whereas the nominal results indicated that [HMIm][Br] synthesis in acetone emitted the lowest quantity of global warming impacts of all solvent systems probed, the Monte Carlo results demonstrated that based on the range of input variables specified, the impacts from both acetone and acetonitrile are nearly equivalent. For these two solvent systems, the synthesis of 1 kg of [HMIm][Br] had an 80% cumulative probability of producing between 3.3 and 3.4 kilograms of CO_2 equivalents. IL synthesis in the DMSO solvent system displayed a narrow distribution of global warming impacts with the highest global warming impact probability of 3.61 kg CO_2 equivalents per functional unit. This value was slightly higher than the nominal value computed for the DMSO system (3.41 kg CO_2 eq.) indicating the importance of understanding how LCA output values are affected by the specified input parameter ranges. Nonetheless, the global warming impacts generated by the production of 1 kg of monoethanolamine still exceed those of IL synthesis in acetone, acetonitrile, and DMSO indicating that even under the least ideal operating conditions investigated IL synthesis is still preferable to the production of an equivalent quantity of MEA. Alternatively, the Monte Carlo results confirmed that production of [HMIm][Br] in dichloromethane is comparatively unsustainable even at the most ideal operating conditions.

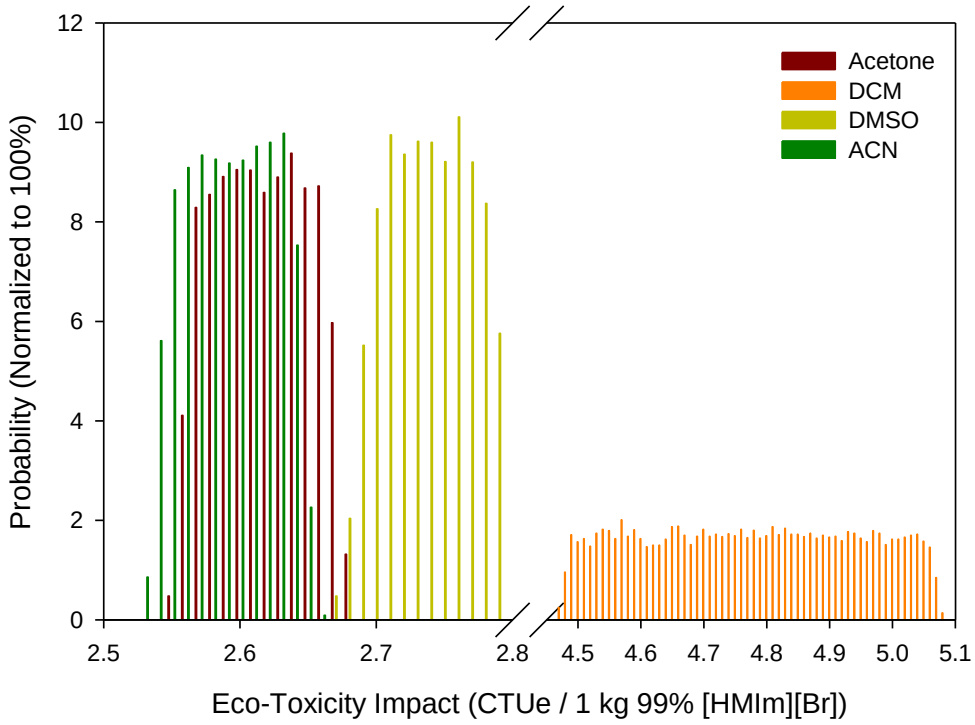

Figure 7.16: Monte Carlo results comparing the life cycle eco-toxicity impact ranges for [HMIm][Br] synthesis in the various reaction solvent systems.

Monte Carlo results for the eco-toxicity impact category are presented in Figure 7.16. The eco-toxicity life cycle impact of producing 1 kg of monoethanolamine was 3.85 comparative toxic units (CTUe). Therefore, despite not being graphically shown, synthesizing an equivalent amount of [HMIm][Br] in acetone, acetonitrile, and DMSO was more sustainable than producing the conventional CO_2 capture solvent. Furthermore, based on the Monte Carlo analysis, the eco-toxicity life cycle impacts of producing [HMIm][Br] in these three solvents were within 0.3 comparative toxic units (*i.e.* +/- 5%). However, the impacts associated with producing the ionic liquid in dichloromethane were significantly greater. Additionally, the range of eco-toxicity impact values for this solvent was significantly broader than what was observed for the other

solvent systems. The observed results are likely due to the significant carcinogenic impacts of dichloromethane production and utilization which significantly outweigh the eco-toxicity contributions from other inputs to the process. As such, the parameter range specified around the recycle ratio for this solvent system is responsible for generating the broad distribution of results and large standard deviation observed for the DCM eco-toxicity impacts.

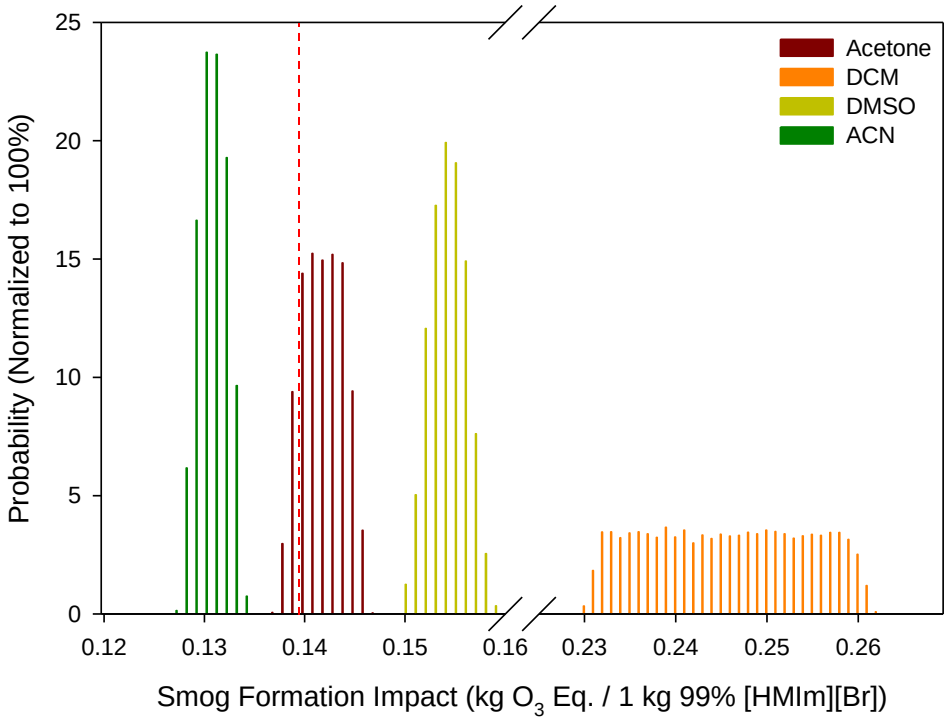

Figure 7.17: Monte Carlo results comparing the life cycle smog formation impact ranges for [HMIm][Br] synthesis in the various reaction solvent systems.

Figure 7.17 displays the Monte Carlo smog formation impacts from [HMIm][Br] production in the various reaction solvents. Unlike the previous two impact categories discussed, the Monte Carlo results for the various solvent systems do not overlap indicating that regardless of input parameter specifications the order of ideal reaction solvents is acetonitrile, followed by acetone,

dimethyl sulfoxide, and dichloromethane. Additionally, only the production of [HMIm][Br] in acetonitrile produces less smog formation impacts compared to the production of monoethanolamine under all Monte Carlo simulation conditions. Alternatively, only under the most ideal input parameter combinations is the production of [HMIm][Br] in acetone more sustainable than producing MEA in this impact category. The ideal LCA results for the acetone solvent system stem from operating conditions containing nearly quantitative solvent recycle and the lowest specified electrical and thermal energy inputs. Based on the assigned parameter ranges the cumulative probability of achieving smog formation emissions for [HMIm][Br] synthesis in acetone that are lower than those produced by the production of MEA was 12% indicating that this operating condition is not likely to be achieved in the specified process.

7.11. Summary

Research on ionic liquids has experienced exponential growth in the past decade indicating that increased industrial demand for ILs in the near future is likely. In order to provide larger quantities of ionic liquids, a sustainable and continuous synthesis method is needed. Therefore, an Aspen Plus process modeling study was presented for the production of 30 metric tons of [HMIm][Br] per day. The mass and energy balance results formed the foundation of a cradle-to-gate life cycle assessment study which indicated that IL synthesis methods utilizing acetone as the reaction solvent were environmentally optimal. The life cycle impacts associated with [HMIm][Br] were compared to those from the production of an equivalent amount of CO_2 capture solvent monoethanolamine. The results indicated that IL production generated less environmental impacts in five of the six categories investigated demonstrating that for select technologies ionic liquids are truly more sustainable than the conventional organic solvent.

References

1. Gonzalez, M.A. and J.T. Ciszewski, *High Conversion, Solvent Free, Continuous Synthesis of Imidazolium Ionic Liquids In Spinning Tube-in-Tube Reactors.* Organic Process Research & Development, 2009. **13**(1): p. 64-66.
2. Garcia-Verdugo, E., et al., *Ionic liquids and continuous flow processes: a good marriage to design sustainable processes.* Green Chemistry, 2015. **17**(5): p. 2693-2713.
3. Sen, N., et al., *On continuous, solvent-free synthesis of ionic liquid [BMIM]Br in a microbore tube.* Journal of Radioanalytical and Nuclear Chemistry, 2016. **307**(2): p. 1001-1009.
4. Schleicher, J.C. and A.M. Scurto, *Kinetics and solvent effects in the synthesis of ionic liquids: imidazolium.* Green Chemistry, 2009. **11**(5): p. 694-703.
5. Waterkamp, D.A., et al., *Synthesis of ionic liquids in micro-reactors - a process intensification study.* Green Chemistry, 2007. **9**(10): p. 1084-1090.
6. Verevkin, S.P., et al., *Does alkyl chain length really matter? Structure-property relationships in thermochemistry of ionic liquids.* Thermochimica Acta, 2013. **562**: p. 84-95.
7. Farahipour, R. and A.T. Karunanithi, *Life Cycle Environmental Implications of CO2 Capture and Sequestration with Ionic Liquid 1-Butyl-3-methylimidazolium Acetate.* Acs Sustainable Chemistry & Engineering, 2014. **2**(11): p. 2495-2500.
8. Imperato, G., B. Konig, and C. Chiappe, *Ionic green solvents from renewable resources.* European Journal of Organic Chemistry, 2007(7): p. 1049-1058.
9. Mehrkesh, A. and A.T. Karunanithi, *Energetic Ionic Materials: How Green Are They? A Comparative Life Cycle Assessment Study.* Acs Sustainable Chemistry & Engineering, 2013. **1**(4): p. 448-455.
10. Righi, S., et al., *Comparative cradle-to-gate life cycle assessments of cellulose dissolution with 1-butyl-3-methylimidazolium chloride and N-methyl-morpholine-N-oxide.* Green Chemistry, 2011. **13**(2): p. 367-375.
11. Mehrkesh, A. and A.T. Karunanithi, *Life-Cycle Perspectives on Aquatic Ecotoxicity of Common Ionic Liquids.* Environmental Science & Technology, 2015.
12. Organization, I., *ISO 14040:2006 - Environmental management - Life cycle assessment - Principles and framework.* 2006.
13. Singh, A., et al., *Key issues in life cycle assessment of ethanol production from lignocellulosic biomass: Challenges and perspectives.* Bioresource Technology, 2010. **101**(13): p. 5003-5012.
14. Hischier, R., et al., *Establishing life cycle inventories of chemicals based on differing data availability.* International Journal of Life Cycle Assessment, 2005. **10**(1): p. 59-67.
15. Geisler, G., T.B. Hofstetter, and K. Hungerbuhler, *Production of fine and speciality chemicals: Procedure for the estimation of LCIs.* International Journal of Life Cycle Assessment, 2004. **9**(2): p. 101-113.
16. Thi, P.T.P., C.W. Cho, and Y.S. Yun, *Environmental fate and toxicity of ionic liquids: A review.* Water Research, 2010. **44**(2): p. 352-372.

17. Stepnowski, P. and A. Zaleska, *Comparison of different advanced oxidation processes for the degradation of room temperature ionic liquids.* Journal of Photochemistry and Photobiology a-Chemistry, 2005. **170**(1): p. 45-50.
18. Morawski, A.W., et al., *Decomposition of ionic liquids by photocatalysis.* Polish Journal of Chemistry, 2005. **79**(12): p. 1929-1935.
19. Fortier, M.O.P., et al., *Life cycle assessment of bio-jet fuel from hydrothermal liquefaction of microalgae.* Applied Energy, 2014. **122**: p. 73-82.

8. Ionic Liquids for CO_2 Capture in Packed Bed Absorption Towers

8.1. Introduction

Population growth and improved quality of life in developing countries continues to result in exponential increases in global energy demand and greenhouse gas (GHG) production. Figure 8.1 shows a plot of annual worldwide carbon emissions from the combustion of fossil resources for energy production.[1] While the correlation between GHG emissions and global climate change remains highly debated, most scientists and politicians agree that reducing the quantity of "new" carbon released to the atmosphere is important for preservation of the environment.

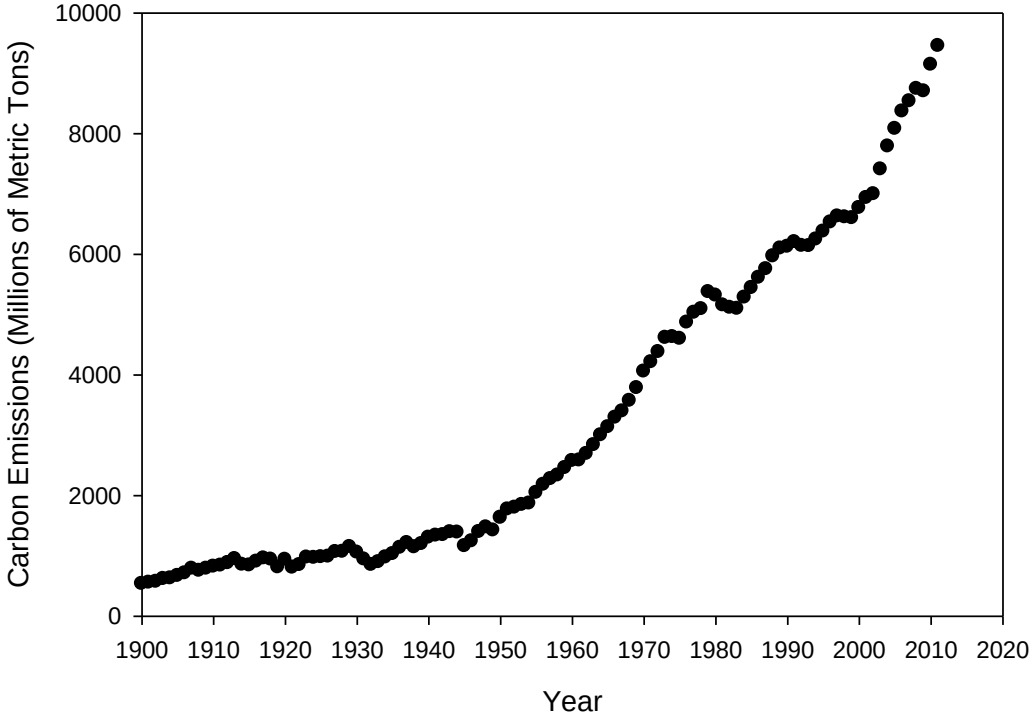

Figure 8.1: Global carbon emissions from the combustion of fossil resources.[1]

In the United States, government imposed policy and regulations continue to lead the forefront of environmentally conscious energy production. For instance, in 2011, approximately 42% of U.S. electrical power generation was sourced from coal-fired power plants generating approximately 2.8 billion tons of carbon dioxide (CO_2) emissions, according to the Environmental Protection Agency.[2, 3] Comparatively, in 2015, only 33% of domestic energy was produced from coal while natural gas utilization increased by 7% to replace the coal based power supply.[2, 3]

Natural gas is a comparatively cleaner energy source relative to coal primarily due to its higher energy density. Whereas coal produces ~215 pounds of CO_2 per million British thermal units (BTUs), natural gas (*i.e.* primarily methane) generates only 115 pounds, a 47% reduction in carbon emissions for the same quantity of energy produced.[4] Nonetheless, energy production from fossil fuels continues to introduce large quantities of CO_2 into the atmosphere and world energy dependence will require the utilization of fossil fuels to meet the growing demand for the foreseeable future. Therefore, as a response, research and development efforts on carbon dioxide capture, storage, and utilization technologies are experiencing rapid growth.[5, 6]

Carbon dioxide capture technologies are applicable to both natural gas and coal based feedstocks. For natural gas, the CO_2 capture process can occur before or after combustion. The pre-combustion conditions are particularly advantageous as CO_2 is increasingly concentrated (45 volume%) at process conditions of approximately 200^{o}C and 20 ATM.[7] Alternatively, pre-combustion CO_2 capture processes are not applicable to coal based feedstocks. Energy production from coal occurs by combusting a mixture of coal and air in a boiler to produce steam. Subsequently, the steam propels a turbine to produce electricity while the low pressure flue gas is sent to a desulfurization unit prior to a CO_2 capture process. Flue gas conditions

leaving the desulfurization unit but prior to the CO_2 capture process are approximately 40°C, 1 ATM, and 15 volume% CO_2.[8]

Packed absorption towers coupled with thermal desorption units, as shown in Figure 8.2, are targeted for CO_2 capture. Post-combustion flue gas leaving the desulfurization unit is fed into the packed absorption tower where it is contacted counter currently by a liquid solvent. Thermodynamically controlled liquid phase absorption of CO_2 occurs inside of the packed tower, producing a CO_2 rich solvent leaving the bottom of the absorption tower and a CO_2 lean flue gas for release to the environment out the top of the column. Solvent regeneration occurs by feeding the solvent into an elevated temperature desorption process where the comparatively high volatility of CO_2 relative to the solvent drives a vapor-liquid separation. CO_2 is sequestered from the top of the desorption column for storage or utilization while the regenerated CO_2 capture solvent is cooled and recycled for multi-pass operation in the absorption tower. [9-13]

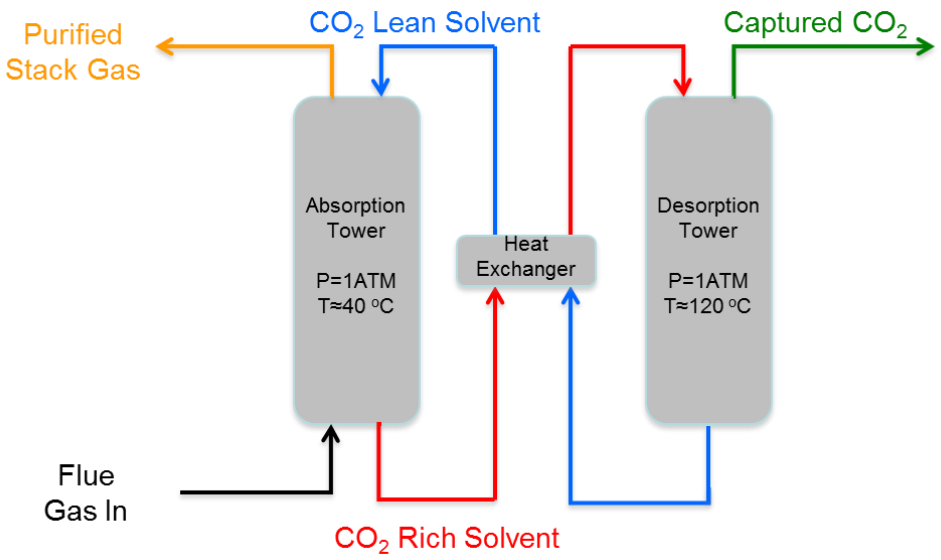

Figure 8.2: Post-combustion CO_2 capture process for flue gas from a coal fired power plant.

8.1.1. Amine Based CO_2 Capture Solvents

Amine based solvents including monoethanolamine (MEA) are most widely applied for post-combustion CO_2 capture processes.[14-16] These solvents are particularly advantageous for CO_2 capture as they sequester the greenhouse gas through chemical and physical absorption routes. For instance, monoethanolamine reacts with CO_2 to produce carbonate and carbamate products allowing MEA to absorb more CO_2 than a comparable solvent which is constrained solely by thermodynamic equilibrium.[17] The properties of MEA, displayed in Table 8.1, demonstrate that this solvent is ideal for CO_2 capture as it has a low pure component viscosity, high CO_2 absorption capacity, and high selectivity for carbon dioxide over other components in the flue gas mixture (N_2, Ar, O_2, *etc.*).

Component	Viscosity (cP) [A]	Density (g/cm^3) [A]	CO_2 Diffusivity (cm^2/sec) [B]	MW (g/mol)	Henry's Constant (CO_2) (ATM) [C]
30 mass% MEA	1.595	1.0035	2.14e-5	61.08	2.75

[A)] Adapted from [18], [B)] Adapted from [19], [C)] Theoretical Henry's constant adapted from [20]

Table 8.1: Properties of monoethanolamine at 40°C and 1 ATM.

Despite the ideal mass transfer and CO_2 capacity of amine based absorbents, specific limitations of these solvents include: their corrosive nature, oxidative and thermal degradation, and high vapor pressures.[21] Furthermore, separation of physically absorbed CO_2 and regeneration of chemically transformed MEA is energy intensive and costly.[22] For instance, the enthalpy of CO_2 absorption in MEA is -85 kJ/mol at 40°C [23] and additional energy input will be required to overcome evaporative losses due to the volatilization of MEA.[24-26] For these reasons, alternative solvents are desired to optimize the absorption of post-combustion carbon dioxide from coal fired power plants.

8.1.2. Ionic Liquids for CO_2 Capture

Select ionic liquids demonstrate significant CO_2 dissolution capacities and therefore are considered potential replacement solvents for MEA in packed absorption CO_2 capture processes. Ionic liquids are especially advantageous for these processes as they possess negligible vapor pressures, are molecularly tunable through cation/anion selection, and do not significantly corrode metals.[24, 27, 28] Significant research into the properties and performance of select conventional and task specific ionic liquids (TSILs) have been performed to identify the applicability of ILs for CO_2 capture processes. The properties of select ILs are presented in Table 8.2. Whereas conventional MEA based absorption-desorption processes are plagued by loss of solvent during the CO_2 stripping process, ionic liquids avoid this problem due to their non-volatile nature. Additionally, select task specific ionic liquids have been designed to achieve superior physical and chemical CO_2 absorption capacities (1:1 mol ratio CO_2:IL) making them thermodynamically better solvents for CO_2 than MEA.[29]

However, while the thermodynamic properties of ILs are ideal for CO_2 capture, ionic liquids demonstrate significantly higher viscosities than amine based solvents and can exceed 1000 cP. [21, 30] Of the ionic liquids investigated herein, 1-ethyl-3-methylimidazolium bistrifluoro(methylsulfonyl)imide [EMIm][Tf_2N] has the lowest pure component viscosity (27 cP) at 40^oC. While comparatively low for an IL, this viscosity is an order of magnitude greater than what is observed for MEA. Furthermore, the viscosity of select task specific ionic liquids has been experimentally shown to increase upon CO_2 absorption.[31] Therefore, the rheological properties of ionic liquids significantly impact the gas-liquid mass transfer rate as evidenced by the slower diffusivities of CO_2 in ILs compared to the amine based MEA solvent.

Ionic Liquid	Viscosity (cm^2/sec)	Density (g/cm^3)	CO_2 Diffusivity (cm^2/sec)	MW (g/mol)	Henry's Constant (ATM)
[EMim][Tf_2N] [A]	21.1	1.50	9.50e-6	391.32	47.7
[BMim][Tf_2N] [A]	27.5	1.42	9.00e-6	419.37	39.4
[HMim][Tf_2N] [A]	37.2	1.36	5.00e-6	447.42	42.0
[EMim][BF_4] [B]	29.4	1.23	5.67e-6	197.97	100
[BMim][BF_4] [A,C]	59.1	1.19	4.30e-6	226.03	76.0

[A)] Adapted from [32] [B)] Adapted from [33] [C)] Adapted from [34]

Table 8.2: Properties of select CO_2 absorbing ionic liquids.

8.2. Overview

Research efforts to this point have primarily focused on the molecular design and testing of ILs for CO_2 capture and few studies have investigated the process design and economic aspects of replacing amine based solvents with ionic liquids.[35-38] Furthermore, most studies have naively assumed that ionic liquids have the potential to act as "drop-in" replacements for conventional solvents in absorption towers.[39] This study explores the complications of applying ionic liquids to CO_2 capture by computationally designing packed absorption towers for use by a range of ionic liquids which were selected to examine the cross section of thermodynamic CO_2 capacity and mass transport limitations (*i.e.* viscosity and diffusivity). In the techno-economic study packed absorption towers are designed with specific heights and diameters to handle the CO_2 output from a 300 MW coal fired power plant. Economic correlations are utilized to examine the cost of various ionic liquid solvents for CO_2 capture relative to a baseline monoethanolamine system.

8.3. Calculation of Packed Tower Diameter

The packed absorption tower diameter was computed by the methods of Sherwood and Leva et al. using appropriate gas and liquid phase mass transfer coefficient correlations.[40-42] Preliminary calculations for the packed column were computed based on the liquid-to-gas kinetic energy ratio developed by Sherwood *et al.*, shown in Eqn. 8.1.[40]

$$F_{LV} = \left(\frac{V*MW_v}{L*MW_L}\right)\left(\frac{\rho_V}{\rho_L}\right)^{0.5} = X \qquad \text{Eqn. 8.1}$$

Where (V) and (L) are the mass flowrates of the vapor and liquid phases respectively, (MW_v) and (MW_L) are similarly the molecular weights of the same two phases, and (ρ_V) and (ρ_L) represent the gas and liquid densities. Eqn. 8.1 and the generalized pressure drop correlation for packed towers developed by Leva *et al.* shown in Figure 8.3 were utilized to determine the y-axis value at column flooding conditions by finding the intersection of the F_{LV} value and the "flooding" condition pressure drop line. Subsequently, Eqn. 8.2 was utilized to back calculate the superficial vapor phase velocity (u_V) at the column flooding condition, where (F_P) is the packing factor determined by the selected packing material properties, (g) is the gravitational constant, and $f\{\rho_L\}$ and $f\{\mu_L\}$ are the correction factors for liquid density and liquid viscosity shown in Figure 8.4 and Figure 8.5 respectively. 25 mm ceramic Raschig rings were selected as the packing material for all trials herein as it is known to generate thin liquid films while minimizing pressure drop throughout the column.

$$Y = \frac{u_V^2 F_P}{g}\left(\frac{\rho_V}{\rho_{H2O,L}}\right) f\{\rho_L\} f\{u_L\} \qquad \text{Eqn. 8.2}$$

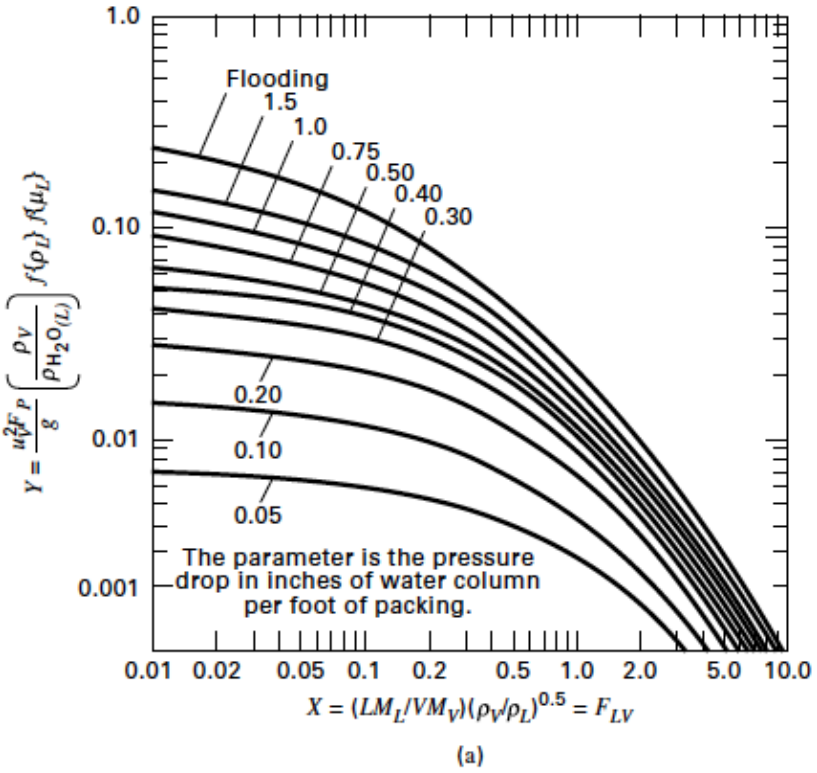

Figure 8.3: Generalized pressure drop correlation for packed columns.[41]

Once the superficial vapor velocity at flooding was calculated an adjusted value was computed at a fractional value of the flooding condition. The flooding condition exists when the entire column is filled with liquid. As this is not an operable scenario for an absorption process, columns are conventionally run at a flooding fraction of 0.5 to 0.7. In this study the fraction of flooding (f) was set at a fixed value of 0.7. Therefore, utilizing the superficial vapor phase velocity at flooding and the flooding fraction, the column diameter was calculated by Eqn. 8.3

$$D_T = \left(\frac{4*V*MW_V}{f*u_{V,f}*\pi*\rho_V}\right)^{0.5} \qquad \text{Eqn. 8.3}$$

The column diameter is primarily a function of the liquid and vapor phase flowrates and physical properties as well as the selected column packing (*i.e.* hydrodynamics).

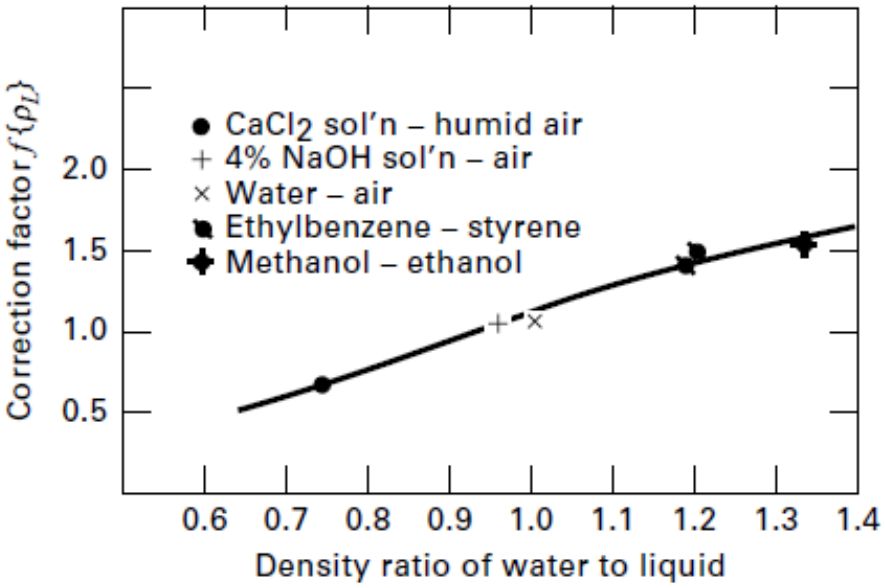

Figure 8.4: Correction factor for liquid density for use in Eqn. 8.2. [43]

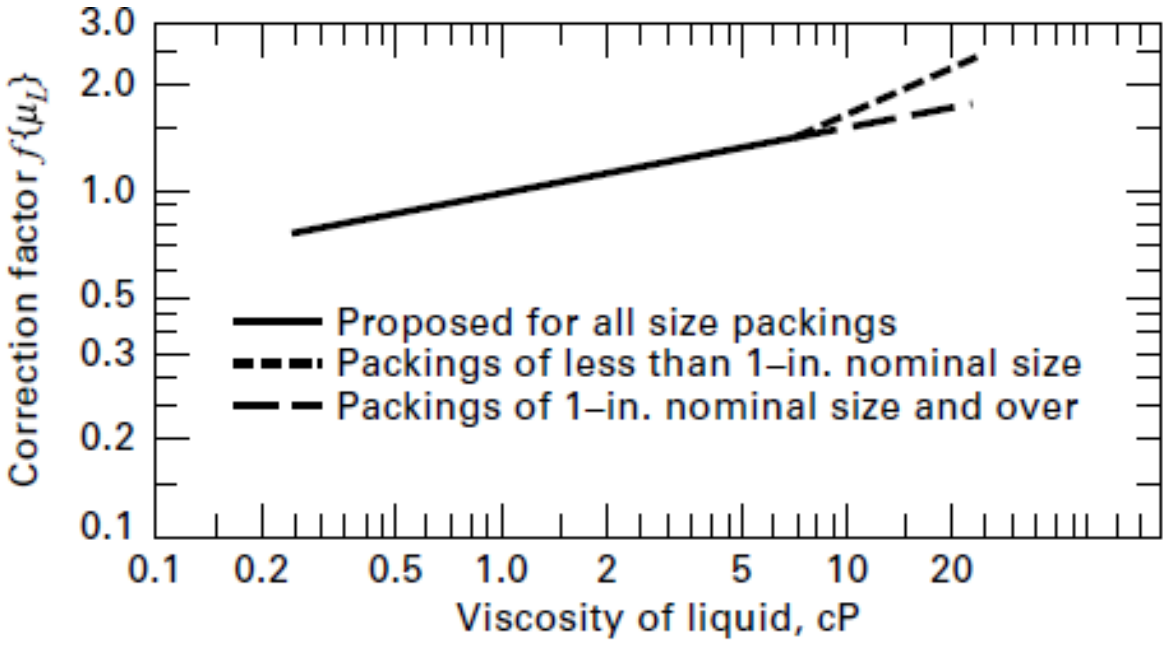

Figure 8.5: Correction factor for liquid viscosity for use in Eqn. 8.2. [43]

8.4. Calculation of Packed Tower Height

The packed absorption tower height is determined by a combination of thermodynamic and mass transfer effects. Maximum CO_2 capacity of the liquid phase solvent, assuming a physical absorption mechanism, is determined by thermodynamic equilibrium. While packed towers do not technically have discrete "transfer units" as compared to trayed towers, the column can be divided into theoretical transfer units where equilibrium is established. The height of a packed tower transfer unit (HTU) is the vertical length of gas-liquid contact required to reach thermodynamic equilibrium. Transfer unit height is therefore controlled by gas-liquid mass transfer resistance. Alternatively, the number of theoretical transfer units required to complete the separation is controlled by thermodynamics. The packed tower height is calculated by multiplying the transfer unit height by the total number of transfer units. A detailed equation list

is provided in the following section to describe how the tower specifications were designed in this case study.

8.4.1. Calculating the Height of a Transfer Unit

Transfer unit height is a direct function of gas and liquid phase mass transfer resistances. The following correlations were obtained from Cussler *et al*.[44] The liquid phase mass transfer coefficient was calculated by Eqn. 8.4 where all properties of the liquid phase were at conditions specified within the absorption column, *i.e.* 40°C and 1 ATM.

$$k_L\left[\frac{cm}{\text{sec}}\right] = (0.0051)(\nu_L g)^{\frac{1}{3}}\left(\frac{{V_L}^o}{a\nu_L}\right)^{0.67}\left(\frac{D_L}{\nu_L}\right)^{0.50}(ad)^{0.40} \qquad \text{Eqn. 8.4}$$

In Eqn. 8.4 (k_L) is the liquid phase mass transfer coefficient in (cm/sec), (ν_L) is the liquid phase kinematic viscosity, $({V_L}^o)$ is the liquid phase velocity, (a) is the packing characteristic, (g) is the gravitational constant, (D_L) is the liquid phase diffusivity of CO_2 in the selected absorbent, and (d) is the packing diameter. The liquid phase mass transfer units were transformed by dividing by the liquid phase molar volume $(\underline{V_L})$ at 40°C as shown in Eqn. 8.5.

$$k_x\left[\frac{mol}{cm^2 sec}\right] = \frac{k_L}{\underline{V_L}} \qquad \text{Eqn. 8.5}$$

The gas phase mass transfer coefficient was calculated by Eqn. 8.6 where (D_g) is the vapor phase diffusion coefficient, (V_G^o) is the vapor phase velocity, (ν_G) is the vapor phase kinematic viscosity, and the remaining variables are as previously defined for the liquid phase mass transfer coefficient.

$$k_G\left[\frac{cm}{\sec}\right] = 3.6(aD_g)\left(\frac{V_G^o}{a\nu_G}\right)^{0.70}\left(\frac{\nu_G}{D_G}\right)^{\frac{1}{3}}(ad)^{-2.0} \qquad \text{Eqn. 8.6}$$

The vapor phase mass transfer coefficient units were transformed as shown in Eqn. 8.7 where $(\underline{V_g})$ is the molar volume of the vapor phase.

$$k_p\left[\frac{cm}{\sec atm}\right] = \frac{k_g\underline{V_g}}{RT} \qquad \text{Eqn. 8.7}$$

Utilizing the previously defined liquid (k_x) and gas (k_p) mass transfer coefficients the overall mass transfer coefficient was calculated by Eqn. 8.8 where the Henry's constant (H) controls the thermodynamic equilibrium for CO_2 in the liquid phase.

$$K_x = \frac{1}{\frac{1}{k_x}+\frac{1}{Hk_p}} \qquad \text{Eqn. 8.8}$$

Finally, the height of a transfer unit was determined by Eqn. 8.9 where (S) is the column diameter and (a) is the interfacial gas-liquid contact area defined by the selected packing material (*i.e.* 25mm ceramic Raschig rings).

$$HTU = \frac{V_L^o}{K_x aS} \qquad \text{Eqn. 8.9}$$

8.4.2. Calculating the Number of Transfer Units

The number of transfer units within a packed tower is determined by thermodynamic equilibrium; approximated by Henry's law in this case study. Due to the large flux of CO_2 transferring from the vapor phase to the liquid phase within the column, constant molal overflow

was not assumed. Instead, a mass balance was performed to determine the driving force of CO_2 absorption throughout the column. The results of the mass balance derivation are presented in Eqns. 8.10-8.14.

Eqn. 8.10 presents the formulation used to compute the composition (mass fraction) of CO_2 exiting the column in the vapor phase which is controlled by the design specification (α), where alpha is the desired percent recovery of CO_2 from the inlet vapor feed.

$$\omega_{CO_2}^{V\,out} = \frac{1}{\left[\frac{\left(1-\omega_{CO_2}^{V\,in}\right)}{(1-\alpha)\left(\omega_{CO_2}^{V\,in}\right)}+1\right]} \qquad \text{Eqn. 8.10}$$

In Eqn. 8.10, $\left(\omega_{CO_2}^{V\,out}\right)$ is the mass fraction of CO_2 exiting the absorption column in the vapor phase, $\left(\omega_{CO_2}^{V\,in}\right)$ is the mass fraction of CO_2 in the flue gas feed entering the column, and alpha (α) is the desired fractional recovery of CO_2 from the feed. Eqn. 8.11 defines the minimum composition of CO_2 (mass fraction) in the liquid absorbent leaving the column $\left(\omega_{CO_2}^{L\,out\,(MIN)}\right)$ and is controlled by thermodynamic equilibrium between the incoming flue gas and CO_2 rich absorbent leaving the column represented by the Henry's constant (H).

$$\omega_{CO_2}^{L\,out\,(MIN)} = \frac{\left(\omega_{CO_2}^{V\,in}\right)(1atm)}{H} \qquad \text{Eqn. 8.11}$$

The minimum liquid flowrate of absorbent entering the column $\left(m_{L\,in}^{MINIMUM}\right)$ was computed in Eqn. 8.12 based on the minimum liquid phase composition of CO_2 leaving the column as determined by the vapor phase flowrate entering the column $(m_{V\,in})$ and thermodynamic equilibrium.

$$m_{L\,in}^{MINIMUM} = (-m_{V\,in})\left[\frac{1-\frac{\left(1-\omega_{CO_2}^{V\,in}\right)}{\left(1-\omega_{CO_2}^{V\,out}\right)}}{1-\frac{\left(1-\omega_{CO_2}^{L\,in}\right)}{\left(1-\omega_{CO_2}^{L\,out\,(MIN)}\right)}}\right] \qquad \text{Eqn. 8.12}$$

While the minimum liquid flowrate is the limiting quantity necessary to satisfy the thermodynamic criterion, conventionally a scale-up fraction is employed to provide additional driving force to achieve the separation. In this study, an actual liquid flowrate entering the column $\left(m_{L\,in}^{ACTUAL}\right)$ of 120% of the minimum was utilized as shown in Eqn. 8.13.

$$m_{L\,in}^{ACTUAL} = 1.2 \cdot (m_{L\,in}^{MIN}) \qquad \text{Eqn. 8.13}$$

Finally, the actual composition of CO_2 in the liquid phase leaving the column $\left(\omega_{CO_2}^{L\,out\,(ACT)}\right)$ was calculated using Eqn. 8.14, based on the actual liquid flowrate determined by Eqn. 8.13.

$$\omega_{CO_2}^{L\,out\,(ACT)} = 1 - \frac{\left(1-\omega_{CO_2}^{L\,in}\right)}{\left[\left(\frac{m_{V\,in}}{m_{L\,in}^{ACT}}\right)\left(1-\frac{\left(1-\omega_{CO_2}^{V\,in}\right)}{\left(1-\omega_{CO_2}^{V\,out}\right)}\right)\right]+1} \qquad \text{Eqn. 8.14}$$

The mass balance calculations presented in Eqns. 8.10-8.14 are essential to determine the composition of CO_2 in the liquid phase leaving the column as well as the liquid flowrate necessary to drive the separation.

A log-mean method, shown in Eqn. 8.15, was applied to compute the theoretical number of equilibrium stages required to absorb the desired quantity of CO_2 after converting the mass based CO_2 compositions in the liquid and vapor phases to molar quantities using the molecular weights of the various streams.

$$NTU = \frac{\left[\frac{(y_1 - y_2)}{(y_1 - y_1^*) - (y_2 - y_2^*)}\right]}{ln\left[\frac{(y_1 - y_1^*)}{(y_2 - y_2^*)}\right]} \quad \text{Eqn. 8.15}$$

Finally, column height (H_T) was determined by multiplying the height of a transfer unit by the number of transfer units as shown in Eqn. 8.16.

$$H_T = HTU * NTU \quad \text{Eqn. 8.16}$$

8.5. Method Validation: Comparison to an Experimental MEA Pilot Plant

Theoretical column diameter and height parameters were computed and compared to experimental pilot plant data (trial 35) for a packed absorption column at 1 ATM and 40^{o}C with an absorbent mixture composed of 32.5 mass% monoethanolamine and 67.5 mass% water to evaluate the validity of the equations presented above.[45] Due to the reactive nature of MEA and CO_2 a theoretical mass based Henry's constant was determined from the phase equilibrium data provided in the experimental study ($H_{MEA\text{-}CO2}$ = 7.17). The experimental CO_2 absorption process had a vapor phase flowrate entering the column of 391.92 kg/hr which contained 25.8 mass% (17.1 mole%) CO_2. The liquid phase flow rate was 2568.0 kg/hr and the absorption process was set to remove 95% of CO_2 fed by the flue gas entering the column. The pilot plant was operated continuously for 48 hours to ensure equilibrium conditions within the process unit. The measured CO_2 loadings on the 32.5% MEA absorbent mixture entering and leaving the absorption column were 0.0336 and 0.0485 mole fraction (x_{CO_2}) respectively. Utilizing the experimental pilot plant process parameters and those of MEA at 40^{o}C, the liquid phase flowrate, column diameter, and column height were computed with the computational method presented above. The results are displayed in Table 8.3.

Property	Pilot Plant	Simulated Plant	% Difference
Liquid Flowrate (kg/hr)	2568.0	2573.5	0.21
Column Diameter (m)	0.427	0.438	2.58
Column Height (m)	6.10	6.89	12.95

Table 8.3: Comparing pilot plant and simulated absorption tower data for CO_2 capture.

The column diameter and height calculations correlate well to the experimentally determined data with deviations of 2.58 and 12.95 percent respectively. Additionally, the simulated and pilot plant liquid flowrates are nearly identical with a deviation of only 0.21%. However, caution should be utilized when comparing the flowrate data in this example since the Henry's constant was determined from the experimental absorption unit's inlet vapor and outlet liquid compositions. Therefore, the computational mass balance calculation was directly influenced by the experimental study leading to the excellent agreement between the values in Table 8.3.

The mass balance method presented herein is designed to be used only with physical absorbing solvents that have well defined Henry's constants at specific operating temperatures and pressures. Applying this methodology to reactive systems and solvents with unknown phase equilibrium constants could lead to inaccurate estimations. However, when used within the appropriate boundaries, the calculation methods appear to accurately compute column diameter and height for packed tower absorption processes.

8.6. Are Ionic Liquids Drop-In Replacements for CO_2 Capture in Packed Towers?

Ionic liquids have been proclaimed as "Drop-In" replacements for amine based solvents in conventional packed tower absorption processes based on their unique non-volatility and non-corrosive properties and excellent thermodynamic CO_2 capacities. However, few studies have performed process design calculations to understand how ionic liquids would theoretically

perform in these systems.[36, 38, 46] Utilizing the previously described computational methodology along with physical property data for select ionic liquids shown in Table 8.2, a comparison of packed tower design specifications has been performed to assess the capital considerations of replacing amine based solvents with ionic liquids for CO_2 capture.

8.6.1. Model Assumptions

The case study presented herein is based on a hypothetical 300 MW coal-fired power plant that generates 216,738 kg of flue gas per hour. It is assumed that the post-combustion flue gas enters a conventional desulfurization unit and exits the process at 40^{o}C and 1 ATM, well cited conditions for the feed gas just prior to entering a CO_2 absorption process unit.[8, 47, 48] The mass and mole based flue gas compositions, based on experimentally acquired power plant data, are presented in Table 8.4. Importantly, the flue gas contains 21.81 mass% CO_2.

Species	Mass% Composition	Mole% Composition
Nitrogen (N_2)	69.77	74.37
Carbon Dioxide (CO_2)	21.81	14.80
Water (H_2O)	4.41	7.31
Oxygen (O_2)	2.81	2.62
Argon (Ar)	1.20	0.90

Table 8.4: Composition of flue gas exiting desulfurization unit at 40^{o}C and 1 ATM.

The simulation presented herein is based on a first pass assumption where the concentration of CO_2 in the liquid phase absorbent entering the column is 0.0000 mass%. Real processes will operate continuously with solvent recycle from the desorption process and therefore, liquid phase CO_2 concentration of recycled absorbent entering the column will almost certainly be greater than the assumed 0.0000 mass% as controlled by the energy intensive desorption process. Equilibrium specifications on CO_2 capture solvents leaving the desorption process are not

currently available for ionic liquid systems. Therefore, a first pass (best-case-scenario) has been developed assuming pure solvent is fed into the top of the absorption tower. The absorption process is operated at 40^{o}C and 1 ATM at 70% of flooding with 25mm ceramic Raschig rings as the packing material. Additionally, 90% of CO_2 fed to the inlet of the process is assumed to be recovered by the liquid absorbent.

8.6.2. Mass Balance for Select ILs and Monoethanolamine

The transport and thermodynamic properties of liquid absorbents directly affect their performance as CO_2 capture solvents. Based on the specified flue gas feed rate (216,738 kg/hr), CO_2 loading (21.81 mass%), and desired percent recovery of CO_2 (90%), the quantity of liquid phase absorbent required to complete the separation was calculated and presented in Table 8.5. As evidenced by the results, the liquid phase flowrate is controlled primarily by the thermodynamic CO_2 capacity of the solvent.

Component	Henry's Constant (ATM)	Viscosity (cP)	Diffusivity (cm^2/sec)	Required Liquid Flow Rate (kg/hr) x 10^{-6}
MEA	2.75	1.59	2.14e-5	0.59
[EMIm][Tf_2N]	47.7	21.1	9.50e-6	11.11
[BMIm][Tf_2N]	39.4	27.5	9.00e-6	9.17
[HMIm][Tf_2N]	42.0	37.2	5.00e-6	9.78
[EMIm][BF_4]	100	29.4	5.67e-6	23.36
[BMIm][BF_4]	76.0	59.1	4.30e-6	17.74
Hypothetical IL	1.09	1.60	5.51e-5	0.20

Table 8.5: Flowrate of liquid absorbent required to remove 90% of CO_2 from flue gas. Solvent properties and absorption presented at 40^{o}C and 1 ATM.

Monoethanolamine, which absorbs CO_2 both chemically and physically, has the lowest theoretical Henry's constant (*i.e.* largest CO_2 absorption capacity) of the "real" solvents tested and requires the least amount of liquid absorbent to meet process specifications. Alternatively,

ILs which absorb CO_2 only by physical mechanisms require significantly higher flowrates compared to MEA. A hypothetical ionic liquid was theorized by selecting optimal parameters for CO_2 capture with the intent to provide a list of IL properties required to develop an IL that is competitive with amine based solvents. For instance, select ILs can absorb up to 1:1 mole ratios of CO_2 relative to the IL. On a mass basis this equates to a CO_2 solubility of ~0.14 mass% (based on an average IL with a molecular weight of approximately 250 g/mol) generating a mass based Henry's constant of approximately 1.07 for the optimized ionic liquid. Transport properties of the hypothetical IL were selected based on practical ILs found in literature. As shown in Table 8.5, ILs are capable of exceeding the performance of amine based solvents when the thermodynamic and transport properties are optimized. Currently no available ionic liquid has the unique combination of properties demonstrated here for the hypothetical IL. Therefore, this case is intended to set guides to direct future research on development of TSILs with optimized properties for CO_2 capture.

8.6.3. Column Diameter for Select Ionic Liquids and Monoethanolamine

As previously discussed in Section 8.3, the packed column diameter is primarily determined by the hydrodynamic properties of the absorbent system. Of the solvents investigated, MEA demonstrates the smallest column diameter, 9.1 meters, as shown in Figure 8.6. Comparatively, the best ionic liquid, [BMIm][Tf_2N], required a column diameter of 13.2 meters, approximately 45% greater than the MEA case. Other [Tf_2N] ionic liquids investigated had marginally larger diameters. However, the [BF_4] ILs demonstrated the worst CO_2 capacities (*i.e.* highest Henry's constants) and required the largest column diameters. For instance, [BMIm][BF_4] required a column diameter of 19.3 meters. Alternatively, the enhanced CO_2 capacity of the hypothetical

IL results in the lowest column diameter of 7.0 meters. From a practical engineering perspective, large column diameters will negatively impact the process economics due to increased material and packing cost. Therefore, absorbents should be selected as to minimize the column diameter when possible.

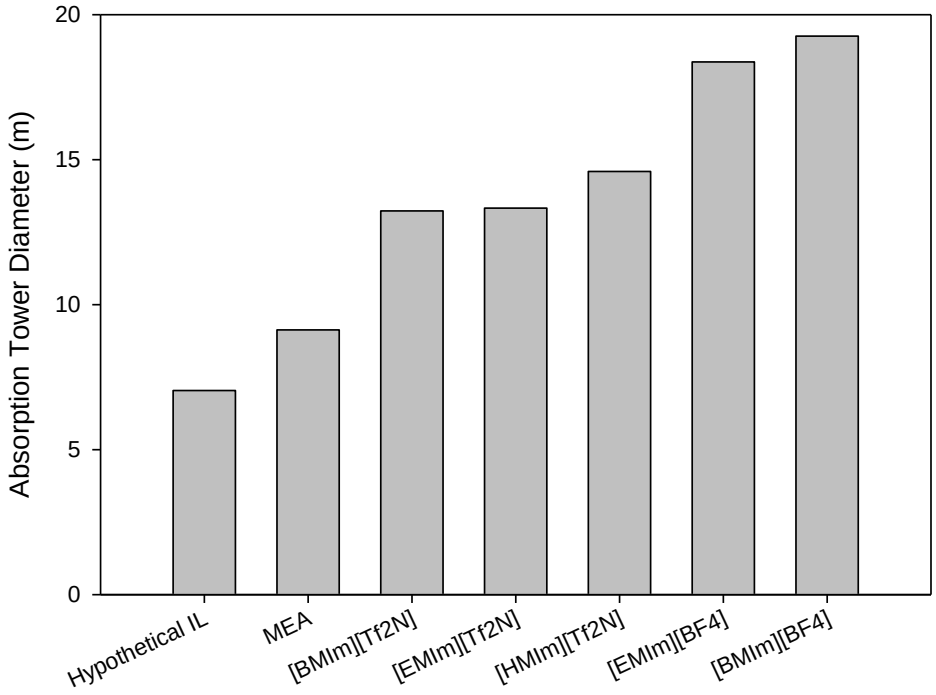

Figure 8.6: Comparison of the packed tower diameter for select absorbents.

The ionic liquid [EMIm][Tf_2N] was selected to examine the impact of temperature on column diameter. Increased temperature significantly reduces mass transport restrictions of the ionic liquid system. For instance, the IL viscosity is reduced by approximately 65% when heated from 30^{o}C to 70^{o}C. However, the enhanced transport phenomena do not positively affect (*i.e.* reduce) the column diameter. Instead, column diameter of the [EMIm][Tf_2N] absorbent system increases

from 13.0 meters to 16.1 meters when the process is operated at 30°C and 70°C respectively as shown in Figure 8.7. Comparing these results to the Henry's constant data it is evident that the driving force for the absorption process is significantly reduced at elevated temperatures. As a result, increasingly large flowrates of liquid absorbent must be fed into the column to reach thermodynamic equilibrium, impacting the hydrodynamics of the process and requiring increasingly large internal column diameters.

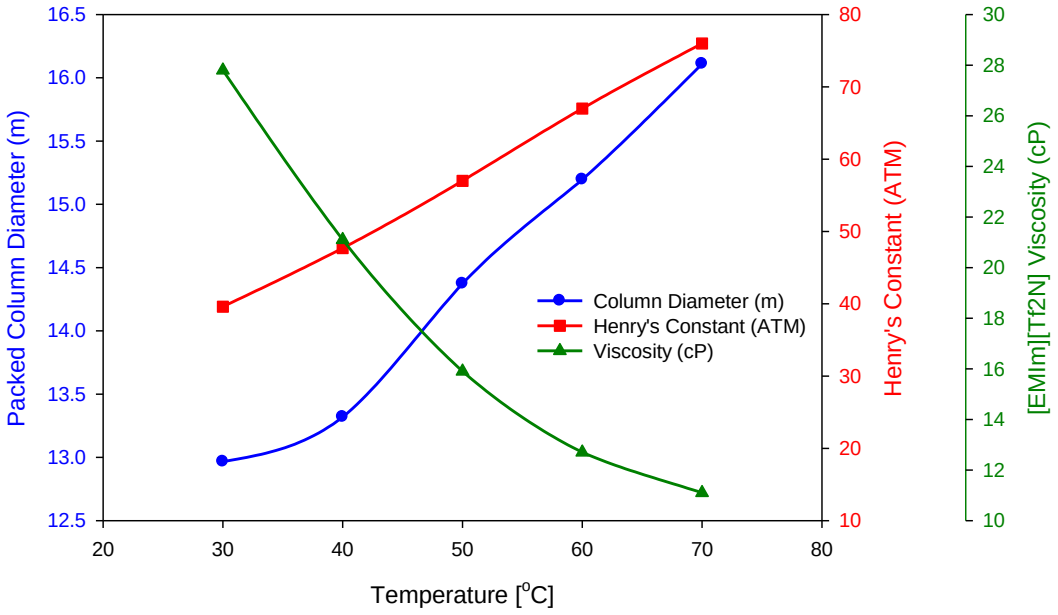

Figure 8.7: Column diameter as a function of temperature, viscosity, and Henry's constant.

8.6.4. Column Height for Select Ionic Liquids and Monoethanolamine

Packed column height is a function of the number of transfer units (NTU) and the height of a transfer unit (HTU). In this study the thermodynamic equilibrium constant and percent recovery of CO_2 were fixed by selecting the absorbent and specifying the process efficiency. Therefore, the concentrations of CO_2 in the vapor and liquid phases entering and exiting the column were

constrained by adjusting the liquid absorbent flowrate through the column. As a result, the various solvents and conditions investigated had an identical number of transfer units (NTUs) which was 7.0. Alternatively, the height of a transfer unit, which depends directly on the rate of gas-liquid mass transfer, varied for the different solvent systems. As column height is a product of the height and number of transfer units, the impact on HTU directly affected the tower height. Therefore, the results have been presented on total tower height with the understanding that HTU is the primary source of the variation.

The packed column height required to remove 90% of CO_2 in the flue gas is reported in Figure 8.8 for a range of ionic liquids and monoethanolamine. None of the "real" ILs were capable of outperforming MEA which had an estimated column height of 9.1 meters. Comparatively, [EMIm][Tf_2N] had the lowest column height (42.6 meters) of the ILs investigated at 40^oC which is considerably larger than the MEA system. The other ILs investigated demonstrated even larger packed column heights as high as 146.4 meters which was observed for [BMIm][BF_4]. It is therefore evident upon inspection that the properties of physical CO_2 absorbing ionic liquids are incapable of matching those of MEA. However, the hypothetical ionic liquid tested which had significantly lower viscosity than the "real" ILs (*i.e.* 1.60 cP) demonstrated a packed column height of only 5.3 meters. Thus, while current physical CO_2 absorbing ILs are not competitive with amine based solvents, a task specific ionic liquid designed with high CO_2 capacity and comparatively low viscosity could be a viable drop-in replacement for amine based solvents.

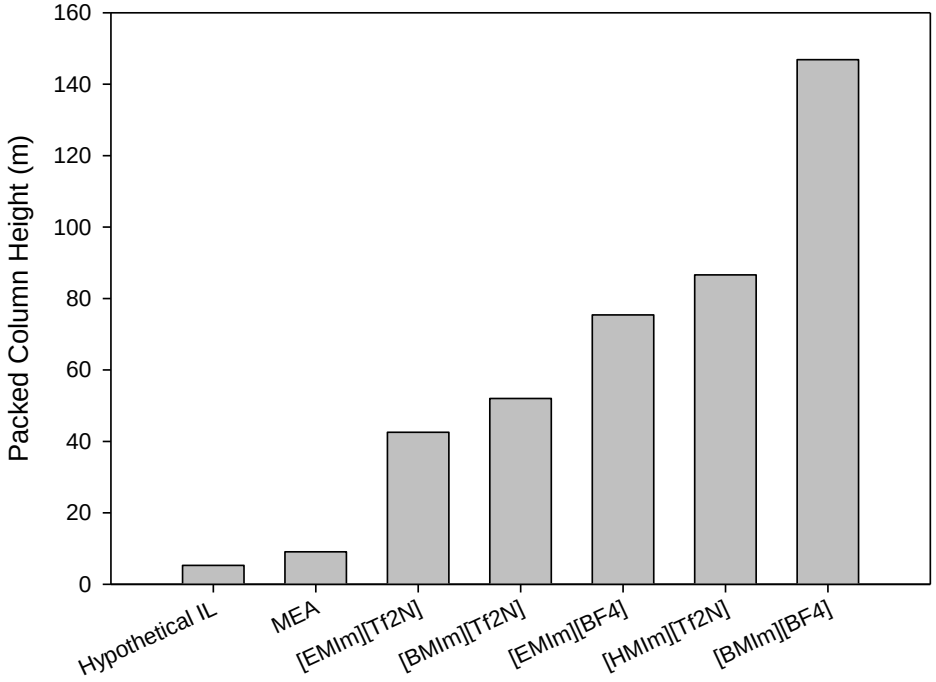

Figure 8.8: Comparison of packed column height for select solvent systems at identical absorption conditions of 40^{o}C and 1 ATM.

The effect of temperature on the packed column height as a function of viscosity and the Henry's constant of CO_2 in [EMIm][Tf_2N] is shown in Figure 8.9. As the temperature of the ionic liquid increases, its inherent viscosity decreases significantly. The reduction in liquid phase viscosity results in a concomitant increase in the diffusivity of CO_2 in the ionic liquid. Therefore, the transport properties of the IL are significantly enhanced at elevated temperatures. Alternatively, increased temperature negatively affects the solubility of CO_2 in the liquid phase as evidenced by the trend of Henry's constant with respect to temperature. Height of a transfer unit is primarily dependent on the liquid phase mass transfer resistance and therefore, Figure 8.9 demonstrates that elevated temperatures favor faster CO_2 absorption and smaller required tower heights to accomplish the desired separation.

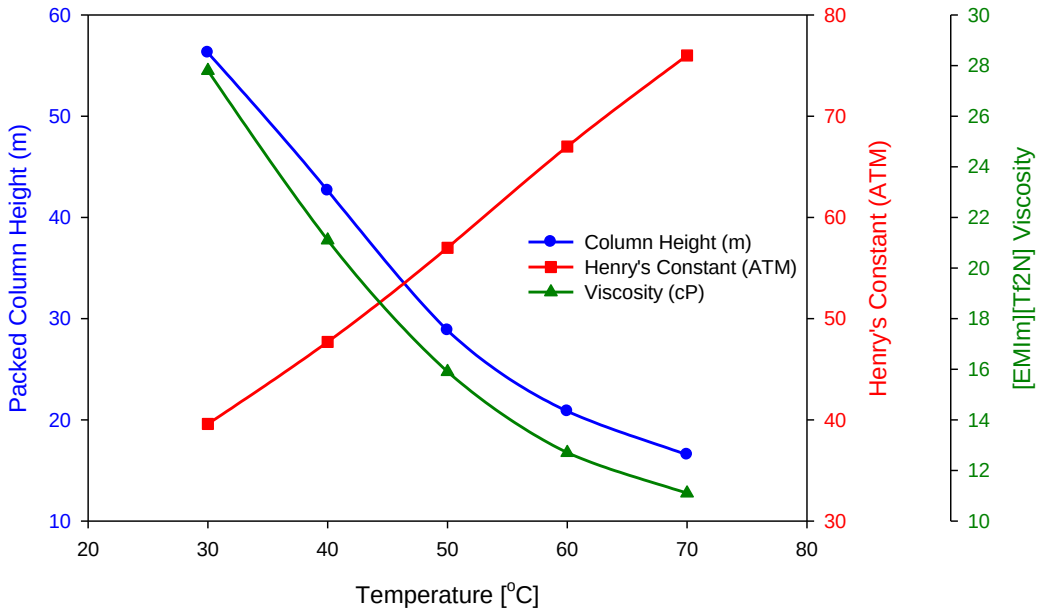

Figure 8.9: Column height as a function of temperature, viscosity, and Henry's constant.

While temperature was previously discussed as the dependent property for reduction of packed column height, [HTU] is directly controlled by the liquid phase viscosity and diffusivity of CO_2. The relationship between column height, diffusivity, and viscosity are displayed in Figure 8.10 and Figure 8.11. The results indicate that tower height is reduced by utilizing absorbents with low viscosities and high CO_2 diffusivities. While thermodynamically favorable ILs have been developed for CO_2 capture, demonstrating equilibrium solubilities as high as 50 mole%, the transport properties of these ILs are less than ideal with viscosities typically greater than 1000 cP and CO_2 diffusivities on the order of 10^{-7} cm^2/sec. As a result, alternative process technologies including those based on rotating baskets and ionic liquid supported membranes have been developed. However, while these modifications successfully overcome the transport limitations of TSILs, they are not "drop-in" technologies for replacing amine based solvents. Therefore, continued research attention should be focused on creating low viscosity ILs for CO_2 capture.

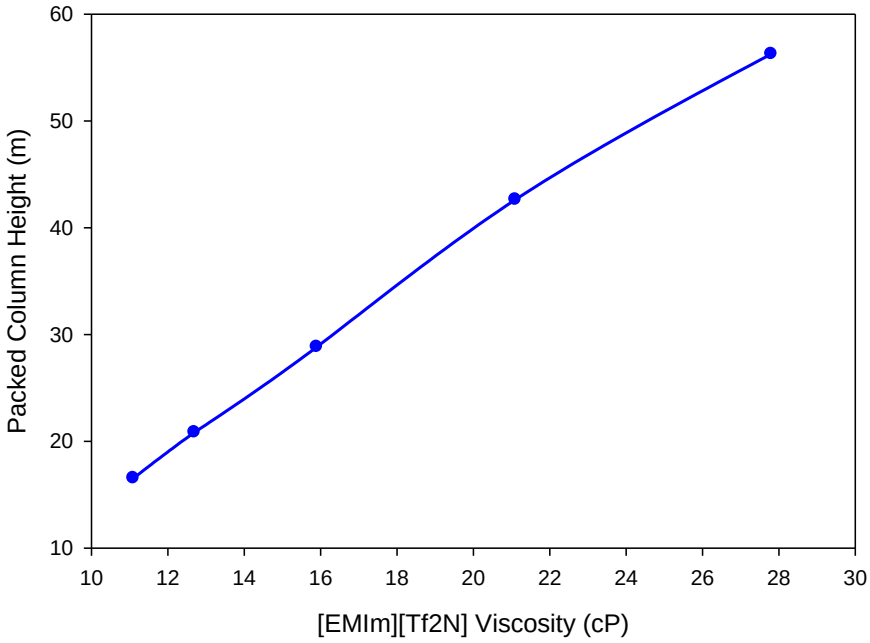

Figure 8.10: Packed column height as a function of ionic liquid viscosity, ceteris paribus.

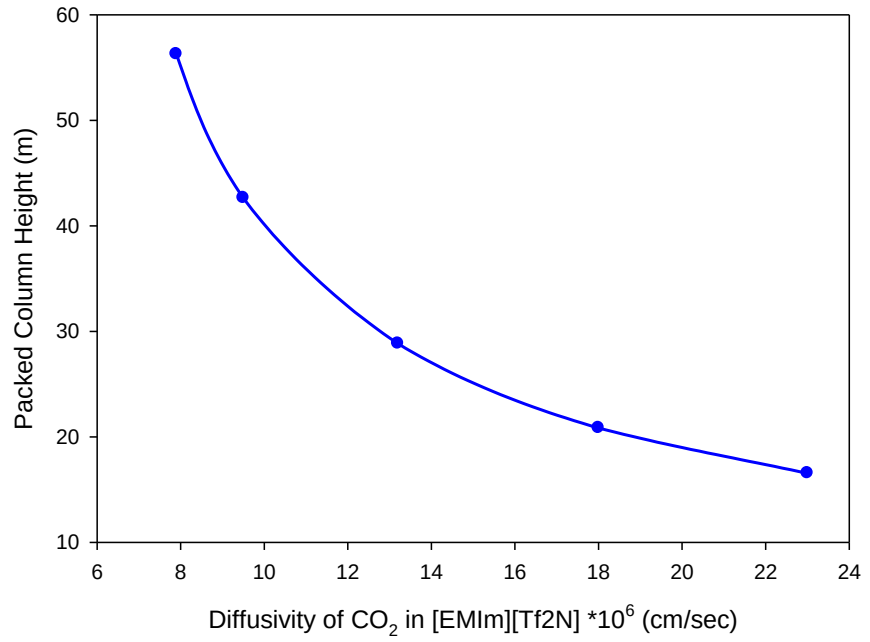

Figure 8.11: Packed column height as a function of CO_2 diffusivity in an IL, ceteris paribus.

8.7. Packed Absorption Tower Design Capital Cost Considerations

The packed column diameter and height have direct impacts on the capital costs of constructing the absorption unit. For instance, the MEA process designed to meet the process specifications to remove 90% of CO_2 from a 300 MW power plant would cost approximately 2.7 million dollars based on Q_1 2003 figures. Comparatively, as shown in Figure 8.12, a packed absorption tower based on even the best performing ionic liquid would cost approximately one order of magnitude more money due to the significantly larger column diameter and height required to complete the separation. These costs only account for the construction of the column and do not include the solvent cost which would penalize the ionic liquids even further.

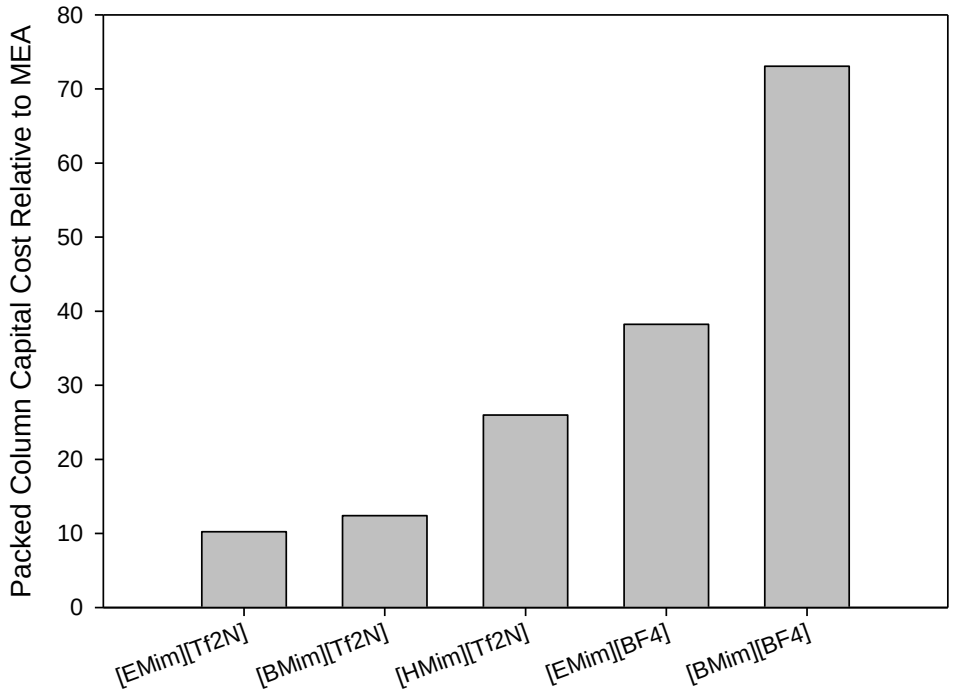

Figure 8.12: Capital costs of constructing a packed tower absorption column based on physical ionic liquids relative to the cost of a comparable process based on MEA.

For instance, in 2014 BASF listed the bulk price of monoethanolamine at ~$2.7 per kg. We estimate that based on current IL production methods even the cheapest ionic liquids would cost ~$5 per kg with [$Tf_2N$] ILs costing approximately $50 per kg and functionalized task specific ILs exceeding $100 per kg. Therefore, the solvent feedstock price must also be considered and efficient recycle processes will be imperative for IL processes to be industrially viable.

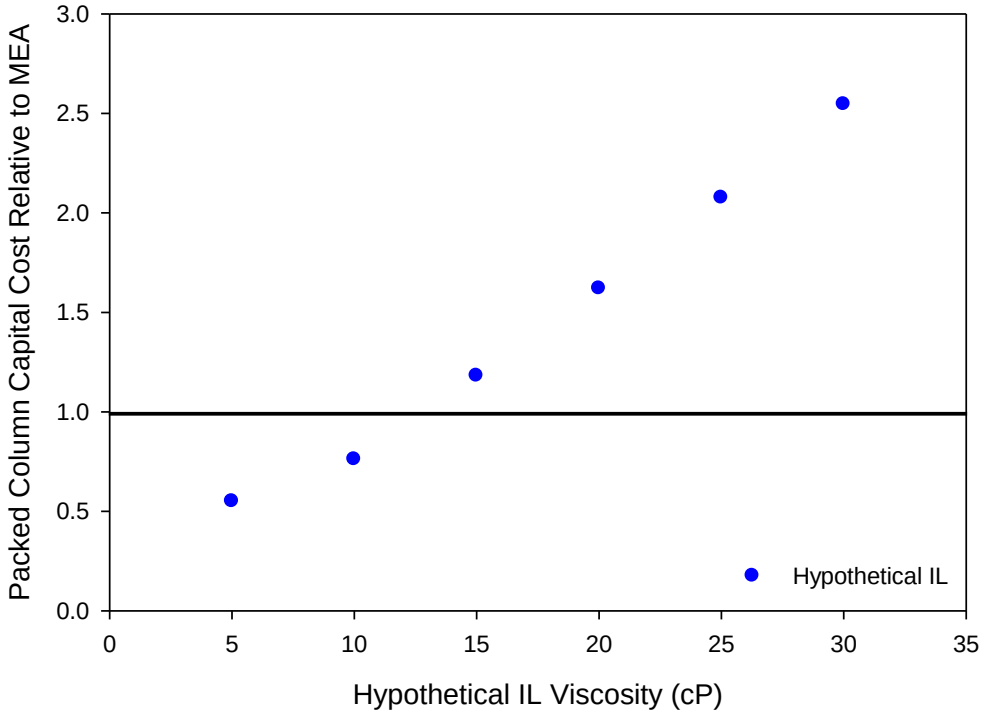

Figure 8.13: Packed tower absorption column capital costs for a hypothetical ionic liquid with a Henry's constant H=1.07 as a function of liquid phase viscosity relative to MEA.

The most significant factors affecting the capital cost of the column were explored and it was determined that liquid phase mass transfer had the most significant impact on column properties and capital costs. Figure 8.13 displays the capital costs of a packed column design for a hypothetical ionic liquid compared to monoethanolamine. The IL was assumed to have optimal

thermodynamic capacity for absorbing CO_2 (*i.e.* H = 1.07) and the transport properties were varied to assess their effects on capital cost. Interestingly, IL viscosity which directly impacts liquid phase CO_2 diffusivity greatly impacted the capital costs of the column. For instance, the IL based process became comparatively cheaper than a process based on MEA when the ionic liquid viscosity was less than approximately 12 cP. Therefore, the design challenge is to create a task specific ionic liquid which can absorb approximately 1:1 (CO_2:IL) molar ratios while maintaining a viscosity below 12 cP and cost of approximately $2 per kg. (All methods for cost calculations were performed according to ASME code).[49, 50]

8.8. Summary

An optimal ionic liquid solvent system will be able to absorb significant quantities of CO_2 (*i.e.* 1:1 mole ratio) while maintaining a low viscosity (*i.e.* less than 12 cP) and high CO_2 diffusivity (*i.e.* faster than 10^{-5} cm^2/sec). Currently available physical CO_2 absorbing ionic liquids are incapable of meeting the process specifications required to replace monoethanolamine as a solvent for CO_2 capture. While select designer task specific ionic liquids demonstrate excellent CO_2 capacities, equal attention must be devoted to creating low viscosity ILs with optimized thermodynamic properties. Theoretical column design results indicate that the capital costs associated with creating an absorption tower process are largely controlled by the liquid phase mass transfer resistance. Process intensification methods including rotating baskets, membranes, and spinning disc contactors could potentially reduce the transport limitations associated with currently available ILs. However, incorporation of these technologies will add complexity and cost to the already comparatively expensive IL based process. Therefore, while current

physically absorbing ILs are not “drop-in” replacements for amine based solvents in CO_2 capture processes, with advances in proper molecular design, ILs possess the potential for future success.

References:

1. Boden, T.A., G. Marland, and R.J. Andres., *Global, Regional, and National Fossil-Fuel CO2 Emissions*, C.D.I.A. Center, Editor 2015: Oak Ridge National Laboratory, U.S. Department of Energy, Oak Ridge, Tenn., U.S.A.
2. United States. Energy Information Administration., et al., *Electric power monthly*, 2016, The Office of Coal and Electric Power Statistics : Supt. of Docs., U.S. G.P.O., distributor: Washington, D.C.
3. United States. Environmental Protection Agency. Office of Policy., *Inventory of U.S. greenhouse gas emissions and sinks*, U.S. Environmental Protection Agency: Washington, DC. p. volumes.
4. Administration, U.S.E.I., *Carbon dioxide emissions per physical unit and million Btu for numerous fuels*, U.S.E.I. Administration, Editor 2016.
5. Wang, J.Y., et al., *Recent advances in solid sorbents for CO2 capture and new development trends.* Energy & Environmental Science, 2014. **7**(11): p. 3478-3518.
6. Dimitriou, I., et al., *Carbon dioxide utilisation for production of transport fuels: process and economic analysis.* Energy & Environmental Science, 2015. **8**(6): p. 1775-1789.
7. Dai, Z., L. Ansaloni, and L. Deng, *Pre-combustion CO2 capture in polymeric hollow fiber membrane contactors using ionic liquids: porous membrane vs. non-porous composite membrane.* Industrial & Engineering Chemistry Research, 2016.
8. Brennecke, J.E. and B.E. Gurkan, *Ionic Liquids for CO2 Capture and Emission Reduction.* Journal of Physical Chemistry Letters, 2010. **1**(24): p. 3459-3464.
9. von der Assen, N., et al., *Selecting CO2 Sources for CO2 Utilization by Environmental-Merit-Order Curves.* Environmental Science & Technology, 2016. **50**(3): p. 1093-1101.
10. Bachu, S., *Identification of oil reservoirs suitable for CO2-EOR and CO2 storage (CCUS) using reserves databases, with application to Alberta, Canada.* International Journal of Greenhouse Gas Control, 2016. **44**: p. 152-165.
11. Luu, M.T., D. Milani, and A. Abbas, *Analysis of CO2 utilization for methanol synthesis integrated with enhanced gas recovery.* Journal of Cleaner Production, 2016. **112**: p. 3540-3554.
12. Ampelli, C., S. Perathoner, and G. Centi, *CO2 utilization: an enabling element to move to a resource- and energy-efficient chemical and fuel production.* Philosophical Transactions of the Royal Society a-Mathematical Physical and Engineering Sciences, 2015. **373**(2037).
13. Yang, N. and R. Wang, *Sustainable technologies for the reclamation of greenhouse gas CO2.* Journal of Cleaner Production, 2015. **103**: p. 784-792.
14. Constantinou, A., S. Barrass, and A. Gavriilidis, *CO2 Absorption in Polytetrafluoroethylene Membrane Microstructured Contactor Using Aqueous Solutions of Amines.* Industrial & Engineering Chemistry Research, 2014. **53**(22): p. 9236-9242.
15. Iliuta, I., F. Bougie, and M.C. Iliuta, *CO2 Removal by Single and Mixed Amines in a Hollow-Fiber Membrane Module-Investigation of Contactor Performance.* Aiche Journal, 2015. **61**(3): p. 955-971.

16. Wang, Z., et al., *Optimization of Blended Amines for CO2 Absorption in a Hollow-Fiber Membrane Contactor.* Industrial & Engineering Chemistry Research, 2013. **52**(34): p. 12170-12182.
17. Goodrich, B.F., et al., *Effect of Water and Temperature on Absorption of CO(2) by Amine-Functionalized Anion-Tethered Ionic Liquids.* Journal of Physical Chemistry B, 2011. **115**(29): p. 9140-9150.
18. Song, J.H., et al., *Solubility of carbon dioxide in monoethanolamine plus ethylene glycol plus water and monoethanolamine plus poly(ethylene glycol) plus water.* Journal of Chemical and Engineering Data, 1996. **41**(3): p. 497-499.
19. Mandal, B.P. and S.S. Bandyopadhyay, *Simultaneous absorption of carbon dioxide and hydrogen sulfide into aqueous blends of 2-amino-2-methyl-1-propanol and diethanolamine.* Chemical Engineering Science, 2005. **60**(22): p. 6438-6451.
20. Tong, D.L., et al., *Solubility of carbon dioxide in aqueous solution of monoethanolamine or 2-amino-2-methyl-1-propanol: Experimental measurements and modelling.* International Journal of Greenhouse Gas Control, 2012. **6**: p. 37-47.
21. Zhang, L.L., et al., *Absorption of Carbon Dioxide with Ionic Liquid in a Rotating Packed Bed Contactor: Mass Transfer Study.* Industrial & Engineering Chemistry Research, 2011. **50**(11): p. 6957-6964.
22. Paul, S., A.K. Ghoshal, and B. Mandal, *Removal of CO2 by single and blended aqueous alkanolamine solvents in hollow-fiber membrane contactor: Modeling and simulation.* Industrial & Engineering Chemistry Research, 2007. **46**(8): p. 2576-2588.
23. Taylor, S.F.R., et al., *CO2 Capture in Wet and Dry Superbase Ionic Liquids.* Journal of Solution Chemistry, 2015. **44**(3-4): p. 511-527.
24. Zhang, X.P., et al., *Carbon capture with ionic liquids: overview and progress.* Energy & Environmental Science, 2012. **5**(5): p. 6668-6681.
25. Pennline, H.W., et al., *Progress in carbon dioxide capture and separation research for gasification-based power generation point sources.* Fuel Processing Technology, 2008. **89**(9): p. 897-907.
26. Zhu, L., G.W. Schade, and C.J. Nielsen, *Real-Time Monitoring of Emissions from Monoethanolamine-Based Industrial Scale Carbon Capture Facilities.* Environmental Science & Technology, 2013. **47**(24): p. 14306-14314.
27. Tan, S.S.Y. and D.R. MacFarlane, *Ionic Liquids in Biomass Processing.* Ionic Liquids, 2009. **290**: p. 311-339.
28. Lee, B.S. and S.T. Lin, *Screening of ionic liquids for CO2 capture using the COSMO-SAC model.* Chemical Engineering Science, 2015. **121**: p. 157-168.
29. Goodrich, B.F., et al., *Effect of Water and Temperature on Absorption of CO2 by Amine-Functionalized Anion-Tethered Ionic Liquids.* Journal of Physical Chemistry B, 2011. **115**(29): p. 9140-9150.
30. Wappel, D., et al., *Ionic liquids for post-combustion CO(2) absorption.* International Journal of Greenhouse Gas Control, 2010. **4**(3): p. 486-494.
31. Wu, C., T.P. Senftle, and W.F. Schneider, *First-principles-guided design of ionic liquids for CO2 capture.* Physical Chemistry Chemical Physics, 2012. **14**(38): p. 13163-13170.

32. Tokuda, H., et al., *How ionic are room-temperature ionic liquids? An indicator of the physicochemical properties.* Journal of Physical Chemistry B, 2006. **110**(39): p. 19593-19600.
33. Guerrero-Sanchez, C., et al., *Magnetorheological fluids based on ionic liquids.* Advanced Materials, 2007. **19**(13): p. 1740-+.
34. Nishida, T., Y. Tashiro, and M. Yamamoto, *Physical and electrochemical properties of 1-alkyl-3-methylimidazolium tetrafluoroborate for electrolyte.* Journal of Fluorine Chemistry, 2003. **120**(2): p. 135-141.
35. Basha, O.M., et al., *Development of a Conceptual Process for Selective Capture of CO2 from Fuel Gas Streams Using Two TEGO Ionic Liquids as Physical Solvents.* Industrial & Engineering Chemistry Research, 2014. **53**(8): p. 3184-3195.
36. Basha, O.M., et al., *Development of a Conceptual Process for Selective CO2 Capture from Fuel Gas Streams Using [hmim][Tf2N] Ionic Liquid as a Physical Solvent.* Energy & Fuels, 2013. **27**(7): p. 3905-3917.
37. Eisinger, R.S. and G.E. Keller, *Process for CO2 Capture Using Ionic Liquid That Exhibits Phase Change.* Energy & Fuels, 2014. **28**(11): p. 7070-7078.
38. Shiflett, M.B., et al., *Carbon Dioxide Capture Using Ionic Liquid 1-Butyl-3-methylimidazolium Acetate.* Energy & Fuels, 2010. **24**: p. 5781-5789.
39. Wang, G.N., et al., *Low-Viscosity Triethylbutylammonium Acetate as a Task-Specific Ionic Liquid for Reversible CO(2) Absorption.* Journal of Chemical and Engineering Data, 2011. **56**(4): p. 1125-1133.
40. Sherwood, T.K., G.H. Shipley, and F.A.L. Holloway, *Flooding velocities in packed columns.* Industrial and Engineering Chemistry, 1938. **30**: p. 765-769.
41. Leva, M., *Flow through Irrigated Dumped Packings - Pressure Drop, Loading, Flooding.* Chemical Engineering Progress Symposium Series, 1954. **50**(10): p. 51-59.
42. Leva, M., *Reconsider Packed-Tower Pressure-Drop Correlations.* Chemical Engineering Progress, 1992. **88**(1): p. 65-72.
43. Seader, J.D.H., E.J.; Roper, D.K., *Separation Process and Principles*. 2011.
44. Cussler, E.L., *Diffusion : mass transfer in fluid systems*. 3rd ed. 2009, Cambridge ; New York: Cambridge University Press. xvii, 631 p.
45. Zhang, Y., et al., *Rate-Based Process Modeling Study of CO2 Capture with Aqueous Monoethanolamine Solution.* Industrial & Engineering Chemistry Research, 2009. **48**(20): p. 9233-9246.
46. Ali, E., et al., *Determination of cost-effective operating condition for CO2 capturing using 1-butyl-3-methylimidazolium tetrafluoroborate ionic liquid.* Korean Journal of Chemical Engineering, 2013. **30**(11): p. 2068-2077.
47. Duan, L.Q., M.D. Zhao, and Y.P. Yang, *Integration and optimization study on the coal-fired power plant with CO2 capture using MEA.* Energy, 2012. **45**(1): p. 107-116.
48. Simon, L.L., et al., *Rate based modeling and validation of a carbon-dioxide pilot plant absorbtion column operating on monoethanolamine.* Chemical Engineering Research and Design, 2011. **89**(9): p. 1684-1692.
49. Couper, J.R., *Chemical process equipment : selection and design*. Rev. 2nd ed. 2010, Amsterdam ; Boston: Elsevier. xvii, 812 p.

50. Seider, W.D. and W.D. Seider, *Product and process design principles : synthesis, analysis, and evaluation*. 3rd ed. 2009, Hoboken, NJ: Wiley. xxxvi, 728 p.

9. Conclusions and Recommendations

9.1. Conclusions

Ionic liquids are traditionally defined as room temperature liquid salts that melt below 100^{o}C. The characteristic ionic interactions between cation and anion constituents of ILs afford them interesting properties including negligible vapor pressures. For this reason, ionic liquids are commonly referred to as environmentally friendly "green" solvents. Ionic liquids also possess excellent thermal stability and have decomposition temperatures greater than 500K allowing them to be applied in high temperature reaction processes without degradation.[1] Furthermore, ionic liquids are deemed "designer solvents" as an estimated 10^{14} unique cation/anion combinations are possible allowing IL functionality to be tailored to the desired application. Despite these advantages, ionic liquids are currently produced by batch synthesis methods yielding small quantities of product at high costs (*i.e.* > \$10 per kg). Therefore, ILs are significantly more expensive than alternative organic solvents which often precludes them from consideration in industrial processes. Additionally, many ILs are hygroscopic and display moderate viscosities which could be problematic in large scale applications. Nonetheless, research on ionic liquids continues to demonstrate excellent performance in extraction, chemical reaction, and materials processing fields. Furthermore, select imidazolium based ionic liquids have shown great potential for lignocellulosic biomass dissolution and conversion.

9.1.1. Mixed Solvent Effects on the Dissolution of Cellulosic Biomass

Select hydrogen bond accepting ionic liquids are excellent solvents for cellulosic biomass. The ionic liquid 1-ethyl-3-methylimidazolium diethyl phosphate [EMIm][DEP] was explored as a

solvent for microcrystalline cellulose. Solid-liquid phase equilibrium results demonstrated that cellulose solubility was proportional to temperature up to 120^{o}C where a maximum of approximately 20 mass% cellulose was observed. Conventional thermodynamic analysis was applied to this system and it is believed that the solid phase activity coefficient greatly increases at high biomass loadings thus reducing the solubility of the polymer in the IL. Furthermore, IL-cellulose bonding scenarios were examined based on the work of Rabideau *et al.*[2] The results demonstrated that cellulose dissolution in an ionic liquid is primarily driven by IL anion – cellulose interactions. Therefore, when all of the IL ions have been bound in solution the temperature independent saturation limit of cellulose is theoretically reached. Based on the computational work of Rabideau *et al.* we estimate this theoretical maximum solubility to be approximately 24 mass%.

As previously discussed, pure ionic liquids are expensive and comparatively viscous relative to organic solvents. Therefore, a strategy was conceptualized to mix ionic liquids and polar aprotic solvents with the goal of merely sustaining the mixed solvent biomass capacity while reducing the quantity of ionic liquid required by the process. Experimental solid-liquid phase equilibrium studies were conducted on mixtures of [EMIm][DEP] with dimethyl sulfoxide, dimethylformamide, and dimethyl imidazolidinone. The results showed that, contrary to the original hypothesis, cellulose solubility in the mixed solvent system increased and was greater than what was observed in the pure IL. For instance, the 25 mass% DMSO system (solute free basis) dissolved 14.2 mass% cellulose (total solution basis) which was 56% greater than the pure IL at the same temperature. Similar results were obtained for DMF and DMI at 40^{o}C and 60^{o}C. However, at 80^{o}C pure [EMIm][DEP] displayed the maximum solubility and cosolvent addition beyond 25 mass% had a negative impact on biomass solubility. It is hypothesized that the

decrease in solubility at high cosolvent loadings is due to the dilution of the IL (most importantly anions) in solution. Regardless, the results presented demonstrate that mixed IL-polar aprotic cosolvent systems are advantageous for dissolution and processing of cellulosic biomass.

Mixed IL-antisolvent systems were also investigated with protic solvents ethanol, methanol, and water. Solid-liquid phase equilibrium results demonstrated that solubility of cellulose in an ionic liquid is significantly impacted by the presence of small quantities of protic solvents. For instance, at 40^{o}C, the presence of only 1 mass% water (solute free basis) reduced the solubility of cellulose in the IL by 55%. Similar results were also observed for ethanol and methanol. Increased temperature at 60^{o}C and 80^{o}C reduced the effect of protic solvents on cellulose solubility but the impact was still evident. For instance, at 80^{o}C, cellulose solubility in [EMIm][DEP] was reduced by 66% when only 5 mass% water was added to the IL. Kamlet Taft solvatochromic parameters, infrared and NMR spectroscopy were applied to understand the observed cellulose solubility trends in the various mixed solvent systems. The results indicated that hydrogen bond accepting ability of the IL anion (*i.e.* basicity) is critical to the biomass dissolving ability of the ionic liquid. Furthermore, mixtures of [EMIm][DEP] with polar aprotic solvents demonstrated enhanced synergistic hydrogen bond accepting behavior whereas polar protic solvent mixtures significantly reduced the basicity of the mixed IL systems.

Some ionic liquids including [EMIm][DEP] dissolve significant quantities of cellulosic biomass. Several potential applications of ILs in biomass processing to fuels and chemicals have been proposed which often include the addition of other liquid solvents. We have demonstrated here that polar aprotic cosolvents can be used to significantly improve the thermodynamic solubility of cellulose depending on the composition and temperature of the system. However, polar protic

solvents, especially water, induce dramatic decreases in cellulose solubility when mixed with ILs at relatively low compositions. Therefore, any process that includes water intentionally or unintentionally will require high levels of IL purification prior to reuse. In IL-cosolvent mixtures the effect of the antisolvent at relatively low compositions is diminished, but still allows precipitation at higher loadings. Solvatochromic probes for determining mixture Kamlet-Taft polarity parameters of IL-cosolvent mixtures seem to correlate nearly quantitatively with these enhanced dissolution properties. However, for antisolvents the *KT* parameters do not exhibit the same dramatic drop as is observed in the solubility measurements with increased antisolvent composition. NMR and FTIR spectroscopic shifts also trend with the behavior of both co- and anti-solvents. Thus, Kamlet-Taft and other spectroscopic techniques may be potential rapid screening tools for designing IL, cosolvent, and antisolvent systems for biomass processing. In addition, we suggest that [EMIm][DEP] should be considered as a "model" ionic liquid for future studies investigating thermodynamic and transport properties of cellulose and potentially other biomass components with ionic liquids.

9.1.2. Gas Antisolvent Process for the Precipitation of Cellulose from an IL

Based on the solid-liquid phase equilibrium data presented in Chapter 3, process modeling was applied to assess the separation costs of purifying [EMIm][DEP] from a 50 mass% water solution. The results indicated that vacuum distillation at 0.01 bar and 175^{o}C were required to purify the IL to 97 mass% consuming more than 17 MJ of heat per kg of cellulose processed, more energy than what is inherently present in cellulose itself (*i.e.* 14-16 MJ/kg). Even at these separation conditions, 3 mass% water still remains in the IL which will have significant impacts on cellulose solubility in the recycled ionic liquid. Based on these results, protic liquid

antisolvents do not appear as a viable separation technique for the precipitation of cellulosic biomass from ionic liquids. Therefore, as an alternative approach, compressed carbon dioxide has been proposed as an energy efficient gas antisolvent method. CO_2 pressures between 26 and 65 bar were applied to mixed IL-cosolvent systems to precipitate approximately 5 mass% cellulose. Most importantly, the separation was completely reversible using CO_2 composition as a separation switch. Therefore, by simply depressurizing the sample, CO_2 concentration was reduced and the cellulose solvation power of the ionic liquid was completely regenerated. Therefore, this study demonstrated the first physical (non-reactive) precipitation of cellulosic biomass from an ionic liquid mixture using compressed carbon dioxide. High pressure NMR confirmed that precipitation does not occur via chemical reaction with CO_2. Solid state NMR indicated an 80+% reduction in cellulose crystallinity. Cellulose precipitation was driven by liquid phase composition of carbon dioxide which dramatically reduced the cellulose solubility after a critical composition was obtained.

9.1.3. Chemical Conversion of Cellulose in Ionic Liquid Solvent Systems

Cellulose and hemicellulose can be chemically converted to value added compounds in ionic liquid and mixed IL-cosolvent systems. Preliminary studies conducted herein investigated the chemical conversion of fructose to 5-HMF in mixed IL-cosolvent systems focusing on [EMIm][DEP] and DMSO with a homogeneous hydrochloric acid catalyst at 100^{o}C. The results indicated that the rate of fructose conversion was first order and significantly accelerated in the mixed solvent systems compared to pure [EMIm][DEP]. Additionally, the mixed solvent systems demonstrated significantly greater yields of 5-HMF (~70 mole%) compared to what was observed in the pure IL solvent system (~10 mole%). Despite successful conversion of biomass

to 5-HMF in [EMIm][DEP], the 5-hydroxymethylfurfural product is relatively unstable in aqueous and ionic liquid systems and decomposed at moderate temperatures to form a combination of levulinic acid, formic acid, and insoluble humins. To assess the stability issues, 5-HMF composition was measured in the pure IL and mixed IL-DMSO solvent systems at 100^{o}C at time increments up to 150 minutes. The results indicated that approximately 87 mole% of 5-hydroxymethylfurfural degraded in the pure [EMIm][DEP] sample after 150 minutes whereas the product was increasingly stabilized in pure DMSO (16 mole% degradation) and the mixed DMSO-IL solvent systems. Therefore, the inclusion of a polar aprotic cosolvent was found to inhibit the degradation of 5-HMF and formation of byproducts.

To this point chemical conversion processes have primarily targeted the production of polar products which are highly miscible with ionic liquids (*i.e.* 5-HMF) requiring energy intensive purification methods for product isolation and recovery. Alternatively, ideal products from lignocellulosic biomass conversion in ionic liquids will be recoverable without the use of energy intensive separation procedures. Products including 2,5-dimethylfuran, 2,5-dimethyltetrahydrofuran, 2-methylfuran, and 2-methyltetrahydrofuran which are produced by hydrogenation of 5-hydroxymethylfurfural and furfural are promising. Compared to 5-hydroxymethylfurfural, these compounds demonstrate low polarities which allow them to naturally partition out of ionic liquids thus generating a bi-phasic separation. Preliminary research presented herein targeted hydrogenation reactions of cellulose derived 5-HMF and hemicellulose based furfural which have been produced in ILs with high selectivity. Transformation of these molecules yields furan products that are applicable as “drop-in” fuel replacements and industrial solvents. To accomplish this, phase equilibrium, mass transport, and kinetic aspects of the respective hydrogenation reactions were explored. Significant emphasis

was placed on tuning hydrogen solubility with compressed CO_2 since previous studies demonstrated that liquid phase H_2 concentration was rate limiting for hydrogenation reactions in ILs. Additionally, phase equilibrium results indicated that, as hypothesized, furan products including 2,5-DMF and 2,5-DMTHF have limited miscibility with [EMIm][DEP] at 25^{o}C. Furthermore, the ionic liquid is completely immiscible with the furan rich phase thus generating an effective separation. Finally, compressed carbon dioxide demonstrated qualitative enhancement of the furan separation process.

9.1.4. VLE, Process, and LCA Modeling of [HMIm][Br] Synthesis

As ionic liquid research and applications increase, continuous IL production methods will be required to meet the forecasted demand. In the interest of investigating a low cost, high volume, IL synthesis method research in the Scurto group previously determined the solvent dependent kinetic rate constants for the [HMIm][Br] synthesis reaction. The results indicated that polar aprotic solvents with high acidity and polarizability are ideal for accelerating the [HMIm][Br] reaction rate. Of the solvents investigated herein, the kinetic studies found that dimethyl sulfoxide provided the fastest reaction rate followed by acetonitrile, acetone, and dichloromethane. While reaction rate optimization is important, separation parameters and environmental impacts of the IL synthesis process are also vital to a complete process design. Therefore, research presented herein investigated the vapor-liquid and liquid-liquid phase equilibrium thermodynamic properties of binary mixtures in the post-reaction [HMIm][Br] synthesis system. The phase equilibrium data was modeled by activity coefficient and Equation of State methodologies and the binary interaction parameters were utilized by Aspen Plus to develop a process model for the continuous synthesis of [HMIm][Br] at a production rate of 30

metric tons per day. The process modeling results demonstrated that solvent selection and operating temperature had significant impacts on the reactor size and separation energy of the process. Whereas, [HMIm][Br] synthesis in DMSO provided the best reaction kinetics and smallest reactor volume, this solvent system required significantly greater separation energy for [HMIm][Br] purification. Alternatively, dichloromethane required the least separation energy of the solvents investigated but required significantly larger reactor volumes due to the comparatively slower kinetics of the IL synthesis reaction. Based on the process modeling results, clear tradeoffs exist between capital and operating expenses when selecting an ideal reaction solvent for the production of [HMIm][Br].

The sustainability of ionic liquid synthesis in various reaction solvents was assessed by a cradle-to-gate life cycle assessment methodology based on the mass and energy balances generated by the Aspen Plus simulations. The LCA results demonstrated that from an environmental perspective, acetone is the most optimal reaction solvent for IL synthesis followed by acetonitrile, dimethyl sulfoxide, and dichloromethane. Therefore, despite having the highest volatility and requiring the lowest separation energy, dichloromethane was the least sustainable IL synthesis reaction solvent due to its high carcinogenetic and eco-toxicity impacts. Based on these results, it is recommended that future IL synthesis procedures utilize acetone or acetonitrile as the reaction solvent. Furthermore, the nominal LCA results for IL synthesis were compared to the impacts associated with the production of monoethanolamine and N-methylmorpholine-N-oxide two conventional solvents for CO_2 capture and cellulose dissolution respectively. The results demonstrated that [HMIm][Br] production in acetone, acetonitrile, and dimethyl sulfoxide were more sustainable than the production of the conventional organic chemicals indicating that ILs are suitable replacements for volatile organic chemicals from a sustainability perspective.

9.1.5. Ionic Liquids as "Drop-In" Replacements for CO_2 Capture

Ionic liquids have been proclaimed as drop in replacements for amine based solvents (*i.e.* monoethanolamine) in packed tower absorption processes for CO_2 capture from post combustion flue gas. The thermodynamic properties of conventional ionic liquids including 1-ethyl-3-methylimidazolium bis(trifluromethylsulfonyl)imide [EMIm][Tf_2N] are less ideal (H_{CO2} = 47.7 ATM @ 40^oC) than MEA which absorbs CO_2 by physical and chemical methods. However, select task specific ionic liquids (TSILs) have been designed which can absorb up to a 1:1 mole ratio of carbon dioxide. Unfortunately the high viscosities of conventional, and especially task specific, ionic liquids create design problems when utilized in packed absorption columns. For instance, the viscosity of [EMIm][Tf_2N] at 40^oC is 21.1 cP, an order of magnitude greater than monoethanolamine. The design of a packed absorption tower is dependent on the height of a transfer unit, the number of transport units, and column diameter. The design presented herein fixed the CO_2 recovery ratio thus manipulating the column specifications to achieve the desired separation. The results demonstrated that column height for ionic liquid systems were 50% to 150% greater than what was required for an amine based solvent at the same process conditions. Column height was directly impacted by the height of a transfer unit (HTU) which was limited by liquid phase mass transfer resistance (*i.e.* IL viscosity). Tower diameter for the IL systems were between 56 and 111% greater than what was required for the MEA system. Due to the comparatively slow gas-liquid mass transport of CO_2 in ILs (*i.e.* 10^{-7} cm^2/sec) increasingly large flowrates of liquid IL absorbent were required to achieve the separation. The considerably larger column heights and diameters required had a direct impact on the capital cost to design a system utilizing ionic liquids. For instance, packed column absorption towers based on ILs were 10 to 75 times more expensive than a system that used monoethanolamine. A list of optimal IL

properties for CO_2 capture were developed based on a hypothetical ionic liquid that demonstrated superior performance compared to MEA. The hypothetical IL maintained a Henry's constant of 1 ATM, a viscosity of 1.6 cP and a diffusivity of $5.51x10^{-5}$ cm^2/sec. The study further demonstrated that creating a low viscosity IL is imperative to successful implementation in conventional packed absorption tower processes. Continued work on the molecular design of ILs for CO_2 capture is strongly encouraged as currently available ILs are not "drop-in" replacements for carbon dioxide capture as commonly proclaimed in the literature.

9.2. Recommendations and Future Work

9.2.1. Mixed Solvent Systems for Biomass Dissolution

The solubility studies presented herein targeted developing optimal solvents for cellulosic biomass dissolution. The results indicated that polar aprotic solvents, when mixed with ILs, enhanced the thermodynamic dissolution capacity of cellulose in IL-cosolvent systems. The following recommendations are made for future work in this area:

- Screen the IL-cosolvent mixtures for their solubilities of hemicellulose and lignin.
- Develop mixed IL-cosolvent systems which readily dissolve cellulose and hemicellulose but do not dissolve lignin.
- Explore mixing multiple ILs to tune the biomass solubility properties as opposed to mixing an ionic liquid with an organic solvent.
- Develop ionic liquids with 2+ cation and anion sites and apply these ILs to biomass dissolution. Investigate if the increased presence of anionic hydrogen bond accepting sites generates a concomitant increase in cellulose solubility.

9.2.2. Chemical Conversion of Cellulosic Biomass in Mixed IL Solvents

Preliminary studies on the production of 5-HMF from fructose were conducted in varying mixed IL-cosolvent systems. The results demonstrated that the reaction rate, 5-HMF stability and yield were all enhanced by the presence of a polar aprotic solvent. Therefore, the following recommendations are made for future work in this area:

- Screen additional cosolvents including acetone, acetonitrile, dimethylformamide, and dimethyl imidazolidinone to compare the reaction performance for the conversion of fructose to 5-HMF.
- Identify what specific solvent characteristics are optimal for the production and stability of 5-HMF in mixed solvent systems potentially utilizing the Kamlet Taft solvatochromic analysis presented herein for [EMIm][DEP]-cosolvent systems.
- Modify the study to begin with cellulose as opposed to the model compound fructose.
- Develop and model the separation energies required to extract 5-HMF from an ionic liquid reaction mixture.
- Based on a complete process flow diagram utilizing the thermodynamic data presented herein for biomass solubility in mixed IL-cosolvent systems, develop a process model to estimate the cost of producing 5-HMF by an ionic liquid processing route.

9.2.3. Hydrogenation of 5-HMF in Mixed IL-Cosolvent Systems

Chapter 5 discusses the current state of cellulosic biomass conversion research in ionic liquids. Based on the results presented it is evident that 5-HMF can be stabilized in ionic liquid-polar aprotic solvent mixtures and that separation of the 5-HMF product from the reaction mixture will

be prohibitively energy intensive. Therefore, future work should evaluate the potential of performing hydrogenation reactions of 5-HMF and furfural to furan products in ionic liquids. Although absent from the initial 2004 National Renewable Energy Laboratory (NREL) report, furan products from cellulose including 2,5-dimethylfuran and 2,5-dimethyltetrahydrofuran as well as hemicellulose derived products 2-methylfuran and 2-methyltetrahydrofuran are receiving increased attention due to their potential as drop-in fuel replacements for gasoline and commercial solvent applications.[3]

Experiments in this study for 5-HMF and furfural conversion should be initially performed independently to simplify the conversion process and to gain an understanding of critical reaction parameters (*i.e.* temperature, H_2 partial pressure, CO_2 partial pressure, catalyst loading *etc.*). However, the extended goal of this research is to convert both cellulose and hemicellulose fractions of biomass to products in a simplified one or two-stage reaction system. To accomplish this, future work should attempt to simultaneously convert 5-HMF and furfural to furan products in a one-pot system. Generating an efficient separation method for isolating the various furan molecules will add complexity to this process since the products have similar nonpolar structures and will theoretically partition into a single product phase. In this case distillation may be required to obtain individual product streams. Alternatively, it is possible that the furan blend could be applied as a potential fuel replacement without separation.

In agreement with the aforementioned task, an additional motivation for future work should be to investigate the effects of compressed carbon dioxide on the conversion of cellulose and hemicellulose to 5-HMF and furfural respectively. Previous studies have shown that the hydrolysis and isomerization reactions which produce 5-HMF and furfural are enhanced by

acidic and less viscous media.[4, 5] It is therefore hypothesized that compressed CO_2 could also benefit these stages of biomass conversion process as CO_2 can form carbonic acid in the presence of water thereby lowering the reaction phase pH.[6] Furthermore, rheology studies have demonstrated that CO_2 is a viscosity reducing agent when mixed with ionic liquids.[7] Carbon dioxide therefore has the potential to diminish mass transport issues that are typically cited as limitations of biomass hydrolysis in ILs.

The overarching goal of this future work is to develop an integrated process which is capable of converting raw lignocellulosic biomass into value-added furan products. Preliminary indications show that compressed gases may be beneficial towards enhanced biomass hydrogenation in ionic liquids. Therefore, further investigations will examine the application of CO_2 to other stages of biomass processing with the hopes of ultimately creating a conversion process that efficiently utilizes the advantages of the ionic liquid and compressed gas technology proposed.

In summary the objective of the proposed future work is to further the current status of biomass conversion in ionic liquids by creating a range of value-added furan products which are recoverable without energy intensive separation processes.

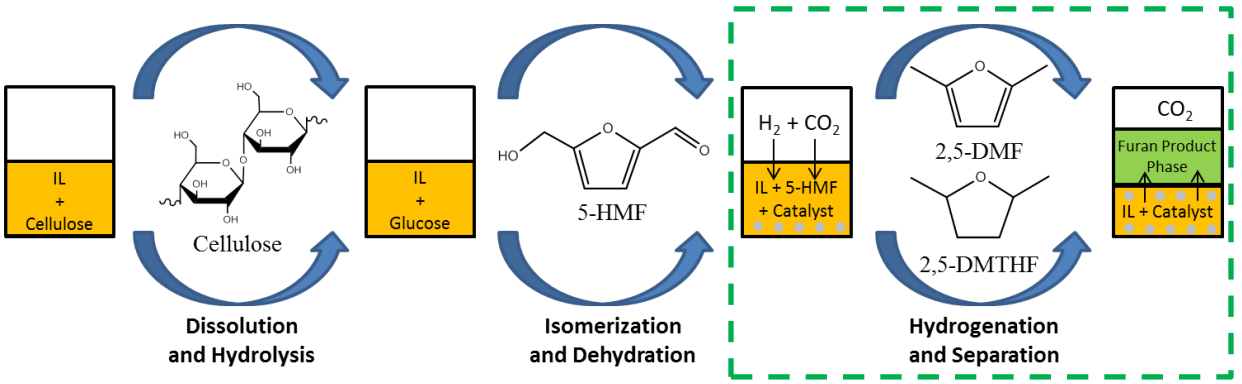

Figure 9.1: Graphical depiction of the cellulose to furan conversion process in ILs.

Future work should address the following five aspects related to hydrogenation reactions in ionic liquids.

- Phase equilibrium studies should be conducted to investigate the solubility of hydrogen in biomass dissolving ionic liquids with and without enhancement by compressed carbon dioxide.
- Independent hydrogenation reactions of 5-HMF and furfural should be conducted in ionic liquids with supported metal catalysts targeting the production of furan products.
- Selective production of hydrogenation products 2,5-DMF and 2,5-DMTHF from 5-hydroxymethylfurfural as well as 2-MF and 2-MTHF from furfural should be investigated by tuning hydrogen solubility in the IL reaction phase along with the system phase equilibrium.
- Polarity induced bi-phasic separations of furan products from IL reaction mixtures should be explored with enhanced separation by compressed CO_2.
- A life cycle assessment study should be conducted to investigate the production of furan molecules by hydrogenation in ionic liquid solvents. Additionally, the LCA study should be extended to encompass complete conversion of biomass (cellulose to target products) in an ionic liquid and compared to alternative biomass conversion technologies potentially including hydrothermal liquefaction and biomass gasification.

9.2.4. IL Synthesis Project

Herein phase equilibrium thermodynamic (vapor-liquid equilibrium) experiments were conducted to assess the post reaction separation of [HMIm][Br] from its reaction mixture. Additionally, process and life cycle assessment modeling was conducted to develop an understanding of the operating costs and environmental impacts associated with continuously producing an ionic liquid. [HMIm][Br] is considered to be a platform IL and functionalized

"task specific" ionic liquids are produced from it using anion exchange techniques. Kinetic parameters for the synthesis of a bis(trifluoromethylsufonyl)imide [Tf_2N] ionic liquid were previously measured in the Scurto laboratory. Therefore, the following recommendations are made for future work in this area:

- Perform vapor-liquid equilibrium measurements to obtain the separation energies required to purify a [Tf_2N] ionic liquid from its reaction mixture.
- In conjunction with previously developed kinetic rate constants conduct process and life cycle assessment modeling studies. Compare the cost and environmental hazards of producing the [Tf_2N] IL to what was presented here for [HMIm][Br].
- Optimize and recalculate the process modeling and LCA impacts for [HMIm][Br] synthesis.

References:

1. Zhang, S.J., et al., *Physical properties of ionic liquids: Database and evaluation.* Journal of Physical and Chemical Reference Data, 2006. **35**(4): p. 1475-1517.
2. Rabideau, B.D. and A.E. Ismail, *Mechanisms of hydrogen bond formation between ionic liquids and cellulose and the influence of water content.* Physical Chemistry Chemical Physics, 2015. **17**(8): p. 5767-5775.
3. Bozell, J.J. and G.R. Petersen, *Technology development for the production of biobased products from biorefinery carbohydrates-the US Department of Energy's "Top 10" revisited.* Green Chemistry, 2010. **12**(4): p. 539-554.
4. Xiao, S.H., et al., *Efficient conversion of cellulose into biofuel precursor 5-hydroxymethylfurfural in dimethyl sulfoxide-ionic liquid mixtures.* Bioresource Technology, 2014. **151**: p. 361-366.
5. Zakrzewska, M.E., E. Bogel-Lukasik, and R. Bogel-Lukasik, *Ionic Liquid-Mediated Formation of 5-Hydroxymethylfurfural-A Promising Biomass-Derived Building Block.* Chemical Reviews, 2011. **111**(2): p. 397-417.
6. Liu, F., et al., *Dehydration of Highly Concentrated Solutions of Fructose to 5-Hydroxymethylfurfural in a Cheap and Sustainable Choline Chloride/Carbon Dioxide System.* Chemsuschem, 2012. **5**(7): p. 1223-1226.
7. Ahosseini, A., et al., *Viscosity of n-alkyl-3-methyl-imidazolium bis(trifluoromethylsulfonyl)amide ionic liquids saturated with compressed CO2.* Fluid Phase Equilibria, 2009. **286**(1): p. 72-78.

Appendices

Appendix 1: Isobaric Vapor-Liquid Equilibrium (*Txy*) for [HMIm][Br] Synthesis

Acetone solvent system phase equilibrium results.

Temperature [K]	X_1	Y_1
329.3	1.0000	1.0000
330.8	0.9345	0.9999
332.3	0.8514	0.9999
333.2	0.8070	0.9999
334.6	0.7284	0.9994
336.4	0.6457	0.9935
338.6	0.5677	0.9896
342.7	0.4590	0.9823
350.8	0.3704	0.9730
355.4	0.3177	0.9560
359.4	0.2781	0.9505
364.4	0.2402	0.9373
372.1	0.1939	0.9051
376.9	0.1692	0.8926
380.4	0.1567	0.8576
386.6	0.1109	0.8136
395.8	0.0922	0.7210
404.2	0.0561	0.6045
409.0	0.0465	0.5375
417.7	0.0211	0.3331
422.1	0.0117	0.1904
428.5	0.0000	0.0000

Table A1: Isobaric vapor–liquid equilibrium at 1.01325 bar for the binary systems **Acetone (1) – 1-Bromohexane (2)** involved in the synthesis of the model IL, [HMIm][Br].

Temperature [K]	X_1	Y_1
329.3	1.0000	1.0000
329.8	0.9366	0.9999
332.2	0.8134	0.9995
333.9	0.7466	0.9990
335.5	0.6874	0.9989
338.7	0.5896	0.9978
341.8	0.5091	0.9968
344.4	0.4445	0.9957
347.9	0.3859	0.9935
353.4	0.3140	0.9913
363.5	0.2323	0.9793
369.3	0.2065	0.9661
390.8	0.1208	0.9157
399.5	0.1045	0.8875
409.9	0.0798	0.8577
422.9	0.0576	0.8116
438.9	0.0360	0.6281
453.4	0.0266	0.5048
460.0	0.0181	0.3479
464.2	0.0143	0.2828
467.9	0.0076	0.1468
471.6	0.0000	0.0000

Table A2: Isobaric vapor–liquid equilibrium at 1.01325 bar for the binary systems **Acetone (1) – 1-Methylimidazole (2)** involved in the synthesis of the model IL, [HMIm][Br].

Temperature [K]	X_1	Y_1
329.3	1.0000	1.0000
330.9	0.9056	1.0000
331.3	0.8658	1.0000
331.8	0.8257	1.0000
332.3	0.7993	1.0000
333.1	0.7587	1.0000
333.3	0.7281	1.0000
334.7	0.6957	1.0000
335.3	0.6479	1.0000
336.7	0.6044	1.0000
338.6	0.5578	1.0000
340.1	0.5201	1.0000
341.8	0.4933	1.0000
343.1	0.4682	1.0000

Table A3: Isobaric vapor–liquid equilibrium at 1.01325 bar for the binary systems **Acetone (1) – [HMIm][Br] (2)** involved in the synthesis of the model IL, [HMIm][Br].

Acetonitrile solvent system phase equilibrium results.

Temperature [K]	X_1	Y_1
355.0	1.0000	1.0000
356.3	0.8613	0.9623
358.3	0.7150	0.9489
361.7	0.5467	0.9353
365.1	0.4282	0.9233
374.6	0.2905	0.8828
381.6	0.2222	0.8419
390.2	0.1706	0.7905
396.1	0.1345	0.7415
403.5	0.1004	0.6638
409.9	0.0707	0.5659
418.2	0.0306	0.4083
423.2	0.0157	0.2108
428.5	0.0000	0.0000

Table A4: Isobaric vapor–liquid equilibrium at 1.01325 bar for the binary systems **Acetonitrile (1) – 1-Bromohexane (2)** involved in the synthesis of the model IL, [HMIm][Br].

Temperature [K]	X_1	Y_1
355.0	1.0000	1.0000
358.1	0.9070	1.0000
362.8	0.7961	1.0000
366.6	0.7012	1.0000
374.2	0.5810	0.9944
382.2	0.4772	0.9847
389.6	0.3997	0.9751
396.2	0.3330	0.9653
404.7	0.2685	0.9455
416.0	0.2013	0.9090
423.0	0.1481	0.8493
430.1	0.1168	0.8028
435.5	0.0970	0.7645
443.9	0.0712	0.6659
451.9	0.0478	0.5154
459.5	0.0285	0.3315
463.6	0.0172	0.2254
465.6	0.0114	0.1607
468.6	0.0036	0.0613
470.4	0.0013	0.0169
471.6	0.0000	0.0000

Table A5: Isobaric vapor–liquid equilibrium at 1.01325 bar for the binary systems **Acetonitrile (1) – 1-Methylimidazole (2)** involved in the synthesis of the model IL, [HMIm][Br].

Temperature [K]	X_1	Y_1
355.0	1.0000	1.0000
356.1	0.9838	1.0000
356.6	0.9635	1.0000
357.1	0.9491	1.0000
357.6	0.9328	1.0000
358.2	0.9097	1.0000
359.1	0.8840	1.0000
360.2	0.8458	1.0000
360.5	0.8377	1.0000
362.0	0.7944	1.0000
362.8	0.7706	1.0000
364.3	0.7277	1.0000
366.3	0.6785	1.0000
368.9	0.6482	1.0000
372.5	0.5743	1.0000
378.2	0.4986	1.0000
386.8	0.4392	1.0000
410.1	0.3873	1.0000

Table A6: Isobaric vapor–liquid equilibrium at 1.01325 bar for the binary systems **Acetonitrile (1) – [HMIm][Br] (2)** involved in the synthesis of the model IL, [HMIm][Br].

Dichloromethane Solvent System Phase Equilibrium Results

Temperature [K]	X_1	Y_1
312.9	1.0000	1.0000
319.0	0.8920	0.9990
324.1	0.7734	0.9973
329.9	0.6586	0.9950
336.4	0.6020	0.9904
344.5	0.4636	0.9841
350.0	0.4341	0.9774
356.5	0.3923	0.9576
364.5	0.2769	0.9395
373.0	0.2172	0.9361
378.7	0.1530	0.8773
384.9	0.1461	0.8482
392.3	0.0963	0.8258
398.7	0.0671	0.7753
404.6	0.0579	0.7107
410.5	0.0403	0.6371
415.4	0.0249	0.5525
420.8	0.0030	0.2501
424.8	0.0072	0.1107
428.5	0.0000	0.0000

Table A7: Isobaric vapor–liquid equilibrium at 1.01325 bar for the binary systems **Dichloromethane (1) – 1-Bromohexane (2)** involved in the synthesis of the model IL, [HMIm][Br].

Temperature [K]	X_1	Y_1
312.9	1.0000	1.0000
313.7	0.9750	0.9998
314.5	0.9500	0.9996
315.6	0.9250	0.9992
316.7	0.9000	0.9988
317.9	0.8750	0.9983
319.2	0.8500	0.9976
320.7	0.8250	0.9968
322.2	0.8000	0.9958
323.9	0.7750	0.9946
325.6	0.7500	0.9932
327.5	0.7250	0.9915
329.5	0.7000	0.9895
331.6	0.6750	0.9872
333.8	0.6500	0.9844
336.2	0.6250	0.9812
338.6	0.6000	0.9774
341.3	0.5750	0.9731
344.0	0.5500	0.9680
347.0	0.5250	0.9621
350.1	0.5000	0.9552
353.4	0.4750	0.9473
356.9	0.4500	0.9380
360.6	0.4250	0.9273
364.5	0.4000	0.9148
368.6	0.3750	0.9002
373.1	0.3500	0.8833
377.8	0.3250	0.8635
382.8	0.3000	0.8405
388.1	0.2750	0.8135
393.8	0.2500	0.7820
399.8	0.2250	0.7451
406.3	0.2000	0.7019
413.2	0.1750	0.6513
420.5	0.1500	0.5921
428.3	0.1250	0.5231
436.5	0.1000	0.4430
445.1	0.0750	0.3507
454.0	0.0500	0.2456
463.1	0.0250	0.1282
471.6	0.0000	0.0000

Table A8: Isobaric vapor–liquid equilibrium at 1.01325 bar for the binary systems **Dichloromethane (1) – 1-Methylimidazole (2)** involved in the synthesis of the model IL, [HMIm][Br].

Temperature [K]	X_1	Y_1
312.9	1.0000	1.0000
314.7	0.9828	1.0000
316.0	0.9619	1.0000
316.5	0.8796	1.0000
320.5	0.8080	1.0000
324.2	0.7528	1.0000
329.0	0.7029	1.0000
332.6	0.6639	1.0000
337.2	0.6226	1.0000
341.5	0.5763	1.0000
348.4	0.5349	1.0000

Table A9: Isobaric vapor–liquid equilibrium at 1.01325 bar for the binary systems **Dichloromethane (1) – [HMIm][Br] (2)** involved in the synthesis of the model IL, [HMIm][Br].

Dimethyl Sulfoxide Solvent System Phase Equilibrium Results

Temperature [K]	X_1	Y_1
462.2	1.0000	1.0000
457.4	0.9750	0.8253
453.1	0.9500	0.7200
450.1	0.9250	0.6497
447.8	0.9000	0.5991
446.1	0.8750	0.5608
444.7	0.8500	0.5303
443.5	0.8250	0.5051
442.5	0.8000	0.4836
441.7	0.7750	0.4647
441.0	0.7500	0.4476
440.3	0.7250	0.4318
439.7	0.7000	0.4170
439.1	0.6750	0.4028
438.6	0.6500	0.3890
438.1	0.6250	0.3755
437.6	0.6000	0.3621
437.1	0.5750	0.3488
436.6	0.5500	0.3355
436.2	0.5250	0.3222
435.8	0.5000	0.3087
435.4	0.4750	0.2951
435.0	0.4500	0.2813
434.6	0.4250	0.2673
434.2	0.4000	0.2531
433.8	0.3750	0.2388
433.4	0.3500	0.2242
433.1	0.3250	0.2094
432.7	0.3000	0.1944
432.4	0.2750	0.1792
432.0	0.2500	0.1639
431.7	0.2250	0.1483
431.4	0.2000	0.1325
431.0	0.1750	0.1165
430.7	0.1500	0.1004
430.4	0.1250	0.0840
430.1	0.1000	0.0676
429.8	0.0750	0.0509
429.5	0.0500	0.0341
429.3	0.0250	0.0171
428.5	0.0000	0.0000

Table A10: Isobaric vapor–liquid equilibrium at 1.01325 bar for the binary systems **Dimethyl Sulfoxide (1) – 1-Bromohexane (2)** involved in the synthesis of the model IL, [HMIm][Br].

Temperature [K]	X_1	Y_1
462.2	1.0000	1.0000
463.3	0.8479	0.9031
464.2	0.7450	0.8197
465.0	0.6362	0.7727
465.7	0.5833	0.6925
466.4	0.4929	0.6297
467.3	0.4452	0.5441
468.0	0.3697	0.4762
468.7	0.3045	0.3929
469.4	0.1952	0.3406
470.2	0.0902	0.2375
471.0	0.0325	0.0927
471.6	0.0000	0.0000

Table A11: Isobaric vapor–liquid equilibrium at 1.01325 bar for the binary systems **Dimethyl Sulfoxide (1) – 1-Methylimidazole (2)** involved in the synthesis of the model IL, [HMIm][Br].

Temperature [K]	X_1	Y_1
462.2	1.0000	1.0000
463.3	0.9494	1.0000
464.0	0.9004	1.0000
465.0	0.8495	1.0000
466.2	0.7730	1.0000
467.2	0.7400	1.0000
468.1	0.7037	1.0000
469.1	0.6466	1.0000
469.6	0.6194	1.0000
471.8	0.5595	1.0000
475.1	0.4766	1.0000

Table A12: Isobaric vapor–liquid equilibrium at 1.01325 bar for the binary systems **Dimethyl Sulfoxide (1) – [HMIm][Br] (2)** involved in the synthesis of the model IL, [HMIm][Br].

Binary phase equilibrium systems common to all solvents:

Temperature [K]	X_1	Y_1
471.6	1.0000	1.0000
473.3	0.9775	1.0000
474.2	0.9368	1.0000
474.9	0.9200	1.0000
475.7	0.9038	1.0000
476.9	0.8755	1.0000
479.5	0.8350	1.0000
479.8	0.8242	1.0000
482.4	0.7781	1.0000
484.3	0.7391	1.0000

Table A13: Isobaric vapor–liquid equilibrium at 1.01325 bar for the binary systems **1-Methylimidazole (1) – [HMIm][Br] (2)** involved in the synthesis of the model IL, [HMIm][Br].

Temperature [K]	X_1	Y_1
428.5	1.0000	1.0000
430.0	0.9406	0.9786
432.0	0.8703	0.9554
434.0	0.8066	0.9172
436.0	0.7479	0.8837
438.0	0.6923	0.8476
440.0	0.6401	0.8095
442.0	0.5901	0.7692
444.0	0.5416	0.7264
446.0	0.4946	0.6816
448.0	0.4480	0.6341
450.0	0.4027	0.5851
452.0	0.3574	0.5340
454.0	0.3134	0.4822
456.0	0.2691	0.4285
458.0	0.2253	0.3739
460.0	0.1836	0.3198
462.0	0.1435	0.2651
464.0	0.1076	0.2124
466.0	0.0752	0.1605
468.0	0.0472	0.1089
470.0	0.0239	0.0596
471.6	0.0000	0.0000

Table A14: Isobaric vapor–liquid equilibrium at 1.01325 bar for the binary systems **1-Bromohexane (1) – 1-Methylimidazole (2)** involved in the synthesis of the model IL, [HMIm][Br].

Temperature [K]	X_1^I	X_1^{II}
298.2	>0.9999	0.023
313.2	>0.9999	0.0625
333.2	>0.9999	0.0785
353.2	>0.9999	0.1111
373.2	>0.9999	0.1448

Table A15: Experimental liquid-liquid equilibrium data for the **1-Bromohexane (1) - [HMIm][Br] (2)** system. Phase I is the upper liquid rich in component 1; phase II is the lower phase rich in component 2.

Appendix 2: Aspen Plus Stream Tables from [HMIm][Br] Synthesis Simulations

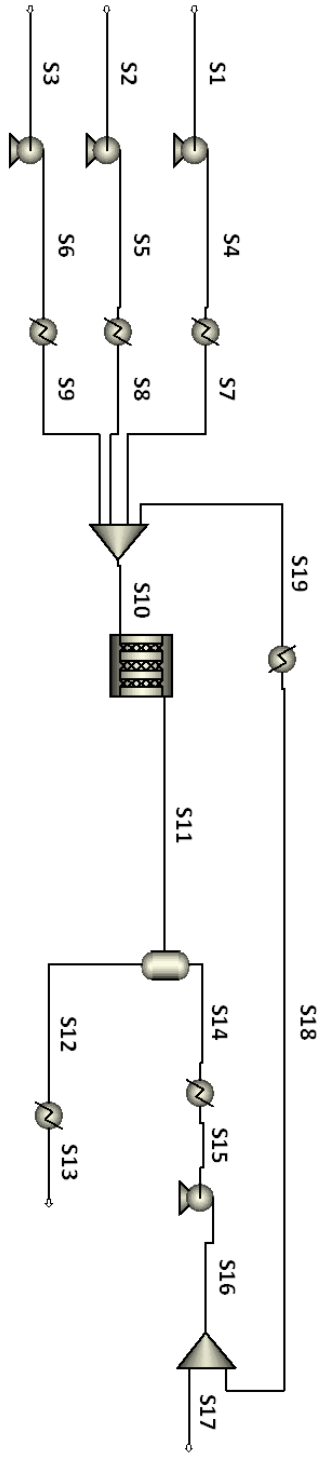

Figure A1: Aspen Plus process model for the continuous synthesis of [HMIm][Br]

Process Specification	Units	S1	S10	S11	S12	S13	S14	S15	S16	S17	S18	S19	S2	S3	S4	S5	S6	S7	S8	S9
From		B7	B8	B9	B10		B11	B12	B13		B14	B7	B2	B3	B1	B2	B3	B4	B5	B6
To		B1	B8	B9	B10		B11	B12	B13		B14	B7	B2	B3	B4	B5	B6	B7	B7	B7
Substream: MIXED																				
Phase:		Liquid	Liquid	Liquid	Liquid	Liquid	Vapor	Liquid	Liquid	Liquid	Liquid	Liquid	Liquid	Liquid	Liquid	Liquid	Liquid	Liquid	Liquid	Liquid
Component Mole Flow																				
1-BH	KMOL/HR	5.06	5.47	0.47	0.03	0.03	0.44	0.44	0.44	0.02	0.42	0.42	0.00	0.00	5.06	0.00	0.00	5.06	0.00	0.00
1-MI	KMOL/HR	0.00	5.06	0.05	0.05	0.05	0.00	0.00	0.00	0.00	0.00	0.00	0.00	5.06	0.00	0.00	5.06	0.00	0.00	5.06
HMIMBR	KMOL/HR	0.00	0.00	5.01	5.01	5.01	0.00	0.00	0.00	0.00	0.00	0.00	0.00	0.00	0.00	0.00	0.00	0.00	0.00	0.00
ACETONE	KMOL/HR	0.00	5.33	5.33	0.07	0.07	5.26	5.26	5.26	0.26	5.00	5.00	0.33	0.00	0.00	0.33	0.00	0.00	0.33	0.00
Mole Flow	KMOL/HR	5.06	15.86	10.85	5.15	5.15	5.70	5.70	5.70	0.29	5.42	5.42	0.33	5.06	5.06	0.33	5.06	5.06	0.33	5.06
Mass Flow	KG/HR	834.78	1628.56	1628.56	1250.14	1250.14	378.42	378.42	378.42	18.92	359.50	359.50	19.17	415.21	834.78	19.17	415.21	834.78	19.17	415.21
Volume Flow	L/MIN	11.22	27.32	24.01	17.86	16.74	3065.89	7.68	7.68	0.38	7.29	7.29	0.41	7.95	11.22	0.41	7.95	11.51	0.42	8.10
Temperature	C	25.00	56.87	50.00	120.00	25.00	120.00	50.00	50.05	50.05	50.05	50.00	25.00	25.00	25.05	25.05	25.04	50.00	50.00	50.00
Pressure	BAR	1.01	1.50	1.50	1.01	1.01	1.01	1.01	1.50	1.50	1.50	1.50	1.01	1.01	1.50	1.50	1.50	1.50	1.50	1.50
Vapor Fraction		0.00	0.00	0.00	0.00	0.00	1.00	0.00	0.00	0.00	0.00	0.00	0.00	0.00	0.00	0.00	0.00	0.00	0.00	0.00
Liquid Fraction		1.00	1.00	1.00	1.00	1.00	0.00	1.00	1.00	1.00	1.00	1.00	1.00	1.00	1.00	1.00	1.00	1.00	1.00	1.00
Solid Fraction		0.00	0.00	0.00	0.00	0.00	0.00	0.00	0.00	0.00	0.00	0.00	0.00	0.00	0.00	0.00	0.00	0.00	0.00	0.00
Molar Enthalpy	KJ/MOL	-192.39	-121.64	-256.42	-239.52	-283.65	-201.66	-239.57	-239.56	-239.56	-239.56	-239.57	-246.87	72.49	-192.38	-246.86	72.50	-186.63	-243.73	77.29
Mass Enthalpy	KJ/KG	-1165.46	-1184.60	-1708.68	-986.67	-1168.48	-3038.72	-3609.86	-3609.76	-3609.76	-3609.76	-3609.86	-4250.45	882.88	-1165.39	-4250.35	882.97	-1130.61	-4196.43	941.41
Enthalpy Flow	KJ/SEC	-270.25	-535.88	-772.97	-342.63	-405.77	-319.42	-379.46	-379.45	-18.97	-360.47	-360.48	-22.63	101.83	-270.24	-22.63	101.84	-262.17	-22.34	108.58
Molar Entropy	KJ/MOL-K	-0.63	-0.43	-0.53	-0.64	-0.81	-0.21	-0.32	-0.32	-0.32	-0.32	-0.32	-0.31	-0.41	-0.63	-0.31	-0.41	-0.61	-0.30	-0.40
Mass Entropy	KJ/KG-K	-3.80	-4.18	-3.54	-2.64	-3.34	-3.19	-4.88	-4.88	-4.88	-4.88	-4.88	-5.35	-5.02	-3.80	-5.35	-5.02	-3.69	-5.18	-4.84
Molar Density	MOL/CC	0.01	0.01	0.01	0.00	0.01	0.00	0.01	0.01	0.01	0.01	0.01	0.01	0.01	0.01	0.01	0.01	0.01	0.01	0.01
Mass Density	GM/CC	1.24	0.99	1.13	1.17	1.25	0.00	0.82	0.82	0.82	0.82	0.82	0.79	0.87	1.24	0.79	0.87	1.21	0.76	0.85
Average Molecular Weight		165.07	102.69	150.07	242.75	242.75	66.36	66.36	66.36	66.36	66.36	66.36	58.08	82.11	165.07	58.08	82.11	165.07	58.08	82.11

Table: A16: Aspen Plus stream table for [HMIm][Br] in acetone at 50^{o}C.

Process Specifications	Units	S1	S10	S11	S12	S13	S14	S15	S16	S17	S18	S19	S2	S3	S4	S5	S6	S7	S8	S9
From		B1	B7	B8	B9	B10	B9	B11	B12	B13	B13	B14	B7	B2	B3	B4	B5	B6	B7	B5	B6	B7
To			B8	B9	B10		B11	B12	B13		B14	B7	B2	B3	B4	B5	B6	B7				
Substream: MIXED																						
Phase:		Liquid	Liquid	Liquid	Liquid	Liquid	Vapor	Liquid	Liquid	Liquid	Liquid	Liquid	Liquid	Liquid	Liquid	Liquid	Liquid	Liquid	Liquid	Liquid	Liquid	Liquid
Component Mole Flow																						
1-BH	KMOL/HR	5.06	5.48	0.47	0.03	0.03	0.44	0.44	0.44	0.02	0.42	0.42	0.00	0.00	5.06	0.00	0.00	5.06	0.00	0.00
1-MI	KMOL/HR	0.00	5.06	0.05	0.05	0.05	0.00	0.00	0.00	0.00	0.00	0.00	0.00	5.06	0.00	0.00	5.06	0.00	0.00	0.00	0.00	5.06
HMIMBR	KMOL/HR	0.00	0.00	5.01	5.01	5.01	0.00	0.00	0.00	0.00	0.00	0.00	0.00	0.00	0.00	0.00	0.00	0.00	0.00	0.00	0.00	0.00
ACETONE	KMOL/HR	0.00	5.33	5.33	0.07	0.07	5.27	5.27	5.27	0.26	5.01	5.01	0.33	0.00	0.00	0.33	0.00	0.00	0.00	0.33	0.00	0.00
Mole Flow	KMOL/HR	5.06	15.87	10.86	5.15	5.15	5.71	5.71	5.71	0.29	5.43	5.43	0.33	5.06	5.06	0.33	5.06	5.06	0.33	0.33	5.06	
Mass Flow	KG/HR	834.78	1629.73	1629.73	1250.10	1250.10	379.63	379.63	379.63	18.98	360.65	360.65	19.17	415.21	834.78	19.17	415.21	834.78	19.17	415.21		
Volume Flow	L/MIN	11.22	28.90	25.09	17.86	16.74	3072.21	7.70	7.70	0.38	7.31	7.96	0.41	7.95	11.22	0.41	7.95	12.17	0.46	8.43		
Temperature	C	25.00	105.24	100.00	120.00	25.00	120.00	50.00	50.28	50.28	50.28	100.00	25.00	25.00	25.30	25.30	25.25	100.00	100.00	100.00		
Pressure	BAR	1.01	4.00	4.00	1.01	1.01	1.01	1.01	4.00	4.00	4.00	4.00	1.01	1.01	4.00	4.00	4.00	4.00	4.00	4.00		
Vapor Fraction		0.00	0.00	0.00	0.00	0.00	1.00	0.00	0.00	0.00	0.00	0.00	0.00	0.00	0.00	0.00	0.00	0.00	0.00	0.00		
Liquid Fraction		1.00	1.00	1.00	1.00	1.00	0.00	1.00	1.00	1.00	1.00	1.00	1.00	1.00	1.00	1.00	1.00	1.00	1.00	1.00		
Solid Fraction		0.00	0.00	0.00	0.00	0.00	0.00	0.00	0.00	0.00	0.00	0.00	0.00	0.00	0.00	0.00	0.00	0.00	0.00	0.00		
Molar Enthalpy	KJ/MOL	-192.39	-111.87	-241.04	-239.47	-283.60	-201.61	-239.53	-239.49	-239.49	-239.49	-231.90	-246.87	72.49	-192.32	-246.83	72.54	-174.24	-236.68	87.31		
Mass Enthalpy	KJ/KG	-1165.46	-1089.51	-1606.87	-986.63	-1168.44	-3034.40	-3605.19	-3604.58	-3604.58	-3604.58	-3490.39	-4250.45	882.88	-1165.06	-4249.82	883.45	-1055.52	-4075.11	1063.37		
Enthalpy Flow	KJ/SEC	-270.25	-493.23	-727.43	-342.61	-405.74	-319.99	-380.18	-380.12	-19.01	-361.11	-349.67	-22.63	101.83	-270.16	-22.63	101.89	-244.76	-21.70	122.64		
Molar Entropy	KJ/MOL-K	-0.63	-0.40	-0.48	-0.64	-0.81	-0.21	-0.32	-0.32	-0.32	-0.32	-0.30	-0.31	-0.41	-0.63	-0.31	-0.41	-0.57	-0.28	-0.37		
Mass Entropy	KJ/KG-K	-3.80	-3.91	-3.18	-2.64	-3.34	-3.19	-4.88	-4.87	-4.87	-4.87	-4.56	-5.35	-5.02	-3.80	-5.35	-5.02	-3.47	-4.84	-4.49		
Molar Density	MOL/CC	0.01	0.01	0.01	0.00	0.01	0.00	0.01	0.01	0.01	0.01	0.01	0.01	0.01	0.01	0.01	0.01	0.01	0.01	0.01		
Mass Density	GM/CC	1.24	0.94	1.08	1.17	1.24	0.00	0.82	0.82	0.82	0.82	0.76	0.79	0.87	1.24	0.79	0.87	1.14	0.69	0.82		
Average Molecular Weight		165.07	102.68	150.01	242.71	242.71	66.44	66.44	66.44	66.44	66.44	66.44	58.08	82.11	165.07	58.08	82.11	165.07	58.08	82.11		

Table A17: Aspen Plus stream table for [HMIm][Br] synthesis in acetone at 100^{o}C.

Process Specification	Units	S1	S10	S11	S12	S13	S14	S15	S16	S17	S18	S19	S2	S3	S4	S5	S6	S7	S8	S9
From		B7	B8	B9	B10		B11	B12	B13		B14	B7	B2	B3	B4	B5	B6	B7	B7	
To		B1	B8	B9	B10		B11	B12	B13		B14	B7	B2	B3	B1	B2	B3	B4	B5	B6
Substream: MIXED																				
Phase:		Liquid	Liquid	Liquid	Liquid	Liquid	Vapor	Liquid	Liquid	Liquid	Liquid	Liquid	Liquid	Liquid	Liquid	Liquid	Liquid	Liquid	Liquid	Liquid
Component Mole Flow																				
1-BH	KMOL/HR	5.06	5.48	0.46	0.01	0.01	0.45	0.45	0.45	0.02	0.42	0.42	0.00	0.00	5.06	0.00	0.00	5.06	0.00	0.00
1-MI	KMOL/HR	0.00	5.06	0.04	0.04	0.04	0.00	0.00	0.00	0.00	0.00	0.00	0.00	5.06	0.00	0.00	5.06	0.00	0.00	5.06
HMIMBR	KMOL/HR	0.00	0.01	5.03	5.02	5.02	0.01	0.01	0.01	0.00	0.01	0.01	0.00	0.00	0.00	0.00	0.00	0.00	0.00	0.00
ACN	KMOL/HR	0.00	5.08	5.08	0.17	0.17	4.91	4.91	4.91	0.25	4.67	4.67	0.41	0.00	0.00	0.41	0.00	0.00	0.41	0.00
Mole Flow	KMOL/HR	5.06	15.63	10.60	5.24	5.24	5.37	5.37	5.37	0.27	5.10	5.10	0.41	5.06	5.06	0.41	5.06	5.06	0.41	5.06
Mass Flow	KG/HR	834.84	1530.84	1530.84	1253.05	1253.05	277.80	277.80	277.80	13.89	263.91	263.91	16.91	415.24	834.84	16.91	415.24	834.84	16.91	415.24
Volume Flow	L/MIN	12.53	24.43	20.43	18.12	16.65	3069.92	5.41	5.41	0.27	5.14	5.14	0.36	6.90	12.53	0.36	6.90	12.84	0.37	7.04
Temperature	C	25.00	58.78	50.00	145.00	25.00	145.00	50.00	50.05	50.05	50.05	50.00	25.00	25.00	25.05	25.05	25.03	50.00	50.00	50.00
Pressure	BAR	1.01	1.50	1.50	1.01	1.00	1.01	1.01	1.50	1.50	1.50	1.50	1.01	1.01	1.50	1.50	1.50	1.50	1.50	1.50
Vapor Fraction		0.00	0.00	0.00	0.00	0.00	1.00	0.00	0.00	0.00	0.00	0.00	0.00	0.00	0.00	0.00	0.00	0.00	0.00	0.00
Liquid Fraction		1.00	1.00	1.00	1.00	1.00	0.00	1.00	1.00	1.00	1.00	1.00	1.00	1.00	1.00	1.00	1.00	1.00	1.00	1.00
Solid Fraction		0.00	0.00	0.00	0.00	0.00	0.00	0.00	0.00	0.00	0.00	0.00	0.00	0.00	0.00	0.00	0.00	0.00	0.00	0.00
Molar Enthalpy	KJ/MOL	-192.39	-29.65	-123.08	-219.50	-275.15	55.08	14.92	14.92	14.92	14.92	14.92	31.45	72.49	-192.37	31.45	72.50	-186.65	33.67	77.29
Mass Enthalpy	KJ/KG	-1165.46	-302.69	-852.61	-917.20	-1149.74	1064.30	288.32	288.41	288.41	288.41	288.32	765.99	882.88	-1165.39	766.09	882.96	-1130.72	820.11	941.41
Enthalpy Flow	KJ/SEC	-270.27	-128.71	-362.56	-319.25	-400.19	82.13	22.25	22.26	1.11	21.14	21.14	3.60	101.83	-270.25	3.60	101.84	-262.21	3.85	108.59
Molar Entropy	KJ/MOL-K	-0.63	-0.38	-0.46	-0.59	-0.80	-0.07	-0.18	-0.18	-0.18	-0.18	-0.18	-0.15	-0.41	-0.63	-0.15	-0.41	-0.61	-0.15	-0.40
Mass Entropy	KJ/KG-K	-3.80	-3.88	-3.20	-2.47	-3.33	-1.40	-3.56	-3.55	-3.55	-3.55	-3.56	-3.73	-5.02	-3.80	-3.73	-5.02	-3.69	-3.56	-4.84
Molar Density	MOL/CC	0.01	0.01	0.01	0.00	0.01	0.00	0.02	0.02	0.02	0.02	0.02	0.02	0.01	0.01	0.02	0.01	0.01	0.02	0.01
Mass Density	GM/CC	1.11	1.04	1.25	1.15	1.25	0.00	0.86	0.86	0.86	0.86	0.86	0.78	1.00	1.11	0.78	1.00	1.08	0.75	0.98
Average Molecular Weight		165.07	97.97	144.36	239.32	239.32	51.75	51.75	51.75	51.75	51.75	51.75	41.05	82.11	165.07	41.05	82.11	165.07	41.05	82.11

Table A18: Aspen Plus stream table for [HMIm][Br] synthesis in acetonitrile at 50^{o}C.

Process Specifications	Units	S1	S10	S11	S12	S13	S14	S15	S16	S17	S18	S19	S2	S3	S4	S5	S6	S7	S8	S9
From		B7	B8	B9	B10		B9	B11	B12	B13	B13	B14	B7	B2	B1	B2	B3	B4	B5	B6
To		B1	B8	B9	B10		B11	B12	B13		B14	B7	B2	B3	B4	B5	B6	B7	B7	B7
Substream: MIXED																				
Phase:		Liquid	Liquid	Liquid	Liquid	Liquid	Vapor	Liquid	Liquid	Liquid	Liquid	Liquid	Liquid	Liquid	Liquid	Liquid	Liquid	Liquid	Liquid	Liquid
Component Mole Flow																				
1-BH	KMOL/HR	5.06	5.52	0.51	0.01	0.01	0.49	0.49	0.49	0.02	0.47	0.47	0.00	0.00	5.06	0.00	0.00	5.06	0.00	0.00
1-MI	KMOL/HR	0.00	5.06	0.04	0.04	0.04	0.00	0.00	0.00	0.00	0.00	0.00	0.00	5.06	0.00	0.00	5.06	0.00	0.00	5.06
HMIMBR	KMOL/HR	0.00	0.01	5.03	5.02	5.02	0.01	0.01	0.01	0.00	0.01	0.01	0.00	0.00	0.00	0.00	0.00	0.00	0.00	0.00
ACN	KMOL/HR	0.00	5.07	5.07	0.16	0.16	4.91	4.91	4.91	0.25	4.66	4.66	0.41	0.00	0.00	0.41	0.00	0.00	0.41	0.00
Mole Flow	KMOL/HR	5.06	15.66	10.65	5.24	5.24	5.41	5.41	5.41	0.27	5.14	5.14	0.41	5.06	5.06	0.41	5.06	5.06	0.41	5.06
Mass Flow	KG/HR	834.84	1537.73	1537.73	1252.60	1252.60	285.13	285.13	285.13	14.26	270.87	270.87	16.83	415.24	834.84	16.83	415.24	834.84	16.83	415.24
Volume Flow	L/MIN	12.53	25.93	21.46	18.11	16.65	3093.59	5.50	5.50	0.28	5.23	5.67	0.36	6.90	12.53	0.36	6.91	13.55	0.41	7.35
Temperature	C	25.00	106.78	100.00	145.00	25.00	145.00	50.00	50.00	50.00	50.00	100.00	25.00	25.00	25.11	25.10	25.07	100.00	100.00	100.00
Pressure	BAR	1.01	2.00	2.00	1.01	1.00	1.01	2.00	2.00	2.00	2.00	2.00	1.01	1.01	2.00	2.00	2.00	2.00	2.00	2.00
Vapor Fraction		0.00	0.00	0.00	0.00	0.00	1.00	0.00	0.00	0.00	0.00	0.00	0.00	0.00	0.00	0.00	0.00	0.00	0.00	0.00
Liquid Fraction		1.00	1.00	1.00	1.00	1.00	0.00	1.00	1.00	1.00	1.00	1.00	1.00	1.00	1.00	1.00	1.00	1.00	1.00	1.00
Solid Fraction		0.00	0.00	0.00	0.00	0.00	0.00	0.00	0.00	0.00	0.00	0.00	0.00	0.00	0.00	0.00	0.00	0.00	0.00	0.00
Molar Enthalpy	KJ/MOL	-192.39	-20.87	-109.32	-219.34	-274.98	53.57	13.22	13.22	13.22	13.22	18.89	31.45	72.49	-192.36	31.45	72.50	-174.32	38.58	87.31
Mass Enthalpy	KJ/KG	-1165.46	-212.60	-756.81	-916.83	-1149.38	1016.37	250.86	250.86	250.86	250.86	358.37	765.99	882.88	-1165.31	766.20	883.04	-1056.03	939.71	1063.37
Enthalpy Flow	KJ/SEC	-270.27	-90.81	-323.27	-319.01	-399.92	80.50	19.87	19.87	0.99	18.88	26.96	3.58	101.83	-270.24	3.58	101.85	-244.89	4.39	122.65
Molar Entropy	KJ/MOL-K	-0.63	-0.36	-0.41	-0.59	-0.80	-0.08	-0.19	-0.19	-0.19	-0.19	-0.17	-0.15	-0.41	-0.63	-0.15	-0.41	-0.57	-0.13	-0.37
Mass Entropy	KJ/KG-K	-3.80	-3.62	-2.85	-2.47	-3.33	-1.43	-3.56	-3.56	-3.56	-3.56	-3.26	-3.73	-5.02	-3.80	-3.73	-5.02	-3.47	-3.23	-4.49
Molar Density	MOL/CC	0.01	0.01	0.01	0.00	0.01	0.00	0.02	0.02	0.02	0.02	0.02	0.02	0.01	0.01	0.02	0.01	0.01	0.02	0.01
Mass Density	GM/CC	1.11	0.99	1.19	1.15	1.25	0.00	0.86	0.86	0.86	0.86	0.80	0.78	1.00	1.11	0.78	1.00	1.03	0.69	0.94
Average Molecular Weight		165.07	98.17	144.45	239.24	239.24	52.71	52.71	52.71	52.71	52.71	52.71	41.05	82.11	165.07	41.05	82.11	165.07	41.05	82.11

Table A19: Aspen Plus stream table for [HMIm][Br] synthesis in acetonitrile at 100^{o}C.

Process Specification	Units	S1	S10	S11	S12	S13	S14	S15	S16	S17	S18	S19	S2	S3	S4	S5	S6	S7	S8	S9
From			B7	B10	B11	B12	B11	B13	B14	B15	B15	B16	B7	B2	B3	B1	B2	B3	B4	B5	B6
To		B1	B10	B11	B12		B13	B14	B15		B16	B7	B2	B3	B4	B5	B6	B7	B7	B7	B7
Substream: MIXED																					
Phase:		Liquid	Liquid	Liquid	Liquid	Liquid	Vapor	Liquid	Liquid	Liquid	Liquid	Liquid	Liquid	Liquid	Liquid	Liquid	Liquid	Liquid	Liquid	Liquid	Liquid
Component Mole Flow																					
1-BH	KMOL/HR	0.00	5.45	0.43	0.02	0.02	0.41	0.41	0.41	0.02	0.39	0.39	0.00	5.06	0.00	0.00	5.06	0.00	0.00	0.00	5.06
1-MI	KMOL/HR	5.06	5.06	0.04	0.04	0.04	0.00	0.00	0.00	0.00	0.00	0.00	0.00	0.00	5.06	0.00	0.00	5.06	0.00	0.00	0.00
HMIMBR	KMOL/HR	0.00	0.00	5.02	5.01	5.01	0.00	0.00	0.00	0.00	0.00	0.00	0.00	0.00	0.00	0.00	0.00	0.00	0.00	0.00	0.00
DCM	KMOL/HR	0.00	5.04	5.04	0.06	0.06	4.99	4.99	4.99	0.25	4.74	4.74	0.31	0.00	0.00	0.31	0.00	0.00	0.00	0.31	0.00
Mole Flow	KMOL/HR	5.06	15.55	10.53	5.14	5.14	5.40	5.40	5.40	0.27	5.13	5.13	0.31	5.06	5.06	0.31	5.06	5.06	0.31	5.06	5.06
Mass Flow	KG/HR	415.21	1743.06	1743.06	1251.48	1251.48	491.59	491.59	491.59	24.58	467.01	467.01	26.07	834.78	415.21	26.07	834.78	415.21	26.07	834.78	834.78
Volume Flow	L/MIN	6.90	26.43	23.73	17.91	16.72	2938.65	6.43	6.43	0.32	6.11	6.24	0.33	12.53	6.90	0.33	12.53	7.04	0.34	12.94	12.94
Temperature	C	25.00	61.19	50.00	125.00	25.00	125.00	35.00	35.10	35.10	35.10	50.00	25.00	25.00	25.07	25.10	25.11	50.00	50.00	50.00	50.00
Pressure	BAR	1.01	2.00	2.00	1.01	1.01	1.01	1.01	2.00	2.00	2.00	2.00	1.01	1.01	2.00	2.00	2.00	2.00	2.00	2.00	2.00
Vapor Fraction		0.00	0.00	0.00	0.00	0.00	1.00	0.00	0.00	0.00	0.00	0.00	0.00	0.00	0.00	0.00	0.00	0.00	0.00	0.00	0.00
Liquid Fraction		1.00	1.00	1.00	1.00	1.00	0.00	1.00	1.00	1.00	1.00	1.00	1.00	1.00	1.00	1.00	1.00	1.00	1.00	1.00	1.00
Solid Fraction		0.00	0.00	0.00	0.00	0.00	0.00	0.00	0.00	0.00	0.00	0.00	0.00	0.00	0.00	0.00	0.00	0.00	0.00	0.00	0.00
Molar Enthalpy	KJ/MOL	72.49	-79.93	-198.07	-236.26	-282.90	-92.78	-129.06	-129.04	-129.04	-129.04	-127.22	-124.54	-192.39	72.50	-124.53	-192.36	77.29	-121.76	-186.65	-186.65
Mass Enthalpy	KJ/KG	882.88	-712.93	-1196.92	-969.63	-1161.03	-1018.63	-1416.84	-1416.71	-1416.71	-1416.71	-1396.68	-1466.34	-1165.46	883.04	-1466.21	-1165.31	941.41	-1433.64	-1130.72	-1130.72
Enthalpy Flow	KJ/SEC	101.83	-345.19	-579.53	-337.08	-403.61	-139.10	-193.47	-193.45	-9.67	-183.78	-181.18	-10.62	-270.25	101.85	-10.62	-270.22	108.58	-10.38	-262.20	-262.20
Molar Entropy	KJ/MOL-K	-0.41	-0.39	-0.48	-0.63	-0.81	-0.10	-0.21	-0.21	-0.21	-0.21	-0.21	-0.18	-0.63	-0.41	-0.18	-0.63	-0.40	-0.17	-0.61	-0.61
Mass Entropy	KJ/KG-K	-5.02	-3.45	-2.87	-2.59	-3.33	-1.10	-2.31	-2.31	-2.31	-2.31	-2.25	-2.14	-3.80	-5.02	-2.14	-3.80	-4.84	-2.04	-3.69	-3.69
Molar Density	MOL/CC	0.01	0.01	0.01	0.00	0.01	0.00	0.01	0.01	0.01	0.01	0.01	0.02	0.01	0.01	0.02	0.01	0.01	0.01	0.01	0.01
Mass Density	GM/CC	1.00	1.10	1.22	1.16	1.25	0.00	1.27	1.27	1.27	1.27	1.25	1.32	1.11	1.00	1.32	1.11	0.98	1.27	1.08	1.08
Average Molecular Weight		82.11	112.11	165.49	243.66	243.66	91.09	91.09	91.09	91.09	91.09	91.09	84.93	165.07	82.11	84.93	165.07	82.11	84.93	165.07	165.07

Table A20: Aspen Plus stream table for [HMIm][Br] synthesis in dichloromethane at 50^{o}C.

Process Specification	Units	S1	S10	S11	S12	S13	S14	S15	S16	S17	S18	S19	S2	S3	S4	S5	S6	S7	S8	S9
From			B7	B8	B9	B10	B9	B11	B12	B13	B13	B14	B2	B1	B2	B3	B4	B5	B6	
To		B1	B8	B9	B10		B11	B12	B13		B14	B7	B3	B4	B5	B6	B7	B7	B7	
Substream: MIXED																				
Phase:		Liquid	Liquid	Liquid	Liquid	Liquid	Vapor	Liquid	Liquid	Liquid	Liquid	Liquid	Liquid	Liquid	Liquid	Liquid	Liquid	Liquid	Liquid	Liquid
Component Mole Flow																				
1-BH	KMOL/HR	0.00	5.48	0.47	0.02	0.02	0.45	0.45	0.45	0.02	0.43	0.43	0.00	5.06	0.00	0.00	5.06	0.00	0.00	5.06
1-MI	KMOL/HR	5.06	5.06	0.05	0.05	0.05	0.00	0.00	0.00	0.00	0.00	0.00	0.00	0.00	5.06	0.00	0.00	5.06	0.00	0.00
HMIMBR	KMOL/HR	0.00	0.00	5.01	5.01	5.01	0.00	0.00	0.00	0.00	0.00	0.00	0.00	0.00	0.00	0.00	0.00	0.00	0.00	0.00
DCM	KMOL/HR	0.00	5.09	5.09	0.06	0.06	5.03	5.03	5.03	0.25	4.78	4.78	0.31	0.00	0.00	0.31	0.00	0.00	0.31	0.00
Mole Flow	KMOL/HR	5.06	15.64	10.62	5.14	5.14	5.49	5.49	5.49	0.27	5.21	5.21	0.31	5.06	5.06	0.31	5.06	5.06	0.31	5.06
Mass Flow	KG/HR	415.21	1753.59	1753.59	1251.19	1251.19	502.39	502.39	502.39	25.12	477.27	477.27	26.33	834.78	415.21	26.33	834.78	415.21	26.33	834.78
Volume Flow	L/MIN	6.90	28.06	24.89	17.91	16.72	2987.13	6.58	6.59	0.33	6.26	6.92	0.33	12.53	6.91	0.33	12.54	7.35	0.38	13.55
Temperature	C	25.00	109.17	100.00	125.00	25.00	125.00	35.00	35.49	35.49	35.49	100.00	25.00	25.00	25.36	25.49	25.55	100.00	100.00	100.00
Pressure	BAR	1.01	6.00	6.00	1.01	1.01	1.01	1.01	6.00	6.00	6.00	6.00	1.01	1.01	6.00	6.00	6.00	6.00	6.00	6.00
Vapor Fraction		0.00	0.00	0.00	0.00	0.00	1.00	0.00	0.00	0.00	0.00	0.00	0.00	0.00	0.00	0.00	0.00	0.00	0.00	0.00
Liquid Fraction		1.00	1.00	1.00	1.00	1.00	0.00	1.00	1.00	1.00	1.00	1.00	1.00	1.00	1.00	1.00	1.00	1.00	1.00	1.00
Solid Fraction		0.00	0.00	0.00	0.00	0.00	0.00	0.00	0.00	0.00	0.00	0.00	0.00	0.00	0.00	0.00	0.00	0.00	0.00	0.00
Molar Enthalpy	KJ/MOL	72.49	-70.80	-182.71	-235.96	-282.56	-93.01	-129.50	-129.44	-129.44	-129.44	-121.07	-124.54	-192.39	72.56	-124.49	-192.26	87.31	-115.77	-174.32
Mass Enthalpy	KJ/KG	882.88	-631.24	-1107.03	-969.12	-1160.54	-1015.65	-1414.10	-1413.44	-1413.44	-1413.44	-1322.07	-1466.34	-1165.46	883.71	-1465.71	-1164.71	1063.37	-1363.10	-1056.03
Enthalpy Flow	KJ/SEC	101.83	-307.48	-539.24	-336.82	-403.35	-141.74	-197.34	-197.25	-9.86	-187.39	-175.28	-10.72	-270.25	101.92	-10.72	-270.08	122.64	-9.97	-244.88
Molar Entropy	KJ/MOL-K	-0.41	-0.36	-0.42	-0.63	-0.81	-0.10	-0.21	-0.21	-0.21	-0.21	-0.19	-0.18	-0.63	-0.41	-0.18	-0.63	-0.37	-0.16	-0.57
Mass Entropy	KJ/KG-K	-5.02	-3.21	-2.55	-2.59	-3.33	-1.12	-2.33	-2.33	-2.33	-2.33	-2.07	-2.14	-3.80	-5.02	-2.14	-3.80	-4.49	-1.84	-3.47
Molar Density	MOL/CC	0.01	0.01	0.01	0.00	0.01	0.00	0.01	0.01	0.01	0.01	0.01	0.02	0.01	0.01	0.02	0.01	0.01	0.01	0.01
Mass Density	GM/CC	1.00	1.04	1.17	1.16	1.25	0.00	1.27	1.27	1.27	1.27	1.15	1.32	1.11	1.00	1.32	1.11	0.94	1.17	1.03
Average Molecular Weight		82.11	112.15	165.05	243.48	243.48	91.58	91.58	91.58	91.58	91.58	91.58	84.93	165.07	82.11	84.93	165.07	82.11	84.93	165.07

Table A21: Aspen Plus stream table for [HMIm][Br] synthesis in dichloromethane at 100^{o}C.

Process Specifications	Units	S1	S10	S11	S12	S13	S14	S15	S16	S17	S18	S19	S2	S3	S4	S5	S6	S7	S8	S9
From		B7	B8	B9	B10		B11	B12	B13		B14	B7	B2	B3	B4	B5	B6	B7	B7	B7
To		B1	B9	B10		B11	B12	B13		B14	B7	B2	B3	B4	B5	B6	B7	B7	B7	B7
Substream: MIXED																				
Phase:		Liquid	Liquid	Liquid	Liquid	Liquid	Vapor	Liquid	Liquid	Liquid	Liquid	Liquid	Liquid	Liquid	Liquid	Liquid	Liquid	Liquid	Liquid	Liquid
Component Mole Flow																				
1-BH	KMOL/HR	0.00	6.45	1.47	0.00	0.00	1.47	1.47	1.47	0.07	1.39	1.39	0.00	5.06	0.00	0.00	5.06	0.00	0.00	5.06
1-MI	KMOL/HR	5.06	5.11	0.13	0.08	0.08	0.06	0.06	0.06	0.00	0.05	0.05	0.00	0.00	5.06	0.00	0.00	5.06	0.00	0.00
HMIMBR	KMOL/HR	0.00	0.95	5.92	4.93	4.93	1.00	1.00	1.00	0.05	0.95	0.95	0.00	0.00	0.00	0.00	0.00	0.00	0.00	0.00
DMSO	KMOL/HR	0.00	5.03	5.03	0.22	0.22	4.81	4.81	4.81	0.24	4.57	4.57	0.47	0.00	0.00	0.47	0.00	0.00	0.47	0.00
Mole Flow	KMOL/HR	5.06	17.54	12.56	5.23	5.23	7.33	7.33	7.33	0.37	6.96	6.96	0.47	5.06	5.06	0.47	5.06	5.06	0.47	5.06
Mass Flow	KG/HR	415.21	2111.42	2111.42	1242.86	1242.86	868.56	868.56	868.56	43.43	825.14	825.14	36.33	834.78	415.21	36.33	834.78	415.21	36.33	834.78
Volume Flow	L/MIN	6.90	24.75	33.22	23.91	22.24	31348.21	11.76	11.76	0.59	11.18	11.18	0.55	6.03	6.90	0.55	6.03	7.04	0.57	6.16
Temperature	C	25.00	38.65	50.00	190.00	25.00	190.00	50.00	50.01	50.01	50.01	50.00	25.00	25.00	25.03	25.04	25.04	50.00	50.00	50.00
Pressure	BAR	1.01	1.50	1.50	0.15	1.01	0.15	1.01	1.50	1.50	1.50	1.50	1.01	1.01	1.50	1.50	1.50	1.50	1.50	1.50
Vapor Fraction		0.00	0.00	0.00	0.00	0.00	1.00	0.00	0.00	0.00	0.00	0.00	0.00	0.00	0.00	0.00	0.00	0.00	0.00	0.00
Liquid Fraction		1.00	1.00	1.00	1.00	1.00	0.00	1.00	1.00	1.00	1.00	1.00	1.00	1.00	1.00	1.00	1.00	1.00	1.00	1.00
Solid Fraction		0.00	0.00	0.00	0.00	0.00	0.00	0.00	0.00	0.00	0.00	0.00	0.00	0.00	0.00	0.00	0.00	0.00	0.00	0.00
Molar Enthalpy	KJ/MOL	72.49	-143.68	-270.54	-204.95	-282.98	-122.46	-259.91	-259.91	-259.91	-259.91	-259.91	-202.92	-202.92	72.50	-202.91	-202.91	77.29	-199.59	-199.59
Mass Enthalpy	KJ/KG	882.88	-1193.53	-1609.34	-862.99	-1191.59	-1033.02	-2192.48	-2192.41	-2192.41	-2192.41	-2192.48	-2597.03	-1229.27	882.96	-2596.95	-1229.23	941.41	-2554.40	-1209.09
Enthalpy Flow	KJ/SEC	101.83	-700.01	-943.89	-297.94	-411.38	-249.24	-528.98	-528.96	-26.45	-502.51	-502.53	-26.21	-285.05	101.84	-26.21	-285.04	108.58	-25.78	-280.37
Molar Entropy	KJ/MOL-K	-0.41	-0.43	-0.63	-0.54	-0.80	-0.18	-0.53	-0.53	-0.53	-0.53	-0.53	-0.35	-0.35	-0.41	-0.35	-0.35	-0.40	-0.34	-0.34
Mass Entropy	KJ/KG-K	-5.02	-3.54	-3.73	-2.25	-3.38	-1.48	-4.46	-4.46	-4.46	-4.46	-4.46	-4.45	-2.11	-5.02	-4.45	-2.11	-4.84	-4.32	-2.04
Molar Density	MOL/CC	0.01	0.01	0.01	0.00	0.00	0.00	0.01	0.01	0.01	0.01	0.01	0.01	0.01	0.01	0.01	0.01	0.01	0.01	0.01
Mass Density	GM/CC	1.00	1.42	1.06	0.87	0.93	0.00	1.23	1.23	1.23	1.23	1.23	1.09	2.31	1.00	1.09	2.31	0.98	1.07	2.26
Average Molecular Weight		82.11	120.38	168.11	237.48	237.48	118.55	118.55	118.55	118.55	118.55	118.55	78.14	165.07	82.11	78.14	165.07	82.11	78.14	165.07

Table A22: Aspen Plus stream table for [HMIm][Br] synthesis in dimethyl sulfoxide at 50^{o}C.

Process Specifications	Units	S1	S10	S11	S12	S13	S14	S15	S16	S17	S18	S19	S2	S3	S4	S5	S6	S7	S8	S9
From			B7	B8	B9	B10	B9	B11	B12	B13	B13	B14	B1	B1	B2	B3	B4	B5	B6	
To		B1	B8	B9	B10		B11	B12	B13		B14	B7	B2	B3	B4	B5	B6	B7	B7	B7
Substream: MIXED																				
Phase:		Liquid	Liquid	Liquid	Liquid	Liquid	Vapor	Liquid	Liquid	Liquid	Liquid	Liquid	Liquid	Liquid	Liquid	Liquid	Liquid	Liquid	Liquid	Liquid
Component Mole Flow																				
1-BH	KMOL/HR	0.00	6.50	1.53	0.00	0.00	1.52	1.52	1.52	0.08	1.44	1.44	0.00	5.06	0.00	0.00	5.06	0.00	0.00	5.06
1-MI	KMOL/HR	5.06	5.11	0.14	0.08	0.08	0.06	0.06	0.06	0.00	0.06	0.06	0.00	0.00	5.06	0.00	0.00	5.06	0.00	0.00
HMIMBR	KMOL/HR	0.00	0.96	5.94	4.93	4.93	1.01	1.01	1.01	0.05	0.96	0.96	0.00	0.00	0.00	0.00	0.00	0.00	0.00	0.00
DMSO	KMOL/HR	0.00	5.07	5.07	0.22	0.22	4.84	4.84	4.84	0.24	4.60	4.60	0.47	0.00	0.00	0.47	0.00	0.00	0.47	0.00
Mole Flow	KMOL/HR	5.06	17.64	12.67	5.23	5.23	7.43	7.43	7.43	0.37	7.06	7.06	0.47	5.06	5.06	0.47	5.06	5.06	0.47	5.06
Mass Flow	KG/HR	415.21	2126.10	2126.10	1242.10	1242.10	884.00	884.00	884.00	44.20	839.80	839.80	36.33	834.78	415.21	36.33	834.78	415.21	36.33	834.78
Volume Flow	L/MIN	6.90	25.88	34.26	23.89	22.23	31809.46	12.37	12.37	0.62	11.75	11.75	0.55	6.03	6.90	0.55	6.03	7.35	0.59	6.44
Temperature	C	25.00	87.02	100.00	190.00	25.00	190.00	100.00	100.01	100.01	100.01	100.00	25.00	25.00	25.03	25.04	25.04	100.00	100.00	100.00
Pressure	BAR	1.01	1.50	1.50	0.15	1.01	0.15	1.01	1.50	1.50	1.50	1.50	1.01	1.01	1.50	1.50	1.50	1.50	1.50	1.50
Vapor Fraction		0.00	0.00	0.00	0.00	0.00	1.00	0.00	0.00	0.00	0.00	0.00	0.00	0.00	0.00	0.00	0.00	0.00	0.00	0.00
Liquid Fraction		1.00	1.00	1.00	1.00	1.00	0.00	1.00	1.00	1.00	1.00	1.00	1.00	1.00	1.00	1.00	1.00	1.00	1.00	1.00
Solid Fraction		0.00	0.00	0.00	0.00	0.00	0.00	0.00	0.00	0.00	0.00	0.00	0.00	0.00	0.00	0.00	0.00	0.00	0.00	0.00
Molar Enthalpy	KJ/MOL	72.49	-125.89	-249.28	-204.77	-282.80	-122.38	-226.47	-226.46	-226.46	-226.46	-226.47	-202.92	-202.92	72.50	-202.91	-202.91	87.31	-192.50	-192.50
Mass Enthalpy	KJ/KG	882.88	-1044.60	-1484.99	-862.39	-1190.99	-1029.25	-1904.59	-1904.52	-1904.52	-1904.52	-1904.59	-2597.03	-1229.27	882.96	-2596.95	-1229.23	1063.37	-2463.67	-1166.14
Enthalpy Flow	KJ/SEC	101.83	-616.92	-877.01	-297.55	-410.92	-252.74	-467.68	-467.66	-23.38	-444.28	-444.30	-26.21	-285.05	101.84	-26.21	-285.04	122.64	-24.86	-270.41
Molar Entropy	KJ/MOL-K	-0.41	-0.37	-0.56	-0.54	-0.80	-0.18	-0.43	-0.43	-0.43	-0.43	-0.43	-0.35	-0.35	-0.41	-0.35	-0.35	-0.37	-0.32	-0.32
Mass Entropy	KJ/KG-K	-5.02	-3.07	-3.31	-2.25	-3.38	-1.48	-3.61	-3.61	-3.61	-3.61	-3.61	-4.45	-2.11	-5.02	-4.45	-2.11	-4.49	-4.06	-1.92
Molar Density	MOL/CC	0.01	0.01	0.01	0.00	0.00	0.00	0.01	0.01	0.01	0.01	0.01	0.01	0.01	0.01	0.01	0.01	0.01	0.01	0.01
Mass Density	GM/CC	1.00	1.37	1.03	0.87	0.93	0.00	1.19	1.19	1.19	1.19	1.19	1.09	2.31	1.00	1.09	2.31	0.94	1.02	2.16
Average Molecular Weight		82.11	120.52	167.87	237.45	237.45	118.91	118.91	118.91	118.91	118.91	118.91	78.14	165.07	82.11	78.14	165.07	82.11	78.14	165.07

Table A23: Aspen Plus stream table for [HMIm][Br] synthesis in dimethyl sulfoxide at 100^{o}C.

Appendix 3: Supplemental Data for Cellulose Solubility Trials

For all solutions solubility data is presented on a total solution basis per the equation:

$$mass\%(X)_i = \frac{mass\ (X)_i}{\sum_{i=1}^{n} mass\ (X)_i} * 100 = \frac{mass\ (X)_i}{Total\ Mass\ of\ Solution} * 100$$

Where $(X)_i$ indicates the particular component of interest and n= total components in solution.

Table A24: Pure component Kamlet-Taft parameters for select solvents of interest compared to published literature values in parentheses.

Solvent	α	β	π^*
Water	1.17 (1.17)[a]	0.17 (0.14)[a]	1.09 (1.09)[a]
Ethanol	0.86 (0.86)[a]	0.75 (0.80)[a]	0.54 (0.54)[a]
DMF	0.17 (0.14)[b]	0.64 (0.69)[b]	0.87 (0.88)[b]
DMSO	0.15 (0.10)[b]	0.69 (0.76)[b]	1.04 (0.99)[b]
DMI	0.16 (N/A)	0.79 (N/A)	0.91 (N/A)
[EMIm][DEP]	0.46 (N/A)	1.07 (N/A)	0.98 (N/A)

Ref. [1] b) Ref. [2].

Table A25: Solubility of microcrystalline cellulose in pure ionic liquid [EMIm][DEP].

Sample	Temp. [K]	Measured on a Total Solution Basis	
		[EMIm][DEP] [mass%]	Cellulose Solubility [mass%]
IL + Cellulose	313.15	90.9	9.1
IL + Cellulose	333.15	86.5	13.5
IL + Cellulose	353.15	81.7	18.3
IL + Cellulose	373.15	80.2	19.8
IL + Cellulose	393.15	80.1	19.9

Table A26: Solubility of microcrystalline cellulose in ionic liquid [EMIm][DEP]-DMSO mixtures.

		Measured on a Total Solution Basis		
Mass% DMSO Binary: Relative to IL	Temp. [K]	[EMIm][DEP] [mass%]	DMSO [mass%]	Cellulose Solubility [mass%]
00.0% DMSO	313.15	90.9	0.0	9.1
25.2% DMSO	313.15	64.2	21.6	14.2
50.0% DMSO	313.15	42.7	42.7	14.6
75.0% DMSO	313.15	23.2	69.5	7.3
85.1% DMSO	313.15	14.9	85.1	0.0
00.0% DMSO	333.15	86.5	0.0	13.5
25.1% DMSO	333.15	61.7	20.6	17.7
50.1% DMSO	333.15	42.7	42.7	14.6
75.0% DMSO	333.15	23.7	71.1	5.2
83.5% DMSO	333.15	16.5	83.5	0.0
00.0% DMSO	353.15	81.7	0.0	18.3
25.0% DMSO	353.15	61.5	20.6	17.9
50.0% DMSO	353.15	43.6	43.7	12.7
75.0% DMSO	353.15	24.1	72.4	3.5
78.1% DMSO	353.15	21.9	78.1	0.0

Table A27: Solubility of microcrystalline cellulose in ionic liquid [EMIm][DEP]-DMF mixtures.

		Measured on a Total Solution Basis		
Mass% DMF Binary: Relative to IL	Temp. [K]	[EMIm][DEP] [mass%]	DMF [mass%]	Cellulose Solubility [mass%]
00.0% DMF	313.15	90.9	0.0	9.1
25.0% DMF	313.15	66.8	22.2	11.0
50.0% DMF	313.15	44.1	44.1	11.8
75.0% DMF	313.15	24.2	72.6	3.2
78.0% DMF	313.15	22.0	78.0	0.0
00.0% DMF	333.15	86.5	0.0	13.5
25.0% DMF	333.15	62.7	20.9	16.4
50.0% DMF	333.15	44.0	44.0	12.0
73.0% DMF	333.15	27.0	73.0	0.0
00.0% DMF	353.15	81.7	0.0	18.3
25.0% DMF	353.15	62.6	21.0	16.4
50.1% DMF	353.15	45.6	45.6	8.8
69.2% DMF	353.15	30.8	69.2	0.0

Table A28: Solubility of microcrystalline cellulose in ionic liquid [EMIm][DEP]-DMI mixtures.

		Measured on a Total Solution Basis		
Mass% DMI Binary: Relative to IL	Temp. [K]	[EMIm][DEP] [mass%]	DMI [mass%]	Cellulose Solubility [mass%]
00.0% DMI	313.15	90.9	0.0	9.1
25.2% DMI	313.15	66.2	22.4	11.4
50.0% DMI	313.15	43.8	43.8	12.4
75.0% DMI	313.15	23.8	71.5	4.7
82.0% DMI	313.15	18.0	82.0	0.0
00.0% DMI	333.15	86.5	0.0	13.5
25.3% DMI	333.15	62.3	21.1	16.6
50.0% DMI	333.15	43.4	43.4	13.2
75.0% DMI	333.15	23.7	71.3	5.0
83.0% DMI	333.15	17.0	83.0	0.0
00.0% DMI	353.15	81.7	0.0	18.3
25.0% DMI	353.15	61.8	20.7	17.5
50.0% DMI	353.15	44.2	44.3	11.5
75.0% DMI	353.15	24.2	72.7	3.1
81.1% DMI	353.15	18.9	81.1	0.0

Table A29: Solubility of microcrystalline cellulose in ionic liquid [EMIm][DEP]-Alcohol mixtures.

		Measured on a Total Solution Basis		
Mass% Alcohol Binary: Relative to IL	Temp. [K]	[EMIm][DEP] [mass%]	Alcohol [mass%]	Cellulose Solubility [mass%]
0.0% MeOH	313.15	90.9	0.0	9.1
1.0% MeOH	313.15	91.4	1.0	7.6
3.0% MeOH	313.15	91.7	2.8	5.5
5.0% MeOH	313.15	92.5	4.7	2.8
0.0% EtOH	313.15	90.9	0.0	9.1
1.1% EtOH	313.15	90.7	1.0	8.3
3.0% EtOH	313.15	90.2	2.9	6.9
5.0% EtOH	313.15	89.5	4.9	5.6

Table A30: Solubility of microcrystalline cellulose in ionic liquid [EMIm][DEP]-H_2O mixtures.

		Measured on a Total Solution Basis		
Mass% H_2O Binary: Relative to IL	Temp. [K]	[EMIm][DEP] [mass%]	H_2O [mass%]	Cellulose Solubility [mass%]
0.0% H_2O	313.15	90.9	0.0	9.1
1.0% H_2O	313.15	92.4	1.0	6.6
3.0% H_2O	313.15	96.5	3.0	0.5
5.0% H_2O	313.15	95.0	5.0	0.0
0.0% H_2O	333.15	86.5	0.0	13.5
1.0% H_2O	333.15	87.1	0.9	12.0
3.0% H_2O	333.15	87.7	2.7	9.6
5.0% H_2O	333.15	90.0	4.7	5.3
0.0% H_2O	353.15	81.7	0.0	18.3
1.0% H_2O	353.15	82.4	0.9	16.7
3.0% H_2O	353.15	84.6	2.7	12.7
5.0% H_2O	353.15	89.0	4.7	6.3

Table A31: Solubility of microcrystalline cellulose in ionic liquid [EMIm][DEP]-DMSO-H_2O mixtures.

Mass% H_2O and		Measured on a Total Solution Basis			
DMSO Ternary Relative to IL	Temp. [K]	[EMIm][DEP] [mass%]	H_2O [mass%]	DMSO [mass%]	Cellulose Solubility [mass%]
1% H_2O, 0% DMSO	313.15	92.4	1.0	0.0	6.6
1% H_2O, 25% DMSO	313.15	64.9	0.9	22.1	12.1
1% H_2O, 50% DMSO	313.15	43.2	0.9	43.8	12.1
3% H_2O, 0% DMSO	313.15	96.5	3.0	0.0	0.5
3% H_2O, 25% DMSO	313.15	65.2	2.7	21.8	10.3
3% H_2O, 50% DMSO	313.15	43.7	2.8	46.5	7.0
5% H_2O, 0% DMSO	313.15	95.0	5.0	0.0	0.0
5% H_2O, 25% DMSO	313.15	66.8	4.8	23.8	4.6
5% H_2O, 50% DMSO	313.15	44.8	5.1	50.1	0.0

Table A32: IL [DEP] Anion: Cellulose –OH ratio and adjusted ratio for mixed IL-DMSO systems.

Mass% DMSO Relative to IL	Temp [K]	Cellulose Solubility [Mass%]	Anion: Cellulose -OH Ratio	Maximum Theoretical Solubility[a]	% of Maximum Theoretical Solubility
00.0% DMSO	313.15	9.1	2.0	24.3	37.4
25.2% DMSO	313.15	14.2	0.9	22.6	62.8
50.0% DMSO	313.15	14.6	0.6	19.9	73.3
75.0% DMSO	313.15	7.3	0.7	14.5	50.3
00.0% DMSO	333.15	13.5	1.3	24.3	55.6
25.1% DMSO	333.15	17.7	0.7	19.4	91.2
50.1% DMSO	333.15	14.6	0.6	13.8	105.8
75.0% DMSO	333.15	5.2	0.9	7.4	70.3
00.0% DMSO	353.15	18.3	0.9	24.3	75.3
25.0% DMSO	353.15	17.9	0.7	19.9	90.0
50.0% DMSO	353.15	12.7	0.7	13.8	92.0
75.0% DMSO	353.15	3.5	1.4	7.4	47.3

[a)] Based on 33% 2:1 Interactions, with an average of 2.54 hydrogen bonds per anhydroglucose unit (AGU).

Table A33: IL [DEP] Anion: Cellulose –OH ratio and adjusted ratio for mixed IL-DMF systems.

Mass% DMF Relative to IL	Temp [K]	Cellulose Solubility [Mass%]	Anion: Cellulose -OH Ratio	Maximum Theoretical Solubility[a]	% of Maximum Theoretical Solubility
00.0% DMF	313.15	9.1	2.0	24.3	37.4
25.0% DMF	313.15	11.0	1.2	22.7	48.5
50.0% DMF	313.15	11.8	0.8	20.1	58.7
75.0% DMF	313.15	3.2	1.5	14.9	21.5
00.0% DMF	333.15	13.5	1.3	24.3	55.6
25.0% DMF	333.15	16.4	0.8	19.4	84.5
50.0% DMF	333.15	12.0	0.7	13.8	87.0
00.0% DMF	353.15	18.3	0.9	24.3	75.3
25.0% DMF	353.15	16.4	0.8	19.4	84.5
50.1% DMF	353.15	8.8	1.1	13.8	63.8

[a)] Based on 33% 2:1 Interactions, with an average of 2.54 hydrogen bonds per anhydroglucose unit (AGU).

Table A34: IL [DEP] Anion: Cellulose –OH ratio and adjusted ratio for mixed IL-DMI systems.

Mass% DMSO Relative to IL	Temp [K]	Cellulose Solubility [Mass%]	Anion: Cellulose -OH Ratio	Maximum Theoretical Solubility[a]	% of Maximum Theoretical Solubility
00.0% DMI	313.15	9.1	2.0	24.3	37.4
25.2% DMI	313.15	11.4	1.2	21.9	52.1
50.0% DMI	313.15	12.4	0.7	18.3	67.8
75.0% DMI	313.15	4.7	1.0	12.3	38.2
00.0% DMI	333.15	13.5	1.3	24.3	55.6
25.3% DMI	333.15	16.6	0.8	19.3	86.0
50.0% DMI	333.15	13.2	0.7	13.8	95.7
75.0% DMI	333.15	5.0	1.0	7.4	67.6
00.0% DMI	353.15	18.3	0.9	24.3	75.3
25.0% DMI	353.15	17.5	0.7	19.4	90.2
50.0% DMI	353.15	11.5	0.8	13.8	83.3
75.0% DMI	353.15	3.1	1.6	7.4	41.9

[a)] Based on 33% 2:1 Interactions, with an average of 2.54 hydrogen bonds per anhydroglucose unit (AGU).

Table A35: IL [DEP] Anion: Cellulose –OH ratio and adjusted ratio for mixed IL-Alcohol systems.

Mass% Alcohol Binary: Relative to IL	Temp [K]	Anion: Cellulose -OH Ratio (single-interaction)	Anion: Antisolvent -OH Ratio
0.0% MeOH	313.15	2.0	N/A
1.0% MeOH	313.15	2.5	12.0
3.0% MeOH	313.15	3.5	3.9
5.0% MeOH	313.15	6.8	2.3
0.0% EtOH	313.15	2.0	N/A
1.1% EtOH	313.15	2.4	17.3
3.0% EtOH	313.15	2.7	5.6
5.0% EtOH	313.15	3.3	3.3

Table A36: IL [DEP] Anion: Cellulose –OH ratio and adjusted ratio for mixed IL-H_2O systems.

Mass% H_2O Binary: Relative to IL	Temp [K]	Anion: Cellulose -OH Ratio (single-interaction)	Anion: Antisolvent -OH Ratio
0.0% H_2O	313.15	2.0	N/A
1.0% H_2O	313.15	2.9	3.4
3.0% H_2O	313.15	38.2	1.1
0.0% H_2O	333.15	1.3	N/A
1.0% H_2O	333.15	1.5	3.4
3.0% H_2O	333.15	1.9	1.1
5.0% H_2O	333.15	3.5	0.6
0.0% H_2O	353.15	0.9	N/A
1.0% H_2O	353.15	1.0	3.4
3.0% H_2O	353.15	1.4	1.1
5.0% H_2O	353.15	2.9	0.6

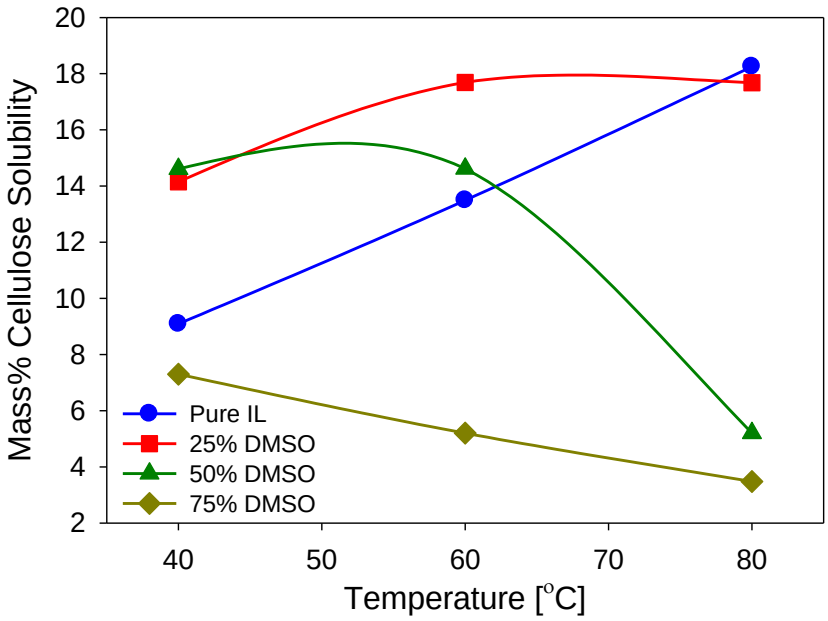

Figure A2: Effect of temperature on cellulose solubility in IL/DMSO mixtures of varying capacity. Lines are smoothed data.

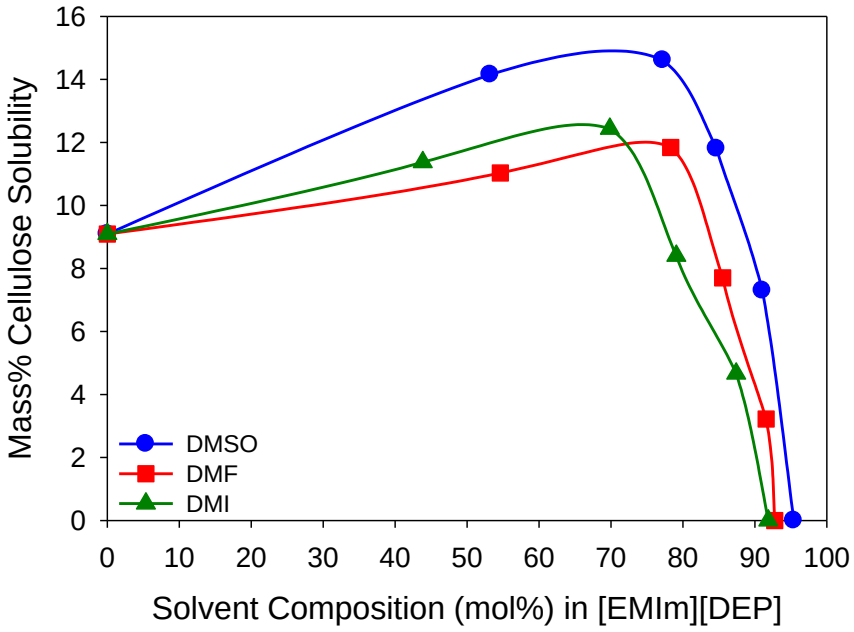

Figure A3: Cellulose solubility in [EMIm][DEP]-cosolvent mixtures at 40°C where cosolvent loading is represented on a molar basis. Lines are smoothed data.

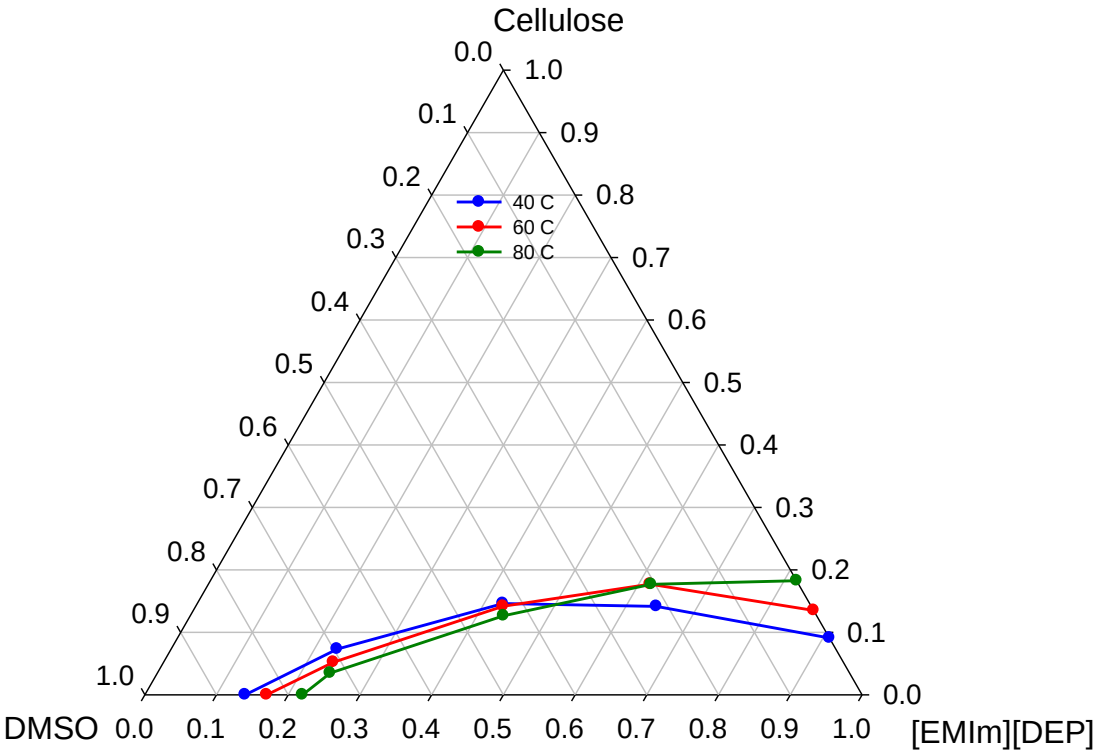

Figure A4: Ternary diagram of cellulose solubility in [EMIm][DEP]-DMSO mixtures. Composition data represented on a mass fraction basis.

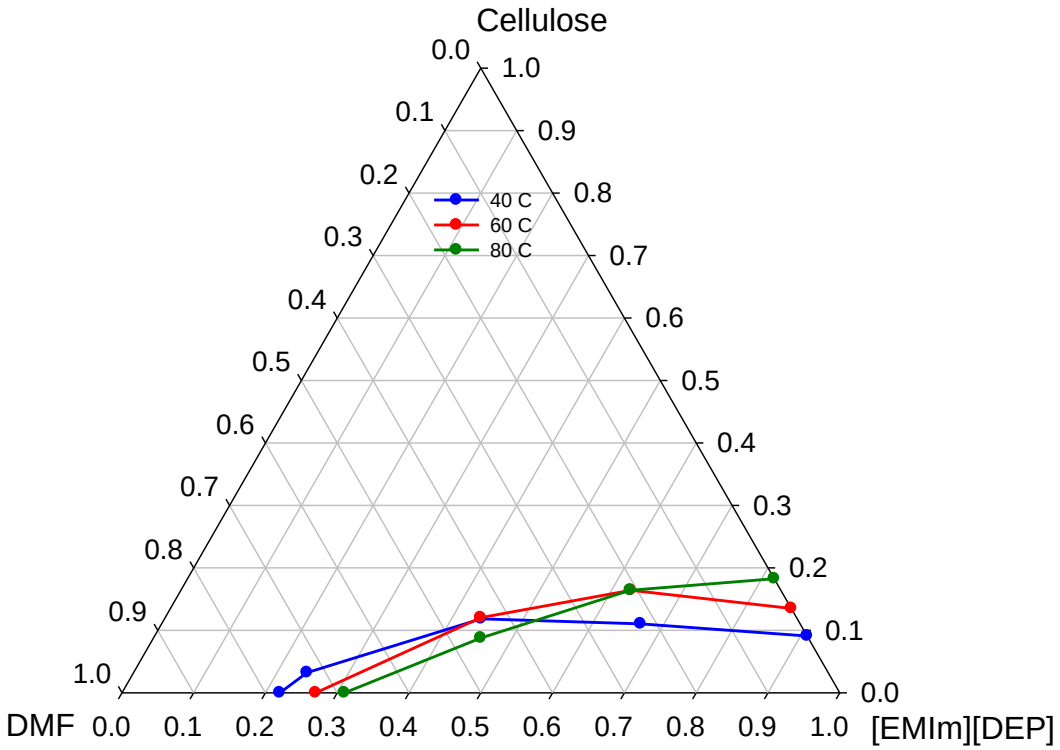

Figure A5: Ternary diagram of cellulose solubility in [EMIm][DEP]-DMF mixtures. Composition data represented on a mass fraction basis.

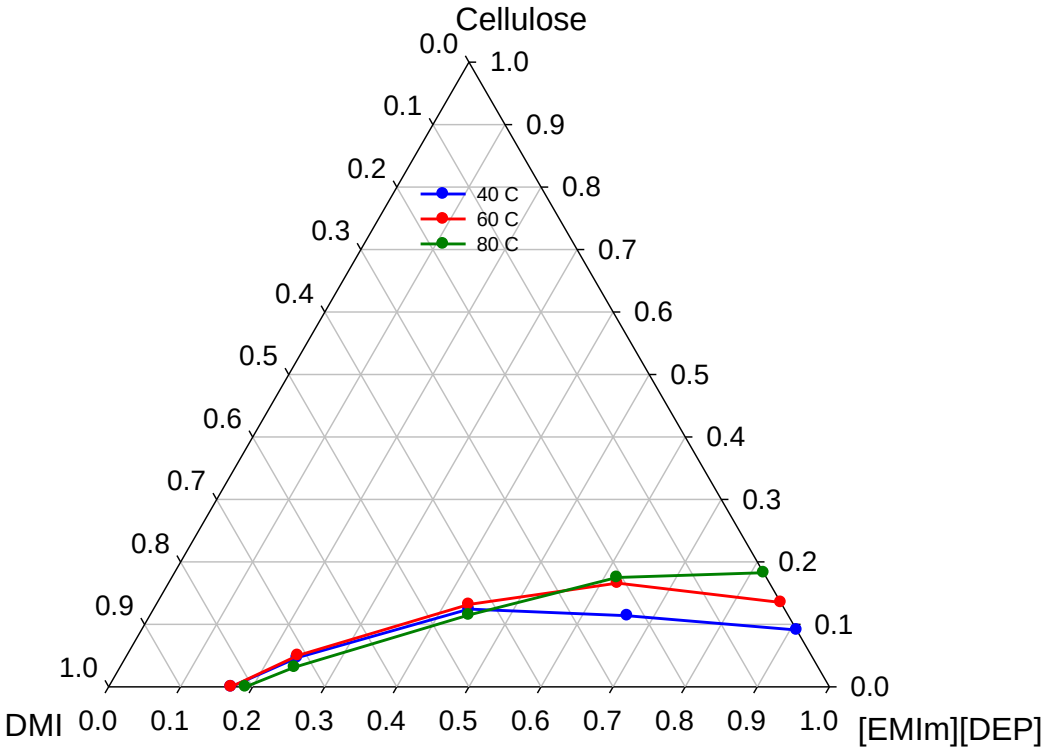

Figure A6: Ternary diagram of cellulose solubility in [EMIm][DEP]-DMI mixtures. Composition data represented on a mass fraction basis.

Appendix 4: Experimental Data Tables for CO_2 Precipitation of Cellulosic Biomass

Table A37: Separation and VLE parameters for mixed [EMIm][DEP]-dimethyl sulfoxide (DMSO) systems. (5 % cellulose loading – total solution basis)

Cosolvent (mass%)	Temp. (^oC)	Separation Pressure (bar)	CO_2 Solubility (X_{CO2})	Volume Expansion (%ΔV)	IL Molarity (mol IL/L)
25% DMSO	25	54	0.5342	28.57	2.18
	40	----	----	----	----
50% DMSO	25	53	0.5472	41.85	1.37
	40	----	----	----	----

"—" indicates that precipitation did not occur at CO_2 pressures up to 250 bar. "N/A" indicates trial not attempted.

Table A38: Separation and VLE parameters for mixed [EMIm][DEP]- dimethylformamide (DMF) systems. (5 % cellulose loading – total solution basis)

Cosolvent (mass%)	Temp. (^oC)	Separation Pressure (bar)	CO_2 Solubility (X_{CO2})	Volume Expansion (%ΔV)	IL Molarity (mol IL/L)
25% DMF	25	32	0.3980	12.07	2.32
	40	49	0.4535	18.27	2.29
50% DMF	25	26	0.3468	16.44	1.53
	40	49	0.4630	28.99	1.40

"—" indicates that precipitation did not occur at CO_2 pressures up to 250 bar. "N/A" indicates trial not attempted.

Table A39: Separation and VLE parameters for mixed [EMIm][DEP]-dimethyl imidazolidinone (DMI) systems. (5 % cellulose loading – total solution basis)

Cosolvent (mass%)	Temp. (^oC)	Separation Pressure (bar)	CO_2 Solubility (X_{CO2})	Volume Expansion (%ΔV)	IL Molarity (mol IL/L)
25% DMI	25	53	0.5565	25.26	2.28
	40	68	0.5839	21.24	2.28
50% DMI	25	40	0.5030	24.95	1.50
	40	57	0.5750	25.92	1.44

"—" indicates that precipitation did not occur at CO_2 pressures up to 250 bar. "N/A" indicates trial not attempted.

Table A40: Separation and VLE parameters for mixed [EMIm][DEP]-Acetone systems. (5 % cellulose loading – total solution basis)

Cosolvent (mass%)	Temp. (^oC)	Separation Pressure (bar)	CO_2 Solubility (X_{CO2})	Volume Expansion (%ΔV)	IL Molarity (mol IL/L)
25% Acetone	25	34	0.4351	23.53	2.00
	40	----	----	----	----
50% Acetone	25	N/A	N/A	N/A	N/A
	40	N/A	N/A	N/A	N/A

"—" indicates that precipitation did not occur at CO_2 pressures up to 250 bar. "N/A" indicates trial not attempted.

Table A41: Separation and VLE parameters for mixed [EMIm][DEP]-Acetonitrile (ACN) systems. (5 % cellulose loading – total solution basis)

Cosolvent (mass%)	Temp. (^oC)	Separation Pressure (bar)	CO_2 Solubility (X_{CO2})	Volume Expansion (%ΔV)	IL Molarity (mol IL/L)
25% ACN	25	43	0.4526	26.74	2.00
	40	62	0.5087	32.55	2.03
50% ACN	25	----	----	----	----
	40	N/A	N/A	N/A	N/A

"—" indicates that precipitation did not occur at CO_2 pressures up to 250 bar. "N/A" indicates trial not attempted.

Table A42: CO_2 Solubility in pure [EMIm][DEP] at 25^oC and associated phase equilibrium parameters.

Temperature (^oC)	Pressure (bar)	CO_2 Solubility (X_{CO2})	Molar Volume (cm^3/mol)	Volume Expansion (100*ΔV/V)	IL Molarity (mol IL/L)
25.01	9.54	0.0856	238.35	1.21	3.84
25.01	19.19	0.2396	200.22	2.24	3.80
25.02	29.61	0.3744	172.31	6.95	3.63
25.02	39.50	0.4652	151.82	10.22	3.52
25.04	49.94	0.5365	134.03	12.29	3.46
25.04	59.83	0.6008	121.70	18.37	3.28

Table A43: CO_2 Solubility in pure [EMIm][DEP] at 40°C and associated phase equilibrium parameters.

Temperature (°C)	Pressure (bar)	CO_2 Solubility (X_{CO2})	Molar Volume (cm^3/mol)	Volume Expansion (100*ΔV/V)	IL Molarity (mol IL/L)
40.00	9.42	0.1320	214.79	0.86	4.04
40.00	19.30	0.2384	192.23	2.88	3.96
40.00	29.43	0.3147	178.63	6.24	3.84
40.00	39.25	0.4014	162.21	10.46	3.69
40.00	49.68	0.4764	145.21	13.03	3.61
40.01	59.82	0.5268	135.13	16.39	3.50
40.00	80.04	0.6297	109.96	21.04	3.37

Table A44: CO_2 Solubility in pure [EMIm][DEP] at 60°C and associated phase equilibrium parameters.

Temperature (°C)	Pressure (bar)	CO_2 Solubility (X_{CO2})	Molar Volume (cm^3/mol)	Volume Expansion (100*ΔV/V)	IL Molarity (mol IL/L)
60.01	9.63	0.1036	230.23	0.87	3.89
60.01	19.29	0.2047	207.45	2.44	3.83
60.01	29.52	0.2995	185.63	4.07	3.77
60.00	39.82	0.3433	176.91	5.81	3.71
60.00	50.00	0.3994	165.12	7.98	3.64
60.00	59.86	0.4503	153.11	9.39	3.59
60.00	79.77	0.5452	130.71	12.87	3.48
60.00	99.96	0.6343	107.82	15.80	3.39

Table A45: CO_2 Solubility in an [EMIm][DEP]-25 mass% Acetone mixture at 25°C and associated phase equilibrium parameters.

Temperature (°C)	Pressure (bar)	CO_2 Solubility (X_{CO2})	Molar Volume (cm^3/mol)	Volume Expansion (100*ΔV/V)	IL Molarity (mol IL/L)
25.00	4.64	0.0850	140.36	1.77	2.59
25.00	9.52	0.1515	133.91	4.71	2.52
25.00	14.61	0.1958	130.19	7.39	2.46
25.00	19.81	0.2480	125.00	10.27	2.39
25.00	24.82	0.3076	118.66	13.69	2.32
25.00	29.67	0.3631	112.78	17.48	2.24
25.00	34.85	0.4351	105.18	23.53	2.14

Table A46: CO_2 Solubility in an [EMIm][DEP]-50 mass% Acetone mixture at 25°C and associated phase equilibrium parameters.

Temperature (°C)	Pressure (bar)	CO_2 Solubility (X_{CO2})	Molar Volume (cm^3/mol)	Volume Expansion (100*ΔV/V)	IL Molarity (mol IL/L)
25.00	7.39	0.1086	100.16	2.79	1.61
25.01	10.14	0.1566	97.34	5.58	1.57
25.00	19.33	0.2994	88.36	15.37	1.43

Table A47: CO_2 Solubility in an [EMIm][DEP]-25 mass% Acetone mixture at 40°C and associated phase equilibrium parameters.

Temperature (°C)	Pressure (bar)	CO_2 Solubility (X_{CO2})	Molar Volume (cm^3/mol)	Volume Expansion (100*ΔV/V)	IL Molarity (mol IL/L)
39.99	9.70	0.1137	135.13	3.14	2.61
39.99	19.81	0.2261	123.09	7.59	2.50
39.99	29.97	0.3248	112.33	12.55	2.39
39.99	39.90	0.4151	102.96	19.08	2.26

Table A48: CO_2 Solubility in an [EMIm][DEP]-50 mass% Acetone mixture at 40°C and associated phase equilibrium parameters.

Temperature (°C)	Pressure (bar)	CO_2 Solubility (X_{CO2})	Molar Volume (cm^3/mol)	Volume Expansion (100*ΔV/V)	IL Molarity (mol IL/L)
40.00	6.93	0.0804	104.02	4.18	1.60
40.00	13.43	0.1557	98.51	7.46	1.55
40.00	22.68	0.2866	88.97	14.86	1.45
40.00	25.06	0.3082	87.74	16.80	1.43

Table A49: CO_2 Solubility in an [EMIm][DEP]-25 mass% Acetonitrile mixture at 25°C and associated phase equilibrium parameters.

Temperature (°C)	Pressure (bar)	CO_2 Solubility (X_{CO2})	Molar Volume (cm^3/mol)	Volume Expansion (100*ΔV/V)	IL Molarity (mol IL/L)
25.01	9.61	0.1091	116.23	3.84	2.44
25.01	19.77	0.2233	105.93	8.55	2.33
25.01	29.84	0.3291	97.30	15.44	2.19
25.01	39.96	0.4272	88.61	23.13	2.05
25.00	42.95	0.4526	87.16	26.74	2.00
25.01	49.96	0.5241	80.51	34.66	1.88

Table A50: CO_2 Solubility in an [EMIm][DEP]-50 mass% Acetonitrile mixture at 25°C and associated phase equilibrium parameters.

Temperature (°C)	Pressure (bar)	CO_2 Solubility (X_{CO2})	Molar Volume (cm^3/mol)	Volume Expansion (100*ΔV/V)	IL Molarity (mol IL/L)
25.00	7.06	0.0712	79.47	3.67	1.57
25.01	12.33	0.1366	76.88	7.91	1.51
25.01	18.42	0.2116	74.26	14.14	1.43
25.02	22.53	0.2594	72.69	18.93	1.37
25.01	27.85	0.3270	70.07	26.16	1.29
25.02	33.91	0.4033	67.09	36.25	1.20
25.02	39.85	0.4818	64.04	49.76	1.09

Table A51: CO_2 Solubility in an [EMIm][DEP]-25 mass% Acetonitrile mixture at 40°C and associated phase equilibrium parameters.

Temperature (°C)	Pressure (bar)	CO_2 Solubility (X_{CO2})	Molar Volume (cm^3/mol)	Volume Expansion (100*ΔV/V)	IL Molarity (mol IL/L)
40.00	10.03	0.0870	110.17	2.25	2.63
40.00	20.06	0.1822	102.66	6.38	2.53
39.99	29.82	0.2654	96.18	10.95	2.43
40.00	40.14	0.3451	89.90	16.34	2.32
40.00	49.88	0.4185	84.26	22.78	2.19
40.00	59.72	0.4926	78.09	30.42	2.07
40.00	61.95	0.5087	76.85	32.55	2.03

Table A52: CO_2 Solubility in an [EMIm][DEP]-50 mass% Acetonitrile mixture at 40°C and associated phase equilibrium parameters.

Temperature (°C)	Pressure (bar)	CO_2 Solubility (X_{CO2})	Molar Volume (cm^3/mol)	Volume Expansion (100*ΔV/V)	IL Molarity (mol IL/L)
40.00	9.94	0.0755	77.57	3.89	1.60
40.00	19.03	0.1632	74.82	10.71	1.50
40.00	31.94	0.2852	70.06	21.37	1.37
40.00	39.27	0.3492	67.72	28.85	1.29
40.00	49.65	0.4452	64.08	43.04	1.16
40.00	59.71	0.5479	60.07	64.53	1.01

Table A53: CO_2 Solubility in an [EMIm][DEP]-25 mass% Dimethyl Sulfoxide mixture at 25°C and associated phase equilibrium parameters.

Temperature (°C)	Pressure (bar)	CO_2 Solubility (X_{CO2})	Molar Volume (cm^3/mol)	Volume Expansion (100*ΔV/V)	IL Molarity (mol IL/L)
24.99	6.63	0.0311	165.03	2.04	2.75
25.00	10.03	0.0567	164.18	4.27	2.69
25.00	14.76	0.1204	156.38	6.50	2.64
25.00	19.94	0.1936	145.67	8.21	2.60
25.00	29.8	0.3091	128.96	11.82	2.51
25.02	39.96	0.4123	115.63	17.86	2.38
25.03	49.78	0.5000	103.85	24.43	2.26
25.03	53.95	0.5342	99.97	28.57	2.18
25.03	59.81	0.5895	92.82	35.47	2.07

Table A54: CO_2 Solubility in an [EMIm][DEP]-50 mass% Dimethyl Sulfoxide mixture at 25°C and associated phase equilibrium parameters.

Temperature (°C)	Pressure (bar)	CO_2 Solubility (X_{CO2})	Molar Volume (cm^3/mol)	Volume Expansion (100*ΔV/V)	IL Molarity (mol IL/L)
25.00	9.57	0.1168	107.20	3.75	1.87
25.01	19.41	0.2213	99.26	8.95	1.78
25.02	29.36	0.3191	93.22	17.02	1.66
25.03	39.71	0.4204	84.74	24.96	1.55
25.04	49.12	0.5106	77.94	36.14	1.43
25.04	52.84	0.5472	75.14	41.85	1.37
25.05	58.35	0.6116	70.17	54.43	1.26

Table A55: CO_2 Solubility in an [EMIm][DEP]-25 mass% Dimethyl Sulfoxide mixture at 40°C and associated phase equilibrium parameters.

Temperature (°C)	Pressure (bar)	CO_2 Solubility (X_{CO2})	Molar Volume (cm^3/mol)	Volume Expansion (100*ΔV/V)	IL Molarity (mol IL/L)
40.00	6.57	0.0507	159.76	1.39	2.79
40.00	11.52	0.1032	153.76	3.29	2.73
40.00	19.72	0.1841	142.62	5.32	2.68
40.00	30.06	0.2757	130.57	8.61	2.60
40.00	41.76	0.3673	118.68	13.00	2.50
40.00	50.55	0.4282	110.55	16.47	2.42
40.00	60.03	0.4900	102.36	20.92	2.34

Table A56: CO_2 Solubility in an [EMIm][DEP]-50 mass% Dimethyl Sulfoxide mixture at 40°C and associated phase equilibrium parameters.

Temperature (°C)	Pressure (bar)	CO_2 Solubility (X_{CO2})	Molar Volume (cm^3/mol)	Volume Expansion (100*ΔV/V)	IL Molarity (mol IL/L)
40.00	7.37	0.0673	111.47	0.97	1.90
40.00	11.98	0.1155	107.47	2.65	1.87
40.00	19.63	0.1830	101.79	5.25	1.82
40.00	29.66	0.2588	95.76	9.15	1.76
40.00	39.69	0.3366	90.22	14.88	1.67
40.00	49.41	0.4008	85.13	20.03	1.60

Table A57: CO_2 Solubility in an [EMIm][DEP]-25 mass% Dimethylformamide mixture at 25°C and associated phase equilibrium parameters.

Temperature (°C)	Pressure (bar)	CO_2 Solubility (X_{CO2})	Molar Volume (cm^3/mol)	Volume Expansion (100*ΔV/V)	IL Molarity (mol IL/L)
25.00	9.63	0.1421	151.63	1.65	2.56
25.00	19.25	0.2691	134.47	5.81	2.46
25.00	29.68	0.3809	119.43	10.95	2.35
25.00	31.88	0.3980	117.31	12.07	2.32
25.00	39.90	0.4682	107.18	15.90	2.25
25.00	49.66	0.5512	96.89	24.15	2.10

Table A58: CO_2 Solubility in an [EMIm][DEP]-50 mass% Dimethylformamide mixture at 25°C and associated phase equilibrium parameters.

Temperature (°C)	Pressure (bar)	CO_2 Solubility (X_{CO2})	Molar Volume (cm^3/mol)	Volume Expansion (100*ΔV/V)	IL Molarity (mol IL/L)
25.00	9.7	0.1413	109.47	4.95	1.70
25.00	14.42	0.2063	103.35	7.20	1.66
25.00	19.71	0.2745	97.96	11.16	1.60
25.01	25.87	0.3468	92.40	16.44	1.53
25.00	29.79	0.3935	88.84	20.60	1.48
25.01	39.81	0.5070	81.00	35.26	1.32
25.02	49.33	0.6244	71.84	57.44	1.13

Table A59: CO_2 Solubility in an [EMIm][DEP]-25 mass% Dimethylformamide mixture at 40°C and associated phase equilibrium parameters.

Temperature (°C)	Pressure (bar)	CO_2 Solubility (X_{CO2})	Molar Volume (cm^3/mol)	Volume Expansion (100*ΔV/V)	IL Molarity (mol IL/L)
40.00	9.69	0.1143	151.24	2.28	2.65
40.00	19.64	0.2151	138.13	5.42	2.57
40.00	29.39	0.3046	126.46	8.92	2.49
40.00	39.85	0.3863	116.34	13.55	2.39
40.00	48.95	0.4488	108.35	17.74	2.30
40.00	49.95	0.4535	107.90	18.27	2.29
40.00	59.77	0.5171	99.55	23.48	2.20

Table A60: CO_2 Solubility in an [EMIm][DEP]-50 mass% Dimethylformamide mixture at 40°C and associated phase equilibrium parameters.

Temperature (°C)	Pressure (bar)	CO_2 Solubility (X_{CO2})	Molar Volume (cm^3/mol)	Volume Expansion (100*ΔV/V)	IL Molarity (mol IL/L)
40.00	9.84	0.0971	111.31	3.06	1.76
40.00	19.62	0.1988	103.29	7.78	1.68
40.00	30.12	0.2971	95.89	14.05	1.59
40.00	39.84	0.3835	88.88	20.52	1.50
40.00	49.21	0.4630	82.87	28.99	1.40
40.00	61.53	0.5644	75.11	44.14	1.26

Table A61: CO_2 Solubility in an [EMIm][DEP]-25 mass% Dimethyl Imidazolidinone mixture at 25°C and associated phase equilibrium parameters.

Temperature (°C)	Pressure (bar)	CO_2 Solubility (X_{CO2})	Molar Volume (cm^3/mol)	Volume Expansion (100*ΔV/V)	IL Molarity (mol IL/L)
25.00	9.94	0.1121	178.35	1.64	2.81
25.00	19.96	0.2415	158.16	5.51	2.71
25.02	29.94	0.3574	140.83	10.90	2.58
25.02	39.95	0.4495	126.64	16.41	2.45
25.00	49.99	0.5355	113.32	23.44	2.32
25.00	53.00	0.5565	109.80	25.26	2.28
25.00	59.98	0.6173	100.45	32.81	2.15

Table A62: CO_2 Solubility in an [EMIm][DEP]-50 mass% Dimethyl Imidazolidinone mixture at 25°C and associated phase equilibrium parameters.

Temperature (°C)	Pressure (bar)	CO_2 Solubility (X_{CO2})	Molar Volume (cm^3/mol)	Volume Expansion (100*ΔV/V)	IL Molarity (mol IL/L)
25.00	9.30	0.1402	140.55	1.84	1.85
25.01	19.67	0.2763	126.19	8.63	1.73
25.00	29.39	0.3827	113.63	14.69	1.64
25.00	41.54	0.5030	99.68	24.95	1.50
25.01	49.69	0.5815	90.72	35.06	1.39

Table A63: CO_2 Solubility in an [EMIm][DEP]-25 mass% Dimethyl Imidazolidinone mixture at 40°C and associated phase equilibrium parameters.

Temperature (°C)	Pressure (bar)	CO_2 Solubility (X_{CO2})	Molar Volume (cm^3/mol)	Volume Expansion (100*ΔV/V)	IL Molarity (mol IL/L)
40.00	9.59	0.1210	181.83	1.33	2.73
40.00	19.64	0.2257	163.85	3.65	2.67
40.00	29.77	0.2998	152.72	6.83	2.59
40.00	39.90	0.3784	139.60	10.01	2.51
40.00	49.79	0.4526	126.82	13.49	2.44
40.00	59.87	0.5191	115.75	17.89	2.35
40.00	69.96	0.5839	103.00	21.24	2.28
40.00	79.73	0.6659	86.14	26.28	2.19

Table A64: CO_2 Solubility in an [EMIm][DEP]-50 mass% Dimethyl Imidazolidinone mixture at 40°C and associated phase equilibrium parameters.

Temperature (°C)	Pressure (bar)	CO_2 Solubility (X_{CO2})	Molar Volume (cm^3/mol)	Volume Expansion (100*ΔV/V)	IL Molarity (mol IL/L)
40.00	9.79	0.1292	184.71	2.45	1.78
40.00	19.67	0.2508	164.13	5.81	1.72
39.99	29.72	0.3625	145.67	10.37	1.65
39.99	39.79	0.4556	129.47	14.87	1.58
40.00	49.88	0.5275	118.11	20.73	1.51
40.00	56.98	0.5750	110.80	25.92	1.44
40.00	59.92	0.5916	108.07	27.80	1.42

Table A65: CO_2 Solubility in an [EMIm][DEP]-50 mass% Dimethyl Imidazolidinone-5 mass% cellulose mixture at 25°C and associated phase equilibrium parameters.

Temperature (°C)	Pressure (bar)	CO_2 Solubility (X_{CO2})	Molar Volume (cm^3/mol)	Volume Expansion (100*ΔV/V)	IL Molarity (mol IL/L)
40.00	9.18	0.0669	114.25	2.68	1.67
40.00	19.16	0.1564	106.84	6.21	1.61
40.00	29.00	0.2397	99.60	9.86	1.56
40.00	41.12	0.3320	91.92	15.39	1.49
40.00	49.77	0.3927	86.66	19.65	1.43
40.00	57.56	0.4434	82.81	24.76	1.37

References:

1. Jessop, P.G., et al., *Solvatochromic parameters for solvents of interest in green chemistry.* Green Chemistry, 2012. **14**(5): p. 1245-1259.
2. Ali, A., et al., *Solvatochromic Absorbance Probe Behavior within Mixtures of the Ionic Liquid 1-Butyl-3-methylimidazolium Bis(trifluoromethylsulfonyl)imide plus Molecular Organic Solvents.* Journal of Chemical and Engineering Data, 2014. **59**(6): p. 1755-1765.